MODERN TOOLS FOR TIME-RESOLVED LUMINESCENCE BIOSENSING AND IMAGING

EDITED BY: Yiqing Lu, Gerard Marriott and Klaus Suhling
PUBLISHED IN: Frontiers in Physics, Frontiers in Chemistry and Frontiers in Molecular Biosciences

frontiers Research Topics

ISSN 1664-8714
ISBN 978-2-88971-252-6
DOI 10.3389/978-2-88971-252-6

About Frontiers

Frontiers is more than just an open-access publisher of scholarly articles: it is a pioneering approach to the world of academia, radically improving the way scholarly research is managed. The grand vision of Frontiers is a world where all people have an equal opportunity to seek, share and generate knowledge. Frontiers provides immediate and permanent online open access to all its publications, but this alone is not enough to realize our grand goals.

Frontiers Journal Series

The Frontiers Journal Series is a multi-tier and interdisciplinary set of open-access, online journals, promising a paradigm shift from the current review, selection and dissemination processes in academic publishing. All Frontiers journals are driven by researchers for researchers; therefore, they constitute a service to the scholarly community. At the same time, the Frontiers Journal Series operates on a revolutionary invention, the tiered publishing system, initially addressing specific communities of scholars, and gradually climbing up to broader public understanding, thus serving the interests of the lay society, too.

Dedication to Quality

Each Frontiers article is a landmark of the highest quality, thanks to genuinely collaborative interactions between authors and review editors, who include some of the world's best academicians. Research must be certified by peers before entering a stream of knowledge that may eventually reach the public - and shape society; therefore, Frontiers only applies the most rigorous and unbiased reviews.
Frontiers revolutionizes research publishing by freely delivering the most outstanding research, evaluated with no bias from both the academic and social point of view. By applying the most advanced information technologies, Frontiers is catapulting scholarly publishing into a new generation.

What are Frontiers Research Topics?

Frontiers Research Topics are very popular trademarks of the Frontiers Journals Series: they are collections of at least ten articles, all centered on a particular subject. With their unique mix of varied contributions from Original Research to Review Articles, Frontiers Research Topics unify the most influential researchers, the latest key findings and historical advances in a hot research area! Find out more on how to host your own Frontiers Research Topic or contribute to one as an author by contacting the Frontiers Editorial Office: frontiersin.org/about/contact

MODERN TOOLS FOR TIME-RESOLVED LUMINESCENCE BIOSENSING AND IMAGING

Topic Editors:
Yiqing Lu, Macquarie University, Australia
Gerard Marriott, University of California, United States
Klaus Suhling, King's College London, United Kingdom

Citation: Lu, Y., Marriott, G., Suhling, K., eds. (2021). Modern Tools for Time-Resolved Luminescence Biosensing and Imaging. Lausanne: Frontiers Media SA. doi: 10.3389/978-2-88971-252-6

Table of Contents

frontiers in Physics

EDITORIAL
published: 29 June 2021
doi: 10.3389/fphy.2021.725234

Editorial: Modern Tools for Time-Resolved Luminescence Biosensing and Imaging

Yiqing Lu[1]*, *Gerard Marriott*[2]* and *Klaus Suhling*[3]*

[1]School of Engineering, Macquarie University, Sydney, NSW, Australia, [2]Department of Bioengineering, University of California Berkeley, Berkeley, CA, United States, [3]Department of Physics, King's College London, London, United Kingdom

Keywords: time-resolved luminescence, luminescence lifetime, exponential decay, fluorescence lifetime imaging (FLIM), Förster resonance energy transfer (FRET), time-correlated single photon counting (TCSPC)

Editorial on the Research Topic

Modern Tools for Time-Resolved Luminescence Biosensing and Imaging

The time evolution of luminescence decay, often described by the parameter of luminescence lifetime assuming first-order kinetics, is among the key characteristics of a luminescence substance. This makes time-resolved luminescence measurement a powerful tool for identifying substances of interest, especially in biological samples where differentiation based on luminescence colors may be inadequate or ineffective [1–3]. Moreover, for quantitative luminescence intensity measurements, the concentration in biological samples is hard to control, and typically needs a calibration, whereas the luminescence decay is largely independent of the luminophore concentration. The kinetics of luminescence decay is also influenced by the environment, enabling various sensing applications of time-resolved luminescence in biology and medicine [4, 5].

In this multidisciplinary Research Topic, a collection of six Original Research, three Brief Research Report, one Technology and Code, and three Review articles are presented, featuring some of the latest advances in time-resolved luminescence instruments, probes, data processing, interpretation, and applications for biosensing and imaging.

Depending on the timescale of the luminescence decay, which varies from nanoseconds for typical fluorophores to seconds and longer for some phosphors, time-resolved luminescence measurement encompasses a diverse range of techniques, probes and devices suited for different temporal resolution. Hirvonen and Suhling provide a detailed overview of the fast timing underpinning fluorescence lifetime imaging (FLIM)—a technique which celebrated its 30th anniversary recently [6], and highlight a few recent examples showcasing applications in life sciences. Meanwhile, Deng et al. survey techniques for measuring long-lived emission, with particular focus on methods using mechanical choppers. Special attention is paid to automatic synchronization based on the same chopper acting as both the pulse generator and the detection shutter, with detailed discussion on their advantages, challenges, and future development prospects. Generally speaking, time-resolved measurement takes longer than steady-state measurement to perform in order to capture the time evolution at the cost of analytical throughput. Bitton et al. review the recent advancements in microscopy and flow cytometry for high-throughput lifetime measurements, and provide their outlook on future developments integrating machine learning.

On the other hand, regardless of the temporal resolution, common principles and methods are applicable to time-resolved luminescence measurement, which can be performed either in the time domain or in the frequency domain [7]. On the former, Ziniuk et al. implement a rapid lifetime determination technique for lifetime imaging of Er-doped nanoparticles emitting shortwave infrared luminescence, which has the potential for *in vivo* bioimaging. Li et al. compare the outputs of several

OPEN ACCESS

Edited by:
Lorenzo Pavesi,
University of Trento, Italy

Correspondence:
Yiqing Lu
yiqing.lu@mq.edu.au
Gerard Marriott
gmlab@berkeley.edu
Klaus Suhling
klaus.suhling@kcl.ac.uk

Specialty section:
This article was submitted to Optics and Photonics, a section of the journal Frontiers in Physics

Received: *15 June 2021*
Accepted: *15 June 2021*
Published: *29 June 2021*

Citation:
Lu Y, Marriott G and Suhling K (2021) Editorial: Modern Tools for Time-Resolved Luminescence Biosensing and Imaging. Front. Phys. 9:725234. doi: 10.3389/fphy.2021.725234

lifetime determination algorithms when the fluorescence follows a multi-exponential decay. They further propose using the ratio of intensity and amplitude-weighted average lifetimes as a new indicator of energy transfer efficiency. On the latter, Sambrano Jr et al. report their progress on developing a flow cytometry method capable of frequency-domain lifetime measurement, based on an acoustic-focusing microfluidic chip to control the flow speed. Sumetsky et al. examine the lifetimes calculated from frequency-domain FLIM, showing a simple linear relationship to the amplitude-weighted lifetime associated with energy transfer efficiency. For calibration purposes, Xiao et al. propose a modified (mirror-symmetric) method to obtain a synthetic instrument response function (IRF) from time-correlated single photon counting data, which offers better performance than the traditional (differential) synthetic IRF for lifetime analysis. In terms of data processing and interpretation, Haas et al. present a multidimensional phasor demixing method for analyzing data from spectral-resolved FLIM microscopy, which is applied to multiplexed biosensing of the cell-death proteases Caspase−2, −3 and −9 on the single cell level.

The versatility of time-resolved luminescence methods keeps inspiring new applications. Mould et al. apply two-photon FLIM microscopy to investigate the effect of cannabidiol on breast cancer cells. They show that at increased concentration of cannabidiol, mitochondrial bound NAD(P)H decreases significantly and correlates to increased oxidative stress. Chorvatova et al. employ endogenous fluorescence of water moss in response to several heavy metal nanoparticles to demonstrate that the fluorescence lifetime of the endogenous fluorescence is a sensitive parameter for detecting environmental pollution. Gallian et al. present an immunoassay platform based on Mn-doped quantum dots and a compact plate reader equipped with a pulsed laser diode and a time-gated detector. They achieve sensitive detection of the capsular polysaccharide from *Burkholderia pseudomallei* (a Tier 1 selected agent) with a detection limit two orders of magnitude lower than steady-state measurements, which can be advantageous for in-field diagnosis. Bhartiya et al. summarize a detailed protocol for multicolour fluorescence *in situ* hybridization combined with DAPI FLIM, allowing study of the structural differences in the 46 chromosomes of the human genome.

We thank all of our contributing authors for their dedication to the Research Topic, and the reviewers for their constructive comments and suggestions. It is hoped that the Research Topic will serve as a useful reference work for a broad audience, encouraging cross-disciplinary collaborations, and accelerating future advances and innovation in Time-Resolved Luminescence Biosensing and Imaging technologies and their applications in the biological, environmental, and health sciences.

AUTHOR CONTRIBUTIONS

All authors listed have made a substantial, direct, and intellectual contribution to the work and approved it for publication.

REFERENCES

1. Soini E, Lövgren T, and Reimer CB. Time-Resolved Fluorescence of Lanthanide Probes and Applications in Biotechnology. *Crit Revs. Anal Chem* (1987) 18: 105–54. doi:10.1080/10408348708085565
2. Marriott G, Clegg RM, Arndt-Jovin DJ, and Jovin TM. Time Resolved Imaging Microscopy. Phosphorescence and Delayed Fluorescence Imaging. *Biophysical J* (1991) 60:1374–87. doi:10.1016/s0006-3495(91)82175-0
3. Fan Y, Wang P, Lu Y, Wang R, Zhou L, Zheng X, et al. Lifetime-engineered NIR-II Nanoparticles Unlock Multiplexed *In Vivo* Imaging. *Nat Nanotech* (2018) 13: 941–6. doi:10.1038/s41565-018-0221-0
4. Berezin MY, and Achilefu S. Fluorescence Lifetime Measurements and Biological Imaging. *Chem Rev* (2010) 110:2641–84. doi:10.1021/cr900343z
5. Suhling K, Hirvonen LM, Levitt JA, Chung P-H, Tregidgo C, Le Marois A, et al. Fluorescence Lifetime Imaging (FLIM): Basic Concepts and Some Recent Developments. *Med Photon* (2015) 27:3–40. doi:10.1016/j.medpho.2014.12.001
6. Ameer-Beg S, Suhling K, and Kuimova M. Special Issue on Fluorescence Lifetime Imaging (FLIM): from Fundamentals to Applications. *Methods Appl Fluoresc* (2020) 8:040401. doi:10.1088/2050-6120/abad19
7. Lakowicz JR. *Principles of Fluorescence Spectroscopy*. 3rd ed. New York: Springer US (2007).

Conflict of Interest: The authors declare that the research was conducted in the absence of any commercial or financial relationships that could be construed as a potential conflict of interest.

frontiers in Physics

REVIEW
published: 13 May 2020
doi: 10.3389/fphy.2020.00161

Fast Timing Techniques in FLIM Applications

Liisa M. Hirvonen[1] *and Klaus Suhling*[2]*

[1] Centre for Microscopy, Characterisation and Analysis (CMCA), The University of Western Australia, Perth, WA, Australia,
[2] Department of Physics, King's College London, London, United Kingdom

Fluorescence lifetime imaging (FLIM) is increasingly used in many scientific disciplines, including biological and medical research, materials science and chemistry. The fluorescence label is not only used to indicate its location, but also to probe its immediate environment, via its fluorescence lifetime. This allows FLIM to monitor and image the cellular microenvironment including the interaction between proteins in their natural environment. It does so with high specificity and sensitivity in a non-destructive and minimally invasive manner, providing both structural and functional information. Time-Correlated Single Photon Counting (TCSPC) is a popular, widely used, robust and mature method to perform FLIM measurements. It is a sensitive, accurate and precise method of measuring photon arrival times after an excitation pulse, with the arrival times not affected by photobleaching, excitation or fluorescence intensity fluctuations. It has a very large dynamic range, and only needs a low illumination intensity. Different methods have been developed to advance fast and accurate timing of photon arrival. In this review a brief history of the development of these methods is given, and their merits are discussed in the context of their applications in FLIM.

Keywords: fluorescence lifetime imaging (FLIM), time-correlated single photon counting (TCSPC), photon counting, single photon detection, fast timing

OPEN ACCESS

Edited by:
Gabriella Carini, Brookhaven National Laboratory (DOE), United States

Reviewed by:
Cristoforo Marzocca, Politecnico di Bari, Italy
Peter R. Hobson, Queen Mary University of London, United Kingdom

***Correspondence:**
Klaus Suhling
klaus.suhling@kcl.ac.uk

Specialty section:
This article was submitted to Radiation Detectors and Imaging, a section of the journal Frontiers in Physics

Received: *20 December 2019*
Accepted: *17 April 2020*
Published: *13 May 2020*

Citation:
Hirvonen LM and Suhling K (2020) Fast Timing Techniques in FLIM Applications. Front. Phys. 8:161. doi: 10.3389/fphy.2020.00161

1. INTRODUCTION

1.1. Early Timing of Light Signals

The quest for precise timing of light signals can be traced back to 1638, when Galileo Galilei (1564-1642), performed an experiment using two observers with lanterns and manual shutters stationed on two well-separated hilltops. Although he suspected that light did not travel instantaneously, this kind of terrestrial approach was far too slow to observe the speed of light experimentally. Astronomical measurements provided a way forward: In 1675, the Danish astronomer Ole Rømer (1644–1710) observed the eclipses of the innermost moon of Jupiter, Io, at different times of the year and proposed a finite speed of light to account for timing differences of the moon emerging from the shadow of Jupiter, as seen from earth. In addition, in another astronomical approach around 50 years later, in 1728, the British astronomer James Bradley (1693–1762) calculated the speed of light from stellar aberration [1].

First terrestrial measurements of the speed of light were performed by Hippolyte Fizeau (1819–1896) in 1848–49 by reflecting an intense beam of light from a mirror 8 km away through a toothed wheel, and in 1850–62 Léon Foucault (1819–1868) improved the experiment by replacing the cog wheel with a rotating mirror, and eventually measured the speed of light within 0.6% of today's accepted value, and Maxwell's calculations [2]. At King's College London, Charles Wheatstone (1802–1875) also experimented with rotating mirrors to measure the duration of electric sparks [3].

1.2. The Photon

After the experimental determination of the speed of light, Maxwell's prediction of electromagnetic waves [2] and their experimental detection by Heinrich Hertz in the 1880s, the nature of light came under increased scrutiny. Max Planck's attempt to explain the blackbody spectrum in 1900 ushered in the idea of quantization of energy. Planck considered hypothetical material oscillators that can only emit and absorb electromagnetic radiation in discrete, quantized form and not in continuously varying quantities, especially not in arbitrarily small amounts. Although he did not explicitly propose that light is quantized, he proposed that the energy ϵ of these oscillators is proportional to their oscillation frequency ν

$$\epsilon = h\nu \tag{1}$$

where h is now known as Planck's constant. In 1905, Albert Einstein [4] introduced the smallest unit of energy of electromagnetic radiation, *Lichtquant* (quantum of light), and explained the photoelectric effect using this concept. The term photon was conceived by the chemist Lewis in 1926 [5], and the existence of light quanta as well as the term photon gained wider acceptance as quantum theory was developed in the 1920s.

In particle physics, the photon is an integer spin particle, a boson, with spin 1. A photon is a "quantized field," it always travels at the speed of light and has a momentum, but no mass, and no charge [6]. It does not decay, once it is emitted, its frequency stays fixed [1].

1.3. Experimental Detection of Photons and Photon Arrival Timing

Experimental detection of single photons requires that the signal from a single photon is converted into an electronic signal. The photoelectric effect, first observed by Heinrich Hertz in 1887 [7], provides the means to do this. While the electronic signal of one photoelectron is too small to be detected, the secondary emission principle, discovered by Austin and Starke [8], allows electron multiplication and hence gain to be introduced. Thus, the photoelectron signal, created by a single photon, can be amplified and measured.

The capability to detect single photons means that it is also possible to time their arrival, similar to timing the arrival of particles. Indeed, the origin of time-correlated single photon counting (TCSPC) lies in particle physics. In 1929, Walther Bothe and Werner Kohlhörster measured the coincidence of penetrating charged particles in cosmic rays [9] leading to the first practical electronic coincidence circuit [10] which became a precursor of the AND logic circuits of electronic computers. By the addition of a delay, this coincidence method evolved to measure delayed coincidence, providing the means for time-resolved measurements and the invention of the "time circuit," nowadays known as the Time-to-Amplitude Converter (TAC) [11]. It became a popular method to measure short radioactive decay times, with time resolution improved to 80 ps in the 1950s [12]. Scintillation decay times, excited by gamma rays, were also reported in the 1950s, using a delayed coincidence method [13].

In 1961, Lowell Bollinger and George Thomas generalized the scintillation measurements to include any type of radiation [14], and flashlamps with optical pulse widths of around 2 ns became available in the 1960s, enabling TCSPC: This is essentially a delayed coincidence method, whereby the arrival time of a single photon is measured relative to an excitation pulse, and this can be done with a few picosecond precision [15]. The accumulation of the arrival time of many single photons then represents the intensity decay of the sample, as long as no photons are lost due to pile-up, and the linearity between intensity and collected photons holds. See **Figure 1** for a timeline of the development of single photon counting and timing technology.

1.4. Fast Timing in Fluorescence

In fluorescence measurements, the sample is excited with a short pulse of light and the decay of fluorescence is measured. This approach can be traced back to the phosphoroscope developed in 1857 by Alexandre-Edmond Becquerel (1820–1891), based on a similar principle to Foucault's speed of light measurement experiments. Becquerel used two rotating disks with a series of holes, and the sample in between, to measure photoluminescence lifetimes. In his apparatus, the sample (e.g., a phosphorescent crystal) was excited by light coming in through one hole, and viewed by the phosphorescent light coming out of the other hole. By varying the speed of rotation, Becquerel was able to measure the short microsecond time interval during which the phosphorescent light is emitted.

In modern time-correlated single photon counting experiments, the photons emitted by the sample are timed one by one and used to build a histogram of the fluorescence decay over time, see **Figure 2A**. In the simplest case, the fluorescence decay is a monoexponential function

$$I(t) = I_0 e^{-\frac{t}{\tau}} \tag{2}$$

where I_0 represents the fluorescence intensity at $t = 0$ [16]. The fluorescence decay time τ is the average time the fluorophore remains in the excited state and is defined by

$$\tau = \frac{1}{k_r + k_{nr}} \tag{3}$$

where k_r is the radiative rate constant which is largely determined by the extinction coefficient, the fluorescence spectrum and the refractive index of the fluorophore's environment [17]. The non-radiative rate constant k_{nr} typically depends on the environment,

Abbreviations: ADC, Analog-to-Digital Converter; APD, Avalanche Photodiode; CCD, Charge-Coupled Device; CMOS, Complementary Metal Oxide Semiconductor; CFD, Constant Fraction Discriminator; FAD, Flavin Adenine Dinucleotide; FLIM, Fluorescence Lifetime Imaging; FRET, Förster Resonance Energy Transfer; FWHM, Full Width at Half Maximum; IRF, Instrument Response Function; LIDAR, Light Detection and Ranging; MCP, Microchannel Plate; MPPC, Multi-Pixel Photon Counters; NADH, Reduced Nicotinamide Adenine Dinucleotide; NADP, Nicotinamide Adenine Dinucleotide Phosphate; PMT, Photomultiplier Tube; SPAD, Single-Photon Avalanche Diode; TAC, Time-to-Amplitude Converter; TCSPC, Time-Correlated Single Photon Counting; TDC, Time-to-Digital Converter; TIRF, Total Internal Reflection Fluorescence; TTS, Transit Time Spread.

[1]The Nature milestone series "Photons" details background and context of the development of the understanding of light and its basic unit, the photon. http://www.nature.com/milestones/milephotons/index.html

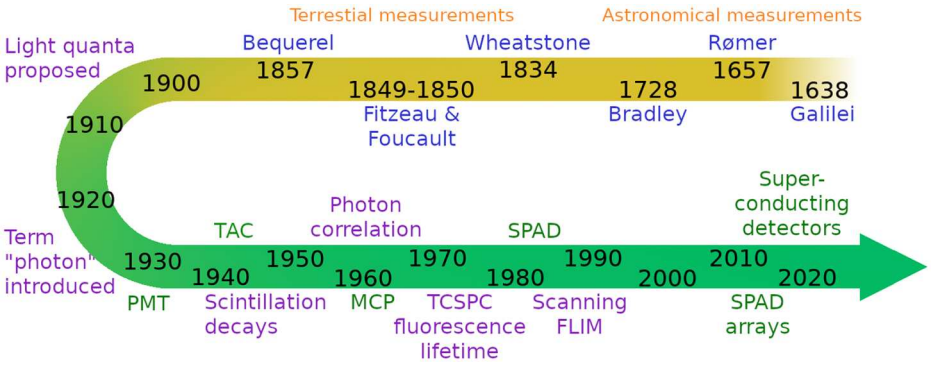

FIGURE 1 | Brief schematic timeline of single photon counting and timing technology from Galilei's work on the speed of light to today's photon detectors and timing electronics. Scientists are indicated in blue, ideas and concepts in purple, and technology developments in green.

and can change with interaction, pH, viscosity, and other parameters [16].

Fluorescence decay measurements in fluorescence spectroscopy or fluorescence microscopy can therefore be used to gain information about the immediate environment of the fluorophore, as well as to probe the proximity of other fluorophores via Förster Resonance Energy Transfer (FRET) [18–20]. Moreover, the fluorescence decay is typically independent of the fluorophore concentration at concentrations low enough to avoid interaction or aggregation.

The first reports that use TCSPC in the measurement of fluorescence decays appear in the early 1970s [21–24], and TCSPC was soon widely used for time-resolved spectroscopy, and in particular the measurement of fluorescence lifetimes in solution [25].

Photon counting techniques are used in many different fields of science and technology, from DNA sequencing [26] to quantum cryptography and interplanetary communications [27], and photon timing applications include light detection and ranging (LIDAR) [28, 29], photon correlation techniques [30], and optical tomography [31]. Single photon detection techniques and applications have been reviewed recently by Buller and Collins [32], Hadfield [33] and Eisaman et al. [34]. Incidentally, the same technology is not only used for photon arrival timing, but also particle arrival timing for particles such as neutrons, where timing can indicate neutron energy [35, 36], and electrons and ions, e.g., in ion velocity mapping [37–39], so there is a growing need for this technology, [40] with applications beyond timing the arrival of photons.

1.5. Fluorescence Lifetime Imaging (FLIM)

The development of laser scanning confocal microscopes [41] enabled TCSPC-based fluorescence lifetime imaging (FLIM), as shown in **Figure 2B**. This method was developed in the late 1980s [42] and early 1990s [43–45] before being more widely applied in the late 1990s [46]. Besides scanning with a point-detector to form an image of the sample, microchannel plate (MCP)-based detectors and more recently single photon avalanche diode (SPAD) arrays can be used for wide-field TCSPC FLIM [47]. The development of both single point and wide-field single photon detection methods has continued over the decades, and while the old technologies continue to be used and improved, there have also been new developments that show great promise, including SPAD arrays and detectors based on superconducting detector technology. See **Figure 1** for a timeline of single photon technology.

The specific requirements for the detectors and the timing electronics depend on the field of application. This review gives an overview of the technology behind the different approaches to fast photon timing and recent developments with a focus on fluorescence decay measurements and particularly FLIM.

1.6. Principles Behind Photon Timing

Photon timing means that the arrival time of a photon at the detector is measured with respect to some reference, typically the excitation laser pulse. A trigger from the laser and the signal from the detector are fed into the timing circuit and their difference is calculated. The photons are then usually assigned a "time bin," i.e., a slot whose width usually depends on the detector precision, the required measurement precision, and the total length of the decay to be measured, see **Figure 3**. The circuit is adjusted such that the entire decay fits into the available time window, typically 5 times the length of the fluorescence lifetime, so that it can decay into the background noise. The measurement is repeated for many photons, until the arrival time histogram—representing the fluorescence decay—contains a statistically significant number of photons for fluorescence decay analysis, and to extract the fluorescence lifetime [48–51].

1.6.1. Instrument Response

A photon timing detector is usually characterized by the full width at half maximum (FWHM) of its instrument response function (IRF), which is measured using a very short pulse of light. In an ideal case, the measured IRF would be a Dirac delta function in a single time bin, but due to experimental uncertainties it is always wider. The width of the instrumental response Δt^2_{IRF} is given by the sum of the squares of the individual time spread contributions [52]

$$\Delta t^2_{IRF} = \Delta t^2_{optical} + \Delta t^2_{tts} + \Delta t^2_{jitter} \quad (4)$$

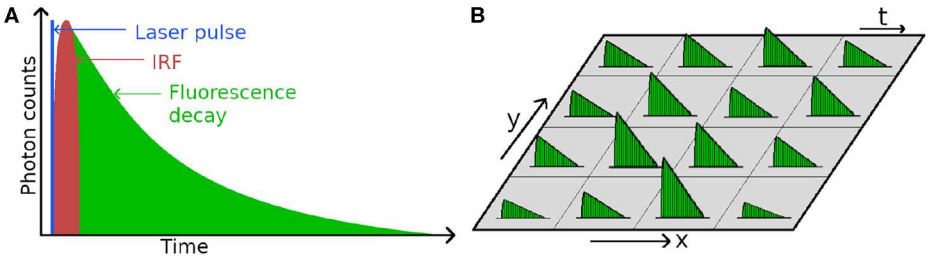

FIGURE 2 | (A) Schematic diagram of a fluorescence decay, **(B)** Basic principle of Fluorescence Lifetime Imaging (FLIM), where a fluorescence decay is measured for every pixel of the image.

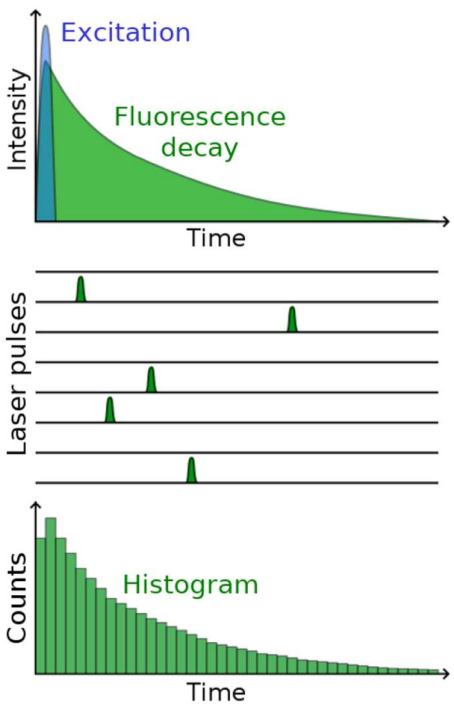

FIGURE 3 | Principle behind photon arrival timing for TCSPC. After repeatedly exciting the sample and timing the arrival of many fluorescence photons (schematically indicated in the middle), a histogram is built up that represents the fluorescence decay.

where $\Delta t_{optical}$ is the optical pulse width of the exciting light, Δt_{tts} is the transit time spread of the detector, and Δt_{jitter} is the jitter of the detection and timing electronics. Optical pulse widths can be as short as femtoseconds, e.g., for two-photon excitation, and the jitter of the electronics can be around 1 ps for the fastest timing systems.

1.6.2. The Poisson Statistics of Photon Counting

One key advantage of photon counting is the well-defined theoretical framework of Poisson statistics, which govern the photon counting process. The photon events are independent, i.e., in ensemble measurements the detection of one photon event does not change the probability of detecting another one. (For single photon work, this idea is modified, and in Hanbury Brown and Twiss-type experiments, this is exploited to gain information about coincident events.) The variance is the mean of the distribution, and the experimental uncertainty in the form of the standard deviation is given by the square root of the number of counts. This also means that the more photons are collected, the smaller the experimental uncertainty, and in practice the dynamic range is only limited by the detector and electronics non-linearities. Poisson statistics also predict how often multiple photon events are detected as a function of the mean count rate. Importantly, the probability that more than one photon occurs after an excitation event is never zero, and there are excitation cycles where this happens. If only one photon can be detected after an excitation event, then the first photon arriving is timed, but subsequent photons are lost. This is known as pile-up which distorts the fluorescence decay toward shorter times [15]. In practice, in the older spectroscopy literature it is recommended to keep the stop-to-start ratio (ratio of fluorescence photon count rate to repetition rate of the excitation laser) to around 1%, for fluorescence decays with typically 10,000 counts in the peak [15].

Again, it is worth emphasizing that pile-up always occurs, the probability to detect several photons after one excitation pulse is never zero—the question is whether the effect emerges from the Poisson noise (square root of the number of counts). For FLIM, with typically fewer counts in the fluorescence decays in each pixel than in spectroscopy measurements, the 1% stop-to-start ratio can be somewhat relaxed, and a 10% stop-to-start ratio only introduces a 2.5% fluorescence lifetime error [49]. If all photons that are emitted after an excitation event are detected, then this is not a problem [53].

2. SINGLE PHOTON DETECTORS

The detection of a single photon requires that (1) the photon is converted into an electronic signal, and (2) that this signal is larger than the noise, so it can easily be measured—in practice, it needs to be amplified. Different detectors have different characteristics regarding transit time spread, detection efficiency, noise, ease-of-use and durability. Detectors used in TCSPC/FLIM applications are discussed in this section, see **Table 1** for a summary.

TABLE 1 | Summary of single photon detectors that are, or could be, used in FLIM.

Method	Principle	Advantages	Disadvantages	Remarks & references
PMT	Photoelectric effect	High gain Large area Low dark count	Requires vacuum Sensitive to magnetic fields	Requires high voltage [58–60, 123]
MCP	Photoelectric effect	Large area High fill factor Short TTS Fast response Low dark count	Requires vacuum Limited lifetime	Requires high voltage [61, 79, 81]
SPAD	Electron-hole pair generation	Low dead-time Fast response	Small active area, high dark count rate Charge carrier diffusion tail in IRF	[124]
SPAD array	Electron-hole pair generation	Large number of parallel detectors	Low fill factor High dark count rate Cross-talk	[84, 95, 102]
SiPM	Electon-hole pair generation	Large number of parallel detectors	Cross-talk	All pixels connected to one readout could be used for scanning FLIM [103–105, 111]
Hybrid PMT	Photoelectric effect and electron-hole pair generation	Low dead-time Low timing jitter No afterpulsing		Requires high voltage [117, 118]
Super conducting detectors	Superconductivity	Low dark count Fast response (nanowires)	Low operating temperature	Still a developing technology, not used for FLIM yet [33, 34, 125]

2.1. Photomultiplier Tube (PMT)

The first working PMTs were produced in the former Soviet Union in the mid-1930s [54–56] in the race to develop electronic television, and were soon shown to be single photon sensitive [57]. A PMT is a vacuum device that consists of a photocathode, up to a dozen discrete dynodes, each at a higher potential than the previous one, and an anode, see **Figure 4** [58–61]. A photon hitting the photocathode can liberate a photoelectron, which in turn releases secondary electrons when it hits the first dynode, attracted to move toward it by the positive potential. The electric signal is amplified in the same way at each dynode, and the overall gain of a PMT can reach values of 10^6 to 10^8 which yields an easily measurable current at the anode, or a pulse. If two photons are detected in quick succession, the output pulses can merge and increase the pulse height. This effect has been exploited to design a so-called pulse pile-up inspector that rejects pulses over a certain pulse height and thus reject multiphoton events which can bias a fluorescence decay [21, 62].

The reproducibility of measurements is affected by the electron transit time, anode pulse rise time, and electron transit time spread. The transit time spread determines the full width half maximum of the IRF. For example, according to its data sheet[2], the Hamamatsu R14755U PMT's single photon pulse has a rise time of 400 ps, but a transit time spread of only 200 ps. Short rise times are advantageous for precise timing. Incidentally, the IRF is much smaller than the width of the single-photon output pulse of the PMT, which is quoted as 680 ps. The spectral response characteristics are determined on the long wavelength side by the photocathode material and on the short wavelength side by the window material. PMTs require a vacuum and a high voltage for their operation, and are sensitive to strong magnetic fields.

Photon detection efficiency of PMTs depends strongly on the photocathode. The detection efficiency of conventional bialkali and multialkali cathodes reaches 20–25% between 400 and 500 nm, but falls off quickly toward longer wavelengths. GaAsP cathodes can reach up to 50% detection efficiency and work up to 700 nm. However, dark current also depends on the cathode material and can become a problem especially with materials that have increased sensitivity toward infrared wavelengths. Typical dead-times of PMTs are in the order of 10 ns, which is generally lower than the dead-time of the electronics used for photon timing and therefore usually not a concern for photon timing applications. They also usually have a large detector area compared to diodes—50 cm diameter for the Super-Kamiokande PMTs [63]—which makes them easy to align in confocal or multiphoton excitation fluorescence microscopes. Multianode PMTs have been produced, with 16 anodes, and have been employed in spectral FLIM [64, 65].

2.2. Microchannel Plate (MCP)

The concept of a microchannel plate (MCP) with a continuous dynode was conceived in the 1930s [66] (coincidentally around the same time as PMTs), although the first working devices were not produced until the early 1960s [67–69]. Like PMTs,

[2]https://www.hamamatsu.com/eu/en/product/type/R14755U-100/index.html

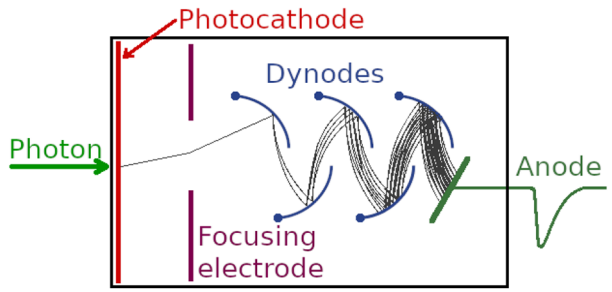

FIGURE 4 | Schematic of a photomultiplier tube. A photon impinging on the photocathode can liberate a photoelectron which is attracted to the first dynode, where further electrons are created by secondary emission. After around 10 dynodes, the gain can be well over 10^6, producing an output pulse that can be timed by timing electronics [58–61].

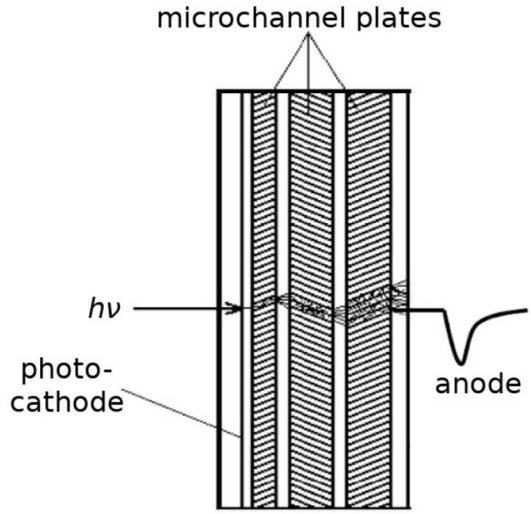

FIGURE 5 | Schematic of a microchannel plate. A photon impinging on the photocathode can liberate a photoelectron, which is attracted into the first microchannel plate where secondary emission inside the microchannels produces more electrons. They can be converted into a timing pulse at the anode.

the operating principle of MCPs is also based on the signal from the emission of a photoelectron from a photocathode and its amplification via secondary emission, but an MCP has continuous dynodes rather than discrete dynodes, as shown in **Figure 5**. This shortens the transit time, and hence also the transit time spread, which is a critical parameter for photon timing applications. MCPs have a regular array of tiny tubes (microchannels) where electrons are accelerated from one side of the plate to the other through a high voltage (typically a few kV). The microchannels are usually straight and round with ∼10 μm in diameter with a center-to-center distance of ∼15 μm [70, 71]. They are arranged at an angle toward the normal (bias angle), so that ion feedback is minimized. Most MCP detectors consist of two (chevron configuration) or three (z-stack configuration) MCPs either pressed together or with a small gap between them, and the bias angles of the plates are rotated 180° with respect to each other to prevent ion feedback. One MCP can have gain up to 10,000, but a 3-MCP intensifier can provide gain $> 10^7$.

MCP detectors do not in principle have "dead-time" when the detector is not capable of detecting new events. However they can be affected by gain depletion where electrons are not delivered fast enough to an area where many events occur, leading to reduced electron gain and consequently reduced output signal amplitude. This can become an issue especially with camera-based read-out which can detect up to 100s of events per frame [47], but this is unlikely to become an issue if the MCP is used for timing photons one by one.

Inside MCPs the electron transit time is short, and consequently, the transit time spread is also short, 10s of ps. Indeed, MCPs are used as fast detectors for timing in TCSPC, and IRFs of <20 ps have been reported [48, 51]. The output electron cloud can then be detected by several methods, depending on the application.

If no position read-out is required, the total current can be converted to a voltage via a resistor and read out as a pulse, as schematically indicated in **Figure 5**. For wide-field TCSPC, a position-sensitive read-out is necessary, and the electrons can be detected with either a position-sensitive anode, or converted to photons with a phosphor screen and detected with a camera [47]. Large area MCPs with dimensions of 20×20 cm^2 have been reported [72].

Although MCPs are a mature technology, they are still widely used and their development continues. For example, unlike PMTs, MCPs can provide spatial resolution, which is advantageous in low light level imaging. Photon counting imaging, where the amplified photon events were imaged with a camera and the image assembled photon by photon, was employed by astronomers due to the exquisite sensitivity this method offered at the time [73]. Indeed, the Hubble space telescope's faint object camera was based on photon counting imaging [74]. The x-ray multimirror satellite's optical monitor [75], the ultra-violet/optical telescope (UVOT) on the *Swift* gamma-ray observatory [76] and the Galaxy Evolution Explorer (GALEX) satellite [77] all employ MCP-based photon counting image intensifiers. Developments in the field are ongoing [78, 79], and recent improvements using atomic layer deposition include robust substrates that able to withstand high processing temperatures, very low background rates, high stable gains, and low outgassing [80, 81].

2.3. Avalanche Photodiodes (APD/SPAD)

In contrast to PMTs and MCPs that are vacuum devices operated at kV voltages, avalanche photodiodes (APDs) are semiconductor solid-state devices based on a p–n junction, for which no vacuum and kV voltages are required. A diode is an electronic component that allows current to flow through it in one direction (when biased in forward mode), but not the other (reverse mode), as schematically shown in **Figure 6A**. A photodiode has a depletion region which is largely free of mobile charge carriers, but when a photon is absorbed in it, an electron-hole pair is created, see **Figure 6B**. Applying an electric field (reverse bias) will allow the

holes to go to the anode, and the electrons to the cathode—thus a flow of current is created by absorbing photons in the depletion region of a photodiode when biased in reverse mode.

By applying a high reverse bias voltage (typically 100–200 V in silicon), APDs show an internal current gain effect (around 100) due to impact ionization (avalanche effect). Gain can be improved by different doping and beveling techniques. A key feature of the electron-hole pair generation is that unlike in the photoelectric effect, this is a process for which no vacuum is required.

SPADs are APDs that are operated with a reverse voltage above a typical APD's breakdown voltage. This is also called Geiger mode, and it can achieve gains of 10^5–10^6. This mode is particularly useful for single-photon detection. Once a photon has been absorbed and an electron-hole pair created, an electron avalanche is initiated which reduces the reverse bias below the breakdown voltage and eventually stops the avalanche. If the SPAD is designed for passive quenching, a large resistor in series to the photodiode quenches the avalanche, whereas in active quenching, an electronic circuit is triggered by the avalanche current to stop it. Single photons thus produce a clear output signal that can be counted and timed. This output signal is typically independent of the number of photons producing electron-hole pairs in the depletion region, so two photons detected in quick succession will not increase the pulse height, and pile-up inspection based on pulse height [21, 62] is not feasible.

SPADs and APDs have a much smaller active area than photomultipliers, typically between 10 and 100 μm in diameter. They can have larger quantum efficiency than photocathode-based photoelectronic vacuum detectors, up to about 80%. SPADs have a low dead-time and consequently high count rate, with transit time spread of 10s of ps comparable to MCPs [82, 83]. However, they do have a charge carrier diffusion tail (a type of afterpulsing) in the IRF. Another characteristic feature of SPADs is their dark noise, typically tens of counts/s depending on the operating voltage and temperature [84] and is a key difference compared to photoelectronic vacuum devices for which 0.02 events $cm^{-2}s^{-1}$ have been quoted [71]. For typical nanosecond fluorescence lifetime measurements in 50 ns time windows, this is not a key issue, but the dark noise consideration gains in importance as the detection window and fluorescence lifetime to be measured increase, and the count rate drops. It is also an important point to consider when enlarging the size of the light sensitive area in SPADs, as the dark noise increases with the area [84].

2.4. Single Photon Avalanche Diode (SPAD) Arrays

SPADs can be arranged into arrays for spectroscopy or imaging, and can be manufactured by complementary metal oxide semiconductor (CMOS) technologies [85]. One-dimensional arrays [86–91] can have a good fill-factor, since the light-sensitive regions can be adjacent, with the timing electronics placed away from the illuminated area. Two-dimensional SPAD arrays can be used as a camera for direct wide-field imaging, where each SPAD is a pixel that can independently perform photon arrival time detection via TCSPC [92–94]. One of the features of such an approach is that it yields enormous overall count rates of GHz [95]. In addition to TCSPC operation, they can be used in gated mode [96]. Two-dimensional arrays built for fast photon timing have a fill factor well below 100% (e.g., from ∼1% [97, 98] to ∼50% [99]) because the majority of the area in each pixel is occupied by electronic circuits to perform the timing. Quantum efficiencies of around 60% have been reported [100], which compares favorably to photocathode-based devices. Large arrays of SPADs have been demonstrated to be suitable for TCSPC [95, 101], and the development of these detectors is currently developing at a fast pace [102].

2.5. Silicon Photomultipliers (SiPM)

Silicon photomultipliers, also known as solid state photomultipliers, or multi-pixel photon counters (MPPCs) are arrays of hundreds to tens of thousands of integrated SPADs, each of which can detect photons individually and independently [103–105]. However, unlike in SPAD arrays, they are all connected to a common readout. Upon detection of a photon in a SPAD, an electrical signal is generated by the SPAD. This can be added to the signal from other SPADs that have detected a photon, to generate a pulse whose amplitude is proportional to the number of photons detected by the SiPM—this is the analog operation of the SiPM, which yields information about the photon flux. Alternatively, the number of SPADs that detected a photon can be counted separately, so that the number SPADs producing a signal is proportional to the number of incident photons, or the photon flux.

Interestingly, SiPMs have a photon number resolving capability: one, two, three or more detected photons can easily be resolved [103]. A pulse height distribution of the SiPM output shows characteristic peaks corresponding to the number of photons detected, in addition to picosecond arrival timing. The latter feature has been used in employing a SiPM with an active area of 1 mm^2 for TCSPC [106].

One feature of SiPMs and SPAD arrays is optical cross-talk. The detection of a photon by the semiconductor can create an infrared photon, which in turn can be detected by a neighboring SPAD [107–109]. However, while the effect exists in principle, it can be minimized with an appropriate SPAD design, and cross-talk as low as 1% has been reported [109].

SPAD arrays and SiPMs can be manufactured by CMOS technologies, but are usually produced using an *ad hoc* technology [85]. This is a photolithographic fabrication process using field effect transistors for logic functions in various integrated circuits, but also for analog circuits in image sensors; for example, the 160×128 SPAD array in Veerappan et al. [92] has been quoted to have 60 million transistors. While the latter SPAD array was manufactured using 130 nm CMOS technology, the latest SPAD arrays have been produced in 40 nm CMOS technology [110], allowing smaller features on the SPAD array. The pixel pitch, for example, 18.4 μm in x and 9.2 μm in y is the smallest one reported for SPAD arrays at the time of writing, much smaller than, for example, the 50 μm pitch used in Veerappan et al. [92]. Since the light-sensitive area

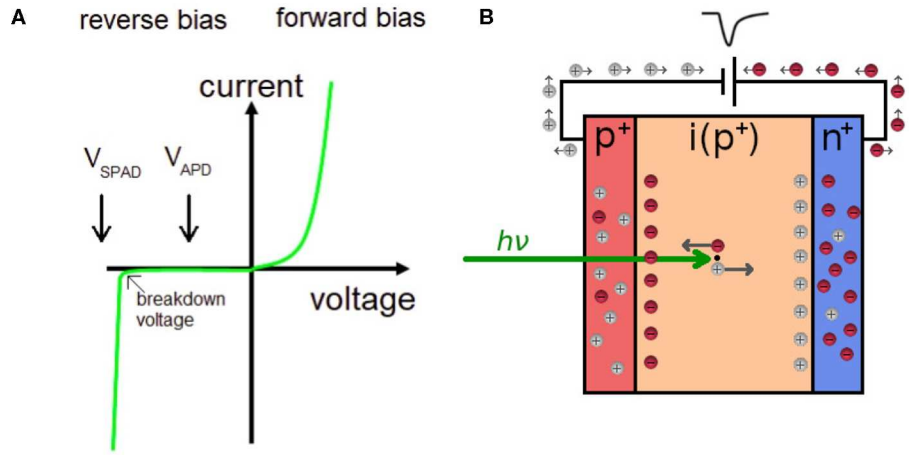

FIGURE 6 | (A) A schematic current-voltage characteristic for a diode. A SPAD is biased above the breakdown voltage of the diode, whereas an APD is biased below the breakdown voltage. **(B)** A schematic of a photodiode in reverse mode. A photon absorbed in the depletion region (i) creates an electron-hole pair, which through impact ionization produces a pulse for timing.

in a pixel has to share the available space with the timing electronics, the fill-factor (i.e., the ratio of light-sensitive area to total pixel area) is less than 100%, if both are implemented in a two-dimensional layer. This is currently the case, but three-dimensional integration, where the light-sensitive part and the electronics are implemented in separate layers which are then put together to form the SPAD array, or SiPM, is an area of active and rapid development, and 100% fill-factor devices will likely be produced in the near future. This would be a very welcome development for many application areas, including biophotonics [102, 111]. Three-dimensional integration will also enable placement of FPGA-like (field programmable gate array) structures beneath the sensor, for detailed analysis of the photon flux, e.g., mean fluorescence lifetime determination without reading out the arrival time of every photon [112–114].

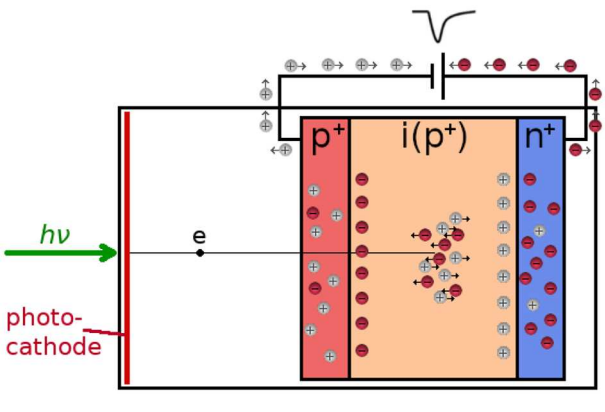

FIGURE 7 | In a hybrid detector, the photoelectron from the photocathode is accelerated through a high voltage into the p-n junction, where it creates a large number of electron-hole pairs. The gain is further increased by impact ionization, producing a timing pulse at the anode.

2.6. Hybrid Detectors

Hybrid photodetectors combine the PMT vacuum tube with photodiode semiconductor technology: a photoelectron liberated from the photocathode is accelerated through a high voltage (up to 10 kV) directly onto an avalanche diode, biased below the breakdown voltage (see **Figure 6A**) where it generates a large number of electron-hole pairs, one per each 3.7 eV [115]. Thus, well over 1,000 electron-hole pairs are created by a single photon, which are further amplified in the diode, see **Figure 7**. One advantage of this technology is that the single gain step produces a narrow pulse height distribution [115, 116], which can be used to detect photon numbers. From the timing point of view, this single gain step results in low transit time spread and therefore low timing jitter [117].

Hybrid detectors feature lower dead-times (<1 ns) compared to either PMTs or SPADs (tens of ns). Also, the IRF of such detectors is, unlike that of a SPAD, PMT or MCP, free of afterpulsing or charge carrier diffusion tails, which reduces counting background and results in a considerably increased lifetime accuracy for a given number of detected photons [117, 118].

Hybrid detectors are now the most commonly used detectors in point-scanning TCSPC FLIM applications. This is due to their high quantum efficiency for GaAsP photocathodes (∼50%), their large area (compared to SPADs) and fast time resolution (20 ps) [51]. Sixteen channel version of hybrid detectors are available. The principle behind hybrid detectors has also been used to create pixelated detectors for imaging (i.e., electron-bombarded CCDs [115, 119, 120] and CMOS cameras [121, 122]) but these devices have not been modified for fast timing applications.

2.7. Superconducting Detectors

Superconducting single photon sensors are a relatively new technology. Superconducting nanowire single photon detectors, developed in 2001 [126], have potential for low jitter, short dead-time and high count rates [125]. In combination with

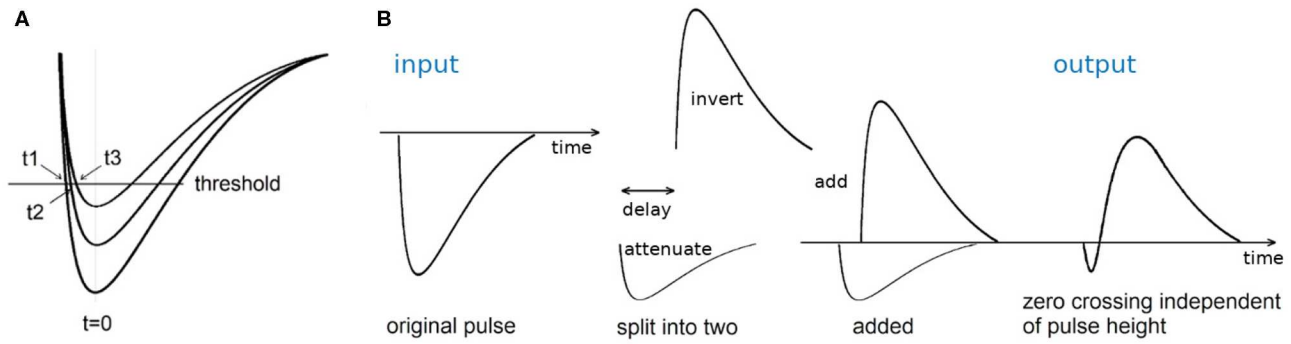

FIGURE 8 | (A) Schematic of leading edge discrimination. The fixed threshold times the pulses (all arriving at the same time t = 0) at different times t1, t2, and t3, depending on the pulse height. **(B)** Schematic of constant fraction discrimination. The original input pulse is split into two, one is attenuated, and one is delayed and inverted. The zero-crossing when the two pulses are added is independent of the pulse height.

TCSPC, an IRF of 2.7 ps has been reported, currently the shortest TCSPC IRF on record [127]. Transition edge sensors were first demonstrated in 1995 [128] and have 100 ns jitter and long dead-time making them unsuitable for fast timing applications [129]. The same is true for superconducting tunnel junction detectors, the single photon events have microsecond rise times, depending on the details of the superconducting material. They do have an intrinsic wavelength resolution, though, which is a very attractive feature. The biggest drawback of superconducting sensors is that they have to be operated at liquid helium temperature. Although they are an exciting development in the field of single photon detection, they currently find applications mostly in quantum optics, astronomy and long distance communications [129]. Consequently their development is aimed more toward the infrared wavelengths rather than visible light currently used in FLIM, to the best of our knowledge have not been used for infrared FLIM and are therefore out of scope for this review. For more information, see recent reviews [33, 34, 125, 129].

3. PHOTON TIMING TECHNOLOGY

3.1. Leading Edge and Constant Fraction Discrimination

After the electronic pulse created by a photon leaves the detector, it may pass through a pre-amplifier before it encounters some kind of discriminator. The discriminator sets the threshold for the pulse to be accepted, and shapes it for detection by the timing circuit. Leading edge discrimination sets a fixed threshold for the incoming pulse, and crossing this threshold provides the timing reference. If the pulses are of a constant amplitude, this is a feasible approach, for example for excitation laser trigger pulses. However, if the pulse height varies, then leading edge discrimination introduces an experimental uncertainty, time walk, which degrades the precision of the timing, as indicated in **Figure 8A**.

This time walk can be minimized by using a constant fraction discriminator (CFD). A CFD splits the input pulse in two, attenuates one of them, and delays and inverts the other, before they are added again, as shown in **Figure 8B**. The zero-crossing is independent of the pulse height. Therefore, for pulses for varying pulse height, as is typical for single photon detectors, a CFD minimizes the dependence of the photon arrival timing on the pulse height. The delay is chosen according to the rise time of the leading edge of the pulses to be timed.

3.2. Time-to-Amplitude Converter (TAC)/ Analog-to Digital Converter (ADC)

As the earliest photon timing technology, the TAC was derived from the delayed coincidence circuit [11]. It measures the time between a laser pulse and the arrival of a photon, and converts this time difference into a measurable voltage amplitude. A TAC typically starts charging a capacitor upon receipt of a "start" pulse, and stops charging it when a "stop" pulse arrives, such that the capacitor charge is proportional to the time elapsed between "start" and "stop." In practice, to avoid resetting the electronics after every laser pulse, TACs are usually operated in reversed start-stop mode where the arrival of the photon starts the TAC and the arrival of the next laser pulse stops it [130].

To record statistics of photon arrival times (e.g., fluorescence decays), the TAC output pulse, the height of which is proportional to the charge on the capacitor, is processed by an analog-to-digital converter (ADC). The ADC resolves the TAC voltage into a digital equivalent of the photon detection time, which is then used to address a memory location for the arrival time bin and increment it by one count. In early TCSPC systems the ADC was the bottleneck both in terms of speed and channel uniformity. This has been resolved by the development of electronics; the electronics required for TAC/ADC systems are relatively complicated, as the TAC requires a highly linear voltage ramp for precise operation, and the ADC has to be able to resolve the voltage into thousands of time channels with equal width [48, 49]. The integral non-linearity of a TAC refers to the actual length of the time window compared to what it should be according to the settings. The differential non-linearity refers to the variation of the counts from time channel to time channel, and this is typically around 1%.

Nowadays TAC/ADC systems can achieve very fast timing in the order of a few ps. In this case the photon timing capabilities

are usually limited by the timing jitter in the detector (i.e., transit time spread), and, with commonly used ps pulsed diode lasers, the optical excitation pulse width.

3.3. Time-to-Digital Converter (TDC)

TDCs are relatively new compared to TAC/ADC technology. As a fully digital system, a TDC counts clock cycles between a start and a stop pulse [131, 132]. The time resolution of a TDC is determined by the clock speed, typically from a few tens to hundreds of ps at best (e.g., a 1 GHz clock has time resolution of 1 ns). In principle, TDC time resolution can be improved by using time interpolation circuits to measure clock cycle fractions, but in this case many advantages, such as simple circuit design and short dead-time are lost.

Although timing resolution of TDCs can be worse than those of TACs, they have some advantages over the TAC/ADC technology. TDCs can have low dead-times in the 1 ns regime, and are favorable in applications where low dead-times are a priority. TDCs can in principle measure any time span, unlike a TAC which has a limited voltage range, and are more robust against environmental changes (e.g., temperature) [53].

TDCs are much easier to upscale than TAC/ADC technology. For this reason TDCs have found widespread use in SPAD arrays, and the development of this technology is expected to continue. Recently a 32-channel TCSPC system has been developed employing the hybrid integration of a custom 32 SPAD array with 32-channel active quench and time to analog converter array [87, 133, 134]. Although the fill-factor and SPAD performance are compromised by having such a large number of detectors and timing electronics on a single substrate, this detector has a TDC in each pixel with 55 ps resolution, allowing independent TCSPC in each pixel of a 32×32 pixel array simultaneously.

TAC/ADC systems, based on charging a capacitor with a constant current source [135], were and are mainly used in fluorescence spectroscopy systems, as they are a mature technology with the best timing precision and good linearity. However, they have a dead-time that does not make it feasible to time the arrival of two photons in one excitation cycle. TDC systems are based on clock cycles, and typically have a lower time resolution and higher differential and integral non-linearities than TACs, but they have a very short dead-time which allows timing of multiple photon arrivals after one excitation pulse [53]. They are also compact, and TDCs are typically the choice of timing circuit used on TCSPC-based SPAD arrays (although TACs have also been implemented [101]). For implementation in CMOS, on a SPAD array, a stable power supply, the power consumption and the heat generated by its operation, the temperature stability as well as non-uniformity across all pixels are all important considerations [135].

3.4. Streak Cameras

Streak cameras differ significantly from the other photon timing methods introduced in this review and are less common, but they are the fastest detectors available and have some uses in FLIM applications where extremely fast timing resolution is needed. Although they can photon count, they do not need TACs and ADCs or TDCs to perform the photon arrival timing, instead they convert photon arrival time into spatial position on a phosphor screen. They can be considered a more integrated or complete imaging system compared to PMTs, MCPs or SPADs which produce a pulse to be timed by appropriate separate electronics. Similar to image intensifiers, photon detection capability of a streak camera is based on electron amplification inside an MCP, but deflector plates and a voltage sweep circuit are placed between a photocathode and the MCP such that the photoelectrons liberated from the photocathode experience a deflecting voltage before hitting the MCP. The voltage experienced by the electron depends on the photon arrival time at the photocathode, therefore photons arriving at different times end up in different locations on the phosphor screen which is imaged by a camera, see **Figure 9**. This detection mode is often combined with spectral dispersion in orthogonal direction, such that the image has time distribution in one axis and spectral distribution in the other.

An obvious disadvantage is that one spatial dimension is taken up by the time axis, and the other possibly by spectral detection, so the camera is capable of measuring only one point at a time. It is possible to operate a streak camera in a line scanning mode, where the one spatial dimension in the camera images the time and the other one of the sample spatial directions, and a line is scanned across the sample for a two-dimensional image [136, 137]. Alternatively, a streak camera can be combined with a point-scanning confocal or two-photon microscope, where the time and spectral coordinates are obtained from the streak camera and the image is formed by usual point-scanning methods [138–140].

The operation of a streak camera is not necessarily based on single photon detection, although they can be operated in single photon mode [140, 141]. The voltage sweep can be adjusted for the required time resolution and dynamic range—timing resolution in the sub-ps regime is possible with this method. Wider use of streak cameras is limited by their cost, also the time

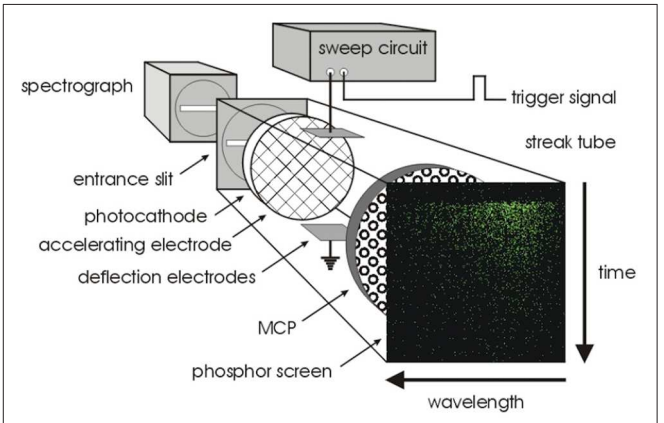

FIGURE 9 | Streak camera principle of operation. A photocathode converts photons into photoelectrons which pass through a pair of deflection plates, before being amplified and converted back into an optical image with a phosphor screen. Due to the deflection plates, timing information is converted into spatial information. Reproduced from Biskup et al. [139].

required for scanning an image and data processing to obtain a FLIM image can be lengthy.

4. FLUORESCENCE LIFETIME IMAGING

In FLIM microscopy, the timing of photons is used to build a histogram of photon arrival times—which is the fluorescence decay—in each pixel of an image, as schematically illustrated in **Figure 2A**. The decay is fitted with an exponential decay function (Equation 2) that yields the fluorescence lifetime, which is typically nanoseconds, and often depends on the microenvironment of the molecule, or the proximity of other fluorescent molecules. Therefore FLIM has found many applications, especially in the biological sciences, for monitoring the microenvironment and/or protein interaction [142–145].

When choosing a detector for FLIM, there is no simple answer for the "best" choice—this depends on the microscope and the sample. Fluorescence lifetimes are typically in the order of a few nanoseconds and in some applications IRFs of several hundred ps may be acceptable, but in order to measure complex multiexponential decays, or detect subtle changes in living specimens, fast timing of photon arrival is essential [51].

Apart from timing of individual photons, the time it takes to acquire a whole image is also very important in FLIM. For biological imaging and especially live cell applications, photon efficiency and light dose are critically important. Usually a compromise has to be found between timing accuracy, data acquisition speed and illumination light dose. FLIM methods can be generally divided into two categories: in scanning FLIM a laser beam is scanned over the image pixel by pixel and the image is recorded with a point detector (**Figure 10A**), whereas wide-field FLIM collects decays for the pixels in parallel fashion (**Figure 10B**) [47, 146].

4.1. Scanning FLIM

While the earliest fast fluorescence timing experiments were point measurements, usually measuring solutions in a cuvette, the development of laser scanning confocal microscopes [41] enabled TCSPC-based FLIM in the 1990s, and opened up new applications for FLIM in biological research. In scanning FLIM a laser beam is scanned over the image pixel by pixel, and the image is recorded with a point detector such as a PMT, SPAD or a hybrid detector. For proper analysis of the decay, a histogram is required for each pixel of the image, with good photon statistics in each pixel. The excitation repetition rate is fundamentally limited by the fluorescence lifetime to be measured so that the sample has time to decay to the ground state before a new excitation pulse, and to avoid photon pile-up, the detection rate is usually limited to 1% of the excitation repetition rate at the brightest pixel. This can make image acquisition slow, typically a few minutes per image. Scanning FLIM is widely used, and it provides the benefits of confocal or multiphoton excitation microscopy, i.e., optical sectioning, reduced background blur and reduced photobleaching outside the focal point. Combination with spectral detection or polarization is also relatively straight-forward.

One limiting factor in acquisition speed is the dead-time of the detector and the timing electronics; this is the time required to reset the electronics, during which any arriving photon will be lost. PMTs can have dead-times of several tens of ns, while SPADs and hybrid detectors have improved this to <1 ns. On TAC/ADC based systems an upper limit to the detection efficiency is usually placed by the TCSPC electronics, which have typical dead-times in the order of 100 ns. TDCs have improved this to <1 ns, albeit with considerable loss of timing resolution [51].

Today, many commercial setups for scanning FLIM use hybrid detectors combined with TAC/ADC electronics. Hybrid detectors combine the advantages of both PMTs and SPADs: they have high gain, short dead-time, and low timing jitter. TAC/ADC electronics, on the other hand, have excellent timing resolution and can achieve IRFs down to 20 ps. While the electronics dead-time is usually in the order of 100 ns, the detection count rate is typically limited by the pile-up restrictions below 1 MHz.

It is possible to improve the overall image acquisition speed by using multiple detectors [147, 148] to reduce the dead-time and distribute the photons over the detectors e.g., by spectral dispersion. Multi-point scanning with SPAD arrays has also been demonstrated [97, 98] which enables real-time imaging of a FRET-based biosensor to study cell signaling, without trade-off between speed, noise and precision [149].

4.2. Wide-Field FLIM

In wide-field FLIM, the entire sample is illuminated to produce fluorescence, and the decay for each pixel is acquired in a parallel

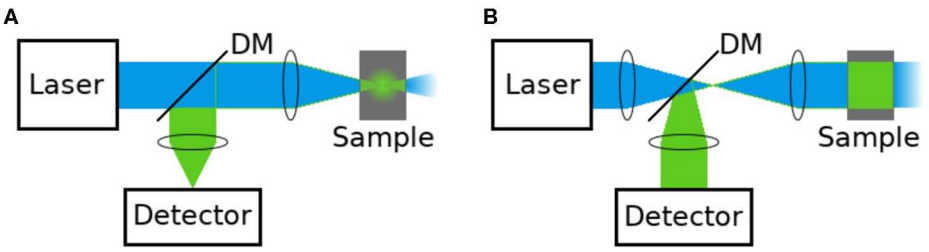

FIGURE 10 | Schematic diagram of the acquisition principle for **(A)** scanning and **(B)** wide-field FLIM. **(A)** In scanning FLIM, a focussed laser beam is raster-scanned over the image pixel by pixel to excite the fluorescence, and the photon arrival timing is performed with a point detector, separately in each pixel. **(B)** In wide-field FLIM, the entire sample is illuminated with a collimated excitation beam to excite the fluorescence, and the photon arrival timing is done with a position-sensitive detector. DM is dichroic mirror.

manner using some kind of camera, i.e., a position-sensitive detector. There are many different methods to perform wide-field FLIM, including time-gating and frequency-domain methods which are not based on timing single photons and are out of scope of this review—for more information see, for example, [20, 150, 151]. Image intensified fast cameras [152, 153], as well as a time-stamping camera, TimepixCam [154, 155], have been used for timing single photons, but the photon timing resolution of these devices is limited from nanoseconds to microseconds, and thus they are more suitable for microsecond phosphorescence lifetime imaging rather than fast timing applications for nanosecond fluorescence decays. However, the latest TimepixCam version has 1.5 ns timing resolution [155] which would be suitable for measuring fluorescence decays of tens of nanoseconds.

For wide-field single photon timing on the picosecond time scale, MCPs and SPAD arrays are the most commonly used detectors. MCPs are a mature technology, and are used in many fields of science. Similar to PMTs, MCPs are capable of high timing resolution with IRFs down to 20 ps [79]. As they provide many channels, the position information is preserved during the signal amplification process. However, the MCPs themselves do not provide positional read-out, so they need to be combined with position read-out anodes [61, 156, 157]. Many different architectures have been designed [47], but usually the position read-out restricts the detection rate to a maximum of one photon per excitation pulse. Although advanced read-out architectures can improve this [158], overall this method does not offer significant improvement to the acquisition speed over scanning methods.

SPAD arrays are a more recent development in wide-field single photon detection. Unlike MCPs where the position read-out often limits the detection rate to a maximum of 1 photon/excitation pulse, SPADs can count a photon/pixel/excitation pulse independently and therefore have potential for enormous count rates, and hence short acquisition times. The TDCs used in SPAD arrays can have an order of magnitude worse timing resolution than MCPs, but this is still acceptable for many FLIM applications where typical lifetimes are in the order of a few nanoseconds. The latest SPAD arrays can have fill factors of 50% [99], a great improvement over the megaframe SPAD arrays with 1% fill factor [97, 98], but they generally do have some non-uniformity across the array. However, these specifications are continuously improving, as this technology is currently developing at a fast pace [102, 110].

Wide-field photon counting methods are especially useful for combining FLIM with microscopy techniques that usually require a wide-field detector, such as TIRF [159] or lightsheet [160] illumination methods. They are also indispensable in live cell imaging, where the uniformly distributed, extremely low light dose enables long term observation of sensitive specimens [61, 156, 161, 162].

5. APPLICATIONS

FLIM with fast timing has a vast range of applications in many different fields of science [143, 163]. FLIM is often used for monitoring the microenvironment of living cells, such as pH [164], ion concentration (Ca^{2+}, Cl^{-}, K, Na,...) [165], viscosity [166, 167], temperature [168, 169], or oxygen levels [170, 171]. FLIM is also the most precise methods for detecting FRET, which can be used for monitoring protein interaction, tension and folding [18]. A number of reviews and textbooks have delved into more details of the technique and its concepts, its implementations, applications and data analysis methods [20, 48, 49, 51, 151, 172–181].

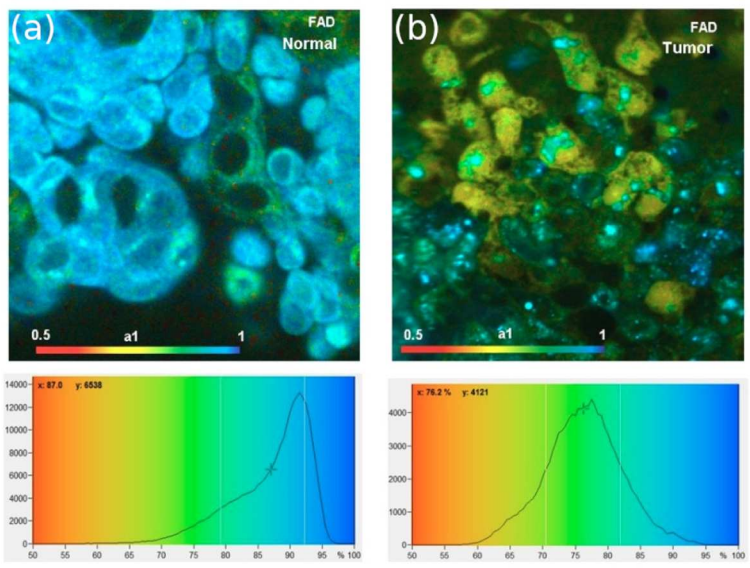

FIGURE 11 | Applications of fast scanning FLIM. **(a,b)** Metabolic state monitoring of cells with fast scanning FLIM. The images show the bound fraction of FAD, which decreases for cancer cells. Reproduced from Becker et al. [183].

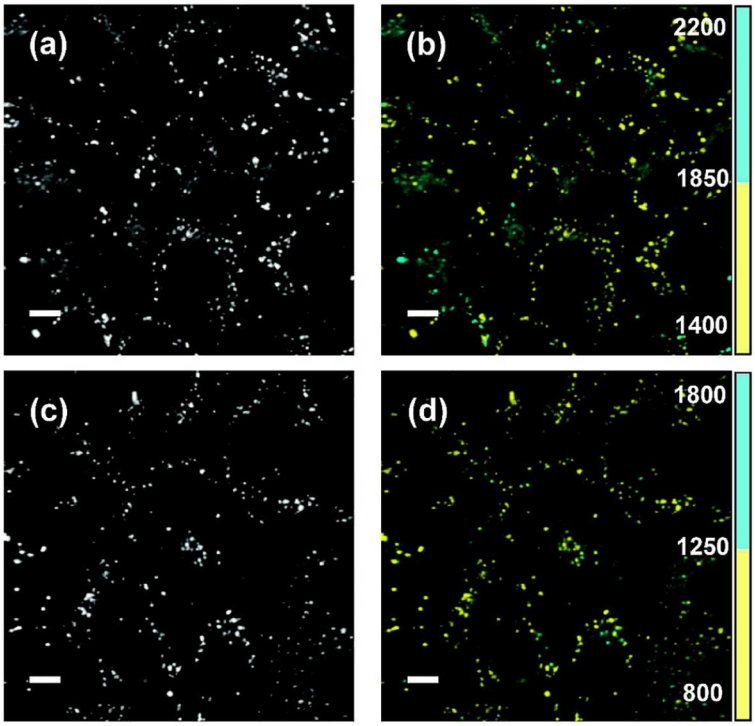

FIGURE 12 | FLIM viscosity measurement. Fluorescence intensity **(a,c)** and FLIM images **(b,d)** for live SK-OV-3 human ovarian carcinoma cells incubated with two different viscosity-sensitive dyes (bottom & top). The fluorescence lifetimes are encoded in two discrete color scales, blue for a long lifetime range, indicating a higher viscosity, and yellow for a short lifetime range, indicating a lower viscosity. The lifetime range for the fluorescent molecular rotor dyes used in **(b)** is 1,400–1,850 ps in yellow and 1,850–2,200 ps in blue, and for the dye used in **(d)** 800–1,250 ps in yellow and 1,250–1,800 ps in blue. Scale bars: 10 μm. Reproduced from [185].

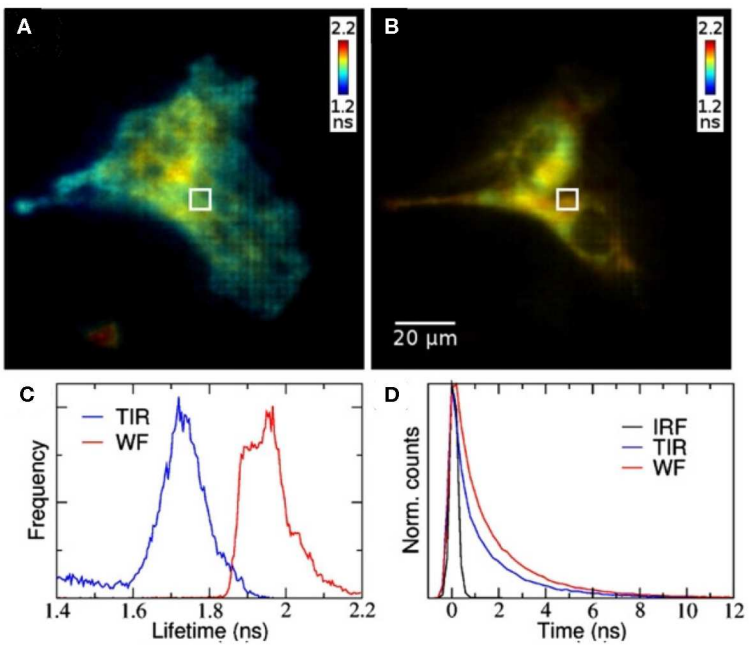

FIGURE 13 | Wide-field TCSPC-based FLIM with TIRF. **(A)** TIRF and **(B)** wide-field FLIM images of HeLa cells. **(C)** Fluorescence lifetime histograms and **(D)** representative fluorescence decays. The fluorescence lifetime difference between the images is due to selective excitation of the membrane-sensitive dye. Reproduced from Hirvonen et al. [159].

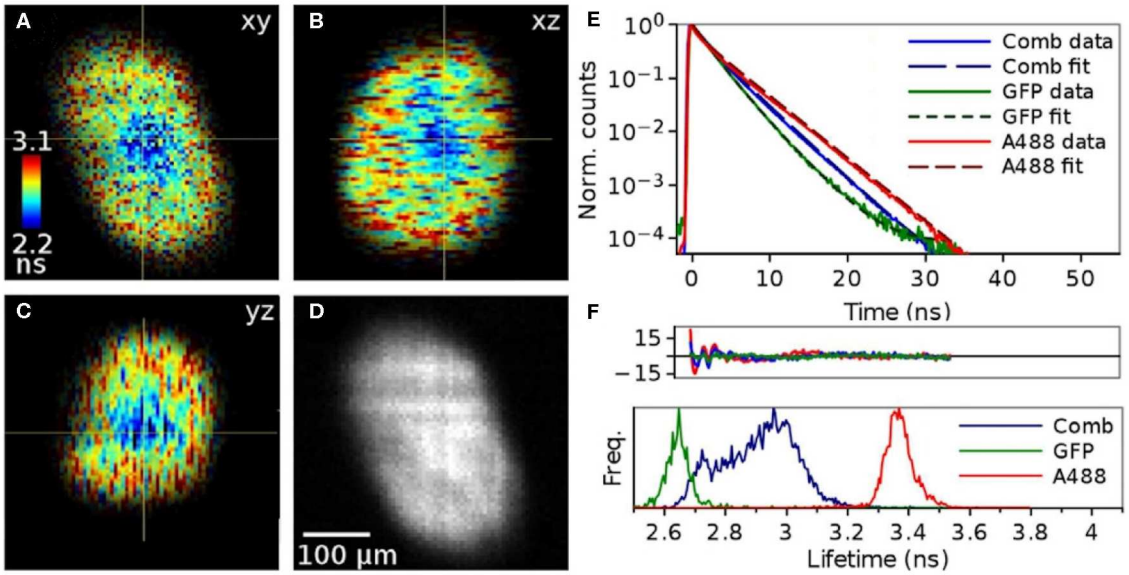

FIGURE 14 | TCSPC-based lightsheet FLIM images of cancer cell spheroids with two different fluorescent labels, one throughout the spheroid and one on the surface only. **(A)** xy FLIM image, with the color-encoded fluorescence lifetime contrast given by the color scale bar on the left, **(B)** xz FLIM image, **(C)** yz FLIM image, and **(D)** xy fluorescence intensity image, with a 100 μm scale bar to indicate spatial dimensions. **(E)** Representative fluorescence decays of samples with one or both fluorescent labels on a semi-logarithmic plot. **(F)** Fluorescence lifetime histograms of samples with one or both fluorescent labels. Reproduced from Hirvonen et al. [160].

Typical fluorescence lifetimes are on the scale of a few nanoseconds which in principle can tolerate IRF widths of a few hundred ps. However, fast ps timing accuracy helps in detecting subtle changes in the microenvironment of living cells, or changes in FRET levels, especially in applications where the overall imaging speed is also a critical parameter [149].

Commercial scanning systems are now available that routinely achieve both fast photon timing accuracy, and fast overall image acquisition times. A confocal FLIM system has been reported with IRF FWHM <25 ps, which achieves count rates of up to 20 MHz [182]. The system uses a single detector but routes the photons into four separate timing channels, thereby shortening the TCSPC electronics dead-time. This system can obtain a 256 × 256 pixel FLIM image in about 0.5 s.

This type of system has been used, for example, for monitoring the metabolic state in living cells [183], see **Figure 11**. This approach allows for an optical biopsy to be obtained, to assess cells for possible signs of disease, without employing mechanical methods for tissue removal or chemical methods for analysis. This so-called autofluorescence FLIM (because the sample does not need to be stained with fluorescence dyes, the intrinsic fluorescence of cells is used) is used for clinical diagnostics of skin [184]. Two lasers were multiplexed to alternatingly excite the endogenous fluorophores NAD(P)H and FAD which provide a read-out of the metabolic state, detected in two FLIM channels. Information on the metabolic state was derived from the fluorescence decays of NAD(P)H and FAD, which both have a fast few 100 ps and a slow ns scale component corresponding to bound and unbound fractions. A fast FLIM system is able to detect subtle changes in the component amplitude ratios and therefore changes in the metabolic state of the cells.

FLIM has also been used for monitoring viscosity in living cells using viscosity-sensitive fluorescent molecular rotor dyes [185], see **Figure 12**. Viscosity is the resistance of a fluid to flow, and is a key parameter determining chemical or biochemical reaction rates. Traditionally, bulk viscosity is measured by mechanical methods, but the use of fluorescent molecular rotors allows optical viscosity measurements. For this approach, only a very small sample is needed, and in combination with fluorescence microscopy and FLIM allows mapping viscosity on a micrometer scale, for example in living cells and their organelles [186].

The FLIM examples in **Figures 11** and **12** are based on raster scanning a single point across the image, and performing TCSPC in each pixel separately, and, depending on the circumstances, it typically takes minutes to acquire a sufficient amount of photons for fluorescence decay analysis. The imaging speed can be improved by multi-point scanning. An 8 × 8 beamlet array was used to illuminate a sample, with a 32 × 32 pixel SPAD array detecting the emission from the spots excited by these beamlets with 55 ps timing resolution. Each beamlet scanned a 32 × 32 pixel area, producing a final image with 256 × 256 pixels. The original system had image acquisition time of 10 s / optical slice, the authors were able to detect FRET and calculate differences in cell biochemistry between sample [97, 98]. An improved version was able to image four optical planes simultaneously with 4 × 4 beamlets in each optical plane, improving overall acquisition speed by a factor of 64 compared to conventional scanning FLIM [187]. With a more powerful laser, the generation of 32 × 32

beamlets could allow 8 × 8 beamlet acquisition of 16 individual planes simultaneously.

In wide-field TCSPC imaging, MCPs provide excellent timing resolution, but they need to be combined with a position-sensitive read-out [61, 156, 157]. Recently an MCP detector with picosecond timing resolution was combined with a delay line anode for position-sensitive read-out, and this detector combined with fluorescence microscopy techniques that are difficult to implement with scanning technologies [188].

TIRF microscopy is a method where an evanescent wave, created by reflection of an excitation beam via total internal reflection on a microscope cover slip, penetrates a few hundred nanometers into the sample. This technique is typically used to excite dyes or fluorescent proteins in or near membranes close to the coverslip, without creating background fluorescence from regions inside the cell. TIRF images are usually recorded with a camera, rather than raster scanning. **Figure 13** shows a comparison of TIRF (left) and wide-field (right) fluorescence lifetime images of HeLa cells where the lifetime difference between the images is due to a membrane-sensitive dye [159]. The TCSPC-based wide-field FLIM approach for TIRF relies on the crossed delay line anode detector, which provides spatial and timing information for each detected photon.

Lightsheet fluorescence microscopy is another microscopy approach which is typically carried out using a camera. **Figure 14** shows lightsheet FLIM images of cancer cell spheroids with two different fluorescent labels, one throughout the spheroid and one on the surface only [160]. Again, without a position-sensitive detector with picosecond time resolution, TCSPC-based lightsheet FLIM is hard to perform.

6. CONCLUSIONS

FLIM is a widely used imaging technique in the life sciences which allows not only the localization of fluorophores, but also the monitoring of their microenvironment and their interaction, typically via their nanosecond fluorescence decay. Photon counting methods allow the measurement of photon arrival time with picosecond time resolution. Both detectors and electronics play a critical role in fast timing of photons. From the detector side, transit time spread in the signal amplification process is a critical parameter for fast timing, whereas low dead-time and high detection efficiency are also important in fluorescence applications. For timing, the mature TAC/ADC technology can now achieve timing accuracy of a few ps, and is the most precise technology to use for fast timing applications. TDCs are a newer technology, whose timing capabilities are still limited to tens of ps by clock speeds, but they are easier to produce, more robust against environmental variations and easier to upscale, for example, to use in megapixel detector array technology for SPADs and SiPMs.

For fluorescence measurements, TCSPC has the best signal-to-noise ratio of the standard time-resolved imaging methods, and is accurate enough to allow multi-exponential fluorescence decay fitting. The extremely low illumination intensity, distributed evenly over the field of view, is beneficial especially in life science applications where it allows long-term monitoring of living cells and organisms. The development of fast TCSPC methods will also benefit fields where single photon or particle time-of-flight measurements are required, for example LIDAR, neutron imaging ion velocity mapping or photon correlation techniques.

AUTHOR CONTRIBUTIONS

All authors listed have made a substantial, direct and intellectual contribution to the work, and approved it for publication.

FUNDING

KS acknowledges funding from BBSRC (BB/R004803/1).

REFERENCES

1. Bradley J. IV. A letter from the Reverend Mr. James Bradley Savilian Professor of Astronomy at Oxford, and F. R. S. to Dr. Edmond Halley Astronom. Reg. &c. giving an Account of a new discovered Motion of the Fix'd Stars. *Philos T R Soc*. (1728) **35**:637–61. doi: 10.1098/rstl.1727.0064
2. Maxwell JC. VIII. A dynamical theory of the electromagnetic field. *Philos T R Soc*. (1865) **155**:459–512. doi: 10.1098/rstl.1865.0008
3. Wheatstone C, Faraday M. An account of some experiments to measure the velocity of electricity and the duration of electric light. *Philos T R Soc*. (1834) **124**:583–91. doi: 10.1098/rstl.1834.0031
4. Einstein A. Über einen die Erzeugung und Verwandlung des Lichtes betreffenden heuristischen Gesichtspunkt. Ann Phys. (1905) **322**:132–48. doi: 10.1002/andp.19053220607
5. Lewis GN. The conservation of photons. Nature. (1926) **118**:874–5. doi: 10.1038/118874a0
6. Roychoudhuri C, Kracklauer AF, Creath K. The Nature of Light: What Is a Photon? Boca Raton, FL: CRC Press (2008).
7. Hertz H. Ueber einen Einfluss des ultravioletten Lichtes auf die electrische Entladung. Ann Phys. (1887) **267**:983–1000. doi: 10.1002/andp.18872670827
8. Austin L, Starke H. Ueber die Reflexion der Kathodenstrahlen und eine damit verbundene neue Erscheinung secundärer Emission. *Ann Phys*. (1902) **314**:271–292. doi: 10.1002/andp.19023141003
9. Bothe W, Kolhörster W. Das Wesen der Höhenstrahlung. *Z Phys*. (1929) **56**:751–77. doi: 10.1007/BF01340137
10. Rossi B. Method of registering multiple simultaneous impulses of several Geiger's counters. Nature. (1930) **125**:636–6. doi: 10.1038/125636a0
11. Rossi B, Nereson N. Experimental determination of the disintegration curve of mesotrons. *Phys Rev*. (1942) **62**:417–22. doi: 10.1103/PhysRev.62.417
12. Bell RE, Graham RL, Petch HE. Design and use of a coincidence circuit of short resolving time. *Can J Phys*. (1952) **30**:35–52. doi: 10.1139/p52-004
13. Lundby A. Scintillation decay times. *Phys Rev*. (1950) **80**:477. doi: 10.1103/PhysRev.80.477
14. Bollinger LM, Thomas GE. Measurement of the time dependence of scintillation intensity by a delayed-coincidence method. *Rev Sci Instrum*. (1961) **32**:1044. doi: 10.1063/1.1717610
15. O'Connor DV, Phillips D. Time-Correlated Single-Photon Counting. New York, NY: Academic Press (1984).
16. Lakowicz JR. *Principles of Fluorescence Spectroscopy*. 3rd edn. New York, NY: Springer (2006). doi: 10.1007/978-0-387-46312-4

17. Toptygin D. Effects of the solvent refractive index and its dispersion on the radiative decay rate and extinction coefficient of a fluorescent solute. *J Fluoresc*. (2003) **13**:201–19. doi: 10.1023/A:1025033731377
18. Algar WR, Hildebrandt N, Vogel SS, Medintz IL. FRET as a biomolecular research tool - understanding its potential while avoiding pitfalls. *Nat Methods*. (2019) **16**:815–29. doi: 10.1038/s41592-019-0530-8
19. Esposito A. How many photons are needed for FRET imaging? *Biomed Opt Express*. (2020) **11**:1186–1202. doi: 10.1364/BOE.379305
20. Gadella TWJ, editor. FRET and FLIM Techniques. Amsterdam, Boston, MA: Elsevier (2009).
21. Schuyler R, Isenberg I. A monophoton fluorometer with energy discrimination. *Rev Sci Instrum*. (1971) **42**:813–7. doi: 10.1063/1.1685237
22. Bachrach RZ. A photon counting apparatus for kinetic and spectral measurements. *Rev Sci Instrum*. (1972) **43**:734. doi: 10.1063/1.1685743
23. Binkert T, Tschanz HP, Zinsli PE. The measurement of fluorescence decay curves with the single-photon counting method and the evaluation of rate parameters. *J Lumin*. (1972) **5**:187–217. doi: 10.1016/0022-2313(72)90041-5
24. Lewis C, Ware WR, Doemeny LJ, Nemzek TL. The measurement of short-lived fluorescence decay using the single photon counting method. *Rev Sci Instrum*. (1973) **44**:107–14. doi: 10.1063/1.1686062
25. Phillips D. A lifetime in photochemistry; some ultrafast measurements on singlet states. Philos R Soc Lond A Mat. (2016) **472**:20160102. doi: 10.1098/rspa.2016.0102
26. Previte MJR, Zhou C, Kellinger M, Pantoja R, Chen CY, Shi J, et al. DNA sequencing using polymerase substrate-binding kinetics. *Nat Commun*. (2015) **6**:5936. doi: 10.1038/ncomms6936
27. Hemmati H. Interplanetary laser communications. *Opt Photon News*. (2007) **18**:22–7. doi: 10.1364/OPN.18.11.000022
28. Buller GS, Wallace AM. Ranging and three-dimensional imaging using time-correlated single-photon counting and point-by-point acquisition. *IEEE J Sel Top Quant*. (2007) **13**:1006–15. doi: 10.1109/JSTQE.2007.902850
29. McCarthy A, Collins RJ, Krichel NJ, Fernández V, Wallace AM, Buller GS. Long-range time-of-flight scanning sensor based on high-speed time-correlated single-photon counting. *Appl Optics*. (2009) **48**:6241. doi: 10.1364/AO.48.006241
30. Turgeman L, Fixler D. Time-averaged fluorescence intensity analysis in fluorescence fluctuation polarization sensitive experiments. *Biomed Opt Express*. (2013) **4**:868–84. doi: 10.1364/BOE.4.000868
31. Schmidt FEW, Fry ME, Hillman EMC, Hebden JC, Delpy DT. A 32-channel time-resolved instrument for medical optical tomography. *Rev Sci Instrum*. (2000) **71**:256–65. doi: 10.1063/1.1150191
32. Buller GS, Collins RJ. Single-photon generation and detection. *Meas Sci Technol*. (2010) **21**:012002. doi: 10.1088/0957-0233/21/1/012002
33. Hadfield RH. Single-photon detectors for optical quantum information applications. *Nat Photonics*. (2009) **3**:696–705. doi: 10.1038/nphoton.2009.230
34. Eisaman MD, Fan J, Migdall A, Polyakov SV. Single-photon sources and detectors. *Rev Sci Instrum*. (2011) **82**:071101. doi: 10.1063/1.3610677
35. Fraser GW, Pearson JF. The direct detection of thermal neutrons by imaging microchannel plate detectors. *Nuclear Instrum Methods A*. (1990) **293**:569–74. doi: 10.1016/0168-9002(90)90325-Z
36. Tremsin AS, McPhate JB, Vallerga JV, Siegmund OHW, Feller WB, Lehmann E, et al. Neutron radiography with sub-15 micron resolution through event centroiding. *Nuclear Instrum Methods A*. (2012) **688**:32–40. doi: 10.1016/j.nima.2012.06.005
37. Vallance C, Brouard M, Lauer A, Slater CS, Halford E, Winter B, et al. Fast sensors for time-of-flight imaging applications. *Phys Chem Chem Phys*. (2014) **16**:383–95. doi: 10.1039/C3CP53183J
38. Dinu L, Eppink ATJB, Rosca-Pruna F, Offerhaus HL, van der Zande WJ, Vrakking MJJ. Application of a time-resolved event counting technique in velocity map imaging. *Rev Sci Instrum*. (2002) **73**:4206–4213. doi: 10.1063/1.1520732
39. Strasser D, Urbain X, Pedersen HB, Altstein N, Heber O, Wester R, et al. An innovative approach to multiparticle three-dimensional imaging. *Rev Sci Instrum*. (2000) **71**:3092–3098. doi: 10.1063/1.1305514
40. Seitz P, Theuwissen AJP. Single Photon Imaging. Heidelberg: Springer (2011). doi: 10.1007/978-3-642-18443-7
41. Amos WB, White JG. How the confocal laser scanning microscope entered biological research. *Biol Cell*. (2003) **95**:335–42. doi: 10.1016/S0248-4900(03)00078-9
42. Bugiel I, König K, Wabnitz H. Investigation of cells by fluorescence laser scanning microscopy with subnanosecond time resolution. *Lasers Life Sci*. (1989) **3**:47–53.
43. Morgan CG, Mitchell AC, Murray JG. Nanosecond time-resolved fluorescence microscopy: principles and practice. *Proc R Microscop Soc*. (1990) **1**:463–66.
44. Wang XF, Periasamy A, Herman B, Coleman DM. Fluorescence lifetime imaging microscopy (FLIM): instrumentation and applications. *Crit Rev Anal Chem*. (1992) **23**:369–95. doi: 10.1080/10408349208051651
45. Gadella TWJ, Jovin TM, Clegg RM. Fluorescence lifetime imaging microscopy (FLIM): spatial resolution of microstructures on the nanosecond time scale. *Biophys Chem*. (1993) **48**:221–39. doi: 10.1016/0301-4622(93)85012-7
46. Becker W, Bergmann A, Hink MA, König K, Benndorf K, Biskup C. Fluorescence lifetime imaging by time-correlated single-photon counting. Microsc Res Tech. (2004) **63**:58–66. doi: 10.1002/jemt.10421
47. Hirvonen LM, Suhling K. Wide-field TCSPC: methods and applications. *Meas Sci Technol*. (2017) **28**:012003. doi: 10.1088/1361-6501/28/1/012003
48. Becker W. Advanced Time-Correlated Single Photon Counting Techniques. Berlin; Heidelberg: Springer (2005). doi: 10.1007/3-540-28882-1
49. Becker W. *Advanced Time-Correlated Single Photon Counting Applications*. Vol. 111. Cham: Springer International Publishing (2015). doi: 10.1007/978-3-319-14929-5
50. Kalisz J. Review of methods for time interval measurements with picosecond resolution. *Meterologia*. (2003) **41**:17–32. doi: 10.1088/0026-1394/41/1/004
51. Liu X, Lin D, Becker W, Niu J, Yu B, Liu L, et al. Fast fluorescence lifetime imaging techniques: a review on challenge and development. *J Innov Opt Heal Sci*. (2019) **12**:1930003. doi: 10.1142/S1793545819300039
52. Birch DJS, Imhof RE. Time-Domain Fluorescence Spectroscopy Using Time-Correlated Single-Photon Counting. In: Lakowicz JR, editor. *Topics in Fluorescence Spectroscopy: Techniques*. Boston, MA: Springer (1999). p. 1–95. doi: 10.1007/0-306-47057-8_1
53. Wahl M. Modern TCSPC electronics: principles and acquisition modes. In: Kapusta P, Wahl M, Erdmann R, editors. *Advanced Photon Counting. Springer Series on Fluorescence (Methods and Applications)*. Cham: Springer (2014). p. 15.
54. Iams H, Salzberg B. The secondary emission phototube. *Proc IRE*. (1935) **23**:55–64. doi: 10.1109/JRPROC.1935.227243
55. Kubetsky LA. Multiple amplifier. *Proc IRE*. (1937) **25**:421–33. doi: 10.1109/JRPROC.1937.229045
56. Zworykin VK, Morton GA, Malter L. The secondary emission multiplier-a new electronic device. *Proc IRE*. (1936) **24**:351–75. doi: 10.1109/JRPROC.1936.226435
57. Allen JS. The detection of single positive ions, electrons and photons by a secondary electron multiplier. *Phys Rev*. (1939) **55**:966–71. doi: 10.1103/PhysRev.55.966
58. Candy BH. Photomultiplier characteristics and practice relevant to photon counting. *Rev Sci Instrum*. (1985) **56**:183–93. doi: 10.1063/1.1138327
59. Hungerford G, Birch DJS. Single-photon timing detectors for fluorescence lifetime spectroscopy. *Meas Sci Technol*. (1996) **7**:121. doi: 10.1088/0957-0233/7/2/002
60. Michalet X, Siegmund OH, Vallerga JV, Jelinsky P, Millaud JE, Weiss S. Detectors for single-molecule fluorescence imaging and spectroscopy. *J Mod Opt*. (2007) **54**:239. doi: 10.1080/09500340600769067
61. Michalet X, Colyer RA, Scalia G, Ingargiola A, Lin R, Millaud JE, et al. Development of new photon-counting detectors for single-molecule fluorescence microscopy. *Philos T R Soc B*. (2013) **368**:1611. doi: 10.1098/rstb.2012.0035
62. van Meurs B, van der Werf R. A circuit for rejecting multiple events detected during a timing cycle in single photon counting experiments. *J Phys E Sci Instrum*. (1976) **9**:437–8. doi: 10.1088/0022-3735/9/6/005
63. Fukuda S, Fukuda Y, Hayakawa T, Ichihara E, Ishitsuka M, Itow Y, et al. The Super-Kamiokande detector. *Nuclear Instrum Methods A*. (2003) **501**:418–462. doi: 10.1016/S0168-9002(03)00425-X

64. Bird DK, Eliceiri KW, Fan CH, White JG. Simultaneous two-photon spectral and lifetime fluorescence microscopy. *Appl Opt*. (2004) **43**:5173–82. doi: 10.1364/AO.43.005173
65. Biskup C, Zimmer T, Kelbauskas L, Hoffmann B, Klocker N, Becker W, et al. Multi-dimensional fluorescence lifetime and FRET measurements. *Microsc Res Tech*. (2007) **70**:442–51. doi: 10.1002/jemt.20431
66. Farnsworth PT. Electron Multiplier (1934). US Patent 1969399.
67. Wiley WC, Hendee CF. Electron multipliers utilizing continuous strip surfaces. *IRE T Nuclear Sci*. (1962) **9**:103–6. doi: 10.1109/TNS2.1962.4315981
68. Goodrich GW, Wiley WC. Continuous channel electron multiplier. *Rev Sci Instrum*. (1962) **33**:761. doi: 10.1063/1.1717958
69. Lampton M. The microchannel image intensifier. *Sci Am*. (1981) **245**:62–71. doi: 10.1038/scientificamerican1181-62
70. Siegmund OHW, Vallerga JV, Tremsin AS, McPhate J, Michalet X, Colyer RA, et al. Microchannel plate imaging photon counters for ultraviolet through NIR detection with high time resolution. *Proc SPIE*. (2011) **8033**:80330V-12. doi: 10.1117/12.884271
71. Siegmund OHW. High-performance microchannel plate detectors for UV/visible astronomy. *Nuclear Instrum Methods A*. (2004) **525**:12–6. doi: 10.1016/j.nima.2004.03.018
72. Wang X, Setru SU, Xie J, Mane A, Demarteau M, Wagner R. Imaging of large-area microchannel plates using phosphor screens. *J Instrum*. (2014) **9**:P11011. doi: 10.1088/1748-0221/9/11/P11011
73. Boksenberg A. Advances in detectors for astronomical spectroscopy. Philos T R Soc S A. (1982) **307**:531–48. doi: 10.1098/rsta.1982.0128
74. Kröger HW, Schmidt GK, Pailer N. Faint object camera: European contribution to the Hubble Space Telescope. *Acta Astronaut*. (1992) **26**:827–34. doi: 10.1016/0094-5765(92)90063-O
75. Mason KO, Breeveld A, Much R, Carter M, Cordova FA, Cropper MS, et al. The XMM-Newton optical/UV monitor telescope. *Astron Astrophys*. (2001) **365**:L36–44. doi: 10.1051/0004-6361:20000044
76. Roming PW, Kennedy TE, Mason KO, et al. The swift ultra-violet/optical telescope. *Space Sci Rev*. (2005) **120**:95–42. doi: 10.1007/s11214-005-5095-4
77. Siegmund OHW, Welsh BY, Martin C, et al. The GALEX mission and detectors. *Proc SPIE*. (2004) **5488**:13–24. doi: 10.1117/12.561488
78. Conti L, Barnstedt J, Hanke L, Kalkuhl C, Kappelmann N, Rauch T, et al. MCP detector development for UV space missions. *Astrophys Space Sci*. (2018) **363**:63. doi: 10.1007/s10509-018-3283-4
79. Tremsin AS, Vallerga JV, Siegmund OHW. Overview of spatial and timing resolution of event counting detectors with Microchannel Plates. *Nuclear Instrum Methods A*. (2020) **949**:162768. doi: 10.1016/j.nima.2019.162768
80. Franco A, Geissbühler J, Wyrsch N, Ballif C. Fabrication and characterization of monolithically integrated microchannel plates based on amorphous silicon. *Sci Rep*. (2014) **4**:4597. doi: 10.1038/srep04597
81. Ertley CD, Siegmund OHW, Hull J, Tremsin A, O'Mahony A, Craven CA, et al. Microchannel plate imaging detectors for high dynamic range applications. *IEEE T Nuclear Sci*. (2017) **64**:1774–80. doi: 10.1109/TNS.2017.2652222
82. Louis T, Schatz GH, Klein-Bölting P, Holzwarth AR, Ripamonti G, Cova S. Performance comparison of a single-photon avalanche diode with a microchannel-plate photomultiplier in time-correlated single-photon counting. *Rev Sci Instrum*. (1988) **59**:1148–52. doi: 10.1063/1.1140258
83. Ceccarelli F, Acconcia G, Gulinatti A, Ghioni M, Rech I. Fully integrated active quenching circuit driving custom-technology SPADs with 6.2-ns dead time. *IEEE Photon Tech*. (2019) **31**:102–5. doi: 10.1109/LPT.2018.2884740
84. Charbon E. Single-photon imaging in complementary metal oxide semiconductor processes. *Philos T R Soc A*. (2014) **372**:20130100. doi: 10.1098/rsta.2013.0100
85. Charbon E, Fishburn M, Walker R, Henderson RK, Niclass C. SPAD-based sensors. In: Remondino F, Stoppa D, editors. *TOF Range-Imaging Cameras*. Berlin; Heidelberg: Springer (2013). p. 11–38. doi: 10.1007/978-3-642-27523-4_2
86. Colyer RA, Scalia G, Rech I, Gulinatti A, Ghioni M, Cova S, et al. High-throughput FCS using an LCOS spatial light modulator and an 8 × 1 SPAD array. *Biomed Opt Express*. (2010) **1**:1408–31. doi: 10.1364/BOE.1.001408
87. Cuccato A, Antonioli S, Crotti M, Labanca I, Gulinatti A, Rech I, et al. Complete and compact 32-channel system for time-correlated single-photon counting measurements. *IEEE Photon J*. (2013) **5**:6801514. doi: 10.1109/JPHOT.2013.2284250
88. Krstajić N, Levitt J, Poland S, Ameer-Beg S, Henderson R. 256 x 2 SPAD line sensor for time resolved fluorescence spectroscopy. *Opt Express*. (2015) **23**:5653–69. doi: 10.1364/OE.23.005653
89. Burri S, Homulle H, Bruschini C, Charbon E. LinoSPAD: a time-resolved 256x1 CMOS SPAD line sensor system featuring 64 FPGA-based TDC channels running at up to 8.5 giga-events per second. In: Berghmans F, Mignani AG, editors. Optical Sensing Detection IV. Vol. 9899. International Society for Optics and Photonics. *Proc SPIE*. (2016). p. 57–66. doi: 10.1117/12.2227564
90. Kufcsák A, Erdogan A, Walker R, Ehrlich K, Tanner M, Megia-Fernandez A, et al. Time-resolved spectroscopy at 19,000 lines per second using a CMOS SPAD line array enables advanced biophotonics applications. *Opt Express*. (2017) **25**:11103–23. doi: 10.1364/OE.25.011103
91. Erdogan AT, Walker R, Finlayson N, Krstajić N, Williams G, Girkin J, et al. A CMOS SPAD line sensor with per-pixel histogramming TDC for time-resolved multispectral imaging. *IEEE J Solid Circ*. (2019) **54**:1705–19. doi: 10.1109/JSSC.2019.2894355
92. Veerappan C, Richardson J, Walker R, Li D, Fishburn MW, Maruyama Y, et al. A 160–128 single-photon image sensor with on-pixel 55ps 10b time-to-digital converter. In: 2011 IEEE International Solid-State Circuits Conference (2011). p. 312–4. doi: 10.1109/ISSCC.2011.5746333
93. Field RM, Realov S, Shepard KL. A 100 fps, time-correlated single-photon-counting-based fluorescence-lifetime imager in 130 nm CMOS. *IEEE J Solid Circ*. (2014) **49**:867–80. doi: 10.1109/JSSC.2013.2293777
94. Tamborini D, Buttafava M, Ruggeri A, Zappa F. Compact, low-power and fully reconfigurable 10 ps resolution, 160 μ range, time-resolved single-photon counting system. *IEEE Sens J*. (2016) **16**:3827–33. doi: 10.1109/JSEN.2016.2535403
95. Krstajić N, Poland S, Levitt J, Walker R, Erdogan A, Ameer-Beg S, et al. 0.5 billion events per second time correlated single photon counting using CMOS SPAD arrays. *Opt Lett*. (2015) **40**:4305–8. doi: 10.1364/OL.40.004305
96. Ulku A, Ardelean A, Antolovic M, Weiss S, Charbon E, Bruschini C, et al. Wide-field time-gated SPAD imager for phasor-based FLIM applications. *Methods Appl Fluoresc*. (2020) **8**:024002. doi: 10.1088/2050-6120/ab6ed7
97. Poland SP, Krstajić N, Coelho S, Tyndall D, Walker RJ, Devauges V, et al. Time-resolved multifocal multiphoton microscope for high speed FRET imaging *in vivo*. *Opt Lett*. (2014) **39**:6013–6. doi: 10.1364/OL.39.006013
98. Poland SP, Krstajić N, Monypenny J, Coelho S, Tyndall D, Walker RJ, et al. A high speed multifocal multiphoton fluorescence lifetime imaging microscope for live-cell FRET imaging. *Biomed Opt Express*. (2015) **6**:277–96. doi: 10.1364/BOE.6.000277
99. Hutchings SW, Johnston N, Gyongy I, Abbas TA, Dutton NAW, Tyler M, et al. A Reconfigurable 3-D-stacked SPAD imager with in-pixel histogramming for flash LIDAR or high-speed time-of-flight imaging. *IEEE J Solid Circ*. (2019) **54**:2947–56. doi: 10.1109/JSSC.2019.2939083
100. Gyongy I, Calder N, Davies A, Dutton NAW, Duncan RR, Rickman C, et al. A 256 × 256, 100-kfps, 61
101. Parmesan L, Dutton N, Krstajic N, Calder N, Holmes A, Grant LA, et al. A 256 x 256 SPAD array with in-pixel Time to Amplitude Conversion for Fluorescence Lifetime Imaging Microscopy. In: Frontiers in Optics. OSA; 2015.
102. Bruschini C, Homulle H, Antolovic IM, Burri S, Charbon E. Single-photon SPAD imagers in biophotonics: review and outlook. *Light Sci Appl*. (2019) **8**:87. doi: 10.1038/s41377-019-0191-5
103. Acerbi F, Gundacker S. Understanding and simulating SiPMs. *Nuclear Instrum Methods A*. (2019) **926**:16–35. doi: 10.1016/j.nima.2018.11.118
104. Klanner R. Characterisation of SiPMs. *Nuclear Instrum Methods A*. (2019) **926**:36–56. doi: 10.1016/j.nima.2018.11.083
105. Piemonte C, Gola A. Overview on the main parameters and technology of modern Silicon Photomultipliers. *Nuclear Instrum Methods A*. (2019) **926**:2–15. doi: 10.1016/j.nima.2018.11.119
106. Martinenghi E, Di Sieno L, Contini D, Sanzaro M, Pifferi A, Dalla Mora A. Time-resolved single-photon detection module based on silicon

photomultiplier: a novel building block for time-correlated measurement systems. *Rev Sci Instrum*. (2016) **87**:073101. doi: 10.1063/1.4954968
107. Rech I, Ingargiola A, Spinelli R, Labanca I, Marangoni S, Ghioni M, et al. Optical crosstalk in single photon avalanche diode arrays: a new complete model. *Opt Express*. (2008) **16**:8381–94. doi: 10.1364/OE.16.008381
108. Nagy F, Mazzillo M, Renna L, Valvo G, Sanfilippo D, Carbone B, et al. Afterpulse and delayed crosstalk analysis on a STMicroelectronics silicon photomultiplier. *Nuclear Instrum Methods A*. (2014) **759**:44–49. doi: 10.1016/j.nima.2014.04.045
109. Xu H, Pancheri L, Braga LHC, Betta GFD, Stoppa D. Crosstalk characterization of single-photon avalanche diode (SPAD) arrays in CMOS 150nm technology. *Proc Eng*. (2014) **87**:1270–3. doi: 10.1016/j.proeng.2014.11.417
110. Henderson RK, Johnston N, Mattioli Della Rocca F, Chen H, Li DDU, Hungerford G, et al. A 192 × 128 time correlated SPAD image sensor in 40-nm CMOS technology. *IEEE J Solid Circ*. (2019) **54**:1907–16. doi: 10.1109/JSSC.2019.2905163
111. Caccia M, Nardo L, Santoro R, Schaffhauser D. Silicon photomultipliers and SPAD imagers in biophotonics: advances and perspectives. *Nuclear Instrum Methods A*. (2019) **926**:101–17. doi: 10.1016/j.nima.2018.10.204
112. Li DU, Bonnist E, Renshaw D, Henderson R. On-chip, time-correlated, fluorescence lifetime extraction algorithms and error analysis. *J Opt Soc Am A*. (2008) **25**:1190–8. doi: 10.1364/JOSAA.25.001190
113. Li DU, Arlt J, Richardson J, Walker R, Buts A, Stoppa D, et al. Real-time fluorescence lifetime imaging system with a 32 × 32 0.13μm CMOS low dark-count single-photon avalanche diode array. *Opt Express*. (2010) **18**:10257–69. doi: 10.1364/OE.18.010257
114. Poland SP, Erdogan AT, Krstajić N, Levitt J, Devauges V, Walker RJ, et al. New high-speed centre of mass method incorporating background subtraction for accurate determination of fluorescence lifetime. *Opt Express*. (2016) **24**:6899–915. doi: 10.1364/OE.24.006899
115. Hirvonen LM, Jiggins S, Sergent N, Zanda G, Suhling K. Photon counting imaging with an electron-bombarded CCD: towards a parallel-processing photoelectronic time-to-amplitude converter. *Rev Sci Instrum*. (2014) **85**:123102. doi: 10.1063/1.4901935
116. Hirvonen L, Suhling K. Photon counting imaging with an electron-bombarded pixel image sensor. *Sensors*. (2016) **16**:617. doi: 10.3390/s16050617
117. Becker W, Su B, Holub O, Weisshart K. FLIM and FCS detection in laser-scanning microscopes: increased efficiency by GaAsP hybrid detectors. *Microsc Res Tech*. (2011) **74**:804–11. doi: 10.1002/jemt.20959
118. Michalet X, Cheng A, Antelman J, Suyama M, Arisaka K, Weiss S. Hybrid photodetector for single-molecule spectroscopy and microscopy. *Proc SPIE*. (2008) **6862**:F8620. doi: 10.1117/12.763449
119. Hirvonen LM, Jiggins S, Sergent N, Zanda G, Suhling K. Photon counting imaging with an electron-bombarded CCD: towards wide-field time-correlated single photon counting (TCSPC). *Nuclear Instrum Methods A*. (2015) **787**:323–7. doi: 10.1016/j.nima.2015.01.031
120. Hirvonen LM, Barber MJ, Suhling K. Photon counting imaging and centroiding with an EBCCD using single molecule localisation software. *Nuclear Instrum Methods A*. (2016) **820**:121–5. doi: 10.1016/j.nima.2016.03.024
121. Barbier R, Baudot J, Chabanat E, et al. Performance study of a MegaPixel single photon position sensitive photodetector EBCMOS. *Nuclear Instrum Methods A*. (2009) **610**:54–6. doi: 10.1016/j.nima.2009.05.054
122. Barbier R, Cajgfinger T, Calabria P, et al. A single-photon sensitive ebCMOScamera: the LUSIPHER prototype. *Nuclear Instrum Methods A*. (2011) **648**:266–74. doi: 10.1016/j.nima.2011.04.018
123. Hamamatsu Photonics K. K. *Photomultiplier Tubes*. 3rd ed. Electron Tube Division (2006).
124. Fisher EMD. Photon counting - fundamentals and applications. In: Britun N, Nikiforov A, editors. *Principles and Early Historical Development of Silicon Avalanche and Geiger-Mode Photodiodes*. InTech (2018). doi: 10.5772/intechopen.72148
125. Holzman I, Ivry Y. Superconducting nanowires for single-photon detection: progress, challenges, and opportunities. *Adv QTM Technol*. (2019) **2**:1800058. doi: 10.1002/qute.201800058
126. Gol'tsman GN, Okunev O, Chulkova G, Lipatov A, Semenov A, Smirnov K, et al. Picosecond superconducting single-photon optical detector. *Appl Phys Lett*. (2001) **79**:705–7. doi: 10.1063/1.1388868
127. Korzh B, Zhao QY, Allmaras JP, Frasca S, Autry TM, Bersin EA, et al. Demonstration of sub-3 ps temporal resolution with a superconducting nanowire single-photon detector. *Nat Photonics*. (2020).
128. Irwin KD. An application of electrothermal feedback for high resolution cryogenic particle detection. *Appl Phys Lett*. (1995) **66**:1998–2000. doi: 10.1063/1.113674
129. Eisenhauer F, Raab W. Visible/infrared imaging spectroscopy and energy-resolving detectors. *Annu Rev Astro Astrophys*. (2015) **53**:155–97. doi: 10.1146/annurev-astro-082214-122442
130. Haugen GR, Wallin BW, Lytle FE. Optimization of data-acquistion rates in time-correlated single-photon fluorimetry. Rev Sci Instruments. (1979) **50**:64–72. doi: 10.1063/1.1135671
131. Mota M, Christiansen J. A high-resolution time interpolator based on a delay locked loop and an RC delay line. *IEEE J Solid Circ*. (1999) **34**:1360–6. doi: 10.1109/4.792603
132. Lampton M, Raffanti R. A high-speed wide dynamic range time-to-digital converter. *Rev Sci Instrum*. (1994) **65**:3577–584. doi: 10.1063/1.1144540
133. Antonioli S, Cuccato A, Miari L, Labanca I, Rech I, Ghioni M. Ultra-compact 32-channel system for time-correlated single-photon counting measurements. *Proc SPIE*. (2013) **8773**:87730D. doi: 10.1117/12.2017408
134. Peronio P, Labanca I, Acconcia G, Ruggeri A, Lavdas AA, Hicks AA, et al. 32-channel time-correlated-single-photon-counting system for high-throughput lifetime imaging. *Rev Sci Instrum*. (2017) **88**:083704. doi: 10.1063/1.4986049
135. Stoppa D, Borghetti F, Richardson JA, Walker R, Henderson RK, Gersbach M, et al. Ultra compact and low-power TDC and TAC architectures for highly-parallel implementation in time-resolved image sensors. In: 2011 International Workshop on ADC Modelling, Testing And Data Converter Analysis and Design and IEEE 2011 ADC Forum (Orvieto) (2011).
136. Krishnan RV, Masuda A, Centonze VFE, Herman BA. Quantitative imaging of protein-protein interactions by multiphoton fluorescence lifetime imaging microscopy using a streak camera. *J Biomed Opt*. (2003) **8**:362–7. doi: 10.1117/1.1577574
137. Krishnan RV, Saitoh H, Terada H, Centonze VE, Herman B. Development of a multiphoton fluorescence lifetime imaging microscopy system using a streak camera. *Rev Sci Instrum*. (2003) **74**:2714–21. doi: 10.1063/1.1569410
138. Biskup C, Zimmer T, Benndorf K. FRET between cardiac Na^+ channel subunits measured with a confocal microscope and a streak camera. *Nat Biotechnol*. (2004) **22**:220–4. doi: 10.1038/nbt935
139. Biskup C, Hoffmann B, Kelbauskas L, Zimmer T, Klocker N, Becker W, et al. Multidimensional fluorescence lifetime measurements. In: Periasamy A, PTC So, editors. Multiphoton Microscopy in the Biomedical Sciences VIII. Vol. 6860. International Society for Optics and Photonics. *Proc SPIE*. (2008). p. 260–71. doi: 10.1117/12.762834
140. Komura M, Itoh S. Fluorescence measurement by a streak camera in a single-photon-counting mode. *Photosyn Res*. (2009) **101**:119–33. doi: 10.1007/s11120-009-9463-x
141. Davis LM, Parigger C. Use of streak camera for time-resolved photon counting fluorimetry. *Meas Sci Technol*. (1992) **3**:85–90. doi: 10.1088/0957-0233/3/1/012
142. Godet J, Mély Y. Exploring protein-protein interactions with large differences in protein expression levels using FLIM-FRET. *Methods Appl Fluoresc*. (2019) **8**:014007. doi: 10.1088/2050-6120/ab5dd2
143. Trinh AL, Ber S, Howitt A, Valls PO, Fries MW, Venkitaraman AR, et al. Fast single-cell biochemistry: theory, open source microscopy and applications. *Methods Appl Fluoresc*. (2019) 7:044001. doi: 10.1088/2050-6120/ab3bd2
144. Lukina MM, Shimolina LE, Kiselev NM, Zagainov VE, Komarov DV, Zagaynova EV, et al. Interrogation of tumor metabolism in tissue samples *ex vivo* using fluorescence lifetime imaging of NAD(P)H. *Methods Appl Fluoresc*. (2019) **8**:014002. doi: 10.1088/2050-6120/ab4ed8
145. Cao R, Wallrabe H, Siller K, Periasamy A. Optimization of FLIM imaging, fitting and analysis for auto-fluorescent NAD(P)H and

FAD in cells and tissues. *Methods Appl Fluoresc*. (2020) **8**:024001. doi: 10.1088/2050-6120/ab6f25
146. Suhling K, Hirvonen LM, Becker W, Smietana S, Netz H, Milnes J, et al. Wide-field time-correlated single photon counting-based fluorescence lifetime imaging microscopy. *Nucl Instrum Meth A*. (2019) **942**:162365. doi: 10.1016/j.nima.2019.162365
147. McLoskey D, Birch DJS, Sanderson A, Suhling K, Welch E, Hicks PJ. Multiplexed single-photon counting. I. A time-correlated fluorescence lifetime camera. *Rev Sci Instrum*. (1996) **67**:2228–37. doi: 10.1063/1.1147041
148. Rinnenthal JL, Barnchen C, Radbruch H, Andresen V, Mossakowski A, Siffrin V, et al. Parallelized TCSPC for dynamic intravital fluorescence lifetime imaging: quantifying neuronal dysfunction in neuroinflammation. PLoS ONE. (2013) **8**:e60100. doi: 10.1371/journal.pone.0060100
149. Levitt JA, Poland SP, Krstajic N, Pfisterer K, Erdogan A, Barber PR, et al. Quantitative real-time imaging of intracellular FRET biosensor dynamics using rapid multi-beam confocal FLIM. *Sci Rep*. (2020) **10**:5146. doi: 10.1038/s41598-020-61478-1
150. Hanley QS, Subramaniam V, Arndt-Jovin DJ, Jovin TM. Fluorescence lifetime imaging: multi-point calibration, minimum resolvable differences, and artifact suppression. *Cytometry*. (2001) **43**:248–60. doi: 10.1002/1097-0320(20010401)43:4<248::AID-CYTO1057>3.0.CO;2-Y
151. Periasamy A, Clegg RM, editors. FLIM Microscopy in Biology and Medicine. Chapman and Hall/CRC (2009). doi: 10.1201/9781420078916
152. Hirvonen LM, Festy F, Suhling K. Wide-field time-correlated single-photon counting (TCSPC) lifetime microscopy with microsecond time resolution. *Opt Lett*. (2014) **39**:5602–5. doi: 10.1364/OL.39.005602
153. Hirvonen LM, Petrášek Z, Beeby A, Suhling K. Sub-μs time resolution in wide-field time-correlated single photon counting microscopy obtained from the photon event phosphor decay. *N J Phys*. (2015) **17**:023032. doi: 10.1088/1367-2630/17/2/023032
154. Hirvonen LM, Fisher-Levine M, Suhling K, Nomerotski A. Photon counting phosphorescence lifetime imaging with TimepixCam. *Rev Sci Instrum*. (2017) **88**:013104. doi: 10.1063/1.4973717
155. Sen R, Hirvonen LM, Zhdanov AV, Svihra P, Andersson-Engels S, Nomerotski A, et al. New luminescence lifetime macro-imager based on a Tpx3Cam optical camera. *Biomed Opt Express*. (2020) **11**:77–88. doi: 10.1364/BOE.11.000077
156. Michalet X, Colyer R, Antelman J, Siegmund O, Tremsin A, Vallerga J, et al. Single-quantum dot imaging with a photon counting camera. *Curr Pharm Biotechnol*. (2009) **10**:543–57. doi: 10.2174/138920109788922100
157. Hartig R, Prokazov Y, Turbin E, Zuschratter W. Wide-field fluorescence lifetime imaging with multi-anode detectors. *Methods Mol Biol*. (2014) **1076**:457–80. doi: 10.1007/978-1-62703-649-8_20
158. Jagutzki O, Cerezo A, Czasch A, Dorner R, Hattass M, Huang M, et al. Multiple hit read-out of a microchannel plate detector with a three-layer delay-line anode. IEEE Nuclear Sci Conf R. (2001) **2**:850–854.
159. Hirvonen LM, Becker W, Milnes J, Conneely T, Smietana S, Le Marois A, et al. Picosecond wide-field time-correlated single photon counting fluorescence microscopy with a delay line anode detector. *Appl Phys Lett*. (2016) **109**:071101. doi: 10.1063/1.4961054
160. Hirvonen LM, Nedbal J, Almutairi N, Phillips TA, Becker W, Conneely T, et al. Lightsheet fluorescence lifetime imaging microscopy with wide-field time-correlated single photon counting. *J Biophotonics*. (2019) **13**:e201960099. doi: 10.1002/jbio.201960099
161. Petrasek Z, Eckert HJ, Kemnitz K. Wide-field photon counting fluorescence lifetime imaging microscopy: application to photosynthesizing systems. *Photosyn Res*. (2009) **102**:157–68. doi: 10.1007/s11120-009-9444-0
162. Vitali M, Picazo F, Prokazov Y, Duci A, Turbin E, Götze C, et al. Wide-Field Multi-Parameter FLIM: long-term minimal invasive observation of proteins in living cells. *PLoS ONE*. (2011) **6**:e15820. doi: 10.1371/journal.pone.0015820
163. Poudel C, Mela I, Kaminski CF. High-throughput, multi-parametric, and correlative fluorescence lifetime imaging. *Methods Appl Fluoresc*. (2020) **8**:024005. doi: 10.1088/2050-6120/ab7364
164. Rodimova SA, Meleshina AV, Kalabusheva EP, Dashinimaev EB, Reunov DG, Torgomyan HG, et al. Metabolic activity and intracellular pH in induced pluripotent stem cells differentiating in dermal and epidermal directions. *Methods Appl Fluoresc*. (2019) **7**:044002. doi: 10.1088/2050-6120/ab3b3d
165. Biskup C, Gensch T. *Fluorescence Lifetime Imaging of Ions in Biological Tissues*. Boca Raton, FL: CRC Press; 2015. doi: 10.1201/b17018-30
166. Kuimova MK. Mapping viscosity in cells using molecular rotors. *Phys Chem Chem Phys*. (2012) **14**:12671–12686. doi: 10.1039/c2cp41674c
167. Vysniauskas A, Kuimova MK. A twisted tale: measuring viscosity and temperature of microenvironments using molecular rotors. *Int Rev Phys Chem*. (2018) **37**:259–85. doi: 10.1080/0144235X.2018.1510461
168. Okabe K, Inada N, Gota C, Harada Y, Funatsu T, Uchiyama S. Intracellular temperature mapping with a fluorescent polymeric thermometer and fluorescence lifetime imaging microscopy. *Nat Commun*. (2012) **3**:705. doi: 10.1038/ncomms1714
169. Jenkins J, Borisov SM, Papkovsky DB, Dmitriev RI. Sulforhodamine nanothermometer for multiparametric fluorescence lifetime imaging microscopy. *Anal Chem*. (2016) **88**:10566–72. doi: 10.1021/acs.analchem.6b02675
170. Wang Xd, Wolfbeis OS. Optical methods for sensing and imaging oxygen: materials, spectroscopies and applications. *Chem Soc Rev*. (2014) **43**:3666–761. doi: 10.1039/C4CS00039K
171. Papkovsky DB, Dmitriev RI. Imaging of oxygen and hypoxia in cell and tissue samples. *Cell Mol Life Sci*. (2018) **75**:2963–80. doi: 10.1007/s00018-018-2840-x
172. Becker W. Fluorescence lifetime imaging-techniques and applications. *J Microsc*. (2012) **247**:119–36. doi: 10.1111/j.1365-2818.2012.03618.x
173. Berezin MY, Achilefu S. Fluorescence lifetime measurements and biological imaging. *Chem Rev*. (2010) **110**:2641–84. doi: 10.1021/cr900343z
174. Borst JW, Visser AJWG. Fluorescence lifetime imaging microscopy in life sciences. *Meas Sci Technol*. (2010) **21**:102002. doi: 10.1088/0957-0233/21/10/102002
175. Chen LC, Lloyd WR, Chang CW, Sud D, Mycek MA. Chapter 20 - Fluorescence Lifetime Imaging Microscopy for Quantitative Biological Imaging. In: Sluder G, Wolf DE, editors. *Digital Microscopy*. *Vol.* 114 *of Methods in Cell Biology*. Oxford: Academic Press (2013). p. 457–88. doi: 10.1016/B978-0-12-407761-4.00020-8
176. Baggaley E, Weinstein JA, Williams JAG. Lighting the way to see inside the live cell with luminescent transition metal complexes. *Coordin Chem Rev*. (2012) **256**:1762–85. doi: 10.1016/j.ccr.2012.03.018
177. Marcu L, French PMW, Elson DS, editors. *Fluorescence Lifetime Spectroscopy and Imaging*. Boca Raton, FL: CRC Press (2015). doi: 10.1201/b17018
178. Suhling K, Hirvonen LM, Levitt JA, et al. Fluorescence lifetime imaging (FLIM): Basic concepts and some recent developments. *Med Photonics*. (2015) **27**:3–40. doi: 10.1016/j.medpho.2014.12.001
179. Kapusta P, Wahl M, Erdmann R, editors. Advanced Photon Counting: Applications, Methods, Instrumentation. Cham: Springer International Publishing (2015). doi: 10.1007/978-3-319-15636-1
180. Wang S, Shen B, Ren S, Zhao Y, Zhang S, Qu J, et al. Implementation and application of FRET-FLIM technology. *J Innov Opt Heal Sci*. (2019) **12**:1930010. doi: 10.1142/S1793545819300106
181. König K, editor. *Multiphoton Microscopy and Fluorescence Lifetime Imaging*. Berlin; Boston, MA: De Gruyter (2018). doi: 10.1515/9783110429985.
182. Becker W, Bergmann A, Smietana S. Fast-acquisition TCSPC FLIM with sub-25-ps IRF width. In: Periasamy A, PTC So, König K, editors. Multiphoton Microscopy in the Biomedical Sciences XIX. Vol. 10882. *Proc SPIE*. (2019). p. 1–7. doi: 10.1117/12.2510272
183. Becker W, Bergmann A, Ibarrola RS, Müller PF, Braun L. Metabolic imaging by simultaneous FLIM of NAD(P)H and FAD. In: Periasamy A, PTC So, König K, editors. *Multiphoton Microscopy in the Biomedical Sciences XIX*. Vol. 10882. *Proc SPIE*. (2019). p. 34–41. doi: 10.1117/12.2510132
184. Sanchez WY, Pastore M, Haridass IN, König K, Becker W, Roberts MS. "Advanced Time-Correlated Single Photon Counting Applications," in *Fluorescence Lifetime Imaging of the Skin*, eds Becker W. Vol.

111. *Springer Series in Chemical Physics* (Cham: Springer) (2015). doi: 10.1007/978-3-319-14929-5_15
185. Levitt JA, Kuimova MK, Yahioglu G, Chung PH, Suhling K, Phillips D. Membrane-bound molecular rotors measure viscosity in live cells via fluorescence lifetime imaging. *J Phys Chem C*. (2009) **113**:11634–42. doi: 10.1021/jp9013493
186. Steinmark IE, James AL, Chung PH, Morton PE, Parsons M, Dreiss CA, et al. Targeted fluorescence lifetime probes reveal responsive organelle viscosity and membrane fluidity. *PLoS ONE*. (2019) **14**:e0211165. doi: 10.1371/journal.pone.0211165
187. Poland SP, Chan GK, Levitt JA, Krstajić N, Erdogan AT, Henderson RK, et al. Multifocal multiphoton volumetric imaging approach for high-speed time-resolved Förster resonance energy transfer imaging *in vivo*. *Opt Lett*. (2018) **43**:6057–60. doi: 10.1364/OL.43.006057
188. Becker W, Hirvonen LM, Milnes JS, Conneely T, Jagutzki O, Netz H, et al. A wide-field TCSPC FLIM system based on an MCP PMT with a delay-line anode. *Rev Sci Instrum*. (2016) **87**:093710. doi: 10.1063/1.4962864

Conflict of Interest: The authors declare that the research was conducted in the absence of any commercial or financial relationships that could be construed as a potential conflict of interest.

frontiers in Chemistry

REVIEW
published: 30 June 2020
doi: 10.3389/fchem.2020.00562

Auto-Phase-Locked Time-Resolved Luminescence Detection: Principles, Applications, and Prospects

Qisheng Deng, Zece Zhu and Xuewen Shu**

Wuhan National Laboratory for Optoelectronics & School of Optical and Electronic Information, Huazhong University of Science and Technology, Wuhan, China

Time-resolved luminescence measurement is a useful technique which can eliminate the background signals from scattering and short-lived autofluorescence. However, the relative instruments always require pulsed excitation sources and high-speed detectors. Moreover, the excitation and detecting shutter should be precisely synchronized by electronic phase matching circuitry, leading to expensiveness and high-complexity. To make time-resolved luminescence instruments simple and cheap, the automatic synchronization method was developed by using a mechanical chopper acted as both of the pulse generator and detection shutter. Therefore, the excitation and detection can be synchronized and locked automatically as the optical paths fixed. In this paper, we first introduced the time-resolved luminescence measurements and review the progress and current state of this field. Then, we discussed low-cost time-resolved techniques, especially chopper-based time-resolved luminescence detections. After that, we focused on auto-phase-locked method and some of its meaningful applications, such as time-gated luminescence imaging, spectrometer, and luminescence lifetime detection. Finally, we concluded with a brief outlook for auto-phase-locked time-resolved luminescence detection systems.

Keywords: time-resolved, luminescence, auto-phase-locked, chopper, imaging

OPEN ACCESS

Edited by:
Klaus Suhling,
King's College London,
United Kingdom

Reviewed by:
Zdenek Petrasek,
Graz University of Technology, Austria
Russell Connally,
Macquarie University, Australia

****Correspondence:***
Zece Zhu
zece@hust.edu.cn
Xuewen Shu
xshu@hust.edu.cn

Specialty section:
This article was submitted to Analytical Chemistry, a section of the journal Frontiers in Chemistry

Received: *03 April 2020*
Accepted: *02 June 2020*
Published: *30 June 2020*

Citation:
Deng Q, Zhu Z and Shu X (2020) Auto-Phase-Locked Time-Resolved Luminescence Detection: Principles, Applications, and Prospects. Front. Chem. 8:562. doi: 10.3389/fchem.2020.00562

INTRODUCTION

Time-resolved techniques have been widely applied to the study of ultrafast photophysical processes (Wirth, 1990; Walker et al., 2013), the research of temporal behavior of chemical systems (Piatkowski et al., 2014), biological detection and imaging (Connally and Piper, 2008; Berezin and Achilefu, 2010; Bünzli, 2010; Cicchi and Pavone, 2011; Strat et al., 2011; Becker, 2012; Yang et al., 2013; Grichine et al., 2014; Lemmetyinen et al., 2014; Lu et al., 2014; Bui et al., 2017; Luo et al., 2017; Zhang et al., 2018; Zhu et al., 2018b; Liu et al., 2019). Since these techniques can detect the luminescence change in time domain, they play a more and more important role as many long-lived luminescence materials and probes were developed (Connally and Piper, 2008; Bünzli, 2010; Yang et al., 2013; Zhang et al., 2018). Time-gated luminescence detection is known as one kind of time-resolved method, which can operate detecting gate after pulse excitation with a delay time (Connally and Piper, 2008; Lemmetyinen et al., 2014; Zhang et al., 2018). Therefore, the background signals caused by scattering and short-lived autofluorescence could be eliminated, and the signal-to-noise ratio would be improved significantly. Luminescence lifetime detection is another mainly used method, which can detect the luminescence decay rates by recording the

luminescence intensity vs. pulse excitation (Cicchi and Pavone, 2011; Becker, 2012; Liu et al., 2019). Since the luminescence lifetimes of many probes are sensitive to microenvironments, lifetime imaging can exhibit significant differences that covered by luminescence intensity, and is more and more widely used in biological imaging to observe functional and molecular events (Connally and Piper, 2008; Berezin and Achilefu, 2010; Bünzli, 2010; Cicchi and Pavone, 2011; Strat et al., 2011; Becker, 2012; Damayanti et al., 2013; Yang et al., 2013; Grichine et al., 2014; Lemmetyinen et al., 2014; Lu et al., 2014; Bui et al., 2017; Luo et al., 2017; Wang et al., 2017; Zhang et al., 2018; Zhu et al., 2018b; Liu et al., 2019).

To achieve the time-resolved luminescence detection, the temporal resolution of related instruments should be high enough, since most luminescence probes exhibit luminescence lifetimes rang from sub-nanoseconds to milliseconds (Berezin and Achilefu, 2010; Bünzli, 2010; Yang et al., 2013; Zhang et al., 2018). With the development of pulse light sources, optical detectors and high-speed shutters, many instruments could achieve nanosecond-resolved luminescence detection (Krishnan et al., 2003; Urayama et al., 2003; Biskup et al., 2004; Connally et al., 2006; Qu et al., 2006; Sun et al., 2009; Gahlaut and Miller, 2010; Strat et al., 2011; Damayanti et al., 2013; Grichine et al., 2014; Hirvonen et al., 2014; Lu et al., 2014; Bergmann et al., 2016; Pominova et al., 2016; Bui et al., 2017; Luo et al., 2017; Wang et al., 2017; Zhu et al., 2018b; Liu et al., 2019). Photon sensitivity is another important factor in time-resolved luminescence detections. Since the luminescence decays exponentially after pulse excitation (Berezin and Achilefu, 2010; Bünzli, 2010; Yang et al., 2013; Zhang et al., 2018), the photon signals are significantly fewer than that under continuous-wave (CW) excitation. Although increasing the exciting power or exposure time could produce more luminescence photons, the photobleaching of many organic dyes would decrease the accuracy of the time-resolved luminescence measurements. Thus, it is necessary to increase the efficiency of photon detecting to improve the signal-to-noise ratio. Particularly in luminescence lifetime detections, a detecting cycle is usually divided into many intervals, each of which should have enough photons for luminescence lifetime analysis (Cicchi and Pavone, 2011; Becker, 2012; Liu et al., 2019).

Because of these requirements, high-speed and sensitive detectors, such as PMT (photomultiplier tube) (Strat et al., 2011; Grichine et al., 2014; Bui et al., 2017; Luo et al., 2017; Zhu et al., 2018b), SPAD (single-photon avalanche diode) (Damayanti et al., 2013; Lu et al., 2014; Wang et al., 2017), streak camera (Krishnan et al., 2003; Biskup et al., 2004; Qu et al., 2006; Bergmann et al., 2016; Pominova et al., 2016) or intensified camera (Urayama et al., 2003; Connally et al., 2006; Sun et al., 2009; Gahlaut and Miller, 2010; Hirvonen et al., 2014) are essential in many instruments for time-correlated single-photon counting (TCSPC). In addition, theses detectors always need to be synchronized with the ultrafast laser sources, leading to highly precise and complicated optical systems. Some reviews have summarized the principle and development of time-resolved luminescence detection techniques (Connally and Piper, 2008; Berezin and Achilefu, 2010; Bünzli, 2010; Cicchi and Pavone, 2011; Becker, 2012; Yang et al., 2013; Lemmetyinen et al., 2014; Zhang et al., 2018; Liu et al., 2019). Most of these techniques are mainly used in detecting nanosecond-delayed fluorescence. As the developments of phosphorescence, delayed fluorescence and upconversion luminescence materials, these materials could emit luminescence with a delay time over microseconds or milliseconds (Marriott et al., 1991, 1994; Verwoerd et al., 1994; Vereb et al., 1998; Connally et al., 2006; Connally and Piper, 2008; Bünzli, 2010; Gahlaut and Miller, 2010; Connally, 2011; Jin, 2011; Jin and Piper, 2011; Damayanti et al., 2013; Yang et al., 2013, 2019; Grichine et al., 2014; Hirvonen et al., 2014; Jin et al., 2014; Lu et al., 2014; Zhang et al., 2014, 2018; Bergmann et al., 2016; Pominova et al., 2016; Zheng et al., 2016; Zhu et al., 2016, 2018a,b; Bui et al., 2017; Chen T. et al., 2017; Wang et al., 2017; Sakiyama et al., 2018; Zhu and Shu, 2018, 2019; Deng et al., 2020; Liu et al., 2020), greatly reducing the requirement of temporal resolution and the cost of the instruments. Combining with the use of low-cost shutters and automatic synchronization methods, CW light sources and common cameras were successfully used to accomplish the time-resolved luminescence detection with the temporal resolution ranging from microseconds to milliseconds (Marriott et al., 1991, 1994; Verwoerd et al., 1994; Vereb et al., 1998; Connally, 2011; Jin, 2011; Jin and Piper, 2011; Jin et al., 2014; Zhang et al., 2014; Zheng et al., 2016; Sakiyama et al., 2018; Zhu and Shu, 2018, 2019; Zhu et al., 2018b; Yang et al., 2019; Deng et al., 2020). In this review, we will focus on these low-cost time-resolved techniques, especially chopper-based time-resolved luminescence detections.

OVERVIEW OF TIME-RESOLVED TECHNIQUES

A time-resolved luminescence detection instrument is usually composed of a pulse source, an optical detector and a synchronous control component (Krishnan et al., 2003; Urayama et al., 2003; Biskup et al., 2004; Connally et al., 2006; Qu et al., 2006; Connally and Piper, 2008; Sun et al., 2009; Gahlaut and Miller, 2010; Cicchi and Pavone, 2011; Strat et al., 2011; Becker, 2012; Damayanti et al., 2013; Grichine et al., 2014; Hirvonen et al., 2014; Lemmetyinen et al., 2014; Lu et al., 2014; Bergmann et al., 2016; Pominova et al., 2016; Bui et al., 2017; Chen T. et al., 2017; Luo et al., 2017; Wang et al., 2017; Zhang et al., 2018; Zhu et al., 2018b; Liu et al., 2019, 2020). To achieve a temporal resolution of nanoseconds, many instruments equipped with a picosecond or even femtosecond laser (Krishnan et al., 2003; Urayama et al., 2003; Biskup et al., 2004; Qu et al., 2006; Sun et al., 2009; Grichine et al., 2014; Pominova et al., 2016; Bui et al., 2017; Luo et al., 2017; Zhu et al., 2018b), which is expensive. In order to increase the repetition rates and shorten the acquisition time, some lasers usually reach a frequency up to dozens of MHz (Damayanti et al., 2013; Luo et al., 2017), which is however not suitable for detecting luminescence with microseconds delay. Nowadays many TTL (transistor-transistor logic) modulated lasers and LEDs (light-emitting diode) could generate pulses within width range from nanoseconds to microseconds (Connally et al., 2006; Gahlaut and Miller, 2010; Hirvonen et al., 2014; Chen T. et al., 2017; Liu

et al., 2020), which may produce more excited states per pulse than picosecond or femtosecond laser when exciting the long luminescence lifetime materials. The laser diodes and LEDs with various wavelength ranges are significantly cheaper than ultrafast lasers. And their emission stability and service life are better than that of mercury and xenon lamps.

Since many laser diode and LED sources are cheap and can be easily equipped in various optical systems, the optical detector becomes a key element in the instruments for time-resolved detection of long-lived luminescence. Various kinds of optical detectors used for time-resolved luminescence imaging are listed in **Table 1**. The temporal resolutions of PMT and SPAD can attain to nanoseconds, even to picoseconds with the sensitivity of single photon, so they are widely used to measure the luminescence lifetimes in TCSPC (Cicchi and Pavone, 2011; Strat et al., 2011; Becker, 2012; Damayanti et al., 2013; Grichine et al., 2014; Lu et al., 2014; Bui et al., 2017; Luo et al., 2017; Wang et al., 2017; Zhu et al., 2018b; Liu et al., 2019). But they could not distinguish photons in different space domain. To achieve luminescence lifetime imaging, these detectors and pulse lasers were usually equipped on the confocal laser scanning systems (Damayanti et al., 2013; Grichine et al., 2014; Lu et al., 2014; Bui et al., 2017; Wang et al., 2017), which have been popularized for luminescence microscopic imaging. However, the luminescence lifetime imaging based on point-by-point scanning is time consuming in detecting lifetimes over microseconds. The low repetition rate usually led to a long acquiring time over several minutes (Grichine et al., 2014; Lu et al., 2014; Bui et al., 2017). However, in some cases, samples with high concentration of luminescence particles can emit enough photons during one pulse cycle (Lu et al., 2014). In other cases, the scanning mode can be controlled flexibly to exclude the dark pixels for time-domain detection (Liu et al., 2019).

To improve the efficiency of time-resolved luminescence imaging, area-array detectors were developed to achieve wide-field time-resolved luminescence imaging of all the pixels (Urayama et al., 2003; Connally et al., 2006; Sun et al., 2009; Gahlaut and Miller, 2010; Li et al., 2010; Guo and Sonkusale, 2012; Hirvonen et al., 2014; Chen et al., 2015; Ingelberts and Kuijk, 2015, 2016; Chen T. et al., 2017; Ulku et al., 2019; Henderson et al., 2020; Liu et al., 2020). A common CCD or CMOS sensor is composed of an area-array of photosensitive silicon diodes, each of which could sense photons in microseconds (Henderson et al., 2020), but the actual frame rate is probably no more than hundreds of frames per second due to the limitation of readout time. To achieve both high gain and nanosecond resolution, micro channel plate (MCP) is developed and serves as a high-speed electronic shutter in the intensified cameras, which are widely used in wide-field time-gated imaging (Urayama et al., 2003; Connally et al., 2006; Sun et al., 2009; Gahlaut and Miller, 2010; Hirvonen et al., 2014; Chen T. et al., 2017; Liu et al., 2020). The streak tubes in streak cameras could distinguish photons in picoseconds (Krishnan et al., 2003; Biskup et al., 2004; Qu et al., 2006; Bergmann et al., 2016; Pominova et al., 2016). But these high-speed cameras are very expensive. In order to image the luminescence lifetime globally, some labs developed a variety of novel CMOS cameras (Henderson et al., 2020), which could implement time-gated control (Ingelberts and Kuijk, 2015, 2016), phase recording (Guo and Sonkusale, 2012; Chen et al., 2015; Ulku et al., 2019) or TCSPC (Li et al., 2010) on their sensor chips. Although these cameras could obtain luminescence lifetime images much faster than the scanning imaging, some of them were limited to detect mono or double exponential luminescence decay. Only a few of them have been used commercially, and their costs are still high.

In addition to the excitation sources and detectors, precise circuit systems with small timing jitter are usually used to synchronize the camera or shutter with the pulse excitation in many time-resolved detection systems (Krishnan et al., 2003; Urayama et al., 2003; Biskup et al., 2004; Connally et al., 2006; Qu et al., 2006; Sun et al., 2009; Gahlaut and Miller, 2010; Cicchi and Pavone, 2011; Strat et al., 2011; Becker, 2012; Hirvonen et al., 2014; Bergmann et al., 2016; Pominova et al., 2016; Chen T. et al., 2017; Luo et al., 2017; Liu et al., 2019, 2020). For

TABLE 1 | Photo detectors used in time-resolved detections.

Detector	Imaging method	Temporal resolution[a]	Luminescence lifetime detected	References
PMT	Scanning	<30 ps	50 ps−1 ms	Strat et al., 2011; Grichine et al., 2014; Bui et al., 2017; Luo et al., 2017; Zhu et al., 2018b
SPAD	Scanning	<1 ns	0.8 ns–ms	Damayanti et al., 2013; Lu et al., 2014; Wang et al., 2017
Streak camera	Scanning	<1 ps	0.26 ns−1 ms	Krishnan et al., 2003; Biskup et al., 2004; Qu et al., 2006; Bergmann et al., 2016; Pominova et al., 2016
Intensified camera	Wide-field	0.2 ns	0.6 ns−1 ms	Urayama et al., 2003; Connally et al., 2006; Sun et al., 2009; Gahlaut and Miller, 2010; Hirvonen et al., 2014; Chen T. et al., 2017; Liu et al., 2020
Gated CMOS	Wide-field	<1 ns	0.45–4 ns	Ingelberts and Kuijk, 2015
Current-assisted CMOS	Wide-field	<1 ns	1.5–4 ns	Ingelberts and Kuijk, 2016
CMOS phase imager	Wide-field	0.11 ns	ns–μs	Guo and Sonkusale, 2012; Chen et al., 2015
SPAD imager CMOS	Wide-field	< 1 ns	1–80 ns	Li et al., 2010; Ulku et al., 2019

[a] *The temporal resolution is represented by the gate time or the delay step of the detector.*

detecting the delayed luminescence within nanoseconds, the related instruments are always composed of elements, such as ultrafast lasers, high-speed cameras and precise control circuits, which are very complicated and expensive to be popularized. However, there is no need to detect the microsecond-delay luminescence with nanosecond shutters, and a wide range of technologies were developed in the past decades to reduce the cost for time-resolved detection of phosphorescence and delayed fluorescence (Marriott et al., 1991, 1994; Verwoerd et al., 1994; Vereb et al., 1998; Connally, 2011; Jin, 2011; Jin and Piper, 2011; Jin et al., 2014; Zhang et al., 2014; Zheng et al., 2016; Sakiyama et al., 2018; Zhu and Shu, 2018, 2019; Zhu et al., 2018b; Yang et al., 2019; Deng et al., 2020).

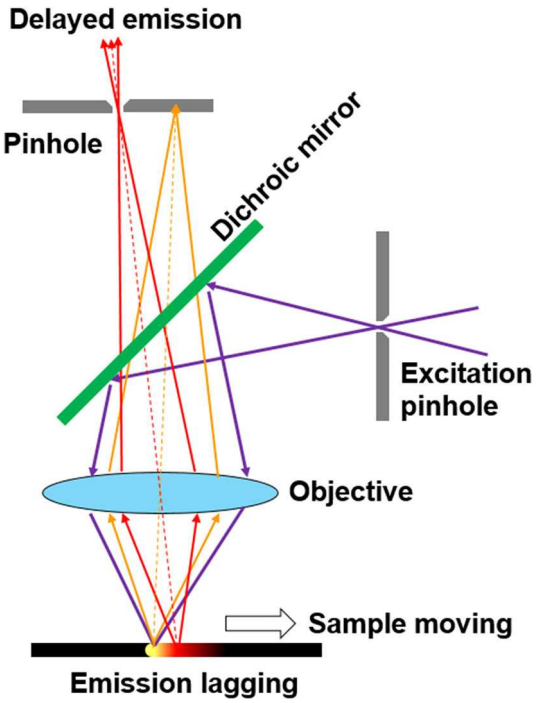

FIGURE 1 | Schematic of pinhole shifting for scanning imaging of the delayed luminescence.

Some methods based on CW excitation were even developed to achieve time-resolved luminescence detection (Nuñez et al., 2013; Petrášek et al., 2016; Zhu, 2019). In 2008, Ramshesh et al. reported a luminescence lifetime imaging on a commercial confocal laser scanning microscope (Ramshesh and Lemasters, 2008). As long as the scanning speed is fast enough, the pixels would emit delayed luminescence lagging behind the excitation spot (**Figure 1**). By just shifting the pinhole of the microscopy, the phosphorescence lifetime imaging of a europium complex was accomplished with sub-millisecond resolution (Grichine et al., 2014). Although a pulsed Ti:Sapphire laser was used for multiphoton excitation, this method can be easily implemented on other confocal microscopes without additional attachments. However, the temporal resolution is limited by the scanning speed, which is in conflict with prolonging the exciting and dwelling time for producing enough photons. Additionally, the interferences caused by the scattering from the exciting spots further limited the improvement of signal-to-noise ratio. In 2016, Petrášek et al. reported a method which realized luminescence lifetime imaging in a standard confocal microscope without any modifications (Petrášek et al., 2016). During pixel scanning, the emitted luminescence would decrease as the scan velocity increased. Based on the dynamical processes of the excited states under CW excitation, the phosphorescence lifetime of a ruthenium complex was estimated to be about microseconds at each pixel.

For wide-field time-resolved imaging, low-cost shutters are used more and more widely for detecting luminescence with a delay over microseconds (Marriott et al., 1991, 1994; Verwoerd et al., 1994; Vereb et al., 1998; Connally, 2011; Jin, 2011; Jin and Piper, 2011; Jin et al., 2014; Zhang et al., 2014; Zheng et al., 2016; Sakiyama et al., 2018; Zhu and Shu, 2018, 2019; Zhu et al., 2018b; Yang et al., 2019; Deng et al., 2020). Notably, a mechanical chopper in combination with a highly sensitive camera is an

TABLE 2 | Chopper-based time-resolved luminescence imaging.

Light source	Camera	Synch control	Temporal resolution[a]	Luminescence lifetime detected	References
488 nm laser	CCD	Circuit	50 μs	~ 1 ms	Marriott et al., 1991
Mercury lamp	CCD	Circuit	210 μs	0.56–0.89 ms	Marriott et al., 1994
UV LED	CCD	Circuit	11–16 μs	>0.1 ms[b]	Jin, 2011; Jin and Piper, 2011
Xenon lamp	Color CCD	Circuit	≤88 μs	>0.1 ms[b]	Zhang et al., 2014
980 nm laser	EMCCD	Circuit	≤23 μs	μs–ms[b]	Zheng et al., 2016
UV LED	CCD	Auto	<260 μs	0.2–0.7 ms	Connally, 2011
980 nm laser	CCD	Auto	50–200 μs	<ms[b]	Zhu et al., 2018b
405 nm laser	Color CCD	Auto	≤10 μs	2–60 μs	Zhu and Shu, 2019
405 nm laser	CCD	Auto	≤128 μs	~200 μs	Sakiyama et al., 2018
405 nm laser	sCMOS	Auto	≤20 μs	16 μs	Yang et al., 2019

[a] *The temporal resolution is represented by the switching time or the delay time.*
[b] *These lifetimes were estimated from the properties of similar luminescence materials.*

alternative in time-gated luminescence imaging (Marriott et al., 1991, 1994; Vereb et al., 1998; Connally, 2011; Jin, 2011; Jin and Piper, 2011; Jin et al., 2014; Zhang et al., 2014; Zheng et al., 2016). The details of the time-resolved luminescence imaging based on some mechanical choppers are shown in **Table 2**. Compared with electro-optic or acousto-optic choppers, the mechanical choppers could provide 100% modulation, which is independent of wavelength (Selzer and Yen, 1976). Although the switching time of commercial mechanical choppers is always shorter than electronic switches and intensifiers in many high-speed detectors, they could be well used in time-resolved luminescence imaging and spectrum detection with a delay time over microseconds (Marriott et al., 1991, 1994; Vereb et al., 1998; Connally, 2011; Jin, 2011; Jin and Piper, 2011; Jin et al., 2014; Zhang et al., 2014; Zheng et al., 2016; Sakiyama et al., 2018; Zhu and Shu, 2018, 2019; Zhu et al., 2018b; Yang et al., 2019; Deng et al., 2020). Now, we will review some principles and applications of mechanical choppers used in time-resolved luminescence detection, particularly the auto-phase-locked method developed in our previous work. Finally, we will give a brief outlook for the auto-phase-locked time-resolved luminescence detection systems, and hope some improvements of the systems and original applications can be realized in future.

INTRODUCTION OF MECHANICAL CHOPPERS

A mechanical chopper is usually composed of a motor which could drive a rotating wheel, mirror or prism to modulate a continuous light beam into light pulses (Hoffmann and Jovin, 1971; Selzer and Yen, 1976; Gembicky et al., 2005; Förster et al., 2015). As shown in **Figure 2**, the rise or fall time of a pulse chopped by a wheel with slots could represent the temporal resolution, which can be expressed as:

$$res_{time} = \frac{r_{beam}}{v}$$

where r_{beam} and v represent the radius of the light beam and the orbital velocity of the disk, respectively. In order to accomplish a temporal resolution as high as possible, a faster rotating speed and bigger wheel is preferred. However, the rotating speed is limited by centrifugal stress and the torque required to overcome aerodynamic drag (Wenthen and Snowman, 1973). Therefore, the wheel size is limited by its tensile strength to prevent it from bursting apart.

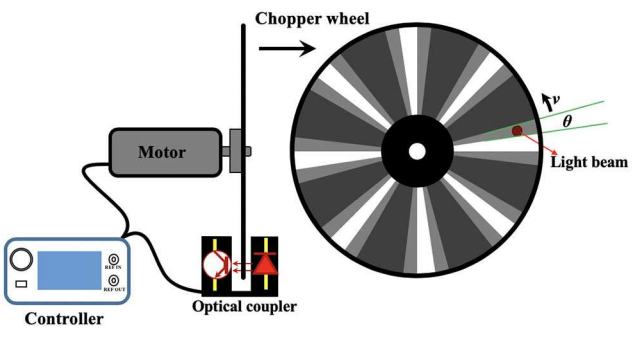

FIGURE 2 | Diagram of commercial chopper and chopper wheel.

In 1971, Hoffmann and Jovin constructed a chopper which can rotate a prism up to 7,000 rounds per second (RPS), further modulating a continuous laser beam to produce nearly 0.5-ns rise-time rectangular-shaped pulses of laser light (Hoffmann and Jovin, 1971). Then in 1976, Selzer and Yen used an air turbine handpiece to develop a chopper which can rotate as fast as 8,300 RPS and span the region from 500 Hz to 300 kHz with a single blade change (Selzer and Yen, 1976). Although the chopper rotated fast, the wheel diameter is only 12.5 mm, so as to reduce the torque load on the turbine. For wheels with diameter over 100 mm, many lab made choppers could spin over hundreds Hz. A 339-mm-diameter wheel with thickness from 30 mm at the center to 0.5 mm at outermost rim could rotate at 998 RPS, which was used to extract picosecond X-ray pulses (Förster et al., 2015).

Although many lab made choppers could rotated over 1,000 RPS (Hoffmann and Jovin, 1971; Selzer and Yen, 1976; Gembicky et al., 2005), the commercial choppers are usually designed to have a max rotating speed of only 100 RPS. Some commercial choppers can rotate at 270 RPS and its frequency can be up to 120 kHz with 445-slot blade (Model-310CD, Scitec Instruments Ltd.). Therefore, the temporal resolutions of many chopper-based time-resolved detection systems were limited to microseconds. To maintain the chopping speed and phase-locking, many choppers have integrated some electrical circuitries to monitor and control the wheel rotation. The commercial choppers usually have a controller which can get the reference signal by the optical switch at the edge of the wheel (**Figure 2**), and convert optical signals into TTL signals, further accomplishing the synchronization with other equipment, such as light sources and signal generators for many optical measurements.

THE CHOPPER-BASED TIME-RESOLVED DETECTION BY ELECTRICAL SYNCHRONIZATION

In many time-resolved luminescence detection systems, the detection shutter and excitation pulse should be synchronized. For the CW light sources, one chopper could be used to generate pulsed excitation, while another chopper acted as a shutter synchronized to the first one for time-gated luminescence detection (**Figure 3**) (Marriott et al., 1991, 1994; Vereb et al., 1998). By using different exciting sources, Marriott et al. used this method to image the delayed luminescence of acridine orange (Marriott et al., 1991) and a Europium (III) complex (Marriott et al., 1994), respectively. The phase difference between the two choppers could be adjusted by the controllers to acquire a series of images with different delay time, so the luminescence lifetime can be measured at each pixel.

Nowadays, many laser and LED sources can be modulated by TTL signals, hence the reference signals of the choppers

can be used to achieve the synchronization of excitations to the chopping cycles. In 2011, Jin used the clock signal from the chopper to achieve the synchronization of the gated detection cycle in a time-gated luminescence microscopy, which was used to achieve real-time direct-visual inspection and true color imaging of *Cryptosporidium parvum* labeled by europium and terbium complexes (Jin, 2011; Jin and Piper, 2011). However, the power or the frequency of currently available UV LEDs at 300–340 nm was not high enough for exciting some terbium complexes. They used a high-power xenon flash lamp synchronized to accomplish dual-color visualization of the time-gated phosphorescence (Zhang et al., 2014). Then this method was applied to synchronize a 980 nm laser to accomplish time-gated upconversion luminescence imaging of mice by Zheng et al. (2016). The lanthanide upconversion nanoparticles always require excitation by high-power lasers over W/cm^2, which usually cause substantial scattering even with the used of filters under CW excitation. While in time-gated imaging, high-contrast upconversion luminescence was visualized with a high signal-to-noise ratio.

THE CHOPPER-BASED TIME-RESOLVED DETECTION BY AUTO SYNCHRONIZATION

The auto synchronization method was developed to avoid phase mismatch between excitation and detection. This method was easier to implement than electrical synchronization, since the excitation and detection paths were modulated by one chopper wheel simultaneously. The phase difference of excitation and detection could be locked even though there were some frequency jitters, which made the method called auto-phase-locked time-resolved detection (Connally, 2011; Sakiyama et al., 2018; Zhu and Shu, 2018, 2019; Zhu et al., 2018b; Yang et al., 2019; Deng et al., 2020). Even before the spread of motor technology, a manual chopper consists of two coaxial wheels was invented by Becquere in 1859 for the detection of phosphorescence with millisecond-delay (Berezin and Achilefu, 2010). The two wheels with holes were not lined up, so the sample between the two wheels was excited by a beam of incident sunlight through one hole, and the phosphorescence was viewed through the other hole. The coaxial wheels ensured the phase difference and achieved a temporal resolution of 0.8 ms.

In 2011, an auto synchronous luminescence time-resolved microscopy equipped with a special chopper was designed by Connally (2011), as shown in **Figure 4**. Two mirror finishes were fabricated by highly polishing the aluminum rotor face and lied at an angle of 45 to the motor axis with a radial sweep at the perimeter of 90, further reflecting the excitation light beam periodically. Then the delayed luminescence emitted from the sample could pass the chopper at intervals between reflections, which could precisely synchronize the excitation pulse, the resolving period, and the detection phase. A compact high-power UV LED was employed as the excitation source, and the images of Giardia lamblia cysts indirectly labeled with a europium chelate/streptavidin conjugate were captured successfully.

To accomplish the auto synchronization with one chopper wheel, Pollak and Maszkiewicz claimed a method in a patent in 1990 (Pollak and Maszkiewicz, 1990). The excitation path was fixed nearly parallel to the detecting path, so that two paths could pass through the slots with different rotation radiuses of only one wheel at the same time, where the outer slots were used to generate pulse excitation and the inner slots act as a detecting shutter (**Figure 5**). The phases of the excitation and detection can be synchronized automatically as long as their optical paths are fixed without the requirement of complex phase matching circuitry or control system. The delayed luminescence could pass the chopper wheel when the excitation was blocked

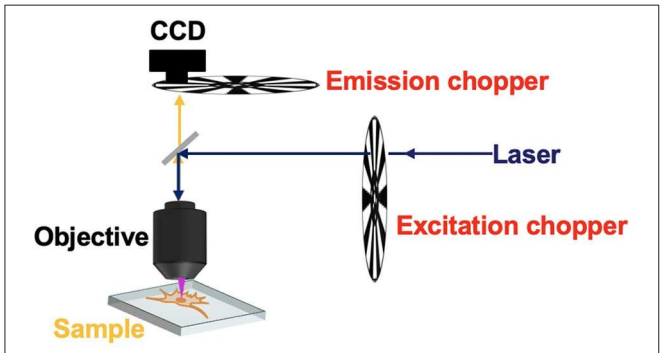

FIGURE 3 | Schematic of the time-gated phosphorescence microscope equipped with two choppers.

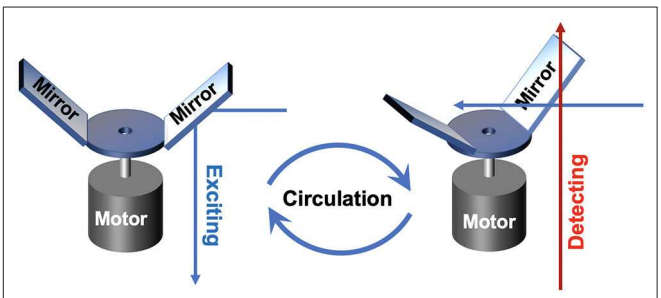

FIGURE 4 | Schematics of gated autosynchronous luminescence detection with the special designed chopper in excitation and detection process.

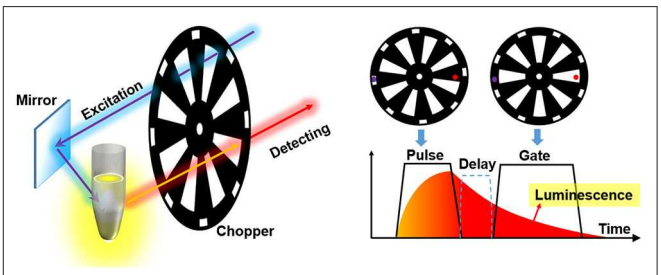

FIGURE 5 | Schematics of gated autosynchronous luminescence detection by a chopper wheel. The diagram (right) shows the time-gated luminescence detection when the wheel rotating.

with appropriate phase difference even if there were some frequency jitters.

The method was also used in a time-gated luminescence spectrometer (Saito et al., 2005). Similarly, the wheels with single circle of slots can also be used to synchronize the excitation and detecting, and the gate time is nearly the same as the pulse width (Sakiyama et al., 2018; Zhu and Shu, 2018, 2019; Zhu et al., 2018b; Yang et al., 2019; Deng et al., 2020). Since the auto synchronization greatly simplified the instruments and reduced the cost, this auto-phase-locked time-resolved technique has been well used in time-gated luminescence imaging (Sakiyama et al., 2018; Zhu et al., 2018b; Yang et al., 2019), spectrometer (Zhu and Shu, 2018) and luminescence lifetime detection (Zhu and Shu, 2019; Deng et al., 2020).

TIME-GATED LUMINESCENCE DETECTION AND IMAGING

The low-cost and auto-phase-locked time-gated luminescence measurement system can be used for time-gated luminescence spectra measurement, which can decrease the scattering interference from exciting light effectively (Sakiyama et al., 2018; Zhu et al., 2018b; Yang et al., 2019). With different types of excitation light sources used, both of background-free downconversion and upconversion delayed luminescence spectra detection can be achieved successfully.

As shown in **Figure 6**, the spectra of Tm/Yb doped $NaYF_4$ nanocrystals at different chopping frequency were measured (Zhu et al., 2018b). Compared to the steady-state spectra, most scattering signals of the exciting laser at about 980 nm were eliminated effectively at time-gated mode (**Figure 6A**). With a low background, there was a clear emission peak caused by the radiative transition of Yb^{3+} ($^2F_{5/2} \rightarrow {}^2F_{5/2}$), while it was covered by the scattering light in the steady state spectrum. No obvious upconversion luminescence was detected at a low chopping frequency, and the delayed luminescence enhanced significantly as the chopping frequency increased (**Figure 6B**), which is resulted from that the delay time was shorten as the chopping frequency increased. This method was also used to measure the downconversion time-gated luminescence spectra of some fluorescence molecules with a delay time of only a few microseconds (Zhu and Shu, 2018).

The auto-phase-locked method was then used to construct an upconversion luminescence microscopy for time-gated luminescence imaging. The delayed luminescence of the Murine B16 melanoma cells incubated by water-dispersed Er/Yb doped $NaYF_4$ nanocrystals was captured by a color CCD (Zhu et al., 2018b). The background of the steady-states was much higher than that of the time-gated images, though the images in steady state mode showed brighter luminescence (**Figure 7**). There were even some signals outside of the cell which was probably the scattering signals from the exciting light, while the time-gated image exhibited a clean background despite the high exciting power. The auto-phase-locked method was also used to accomplish the time-gated imaging of silicon quantum dots with downconversion long-lived luminescence in biological tissue, and greatly increased the signal-to-noise ratio (Sakiyama et al., 2018; Yang et al., 2019).

LUMINESCENCE LIFETIME DETECTION AND IMAGING

Although time-gated method can detect delayed luminescence, it can hardly distinguish the delayed signals with similar luminescence lifetimes, to measure which the luminescence intensity change in time domain should be recorded. Therefore, we developed a simple way to adjust the delay time to achieve luminescence lifetime analysis on the time-gated system. Since the chopper can be placed on a displacement platform, it can be moved vertically, hence the phase difference between pulse excitation and shutter can be adjusted easily and flexibly (**Figure 8**). As shown in **Figure 9A**, when the altitude of the chopper changed with a variation of h which is much less than the distance between the light path and the chopper center ($h \ll$

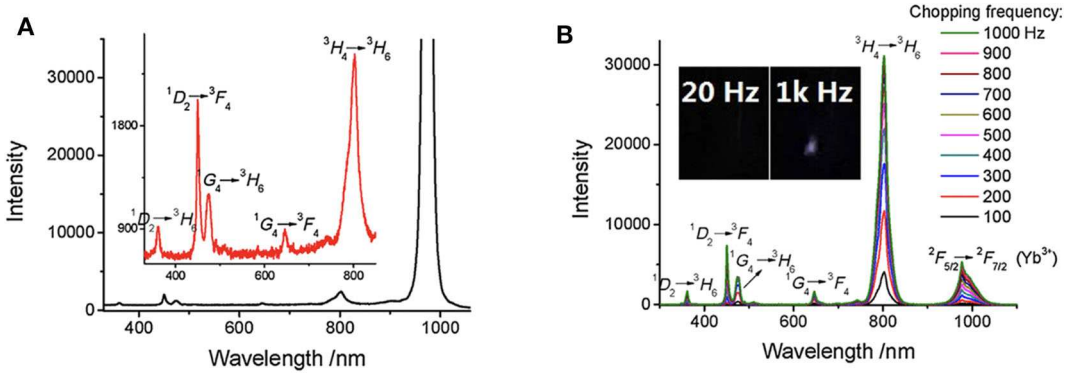

FIGURE 6 | Steady-state emission spectra **(A)** and time-gated emission spectra **(B)** of Tm/Yb doped nanocrystals (Tm 2%, Yb 18%). $\lambda_{ex} = 980$ nm. The exciting power is about 1 W. Inset: the delayed luminescence emission at different chopping frequency. Reprinted from Zhu et al. (2018b). Copyright (2018), with permission from Elsevier.

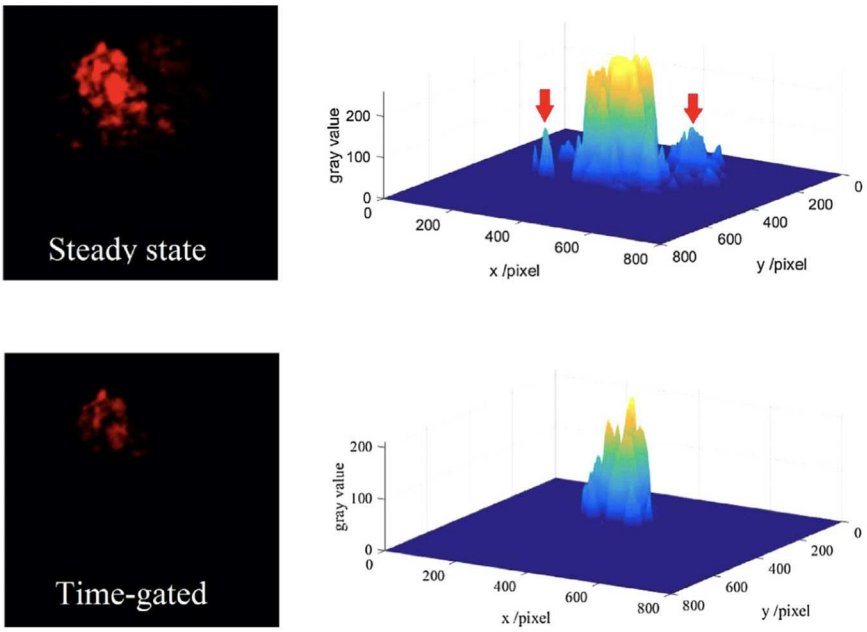

FIGURE 7 | The red channels and their gray distributions of the microscopic images at steady state (the inset arrow indicating some scattering signals) and time-gated with a chopping speed of 1,000 Hz. Reprinted from Zhu et al. (2018b). Copyright (2018), with permission from Elsevier.

l_1, l_2), the variation of the phase difference (φ) can be expressed as (Zhu and Shu, 2019):

$$\Delta\varphi = \frac{\Delta\theta}{2\pi/n} = \left(\frac{l_1}{l_1^2 + h_1^2} + \frac{l_2}{l_2^2 + h_2^2}\right)\frac{nh}{2\pi}$$

where n represents the number of the chopper slots and $\Delta\theta$ is central angle variation. By using an oscilloscope equipped with two parallel silicon photodiodes to measure the phase difference (**Figure 9B**), the phase difference variation ($\Delta\varphi$) was proved to be linear with the altitude variation of the chopper (h), which also means that the delay time (Δt) was also linear with the altitude variation of the chopper, since the delay time can be calculated by:

$$\Delta t = T \bullet \Delta\varphi$$

where T is the chopping period. Herein, a simplified method was developed later for measuring the delay time with no additional detectors. Firstly, the altitude variation (H) of one period which corresponds to 2π phase difference was measured. Therefore, the change of the delay time can also be calculated by (Deng et al., 2020):

$$\Delta t = T \bullet \frac{h}{H}$$

Combining the phase difference adjustment with the time-gated detection, the spectrally resolved luminescence lifetimes can be measured. As shown in **Figure 10A**, the spectra of a classical TADF (thermally-activated delayed fluorescence)

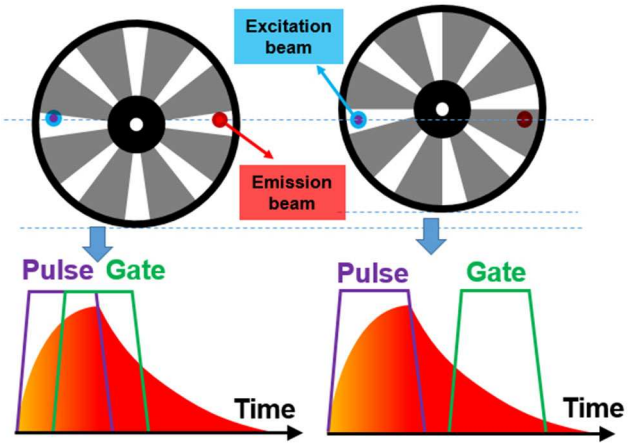

FIGURE 8 | Schematics of the phase modulation by changing the altitude of the chopper wheel.

molecule, BTZ-DMAC, at different delay time were recorded by a spectrograph (Deng et al., 2020). Two long-lived excited states with lifetimes of 30 and 120 μs, respectively, were revealed by fitting the integral of luminescence signals at all wavelengths at different delay time. It is easy to find that the longer-lifetime excited state occupies a larger proportion, and the maximum intensity of the two excited states were gained at 608 and 616 nm, respectively (**Figure 10B**), suggesting a small energy gap between different excited states probably caused by conformation differences.

Using a CCD camera as a detector, global luminescence lifetime imaging was achieved with a temporal resolution of

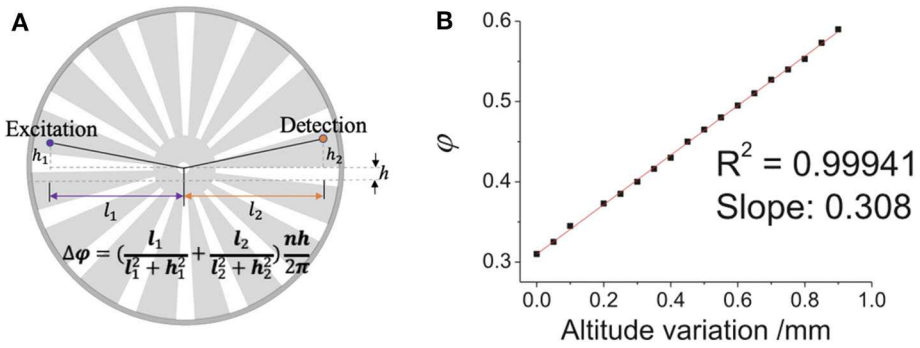

FIGURE 9 | Diagram of the change of the chopper altitude. **(A)** Schematic diagram of adjusting the phase difference between pulse excitation (left spot) and shutter (right spot). **(B)** The phase difference (ϕ) vs. the altitude variation of the chopper wheel (the delay time $\Delta t = T \bullet \varphi$). Reprinted from Zhu and Shu (2019). Copyright (2019), with permission from Elsevier.

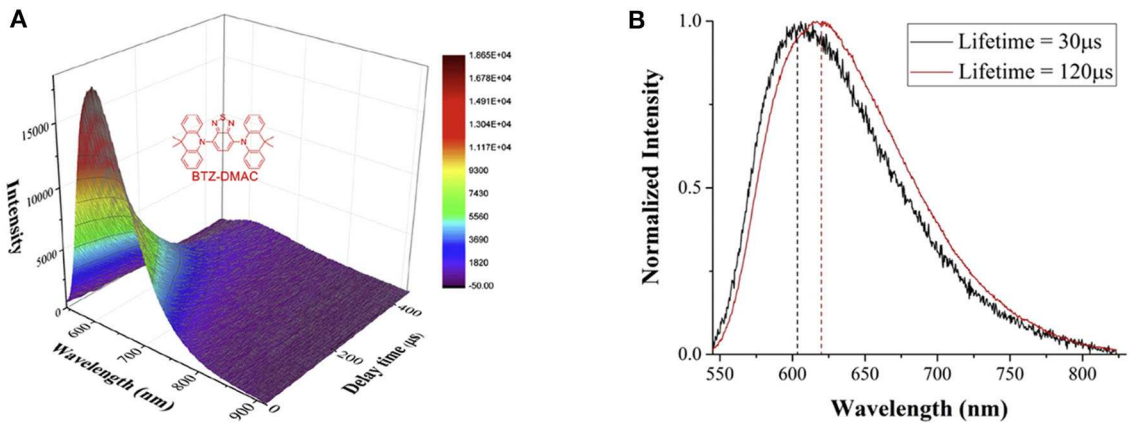

FIGURE 10 | (A) Time-gated luminescence spectra of BTZ-DMAC measured at different delay time at chopping frequency of 1 kHz. Inset: the structure of BTZ-DMAC. **(B)** The luminescence spectra of the two excited states with different lifetimes. Reprinted from Deng et al. (2020). Copyright (2020), with permission from Elsevier.

microseconds (Zhu and Shu, 2019). As the phase difference was adjusted by changing the altitude of the chopper, a series of time-gated luminescence images with different phase difference can be gained and used for luminescence lifetime imaging of a typical thermally activated delayed fluorescence materials, 4CzIPN. As shown in **Figure 11**, the time-gated image exhibited low scattering light and background which was accomplished by the auto-phase-locked principle. The delay time increased as the phase difference increased, further leading to a decrease of the luminescence intensity. The luminescence lifetimes at each pixel were estimated by fitting the luminescence intensity represented by the grayscales at each pixel at different delay time with the exponential function. In this way, the luminescence lifetime imaging of 4CzIPN powders could be constructed, as shown in **Figure 11**, where different colors were used to represent different lifetimes ranging from 2 to 3.5 μs. Practically, the delay time was adjusted in steps much smaller than the gate width (>50 μs) in these experiments, resulting in overlapping gates. However, the lifetimes within a few microseconds could be well-measured, because a moving resolution of 10 μm of the stage could achieve a temporal resolution of sub-microseconds for the delay control. In addition, the rise and fall time of the shutter was proved to have little effect on the exponential fitting at a constant chopping frequency (Zhu and Shu, 2019). Compared to luminescence lifetime imaging systems based on confocal laser scanning systems (Cicchi and Pavone, 2011; Strat et al., 2011; Becker, 2012; Damayanti et al., 2013; Grichine et al., 2014; Lu et al., 2014; Bui et al., 2017; Luo et al., 2017; Wang et al., 2017; Zhu et al., 2018b; Liu et al., 2019), this method will save much time in luminescence lifetime imaging of long-lifetime luminescence.

CHALLENGES AND PROSPECTS

The auto-phase-locked method exhibited great potential in time-resolved luminescence detection and imaging. Since the method could significantly reduce the phase jitters, the temporal resolution is mainly limited by the rotational speed of the chopper. To our knowledge, the fastest orbital velocity of a wheel driven by a chopper was 1,063 m/s (Förster et al., 2015),

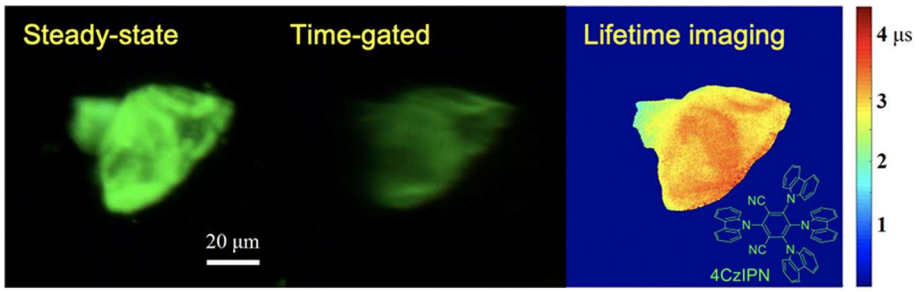

FIGURE 11 | Steady-state, time-gated and luminescence lifetime imaging of 4CzIPN. Inset: the structure of 4CzIPN. Reprinted from Zhu and Shu (2019). Copyright (2019), with permission from Elsevier.

suggesting a rise time of 95 ns for opening a 0.1-mm-wide light beam, which can be used to test most phosphorescent and delayed luminescence (Bünzli, 2010; Yang et al., 2013; Zhang et al., 2018). Another important feature of this method is that the temporal accuracy of the delay time or the phase difference depends on the moving accuracy of the stages. This method is absolutely different with the phase modulation based on circuit control. With a high-precision stage, the time step could be much shorter than the chopper shutter. Combining with the ultrafast mechanical chopper, the auto-phase-locked method may be used to measure the luminescence lifetimes of tens of nanoseconds.

Despite some defects of the mechanical chopper, such as the rotating instability, there are no other shutters with both low cost and high modulation depth for broadband light. Some MEMS (micro electromechanical system) choppers may reach a much higher frequency than mechanical choppers (Chao et al., 2007; Tsuchiya et al., 2016; Chen P. et al., 2017; Chen T. et al., 2017), but they were mainly used for modulating light sources. These vibration-based choppers are safer to be used than the ultrafast mechanical chopper. If two incoherent light beams were modulated by a MEMS chopper, the auto synchronization could be implemented for time-gated luminescence detection.

As the developments and applications of luminescence materials, such as phosphorescence, delayed fluorescence and upconversion luminescence materials become more and more widely, we believe the time-resolved techniques would be more and more used for measuring luminescence lifetimes and spectra. And the time-resolved luminescence imaging would be a powerful method for their applications in biological imaging and detections. To detect the long-lived luminescence of these materials, there is no need to use high-speed detectors and ultrafast light sources. A laser or LED modulated by a chopper with a pulse width of a few microseconds may be more suitable than ultrafast lasers to excite the luminescence with lifetime over sub-millisecond. Compared to the approaches based on electrical synchronization, the auto synchronization method avoids the phase jitters caused by the mechanical jitters of the choppers. Because the auto-phase-locked method needs no synchronization circuits, the control element could be simple, which could be propitious to construct miniaturized apparatuses for time-resolved detection.

In addition to the development of device hardware, the backward analysis of the dynamical photophysical process may be used to develop novel methods for time-resolved luminescence detection. It is possible to use Petrášek's method (Petrášek et al., 2016) on some chopper-based systems for luminescence lifetime imaging by setting no phase difference between excitation and detection. By changing the chopping frequency instead of the phase difference, the approximations of the luminescence lifetimes may be estimated. The ideas and principles are still being developed. We believe the methods as well as choppers would be useful to construct low-cost instruments for microsecond-resolved luminescence detection and imaging.

AUTHOR CONTRIBUTIONS

QD wrote the manuscript and prepared the figures. ZZ applied for the permission of the use of the images in other published journals and helped to prepare the figures. XS took the primary responsibility for communication with the journal and editorial office during the submission process, throughout peer review and during publication. All authors contributed to the article and approved the submitted version.

FUNDING

This work was supported by National Natural Science Foundation of China (NSFC) (61775074); National Key R&D Program of China (2018YFE0117400); China Post-doctoral Science Foundation (2017M620315 and 2018T110757).

REFERENCES

Becker, W. (2012). Fluorescence lifetime imaging–techniques and applications. *J. Microsc.* 247, 119–136. doi: 10.1111/j.1365-2818.2012.03618.x

Berezin, M., and Achilefu, S. (2010). Fluorescence lifetime measurements and biological imaging. *Chem. Rev.* 110, 2641–2684. doi: 10.1021/cr900343z

Bergmann, L., Hedley, G. J., Baumann, T., Bräse, S., and Samuel, I. D. W. (2016). Direct observation of intersystem crossing in a thermally activated

delayed fluorescence copper complex in the solid state. *Sci. Adv.* 2:e1500889. doi: 10.1126/sciadv.1500889

Biskup, C., Zimmer, T., and Benndorf, K. (2004). FRET between cardiac Na^+ channel subunits measured with a confocal microscope and a streak camera. *Nat. Biotechnol.* 22, 220–224. doi: 10.1038/nbt935

Bui, A. T., Grichine, A., Duperray, A., Lidon, P., Riobé, F., Andraud, C., et al. (2017). Terbium (III) luminescent complexes as millisecond-scale viscosity probes for life-time imaging. *J. Am. Chem. Soc.* 139, 7693–7696. doi: 10.1021/jacs.7b02951

Bünzli, J. G. (2010). Lanthanide luminescence for biomedical analyses and imaging. *Chem. Rev.* 110, 2729–2755. doi: 10.1021/cr900362e

Chao, S., Holl, M. R., McQuaide, S. C., Ren, T. T. H., Gales, S. A., and Meldrum, D. R. (2007). Phosphorescence lifetime based oxygen microsensing using a digital micromirror device. *Optics Express* 15, 10681–10689. doi: 10.1364/OE.15.010681

Chen, H., Holst, G., and Gratton, E. (2015). Modulated CMOS camera for fluorescence lifetime microscopy. *Microsc. Res. Tech.* 78, 1075–1081. doi: 10.1002/jemt.22587

Chen, P., Walko, D. A., Jung, I. W., Li, Z., Gao, Y., Shenoy, G. K., et al. (2017). Application of MEMS-based x-ray optics as tuneable nanosecond choppers. *Proc. SPIE* 10386:103860M. doi: 10.1117/12.2273026

Chen, T., Hong, R., Magda, D., Bieniarz, C., Morrison, L., and Miller, L. W. (2017). Time gated luminescence imaging of immunolabeled human tissues. *Anal. Chem.* 89, 12713–12719. doi: 10.1021/acs.analchem.7b02734

Cicchi, R., and Pavone, F. S. (2011). Non-linear fluorescence lifetime imaging of biological tissues. *Anal. Bioanal. Chem.* 400, 2687–2697. doi: 10.1007/s00216-011-4896-4

Connally, R. (2011). A device for gated autosynchronous luminescence detection. *Anal. Chem.* 83, 4782–4787. doi: 10.1021/ac200281h

Connally, R., Jin, D., and Piper, J. (2006). High intensity solid-state UV source for time-gated luminescence microscopy. *Cytometry A* 69, 1020–1027. doi: 10.1002/cyto.a.20326

Connally, R. E., and Piper, J. A. (2008). Time-gated luminescence microscopy. *Ann. N. Y. Acad. Sci.* 1130, 106–116. doi: 10.1196/annals.1430.032

Damayanti, N. P., Parker, L. L., and Irudayaraj, J. M. K. (2013). Fluorescence lifetime imaging of biosensor peptide phosphorylation in single live cells. *Angew. Chem. Int. Ed.* 52, 3931–3934. doi: 10.1002/anie.201209303

Deng, Q., Zhu, Z., and Shu, X. (2020). Spectrally resolved luminescence lifetime detection for measuring the energy splitting of the long-lived excited states. *Spectrochim. Acta A Mol. Biomol. Spectrosc.* 224:117434. doi: 10.1016/j.saa.2019.117434

Förster, D. F., Lindenau, B., Leyendecker, M., Janssen, F., Winkler, C., Schumann, F. O., et al. (2015). Phase-locked MHz pulse selector for X-ray sources. *Opt. Lett.* 40, 2265–2268. doi: 10.1364/OL.40.002265

Gahlaut, N., and Miller, L. W. (2010). Time-resolved microscopy for imaging lanthanide luminescence in living cells. *Cytometry A* 77, 1113–1125. doi: 10.1002/cyto.a.20964

Gembicky, M., Oss, D., Fuchs, R., and Coppens, P. (2005). A fast mechanical shutter for submicrosecond time-resolved synchrotron experiments. *J. Synchrotron Radiat.* 12, 665–669. doi: 10.1107/S090904950501770X

Grichine, A., Haefele, A., Pascal, S., Duperray, A., Michel, R., Andraud, C., et al. (2014). Millisecond lifetime imaging with a europium complex using a commercial confocal microscope under one or two-photon excitation. *Chem. Sci.* 5, 3475–3485. doi: 10.1039/C4SC00473F

Guo, J., and Sonkusale, S. (2012). A 65 nm CMOS digital phase imager for time-resolved fluorescence imaging. *IEEE J. Solid State Circuits* 47, 1731–1742. doi: 10.1109/JSSC.2012.2191335

Henderson, R. K., Rae, B. R., and Li, D. U. (2020). "CMOS sensors for fluorescence lifetime imaging," in *High Performance Silicon Imaging*, ed D. Durini (Cambridge: Woodhead Publishing), 377–412. doi: 10.1016/B978-0-08-102434-8.00012-X

Hirvonen, L. M., Festy, F., and Suhling, K. (2014). Wide-field time-correlated single-photon counting (TCSPC) lifetime microscopy with microsecond time resolution. *Opt. Lett.* 39, 5602–5605. Intensified CMOS doi: 10.1364/OL.39.005602

Hoffmann, G. W., and Jovin, T. M. (1971). A nanosecond rise-time mechanical chopper for laser light. *Appl. Opt.* 10, 218–219. doi: 10.1364/AO.10.000218

Ingelberts, H., and Kuijk, M. (2015). High-speed gated CMOS detector for fluorescence lifetime microscopy extending to near-infrared wavelengths. *IEEE Sensors* 1863–1866. doi: 10.1109/ICSENS.2015.7370660

Ingelberts, H., and Kuijk, M. (2016). A current-assisted CMOS photonic sampler with two taps for fluorescence lifetime sensing. *Proc. SPIE* 9896:98960Y. doi: 10.1117/12.2227819

Jin, D. (2011). Demonstration of true-color high-contrast microorganism imaging for terbium bioprobes. *Cytometry A* 79, 392–397. doi: 10.1002/cyto.a.21052

Jin, D., Lu, Y., Leif, R. C., Yang, S., Rajendran, M., and Miller, L. W. (2014). How to build a time-gated luminescence microscope. *Curr. Protoc. Cytometry* 67, 2.22.1–2.22.36. doi: 10.1002/0471142956.cy0222s67

Jin, D., and Piper, J. A. (2011). Time-gated luminescence microscopy allowing direct visual inspection of lanthanide-stained microorganisms in background-free condition. *Anal. Chem.* 83, 2294–2300. doi: 10.1021/ac103207r

Krishnan, R. V., Masuda, A., Centonze, V. E., and Herman, B. (2003). Quantitative imaging of protein-protein interactions by multiphoton fluorescence lifetime imaging microscopy using a streak camera. *J. Biomed. Opt.* 8, 362–367. doi: 10.1117/1.1577574

Lemmetyinen, H., Tkachenko, N. V., Valeur, B., Hotta, J., Ernsting, N. P., Gustavsson, T., et al. (2014). Time-resolved fluorescence methods. *Pure Appl. Chem.* 86, 1969–1998. doi: 10.1515/pac-2013-0912

Li, D. U., Arlt, J., Richardson, J., Walker, R., Buts, A., Stoppa, D., et al. (2010). Real-time fluorescence lifetime imaging system with a 32×32 0.13 μm CMOS low dark-count single-photon avalanche diode array. *Opt. Express* 18, 10257–10269. doi: 10.1364/OE.18.010257

Liu, X., Lin, D., Becker, W., Niu, J., Yu, B., Liu, L., et al. (2019). Fast fluorescence lifetime imaging techniques: a review on challenge and development. *J. Innov. Opt. Health Sci.* 12:1930003. doi: 10.1142/S1793545819300039

Liu, Y., Gu, Y., Yuan, W., Zhou, X., Qiu, X., Kong, M., et al. (2020). Quantitative mapping of liver hypoxia in living mice using time-resolved wide-field phosphorescence lifetime imaging. *Adv. Sci.* 7:1902929. doi: 10.1002/advs.201902929

Lu, Y., Zhao, J., Zhang, R., Liu, Y., Liu, D., Goldys, E. M., et al. (2014). Tunable lifetime multiplexing using luminescent nanocrystals. *Nat. Photon.* 8, 32–36. doi: 10.1038/nphoton.2013.322

Luo, T., Lu, Y., Liu, S., Lin, D., and Qu, J. (2017). Phasor-FLIM as a screening tool for the differential diagnosis of actinic keratosis, bowens disease, and basal cell carcinoma. *Anal. Chem.* 89, 8104–8111. doi: 10.1021/acs.analchem.7b01681

Marriott, G., Clegg, R. M., Arndt-Jovin, D. J., and Jovin, T. M. (1991). Time resolved imaging microscopy. Phosphorescence and delayed fluorescence imaging. *Biophys. J.* 60, 1374–1387. doi: 10.1016/S0006-3495(91)82175-0

Marriott, G., Heidecker, M., Diamandis, E. P., and Yan-Marriott, Y. (1994). Time-resolved delayed luminescence image microscopy using an europium ion chelate complex. *Biophys. J.* 67, 957–965. doi: 10.1016/S0006-3495(94)80597-1

Nuñez, V., Upadhyayula, S., Millare, B., Larsen, J. M., Hadian, A., Shin, S., et al. (2013). Microfluidic space-domain time-resolved emission spectroscopy of Terbium(III) and Europium(III) Chelates with Pyridine-2,6-Dicarboxylate. *Anal. Chem.* 85, 4567–4577. doi: 10.1021/ac400200x

Petrášek, Z., Bolivar, J. M., and Nidetzky, B. (2016). Confocal luminescence lifetime imaging with variable scan velocity and its application to oxygen sensing. *Anal. Chem.* 88, 10736–10743. doi: 10.1021/acs.analchem.6b03363

Piatkowski, L., Hugall, J. T., and Hulst, N. F. (2014). Raman spectroscopy: watching a molecule breathe. *Nat. Photon.* 8, 589–591. doi: 10.1038/nphoton.2014.174

Pollak, A., and Maszkiewicz, M. (1990). *Apparatus for Time-Resolved Photography of Fluorescence*. U. S. Patent No 4,954,714. Washington, DC: U.S. Patent and Trademark Office.

Pominova, D. V., Ryabova, A. V., Grachev, P. V., Romanishkin, I. D., Kuznetsov, S. V., Rozhnova, J. A., et al. (2016). Upconversion microparticles as time resolved luminescent probes for multiphoton microscopy: desired signal extraction from the streaking effect. *J. Biomed. Opt.* 21:096002. doi: 10.1117/1.JBO.21.9.096002

Qu, J. L., Liu, L. X., Chen, D. N., Lin, Z. Y., Xu, G. X., Guo, B. P., et al. (2006). Temporally and spectrally resolved sampling imaging with a specially designed streak camera. *Opt. Lett.* 31, 368–370. doi: 10.1364/OL.31.000368

Ramshesh, V. K., and Lemasters, J. J. (2008). Pinhole shifting lifetime imaging microscopy. *J. Biomed. Opt.* 13:064001. doi: 10.1117/1.3027503

Saito, M., Takahashi, S., and Matsumoto, K. (2005). *Light Measuring Device Avoiding Influence of Fluorescence or Phosphorescence of Lenses and Filters in*

Optical Path. U. S. Patent No US 6,839,134,B2. Washington, DC: U.S. Patent and Trademark Office.

Sakiyama, M., Sugimoto, H., and Fujii, M. (2018). Long-lived luminescence of colloidal silicon quantum dots for time-gated fluorescence imaging in the second near infrared window in biological tissue. *Nanoscale* 10, 13902–13907. doi: 10.1039/C8NR03571G

Selzer, P. M., and Yen, E. M. (1976). High-speed light chopper wheel for modulation spectroscopy. *Rev. Sci. Instr.* 47, 749–750. doi: 10.1063/1.1134728

Strat, D., Dolp, F., Rueck, A. C., Einem, B., Steinmetz, C., and Arnim, C. A. F. (2011). Spectrally resolved fluorescence lifetime imaging microscopy: Förster resonant energy transfer global analysis with a one- and two-exponential donor model. *J. Biomed. Opt.* 16:026002. doi: 10.1117/1.3533318

Sun, Y., Phipps, J., Elson, D. S., Stoy, H., Tinling, S., Meier, J., et al. (2009). Fluorescence lifetime imaging microscopy: *in vivo* application to diagnosis of oral carcinoma. *Opt. Lett.* 34, 2081–2083. doi: 10.1364/OL.34.002081

Tsuchiya, T., Kogita, Y., Taniyama, A., Hirai, Y., Sugano, K., and Tabata, O. (2016). Time-resolved micro-Raman stress spectroscopy for single-crystal silicon resonators using a MEMS optical chopper. *J. Microelectromech. Syst.* 25, 188–196. doi: 10.1109/JMEMS.2015.2503723

Ulku, A. C., Bruschini, C., Antolovic, I. M., Weiss, S., Michalet, X., and Charbon, E. (2019). Phasor-based widefield FLIM using a gated 512×512 single-photon SPAD imager. *Proc. SPIE* 10882:108820M. doi: 10.1117/12.2511148

Urayama, P., Zhong, W., Beamish, J. A., Minn, F. K., Sloboda, R. D., Dragnev, K. H., et al. (2003). A UV–visible–NIR fluorescence lifetime imaging microscope for laser-based biological sensing with picosecond resolution. *Appl. Phys. B* 76, 483–496. doi: 10.1007/s00340-003-1152-4

Vereb, G., Jares-Erijman, E., Selvin, P. R., and Jovin, T. M. (1998). Temporally and spectrally resolved imaging microscopy of lanthanide chelates. *Biophys. J.* 74, 2210–2222. doi: 10.1016/S0006-3495(98)77930-5

Verwoerd, N. P., Hennink, E. J., Bonnet, J., Van der Geest, C. R. G., and Tanke, H. J. (1994). Use of Ferro-electric liquid crystal shutters for time-resolved fluorescence microscopy. *Cytometry* 16, 113–117. doi: 10.1002/cyto.990160204

Walker, B. J., Musser, A. J., Beljonne, D., and Friend, R. H. (2013). Singlet exciton fission in solution. *Nat. Chem.* 5, 1019–1024. doi: 10.1038/nchem.1801

Wang, J., Xue, J., Yan, Z., Zhang, S., Qiao, J., and Zhang, X. (2017). Photoluminescence lifetime imaging of synthesized proteins in living cells using an iridium-alkyne probe. *Angew. Chem. Int. Ed.* 129, 15124–15128. doi: 10.1002/ange.201708566

Wenthen, F. T., and Snowman, L. R. (1973). High speed light choppers. *Appl. Opt.* 12, 822–824. doi: 10.1364/AO.12.000822

Wirth, M. J. (1990). Ultrafast spectroscopy. *Anal. Chem.* 62, 270A—277A. doi: 10.1021/ac00203a716

Yang, W., Srivastava, P. K., Han, S., Jing, L., Tu, C. C., and Chen, S. L. (2019). Optomechanical time-gated fluorescence imaging using long-lived silicon quantum dot nanoparticle. *Anal. Chem.* 91, 5499–5503. doi: 10.1021/acs.analchem.9b00517

Yang, Y., Zhao, Q., Feng, W., and Li, F. (2013). Luminescent chemodosimeters for bioimaging. *Chem. Rev.* 113, 192–270. doi: 10.1021/cr2004103

Zhang, K. Y., Yu, Q., Wei, H., Liu, S., Zhao, Q., and Huang, W. (2018). Long-lived emissive probes for time-resolved photoluminescence bioimaging and biosensing. *Chem. Rev.* 118, 1770–1839. doi: 10.1021/acs.chemrev.7b00425

Zhang, L., Zheng, X., Deng, W., Lu, Y., Lechevallier, S., Ye, Z., et al. (2014). Practical implementation, characterization and applications of a multi-colour time-gated luminescence microscope. *Sci. Rep.* 4:6597. doi: 10.1038/srep06597

Zheng, X., Zhu, Z., Lu, Y., Zhao, J., Feng, W., Jia, G., et al. (2016). High-contrast visualization of upconversion luminescence in mice using time-gating approach. *Anal. Chem.* 88, 3449–3454. doi: 10.1021/acs.analchem.5b04626

Zhu, Z. (2019). Smartphone-based apparatus for measuring upconversion luminescence lifetimes. *Anal. Chim. Acta* 1054, 122–127. doi: 10.1016/j.aca.2018.12.016

Zhu, Z., and Shu, X. (2018). Auto-phase-locked measurement of time-gated luminescence spectra with a microsecond delay. *Opt. Lett.* 43, 2575–2578. doi: 10.1364/OL.43.002575

Zhu, Z., and Shu, X. (2019). Global luminescence lifetime imaging of thermally activated delayed T fluorescence on an auto-phase-locked time-gated microscope. *Sens. Actuators B Chem.* 280, 177–182. doi: 10.1016/j.snb.2018.10.071

Zhu, Z., Song, B., Yuan, J., and Yang, C. (2016). Enabling the triplet of tetraphenylethene to sensitize the excited state of europium (III) for protein detection and time-resolved luminescence imaging. *Adv. Sci.* 3:1600146. doi: 10.1002/advs.201600146

Zhu, Z., Tian, D., Gao, P., Wang, K., Li, Y., Shu, X., et al. (2018a). Cell-penetrating peptides transport noncovalently linked thermally activated delayed fluorescence nanoparticles for time-resolved luminescence imaging. *J. Am. Chem. Soc.* 140, 17484–17491. doi: 10.1021/jacs.8b08438

Zhu, Z., Tian, D., and Shu, X. (2018b). Auto-phase-locked time-gated luminescence detection for background-free upconversion spectra measurement and true-color biological imaging. *Sens. Actuators B Chem.* 260, 289–294. doi: 10.1016/j.snb.2018.01.012

Conflict of Interest: The authors declare that the research was conducted in the absence of any commercial or financial relationships that could be construed as a potential conflict of interest.

frontiers in Physics

REVIEW
published: 26 April 2021
doi: 10.3389/fphy.2021.648553

A Review of New High-Throughput Methods Designed for Fluorescence Lifetime Sensing From Cells and Tissues

Aric Bitton†, *Jesus Sambrano*†, *Samantha Valentino and Jessica P. Houston**

Department of Chemical and Materials Engineering, New Mexico State University, Las Cruces, NM, United States

Though much of the interest in fluorescence in the past has been on measuring spectral qualities such as wavelength and intensity, there are two other highly useful intrinsic properties of fluorescence: lifetime (or decay) and anisotropy (or polarization). Each has its own set of unique advantages, limitations, and challenges in detection when it comes to use in biological studies. This review will focus on the property of fluorescence lifetime, providing a brief background on instrumentation and theory, and examine the recent advancements and applications of measuring lifetime in the fields of high-throughput fluorescence lifetime imaging microscopy (HT-FLIM) and time-resolved flow cytometry (TRFC). In addition, the crossover of these two methods and their outlooks will be discussed.

Keywords: fluorescence lifetime, high-throughput approaches, fluorescence lifetime imaging microscopy, flow cytometry, frequency domain, time domain

OPEN ACCESS

Edited by:
Gerard Marriott, University of California, Berkeley, United States

Reviewed by:
Nirmal Mazumder, Manipal Academy of Higher Education, India
Edoardo De Tommasi, National Research Council (CNR), Italy

***Correspondence:**
Jessica P. Houston
jph@nmsu.edu

†*These authors have contributed equally to this work*

Specialty section:
This article was submitted to Optics and Photonics, a section of the journal Frontiers in Physics

Received: *31 December 2020*
Accepted: *15 March 2021*
Published: *26 April 2021*

Citation:
Bitton A, Sambrano J, Valentino S and Houston JP (2021) A Review of New High-Throughput Methods Designed for Fluorescence Lifetime Sensing From Cells and Tissues. Front. Phys. 9:648553. doi: 10.3389/fphy.2021.648553

INTRODUCTION

The fluorescence lifetime is a unique optical parameter that has been exploited for many decades for a variety of biological applications. The fluorescence lifetime is defined as the average time a molecule spends in an excited state prior to returning back to its relaxed ground state. When measured, most organic fluorophores have a fluorescence lifetime that ranges between 100 ps and 15 ns [1]. When this lifetime is measurable, the information that it encodes reveals direct or indirect changes of the fluorophore itself, as well as its surroundings. Every fluorescence molecule has a unique fluorescence lifetime, and the value of the lifetime is reflected by the chemical and physical characteristics of the microenvironment in which the fluorophore resides [2]. Moreover, the fluorescence lifetime is independent of fluorescence brightness; thus, the fluorescence lifetime can be detected from dim fluorescence signals, making accurate measurements of fluorophores that are dim or in low concentrations possible. With these unique characteristics, the lifetime of a fluorophore has become quite valuable in life sciences. For example, Förster resonance energy transfer (FRET), a phenomenon where fluorescence properties are altered when two fluorophores are in close proximity (<10 nm), can be more accurately quantified using lifetime compared to other fluorescence properties [3]. This and other advantages have led to a variety of novel bio-inspired applications where the resulting lifetime data reveal new discoveries. Since the fluorescence lifetime continues to be a sought-after optical parameter, we use this review to focus on technologies that measure fluorescence lifetime with a focus on higher-throughput systems.

The applications of fluorescence lifetime measurements range significantly. Some examples include separating fluorophores that have similar spectra but different lifetimes [4–13], exploiting

the difference in lifetime of free and bound metabolites for metabolic study and diagnosis [14–24], using FRET to screen for binding or inhibition of exogenous and endogenous molecules of interest [2, 5, 25–35], evaluating the conformation and stability of proteins or other molecules in varying environments [31, 36], or even using lifetime as an additional parameter in fluorescent inks for anti-counterfeiting [37], though this list is far from exhaustive. New methods and technologies continue to be discovered, further establishing the wide-reaching significance and potential of fluorescence lifetime. Along with these distinct advantages and potential, there are unique challenges present in measuring fluorescence lifetime. Most of these difficulties arise from the short timescale of fluorescence decay, though these are now much easier to overcome given the current state of the modern laser, microchip, and other optoelectronic technologies. Ranging from hundreds of picoseconds to tens of nanoseconds, recording the process requires high-speed excitation, detection, and data acquisition hardware and techniques.

Measuring the fluorescence lifetime is traditionally approached in one of the two ways: with optoelectronics that involves either time-domain or frequency-domain measurements (see **Figure 1**). In the time domain, the timing of fluorescence photons is directly measured, often against a pulse of excitation light, as if the excitation light is starting a clock or a timer. A few of the most common time-domain methods are time-correlated single-photon counting (TCSPC), time gating, and direct waveform recording or pulse sampling. TCSPC uses fast electronics and/or fast detectors to measure the arrival time of individual photons. These arrival times of the photons are then gathered into time bins and visualized with a histogram. As shown in **Figure 2**, less photons will be present in the time bins as the fluorescence decays, causing the shape of the histogram to be representative of the decay curve and showing graphically the probability density function of the photon arrival times [38]. Though TCSPC can be very accurate and have a high temporal resolution, the throughput is heavily dependent on the ability of the detector and electronics to avoid photon pile-up. This is caused by the dead time, a period after initial triggering where no photons will be recorded until the detector and electronics are re-primed. Reducing dead time has been a main source of innovation for increasing throughput and will be discussed further along with detection devices. Unlike TCSPC, time gating does not record the fluorescence decay in terms of individual photon timing but handles the measurements in short sections of time that cover a set portion of the decay curve, stitching those sections together digitally for the full picture. Direct waveform recording uses high-speed digitizers and records the entire waveform of the fluorescence signal, from which the lifetime information is then extracted. The latter two methods are not as affected by, or avoid entirely, the issue of detector dead time and thus can have faster acquisition speeds, but they are generally not as sensitive or accurate as TCSPC.

To measure fluorescence lifetime in the frequency domain, the excitation source intensity is modulated, causing the resulting fluorescence signal to follow the same pattern. However, due to the fluorescence decay time, the fluorescence signal will be shifted compared to the excitation source signal. This phase shift is directly proportional to the fluorescence lifetime and can be extracted mathematically, i.e., using Fourier transforms [39]. Since this method employs continuous fluorescence detection rather than pulsed or gated detection seen in most time-domain methods, photon pile-up does not occur and frequency-domain lifetime detection can be used at much higher throughputs, such as those seen in flow cytometry [40]. However, the performance is more dependent on the brightness of the sample

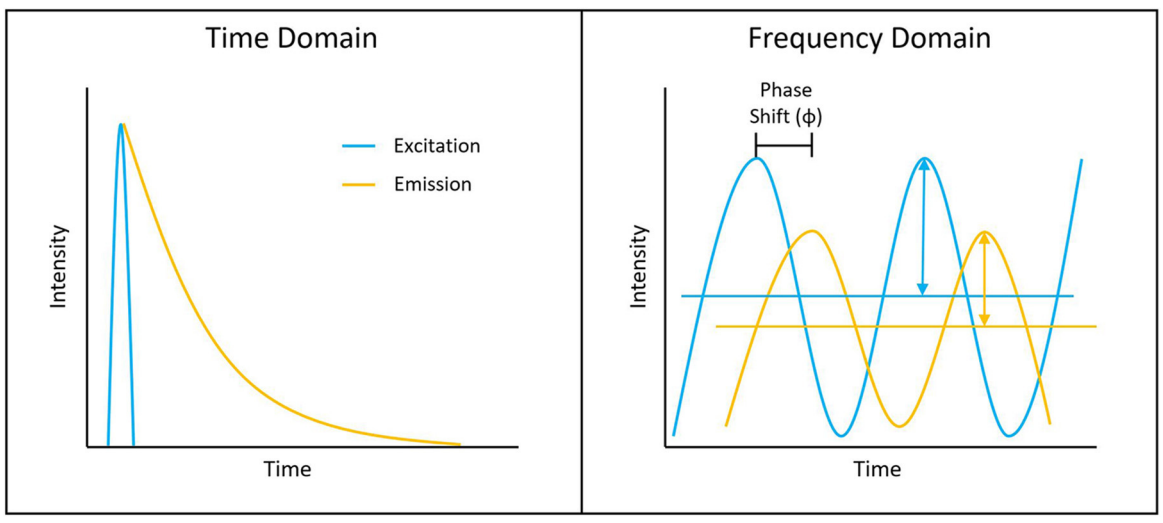

FIGURE 1 | Depiction of typical time-domain data **(left)** and frequency-domain data **(right)**. Lifetime determination in the time domain is a function of the decay curve created by a histogram of photon arrival times. For the frequency domain, the lifetime is a function of the phase shift between the laser excitation and fluorescence emission light.

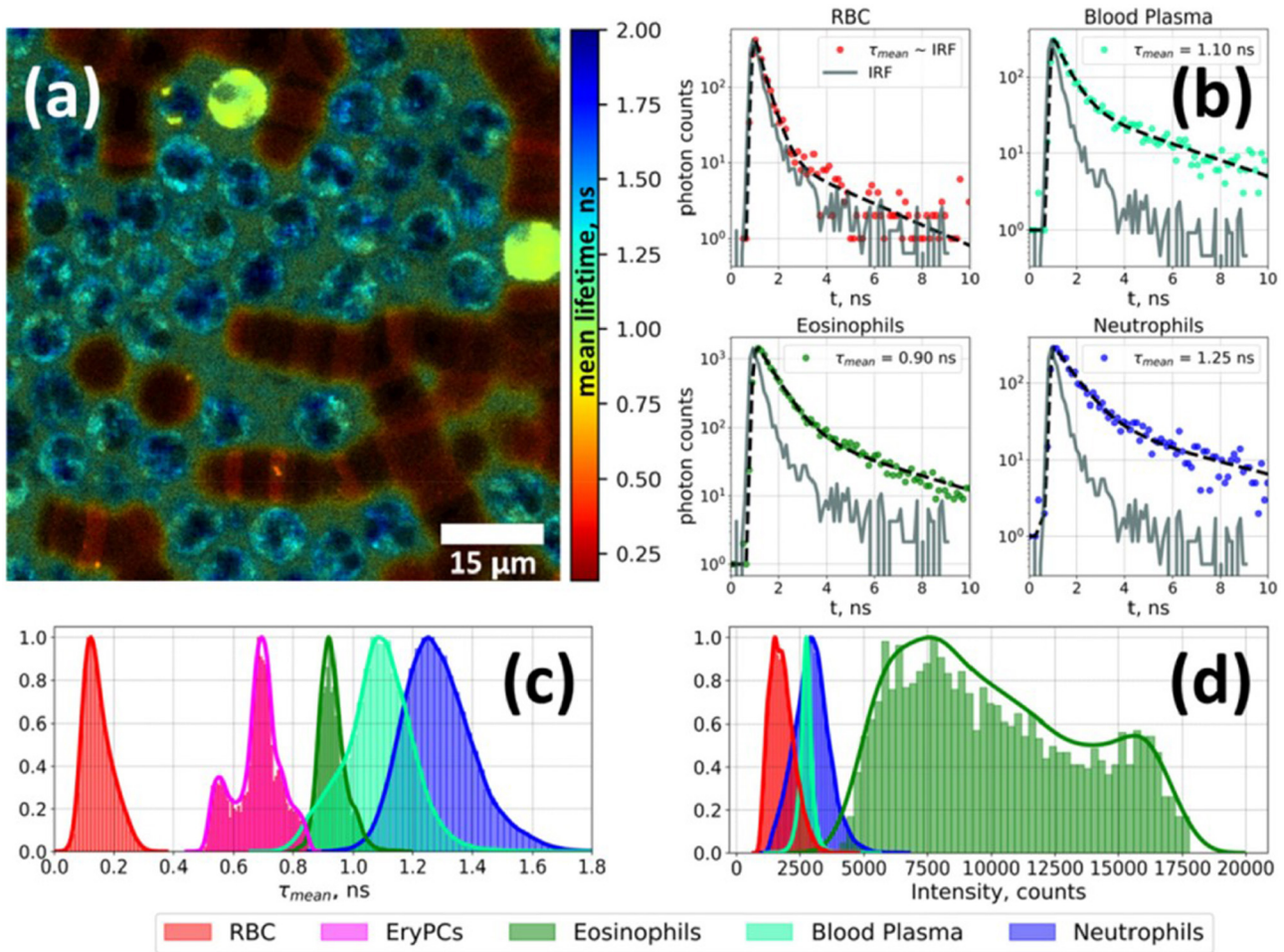

FIGURE 2 | Fluorescence lifetime imaging microscopy image of autofluorescence from a white blood cell-enriched sample excited at 402 nm and collected at >520 nm **(a)**. Fluorescence decay curves for each blood-cell type was generated using time-correlated single-photon counting (TCSPC) along with a biexponential decay curve fit **(b)**. Plots of average fluorescence lifetime **(c)** and integral fluorescence intensity for each cell type **(d)**. Adapted with permission from [23] © The Optical Society.

and measurements are generally lower in accuracy, resolution, or both compared to what is achievable in the time domain.

Both time-domain and frequency-domain high-throughput methods will be discussed in the context of fluorescence lifetime imaging microscopy (FLIM) and time-resolved flow cytometry (TRFC) in the following sections of the review. A summary of the lifetime techniques to be discussed is provided in **Table 1**.

HIGH-THROUGHPUT FLIM (HT-FLIM)

The large field of FLIM that encompasses many different methods, instruments, and applications is attributed to the long-standing history of fluorescence microscopy. Increasing the speed and throughput capabilities of FLIM systems reduces the imaging time and can increase multiplexing capabilities, magnifying its usefulness in many applications, particularly those that are time-sensitive, such as real-time imaging or clinical diagnosis. However, increasing speed and/or throughput usually entails compromises, typically in the form of reduced temporal or spatial resolution and accuracy. The opposite is also generally true; if high accuracy and resolution are desired, then image acquisition time is long. These compromises can often be a function of the microscopy platform used, such as widefield vs. confocal, or be a result of the detection and data acquisition systems. **Figure 3** contains a schematic picture of a general FLIM setup. This review focuses on more recent systems from literature in the past decade or on those leading the advancement in HT-FLIM methods and technology with discussions on capabilities, innovations, trade-offs, and current applications. Since TCSPC is to some extent a gold standard and is heavily utilized in FLIM [11], discussion of systems and applications will be separated by those that are TCSPC-based and those that are not, including frequency-domain FLIM.

TABLE 1 | Common fluorescence lifetime sensing techniques.

Technique	Theory/Principle	Detection method	Advantages	Limitations
TCSPC (Time domain)	Timing of fluorescence photons is measured against a pulsed excitation source and organized into a histogram representing the fluorescence decay curve.	Timing electronics paired with detectors (PMTs, hybrid PMTs, APDs), or silicon-based detectors with built-in timing circuitry (SPADs with TDCs).	Very high accuracy and temporal resolution	Photon pile-up/detector dead time. Lower throughput.
Time gating (Time domain)	Similar to TCSPC, but only small sections of the fluorescence decay curve are measured at a given time or across a given detection channel.		Limits or eliminates issues of pile-up and/or dead time for faster acquisition.	Typically less sensitive and/or accurate compared to TCSPC.
Direct waveform recording	Entire fluorescence waveform is captured and used to extract the fluorescence lifetime.	Fast detectors paired with high-speed digitizers to convert the analog signal real-time.		
Frequency domain	Decay time results in a phase shift between fluorescence and excitation source that is directly proportional fluorescence lifetime and can be calculated using Fourier transforms.	Function generators required to modulate excitation source. Standard fluorescence detectors and high speed data acquisition systems.	Continuous detection with very high throughput.	Accuracy, resolution, or both are more dependent on fluorophore brightness.

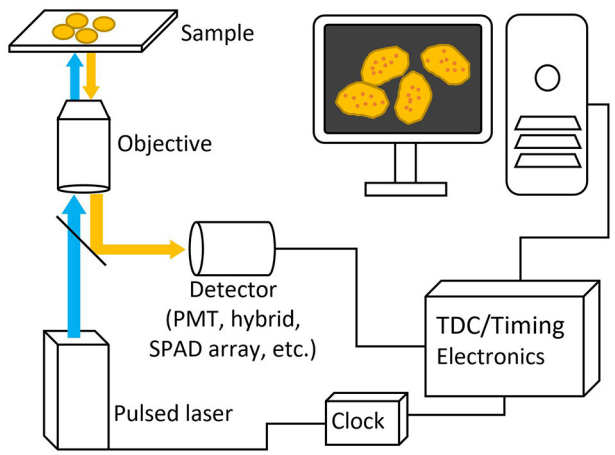

FIGURE 3 | Basic schematic picture of a generalized FLIM system. Pulsed excitation light passes through the microscope to the sample and the excitation light travels back through and is deflected to a detector with a dichroic mirror. Both laser and detector setups are then connected to timing electronics for lifetime calculation.

TCSPC in HT-FLIM

TCSPC is a long-used and extensively researched method in FLIM due to its hardware availability, high sensitivity, resolution, and various possible implementations. The main setback for TCSPC with regard to throughput is photon pile-up caused by dead time in the detector and timing electronics, during which valuable information is lost from the photons that are not detected. As a result, much of the research involved in increasing TCSPC throughput is centered on either decreasing the dead time or finding ways to mitigate the effects of dead time and reduce photon pile-up. Traditionally, photomultiplier tubes (PMTs) are used, operating in single-photon counting mode with separate electronics for signal processing and analysis. In the context of TCSPC, this only provides one channel for photon timing with limited throughput [41]. One solution to this issue is parallelization, which theoretically can be applied to any detector/timing electronic setup, given there is enough funding, space, and power available. In 2012, however, one group presented a more elegant, highly parallelized solution capable of 10× the photon counting rates of traditional TCSPC using an iteration of their novel single-photon avalanche diode (SPAD) array that included an accompanying array of time-to-digital converters (TDCs) and circuitry to perform lifetime estimations in real time on one chip made using a CMOS process [42]. Since then, the technology has been continuously improved through increasing the SPAD array pixel count [43], creating a multi-focal system to increase resolution and detector efficiency, and moving from a widefield to a laser-scanning approach for live FRET studies [26]. The attractiveness of having a scalable, accurate, all-in-one TCSPC solution built into a microchip has encouraged others to develop their own SPAD array systems using similar CMOS processes for specific applications, such as a high-speed, large pixel count camera for fluorescence lifetime imaging at high frame rates [44]. For a more in-depth look at the history, architecture, and application of SPADs in FLIM and other fields, the recent review by Bruschini et al. is recommended [45].

Although integrated silicon photomultiplier SPAD arrays are highly versatile and provide great temporal resolution, they are not a universal answer for TCSPC. Apart from the standard PMT and counting hardware setup, there are hybrid detectors (called hybrid PMTs) that combine the photocathode and vacuum tube from PMTs with avalanche diodes, similar to those seen in SPADs but operated at lower voltages, resulting in much lower detector dead times (<1 ns) compared to PMTs and SPADs alone (>10 ns) [41]. When paired with fast timing electronics, such as fast

TDCs, systems employing hybrid detectors for TCSPC can have count rates comparable to some SPAD arrays while being simpler and made entirely from off-the-shelf products [11]. As a result, system complexity and cost can be more dependent on the timing electronics than the hybrid PMTs and be chosen to fit the needs of the application.

Non-TCSPC-Based HT-FLIM

Time-gated approaches to FLIM involve recording the fluorescence decay kinetics in small sections of time (gates) and then combining those sections. This gives the same final result as TCSPC: a decay curve that represents the probability density function of photon arrival times used to calculate the fluorescence lifetime. These gates can be measured sequentially using one channel or simultaneously using multiple timing channels for higher acquisition throughputs. As a result, detector dead time is less of an issue than in TCSPC, but photon efficiency is lower since only part of the decay curve is being recorded at a time, though the multichannel techniques lessen this loss of photon efficiency. Analogous to integral approximation methods in calculus, having more time gates with smaller widths results in higher lifetime accuracy, particularly for fluorophores with short lifetimes or multiexponential decay, while having a longer overall detection time improves accuracy for longer fluorescence lifetimes [46]. Adding more gates or increasing the detection window size leads to longer acquisition times and lower throughput; however, analysis algorithms [21, 47] and even deep learning [22] have been implemented to maintain accuracy while collecting less images or gates. Similar detectors used for TCSPC can be used in time-gated FLIM, including modified SPAD arrays with gating electronics.

Select methods that do not fall under the main umbrellas of TCSPC or time gating are direct waveform recording (DWR) and frequency-domain FLIM (fd-FLIM). Similar to TCSPC and time gating, a pulsed laser source and common detectors, like PMTs, are used, but instead of the typical timing electronics following the detector, a high-speed digitizer records the entire analog waveform coming out of the detector, largely avoiding the issue of dead time inherent in photon counting. One recent application of DWR can be found in a fluorescence lifetime microplate reader using a high-intensity laser to allow for a fast and accurate lifetime recording and FRET recording, covering a 384-well-plate in 3 min in the early designs and, more recently, a 1,536-well-plate in the same amount of time [6, 29, 30, 32]. Generally being a simpler option to acquire fluorescence lifetime images at high frame rates, fd-FLIM remains viable for those who require speed over the high accuracy or sensitivity. Some recent implementations of fd-FLIM include an automated wide-field system built from commercial parts for FRET analysis of samples in 96-well-plates or microscope slides [28] and the use of a modulated laser in light-sheet microscopy with a CMOS camera to perform real-time, 3D fluorescence lifetime imaging [48].

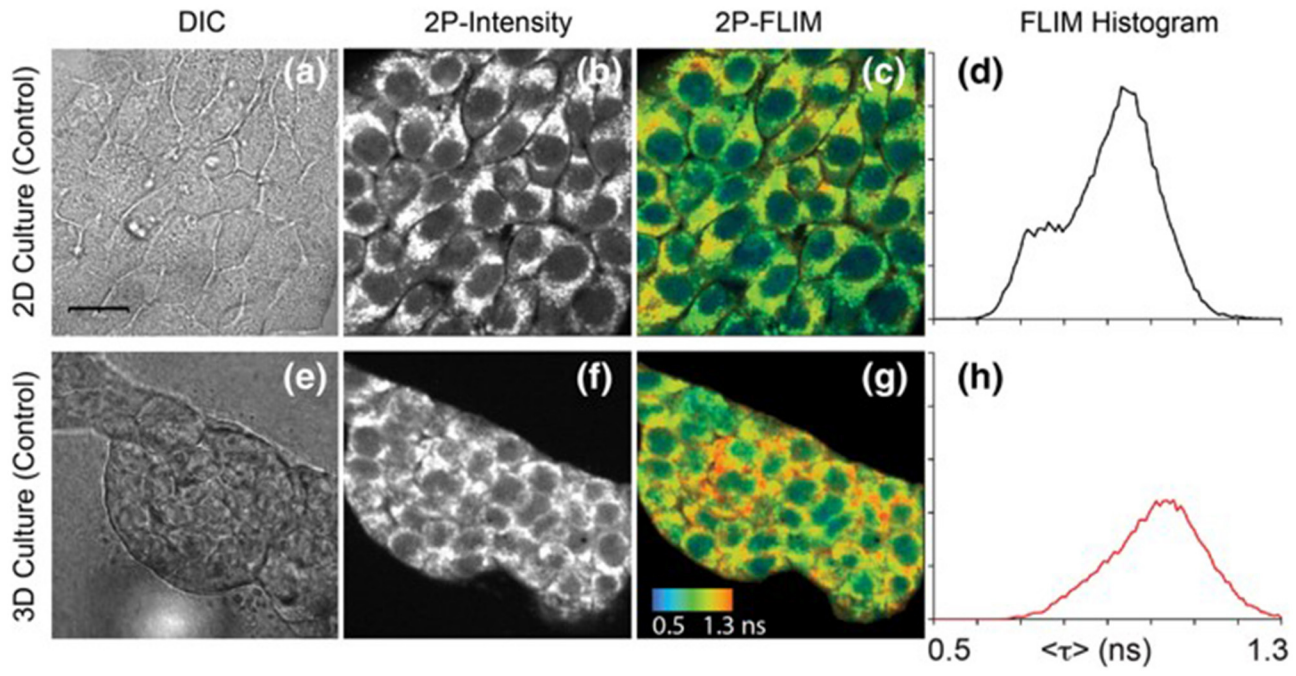

FIGURE 4 | Images of NAD(P)H in 4T1 cells taken from a 2D monolayer culture and 3D matrix culture showing differential interference contrast microscopy **(a,e)**, two-photon fluorescence intensity **(b,f)**, and two-photon FLIM **(c,g)** along with histograms of the fluorescence lifetimes from the FLIM images **(d,h)**. These images highlight the usefulness of two-photon excitation to image live cells *in vivo* as there were differences in cell metabolism, as indicated by NAD(P)H fluorescence, between cells cultured in a typical lab environment (2D monolayer) and those cultured in a more realistic environment (3D culture). Adapted with permission from [20] © 2018 International Society for Advancement of Cytometry.

Multiphoton Excitation

Another notable facet of FLIM technologies is the capability of multiphoton excitation. Traditional FLIM systems use one-photon excitation, where the absorption event of one photon provides the energy required to raise an electron to an excited state. However, as first theorized in 1929 and later proven in 1961, it is possible for two (or more) lower-energy, longer-wavelength photons to simultaneously interact with an electron to result in excitation [49]. This results in a number of benefits, such as less damage and deeper penetration in live samples, given the longer excitation wavelength, greater spectral separation between the excitation light and emission light, and the inherent ability to perform optical sectioning due to the non-linear relationship between excitation light intensity and multiphoton absorption [50]. Since much greater light intensity is required to make up for the lower probability of more than one photon simultaneously being absorbed, multiphoton excitation typically employs the use of highly focused, femtosecond-pulsed lasers. This allows for moments of very high intensity and low overall laser power felt by the sample and, consequently, is already an ideal excitation setup to perform FLIM and can utilize the lifetime detection methods discussed previously. Due to the nature of the advantages fundamental to multiphoton excitation, applications often involve *in vivo* imaging (see **Figure 4**), viewing dynamic biological processes over time, or imaging fluorophores with short-wavelength absorption within delicate live samples [13, 17, 19, 20, 26, 51].

TIME-RESOLVED FLOW CYTOMETRY

Time-resolved flow cytometry remains a niche field when compared to FLIM, mainly owing to the high-throughput nature of flow cytometry methods. TRFC was first demonstrated in the 1990s in the form of "phase-sensitive flow cytometry" (PSFC) [52, 53]. PSFC used analog phase-sensitive detection electronics, in which the excitation source and photodetectors were homodyned to resolve phase shifts between the modulated excitation source and the fluorescence emission (see **Figure 5**). The amplitude-demodulated fluorescence signal was phase-shifted to $\pi/2+\varphi_1$ with respect to the reference signal to directly calculate the fluorescence lifetime value. This concept was demonstrated using Chinese hamster ovary (CHO) cells that were exogenously labeled with fluorescein isothiocyanate (FITC) and propidium iodide (PI). After binding, a mean lifetime of 3.5 ns was reported for FITC, whereas the mean lifetime of bound PI was measured to be at 15.0 ns. Digitalization of time-resolved waveforms shortly followed [54], allowing for more rapid analysis including the introduction of dual-frequency analysis [55] for improved single-cell analysis and the first chromophore quenching study in TRFC [56]. DNA content was analyzed in viable cells with exogenous DNA-binding probes [57], bringing about cell-cycle analysis using TRFC, and it progressed to the analysis of fixed cells to quantify and discriminate DNA and RNA content [58, 59]. TRFC emerged from NFCR during the late 2000s, and the niche technology began to mature and became a more versatile technology that focused on overcoming limitations found in conventional flow cytometry [60].

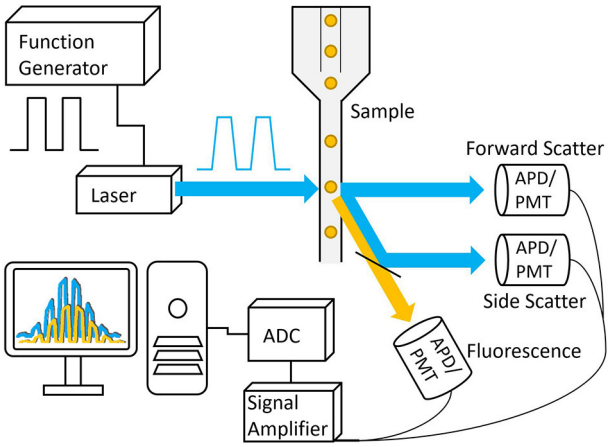

FIGURE 5 | Basic schematic of a frequency-domain TRFC system. A function generator is used to modulate the laser that is then focused onto a small interrogation point in the flow path of the sample. The scattered excitation light and fluorescence emission light are directed toward the detectors, producing analog signals that are amplified and digitized by the analog-to-digital converter.

Frequency-Domain TRFC

The advancements in electro-optical technologies and instruments have facilitated a currently widespread use of frequency-domain flow cytometry (fd-FCM) systems [39]. Some examples of these advancements include the ability to directly modulate a solid-state laser at radiofrequency, modular high-speed transimpedance amplifiers, high-speed analog-to-digital conversion with field programmable gating array (FPGA) capabilities, and the overall size reduction of processing hardware [40]. The main advancement that has benefited from TRFC is the data-acquisition systems with digital sampling rates in excess of 100 mega samples per second (MSPS). Using these systems enabled researchers to perform TRFC for lifetime analysis as well as sorting with modified commercial systems [4, 7, 39]. For example, sorting based on the fluorescence lifetime was made possible using digital signal processing (sort purities >90%) as well as the development of pseudophasor analyses [4, 7, 61]. The sorting feasibility study which was performed involved separating yeast cells that expressed fluorescence proteins (XFPs) having co-spectral emission [7]. That is, different XFPs with similar emission spectra were measured and separated based on their fluorescence lifetime values. The observed difference is illustrated in the pseudophasor graphs given in **Figure 6**.

Sorting-based TRFC and non-sorting TRFC measurements both benefit from the use of phasor analysis (**Figure 7**). Phasor graphing is quite useful to TRFC because a phasor plot is comparable to a cytometry scatter plot. Scatter plots are useful for setting sort gates and for drawing conclusions about population distributions. Phasor plots were first introduced

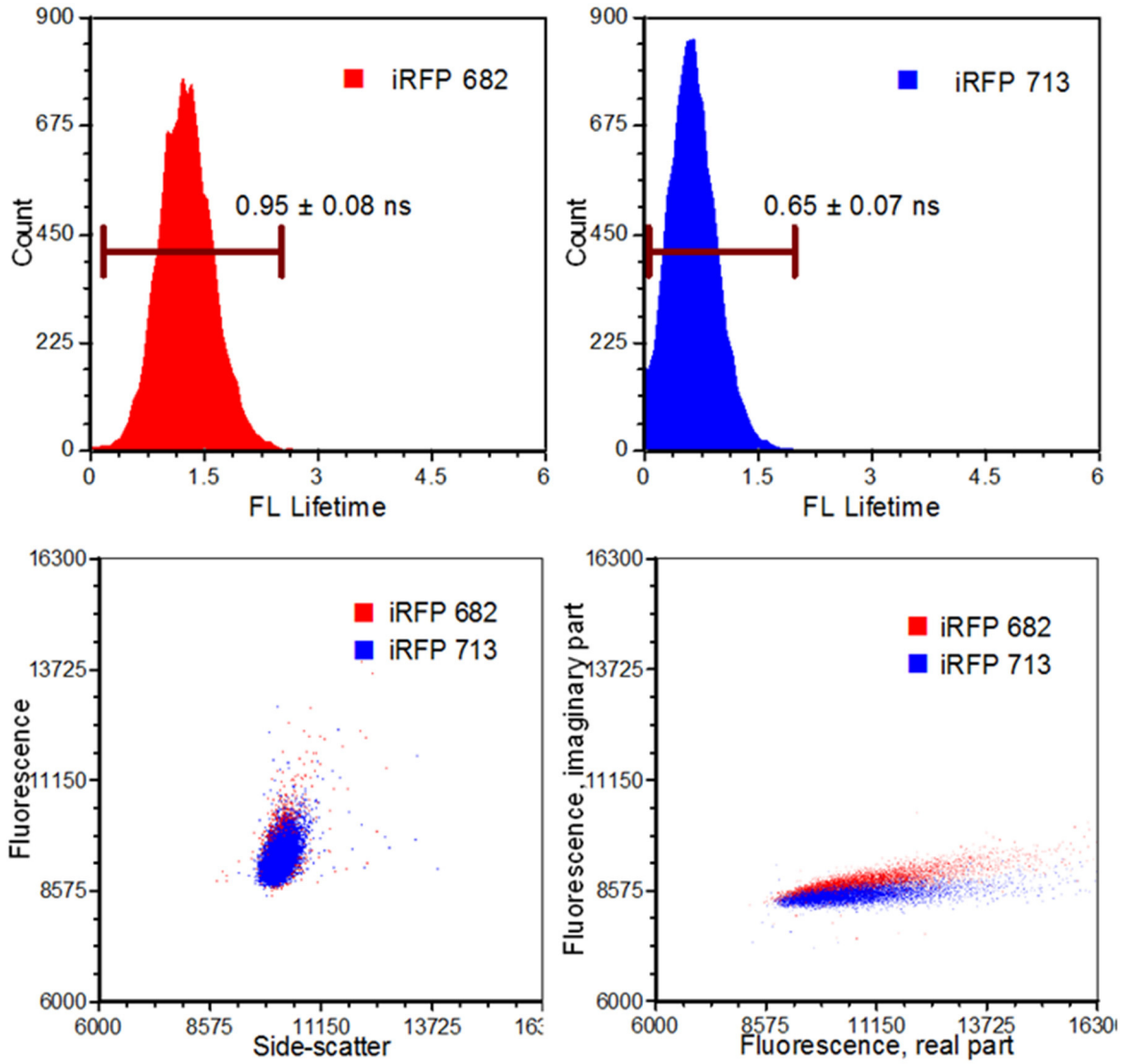

FIGURE 6 | Results from an infrared fluorescent protein study (iRFP). Left, top: An iRFP with an emission maximum of 682 nm expressed a fluorescence lifetime value of 0.95 ± 0.08 ns. Right, top: An iRFP with an emission maximum of 713 nm expressed a fluorescence lifetime value of 0.65 ± 0.07 ns. Bottom, left: Dot-plot illustrating fluorescence vs. side-scatter for both the iRFP populations. Conventional fluorescence-activated cell sorting applies population gating to sort and enrich populations of interest. Significant overlap would inhibit users from achieving high sort yields. Authors from Yang et al. [62] applied time-resolved sorting to achieve maximum sort yields. Time-resolved data is processed by a fast Fourier transform and is transposed to frequency spectrums. Direct current and modulating frequencies are identified to calculate the phase value on a per-event basis. The subtle differences with respect to phase values between the two iRFPs illustrate two distinctive populations that permit sorting. Figure adapted with permission from The Optical Society ® [62].

with FLIM data. With phasor analysis, the lifetime data are coordinate-transformed such that the magnitude of the demodulation value is represented as a magnitude (point) in the phasor space, and the phase-shift value is represented by the angle of the vector relative to the horizontal axis of the phasor graph. With TRFC, each point on the phasor graph is representative of the signal from a single cell; thus, for each cell, the intensity-weighted average of all present lifetime components [8] is considered. If the weighted value falls at the outer semi-circle, the signal obtained is a single fluorescence lifetime, not a combination of more than one. When the weighted phasor value for a given cell is observed to be inside the semi-circle, it can be inferred that multiple decay kinetics are present. Thus, the value represents the presence of multiple fluorescence lifetimes [63]. The robustness of phasor graphing was demonstrated in a TRFC FRET integrin study where surface integrins varied in their conformational states in the absence and presence of artificial stimuli. The study found the existence of multiple photophysical states of an antigen-conjugated chromophore that were not easily resolved with TRFC alone (see **Figure 8**) [31]. Phasor analyses can generally improve TRFC data collection and provide a way to statistically map lifetime changes, which is important for many biological applications.

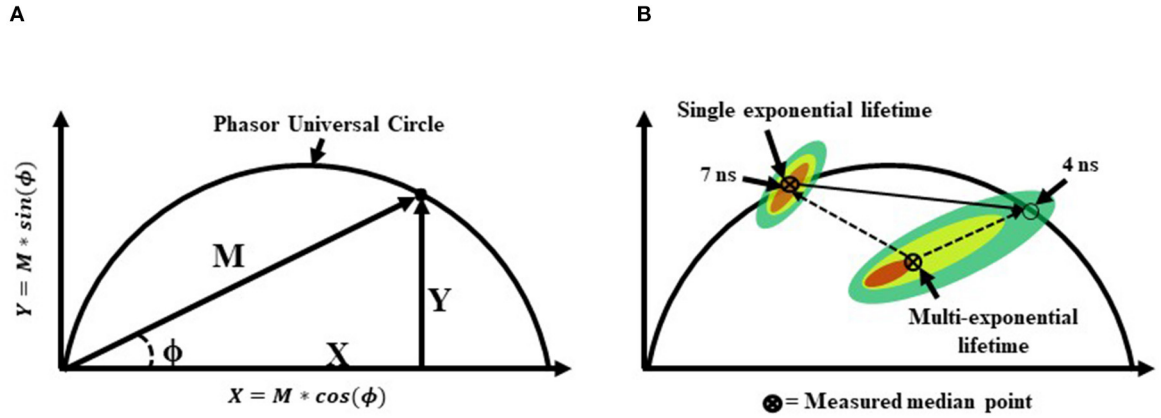

FIGURE 7 | (A) A graphical representation of a phasor graph. Raw data is transposed to the frequency domain by applying a discrete Fourier transform. Data are visualized in a frequency spectrum where the phase (ϕ) and modulation (M) factors are extrapolated to construct the phasor graphs. Calculated events that fall directly on the phasor universal circle represent a single exponential lifetime, whereas calculated events falling within the phasor universal circle represent multiple exponential lifetimes. Alternatively, it is possible to gain insight into the weighted mean lifetime by calculating fractional contributions of different lifetime components using lifetime component vectors as represented in part **(B)**.

The many single-cell analysis and sorting applications that have benefited from the use of TRFC include both digital frequency-domain and time-domain (described later) approaches. Some examples of frequency-domain TRFC include the measurement of fluorescence protein translocation within cells. TRFC measurements of protein movement were studied in the context of autophagy [25], in which the lifetime of enhanced green fluorescence protein (EGFP) when bound to the LC3 protein was affected depending on how the fusion protein was sequestered inside the cell. Thus, the lifetime was an indirect measure of the punctae localization of EGFP-LC3 into autophagosomes. In other examples, TRFC was used to study enzyme activity during apoptosis with the aid of tunable-FRET bioprobes [27]. The goal of the specialty bioprobes was to enable quantitative analysis of enzyme activity for high-content screening toward the discovery of potent anti-cancer agents. This work was later extended by the inclusion of TRFC phasor analyses, which provided statistical "fingerprints" of the loss of FRET, which was correlated to caspase enzyme activity at the onset of apoptosis [34]. In other fd-FCM studies, apoptosis-dependent phagocytosis of bacteria-inoculated cells was examined to determine if EGFP lifetimes could be used as a pH indicator, since pH changes are often expected in the phagosome microenvironment during phagocytosis of bacteria cells by macrophages [9]. A decrease in the EGFP fluorescence lifetime by ∼1 ns was measured with fd-FCM as EGFP-labeled bacteria were taken in by the macrophage cells. Finally, in more recent studies, lifetime changes in the metabolic cofactor, NAD(P)H, have been measurable with TRFC. These metabolic mapping studies contribute to a growing body of FLIM research on the bound and free states of NAD(P)H, which influences the decay kinetics of this endogenous fluorophore. When measured with a cytometry system, the NAD(P)H fluorescence lifetime can be screened for large numbers of cells, thereby revealing the heterogeneity in the metabolic state from cell to cell [18]. The lifetime measurement of NAD(P)H as well as flavin adenine dinucleotide is common in FLIM and is now being studied using fd-FCM.

Time-Domain TRFC

Time-resolved flow cytometry with time-domain systems has also been designed and optimized for a variety of biological applications. Time-domain flow cytometry (td-FCM) systems excite cells with consecutive excitation pulses, and the fluorescence decay is measured over a given time resolution. These cytometers perform photon counting with optoelectronics that capture photons and bin them with respect to their arrival time [64]. As discussed previously, in time-domain FLIM, the systems that acquire time decay kinetics can be slower than their frequency domain counterparts due to dead times between detection windows. In td-FCM, pulse back-up occurs, resulting in the counting of losses as the event rate increases. However, in the time domain, multiple lifetimes can be readily calculated cell by cell. In a recent example, td-FCM was demonstrated with PMT detectors, TCSPC control modules, and microfluidic-based flow control. This work, by Nedbal et al., captured photons in 20 μs time bins and fit data with exponential decay models. The throughput of this system reached approximately 3,000 events min^{-1}; in contrast, fd-FCM systems count at rates up to 60,000 s^{-1}. However, in 2016, advancements were made with respect to CMOS sensors, providing higher-resolution timing through embedded FPGAs and reducing data transfer rates and CPU power needed to process raw data. The implementation of a CMOS SPAD array in conjunction with a series of eight time-interleaved TDCs greatly reduced signal pile-up, allowing for a maximum sample rate of 60,000 s^{-1} with very low error rates [65].

Other unique hybrid td-FCM systems have been developed in order to enhance the ability of a cytometer to capture multiple-decay kinetic signals while retaining a high event rate. One

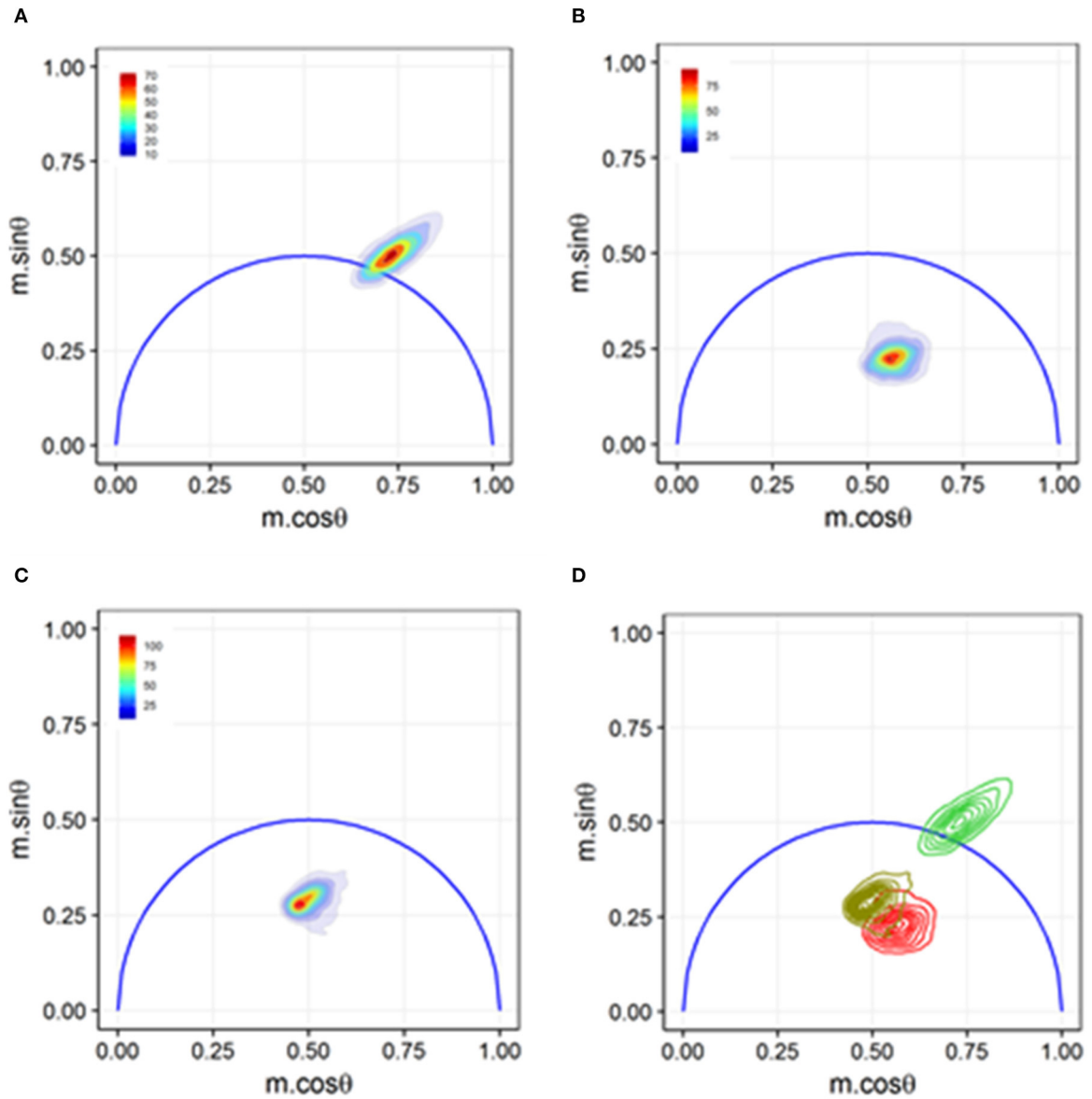

FIGURE 8 | Phasor graph analysis for a Förster resonance energy transfer (FRET) study that resolved integrin conformational changes in the presence of artificial stimuli. **(A)** Transfected U937 ΔST cells were labeled with conjugated donor probe Leucine-Aspartic Acid-Valine binding residue conjugated to fluorescein isothiocyanate (LDV-FITC). The LDV residue has an affinity for the binding site on the inactive $\alpha 4$ integrin. **(B)** Acceptor probe PKH-26 (red, lipophilic fluorescent cell membrane dye), which binds to the cell membrane, was introduced to the cell suspension. Immediate quenching occurs because of the proximity of the donor probe to the acceptor probe. The population transits to the center of the phasor graph, indicating the presence of multiple fluorescence lifetimes as some cells are undergoing FRET and some are unaffected. **(C)** Artificial stimuli formyl Methionine-Leucine-Phenylalanine-Phenylalanine (fMLFF) elicits activation of $\alpha 4$ integrins. Integrins extend to their activated state, effectively removing the donor probe out of the proximity of the acceptor probe. Significant heterogeneity was present due to cell response or lack thereof to the artificial stimuli. **(D)** Contour plots illustrating the distribution and overlap of FRET and loss of FRET populations. Noticeable shifts were seen between the two populations, indicating a general response to the artificial stimuli. Figure adapted with permission from The Optical Society ® [31].

example of this was a td-FCM system in which the excitation source was "pulsed" over the moving cell multiple times with the aid of acousto-optic deflection [5]. The laser was "rastered" across the cell several times in the span of 25 ns, enabling the ability to acquire multiple single exponential decay and dual exponential decay waveforms per cell in a single spectral channel. To resolve the decay kinetics of the excited fluorophores, a post-processing deconvolution analysis was applied to the scatter and fluorescence waveforms. If a single exponential decay is assumed to be present, a convolution of the Gaussian function gives the exponential curve of the former Gaussian curve, allowing the calculation of the fluorescence lifetime value. If multiple decays are present, re-convolution is performed using the Fourier convolution theorem. A Gaussian function is

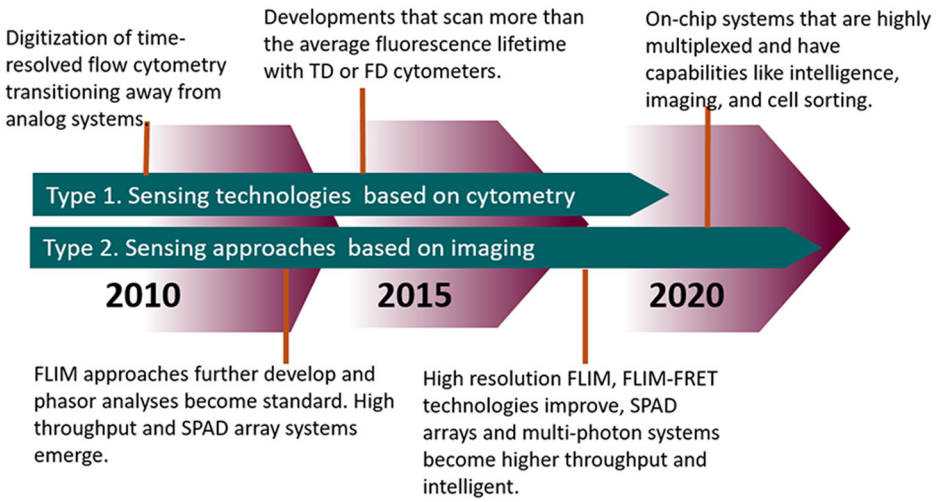

FIGURE 9 | Timeline highlighting the advances in FLIM and TRFC from the past decade and moving forward.

first convoluted with the proper multi-exponential decay model and then deconvoluted to separate instrument response from species that contribute to the measured fluorescence lifetime. In similar examples, digital signal processing (DSP) approaches were used to calculate the fluorescence lifetime in the time domain by estimating the time delay between a fluorescence and scattered light signal [61, 66]. Light pulse signals collected from conventional cytometry (forward scattered light waveforms and fluorescence waveforms) were compared offline [61] with a variety of interpolation or fitting algorithms to prove that this value correlates to the average fluorescence lifetime [61]. Other advanced processing approaches were demonstrated by using a modified chirp Z-transform (MCZT) to acquire high-resolution spectral data. This was followed by a fine-interpolated correlation peak (FICP) algorithm applied and integrated with a time-domain cross-correlation function to permit the calculation of time delay between the forward scattered light and fluorescence signal [66].

Sample isolation and enrichment through fluorescence-activated cell sorting (FACS) is also possible with td-FCM using a technique known as fluorescence-activated droplet sorting (FADS). A recent study employed TCSPC [67] for oil droplet-based microfluidic sorting and sample encapsulation. The sample was measured based on the emitted spectra and fluorescence lifetime value. Sort decisions were made using multiparametric information. Fluorescence intensity and lifetime measurements within an acceptable value triggered the FPGA of the data acquisition system to send a signal to a function generator that activated dielectrophoresis electrodes to isolate the cells that fall within the targeted threshold. Sort purities achieved for mScarlet and mCherry RFPs at a sort rate of 2,500 events min^{-1} were 80 $\pm$ 1% and 97 $\pm$ 1%, respectively. Furthermore, Hung et al. demonstrated an approach that would permit the encapsulation of multiple cells per droplet, permitting the system to achieve sorting times for RFP libraries ($\sim$108 events) within 3 h, which is three times faster than state-of-the-art cell sorters.

Aside from fluorescence-based measurements, it is possible to acquire longer luminescence lifetime values with slightly altered electronic and td-FCM instrumentation setup. As a recent example of this, autofluorescence crosstalk was resolved using Europium-doped polystyrene beads and THP-1 cells. A td-FCM system was designed to measure the long lanthanide lifetimes of Eu (range of μs or ms). The luminescence decay was long enough to not interfere with shorter fluorescence signals [68]. The long-lifetime td-FCM instrument measured the focused cells acoustically, and the throughput was lower compared to conventional cytometry. Similarly, Kage et al. [69] developed a td-FCM system to measure the lifetime values of four types of quantum-dot-doped polymer beads. In this study, it was demonstrated that longer lifetimes of the quantum-dot-doped beads can be discriminated from shorter lifetimes found in dye-based beads by measuring the respective decay by separate tempo-spectral channels.

DISCUSSION (FLIM AND TRFC CROSSOVER AND FUTURE)

The measurement of fluorescence lifetime is becoming an increasingly useful and necessary tool for studying biological characteristics and phenomena from the tissue level down to the protein level. **Tables 1**, **2** highlights modern innovations in fluorescence lifetime instrumentation and applications, which are also depicted by the flow diagram in **Figure 9**. Many of the limitations in using fluorescence lifetime are related to throughput, particularly in the realm of detection hardware and computational processing power. This review discussed the evolution of fluorescence lifetime techniques in the fields of FLIM and TRFC, which are technologies that are raising the bar for

TABLE 2 | Fluorescence lifetime measuring technology and methods in the past decade.

References	Technology and methods	Brief summary
Yuan et al. [70]	Fluorescence spectrometer, AOTF, optical biopsy	AOTF and collection of first-order diffraction beams. Acquisition of 200 nm time-resolved spectra in 4 s.
Houston et al. [39]	Frequency domain TRFC, lifetime-based sorting, ORCAS	Open reconfigurable cytometric acquisition system (ORCAS) adds capability to perform lifetime analysis on any cytometer with a laser that can be modulated.
Tyndall et al. [42]	TCSPC, SPAD Array, integrated silicon photomultiplier (SiPM)	Parallelization of TCSPC to overcome photon pile-up. CMOS process used to make a SiPM with SPAD array, TDCs, and lifetime estimation on-chip.
Li et al. [5]	fd-TRFC, fluorescence lifetime excitation cytometry by kinetic dithering (FLECKD)	Rapid scanning of laser across sample passing through flow cytometer. Able to discriminate multiple fluorescence lifetimes simultaneously.
Petersen et al. [6]	High throughput fluorescence lifetime plate reader. DIrect waveform recording (DWR)	Waveforms are direclty digitized for lifetime calculation. Fluorescence lifetime plate reader can image 384-well microplate in 3 minutes with better than 1% accuracy.
Nedbal et al. [2]	TCSPC, microfluidic FLIM, Burst-Integrated Fluorescence Lifetime (BIFL)	Epifluorescent microscope with associated BIFL software used to determine intensity of fluorescence, photon rate, lifetime, and burst duration for each cell.
Poland et al. [26]	Multifocal multiphoton FLIM (MM-FLIM), SPAD array, TCSPC, FRET	Parellelized MM-FLIM in both excitation and detection. Technique showed increased speed in comparison to confocal FLIM and widefield FLIM.
Rocca et al. [65]	TCSPC, CMOS SPAD array, SiPM, BIFL, Field Programmable gate arrays (FPGA)	A single-chip is equiped with SiPM capable of BIFL using TCSPC for detection and real-time sorting with FPGA using CMM for lifetime calcuation.
Lee et al. [15]	Phasor-FLIM based single cell screening	Single-cell traps within a microfluidic device allow for differentiation of cells based on metabolic differences in NAD(P)H without any labeling using phasor-FLIM
Mikami et al. [71]	Frequency-division multiplexing (FDM) confocal microscope, imaging flow cytometry	Integration of a dual-frequeny comb that was spatially distributed along with QAM into FDM. 16,000 frames/s surpassed the fluorescence lifetime limit
Schaaf et al. [32]	Red-shifted FRET biosensors (OFP and MFP), high throughput screening/plate reader	The FRET pair developed increased efficiency, dynamic range, and signal-to-background of HTS. Can image 1536 well-plate in 3 minutes
Shen et al. [17]	Custom continuous-flow bioreactor, real time two-photon FLIM (2P-FLIM)	2P-FLIM was implemented to continuously monitor live cultures under shear stress, eliminating traditional interuptions of the bioreactor
Esposito and Venkitaraman [10]	Hyperdimensional imaging microscopy (HDIM)	Parallel detection of orthogonal fluorescence characteristics (lifetime, polarization, and spectra). Hyperdimensional traits detected with two multiwavelength TCSPC detectors.
Yao et al. [24]	A deep convolution neural network (CNN) called Net-FLICS (FLIM with compressed sensing)	Reconstruction of intensity and FLI maps using deep learning. Reconstruction times of <3 ms/sample, 4 orders of magnitude faster than previous methodologies
Hirmiz et al. [33]	FLIM-FRET combined technology with a highly-multiplexed confocal microscope	Microscope was coupled to an SPAD array for high resolution and rapid imaging of FLIM
Karpf et al. [13]	Spectro-Temporal Laser Imaging by Difracted Excitation (SLIDE), imaging flow cytometry	Non-linear microscope with kHz frame rate using a pulse-modulated, sweeping laser with inertia-free steering. Lifetime recording of $88x10^6$ pixels/s.

high throughput and high content analysis. Currently, there are still pitfalls (i.e., resolution, accuracy) to increasing the speed of lifetime acquisition. Nonetheless, advances in technology and software hint at a future in which the fluorescence lifetime will be precisely measured at a reasonable throughput without much compromise.

The future of high-throughput FLIM and cytometry is indeed foreshadowed by novel machinations of deep learning, imaging, multiplexing, and intelligent hardware. Use cases in which lifetime imaging cytometry is possible are emerging (e.g., FLIM systems that capture multiple fluorescence parameters simultaneously at a high throughput [10]). Deep learning is also trending as it can increase the speed of lifetime analysis by reducing the number of images acquired without compromising accuracy or resolution [22, 24]. Hybridization of instruments, such as combining multiphoton wavelength-swept excitation, diffraction grating, and galvanometric beam scanners to perform rapid multiplexed imaging, is also advancing this field [13]. Many opportunities are possible with these technologies, as well as SPAD arrays and other high-speed, high-resolution time-domain lifetime detection methods [2, 65].

The future of high-throughput fluorescence lifetime will involve huge advancements in instrument and data analysis. These advancements will likely be built upon existing, established methods as well as novel innovations in instrument speed and resolution. The physical tools that enable high-throughput lifetime analyses will perhaps uncover traits of cells, cellular processes, and other biochemical interactions that otherwise are not currently detectable. The eventual dissemination of such tools will certainly influence bioscience and will lead to eventual clinical translation for a true biomedical impact.

AUTHOR CONTRIBUTIONS

AB wrote the review, prepared the synthesis of the literature, and prepared figures. SV and JS assisted in writing, interpretation, and discussion. JH directed the review and its interpretation of the literature and guarantee the integrity of all discussed results. All authors contributed to the article and approved the submitted version.

FUNDING

This work was funded by National Institutes of Health Grant R01GM129859.

REFERENCES

1. Yankelevich DR, Ma D, Liu J, Sun Y, Sun Y, Bec J, et al. Design and evaluation of a device for fast multispectral time-resolved fluorescence spectroscopy and imaging. *Rev Sci Instrum.* (2014) 85:034303. doi: 10.1063/1.4869037
2. Nedbal J, Visitkul V, Ortiz-Zapater E, Weitsman G, Chana P, Matthews DR, et al. Time-domain microfluidic fluorescence lifetime flow cytometry for high-throughput Forster resonance energy transfer screening. *Cytometry A.* (2015) 87:104–18. doi: 10.1002/cyto.a.22616
3. Schuermann KC, Grecco HE, flatFLIM: enhancing the dynamic range of frequency domain FLIM. *Opt Express.* (2012) 20:20730–41. doi: 10.1364/OE.20.020730
4. Cao R, Pankayatselvan V, Houston JP. Cytometric sorting based on the fluorescence lifetime of spectrally overlapping signals. *Opt Express.* (2013) 21:14816–31. doi: 10.1364/OE.21.014816
5. Li W, Vacca G, Castillo M, Houston KD, Houston JP. Fluorescence lifetime excitation cytometry by kinetic dithering. *Electrophoresis.* (2014) 35:1846–54. doi: 10.1002/elps.201300618
6. Petersen KJ, Peterson KC, Muretta JM, Higgins SE, Gillispie GD, Thomas DD. Fluorescence lifetime plate reader: resolution and precision meet high-throughput. *Rev Sci Instrum.* (2014) 85:113101. doi: 10.1063/1.4900727
7. Sands B, Jenkins P, Peria WJ, Naivar M, Houston JP, Brent R. Measuring and sorting cell populations expressing isospectral fluorescent proteins with different fluorescence lifetimes. *PLoS ONE.* (2014) 9:e109940. doi: 10.1371/journal.pone.0109940
8. Cao R, Jenkins P, Peria W, Sands B, Naivar M, Brent R, et al. Phasor plotting with frequency-domain flow cytometry. *Opt Express.* (2016) 24:14596–607. doi: 10.1364/OE.24.014596
9. Li W, Houston KD, Houston JP. Shifts in the fluorescence lifetime of EGFP during bacterial phagocytosis measured by phase-sensitive flow cytometry. *Sci Rep.* (2017) 7:40341. doi: 10.1038/srep40341
10. Esposito A, Venkitaraman AR. Enhancing biochemical resolution by hyperdimensional imaging microscopy. *Biophys J.* (2019) 116:1815–22. doi: 10.1016/j.bpj.2019.04.015
11. Trinh AL, Ber S, Howitt A, Valls PO, Fries MW, Venkitaraman AR, et al. Fast single-cell biochemistry: theory, open source microscopy and applications. *Methods Appl Fluoresc.* (2019) 7:044001. doi: 10.1088/2050-6120/ab3bd2
12. Brodwolf R, Volz-Rakebrand P, Stellmacher J, Wolff C, Unbehauen M, Haag R, et al. Faster, sharper, more precise: Automated Cluster-FLIM in preclinical testing directly identifies the intracellular fate of theranostics in live cells and tissue. *Theranostics.* (2020) 10:6322–36. doi: 10.7150/thno.42581
13. Karpf S, Riche CT, Di Carlo D, Goel A, Zeiger WA, Suresh A, et al. Spectro-temporal encoded multiphoton microscopy and fluorescence lifetime imaging at kilohertz frame-rates. *Nat Commun.* (2020) 11:2062. doi: 10.1038/s41467-020-15618-w
14. Stringari C, Sierra R, Donovan PJ, Gratton E. Label-free separation of human embryonic stem cells and their differentiating progenies by phasor fluorescence lifetime microscopy. *J Biomed Opt.* (2012) 17:046012. doi: 10.1117/1.JBO.17.4.046012
15. Lee DH, Li X, Ma N, Digman MA, Lee AP. Rapid and label-free identification of single leukemia cells from blood in a high-density microfluidic trapping array by fluorescence lifetime imaging microscopy. *Lab Chip.* (2018) 18:1349–58. doi: 10.1039/C7LC01301A
16. Li X, Lee AP. High-throughput microfluidic single-cell trapping arrays for biomolecular and imaging analysis. *Methods Cell Biol.* (2018) 148:35–50. doi: 10.1016/bs.mcb.2018.09.010
17. Shen N, Riedl JA, Carvajal Berrio DA, Davis Z, Monaghan MG, Layland SL, et al. A flow bioreactor system compatible with real-time two-photon fluorescence lifetime imaging microscopy. *Biomed Mater.* (2018) 13:024101. doi: 10.1088/1748-605X/aa9b3c
18. Alturkistany F, Nichani K, Houston KD, Houston JP. Fluorescence lifetime shifts of NAD(P)H during apoptosis measured by time-resolved flow cytometry. *Cytometry A.* (2019) 95:70–79. doi: 10.1002/cyto.a.23606
19. Bower AJ, Sorrells JE, Li J, Marjanovic M, Barkalifa R, Boppart SA. Tracking metabolic dynamics of apoptosis with high-speed two-photon fluorescence lifetime imaging microscopy. *Biomed Opt Express.* (2019) 10:6408–21. doi: 10.1364/BOE.10.006408
20. Cong A, Pimenta RML, Lee HB, Mereddy V, Holy J, Heikal AA. Two-photon fluorescence lifetime imaging of intrinsic NADH in three-dimensional tumor models. *Cytometry A.* (2019) 95:80–92. doi: 10.1002/cyto.a.23632
21. Silva SF, Domingues JP, Morgado AM. Can we use rapid lifetime determination for fast, fluorescence lifetime based, metabolic imaging? Precision and accuracy of double-exponential decay measurements with low total counts. *PLoS ONE.* (2019) 14:e0216894. doi: 10.1371/journal.pone.0216894
22. Smith JT, Yao R, Sinsuebphon N, Rudkouskaya A, Un N, Mazurkiewicz J, et al. Fast fit-free analysis of fluorescence lifetime imaging via deep learning. *Proc Natl Acad Sci USA.* (2019) 116:24019–30. doi: 10.1073/pnas.1912707116
23. Yakimov BP, Gogoleva MA, Semenov AN, Rodionov SA, Novoselova MV, Gayer AV, et al. Label-free characterization of white blood cells using fluorescence lifetime imaging and flow-cytometry: molecular heterogeneity and erythrophagocytosis [Invited]. *Biomed Opt Express.* (2019) 10:4220–36. doi: 10.1364/BOE.10.004220
24. Yao R, Ochoa M, Yan P, Intes X. Net-FLICS: fast quantitative wide-field fluorescence lifetime imaging with compressed sensing - a deep learning approach. *Light Sci Appl.* (2019) 8:26. doi: 10.1038/s41377-019-0138-x
25. Gohar AV, Cao R, Jenkins P, Li W, Houston JP, Houston KD. Subcellular localization-dependent changes in EGFP fluorescence lifetime measured by time-resolved flow cytometry. *Biomed Opt Express.* (2013) 4:1390–400. doi: 10.1364/BOE.4.001390
26. Poland SP, Krstajic N, Monypenny J, Coelho S, Tyndall D, Walker RJ, et al. A high speed multifocal multiphoton fluorescence lifetime imaging microscope for live-cell FRET imaging. *Biomed Opt Express.* (2015) 6:277–96. doi: 10.1364/BOE.6.000277
27. Suzuki M, Sakata I, Sakai T, Tomioka H, Nishigaki K, Tramier M, et al. A high-throughput direct fluorescence resonance energy transfer-based assay for analyzing apoptotic proteases using flow cytometry and fluorescence lifetime measurements. *Anal Biochem.* (2015) 491:10–7. doi: 10.1016/j.ab.2015.08.022
28. Guzman C, Oetken-Lindholm C, Abankwa D. Automated high-throughput fluorescence lifetime imaging microscopy to detect protein-protein interactions. *J Lab Autom.* (2016) 21:238–45. doi: 10.1177/2211068215606048
29. Lo CH, Vunnam N, Lewis AK, Chiu TL, Brummel BE, Schaaf TM, et al. An innovative high-throughput screening approach for discovery of small molecules that inhibit TNF receptors. *SLAS Discov.* (2017) 22:950–61. doi: 10.1177/2472555217706478
30. Schaaf TM, Peterson KC, Grant BD, Bawaskar P, Yuen S, Li J, et al. High-throughput spectral lifetime-based fret screening in living cells to identify small-molecule effectors of SERCA. *SLAS Discov.* (2017) 22:262–73. doi: 10.1177/1087057116680151
31. Sambrano J, Chigaev A, Nichani KS, Smagley Y, Sklar LA, Houston JP. Evaluating integrin activation with time-resolved flow cytometry. *J Biomed Opt.* (2018) 23:1–10. doi: 10.1117/1.JBO.23.7.075004
32. Schaaf TM, Li A, Grant BD, Peterson K, Yuen S, Bawaskar P, et al. Red-shifted FRET biosensors for high-throughput fluorescence lifetime screening. *Biosensors.* (2018) 8:99. doi: 10.3390/bios8040099

33. Hirmiz N, Tsikouras A, Osterlund EJ, Richards M, Andrews DW, Fang Q. Highly multiplexed confocal fluorescence lifetime microscope designed for screening applications. *IEEE J Selected Topics Quantum Electron.* (2020) 27:1–9. doi: 10.1109/JSTQE.2020.2997834
34. Nichani K, Li J, Suzuki M, Houston JP. Evaluation of Caspase-3 activity during apoptosis with fluorescence lifetime-based cytometry measurements and phasor analyses. *Cytometry A.* (2020) 97:1265–1275. doi: 10.1002/cyto.a.24207
35. Rohilla S, Kramer B, Koberling F, Gregor I, Hocke AC. Multi-target immunofluorescence by separation of antibody cross-labelling via spectral-FLIM-FRET. *Sci Rep.* (2020) 10:3820. doi: 10.1038/s41598-020-60877-8
36. Wei Y, Larson NR, Angalakurthi SK, C. Russell middaugh, improved fluorescence methods for high-throughput protein formulation screening. *SLAS Technol.* (2018) 23:516–28. doi: 10.1177/2472630318780620
37. Kalytchuk S, Wang Y, Polakova K, Zboril R. Carbon dot fluorescence-lifetime-encoded anti-counterfeiting. *ACS Appl Mater Interfaces.* (2018) 10:29902–8. doi: 10.1021/acsami.8b11663
38. Microscopy Techniques. 1 ed. *Advances in Biochemical Engineering/Biotechnology*. Scheper T, editor. Berlin: Springer-Verlag Berlin Heidelberg (2005).
39. Houston JP, Naivar MA, Freyer JP. Digital analysis and sorting of fluorescence lifetime by flow cytometry. *Cytometry A.* (2010) 77:861–72. doi: 10.1002/cyto.a.20930
40. Houston JP, Naivar MA, Jenkins P, Freyer JP. Capture of fluorescence decay times by flow cytometry. *Curr Protoc Cytom.* (2012) 50:1.25.1–1.25.21. doi: 10.1002/0471142956.cy0125s59
41. Poudel C, Mela I, Kaminski CF. High-throughput, multi-parametric, and correlative fluorescence lifetime imaging. *Methods Appl Fluoresc.* (2020) 8:024005. doi: 10.1088/2050-6120/ab7364
42. Tyndall D, Rae BR, Li DD, Arlt J, Johnston A, Richardson JA, et al. A high-throughput time-resolved mini-silicon photomultiplier with embedded fluorescence lifetime estimation in 0.13 mum CMOS. *IEEE Trans Biomed Circuits Syst.* (2012) 6:562–70. doi: 10.1109/TBCAS.2012.2222639
43. Krstajic N, Poland S, Levitt J, Walker R, Erdogan A, Ameer-Beg S, et al. 0.5 billion events per second time correlated single photon counting using CMOS SPAD arrays. *Opt Lett*. (2015) 40:4305–8. doi: 10.1364/OL.40.004305
44. Burri S, Powolny F, Bruschini C, Michalet X, Regazzoni F, Charbon E. A 65k pixel, 150k frames-per-second camera with global gating and micro-lenses suitable for fluorescence lifetime imaging. *Proc SPIE Int Soc Opt Eng.* (2014) 9141:914109. doi: 10.1117/12.2052862
45. Bruschini C, Homulle H, Antolovic IM, Burri S, Charbon E. Single-photon avalanche diode imagers in biophotonics: review and outlook. *Light Sci Appl.* (2019) 8:87. doi: 10.1038/s41377-019-0191-5
46. Fereidouni F, Reitsma K, Gerritsen HC. High speed multispectral fluorescence lifetime imaging. *Opt Express.* (2013) 21:11769–82. doi: 10.1364/OE.21.011769
47. Silva SF, Domingues JP, Morgado AM. Accurate rapid lifetime determination on time-gated FLIM microscopy with optical sectioning. *J Healthc Eng.* (2018) 2018:1371386. doi: 10.1155/2018/1371386
48. Mitchell CA, Poland SP, Seyforth J, Nedbal J, Gelot T, Huq T, et al. Functional *in vivo* imaging using fluorescence lifetime light-sheet microscopy. *Opt Lett*. (2017) 42:1269–72. doi: 10.1364/OL.42.001269
49. Baldeweck T, Balu M, Batista A, Vecker W, Belousov VV, Breinig HG, et al. *Multiphoton Microscopy and Fluorescence Lifetime Imaging: Applications in Biology and Medicine*. Berlin: Walter de Gruyter GmbH & Co KG (2018).
50. Masters BR. *Confocal Microscpoy Multiphoton Exciation Microscopy: The Genesis of Live Cell Imaging*. Bellingham, WA: SPIE (2006). doi: 10.1117/3.660403
51. Cao R, Wallrabe H, Periasamy A. Multiphoton FLIM imaging of NAD(P)H and FAD with one excitation wavelength. *J Biomed Opt.* (2020) 25:1–16. doi: 10.1117/1.JBO.25.1.014510
52. Steinkamp JA, Crissman HA. Resolution of fluorescence signals from cells labeled with fluorochromes having different lifetimes by phase-sensitive flow cytometry. *Cytometry.* (1993) 14:210–6. doi: 10.1002/cyto.990140214
53. Steinkamp JA, Yoshida TM, Martin JC. Flow cytometer for resolving signals from heterogeneous fluorescence emissions and quantifying lifetime in fluorochrome-labeled cells/particles by phase-sensitive detection. *Rev Scic Instruments.* (1993) 64:3440. doi: 10.1063/1.1144265
54. Deka C, Sklar LA, Steinkamp JA. Fluorescence lifetime measurements in a flow cytometer by amplitude demodulation using digital data acquisition technique. *Cytometry.* (1994) 17:94–101. doi: 10.1002/cyto.990170112
55. Deka C, Cram LS, Habbersett R, Martin JC, Sklar LA, Steinkamp JA. Simultaneous dual-frequency phase-sensitive flow cytometric measurements for rapid identification of heterogeneous fluorescence decays in fluorochrome-labeled cells and particles. *Cytometry.* (1995) 21:318–28. doi: 10.1002/cyto.990210403
56. Deka C, Lehnert BE, Lehnert NM, Jones GM, Sklar LA, Steinkamp JA. Analysis of fluorescence lifetime and quenching of FITC-conjugated antibodies on cells by phase-sensitive flow cytometry. *Cytometry.* (1996) 25:271–9. doi: 10.1002/(SICI)1097-0320(19961101)25:3<271::AID-CYTO8>3.0.CO;2-I
57. Sailer BL, Steinkamp JA, Crissman HA. Flow cytometric fluorescence lifetime analysis of DNA-binding probes. *Europ J Histochem.* (1998) 42:19–27.
58. Keij JF, Bell-Prince C, Steinkamp JA. Simultaneous analysis of relative DNA and glutathione content in viable cells by phase-resolved flow cytometry. *Cytometry.* (1999) 35:48–54. doi: 10.1002/(SICI)1097-0320(19990101)35:1<48::AID-CYTO7>3.0.CO;2-5
59. Cui HH, Valdez JG, Steinkamp JA, Crissman HA. Fluorescence lifetime-based discrimination and quantification of cellular DNA and RNA with phase-sensitive flow cytometry. *Cytometry A.* (2003) 52A:46–55. doi: 10.1002/cyto.a.10022
60. Houston J, Naivar M, Martin J, Goddard G, Carpenter S, Mourant J, et al. *Endogenous Fluorescence Lifetime of Viable Cells by Flow Cytometry*. SPIE BiOS. Vol. 6859. SPIE (2008). doi: 10.1117/12.763816
61. Cao R, Naivar MA, Wilder M, Houston JP. Expanding the potential of standard flow cytometry by extracting fluorescence lifetimes from cytometric pulse shifts. *Cytometry A.* (2014) 85:999–1010. doi: 10.1002/cyto.a.22574
62. Yang Z, Shcherbakova DM, Verkhusha VV, Houston JP. Developing a time-resolved flow cytometer for fluorescence lifetime measurements of near-infrared fluorescent proteins. In *2016 Conference on Lasers and Electro-Optics (CLEO)*. Piscataway, NJ: IEEE (2016). doi: 10.1364/CLEO_SI.2016.SW4G.1
63. Jenkins P, Naivar MA, Houston JP. Toward the measurement of multiple fluorescence lifetimes in flow cytometry: maximizing multi-harmonic content from cells and microspheres. *J Biophotonics.* (2015) 8:908–17. doi: 10.1002/jbio.201400115
64. Steinkamp J. *Flow Cytometers, in eLS*. Somerset, NJ: John Wiley & Sons Ltd (2001). doi: 10.1038/npg.els.0002971
65. Rocca FM, Nedbal J, Tyndall D, Krstajic N, Li DD, Ameer-Beg SM, et al. Real-time fluorescence lifetime actuation for cell sorting using a CMOS SPAD silicon photomultiplier. *Opt Lett.* (2016) 41:673–6. doi: 10.1364/OL.41.000673
66. Zhu L, Zhang W, Dong M, Lou X. Analysis of flow cytometric fluorescence lifetime with time-delay estimation of pulse signals. *Sensors.* (2018) 18:442. doi: 10.3390/s18020442
67. Hung, S.-T., Mukherjee S, Jimenez R. Enrichment of rare events using a multi-parameter high throughput microfluidic droplet sorter. *Lab Chip.* (2020) 20:834–43. doi: 10.1039/C9LC00790C
68. Wang Y, Sayyadi N, Zheng X, Woods TA, Leif RC, Shi B, et al. Time-resolved microfluidic flow cytometer for decoding luminescence lifetimes in the microsecond region. *Lab Chip.* (2020) 20:655–64. doi: 10.1039/C9LC00895K
69. Kage D, Hoffmann K, Borcherding H, Schedler U, Resch-Genger U. Lifetime encoding in flow cytometry for bead-based sensing of biomolecular interaction. *Sci Rep.* (2020) 10:19477. doi: 10.1038/s41598-020-76150-x
70. Yuan Y, Hwang JY, Krishnamoorthy M, Ye K, Zhang Y, Ning J, et al. High-throughput acousto-optic-tunable-filter-based time-resolved fluorescence spectrometer for optical biopsy. *Optics Lett.* (2009) 34:1132–4. doi: 10.1364/ol.34.001132
71. Mikami H, Harmon J, Kobayashi H, Hamad S, Wang Y, Iwata O, et al. Ultrafast confocal fluorescence microscopy beyond the fluorescence lifetime limit. *Optica.* (2018) 5:117–26. doi: 10.1364/OPTICA.5.000117

Conflict of Interest: The authors declare that the research was conducted in the absence of any commercial or financial relationships that could be construed as a potential conflict of interest.

frontiers in Chemistry

ORIGINAL RESEARCH
published: 26 April 2021
doi: 10.3389/fchem.2021.659553

Real-Time Imaging of Short-Wave Infrared Luminescence Lifetimes for Anti-counterfeiting Applications

*Roman Ziniuk[1], Artem Yakovliev[1], Hui Li[2], Guanying Chen[2], Junle Qu[1] and Tymish Y. Ohulchanskyy[1]**

[1] Key Laboratory of Optoelectronic Devices and Systems, Center for Biomedical Photonics and College of Physics and Optoelectronic Engineering, Shenzhen University, Shenzhen, China, [2] School of Chemistry and Chemical Engineering, Harbin Institute of Technology, Harbin, China

Rare-earth doped nanoparticles (RENPs) have been widely used for anti-counterfeiting and security applications due to their light frequency conversion features: they are excited at one wavelength, and they display spectrally narrow and distinguished luminescence peaks either at shorter wavelengths (i.e., frequency/energy upconversion) or at longer wavelengths (frequency/energy downconversion). RENPs with a downconversion (DC) photoluminescence (PL) in short-wave infrared (SWIR) spectral range (∼1,000–1,700 nm) have recently been introduced to anti-counterfeiting applications, allowing for multilevel protection based on PL imaging through opaque layers, due to a lesser scattering of SWIR PL emission. However, as the number and spectral positions of the discrete PL bands exhibited by rare-earth ions are well-known, it is feasible to replicate luminescence spectra from RENPs, which results in a limited anti-counterfeiting security. Alternatively, lifetime of PL from RENPs can be used for encoding, as it can be finely tuned in broad temporal range (i.e., from microseconds to milliseconds) by varying type of dopants and their content in RENPs, along with the nanoparticle morphology and size. Nevertheless, the current approach to decoding and imaging the RENP luminescence lifetimes requires multiple steps and is highly time-consuming, precluding practical applications of PL lifetime encoding for anti-counterfeiting. Herein, we report the use of a rapid lifetime determination (RLD) technique to overcome this issue and introduce real-time imaging of SWIR PL lifetime for anti-counterfeiting applications. $NaYF_4$:20% Yb, x% Er (x = 0, 2, 20, 80)@$NaYF_4$ core@shell RENPs were synthesized and characterized, revealing DC PL in SWIR region, with maximum at ∼1,530 nm and PL lifetimes ranging from 3.2 to 6 ms. Imaging of the nanoparticles with different lifetimes was performed by the developed time-gated imaging system engaging RLD method and the precise manipulation of the delay between the excitation pulses and camera gating windows. Moreover, it is shown that imaging and decrypting can be performed at a high rate (3–4 fps) in a cyclic manner, thus allowing for real-time temporal decoding. We believe that the demonstrated RLD-based fast PL lifetime imaging approach can be employed in other applications of photoluminescent RENPs.

Keywords: photoluminescence, time-gated imaging, short-wave infrared, rare-earth ions, nanoparticles, anti-counterfeiting, rapid lifetime determination

OPEN ACCESS

Edited by:
Klaus Suhling, King's College London, United Kingdom

Reviewed by:
Dayong Jin, University of Technology Sydney, Australia
Stan Botchway, Science and Technology Facilities Council, United Kingdom

***Correspondence:**
Tymish Y. Ohulchanskyy
tyo@szu.edu.cn

Specialty section:
This article was submitted to Analytical Chemistry, a section of the journal Frontiers in Chemistry

Received: *27 January 2021*
Accepted: *08 March 2021*
Published: *26 April 2021*

Citation:
Ziniuk R, Yakovliev A, Li H, Chen G, Qu J and Ohulchanskyy TY (2021) Real-Time Imaging of Short-Wave Infrared Luminescence Lifetimes for Anti-counterfeiting Applications. Front. Chem. 9:659553. doi: 10.3389/fchem.2021.659553

INTRODUCTION

The forgery and counterfeiting of all kinds have become a real threat to a number of industries including banking, pharmaceuticals, electronics, and packaging (Chaudhrya et al., 2005; Fincham, 2014; Fink et al., 2016). To protect and ensure legitimacy of valuable commodities, various protection techniques were introduced, including watermarking, laser holography, radio-frequency identification, and luminescent anti-fake patterns. Luminescence-based anti-counterfeiting strategy has attracted attention due to advantages of good concealment, difficulty of faking, low production cost, and feasibility of large-scale production. Luminescent materials can be used to create protective tags, labels, or packages; unique patterns [e.g., barcodes or quick response (QR) codes] can be created, revealing encoded information either under photoexcitation (with light at certain wavelength or by natural day/room light) or under specific external stimuli (e.g., pressure) (Kumar et al., 2014; Liu et al., 2017; Sun et al., 2017; Han et al., 2019; Abdollahi et al., 2020). Optical properties of those materials (luminescence spectra, lifetime, etc.) play a crucial role in optical information encoding and determine properties of the security patterns.

Rare-earth ion doped nanoparticles (RENPs) are well-known and widely used due to their light conversion feature that leads to the spectral fingerprint of their photoluminescence (PL), distinguishable by large Stokes (downconversion, DC) and anti-Stokes (upconversion, UC) shifts (Liu et al., 2011; Andres et al., 2014; Kaczmarek et al., 2017; Mei et al., 2019; Xie et al., 2019; You et al., 2019). RENPs provide a number of unique features for anti-counterfeiting and security applications, such as a color-tunable UC/DC luminescence with long decay time and excellent stability. In addition, RENPs can feasibly be introduced into polymeric/polymerizable materials for UC/DC PL pattern fabrication or transferred to the ink-like solutions compatible with commercially available inkjet printers for further pattern printing (da Luz et al., 2015; You et al., 2015; Jee et al., 2020).

Among all the RENPs, Yb^{3+}/Er^{3+} doped UC nanoparticles have been widely recognized, extensively studied, and used in various applications due to their bright UC/DC emission. Being excited in the intense absorption peak at ∼980 nm, Yb^{3+} sensitizes Er^{3+}, which manifest UC PL in visible spectral range, as well as DC PL peaked at ∼1,530 nm (Yi et al., 2004; Li et al., 2017; Secu et al., 2019). It should be noted that RENPs with DC PL in short-wave infrared (SWIR) spectral range are increasingly employed in various imaging applications, due to lesser scattering. SWIR light can penetrate deeper through opaque media in comparison with visible and near-infrared one (Bashkatov et al., 2005; Laurenzis and Christnacher, 2013; Göhler and Lutzmann, 2016; Golovynskyi et al., 2018). SWIR is usually defined by the hardware manufacturers as ∼1,000–1,700 nm spectral range, which is associated with a range of sensitivity of InGaAs detectors and, correspondingly, InGaAs-based imaging cameras. At the same time, the SWIR term specifically defines the spectral range beyond 1,500 nm (Golovynskyi et al., 2018), especially in rapidly emerging bioimaging field that utilizes exogenous photoluminescent probes, including Yb^{3+}/Er^{3+} doped RENPs (Wang et al., 2018a; Lv et al., 2019; Hazra et al., 2020; Li et al., 2020). Along with this, anti-counterfeiting applications of the SWIR emitting nanoparticles have also been recently reported, suggesting PL imaging of 3D patterns and multilevel anti-counterfeiting protection based on imaging through opaque layers (Tan et al., 2020; Platel et al., 2021).

Despite all advantages, use of RENPs for anti-counterfeiting has some limitations. In particular, the number and spectral positions of the discrete luminescence bands provided by rare-earth ions are well-defined and known, making a replication of the luminescence spectra relatively feasible and limiting security of an anti-counterfeit coding. On the other hand, lifetime of UC/DC PL from RENPs can be finely tuned in broad temporal range (from microseconds to milliseconds) by multiple methods, including the changes of dopant types and content, along with tailoring nanoparticle morphology and size (Wang and Liu, 2008; Deng et al., 2015; Fan, 2018; Ortgies et al., 2018; Wang et al., 2018b, 2019; Liang et al., 2019; Mei et al., 2019). This provides much broader range of possibilities for anti-counterfeiting patterns in comparison with the encoding based on PL spectra. The PL lifetime encoding dimension has recently been demonstrated for the anti-counterfeiting applications, exploiting time-domain PL lifetime measurement and time-gated imaging of anti-counterfeiting patterns created with SWIR emitting RENPs (Tan et al., 2020). At the same time, a decrypting of PL lifetime encoded information, as well as practical use of time-gated PL imaging systems in anti-counterfeiting applications depend on the precision of time-gated imaging setup and the image acquisition/processing time. The main part of the time gated imaging method is a precise synchronization of imaging camera shutter with the excitation pulse along with an introduction of a controllable delay between the excitation pulse and start of camera exposure to distinguish the decaying PL signal (**Figure 1A**). Time-gated PL imaging data (i.e., sequence of PL images) can be acquired through a stepwise increase in the delay time, with sequential acquisition of PL image for every delay (**Figure 1B**). Next, the obtained hypercube (stack of PL images acquired with different delays) is processed, revealing the encrypted PL lifetime information (Fan, 2018; Ortgies et al., 2018; Ziniuk et al., 2019). Processing of the hypercube can involve different PL lifetime unmixing protocols, from simple monoexponential fitting to linear mixture analysis to multiexponential fitting, or even more sophisticated approaches. These lifetime unmixing methods are applied for each pixel of the images and include complicated calculations, resulting in highly time-consuming process and revealing one of the major drawbacks of using PL lifetime in anti-counterfeit coding: the inability of instant (real-time) interpretation of the encrypted information. A scanning time-gated setup with point-to-point PL decay acquisition with consequent lifetime determination was recently proposed as a powerful solution for real-time discrimination of the PL lifetimes from multiple particles (Lu et al., 2014); however, the real-time wide-field PL lifetime imaging remains a challenge. To overcome this issue, we propose to employ a rapid lifetime determination (RLD) approach. Following this approach, lifetime of a monoexponential PL decay can be calculated from as few as two points of an exponent and PL

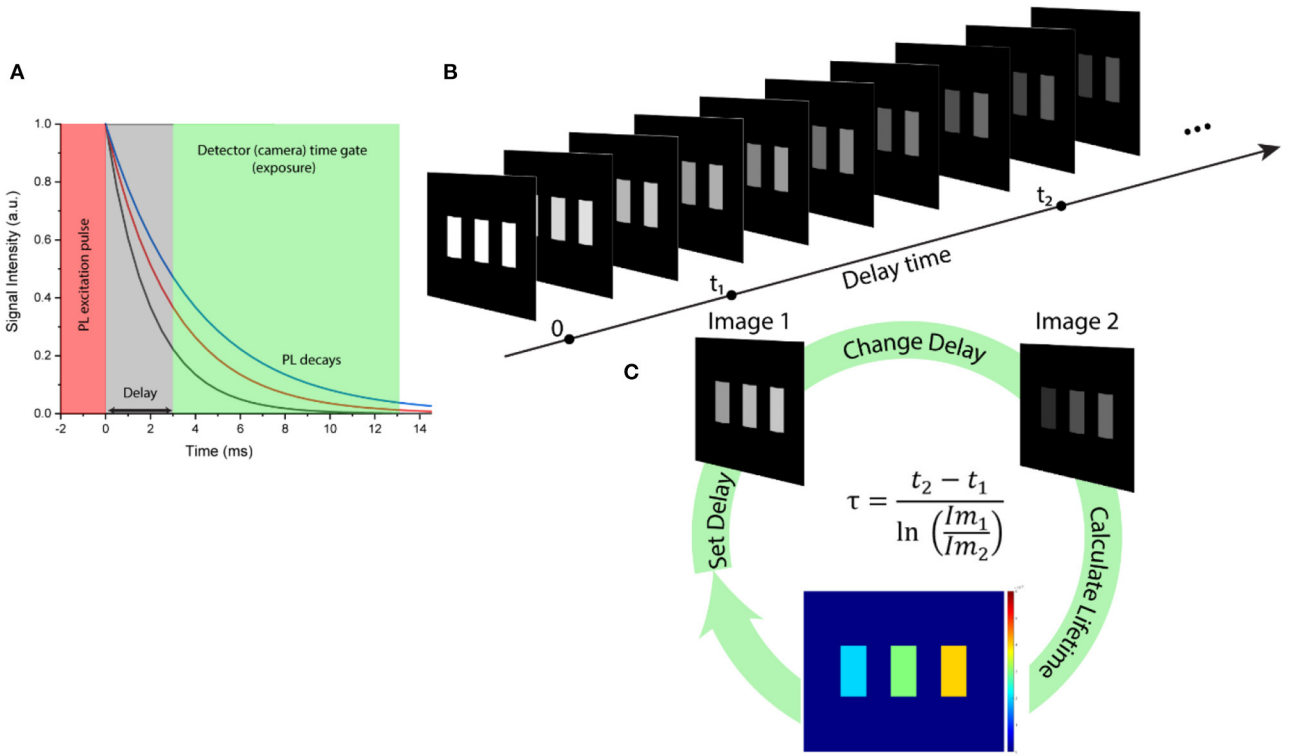

FIGURE 1 | (A) Schematic representation of the PL signal selection using time-domain filtering. **(B)** Stack of time-gated PL images acquired with gradually increased delay time. **(C)** Three-step rapid lifetime determination scheme for real-time anti-counterfeiting imaging, where t_1 and t_2 are delay times for acquiring Image 1 and Image 2 with Im_1 and Im_2 intensity values, respectively, and τ is PL lifetime calculated for each pixel.

lifetime mapping can be feasibly obtained (Sharman et al., 1999; Chan et al., 2001; Liu et al., 2014):

$$\tau = \frac{t_2 - t_1}{\ln\left(\frac{Im_1}{Im_2}\right)},$$

where t_1 and t_2 are delay times for acquisition of Image 1 and Image 2 with Im_1 and Im_2 intensity values, respectively, and τ is the PL lifetime (**Figure 1C**). Furthermore, by simultaneously applying the RLD approach to each pixel of an image and repeating imaging process in the cyclic manner, a real-time PL lifetime imaging can be achieved. Herein, we report on applications of the RLD approach for real-time imaging of SWIR luminescence temporal codes created using RENPs doped with Yb^{3+}/Er^{3+} and emitting in 1,500–1,600 nm spectral region under 975-nm pulsed excitation for anti-counterfeiting and security applications.

RESULTS

Core@shell RENPs of $NaYF_4$:20% Yb^{3+}, x% Er^{3+} (x = 0, 2, 20, 80)@$NaYF_4$ were synthesized using the co-precipitation method at high temperature, as described in the Materials and Methods section. Representative transmission electron microscopy images (TEM) of the parent core $NaYF_4$:Yb^{3+}/Er^{3+} and core@shell $NaYF_4$:Yb^{3+}/Er^{3+}@$NaYF_4$ nanoparticles are presented in **Figures 2B,C**, revealing uniform size (around 5.5 and 11.5 nm, respectively) and morphology of the resulting nanoparticles.

According to the energy level diagram for Yb^{3+}/Er^{3+} (**Figure 2A**), under excitation at 975 nm, the synthesized core@shell RENPs manifest multiphoton UC PL peaked at 650, 540, and 410 nm and originated from higher energy levels of Er^{3+} (**Figure 2D**). At the same time, an intense DC PL peaked at ~1,530 nm (Er^{3+} emission) is observed, along with a weaker Yb^{3+}emission band at ~1,000 nm (**Figure 2E**). As the efficiency of excitation energy transfer between Yb^{3+} and Er^{3+} in $NaYF_4$:Yb^{3+}/Er^{3+} RENPs is known to depend on the dopant concentrations, an observed change in the intensities of UC/DC PL from Yb^{3+} and Er^{3+} is expected when varying Er^{3+} dopant concentrations. Indeed, when the concentration of Er^{3+} in the core was increased from 0, 2, 20, to 80%, the emission of Yb^{3+} at ~1,000 nm decreases, evidencing an increase in the efficiency of the excitation energy transfer from Yb^{3+} to Er^{3+} (**Figure 2E**). This was also confirmed by the shortening of the Yb^{3+} PL lifetime with an increase in Er^{3+} concentrations (**Figure 2F**). It is worth noting that UC/DC PL from Er^{3+} has been detected even for the RENPs that are suggested to have no Er^{3+}, indicating Er^{3+} impurity of unidentified concentration, which was introduced during RENP synthesis. At the same time, as one can see in **Figures 2D,E**, an increase in Er^{3+} concentration from 2 to 20 and 80% resulted in a noticeable decrease in the ratio of UC and DC PL intensities. The intensity of UC PL

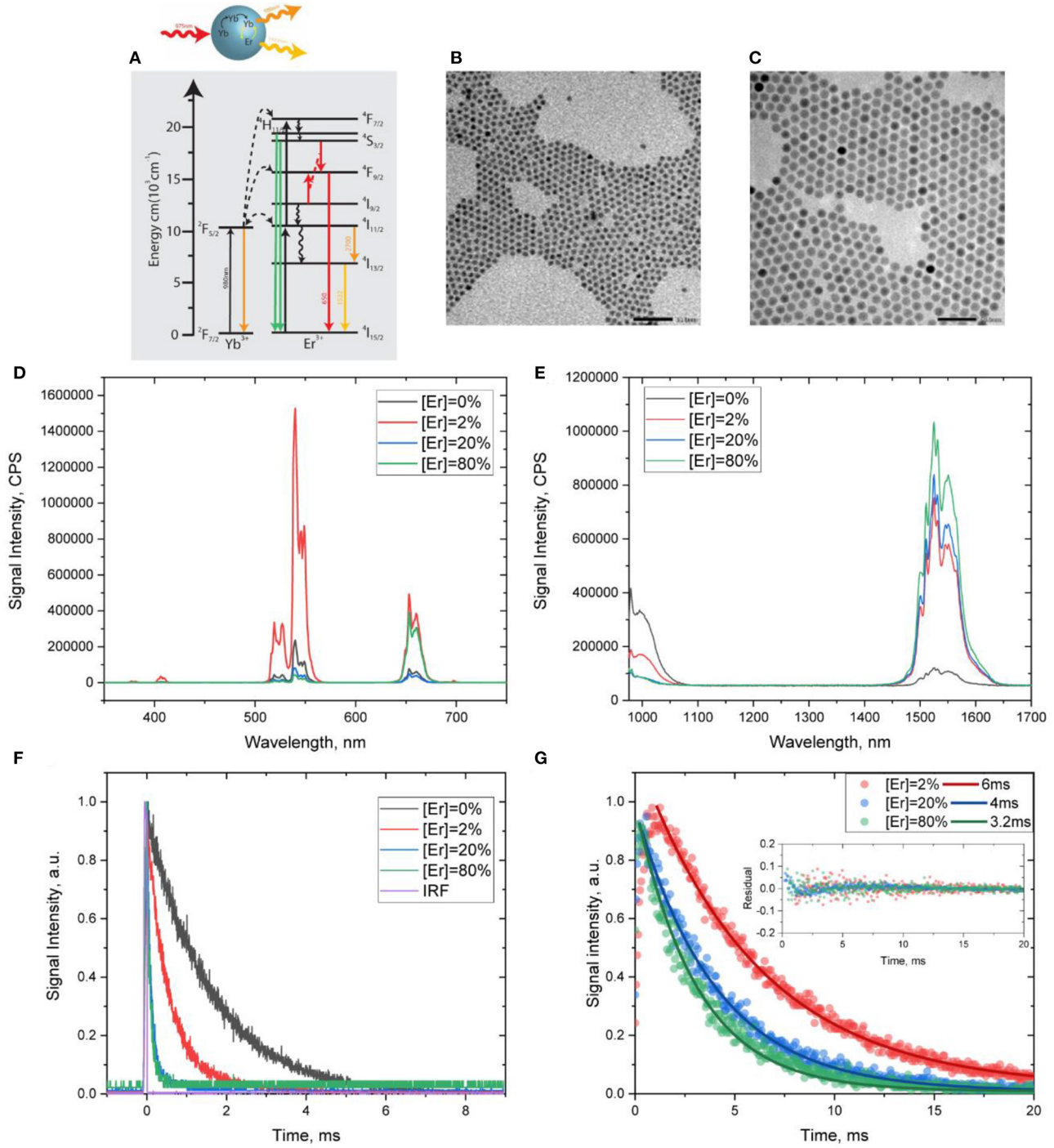

FIGURE 2 | (A) Scheme of energy levels along with activation/deactivation pathways in Yb^{3+}/Er^{3+} co-doped nanoparticles. **(B,C)** Representative TEM images of $NaYF_4$: Yb^{3+}, Er^{3+} core and $NaYF_4$:Yb^{3+},Er^{3+}@$NaYF_4$ core@shell RENPs, respectively. **(D,E)** UC PL and DC PL spectra of $NaYF_4$:Yb^{3+},Er^{3+}@ $NaYF_4$ core@shell nanoparticles under 975-nm excitation. **(F)** PL decays acquired at 1,000 nm (Yb^{3+} emission), **(G)** DC PL decays acquired at 1,530 nm (Er^{3+} emission), along with the monoexponential fits and corresponding residuals.

relatively to DC PL is significantly higher for $NaYF_4$:20%Yb^{3+}, 2% Er^{3+}@$NaYF_4$ RENPs than for $NaYF_4$:20%Yb^{3+}, x% Er^{3+} @$NaYF_4$ (x = 20, 80). This is evidently associated with the concentration quenching effect (Ding et al., 2014; Rabouw et al., 2018), which is also confirmed by the decrease in the lifetime of DC PL of Er^{3+} ions. Using monoexponential fitting, the

lifetime values were found to be ∼6 ms for $NaYF_4$:20%Yb^{3+}, 2% Er^{3+}@$NaYF_4$ RENPs and 4 and 3.2 ms for RENPs with 20 and 80% of Er^{3+}. The DC PL decays are shown in **Figure 2G** along with fitting curves and residuals. It should be noted that the coefficients of determination (R^2) were calculated to be 99.36, 99.35, and 99.59% for 6, 4, and 3.2 ms, respectively, confirming the accuracy of the monoexponential fitting.

The synthesized Er^{3+} doped core@shell nanoparticles with intense SWIR luminescence of long and tunable monoexponential lifetimes can be considered as promising constituents providing temporal codes for anti-counterfeiting patterning in scattering (opalescent) media, which is based on time-gated PL SWIR imaging (Tan et al., 2020). We have previously reported a home-built time-gated SWIR imaging system capable of collecting precisely delayed optical images of SWIR PL from RENPs excited by a pulsed laser at 975 nm (Ziniuk et al., 2019). For real-time imaging of SWIR PL lifetimes, the setup was set to acquire two PL intensity images with different delays and RLD algorithm was applied to images in order to reveal lifetimes encoded in each image pixel. To validate this concept, we imaged three Eppendorf tubes filled with suspensions of RENPs with 2, 20, and 80% of Er^{3+} and DC PL lifetimes of 6, 4, and 3.2 ms, respectively (**Figures 3A,B**). Utilizing two SWIR PL intensity images acquired with 1- and 5-ms delays and RLD algorithm (**Figure 1**), lifetime images were acquired at the rate of 4 fps, demonstrating the possibility to employ the SWIR PL lifetimes as coding (patterning) parameter in real-time anti-counterfeiting application (**Figure 3C**). The lifetime histogram obtained in post-imaging processing from the lifetime image file clearly visualizes the presence of three separate components in the lifetime images (**Figure 3D**). It is worth noting that due to the scattering of the emitted light, some area of the image (e.g., edges of Eppendorf tubes) shows different lifetimes arising from a mixture of PL signals from different samples.

Next, a model of an anti-counterfeiting pattern was fabricated. The letters "S," "Z," and "U" were cut from a printing paper, soaked in the suspensions of RENPs with 2, 20, and 80% of Er^{3+} and glued between two sheets of paper. In such a way, an "SZU" pattern (**Figure 4A**) invisible to the naked eye was created, in which a different type of nanoparticle marked every letter. Next, steady-state and time-gated SWIR PL imaging

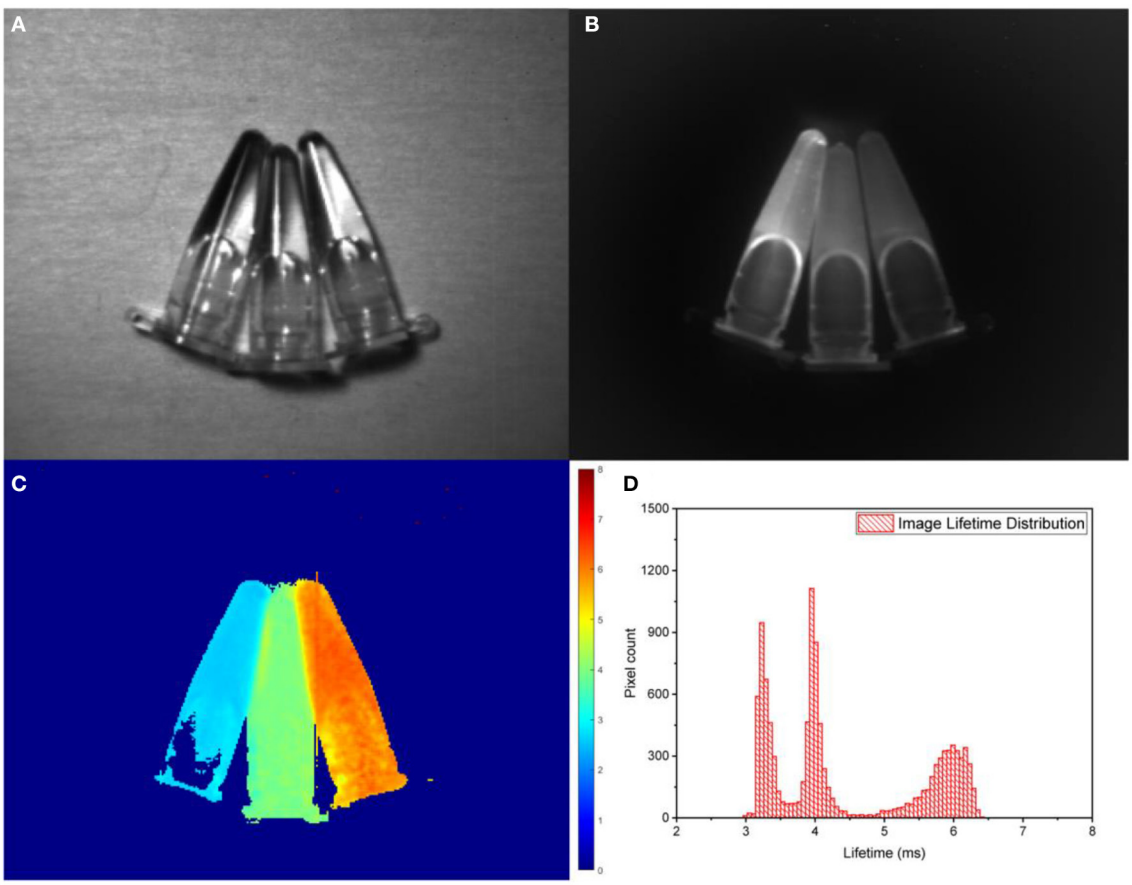

FIGURE 3 | (A) Bright-field imaging of Eppendorf tubes with $NaYF_4$:20%Yb, x%Er@$NaYF_4$ (x = 2, 20, 80% right to left). **(B)** Steady-state SWIR PL imaging of Eppendorf tubes with RENPs suspensions acquired by the SWIR camera with 975-nm excitation and 1,200-nm long-pass filter. **(C,D)** PL lifetime image obtained using RLD approach and corresponding lifetime histogram.

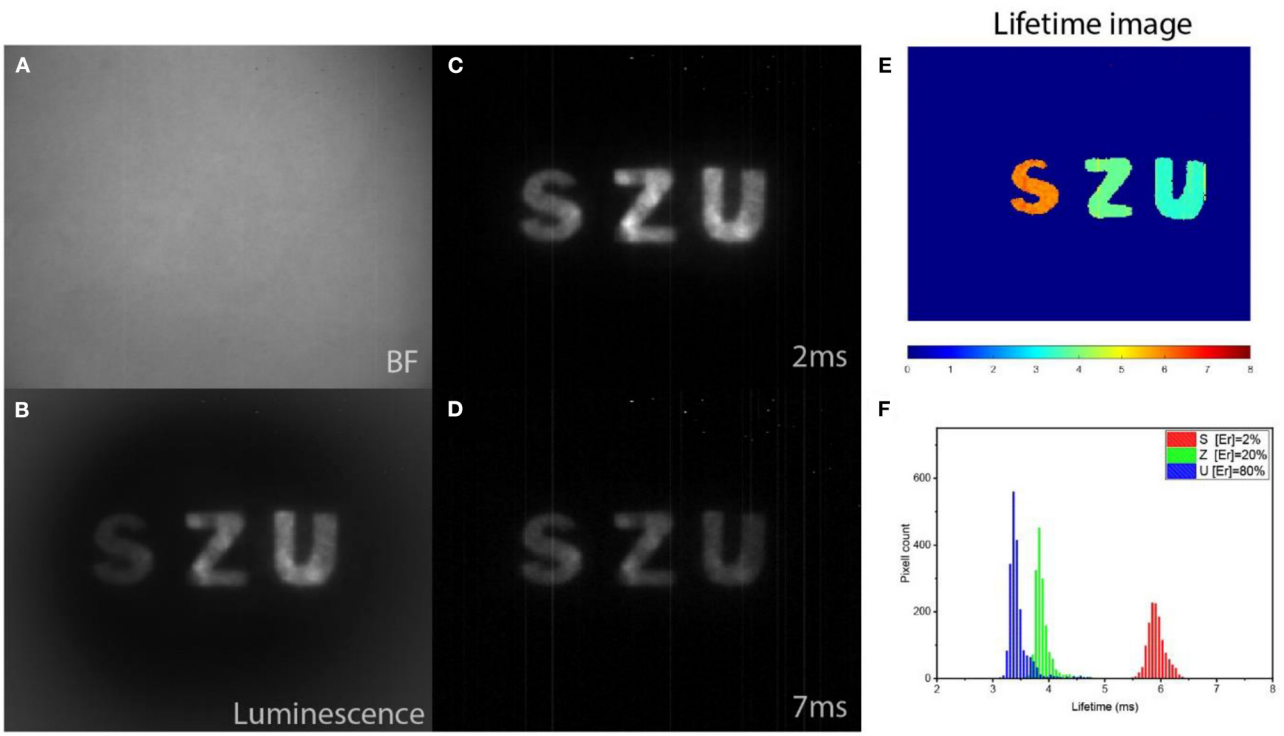

FIGURE 4 | (A) Bright-field image of paper with invisible patterns acquired by SWIR camera at room illumination. **(B)** Steady-state PL intensity imaging revealing a SWIR PL pattern hidden under paper layer and excited by continuous wave laser irradiation at 975 nm. **(C,D)** Time-gated SWIR PL images acquired with 2- and 7-ms delays after pulsed excitation at 975 nm, respectively. **(E)** SWIR PL lifetime image generated with using RLD algorithm using images shown as **(C,D)**. **(F)** Lifetime image histogram illustrating pattern of three separate lifetime-encoded letters.

of the pattern coded by SWIR PL lifetime were performed, using 975-nm excitation from laser diode in continuous wave (CW) and pulsed modes. When comparing steady-state and time-gated PL images, significantly improved signal-to-noise ratio for time-gated images can be clearly seen, demonstrating advantage of time-gating to cut off scattering of the excitation light (**Figures 4B,C**). Two time-gated SWIR PL images obtained for 2- and 7-ms delays (**Figures 4C,D**) were further processed by RLD-based software to determine lifetimes in each pixel (thus, revealing coded information) and produce the lifetime image shown in **Figure 4E**. Lifetime distribution histogram obtained from the lifetime image clearly shows encoding of each photoluminescent letter (**Figure 4F**).

Finally, we have demonstrated the ability of the time-gated SWIR PL imaging setup and the RLD-based software, which process two PL intensity images of different delays to generate PL lifetime image, to working in real time. Two videos were acquired with this aim: (1) video of physical movement of the paper with the pattern in and out of the SWIR camera field of view (acquired by a cell phone camera); (2) computer screen recording with the LabVIEW-based software, which controls the SWIR camera, processes PL intensity images, and generates PL lifetime image using the RLD algorithm. These two videos were synchronized afterwards and four frames of each one were extracted and positioned next to each other to illustrate real-time PL lifetime imaging of anti-counterfeiting pattern. The stages of the anti-counterfeiting SWIR PL imaging, illustrated by combinations of the synchronized video frames, are presented in **Figure 5**. It shows the images when the patterned paper is about to be moved into the imaged area (**Figure 5A**), the pattern is moved into the SWIR camera field of view (imaged area), PL intensity image is acquired (**Figure 5B**), PL lifetime image is generated (**Figure 5C**), and the patterned paper is removed out of the imaged area (**Figure 5D**). The timecodes, which are seen in every selected video frame, are in a format of "hours:minutes:seconds:frames" (frames from 0 to 30 are counted within the current second). The total time between inserting patterned paper in the imaged area and removing it from there is <3 s, while PL lifetime image is seen to be generated in <1 s, as also confirmed by **Supplementary Video 1**.

DISCUSSION

We report on the real-time determination/imaging of SWIR PL lifetimes for anti-counterfeiting applications using time-gated SWIR PL imaging setup with pulsed laser diode as an excitation source, RENPs as anti-counterfeiting temporal tags, and an RLD method for fast decoding. It is worth noting that while the developed approach is applicable in broad temporal range (from tens and hundreds of microseconds to tens of milliseconds), the use of lifetimes of several milliseconds makes this method highly beneficial, due to combined advantages of simplicity, high

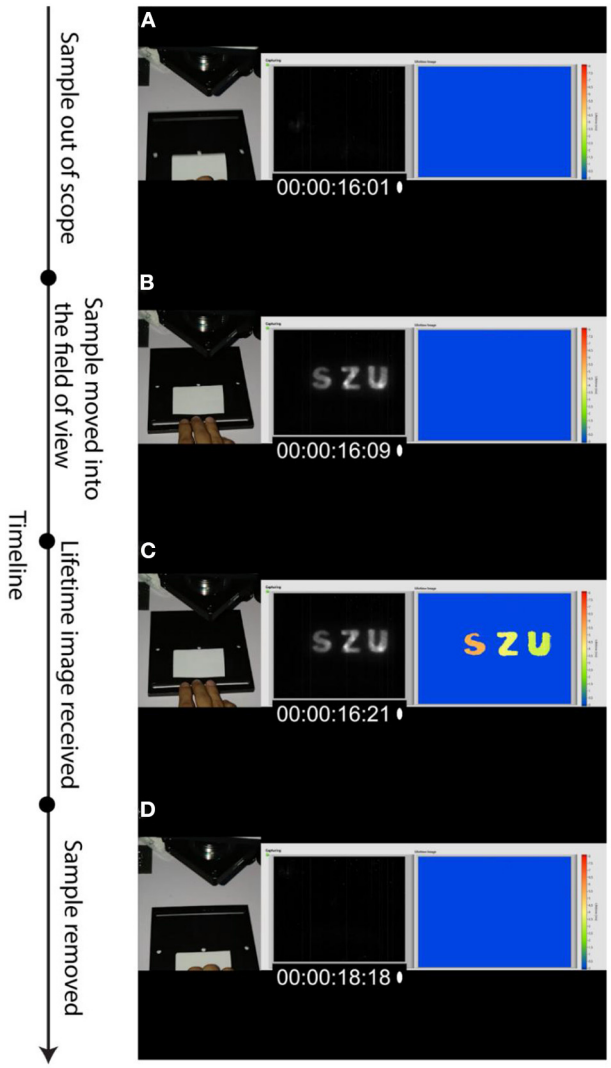

FIGURE 5 | Timeline and major stages of RLD-assisted real-time decoding of SWIR PL pattern illustrated by the photographic images, selected video frames, and corresponding screens of the RLD-based software decoding lifetimes. Timecode (00:00:xx:yy) in every presented video frame shows seconds of the video (xx) and number of the frame within current second (yy). **(A)** The paper with invisible pattern is to be moved into the imaged area (time: 16 s, frame 1). **(B)** SWIR PL intensity image appearing when the pattern is moved into the imaging area (time: 16 s, frame 9). **(C)** Lifetime image generated after receiving two sequential time-gated images with different delays followed by RLD-based processing (time: 16 s, frame 21). **(D)** The paper with invisible pattern is moved out of the imaged area (time: 18 s, frame 18).

speed, and accuracy. Throughout the conducted experiments with $NaYF_4$:20%Yb^{3+}, x%Er^{3+}@$NaYF_4$, the usability of such SWIR emitting RENPs as SWIR PL lifetime-coded tags for real-time anti-counterfeiting and security applications was shown. The Yb^{3+}/Er^{3+} doped RENPs exhibit bright SWIR PL peaked at ∼1,530 nm, with a lifetime that can be precisely tuned in a wide range by manipulation of Er^{3+} content, making these RENPs a highly promising material for anti-counterfeiting and security applications. Use of RLD algorithm allowed us to perform real-time imaging of PL lifetimes of RENPs both suspended in liquid and deposited on a paper. Three samples of RENPs with different SWIR PL lifetimes were clearly distinguished and lifetime values were determined in the post-processed images as well as in real-time running test with SWIR photoluminescent pattern.

It should be noted, however, that the use of the RLD method has its own limitations. First, it requires the PL decays to be monoexponential (Chan et al., 2001). In this regard, the employed RENPs are suitable as their PL decays can be well-fitted with a single exponent (**Figure 2G**). This also leads to an inability of RLD approach to separate (unmix) multiple signals in the single image pixel. This limitation can be addressed by utilization of dual lifetime determination (DLD) method, which can be considered as a modified version of RLD. In DLD, four PL images with different delay times are acquired and the RLD method is repeated twice for two different components in single pixel (two images to determine shorter component and two images for longer component) (Nagl et al., 2009), which results in longer data acquisition in comparison with simple RLD. However, DLD application is not needed when the PL in the imaged pattern is known to decay monoexponentially, as in our work. Another limitation of the RLD (and DLD) method is that the lifetime values are to be known preliminarily before the experiment (testing) in order to maximize the signal-to-noise ratio and, hence, the precision of the measurements. Nevertheless, this appears to be feasible in anti-counterfeiting applications.

In conclusion, our results open the pathway to real-time imaging of PL lifetimes for anti-counterfeiting applications. A combination of the PL time-gating system with RLD-based approach appears to be highly promising for applications in various fields, including information storage, real-time *in vivo* bioimaging, and particle tracking.

MATERIALS AND METHODS

Synthesis of RENPs

The $NaYF_4$: 20% Yb^{3+}, x% Er^{3+} NPs (x = 0, 2, 20, 80) were prepared following the method previously reported (Li et al., 2017). First, RE-OA precursor was prepared using the following procedure. (0.8-x) mmol $YCl_3{\cdot}6H_2O$, 0.2 mmol $YbCl_3{\cdot}6H_2O$, x mmol $ErCl_3{\cdot}6H_2O$, and 3 mmol sodium oleate were mixed with 3 ml of deionized water, 3.5 ml of absolute ethyl alcohol, and 7 ml of hexane, and the resulting mixture was heated at 60°C overnight. The organic phase solvent containing Ln-OA (Ln = Y, Yb, Er) was collected through a separatory funnel, and washed three times with deionized water in a separatory funnel. Second, the obtained Ln-OA precursor was mixed with 8 mmol sodium oleate, 5.2 ml of OA, 5.1 ml of OM, and 9 ml of ODE. The solution was then heated up to 100°C under argon gas protection with vigorous magnetic stirring for 60 min. Subsequently, 8 mmol solid ammonium fluoride was added to the solution and kept at 100°C for another 30 min. Last, the reaction mixture was heated to 300°C at a rate of 10 $K{\cdot}min^{-1}$, kept at this temperature for 30 min, and then allowed to cool down to room temperature naturally. The resulting products were precipitated by addition of 20 ml of ethanol, collected via centrifugation at 6,000 rpm for

10 min, washed twice with a 1:6 hexane/ethanol mixture, and finally dispersed in 10 ml of hexane for further use.

Preparation of $NaYF_4$: Yb, Er@ $NaYF_4$ RENPs

The thermal decomposition method was utilized to coat the NaYF4 shell with a thickness of about 3 nm on $NaYF_4$: Yb, Er core. Typically, 0.5 mmol Y_2O_3 dissolved in 10 ml of trifluoroacetic acid (TFA) aqueous solution with a concentration of 50%. The solution was heated at 90°C under stirring until the solution transformed into transparency, and then, the solution was evaporated to dryness under argon gas, yielding the shell precursor $(CF_3COO)_3Y$. Afterwards, 2 mmol of sodium trifluoroacetate (0.272 g) was added to $(CF_3COO)_3Y$ precursor, together with 10 ml of OA, 10 ml of ODE, and 2.5 ml (0.25 mmol) of the pre-prepared $NaYF_4$: 20% Yb^{3+}, x% Er^{3+} NPs (x = 0, 2, 20, 50, 80); the mixture was then heated at 120°C for 30 min to distill low-boiling liquid, such as water and hexane. Then, the solution was heated to 300°C at a rate of 10 K·min^{-1} under argon protection. After keeping 30 min at 300°C, the reaction mixture was cooled to room temperature and the product was isolated as described above for the $NaYF_4$: Yb^{3+}, Er^{3+} core NPs.

Measurements of PL Spectra and Lifetimes

UC and DS PL spectra in visible and NIR range were obtained using HORIBA Fluorolog-3 spectrofluorometer attached to an iHR320 spectrometer (Horiba) coupled with thermoelectrically cooled NIR-PMT detector (H10330B-75, Hamamatsu). As an excitation source, the fiber-coupled laser diode emitting at 975 nm (QSP-975-10, QPhotonics, USA) controlled by a laser driver (Arroyo Instruments, 4308-QCW) was employed: a collimated beam from the diode was introduced inside the sample chamber of the Fluorolog-3 and directed on the sample cuvette. Laser diode was used in CW mode for the PL spectra acquisition and in pulsed mode (100 μs pulse width) during PL lifetime measurements. In the latter case, signal from the output of the NIR PMT was recorded by the Digital Phosphor Oscilloscope (TDS 3034C, Tektronix) using a variable feed-through terminator (VT2, Thorlabs), and the PL decays were averaged over 128 excitation pulses. The iHR320 spectrometer was set to 1,000 and 1,530 nm for Yb^{3+} and Er^{3+}, respectively. In addition, sync out signal from the laser driver was directly connected to an oscilloscope for external triggering. The experimentally obtained PL decays were fitted monoexponentially using Origin Pro software (OriginLab).

Security Labeling

The imaging pattern was obtained by the direct deposition of RENP hexane suspension onto a commercially available printing paper, which was cut to form the "SZU." Furthermore, those letters with deposited nanoparticles were placed between two sheets of the same white printing paper. This step allows our pattern to be invisible to the naked eye.

SWIR PL Imaging

A home-built SWIR time-gated imaging system was developed based on a NIR-SWIR camera (Xeva-1.7-320, Xenics, Belgium), which is equipped with focusing optics (TEC-M55MPW, Computar, USA) and operates in 900–1,700 nm spectral range (Ziniuk et al., 2019). During imaging, the 1,200-nm long-pass filter (1200LP from Edmunds Optics.) was used in order to cut off Yb^{3+} emission and scattering from the exciting laser. A 975-nm fiber-coupled laser diode (QSP-975-10) powered by a QCW capable laser driver (Arroyo Instruments, 4308-QCW) was used as an excitation source, providing a power density of 30 mW/cm^2 at the sample. Pulse modulation with 10-Hz repetition rate was performed in a burst mode in order to achieve one pulse per trigger received from the LabVIEW developed software. An InGaAs camera was synchronized with laser diode pulses using the "Sync out" output of the laser driver and triggered to capture image at precisely controlled delay times (10 μs to few seconds) and kept integrating for 10 ms. For the RLD, pairs of images with different delay times were obtained. For the image involving a single lifetime, the lifetime of each pixel can be determined by equation (**Figure 1C**). By synchronizing laser triggering, image acquisitions, and data processing, the process can be repeated, thus giving the real-time lifetime data as fast as four frames per second. All the mentioned operations were carried out using LabVIEW software.

DATA AVAILABILITY STATEMENT

The original contributions presented in the study are included in the article/**Supplementary Material**, further inquiries can be directed to the corresponding author/s.

AUTHOR CONTRIBUTIONS

RZ conceived the idea, developed the experimental setup and analyzing software, performed experiments, and drafted the manuscript. AY contributed to the development of the experimental setup and analyzing software. HL and GC synthesized the RENPs and characterized them with TEM. JQ supervised the project and revised and edited the manuscript. TO initiated the study, contributed to the idea development, supervised the project, and revised and edited the manuscript. All authors approved the final version of the manuscript.

FUNDING

This work has been partially supported by the National Natural Science Foundation of China (61620106016/61875135/61835009/61950410610/51972084); the Shenzhen Basic Research Project (JCYJ20170818090620324), and the Shenzhen International Cooperation Project (GJHZ20180928161811821).

SUPPLEMENTARY MATERIAL

The Supplementary Material for this article can be found online at: https://www.frontiersin.org/articles/10.3389/fchem.2021.659553/full#supplementary-material

REFERENCES

Abdollahi, A., Roghani-Mamaqani, H., Razavi, B., and Salami-Kalajahi, M. (2020). Photoluminescent and chromic nanomaterials for anticounterfeiting technologies: recent advances and future challenges. *ACS Nano* 14, 14417–14492. doi: 10.1021/acsnano.0c07289

Andres, J., Hersch, R. D., Moser, J.-E., and Chauvin, A.-S. (2014). A new anti-counterfeiting feature relying on invisible luminescent full color images printed with lanthanide-based inks. *Adv. Funct. Mater.* 24, 5029–5036. doi: 10.1002/adfm.201400298

Bashkatov, A. N., Genina, E. A., Kochubey, V. I., and Tuchin, V. V. (2005). Optical properties of human skin, subcutaneous and mucous tissues in the wavelength range from 400 to 2000 nm. *J. Phys. D Appl. Phys.* 38, 2543–2555. doi: 10.1088/0022-3727/38/15/004

Chan, S. P., Fuller, Z. J., Demas, J. N., and DeGraff, B. A. (2001). Optimized gating scheme for rapid lifetime determinations of single-exponential luminescence lifetimes. *Anal. Chem.* 73, 4486–4490. doi: 10.1021/ac0102361

Chaudhrya, P., Cordellb, V., and Zimmermanc, A. (2005). Modelling anti-counterfeiting strategies in response to protecting intellectual property rights in a global environment. *Mark. Rev.* 5, 59–72. doi: 10.1362/1469347053294832

da Luz, L. L., Milani, R., Felix, J. F., Ribeiro, I. R. B., Talhavini, M., Neto, B. A. D., et al. (2015). Inkjet printing of lanthanide–organic frameworks for anti-counterfeiting applications. *ACS Appl. Mater. Interfaces* 7, 27115–27123. doi: 10.1021/acsami.5b06301

Deng, R., Qin, F., Chen, R., Huang, W., Hong, M., and Liu, X. (2015). Temporal full-colour tuning through non-steady-state upconversion. *Nat. Nanotechnol.* 10, 237–242. doi: 10.1038/nnano.2014.317

Ding, Y., Zhang, X., Gao, H., Xu, S., Wei, C., and Zhao, Y. (2014). Enhancement on concentration quenching threshold and upconversion luminescence of β-NaYF4:Er3+/Yb3+ codoping with Li+ ions. *J. Alloys Compounds* 599, 60–64. doi: 10.1016/j.jallcom.2014.02.050

Fan, Y. (2018). Lifetime-engineered NIR-II nanoparticles unlock multiplexed *in vivo* imaging. *Nat. Nanotechnol.* 13:11. doi: 10.1038/s41565-018-0221-0

Fincham, J. E. (2014). Counterfeit medications and their negative impacts on health care. *Am. J. Pharm. Educ.* 78:48. doi: 10.5688/ajpe78348

Fink, C. M., Keith, E., and Qian, Y. (2016). The economic effects of counterfeiting and piracy: a review and implications for developing countries. *World Bank Res. Observ.* 31, 1–28. doi: 10.1596/1813-9450-7586

Göhler, B., and Lutzmann, P. (2016). Review on short-wavelength infrared laser gated-viewing at fraunhofer IOSB. *OE* 56:031203. doi: 10.1117/1.OE.56.3.031203

Golovynskyi, S., Golovynska, I., Stepanova, L. I., Datsenko, O. I., Liu, L., Qu, J., et al. (2018). Optical windows for head tissues in near-infrared and short-wave infrared regions: approaching transcranial light applications. *J. Biophoton.* 11:e201800141. doi: 10.1002/jbio.201800141

Han, X., Song, E., Zhou, B., and Zhang, Q. (2019). Color tunable upconversion luminescent perovskite fluoride with long-/short-lived emissions toward multiple anti-counterfeiting. *J. Mater. Chem. C* 7, 8226–8235. doi: 10.1039/C9TC02171J

Hazra, C., Skripka, A., Ribeiro, S. J. L., and Vetrone, F. (2020). Erbium single-band nanothermometry in the third biological imaging window: potential and limitations. *Adv. Optic. Mater.* 8:2001178. doi: 10.1002/adom.202001178

Jee, H., Chen, G., Prasad, P. N., Ohulchanskyy, T. Y., and Lee, J. (2020). *In situ* ultraviolet polymerization using upconversion nanoparticles: nanocomposite structures patterned by near infrared light. *Nanomaterials* 10:2054. doi: 10.3390/nano10102054

Kaczmarek, A. M., Liu, Y.-Y., Wang, C., Laforce, B., Vincze, L., Voort, P. V. D., et al. (2017). Lanthanide "Chameleon" multistage anti-counterfeit materials. *Adv. Funct. Mater.* 27:1700258. doi: 10.1002/adfm.201700258

Kumar, P., Dwivedi, J., and Gupta, B. K. (2014). Highly luminescent dual mode rare-earth nanorod assisted multi-stage excitable security ink for anti-counterfeiting applications. *J. Mater. Chem. C* 2, 10468–10475. doi: 10.1039/C4TC02065K

Laurenzis, M., and Christnacher, F. (2013). Laser gated viewing at ISL for vision through smoke, active polarimetry, and 3D imaging in NIR and SWIR wavelength bands. *Adv. Optic. Technol.* 2, 397–405. doi: 10.1515/aot-2013-0040

Li, H., Xu, L., and Chen, G. (2017). Controlled synthesis of monodisperse hexagonal NaYF4:Yb/Er nanocrystals with ultrasmall size and enhanced upconversion luminescence. *Molecules* 22:2113. doi: 10.3390/molecules22122113

Li, Y., Jiang, M., Xue, Z., and Zeng, S. (2020). 808 nm light triggered lanthanide nanoprobes with enhanced down-shifting emission beyond 1500 nm for imaging-guided resection surgery of tumor and vascular visualization. *Theranostics* 10, 6875–6885. doi: 10.7150/thno.41967

Liang, L., Qin, X., Zheng, K., and Liu, X. (2019). Energy flux manipulation in upconversion nanosystems. *Acc. Chem. Res.* 52, 228–236. doi: 10.1021/acs.accounts.8b00469

Liu, X., Wang, Y., Li, X., Yi, Z., Deng, R., Liang, L., et al. (2017). Binary temporal upconversion codes of Mn 2+ -activated nanoparticles for multilevel anti-counterfeiting. *Nat. Commun.* 8, 1–7. doi: 10.1038/s41467-017-00916-7

Liu, Y., Ai, K., and Lu, L. (2011). Designing lanthanide-doped nanocrystals with both up- and down-conversion luminescence for anti-counterfeiting. *Nanoscale* 3, 4804–4810. doi: 10.1039/c1nr10752f

Liu, Y., Zhou, Y., and Liu, Y. (2014). "A rapid fluorescence lifetime image acquistion method based on time-gated fluorescence lifetime imaging microscopy," in: *The 2014 2nd International Conference on Systems and Informatics (ICSAI 2014)*, 808–812.

Lu, Y., Lu, J., Zhao, J., Cusido, J., Raymo, F. M., Yuan, J., et al. (2014). On-the-fly decoding luminescence lifetimes in the microsecond region for lanthanide-encoded suspension arrays. *Nat. Commun.* 5:3741. doi: 10.1038/ncomms4741

Lv, R., Feng, M., Liu, J., Jiang, X., Yuan, H., Yan, R., et al. (2019). Improved red emission and short-wavelength infrared luminescence under 808 nm laser for tumor theranostics. *ACS Biomater. Sci. Eng.* 5, 4683–4691. doi: 10.1021/acsbiomaterials.9b00688

Mei, Q., Bansal, A., Jayakumar, M. K. G., Zhang, Z., Zhang, J., Huang, H., et al. (2019). Manipulating energy migration within single lanthanide activator for switchable upconversion emissions towards bidirectional photoactivation. *Nat. Commun.* 10, 1–11. doi: 10.1038/s41467-019-12374-4

Nagl, S., Stich, M. I. J., Schäferling, M., and Wolfbeis, O. S. (2009). Method for simultaneous luminescence sensing of two species using optical probes of different decay time, and its application to an enzymatic reaction at varying temperature. *Anal. Bioanal. Chem.* 393, 1199–1207. doi: 10.1007/s00216-008-2467-0

Ortgies, D. H., Tan, M., Ximendes, E. C., del Rosal, B., Hu, J., Xu, L., et al. (2018). Lifetime-encoded infrared-emitting nanoparticles for *in vivo* multiplexed imaging. *ACS Nano* 12, 4362–4368. doi: 10.1021/acsnano.7b09189

Platel, R., Vaure, L., Palleau, E., Raffy, S., Guérin, F., Lagarde, D., et al. (2021). Synthesis of hybrid colloidal nanoparticles for a generic approach to 3D electrostatic directed assembly: application to anti-counterfeiting. *J. Colloid Interface Sci.* 582, 1243–1250. doi: 10.1016/j.jcis.2020.08.098

Rabouw, F. T., Prins, P. T., Villanueva-Delgado, P., Castelijns, M., Geitenbeek, R. G., and Meijerink, A. (2018). Quenching pathways in NaYF4:Er3+,Yb3+ upconversion nanocrystals. *ACS Nano* 12, 4812–4823. doi: 10.1021/acsnano.8b01545

Secu, C. E., Matei, E., Negrila, C., and Secu, M. (2019). The influence of the nanocrystals size and surface on the Yb/Er doped LaF3 luminescence properties. *J. Alloys Compounds* 791, 1098–1104. doi: 10.1016/j.jallcom.2019.03.267

Sharman, K. K., Periasamy, A., Ashworth, H., and Demas, J. N. (1999). Error analysis of the rapid lifetime determination method for double-exponential decays and new windowing schemes. *Anal. Chem.* 71, 947–952. doi: 10.1021/ac981050d

Sun, T., Xu, B., Chen, B., Chen, X., Li, M., Shi, P., et al. (2017). Anti-counterfeiting patterns encrypted with multi-mode luminescent nanotaggants. *Nanoscale* 9, 2701–2705. doi: 10.1039/C6NR09083D

Tan, M., Li, F., Wang, X., Fan, R., and Chen, G. (2020). Temporal multilevel luminescence anticounterfeiting through scattering media. *ACS Nano* 14, 6532–6538. doi: 10.1021/acsnano.9b08326

Wang, F., and Liu, X. (2008). Upconversion multicolor fine-tuning: visible to near-infrared emission from lanthanide-doped NaYF4 nanoparticles. *J. Am. Chem. Soc.* 130, 5642–5643. doi: 10.1021/ja800868a

Wang, X., Yakovliev, A., Ohulchanskyy, T. Y., Wu, L., Zeng, S., Han, X., et al. (2018a). Efficient erbium-sensitized core/shell nanocrystals for short wave infrared bioimaging. *Adv. Optic. Mater.* 6:1800690. doi: 10.1002/adom.201800690

Wang, Y., Zheng, K., Song, S., Fan, D., Zhang, H., and Liu, X. (2018b). Remote manipulation of upconversion luminescence. *Chem. Soc. Rev.* 47, 6473–6485. doi: 10.1039/C8CS00124C

Wang, Y., Zhou, J., Gao, J., Zhang, K., Gao, C., Xie, X., et al. (2019). Physical manipulation of lanthanide-activated photoluminescence. *Ann. Phys.* 531:1900026. doi: 10.1002/andp.201900026

Xie, S., Gong, G., Song, Y., Tan, H., Zhang, C., Li, N., et al. (2019). Design of novel lanthanide-doped core–shell nanocrystals with dual up-conversion and down-conversion luminescence for anti-counterfeiting printing. *Dalton Trans.* 48, 6971–6983. doi: 10.1039/C9DT01298B

Yi, G., Lu, H., Zhao, S., Ge, Y., Yang, W., Chen, D., et al. (2004). Synthesis, characterization, and biological application of size-controlled nanocrystalline NaYF4:Yb,Er infrared-to-visible up-conversion phosphors. *Nano Lett.* 4, 2191–2196. doi: 10.1021/nl048680h

You, M., Zhong, J., Hong, Y., Duan, Z., Lin, M., and Xu, F. (2015). Inkjet printing of upconversion nanoparticles for anti-counterfeit applications. *Nanoscale* 7, 4423–4431. doi: 10.1039/C4NR06944G

You, W., Tu, D., Li, R., Zheng, W., and Chen, X. (2019). "Chameleon-like" optical behavior of lanthanide-doped fluoride nanoplates for multilevel anti-counterfeiting applications. *Nano Res.* 12, 1417–1422. doi: 10.1007/s12274-019-2366-z

Ziniuk, R., Yakovliev, A., Qu, J., and Ohulchanskyy, T. Y. (2019). "Time-gated and lifetime-unmixed imaging of near- and short wave infrared photoluminescence from rare-earth ion doped nanoparticles," in: *Eleventh International Conference on Information Optics and Photonics (CIOP 2019); International Society for Optics and Photonics*, Vol. 11209, 112095E.

Conflict of Interest: The authors declare that the research was conducted in the absence of any commercial or financial relationships that could be construed as a potential conflict of interest.

frontiers in Physics

ORIGINAL RESEARCH
published: 16 October 2020
doi: 10.3389/fphy.2020.576862

Investigations on Average Fluorescence Lifetimes for Visualizing Multi-Exponential Decays

Yahui Li[1,2,3], *Sapermsap Natakorn*[4], *Yu Chen*[4], *Mohammed Safar*[1], *Margaret Cunningham*[1], *Jinshou Tian*[2,3] *and David Day-Uei Li*[1]*

[1] Strathclyde Institute of Pharmacy and Biomedical Sciences, University of Strathclyde, Glasgow, United Kingdom, [2] Key Laboratory of Ultra-fast Photoelectric Diagnostics Technology, Xi'an Institute of Optics and Precision Mechanics, Xi'an, China, [3] University of Chinese Academy of Sciences, Beijing, China, [4] Department of Physics, Scottish Universities Physics Alliance, University of Strathclyde, Glasgow, United Kingdom

Intensity- and amplitude-weighted average lifetimes, denoted as τ_I and τ_A hereafter, are useful indicators for revealing Förster resonance energy transfer (FRET) or fluorescence quenching behaviors. In this work, we discussed the differences between τ_I and τ_A and presented several model-free lifetime determination algorithms (LDA), including the center-of-mass, phasor, and integral equation methods for fast τ_I and τ_A estimations. For model-based LDAs, we discussed the model-mismatch problems, and the results suggest that a bi-exponential model can well approximate a signal following a multi-exponential model. Depending on the application requirements, suggestions about the LDAs to be used are given. The instrument responses of the imaging systems were included in the analysis. We explained why only using the τ_I model for FRET analysis can be misleading; both τ_I and τ_A models should be considered. We also proposed using τ_A/τ_I as a new indicator on two-photon fluorescence lifetime images, and the results show that τ_A/τ_I is an intuitive tool for visualizing multi-exponential decays.

Keywords: fluorescence lifetime imaging, lifetime determination algorithm, average lifetimes, multi-exponential decays, lifetime image visualization, FRET—fluorescence resonance energy transfer

OPEN ACCESS

Edited by:
Klaus Suhling, King's College London, United Kingdom

Reviewed by:
Nirmal Mazumder, Manipal Academy of Higher Education, India
Ilia L. Rasskazov, University of Rochester, United States

***Correspondence:**
David Day-Uei Li
david.li@strath.ac.uk

Specialty section:
This article was submitted to Optics and Photonics, a section of the journal Frontiers in Physics

Received: *27 July 2020*
Accepted: *09 September 2020*
Published: *16 October 2020*

Citation:
Li Y, Natakorn S, Chen Y, Safar M, Cunningham M, Tian J and Li DD-U (2020) Investigations on Average Fluorescence Lifetimes for Visualizing Multi-Exponential Decays. Front. Phys. 8:576862. doi: 10.3389/fphy.2020.576862

1. INTRODUCTION

Fluorescence lifetime imaging (FLIM) is a crucial technique for assessing microenvironments of fluorescent molecules [1, 2], such as pH [3], Ca^{2+} [4, 5], O_2 [6], viscosity [7], or temperature [8]. Combining with Förster Resonance Energy Transfer (FRET) techniques, FLIM can be a powerful "quantum ruler" to measure protein conformations and interactions [9–12]. Compared with fluorescence intensity imaging, FLIM is independent of the signal intensity and fluorophore concentrations, making FLIM a powerful quantitative imaging technique for applications in life sciences [13], medical diagnosis [14–16], drug developments [17–19], and flow diagnosis [20–22]. FLIM techniques can build on time-correlated single-photon counting (TCSPC) [23–25], time-gating [26–28], or streak cameras [29]; they record time-resolved fluorescence intensity profiles to extract lifetimes with a lifetime determination algorithm (LDA) [1]. There is a rapid growth of real-time applications that fast analysis is sought after [12, 30]. Traditional LDAs usually use the least square method (LSM) or maximum likelihood estimation (MLE) [31] to analyze decay models chosen by users, and model-fitting analysis follows a reduced chi-squared criterion [1]. In reality, however, it is difficult to know the exact decay model as fluorescent molecules in biological systems can demonstrate

complex multi-exponential decay profiles. For instance, a mixture of fluorophores, a multi-tryptophan protein, single fluorophores in varied environments, and single-tryptophan proteins in multiple conformational states [1] can show multi-exponential decays as

$$f(t) = A\sum_{i=1}^{p} q_i \exp(-t/\tau_i), \text{where} \sum_{i=1}^{p} q_i = 1, \tag{1}$$

where A represents the amplitude, q_i and τ_i ($i = 1, \ldots, p$) denote the amplitude fractions and lifetimes, respectively, and p is the number of lifetime components. There are time-domain or frequency-domain [32–35] FLIM systems to measure a fluorescence decay. In this work, we focus on time-domain approaches.

Suppose the instrument response function (IRF) of the measurement system is $irf(t)$, the task performed by FLIM analysis tools is to extract $f(t)$ from the measured decay $h(t)$, as

$$h(t) = irf(t) * f(t). \tag{2}$$

The problems with traditional LSM or MLE are two-fold. (1) It is challenging to categorize a fluorescence emission into a specific exponential model described by Equation (1) in complex biological processes. An arbitrary choice of p in Equation (1) simply based on reduced chi-squared tests [36] would lead to totally different interpretations. As the fitting routine is not mathematically unique; a measured decay could be fitted equally well with a bi-exponential or a tri-exponential model. (2) To ensure the accuracy, it usually needs a high photon count (long acquisition time) when $p \geq 2$ [37]. Instead of completely extracting q_i and τ_i ($i = 1, \ldots, p$), which is doubtful as mentioned above and time-consuming, in many applications, it is often useful to determine only the average lifetime which can be expressed in two forms [1]: the intensity-weighted average lifetime

$$\tau_I = \sum_{i=1}^{p} q_i \tau_i^2 / \sum_{i=1}^{p} q_i \tau_i, \tag{3}$$

and the amplitude-weighted average lifetime

$$\tau_A = \sum_{i=1}^{p} q_i \tau_i / \sum_{i=1}^{p} q_i = \sum_{i=1}^{p} q_i \tau_i. \tag{4}$$

The question about which average lifetime we should use according to the applications has been investigated in [38]. For instance, they suggested:

(a) τ_A can estimate the energy transfer efficiency in FRET [39],

$$E = 1 - \frac{I_{DA}}{I_D} = 1 - \frac{\tau_{DA,A}}{\tau_{D,A}}, \tag{5}$$

where E is the energy transfer efficiency, I_{DA} and I_D are the fluorescence intensities of the donor in the presence and absence of energy transfer, respectively, and $\tau_{DA,A}$ and $\tau_{D,A}$ are τ_A of the donor in the presence and absence of energy transfer, respectively. E can further estimate the donor-acceptor distance.

(b) τ_A can also assess dynamic quenching behaviors, described by the Stern-Volmer equation [40],

$$\frac{I_0}{I_1} = 1 + K_D[Q] = \frac{\tau_{0,A}}{\tau_{1,A}}, \tag{6}$$

where I_0 and I_1 are fluorescence intensities, $\tau_{0,A}$ and $\tau_{1,A}$ are τ_A of the fluorophore in the absence and presence of the quencher, respectively, K_D is the Stern-Volmer quenching constant, and $[Q]$ is the concentration of the quencher. Additionally, the average radiative rate constant can be expressed as, $k_r = QE/\tau_{1,A}$, where QE is the quantum yield.

(c) τ_I can be used to estimate the average collisional constant k_q from the Stern-Volmer constant K_D.

Average lifetimes can either be calculated by extracting the lifetime components using model-based LDAs and then using Equations (3) and (4). Or they can be directly obtained with model-free LDAs, such as hardware-friendly center-of-mass methods (CMM) [41–44], the phasor method (Phasor) [45–47], the rapid lifetime determination method (RLD) [30, 48–51], or the integral extraction method (IEM) [52, 53], without assuming any decay model.

In this work, we theoretically investigated two types of average lifetimes evaluated by model-free LDAs, examined the performances of τ_A and τ_I estimations using different LDAs, and suggested the choices of LDAs in terms of accuracy, precision, and estimation speeds according to the applications. We also described a multi-exponential decay visualization tool using the ratio τ_A/τ_I. Experimental results demonstrate the performance of τ_A/τ_I in comparison with Phasor.

2. THEORY

In this section, we derived the average lifetimes determined by the model-free methods, CMM, Phasor, and IEM and described the general work flow of average lifetime estimations with the model-free and model-based LDAs.

As Equation (2), the measured signal $h(t)$ is the convolution of $f(t)$ with $irf(t)$. Here we focus on the signal h_m and irf_m obtained from a TCSPC system, as shown in **Figure 1**,

$$\begin{aligned} h_m &= \sum_{k=0}^{m} irf_{k-m} \cdot f_m, m = 0, 1, 2, \ldots, M-1, \\ irf_m &= \int_{m\Delta t}^{(m+1)\Delta t} irf(t)dt, \\ f_m &= \int_{m\Delta t}^{(m+1)\Delta t} f(t)dt = A\sum_{i=1}^{p} q_i \tau_i e^{-\frac{m\Delta t}{\tau_i}}[1 - e^{-\frac{\Delta t}{\tau_i}}], \end{aligned} \tag{7}$$

where h_m is the photon count collected in Bin m at $t_m = (m + 1/2)\Delta t$, M is the number of bins, and Δt is the time resolution.

(a) CMM

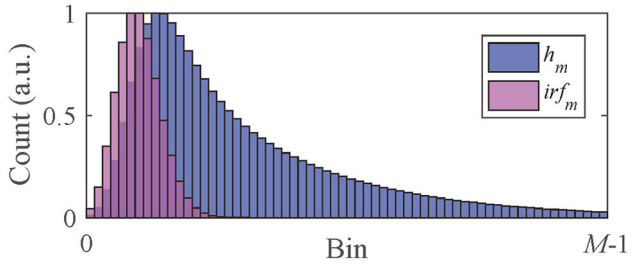

FIGURE 1 | Illustration of h_m and irf_m obtained with a TCSPC system.

The average lifetime evaluated with CMM is

$$\tau_{CMM} = \frac{\int_0^\infty t \cdot h(t)dt}{\int_0^\infty h(t)dt} - \frac{\int_0^\infty t \cdot irf(t)dt}{\int_0^\infty irf(t)dt} = \frac{\sum_{i=1}^p q_i\tau_i^2}{\sum_{i=1}^p q_i\tau_i} \simeq \frac{\sum_{m=0}^{M-1} t_m \cdot h_m}{\sum_{m=0}^{M-1} h_m} - \frac{\sum_{m=0}^{M-1} t_m \cdot irf_m}{\sum_{m=0}^{M-1} irf_m}, \quad (8)$$

which is equal to τ_I. The derivation of Equation (8) is shown in the **Appendix**.

(b) Phasor

The average lifetime evaluated with Phasor is

$$\tau_P = \frac{s}{g\omega} = \frac{\sum_{i=1}^p q_i\tau_i^2/(1+\omega^2\tau_i^2)}{\sum_{i=1}^p q_i\tau_i/(1+\omega^2\tau_i^2)}, \quad (9)$$

where $\omega = 2\pi/T$, $T = M\Delta t$ is the measurement window, and g and s are the phasor components expressed as

$$g = \frac{\int_0^\infty f(t)\cdot\cos(\omega t)dt}{\int_0^\infty f(t)dt} = \frac{\sum_{i=1}^p q_i\tau_i/(1+\omega^2\tau_i^2)}{\sum_{i=1}^p q_i\tau_i} = \frac{R_h + s\cdot I_{irf}}{R_{irf}},$$

$$s = \frac{\int_0^\infty f(t)\cdot\sin(\omega t)dt}{\int_0^\infty f(t)dt} = \frac{\sum_{i=1}^p \omega q_i\tau_i^2/(1+\omega^2\tau_i^2)}{\sum_{i=1}^p q_i\tau_i} = \frac{I_h\cdot R_{irf} - R_h\cdot I_{irf}}{R_{irf}^2 + I_{irf}^2},$$

where

$$R_h = \frac{\int_0^\infty h(t)\cdot\cos(\omega t)dt}{\int_0^\infty h(t)dt} \simeq \frac{\sum_{m=0}^{M-1} h_m\cdot\cos(\omega t_m)}{\sum_{m=0}^{M-1} h_m},$$

$$I_h = \frac{\int_0^\infty h(t)\cdot\sin(\omega t)dt}{\int_0^\infty h(t)dt} \simeq \frac{\sum_{m=0}^{M-1} h_m\cdot\sin(\omega t_m)}{\sum_{m=0}^{M-1} h_m},$$

$$R_{irf} = \frac{\int_0^\infty irf(t)\cdot\cos(\omega t)dt}{\int_0^\infty irf(t)dt} \simeq \frac{\sum_{m=0}^{M-1} irf_m\cdot\cos(\omega t_m)}{\sum_{m=0}^{M-1} irf_m},$$

$$I_{irf} = \frac{\int_0^\infty irf(t)\cdot\sin(\omega t)dt}{\int_0^\infty irf(t)dt} \simeq \frac{\sum_{m=0}^{M-1} irf_m\cdot\sin(\omega t_m)}{\sum_{m=0}^{M-1} irf_m}.$$

τ_P is a weighted average lifetime whose weights are $q_i\tau_i/(1+\omega^2\tau_i^2)$. If $\tau_i \ll T$, then the weights are approximately equal to $q_i\tau_i$, i.e., τ_P is close to τ_I.

(c) IEM

For IEM, the underlying exponential decay should be extracted by a model-free deconvolution method. With the estimated exponential decay $\hat{f}_m$, the average lifetime with IEM is

$$\tau_{IEM} = -\frac{\int_0^\infty g(t)dt}{\int_0^\infty g'(t)dt} = \frac{\sum_{i=1}^p q_i\tau_i}{\sum_{i=1}^p q_i} \simeq -\frac{\Delta t\sum_{m=0}^{M-1} S_m\cdot\hat{f}_m}{\hat{f}_{M-1} - \hat{f}_0} \quad (10)$$

$$g(t) = A\sum_{i=1}^p q_i\tau_i e^{-t/\tau_i}[1 - e^{-\Delta t/\tau_i}],$$

where $S_m = [1/3,\ 4/3,\ 2/3,\ 4/3,\ 1/3]$ are the coefficients for numerical integration based on Simpson's rule. τ_{IEM} is actually an estimator for τ_A.

Figure 2 summarizes the flow diagram for τ_I and τ_A estimations with different algorithms used in this study. The simulated signals h_m and irf_m are directly sent into CMM and Phasor blocks to estimate τ_I. The estimated f_m (from h_m and irf_m with the Laguerre expansion deconvolution method with $L = 16$ and $\alpha = 0.912$ [54, 55]) is sent to IEM to estimate τ_A and sent to the bi-decay center-of-mass method (BCMM; $j = 2$) [56], the variable projection method (VPM; $j = 2$) [57], or LSM with a j-exponential model (denoted as LSM-j), to estimate τ_I and τ_A. CMM and Phasor are fast as no deconvolution routine is needed, whereas IEM, BCMM, VPM, and LSM are direct or iterative estimation approaches once f_m is extracted. Artificial neural network assisted analysis tools [58, 59] can be included in this diagram, but they are out of the scope of this work.

3. RESULTS

3.1. Simulations

In reality, it is difficult to characterize a real fluorescence profile with a suitable exponential model described in Equation (1). To demonstrate how model-free analysis can be beneficial, we examined two scenarios. Case A: we used exponential decay signals with $p = 1 \sim 4$ to assess the influence of the model mismatch between the signal and the algorithm on τ_I and τ_A estimations. This study is to investigate the scenario when users select a j-exponential model to analyze a p-exponential decay (p can be different from j). Case B: we generated synthetic bi-exponential ($p = 2$) decay signals to assess the performances of τ_I and τ_A estimations with the model-free and model-based LDAs.

The performances of lifetime estimations can be assessed in two aspects: (1) the accuracy $B_n = |\hat{\tau}_n - \tau_n|/\tau_n$ and the precision $F_n = \sqrt{N_{tot}}\sigma_{\hat{\tau}_n}/\hat{\tau}_n$ [60], where $n = I$ or A for the intensity- or the amplitude-weighted lifetimes, τ_n and $\hat{\tau}_n$ are actual and estimated values, $\sigma_{\hat{\tau}_n}$ is the standard deviation of $\hat{\tau}_n$, and N_{tot} is the total photon count. The lower the F, the higher the precision ($F = 1$ for the ideal case).

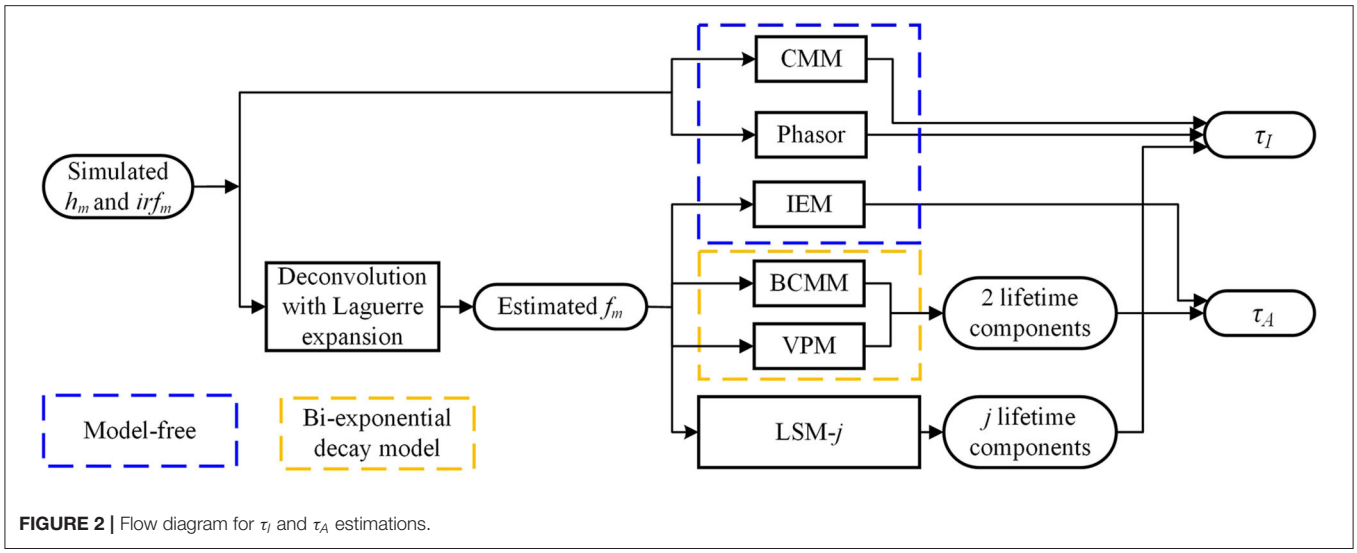

FIGURE 2 | Flow diagram for τ_I and τ_A estimations.

TABLE 1 | τ_i, τ_I, and τ_A for $p = 1 \sim 4$ with $q_i = 1/p$.

p	τ_i (ns)	τ_I (ns)	τ_A (ns)
1	2.5	2.5	2.5
2	0.1, 2.5	2.40	1.3
3	0.1, 1.3, 2.5	2.04	1.3
4	0.1, 0.9, 1.7, 2.5	1.92	1.3

3.1.1. Case A: Model Mismatch

Ideally, a bi-exponential signal should be analyzed by a bi-exponential model. For instance, BCMM, VPM, and LSM-2 are used for bi-exponential decay models, and LSM-j for j-exponential models, $j > 2$. However, in realistic biological processes, it is difficult to know precisely how many lifetime components a decay profile contains. In traditional FLIM analysis tools, users usually need to select an exponential model to fit measured decays and use the reduced chi-squared to evaluate the goodness-of-fit. If the reduced chi-squared is not satisfactory, then a different exponential model is chosen. This process continues until the reduced chi-squared is acceptable. Often different exponential models can produce similar reduced chi-squared values, and the question is which fitting we should use? It is quite common that a j-exponential model might analyze a signal containing p lifetime components and $j \neq p$. We would like to know if p is unknown to the user, whether using a different analysis model ($j \neq p$) would lead to a different biological story.

We generated exponential decay signals h_m ($m = 0,\ldots, M$-1) to test the LDAs for τ_I and τ_A estimations. h_m can be artificially generated with $f(t) = A\sum_{i=1}^{p} q_i \exp(-t/\tau_i)$, where $p = [1, 2, 3, 4]$, $q_i = 1/p$, and the IRF is approximated with a Poisson distribution $irf_m = \exp(\lambda)\lambda^m/m!$ with $\lambda = 500$ ps, FWHM $\simeq$ 300 ps, and $M = 256$. The measurement window $T = 10$ ns, and the total photon count $N_{tot} = 10^3$. τ_i, τ_I, and τ_A for each p are summarized in **Table 1**.

The performances of τ_I and τ_A estimations with the simulated exponential decays are shown in **Figures 3A–D** for B_I, F_I, B_A, and F_A, respectively. For model-free LDAs, B_I and B_A are below 10% and are independent of p. For LSM-1, when $p = 1$, B_I, and B_A are zero, whereas when $p > 1$, B_I and B_A increase especially for $p = 2$. For model-based LDAs where $j > 1$, BCMM, VPM, and LSM-j have similar performances even for $p \neq j$, seemingly suggesting that a bi-exponential model can well approximate a signal following an arbitrary p-exponential model. We generated 100 signals with τ_i and q_i chosen randomly in the ranges of $0.1 \sim 2.5$ ns and $0.1 \sim 0.9$, respectively, for each p. BCMM, VPM, and LSM-2 were used to fit the signals with bi-exponential decays. The goodness-of-fit is judged by the reduced chi-squared $\chi^2 = \frac{1}{M}\sum_{m=0}^{M-1}(f_m - f_{c,m})^2/f_m$, where f_m and $f_{c,m}$ are actual and fitted signals of Bin m. The box plots of χ^2 for BCMM, VPM, and LSM-2 are shown in **Figures 3E–G**, respectively. The χ^2 values are insensitive to p for the three LDAs so that we conclude that a bi-exponential decay is suitable to approximate an arbitrary p-exponential decay ($p \leq 4$).

Therefore, if the decay model of the signal is inaccessible, model-free and model-based LDAs, BCMM, VPM, and LSM-2 are enough for τ_I and τ_A estimations.

In practice, users can choose an optimization algorithm and set initial conditions to analyze FLIM images when LSM-2 is used. We would like to know how they can affect τ_I and τ_A estimations. Four bi-exponential decays, Decays $1 \sim 4$, with different parameters (q_1, τ_1, τ_2) were analyzed using LSM-2 with different initial conditions (q_{10}, τ_{10}, τ_{20}), denoted as Init. $1 \sim 4$ listed in **Table 2** with $N_{tot} = 10^3$. When either of the estimated τ_1 and τ_2 is larger than T (10 ns), we say that the estimation fails. The probabilities of producing a failed trial, $P(\tau_1$ or $\tau_2 > 10)$ and producing biased τ_I and τ_A with B_I and $B_A > 0.3$, i.e., $P(B_n > 0.3)$, $n = I$ or A, are shown in **Figure 4**. **Figures 4A–F** are the LSM-2 results with the unconstrained and constrained trust-region-reflective (TRR) algorithms, respectively. The constraints are $0 < q_1 < 1$ and $0 < \tau_1, \tau_2 < 10$ ns. **Figures 4G–I** are the LSM-2 results using the Levenberg-Marquardt (LM) algorithm. For the unconstrained TRR, the performances are relatively sensitive to initial conditions. $P(\tau_1$ or $\tau_2 > 10)$ for Init. 4 is quite significant which results in large $P(B_n > 0.3)$, $n = I$

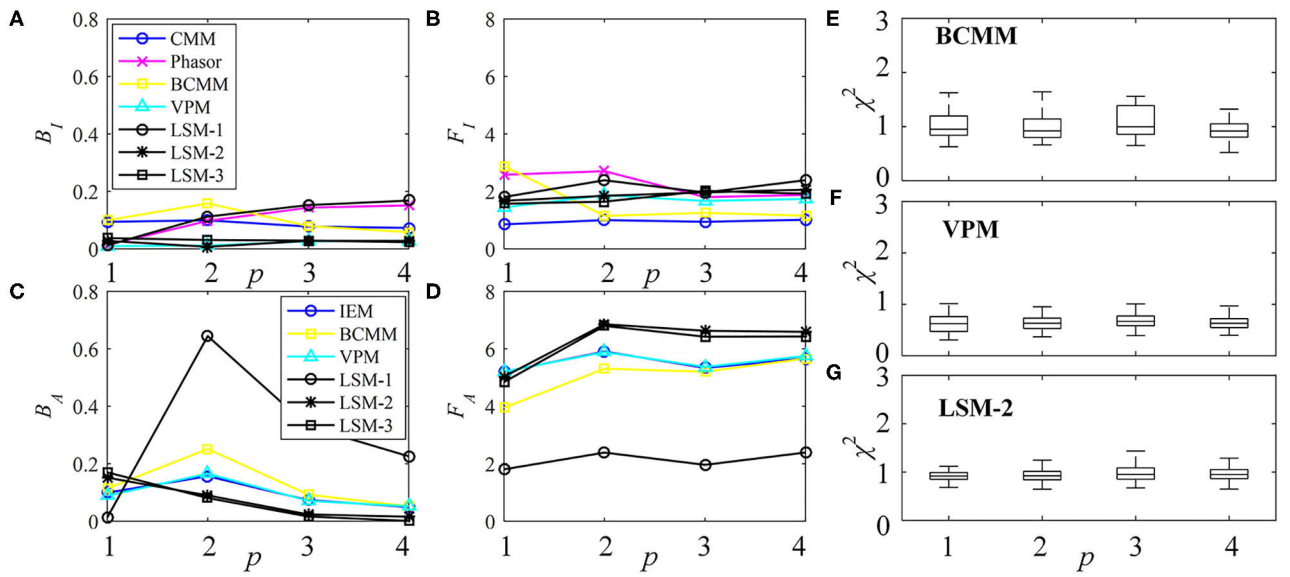

FIGURE 3 | Performances of τ_I and τ_A estimations with exponential decay signals using different algorithms, **(A)** B_I, **(B)** F_I, **(C)** B_A, and **(D)** F_A. **(E–G)** Box plots of χ^2 for BCMM, VPM, and LSM-2.

TABLE 2 | Bi-exponential decays and initial conditions for τ_I and τ_A estimations with LSM-2.

Decay	Parameters			Init.	Initial conditions		
	q_1	τ_1	τ_2		q_{10}	τ_{10}	τ_{20}
1	1/2	0.1	2.5	1	1/2	0.1	0.5
2	4/5	0.1	2.5	2	1/2	0.1	2.5
3	1/2	0.5	1	3	1/2	2	4
4	1/2	1	2.5	4	1/2	4	6

or A, for all four decays. Although Init. 3 leads to a low P for Decays $2 \sim 3$, $P(B_A > 0.3)$ for Decay 1 rises to 0.7. Thus, if the initial conditions are not chosen properly, the quality of τ_I and τ_A images cannot be guaranteed. The constrained TRR and LM are insensitive to initial conditions. Although the LM has failed trials, they barely affect $P(B_n > 0.3)$, $n = I$ or A. Therefore, to ensure accurate τ_I and τ_A estimations, the constrained TRR and LM are recommended for LSM-2.

3.1.2. Case B: Performances of Average Lifetime Estimations

As mentioned above, it might be challenging to use a proper exponential model to describe realistic biological processes; a bi-exponential model might well approximate them. Here we will use a bi-exponential model to explain why model-free LDAs have the benefits of higher photon efficiency and faster analysis than model-based LDAs for τ_I and τ_A estimations.

h_m can be artificially generated with the same IRF used in Case A and $f(t) = A[q_1 \exp(-t/\tau_1) + (1-q_1)\exp(-t/\tau_2)]$, where $\tau_1 < \tau_2$ and q_1 is the amplitude fraction of τ_1. **Figure 5A** shows the signal and IRF. In FRET and dynamic quenching applications, the fluorescence lifetime of the donor fluorophore is in general decreasing, and we assume $\tau_2 = 2.5$ ns and τ_1 varying from 0.1 to 2.5 ns to emulate FRET or quenching. The theoretical τ_I, τ_A, and τ_P with $q_1 = 0.5$ are shown in **Figure 5B**. τ_P has a negative bias from τ_I. With T/τ_2 increasing, τ_P approaches τ_I. **Figure 5B** that two different (τ_1, τ_2) sets can deliver the same τ_I, for instance, (0.32, 2.5) ns and (2.1, 2.5) ns have the same τ_I of 2.3 ns.

Therefore, only estimating τ_I can be misleading. **Figure 5B** also shows that the dynamic range of τ_I is only 2.5–2.23 = 0.27 ns and within which the above problem persists. Whereas τ_A does not have this problem for this case. We conducted Monte Carlo simulations to estimate τ_I and τ_A with the simulated signals, including Poisson noise under different conditions $q_1 = 0.2$, 0.5, and 0.8.

The performances of τ_I and τ_A estimations with bi-exponential decay signals are shown in **Figures 6A–D** for B_I, F_I, B_A, and F_A, respectively. For $\hat{\tau}_I$, $B_{I,CMM}$, and $B_{I,BCMM}$ are roughly 10 and 8%, respectively determined by T/τ_2. The larger T/τ_2 is, the smaller B_I becomes (with $F_{I,CMM}$ and $F_{I,BCMM}$ being closer to 1). Phasor has a lower accuracy when q_1 becomes larger and τ_1 smaller, and it is less precise than CMM. VPM and LSM-2 both have a smaller $B_I = 3\%$ but higher F_I ($1.5 \sim 5$) than CMM and BCMM. For $\hat{\tau}_A$, B_A is 7% except for $\tau_1 = 0.1$ ns, and F_A is around 5 for the four LDAs. **Figures 6C,D** show that if only τ_A is needed, there is no need to resort to slower model-based LDAs.

For τ_I estimations, LSM-2 and VPM are preferred when high accuracy is required. Still, they are slower and have lower photon efficiency than CMM and BCMM which means the photon count should be higher to have similar precision, for instance, a relative standard deviation of 5% can be reached with $N_{tot} = 3{,}600$ for LSM-2 and $N_{tot} = 500$ for CMM and BCMM. When the

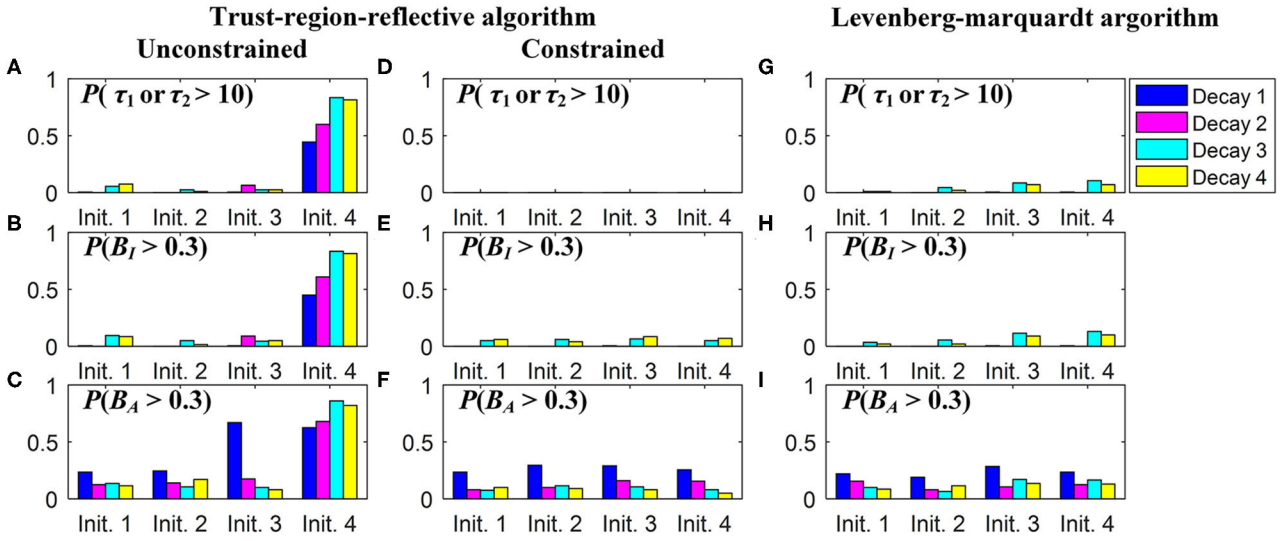

FIGURE 4 | (A,D,G) $P(\tau_1$ or $\tau_2 > 10)$, **(B,E,H)** $P(B_I > 0.3)$, and **(C,F,I)** $P(B_A > 0.3)$, for estimations of Decays 1 ∼ 4 with Init. 1 ∼ 4 using **(A–C)** the unconstrained TRR, **(D–F)** the constrained TRR, and **(G–I)** the LM algorithms.

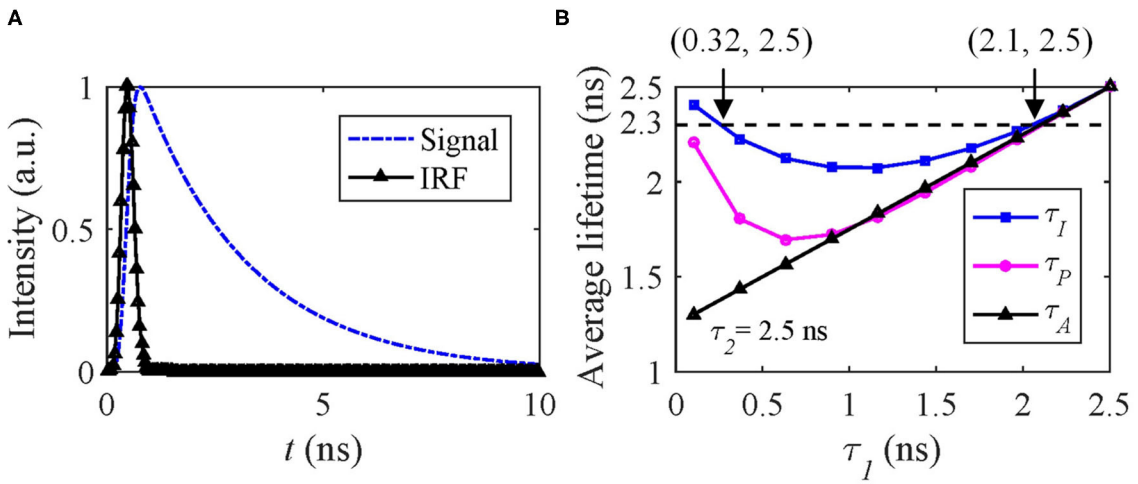

FIGURE 5 | (A) Simulated signal (blue) and IRF (black), **(B)** theoretical τ_I (blue), τ_A (black), and τ_P (magenta) average lifetimes with $q_1 = 0.5$.

accuracy of CMM or BCMM (10% @ $T/\tau_2 = 4$) is acceptable, CMM or BCMM should be employed for their high photon efficiency and estimation speeds. CMM is faster than BCMM as it can work without deconvolution. For τ_A estimations, since the performances of IEM, BCMM, VPM, LSM-2 are similar, IEM can be the right candidate for fast analysis. Notice that the τ_A method is less photon efficient than the τ_I method as F_A is higher than F_I.

3.2. Experimental Results

tSA201 cells, which are a transformed human kidney cell line, were co-transfected with $hP2Y_{12}$-eCFP and $hP2Y_1$-eYFP receptors. After 48 h of transfection, the cells on the coverslips were washed once gently with PBS followed by fixation with ice-cold methanol for 10 min at room temperature. After being washed three times with PBS, they were mounted on to glass microscope slides with Mowiol. The microscope slides were then stored in the dark at room temperature overnight to allow the coverslips to dry, then stored at 4°C for later use.

Cells were imaged on LSM510 (Carl Zeiss) equipped with a TCSPC module (SPC-830, Becker & Hickl GmbH), to determine the fluorescence lifetime and consequently the amount of FRET. The donor is CFP with the excitation wavelength range of 350 ∼ 500 nm and the emission wavelength range of 450 ∼ 600 nm. The acceptor is YFP. The sample is scanned pixel by pixel by a femtosecond Ti:Sapphire laser (Chameleon,

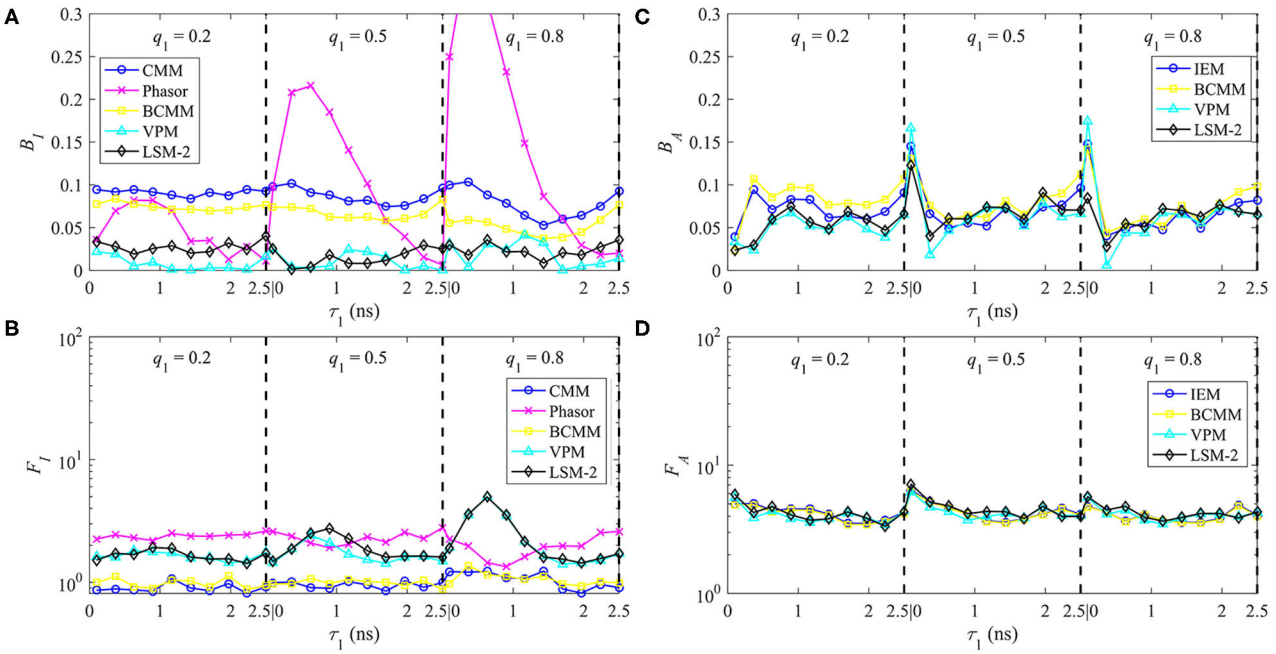

FIGURE 6 | The performances of τ_I and τ_A estimations with bi-exponential decay signals with $\tau_1 = 0.1 \sim 2.5$ ns, $\tau_2 = 2.5$ ns, $q_1 = 0.2, 0.5, 0.8$, **(A)** B_I, **(B)** F_I and **(C)** B_A, **(D)** F_A.

Coherent) with an average output laser power of 3.8 W at 800 nm, as a two-photon excitation source to reduce cellular damage. The laser power is controlled with two polarizers. The repetition rate is 80 MHz with illuminating duration <200 fs. The emitted fluorescence signal from the donor is collected through a 63× water-immersion objective lens (N.A. = 1.0), a 480 ∼ 520 nm bandpass filter, and transferred into a photomultiplier tube (PMT) detector. The FLIM scanning was performed in a dark room containing the microscope. A set of experimental data (256 × 256 pixels, $M = 256$, $T = 10$ ns) was collected over an exposure period of up to 15 min. The IRF is obtained from the measurement of dried urea [$(NH_2)_2CO$] [61].

3.2.1. Average Lifetime Images With LSM, CMM, and IEM

Figures 7A,C show the τ_I and τ_A images of the data evaluated by LSM-2 with an execution time of 410 s. The lifetime images were evaluated on Matlab R2016a, 64-bit with the Intel(R) Celeron(R) CPU (2950M @ 2 GHz) with 20923 pixels above an intensity threshold. **Figures 7B,D** show the τ_I and τ_A images evaluated by CMM and IEM with execution times of 0.25 and 92.3 s, respectively. IEM can be further accelerated to 0.6 s per image with histogram classification methods (we will report the details soon), as shown in **Figure 7E**. Although Fast-IEM causes a small bias in some pixels, the mean square error is acceptable with 0.005 ns^2. The color bar represents lifetimes and the pixel brightness represents photon counts. The **Figures 7F,G** are histograms of τ_I and τ_A, respectively. Although the histogram of τ_I with CMM deviates slightly from the one with LSM-2, CMM is 1,800-fold faster than LSM-2. If $T/\tau_i > 4$, the bias of τ_I with CMM would become smaller. The τ_A images are almost the same with IEM and LSM-2, whereas IEM and Fast-IEM are much faster than LSM-2.

Since the FRET efficiency E has a linear relationship with the average lifetimes as shown in Equation (5), **Figures 7A–E** can also be used to represent E images with the color bar in the range of 0 ∼ 100%. As we mentioned in Introduction, it is straightforward to obtain E images from τ_A images, so that **Figures 7C–E** are proper E images. If τ_I images are misused for E, the results would be different, as shown in **Figures 7A,B**, leading to a different biological story.

3.2.2. Visualization of Multi-Exponential Decays With τ_A/τ_I

τ_I and τ_A can not only access the essential parameters in FRET and dynamic quenching processes but also indicate the positions where multi-exponential decays occur. As mentioned previously, a fluorescence signal can be approximated by a bi-exponential decay, so that the ratio of τ_I and τ_A can be expressed as

$$\frac{\tau_A}{\tau_I} = \frac{[1 + q_1(R-1)]^2}{1 + q_1(R^2-1)}, \tag{11}$$

where $R = \tau_1/\tau_2$. The distribution of τ_A/τ_I (**Figure 8**) shows that when $R \simeq 1$ or $q_1 \simeq 0$ or 1, $\tau_A/\tau_I \simeq 1$. With a decrease of R or an increase of q_1, τ_A/τ_I decreases. Therefore, the ranges of q_1 and R of a pixel can be determined by τ_A/τ_I.

To present the multi-exponential decay visualization performance of τ_A/τ_I, the τ_I and τ_A images evaluated by LSM-2,

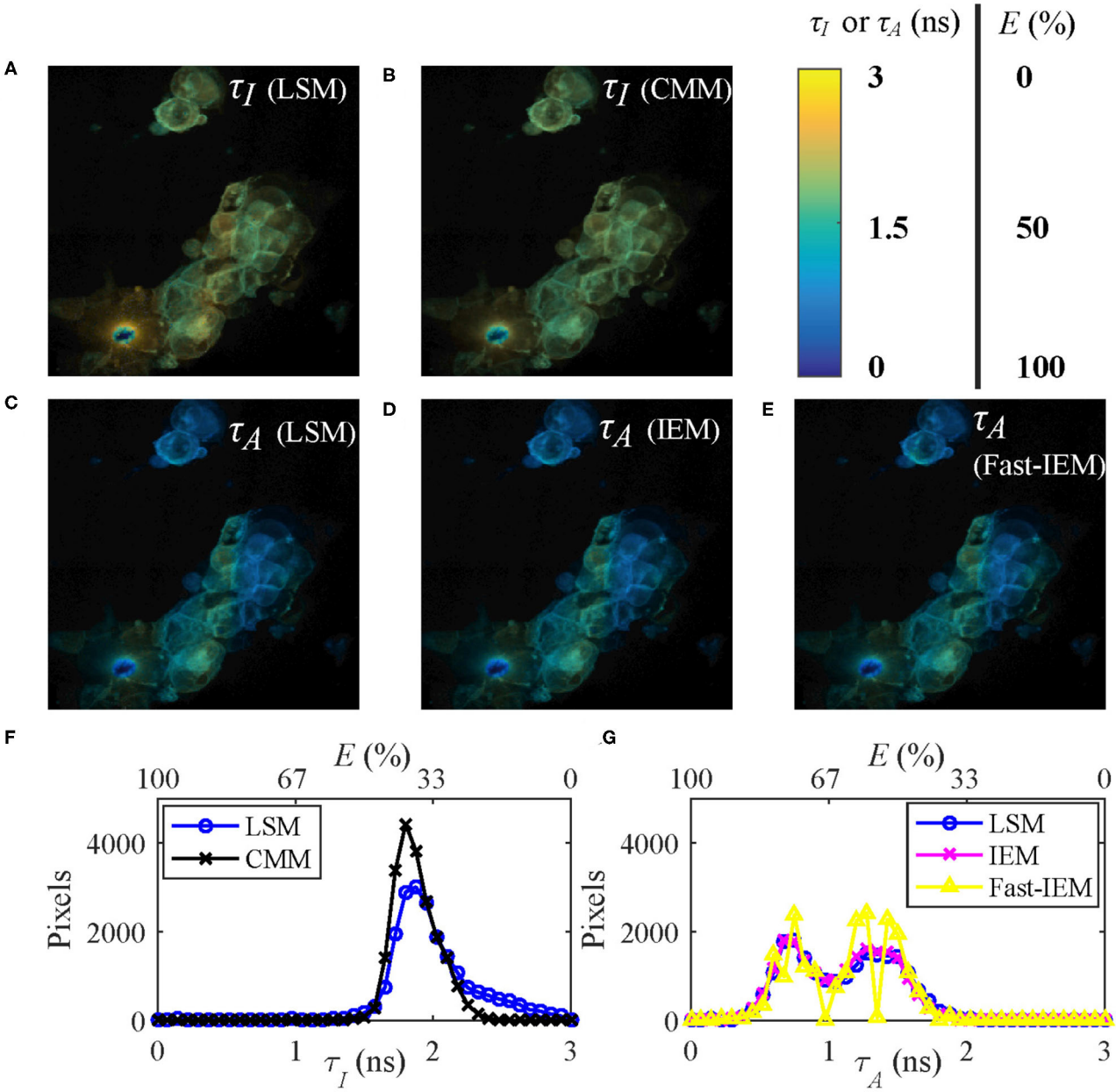

FIGURE 7 | (A,C) τ_I and τ_A images evaluated with LSM-2, **(B,D)** τ_I and τ_A images evaluated with CMM and IEM, respectively. **(E)** τ_A image with Fast-IEM. **(F)** Histograms of τ_I with LSM-2 (blue) and CMM (black). **(G)** Histograms of τ_A with LSM-2 (blue), IEM (magenta), and Fast-IEM (yellow). The color bar represents lifetimes and the pixel brightness represents photon counts. **(A–E)** Can also represent FRET efficiency (E) images evaluated with the corresponding lifetime images with the color bar representing the range of E, 0 ~ 100%. **(F,G)** Can also be used to show the histograms of E with the upper x label.

Figures 9A,B, were used to generate the τ_A/τ_I image as shown in **Figure 9C**. The histograms of τ_I and τ_A and the phasor plot are shown in **Figures 9D,E**. **Figure 9F** shows the possible range of q_1 and R of the selected pixels in **Figure 9C**. **Figures 9C,F** share the same color bar. **Figure 9D** shows that τ_A has a broader lifetime dynamic range than τ_I, which is consistent with the theoretical lines shown in **Figure 5B**. The τ_A histogram shows two clusters with different peaks, whereas the τ_I histogram only indicates a single merged group, meaning that there is no way to differentiate these two clusters. It is why using τ_I to analyze samples with a strong FRET can be misleading.

The results of the selected pixels within different τ_A/τ_I ranges are shown in **Figure 10**, $\tau_A/\tau_I = 0.2 \sim 0.5$, and **Figure 11**, $\tau_A/\tau_I = 0.5 \sim 1$. For the pixels with $\tau_A/\tau_I = 0.2 \sim 0.5$, the histograms clearly show that τ_A is much smaller than τ_I, which means the difference between τ_1 and τ_2 is significant. **Figure 10F** shows that

the ranges of q_1 and R are approximately $0.5 \sim 1$ and $0 \sim 0.2$, respectively. For the pixels with $\tau_A/\tau_I = 0.5 \sim 1$, τ_A is closer to τ_I, meaning the pixels have decays close to mono-exponential. Separating the average lifetime images with τ_A/τ_I is easier than phasor plots because τ_A/τ_I is one dimensional and phasors are two dimensional. Furthermore, τ_A/τ_I can show the q_1 and R ranges more intuitively than phasor plots. τ_A/τ_I can be a useful tool to visualize the properties of the fluorescence decays within a lifetime image.

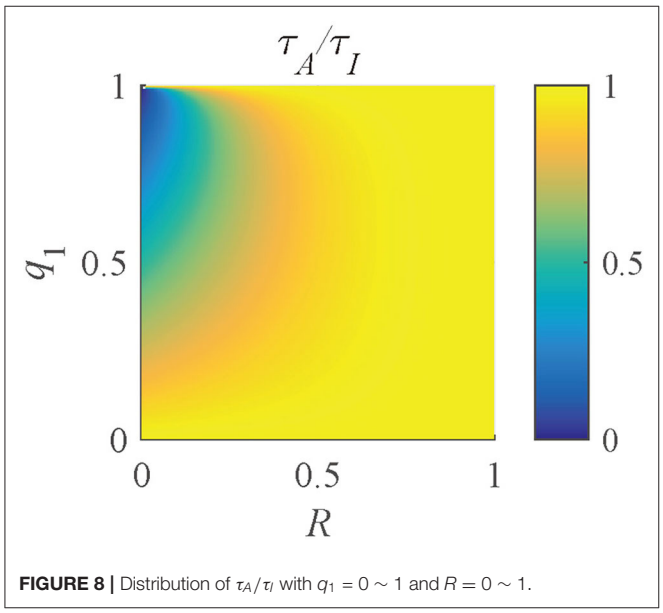

FIGURE 8 | Distribution of τ_A/τ_I with $q_1 = 0 \sim 1$ and $R = 0 \sim 1$.

4. DISCUSSION

In realistic samples, fluorescence signals always follow multi-exponential decay models. However, extracting lifetime components with a traditional fitting method is a time-consuming process. For some applications that require calculating FRET efficiency and accessing dynamic quenching behaviors, average lifetimes are satisfactory. Model-free lifetime determination algorithms can be used to evaluate average lifetimes directly, for instance, CMM and Phasor for intensity-weighted average lifetimes τ_I and IEM for amplitude-weighted average lifetimes τ_A. Discussions of the influence of the model mismatch between the real signal and the model-based LDAs on τ_I and τ_A estimations suggest that a bi-exponential model can well-approximate a signal following a multiple-exponential model. The results of the Monte-Carlo simulations suggest that VPM and LSM based on a bi-exponential model can be used for applications requiring high accuracy. The constrained TRR and LM algorithms with proper initial conditions are supported for LSM to guarantee accuracy. In contrast, CMM and IEM are recommended for applications requiring high estimation speeds.

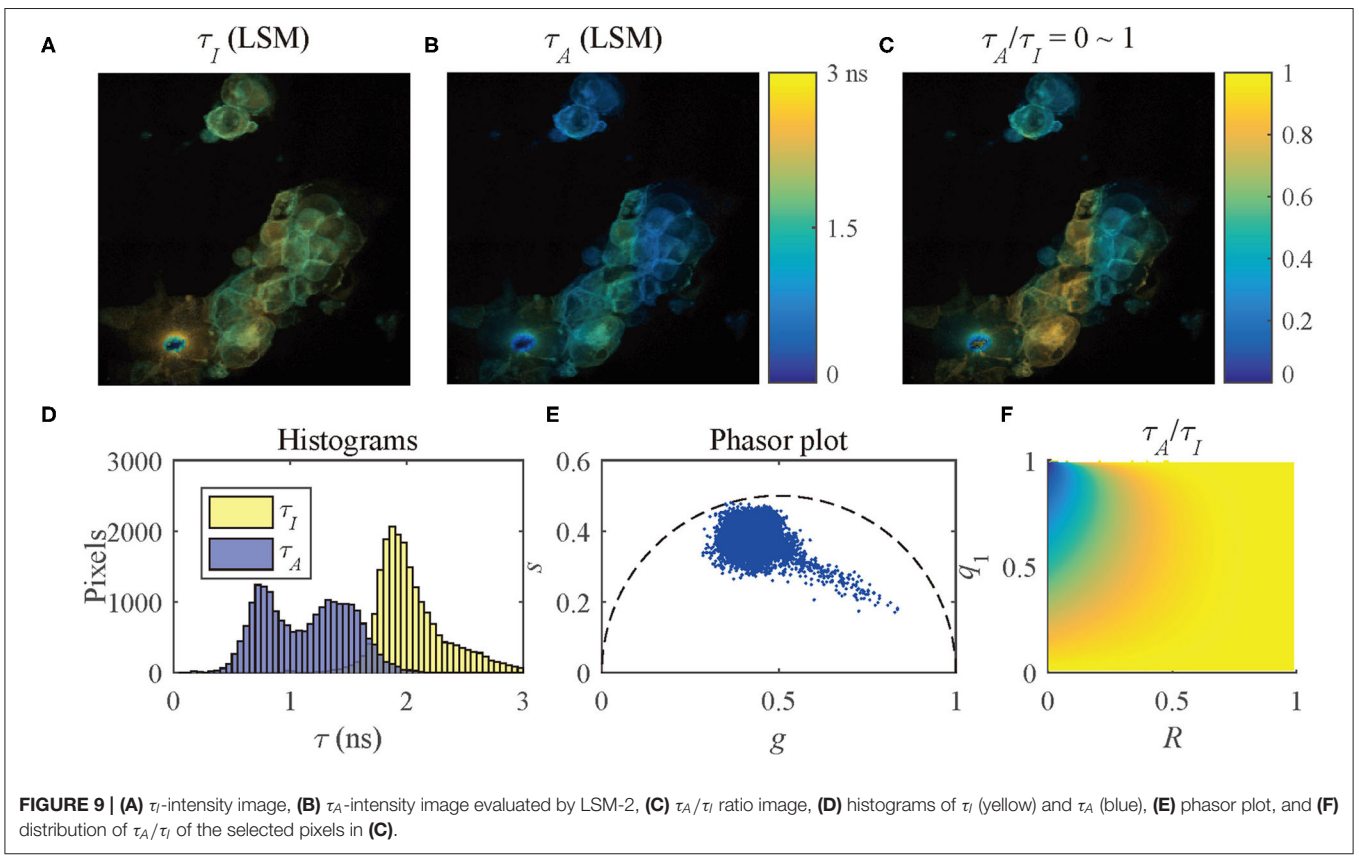

FIGURE 9 | (A) τ_I-intensity image, **(B)** τ_A-intensity image evaluated by LSM-2, **(C)** τ_A/τ_I ratio image, **(D)** histograms of τ_I (yellow) and τ_A (blue), **(E)** phasor plot, and **(F)** distribution of τ_A/τ_I of the selected pixels in **(C)**.

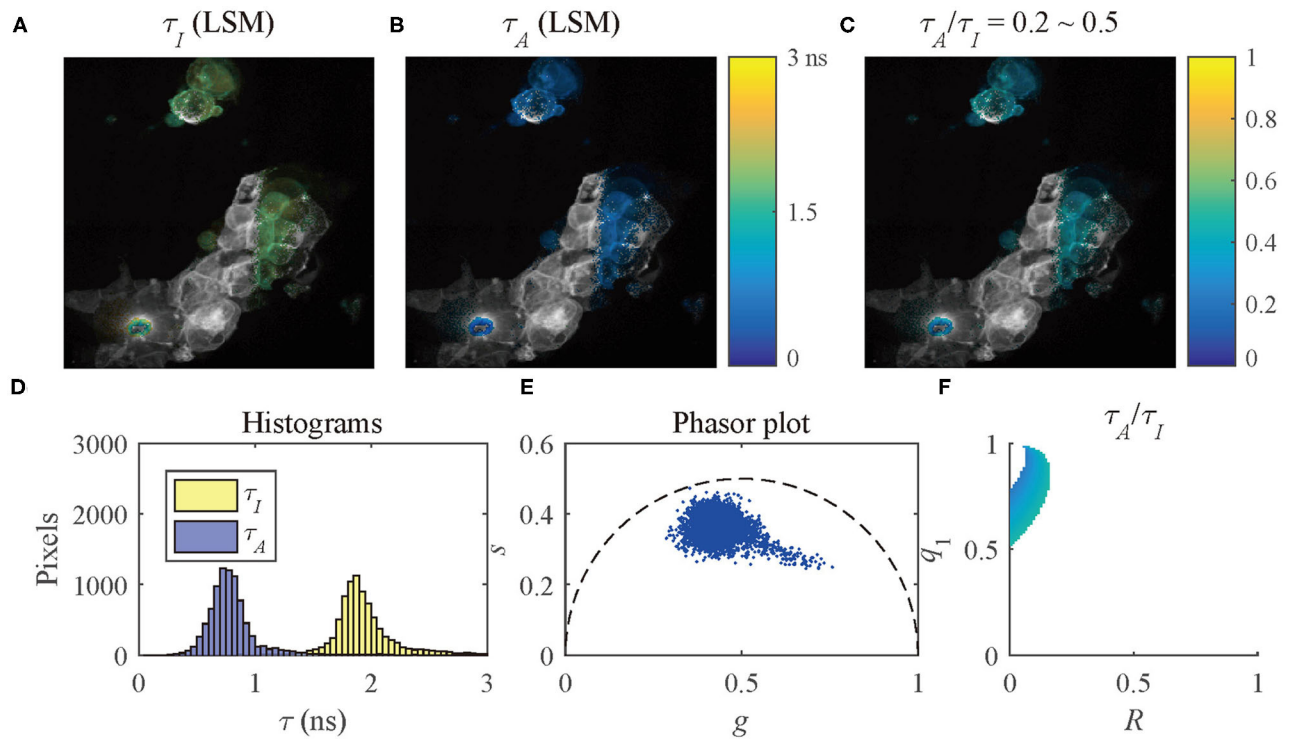

FIGURE 10 | (A) τ_I-intensity image, **(B)** τ_A-intensity image evaluated by LSM-2, **(C)** τ_A/τ_I ratio image, **(D)** histograms of τ_I (yellow) and τ_A (blue), **(E)** phasor plot, and **(F)** distribution of τ_A/τ_I of the selected pixels in **(C)** with $\tau_A/\tau_I = 0.2 \sim 0.5$.

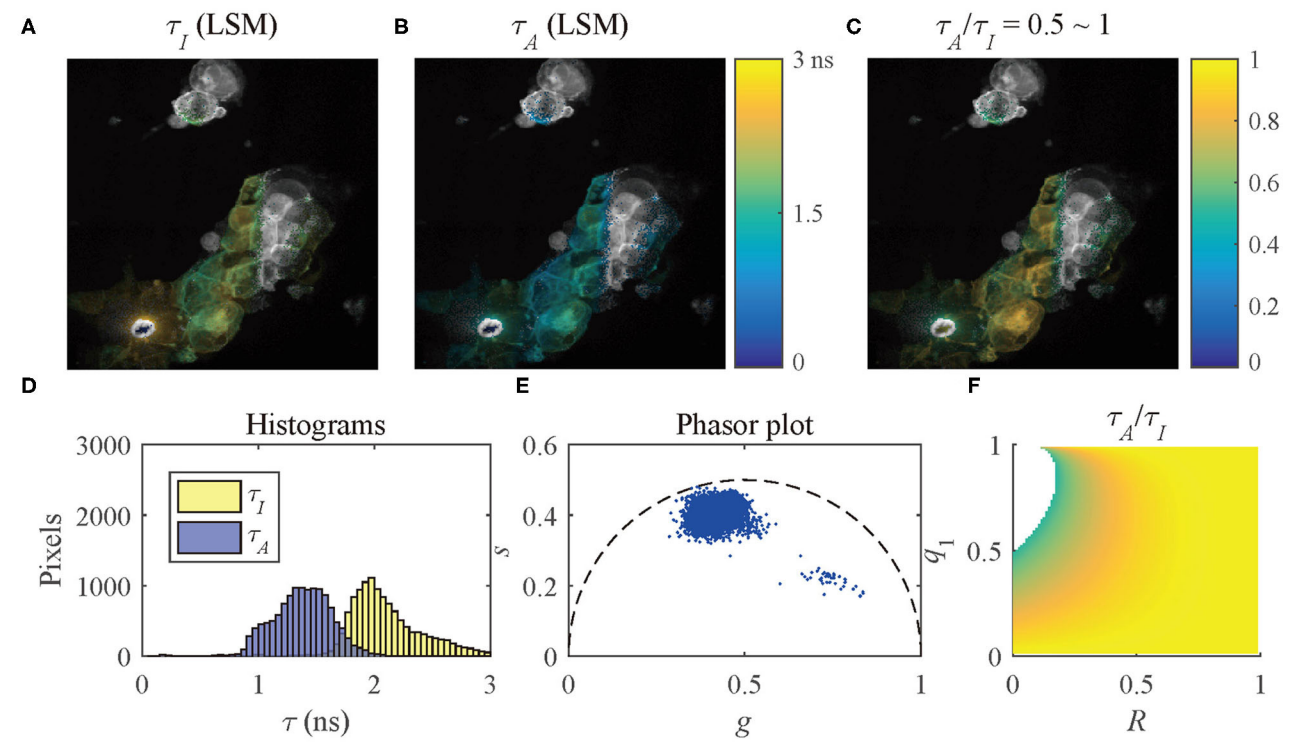

FIGURE 11 | (A) τ_I-intensity image, **(B)** τ_A-intensity image evaluated by LSM-2, **(C)** τ_A/τ_I ratio image, **(D)** histograms of τ_I (yellow) and τ_A (blue), **(E)** phasor plot, and **(F)** distribution of τ_A/τ_I of the selected pixels in **(C)** with $\tau_A/\tau_I = 0.5 \sim 1$.

We also explained why τ_I models can be misleading, and τ_I and τ_A models should be considered. Experimental data were used to compare the performances of LSM-2, CMM, and IEM for evaluating τ_I and τ_A images. Similar τ_I and τ_A images were generated, whereas CMM and IEM are much faster than LSM-2. The data were further analyzed with τ_A/τ_I, which is capable of indicating the possible ranges of the amplitude proportion of the short lifetime and the ratio of the short and long lifetimes. We believe τ_A/τ_I is a useful and intuitive tool for visualizing multi-exponential decays in a lifetime image.

DATA AVAILABILITY STATEMENT

FLIM image raw data and the instrument response are available at https://doi.org/10.15129/062e9e11-9d7f-49e5-a332-2b10d695bdcd.

AUTHOR CONTRIBUTIONS

YL conducted theoretical and experimental analysis and developed analysis tools. MS and MC conceived FRET experiments and prepared samples. SN and YC contributed to FRET-FLIM experiments. JT contributed to tool developments. DL initiated the research concept and supervised the project. All authors wrote and revised the paper.

FUNDING

We would like to acknowledge support from Medical Research Scotland, China Scholarship Council, and Engineering and Physical Sciences Research Council (EP/M506643/1).

REFERENCES

1. Lakowicz JR. *Principles of Fluorescence Spectroscopy*. New York, NY: Springer (2006). doi: 10.1007/978-0-387-46312-4
2. Berezin MY, Achilefu S. Fluorescence lifetime measurements and biological imaging. *Chem Rev*. (2010) **110**:2641–84. doi: 10.1021/cr900343z
3. Ning Y, Cheng S, Wang JX, Liu YW, Feng W, Li F, et al. Fluorescence lifetime imaging of upper gastrointestinal pH *in vivo* with a lanthanide based near-infrared τ probe. *Chem Sci*. (2019) **10**:4227–35. doi: 10.1039/C9SC00220K
4. Agronskaia AV, Tertoolen L, Gerritsen HC. Fast fluorescence lifetime imaging of calcium in living cells. *J Biomed Opt*. (2004) **9**:1230–7. doi: 10.1117/1.1806472
5. Zheng K, Jensen TP, Rusakov DA. Monitoring intracellular nanomolar calcium using fluorescence lifetime imaging. *Nat Protoc*. (2018) **13**:581–97. doi: 10.1038/nprot.2017.154
6. Hosny NA, Lee DA, Knight MM. Single photon counting fluorescence lifetime detection of pericellular oxygen concentrations. *J Biomed Opt*. (2012) **17**:016007. doi: 10.1117/1.JBO.17.1.016007
7. Peng X, Yang Z, Wang J, Fan J, He Y, Song F, et al. Fluorescence ratiometry and fluorescence lifetime imaging: using a single molecular sensor for dual mode imaging of cellular viscosity. *J Am Chem Soc*. (2011) **133**:6626–35. doi: 10.1021/ja1104014
8. Okabe K, Inada N, Gota C, Harada Y, Funatsu T, Uchiyama S. Intracellular temperature mapping with a fluorescent polymeric thermometer and fluorescence lifetime imaging microscopy. *Nat Commun*. (2012) **3**:705. doi: 10.1038/ncomms1714
9. Fruhwirth GO, Fernandes LP, Weitsman G, Patel G, Kelleher M, Lawler K, et al. How förster resonance energy transfer imaging improves the understanding of protein interaction networks in cancer biology. *ChemPhysChem*. (2011) **12**:442–61. doi: 10.1002/cphc.201000866
10. Marcu L. Fluorescence lifetime techniques in medical applications. *Ann Biomed Eng*. (2012) **40**:304–31. doi: 10.1007/s10439-011-0495-y
11. Nobis M, McGhee EJ, Morton JP, Schwarz JP, Karim SA, Quinn J, et al. Intravital FLIM-FRET imaging reveals Dasatinib-induced spatial control of Src in pancreatic cancer. *Cancer Res*. (2013) **73**:4674–86. doi: 10.1158/0008-5472.CAN-12-4545
12. Levitt JA, Poland SP, Krstajic N, Pfisterer K, Erdogan A, Barber PR, et al. Quantitative real-time imaging of intracellular FRET biosensor dynamics using rapid multi-beam confocal FLIM. *Sci Rep*. (2020) **10**:5146. doi: 10.1038/s41598-020-61478-1
13. Becker W. Fluorescence lifetime imaging-applications and instrumental principles. In: Bradshaw RA, Stahl PD, editors. *Encyclopedia of Cell Biology*. Vol. 2. Waltham, MA: Elsevier. (2016). p. 107–20. doi: 10.1016/B978-0-12-394447-4.20095-3
14. Coda S, Thompson AJ, Kennedy GT, Roche KL, Ayaru L, Bansi DS, et al. Fluorescence lifetime spectroscopy of tissue autofluorescence in normal and diseased colon measured *ex vivo* using a fiber-optic probe. *Biomed Opt Express*. (2014) **5**:515. doi: 10.1364/BOE.5.000515
15. Canals J, Franch N, Alonso O, Vilá A, Diéguez A. A point-of-care device for molecular diagnosis based on CMOS SPAD detectors with integrated microfluidics. *Sensors*. (2019) **19**:445. doi: 10.3390/s19030445
16. Alonso O, Franch N, Canals J, Arias-Alpízar K, de la Serna E, Baldrich E, et al. An internet of things-based intensity and time-resolved fluorescence reader for point-of-care testing. *Biosens Bioelectron*. (2020) **154**:112074. doi: 10.1016/j.bios.2020.112074
17. Heger Z, Kominkova M, Cernei N, Krejcova L, Kopel P, Zitka O, et al. Fluorescence resonance energy transfer between green fluorescent protein and doxorubicin enabled by DNA nanotechnology. *Electrophoresis*. (2014) **35**:3290–301. doi: 10.1002/elps.201400166
18. Karpf S, Riche CT, Di Carlo D, Goel A, Zeiger WA, Suresh A, et al. Spectro-temporal encoded multiphoton microscopy and fluorescence lifetime imaging at kilohertz frame-rates. *Nat Commun*. (2020) **11**:2062. doi: 10.1038/s41467-020-15618-w
19. Hirmiz N, Tsikouras A, Osterlund EJ, Richards M, Andrews DW, Fang Q. Highly multiplexed confocal fluorescence lifetime microscope designed for screening applications. *IEEE J Select Top Quant Electron*. (2020) **27**:1–9. doi: 10.1109/JSTQE.2020.2997834
20. Ehn A, Johansson O, Arvidsson A, Aldén M, Bood J. Single-laser shot fluorescence lifetime imaging on the nanosecond timescale using a Dual Image and Modeling Evaluation algorithm. *Opt Exp*. (2012) **20**:3043. doi: 10.1364/OE.20.003043
21. Jonsson M, Ehn A, Christensen M, Aldén M, Bood J. Simultaneous one-dimensional fluorescence lifetime measurements of OH and CO in premixed flames. *Appl Phys B*. (2014) **115**:35–43. doi: 10.1007/s00340-013-5570-7
22. Ehn A, Zhu J, Li X, Kiefer J. Advanced laser-based techniques for gas-phase diagnostics in combustion and aerospace engineering. *Appl Spectrosc*. (2017) **71**:341–66. doi: 10.1177/0003702817690161
23. Becker W. *Advanced Time-Correlated Single Photon Counting Techniques*. Heidelberg: Springer (2005). doi: 10.1007/3-540-28882-1
24. Rinnenthal JL, Börnchen C, Radbruch H, Andresen V, Mossakowski A, Siffrin V, et al. Parallelized TCSPC for dynamic intravital fluorescence lifetime imaging: quantifying neuronal dysfunction in neuroinflammation. *PLoS ONE*. (2013) **8**:e60100. doi: 10.1371/journal.pone.0060100
25. Erdogan AT, Finlayson N, Williams GS, Williams E, Henderson RK. Video rate spectral fluorescence lifetime imaging with a 512 x 16 SPAD line sensor. In: Goda K, Tsia KK, editors. *High-Speed Biomedical Imaging and Spectroscopy IV*. San Francisco, CA: SPIE (2019). p. 22. doi: 10.1117/12.2509607
26. Cole MJ, Siegel J, Webb SED, Jones R, Dowling K, Dayel MJ, et al. Time-domain whole-field fluorescence lifetime imaging with optical sectioning. *J Microsc*. (2001) **203**:246–57. doi: 10.1046/j.1365-2818.2001.00894.x
27. Grant DM, McGinty J, McGhee EJ, Bunney TD, Owen DM, Talbot CB, et al. High speed optically sectioned fluorescence lifetime imaging

permits study of live cell signaling events. *Opt Exp*. (2007) **15**:15656. doi: 10.1364/OE.15.015656
28. Gu L, Hall DJ, Qin Z, Anglin E, Joo J, Mooney DJ, et al. *In vivo* time-gated fluorescence imaging with biodegradable luminescent porous silicon nanoparticles. *Nat Commun*. (2013) **4**:2326. doi: 10.1038/ncomms3326
29. Camborde L, Jauneau A, Briére C, Deslandes L, Dumas B, Gaulin E. Detection of nucleic acid-protein interactions in plant leaves using fluorescence lifetime imaging microscopy. *Nat Protoc*. (2017) **12**:1933–50. doi: 10.1038/nprot.2017.076
30. Li DDU, Ameer-Beg S, Arlt J, Tyndall D, Walker R, Matthews DR, et al. Time-Domain fluorescence lifetime imaging techniques suitable for solid-state imaging sensor arrays. *Sensors*. (2012) **12**:5650–69. doi: 10.3390/s120505650
31. Bajzer Ž, Prendergast FG. [10] Maximum likelihood analysis of fluorescence data. *Methods Enzymol*. (1992) **210**:200–37. doi: 10.1016/0076-6879(92)10012-3
32. Verveer PJ, Hanley QS. Chapter 2: Frequency domain FLIM theory, instrumentation, and analysis. In: Gadella TWJ, editor. *Laboratory Techniques in Biochemistry and Molecular Biology*. New York, NY: Elesvier B.V. (2009). p. 59–94. doi: 10.1016/S0075-7535(08)00002-8
33. Zhao Q, Schelen B, Schouten R, van den Oever R, Leenen R, van Kuijk H, et al. Modulated electron-multiplied fluorescence lifetime imaging microscope: all-solid-state camera for fluorescence lifetime imaging. *J Biomed Opt*. (2012) **17**:126020. doi: 10.1117/1.JBO.17.12.126020
34. Howard SS, Straub A, Horton NG, Kobat D, Xu C. Frequency-multiplexed *in vivo* multiphoton phosphorescence lifetime microscopy. *Nat Photon*. (2013) **7**:33–7. doi: 10.1038/nphoton.2012.307
35. Serafino MJ, Applegate BE, Jo JA. Direct frequency domain fluorescence lifetime imaging using field programmable gate arrays for real time processing. *Rev Sci Instrum*. (2020) **91**:033708. doi: 10.1063/1.5127297
36. James F. *Statistical Methods in Experimental Physics*. Singapore: World Scientific (2008).
37. Fišerová E, Kubala M. Mean fluorescence lifetime and its error. *J Luminesc*. (2012) **132**:2059–64. doi: 10.1016/j.jlumin.2012.03.038
38. Sillen A, Engelborghs Y. The correct use of "average" fluorescence parameters. *Photochem Photobiol*. (1998) **67**:475–486. doi: 10.1111/j.1751-1097.1998.tb09082.x
39. Gadella T. *FRET and FLIM Techniques*. Amsterdam: Elsevier B.V. (2009).
40. Gehlen MH. The centenary of the Stern-Volmer equation of fluorescence quenching: from the single line plot to the SV quenching map. *J Photochem Photobiol C*. (2020) **42**:100338. doi: 10.1016/j.jphotochemrev.2019.100338
41. Li DDU, Arlt J, Tyndall D, Walker R, Richardson J, Stoppa D, et al. Video-rate fluorescence lifetime imaging camera with CMOS single-photon avalanche diode arrays and high-speed imaging algorithm. *J Biomed Opt*. (2011) **16**:096012. doi: 10.1117/1.3625288
42. Padilla-Parra S, Auduge N, Coppey-Moisan M, Tramier M. Non fitting based FRET-FLIM analysis approaches applied to quantify protein-protein interactions in live cells. *Biophys Rev*. (2011) **3**:63–70. doi: 10.1007/s12551-011-0047-6
43. Won Y, Moon S, Yang W, Kim D, Han WT, Kim DY. High-speed confocal fluorescence lifetime imaging microscopy (FLIM) with the analog mean delay (AMD) method. *Opt Exp*. (2011) **19**:3396. doi: 10.1364/OE.19.003396
44. Hwang W, Kim D, Lee S, Won YJ, Moon S, Kim DY. Analysis of biexponential decay signals in the analog mean-delay fluorescence lifetime measurement method. *Opt Commun*. (2019) **443**:136–43. doi: 10.1016/j.optcom.2019.02.059
45. Digman MA, Caiolfa VR, Zamai M, Gratton E. The phasor approach to fluorescence lifetime imaging analysis. *Biophys J*. (2008) **94**:L14–6. doi: 10.1529/biophysj.107.120154
46. Stringari C, Cinquin A, Cinquin O, Digman MA, Donovan PJ, Gratton E. Phasor approach to fluorescence lifetime microscopy distinguishes different metabolic states of germ cells in a live tissue. *Proc Natl Acad Sci USA*. (2011) **108**:13582–7. doi: 10.1073/pnas.1108161108
47. Ranjit S, Malacrida L, Jameson DM, Gratton E. Fit-free analysis of fluorescence lifetime imaging data using the phasor approach. *Nat Protoc*. (2018) **13**:1979–2004. doi: 10.1038/s41596-018-0026-5
48. Ballew RM, Demas JN. An error analysis of the rapid lifetime determination method for the evaluation of single exponential decays. *Analyt Chem*. (1989) **61**:30–3. doi: 10.1021/ac00176a007
49. Elangovan M, Day RN, Periasamy A. Nanosecond fluorescence resonance energy transfer-fluorescence lifetime imaging microscopy to localize the protein interactions in a single living cell. *J Microsc*. (2002) **205**:3–14. doi: 10.1046/j.0022-2720.2001.00984.x
50. Moore C, Chan SP, Demas JN, DeGraff BA. Comparison of methods for rapid evaluation of lifetimes of exponential decays. *Appl Spectrosc*. (2004) **58**:603–7. doi: 10.1366/000370204774103444
51. Elson DS, Munro I, Requejo-Isidro J, McGinty J, Dunsby C, Galletly N, et al. Real-time time-domain fluorescence lifetime imaging including single-shot acquisition with a segmented optical image intensifier. *New J Phys*. (2004) **6**:180. doi: 10.1088/1367-2630/6/1/180
52. Li DDU, Bonnist E, Renshaw D, Henderson R. On-chip, time-correlated, fluorescence lifetime extraction algorithms and error analysis. *J Opt Soc Am A*. (2008) **25**:1190. doi: 10.1364/JOSAA.25.001190
53. Li DDU, Arlt J, Richardson J, Walker R, Buts A, Stoppa D, et al. Real-time fluorescence lifetime imaging system with a 32 × 32 0.13μm CMOS low dark-count single-photon avalanche diode array. *Opt Exp*. (2010) **18**:10257. doi: 10.1364/OE.18.010257
54. Liu J, Sun Y, Qi J, Marcu L. A novel method for fast and robust estimation of fluorescence decay dynamics using constrained least-squares deconvolution with Laguerre expansion. *Phys Med Biol*. (2012) **57**:843–65. doi: 10.1088/0031-9155/57/4/843
55. Zhang Y, Chen Y, Li DDU. Optimizing Laguerre expansion based deconvolution methods for analysing bi-exponential fluorescence lifetime images. *Opt Exp*. (2016) **24**:13894. doi: 10.1364/OE.24.013894
56. Li DDU, Yu H, Chen Y. Fast bi-exponential fluorescence lifetime imaging analysis methods. *Opt Lett*. (2015) **40**:336–9. doi: 10.1364/OL.40.000336
57. Zhang Y, Cuyt A, Lee W, Lo Bianco G, Wu G, Chen Y, et al. Towards unsupervised fluorescence lifetime imaging using low dimensional variable projection. *Opt Exp*. (2016) **24**:26777. doi: 10.1364/OE.24.026777
58. Wu G, Nowotny T, Zhang Y, Yu HQ, Li DDU. Artificial neural network approaches for fluorescence lifetime imaging techniques. *Opt Lett*. (2016) **41**:2561. doi: 10.1364/OL.41.002561
59. Smith JT, Yao R, Sinsuebphon N, Rudkouskaya A, Un N, Mazurkiewicz J, et al. Fast fit-free analysis of fluorescence lifetime imaging via deep learning. *Proc Natl Acad Sci USA*. (2019) **116**:24019–30. doi: 10.1073/pnas.1912707116
60. Draaijer A, Sanders R, Gerritsen HC. Fluorescence lifetime imaging, a new tool in confocal microscopy. In: Pawley JB, editor. *Handbook of Biological Confocal Microscopy*. Boston, MA: Springer US (1995). p. 491–505. doi: 10.1007/978-1-4757-5348-6_31
61. Sapermsap N, Li DDU, Al-Hemedawi R, Li Y, Yu J, Birch DJ, et al. A rapid analysis platform for investigating the cellular locations of bacteria using two-photon fluorescence lifetime imaging microscopy. *Methods Appl Fluoresc*. (2020) **8**:034001. doi: 10.1088/2050-6120/ab854e

Conflict of Interest: The authors declare that the research was conducted in the absence of any commercial or financial relationships that could be construed as a potential conflict of interest.

APPENDIX

Derivation of τ_{CMM}. Take the integration of $t \cdot h(t)$ and $h(t)$,

$$\begin{aligned}\int_0^\infty t \cdot h(t)dt &= \int_0^\infty t \int_0^\infty irf(t-t') \cdot f(t')dt'dt \\ &= \int_0^\infty \int_0^\infty (t-t') \cdot irf(t-t') \cdot f(t')dt'dt \\ &+ \int_0^\infty \int_0^\infty irf(t-t') \cdot t' \cdot f(t')dt'dt \\ &= \int_0^\infty [t \cdot irf(t)] * f(t)dt + \int_0^\infty irf(t) * [t \cdot f(t)]dt \\ &= \int_0^\infty t \cdot irf(t)dt \int_0^\infty f(t)dt \\ &+ \int_0^\infty irf(t)dt \int_0^\infty t \cdot f(t)dt, \end{aligned} \tag{A1}$$

$$\int_0^\infty h(t)dt = \int_0^\infty irf(t)dt \int_0^\infty f(t)dt. \tag{A2}$$

Dividing Equation (A1) by Equation (A2) gives

$$\frac{\int_0^\infty t \cdot h(t)dt}{\int_0^\infty h(t)dt} = \frac{\int_0^\infty t \cdot irf(t)dt}{\int_0^\infty irf(t)dt} + \frac{\int_0^\infty t \cdot f(t)dt}{\int_0^\infty f(t)dt}. \tag{A3}$$

Then,

$$\begin{aligned}\tau_{CMM} &= \frac{\int_0^\infty t \cdot f(t)dt}{\int_0^\infty f(t)dt} = \frac{\sum_{i=1}^p q_i\tau_i^2}{\sum_{i=1}^p q_i\tau_i} \\ &= \frac{\int_0^\infty t \cdot h(t)dt}{\int_0^\infty h(t)dt} - \frac{\int_0^\infty t \cdot irf(t)dt}{\int_0^\infty irf(t)dt} \\ &\simeq \frac{\sum_{m=0}^{M-1} t_m \cdot h_m}{\sum_{m=0}^{M-1} h_m} - \frac{\sum_{m=0}^{M-1} t_m \cdot irf_m}{\sum_{m=0}^{M-1} irf_m}. \end{aligned} \tag{A4}$$

frontiers in Physics

CORRECTION
published: 15 February 2021
doi: 10.3389/fphy.2020.637953

Corrigendum: Investigations on Average Fluorescence Lifetimes for Visualizing Multi-Exponential Decays

Yahui Li[1,2,3], *Sapermsap Natakorn*[4], *Yu Chen*[4], *Mohammed Safar*[1], *Margaret Cunningham*[1], *Jinshou Tian*[2,3] *and David Day-Uei Li*[1]*

[1]*Strathclyde Institute of Pharmacy and Biomedical Sciences, University of Strathclyde, Glasgow, United Kingdom,* [2]*Key Laboratory of Ultra-fast Photoelectric Diagnostics Technology, Xi'an Institute of Optics and Precision Mechanics, Xi'an, China,* [3]*University of Chinese Academy of Sciences, Beijing, China,* [4]*Department of Physics, Scottish Universities Physics Alliance, University of Strathclyde, Glasgow, United Kingdom*

Keywords: fluorescence lifetime imaging, lifetime determination algorithm, average lifetimes, multi-exponential decays, lifetime image visualization, FRET—fluorescence resonance energy transfer

OPEN ACCESS

Approved by:
Frontiers Editorial Office, Frontiers Media SA, Switzerland

***Correspondence:**
David Day-Uei Li
David.Li@strah.ac.uk

Specialty section:
This article was submitted to Optics and Photonics, a section of the journal Frontiers in Physics

Received: *04 December 2020*
Accepted: *07 December 2020*
Published: *15 February 2021*

Citation:
Li Y, Natakorn S, Chen Y, Safar M, Cunningham M, Tian J and Li DD-U (2021) Corrigendum: Investigations on Average Fluorescence Lifetimes for Visualizing Multi-Exponential Decays. Front. Phys. 8:637953. doi: 10.3389/fphy.2020.637953

A Corrigendum on

Investigations on Average Fluorescence Lifetimes for Visualizing Multi-Exponential Decays *by Li, Y., Natakorn, S., Chen, Y., Safar, M., Cunningham, M., Tian, J., and Li, D. D.-U. (2020). Front. Phys. 8:576862. doi: 10.3389/fphy.2020.576862*

In the original article, there was a missing data link in the **Data Availability Statement**. A correction has been made in the statement below.

DATA AVAILABILITY STATEMENT

FLIM image raw data and the instrument response are available at https://doi.org/10.15129/062e9e11-9d7f-49e5-a332-2b10d695bdcd.

The authors apologize for this error and state that it does not change the scientific conclusions of the article in any way. The original article has been updated.

frontiers in Physics

BRIEF RESEARCH REPORT
published: 14 May 2021
doi: 10.3389/fphy.2021.647985

Toward the Development of an On-Chip Acoustic Focusing Fluorescence Lifetime Flow Cytometer

Jesus Sambrano Jr.[1], *Felicia Rodriguez*[1], *John Martin*[2] *and Jessica P. Houston*[1]*

[1] Department of Chemical and Materials Engineering, New Mexico State University, Las Cruces, NM, United States, [2] Tiber Plasma Diagnostics, Las Cruces, NM, United States

Conventional flow cytometry is a valuable quantitative tool. Flow cytometers reveal physical and biochemical information from cells at a high throughput, which is quite valuable for many biomedical, biological, and diagnostic research fields. Flow cytometers range in complexity and typically provide multiparametric data for the user at rates of up to 50,000 cells measured per second. Cytometry systems are configured such that fluorescence or scattered light signals are collected per-cell, and the integrated optical signal at a given wavelength range indicates a particular cellular feature such as phenotype or morphology. When the timing of the optical signal is measured, the cytometry system becomes "time-resolved." Time-resolved flow cytometry (TRFC) instruments can detect fluorescence decay kinetics, and such measurements are consequential for Förster Resonance Energy Transfer (FRET) studies, multiplexing, and metabolic mapping, to name a few. TRFC systems capture fluorescence lifetimes at rates of thousands of cells per-second, however the approach is challenged at this throughput by terminal cellular velocities. High flow rates limit the total number of photons integrated per-cell, reducing the reliability of the average lifetime as a cytometric parameter. In this contribution, we examine an innovative approach to address this signal-to-noise issue. The technology merges time-resolved hardware with microfluidics and acoustics. We present an "acoustofluidic" time-resolved flow cytometer so that cellular velocities can be adjusted on the fly with a standing acoustic wave (SAW). Our work shows that acoustic control can be combined with time-resolved features to appropriately balance the throughput with the optical signals necessary for lifetime data.

Keywords: flow cytometry, FRET, time-resolved flow cytometry, fluorescence lifetime, acoustofluidic

OPEN ACCESS

Edited by:
Klaus Suhling,
King's College London,
United Kingdom

Reviewed by:
Yuhwa Lo,
University of California, San Diego,
United States
Jianming Wen,
Kennesaw State University,
United States
Jim Piper,
Macquarie University, Australia

***Correspondence:**
Jessica P. Houston
jph@nmsu.edu

Specialty section:
This article was submitted to Optics and Photonics, a section of the journal Frontiers in Physics

Received: *30 December 2020*
Accepted: *21 April 2021*
Published: *14 May 2021*

Citation:
Sambrano J Jr, Rodriguez F, Martin J and Houston JP (2021) Toward the Development of an On-Chip Acoustic Focusing Fluorescence Lifetime Flow Cytometer. Front. Phys. 9:647985. doi: 10.3389/fphy.2021.647985

INTRODUCTION

Flow cytometry is a robust statistical apparatus common to many research fields as well as the medical industry. Cytometry methods involve analyzing individual cells with the aid of laser excitation light, which excites fluorophores conjugated to the cell of interest. Specialty photo- detectors measure the intensity of the emitted fluorescence signal or excitation light that is scattered by the cell. This high-throughput technique is also used to separate subpopulations of a heterogeneous population of cells based on the fluorescence signal measured. The excitation light

that is scattered by the cell is directionally measured (forward scatter and side scatter) and also provides information about the cell—generally morphological changes such as size, granularity, etc. [1].

Recent advances in lasers and data acquisition systems have led to the ability to measure, cytometrically, an additional fluorescence parameter, this being the fluorescence lifetime [2]. Uniquely designed cytometry approaches that extract fluorescence lifetimes are known as time-resolved flow cytometry (TRFC) systems. The fluorescence lifetime parameter is independent of the fluorescence intensity and can provide additional multiplexing capabilities [3–5]. For example, TRFC was recently employed in an application in which the endogenous fluorophore, NAD(P)H, was measured to identify metabolic changes during apoptosis since it is well-known that this metabolite undergoes fluorescence lifetime shifts during enzymatic reactions important for energy generation [6]. To obtain the fluorescence lifetime of a fluorescent compound, a modulated laser excites the fluorophore on or within the cell. This modulated excitation source leads to a fluorescence signal modulated at the same frequency and a similarly modulated scattered light signal [2, 7, 8]. Due to the fluorescence decay, a phase difference between the scattered laser light and the emitted fluorescence results. The fluorescence lifetime is thus calculated from the difference in these phases.

One other significant area of development in flow cytometry is throughput and synergism with imaging and on-chip detection. Many advancements have been made with cytometers that employ micron-sized channels to control and manipulate cells. Microfluidic devices have an abundance of advantages over disadvantages. When small volumes and quantities are used, then sample analysis and sorting becomes facile. Additionally, microfluidic systems are favored because miniaturization leads to reduce operational costs. Biomedicine has been most significantly impacted by microfluidic approaches [9, 10] that also contain microelectromechanical systems (MEMS), or more commonly, "lab on a chip" [11] devices. MEMS provide a way to perform analytical measurements based on passive and proactive interrogation. These lab-on-a-chip systems thus enable cells to be aligned, stretched, deflected, labeled, treated, excited, lysed, sequenced, and more. In other words, the control and manipulation of cells is quite impressive with microfluidics, and the clever chip-based systems found today are not only versatile but also portable, low-cost, and massively parallelized. In general, the MEMS systems that incorporate optical signals for cell interrogation involve careful control of the cell as it is moved through small channels and across a focused laser beam. For single-cell analyses, cells must be aligned and ideally move in single file. The alignment can be accomplished by dielectrophoretic focusing [12], inertial focusing [13], magnetophoresis [14], or acoustophoresis [15], to name a few of the most widely used approaches. The end goal for such systems is to achieve high spatiotemporal resolution resulting in a crisp image of a single cell, or an ample optical signal that can be used to make interpretations about the cell (i.e., phenotype, genotype, etc.).

Herein we combine both emerging areas of flow cytometry: time-resolved measurements and microfluidics. These technologies are merged and discussed in this contribution for the purpose of achieving higher fluorescence lifetime resolution and to enable the detection of low-level optical signals from cells. Our objective is to adapt TRFC onto a microfluidic platform for control with acoustics to achieve the necessary fluorescence sensitivity and high temporal resolution (∼100 s of picoseconds) during cell counting and eventually sorting. Interestingly, there have been very few TRFC systems designed onto microfluidic chips that measure real-time fluorescence lifetimes. The fluorescence lifetime is challenging to read-out during cell measurements because the timing of decay must be calculated with on-chip digital signal processing using frequency-domain analyses. Although in past work we implemented the fluorescence lifetime as a sorting parameter on a traditional cytometer, we found it challenging to sample the optical signals at an adequate level. A higher signal-to-noise is necessary for higher timing resolution. Unfortunately the tradeoff remains; cells can either be moved through a laser at a high throughput (∼1–10 μs), or slowed down so that the amount of time that photons can be collected is increased (100 μs−100 ms) for a robust lifetime read-out.

In this contribution we adopt microfluidics in order to evaluate how a slower flow rate might improve our ability to perform TRFC. We thus apply standing acoustic waves (SAW) for cell movement and alignment. This acoustophoretic approach works synergistically with quiescent and laminar flow regimes. Particles/cells are transported by a laminar flow, and their motion is controlled dependent on a set of cellular physical properties such as particle compressibility, particle size, and density. With SAW, piezoceramic actuators composed of perovskite crystals are mechanically excited to propagate an ultrasonic sound wave that permeates through a matching layer, meeting, and reflecting off the reflecting layer to produce a SAW with respect to the microchannel geometry, composite material of the microchannel, and the speed of sound in the fluid. With more control over photon collection and cell movement, we plan to make it possible to calculate more than one fluorescence lifetime per cell (i.e., multiple decay kinetic acquisition), and address outstanding questions in the fluorescence lifetime field. The following report discusses work toward this goal.

METHODS AND MATERIALS

System Overview

The time-resolved acoustofluidic flow cytometer (TRAFFC) described herein (see **Figure 1**) was designed to be modular. Each component was procured, assembled, and optimized to fit onto a standard 2 × 2 optical breadboard. The components include the chip, optics, detectors, electronics, and data system described herein.

BennuBio, Inc (Albuquerque, NM) kindly gifted us the acoustic chip, which consisted of an aluminum core (125 × 12 mm) with a 500 μm wide microchannel. The aluminum core is bonded between two borosilicate slides (125 × 12 mm) which create the matching and reflecting layer for acoustic focusing.

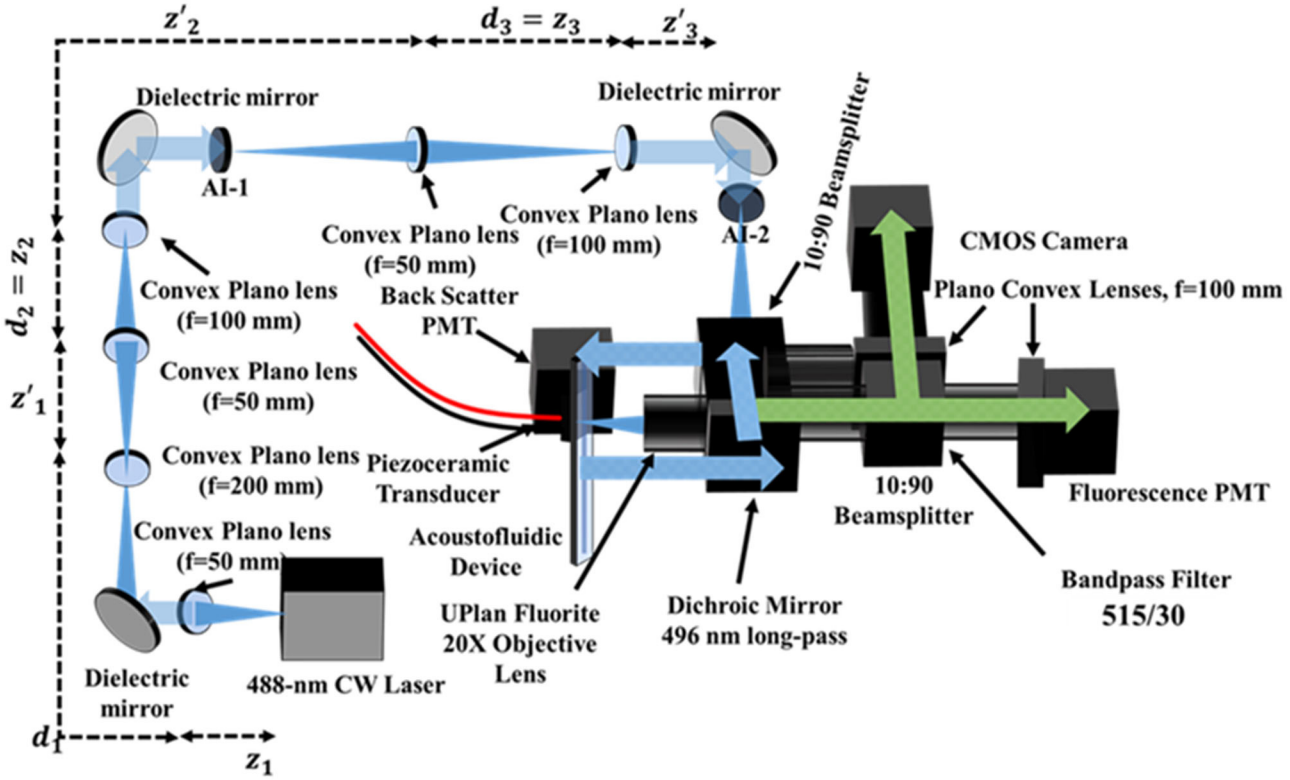

FIGURE 1 | Schematic representation of the TRAFFC system. The system is an epifluorescence-like arrangement where emission light is reflected and collected at 0° (fluorescence and imaging CMOS camera). Light scatter is collected through low angle scattering through the dichroic beam splitter and plate beam splitter. To achieve a laser spot size commonly found in commercial cytometers, the laser beam is expanded three times before being focused down onto the sample plane on the acoustofluidic device. Optical aberrations are cleaned with adjustable irises (AI).

The inlet and outlets contain luers (IDEX Corp., Northbrook, IL) epoxied onto respective outlets. On the reverse side of the device is a piezoceramic (PZT, lead zirconate titanate) transducer (30 × 30 mm). Two leads extend outward from the PZT and are connected to a power amplifier (Electronics and Innovation, LTD, Rochester, NY) and arbitrary function generator (Tektronix, Beaverton, OR), respectively. Sample is introduced to the acoustofluidic device using a Chemyx Fusion 200 syringe pump (Stafford, TX). When initially optimizing the system and establishing a fluorescence baseline, a flow rate of 50–100 μL/min was used. As fluorescence detection was established, flow rates were varied between 10 and 500 μL/min. This work used flow rates of 250 μL/min.

The TRAFFC optical system was developed with a single laser excitation source, a 2-channel detector arrangement (fluorescence and light scatter), and a CCD camera for imaging. The excitation source was a blue diode laser (OBIS LX 488 nm, Coherent Inc., Santa Clara, CA) with a maximum optical power output of 150 mW. To assure minimal reflection from the device channel walls, the laser spot was minimized to a Gaussian-like profile with a diameter of ∼180 μm through a series of three-lens expansion systems. The first expansion set of lenses had focal lengths of 50 and 200 mm, respectively. The second and third set of lenses consisted of lenses with focal lengths of 50 and 100 mm as diagrammed in **Figure 1**. The laser reflected off a dichroic beam splitter (495LP, Semrock, Rochester, NY) and was directed to the acoustofluidic device. For steady-state fluorescence measurements, the laser operated at 50 mW in continuous wave mode. For acquisition of fluorescence decay kinetics (fluorescence lifetime), the laser operated in digital modulation mode and was modulated at a sinusoidal radio frequency of 195 kHz by an arbitrary function generator. Fluorescence was collected by an objective (LMPLFLN 20X, NA=0.4, Olympus, Waltham, MA), passed through a bandpass filter (515/30 nm, Semrock, Rochester, NY), and was split into two image components (10:90 plate beam splitter, Thorlabs, Newton, NJ). The emission signal was captured by a photomultiplier tube (PMT, Hamamatsu model type R928) and a CMOS camera (ORCA-Flash4.0 V3 CMOS Hamamatsu Photonics, San Jose, CA). Light was focused onto the camera sensor and PMT window through respective Plano convex lenses (f = 100 mm, Thorlabs, Newton, NJ). A PMT for optical backscatter was positioned after a second 10:90 plate beam splitter. The fluorescence PMT voltage was set at an offset of −480V, and the exposure time for the CMOS camera was 32 ms (∼40 frames per second). The camera was operated using HCImage Live software suite (Hamamatsu Corporation, Sewickley, PA) with a Dell OptiPlex computer (32 GB of RAM,

Round Rock, TX. Data were collected using a custom data acquisition system with a sampling rate of up to 50 megasamples per second (50 MSPS); data transfer was through a FireWire 400 cable to a FireWire PCIe adapter.

Testing Samples

Fluorescent microspheres as well as fluorescently labeled cells were used to evaluate the performance of the preliminary TRAFFC system. Standard flow cytometry microspheres with known fluorescence lifetimes included FlowCheck® fluorospheres (Beckman Coulter, Indianapolis, IN) and Yellow-Green (YG) fluorospheres (Polysciences Inc., Warrington, PA). All microspheres and cells were prepared at a concentration of $\sim 1.0 \times 10^6$ particles/mL. The cells used for testing included a MCF-7 breast cancer line. Cells were cultured in 5 mL DMEM containing 10% by volume fetal bovine serum, 1 mM of sodium pyruvate, and 2 mM of L-glutamine to make a final concentration of 1× for the latter two components. The cells, cultured in a 37°C, 5% (v/v) CO_2 environment, were harvested when concentrations reached ∼1.5 × 10 cells/mL. Additional cell preparation for TRAFFC measurements included fixation and labeling with the fluorescence dye, propidium iodide (PI). The protocol included removing cells from culture and centrifuging at 350 × G for 5 min. Cells were then washed twice with DPBS, gently vortexed and fixed with 3 mL of 70% ethanol. Fixation included storing cells for ∼1 h in a −20°C freezer. Cells were then centrifuged at 1,150 RPM for 5 min and re-suspended in 7 mL of 50 µg/mL RNase. Fluorescence labeling included adding 35 uL of propidium iodide at 37°C for 30 min. The final working concentration for the MCF-7 cells was verified by a hemocytometer and the Countess II Automated Cell Counter (Thermo Fisher Scientific, Waltham, MA,). Fluorescent labeling

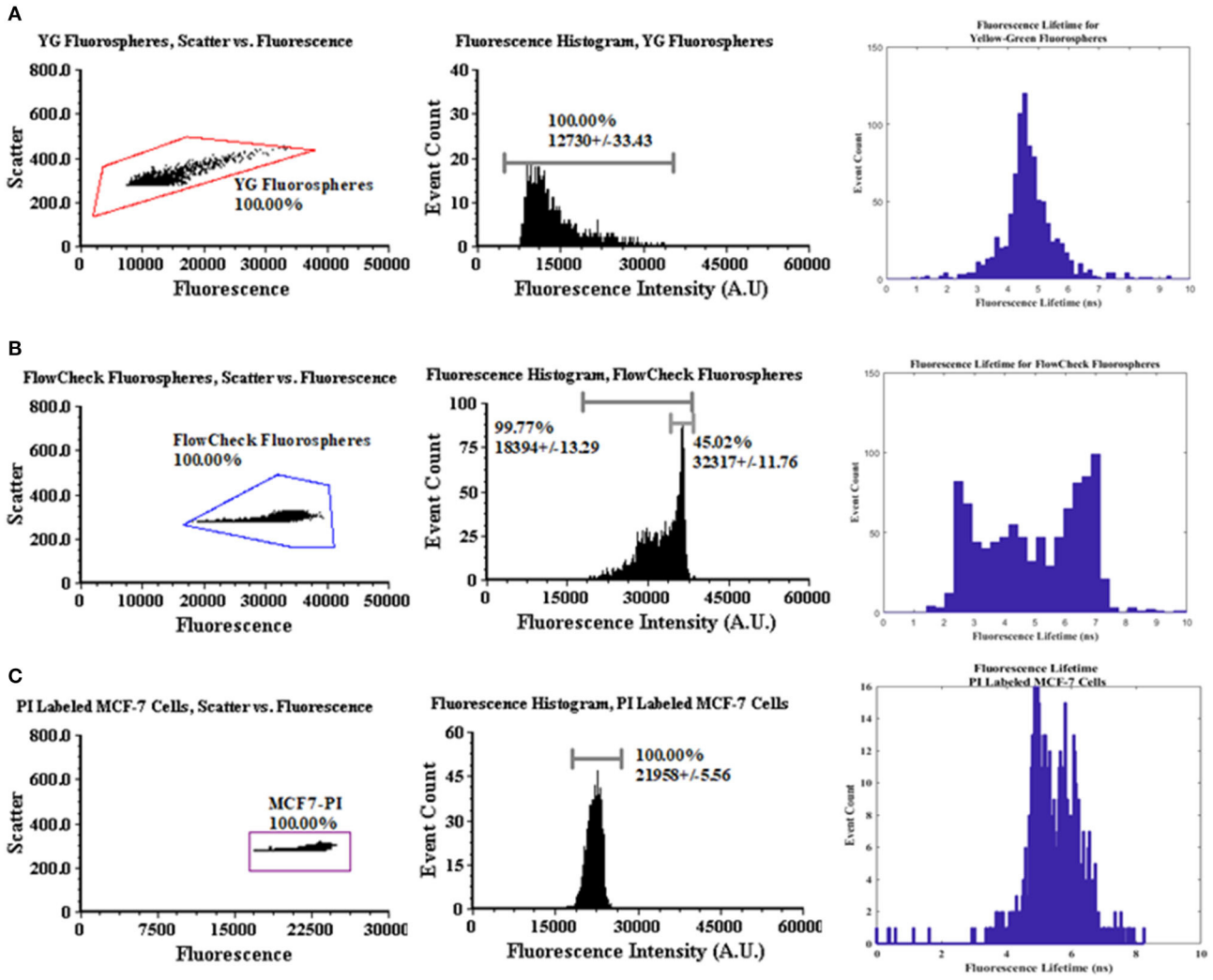

FIGURE 2 | Fluorescence and reference waveforms plotted, and resultant frequency spectrums analyzed offline in MATLAB for **(A)** YG fluorospheres, **(B)** FlowCheck® fluorospheres, and **(C)** PI-labeled MCF-7 cells.

for MCF-7 cells were also checked prior to experiments with an ECHO Revolve Microscope (ECHO, San Diego, CA.) with a 10X objective in both upright mode and under fluorescence inverted mode (data not included).

RESULTS

General Fluorescence Measurements

The preliminary tests performed on the TRAFFC system included fluorescence measurements detected from both fluorescence microspheres and the PI-labeled cells. Future work will optimize the of capture backscattered light, which is important for cell characterization and robust fluorescence lifetime calculations and is discussed later. The fluorescence signals from the PMT were amplified with a transimpedance amplifier (TIA, DC-100, ARI Corp.) with a low noise 60 dB gain and overall low voltage signal contribution of 1mV, peak-to-peak. The fluorescence signals after amplification were observed using an oscilloscope as well as the custom DAQ system described previously. **Figure 2** is a graph showing examples of the fluorescence data collected. The signals have a "modulated pulse" shape, similar to standard digital cytometry measurements we have performed previously [8]. The signals expectedly follow an increase in fluorescence and decrease as an acoustically focused microsphere and/or cell enters the laser excitation site and rapidly exits. These waveforms after collection can be compiled and stored as comma separated value files (.csv) for off-line analysis. Accordingly, MATLAB (Natick, MA) was used to read and plot the waveforms for further investigation. As can be seen by **Figure 2**, the pulse width is wide, which indicates a mean flow velocity ($0.16670.1 \cdot m\ s^{-1}$) and mean differential pressure of ∼11 PSI that fosters a longer dwell time in the beam. An item to note is how the outlet of sample to waste may affect these dwell times. The outlet waste tube is submerged in fluid at all times to negate backpressure "shockwaves" up through the outlet tube that would be incurred by break-off droplets. However, by keeping the outlet tube submerged, it is possible that changes in differential pressure occur and may affect sample velocity and signal duration (pulse widths).

In addition, the TRAFFC system uses standing acoustic wave (SAW) focusing, an alternative to sheath-driven hydrodynamic focusing. A more in-depth analysis of acoustic focusing is discussed later. Briefly, SAWs generated a pressure node across the center cross-section of the microchannel. A modest flow rate was used to assure particles/cells had sufficient time to be captured by the SAW. Finally, to enable optimized acoustic focusing and, maximum dwell time within the detection aperture, particle focusing was initiated 3 mm downstream from the detection aperture. **Figure 2** includes the modulated reference signal plotted with the fluorescence pulse to demonstrate DAQ capture of both for fluorescence lifetime measurements. Finally, **Figure 2** includes the frequency spectrum results of the Fourier analysis, which is one step toward calculating the fluorescence lifetime (further described below). Transit times are also plotted against fluorescence intensities.

Intensity and Lifetime Measurements

Figure 3 provides a statistical summary of the fluorescence intensity and lifetime measured of the fluorescence microspheres and fluorescently labeled cells. Microsphere data collection was repeated 6 times after calibration. To calibrate the lifetime measurements, we used YG fluorospheres as a calibration reference, which have a known lifetime value ∼3 ns. Thus, we calculated the anticipated phase shift value ($\Delta\phi_{expected}$) to adjust the signals prior to measuring other microspheres and cells. For the calibration analysis, ∼3,000 events were collected. Data were analyzed offline in MATLAB (as seen in **Figure 2**). A Discrete Fourier Transform (DFT) was applied to the fluorescence and reference waveforms. The frequency spectrum revealed the DC and modulation frequencies for each respective waveform. Phase angles were extracted for each waveform and the phase shift value was calculated (ϕ_{FL}- $\phi_{Reference} = \Delta\ \phi_{calculated}$). Phase correction was then made and applied to all experiments for the remainder of the measurements made.

Also After calibration, FlowCheck® fluorospheres were measured with the TRAFFC system (∼3,000 events for $n = 6$ experiments). Data included the mean intensity, event count, and percent coefficient of variation (standard deviation/mean × 100). The FlowCheck® fluorospheres displayed a bright intensity at a mean intensity of 32317 A.U. with a CV of +/−11.76%. This is in comparison to YG fluorospheres (mean fluorescence intensity = 12730 a.u and cv = 33.43%). Finally, MCF-7 breast cancer cells were evaluated ($n = 6$ trials, and ∼1,000 events). The mean fluorescence intensity from the labeled cells was measured to be 21958 a.u. with a cv of 5.56%.

Fluorescence lifetime analyses were performed on FlowCheck® Fluorospheres, YG fluorospheres and PI-labeled MCF-7 cells. We collected waveforms at a low sampling frequency (195 kHz) to adjust for digitization of long pulse widths. Waveforms were analyzed when collected by both the laboratory oscilloscope as well as a DAQ system. Data acquired by the oscilloscope included only a single particle/cell measurement whereas DAQ-recorded waveforms included up to 1,000 events. Lifetimes calculated from the oscilloscope are provided in **Table 1**. The FlowCheck® and YG fluorospheres recorded a mean lifetime value of 6.25 ± 1.66 ns and 5.16 ± 1.51 ns, respectively. These values are close to many previous reports for these fluorescence microspheres [4]. DAQ-derived lifetimes were calculated to be 5.07 ± 1.66 ns for FlowCheck® fluorospheres and 3.01 ± 7.63 ns for YG fluorospheres. The PI-labeled MCF-7 cells were measured similiarly and processed for average fluorescence lifetime measurements. The oscilloscope-derived mean lifetime for the PI when intercalated into a cell was calculated to be 8.38 ± 2.09 ns. When the PI-labeled cells were processed in bulk after collection by the DAQ, a calculated mean lifetime value was found to be 5.73 ± 0.76 ns. Propidium iodide is known to have an average fluorescence lifetime when intercalated into the DNA of a cell that ranges from 8 to 12 nanoseconds. Our results include a wider lifetime range, which suggests the need to optimize the modulation frequency and make digitization adjustments when longer pulses are collected.

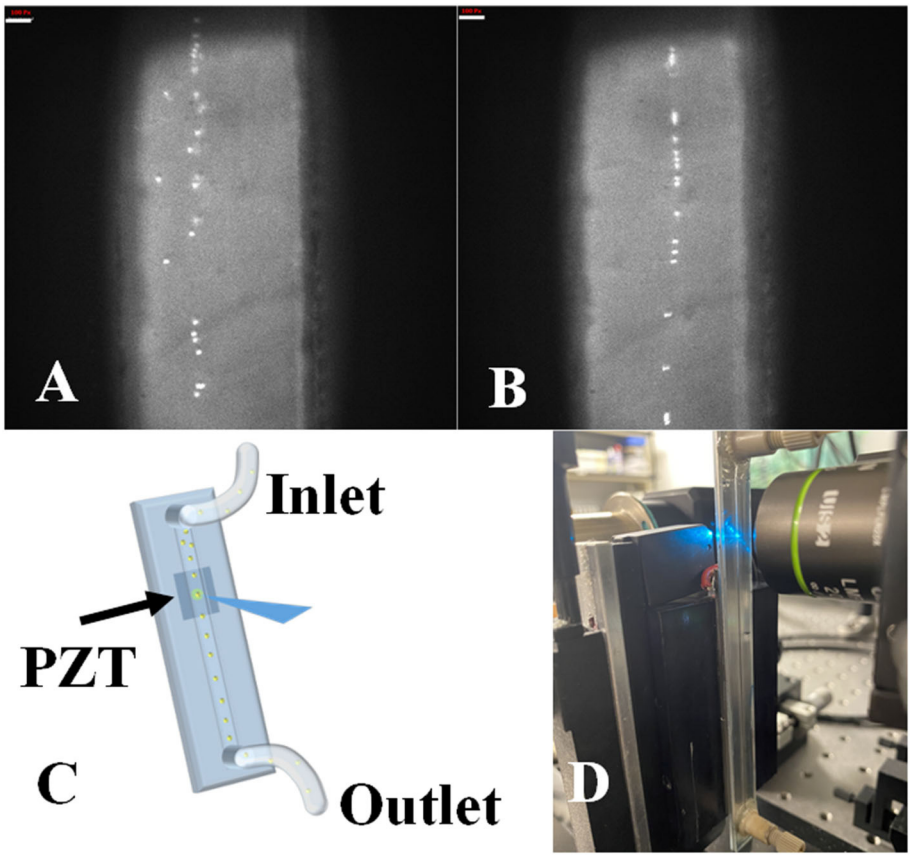

FIGURE 3 | Dot plot, intensity, and lifetime histogram data for fluorospheres and MCF-7 cells. **(A)** A polygon gate was applied to the entire dot plot population for YG fluorospheres. The mean intensity was recorded at 12730 A.U. with a CV of 33.43%. The corrected mean lifetime was recorded as 5.07 ± 1.66 ns from DAQ acquisition. **(B)** The same method was applied for FlowCheck® fluorospheres with respect to the dot plot gating. Mean intensity value was measured at 18394 A.U. with a CV of 13.29%. The mean corrected lifetime was measured at 5.07 ± 1.66 ns with visible bi-modal populations. **(C)** Propidium-labeled MCF-7 cells were acquired for up to 1,000 events. Mean fluorescence intensity was measured at 21958 A.U. with a CV of 5.56%. Mean corrected lifetime was measured at 5.73 ± 0.76 ns. **(D)** The acoustofluidic device used in the modular TRAFFC system.

TABLE 1 | Mean fluorescence intensity values, oscilloscope and DAQ calculated fluorescence lifetime values for FlowCheck fluorospheres, yellow-green fluorospheres and PI-labled MCF-7 cells.

Particle	Mean intensity (A.U.)	CV%	Rigol oscilloscope calculated τ (ns)	DAQ calculated τ (ns)
FlowCheck® fluorospheres	32317	11.76	6.25 ± 1.66	5.07 ± 1.66
Yellow-green fluorospheres	12730	33.43	5.16 ± 1.51	3.01 ± 7.63
PI Labeled MCF-7 Cells	21958	5.56	8.38 ± 2.09	5.73 ± 0.76

Acoustic Focusing

Upon evaluating the acoustic focusing component of the system, we found optimal settings necessary for measuring cell and microsphere signals. The TRAFFC system used one-dimensional acoustic focusing as opposed to two-dimensional focusing as found in recent studies by others [16]. One dimensional focusing involves acoustic focusing applied only across the width of the channel as opposed to the width and height of the channel. From here, we calculate the theoretical frequency needed to create a pressure node (SAW) at the center of the microchannel. The equation is as follows:

$$f = \frac{c_m}{2D}$$

where c_m is a constant and is the speed of sound in water which is 1,480 m s^{-1}. The width of the channel for our acoustofluidic device is 0.5 mm. After calculating with these numerical values, we concluded a frequency of 1.48 MHz that is needed to generate a single pressure node for acoustic focusing. In experimental analysis, we found that best focusing for polystyrene beads >5 μm was found at 1.53 MHz with amplitude of −9 dB that yielded power amplified output of 12 V_{p-p}. Our one-micron beads required an amplitude of −2.5 dB, leading to a power amplified a 16 $V_{p-p.}$ MCF-7 cells required a 1.51 MHz driving

frequency but a lower amplitude of −12 dB, netting a voltage of 9 V_{p-p}.

DISCUSSION

The data collected from the TRAFFC system described herein are preliminary, and although this modular cytometer requires further optimization, many steps have been achieved to establish lifetime measurements in combination with acoustically-driven flow of samples through a microchip. The TRAFFC system is capable of slower flow velocities and can adequately focus cells and microspheres for measurement. We observed longer integration times compared to conventional TRFC systems we have developed in past work. Importantly, the larger pulse widths, required us to reduce the digitization rate; this limitation will be a focus of our future work. In general, the significance of this preliminary work is that acoustic focusing can be accomplished for lifetime analysis with cells and microspheres, and this is an important step toward control of sample for eventual multi-lifetime analyses and sorting. With the FlowCheck® and YG fluorospheres, as well as PI-labeled cells, we measured bright and reproducible fluorescence intensity and fluorescence lifetime measurements. In the following sections we draw conclusions from this work related to the areas that require significant improvement, which include detection of light scatter, data acquisition, and acoustic control.

LIGHT SCATTER

The current design we present herein is that of an acoustically focused cytometer without the ability to collect light scattered from cells. Scattered light from the laser excitation source is important in cytometry because it roughly provides morphological and cytoplasmic features synergistically with fluorescence. The scatter parameter may also be of importance for sorting and separation of cells from debris. The TRAFFC system we present is designed to capture optical backscatter, which is currently challenged by de-focused background light. One way to optimize this is to design the TRAFFC system such that the acoustofluidic device is oriented horizontally (angling the device for low angle scattering capture) so as to negate background laser intrusion into the scatter optical channel. While it is possible to fabricate a device with optical waveguides or use of ultrasonic backscatter, we seek to reduce the complexity and costs associated with modular cytometry system.

DATA ACQUISITION

During the acquisition of fluorescence data we found that the transit time of the cell through the excitation source was indeed slower (relative to traditional cytometry). Yet this slow-down led to long cytometric pulses. The width of the pulse required down sampling of the digitized pulses thus limiting our real-time

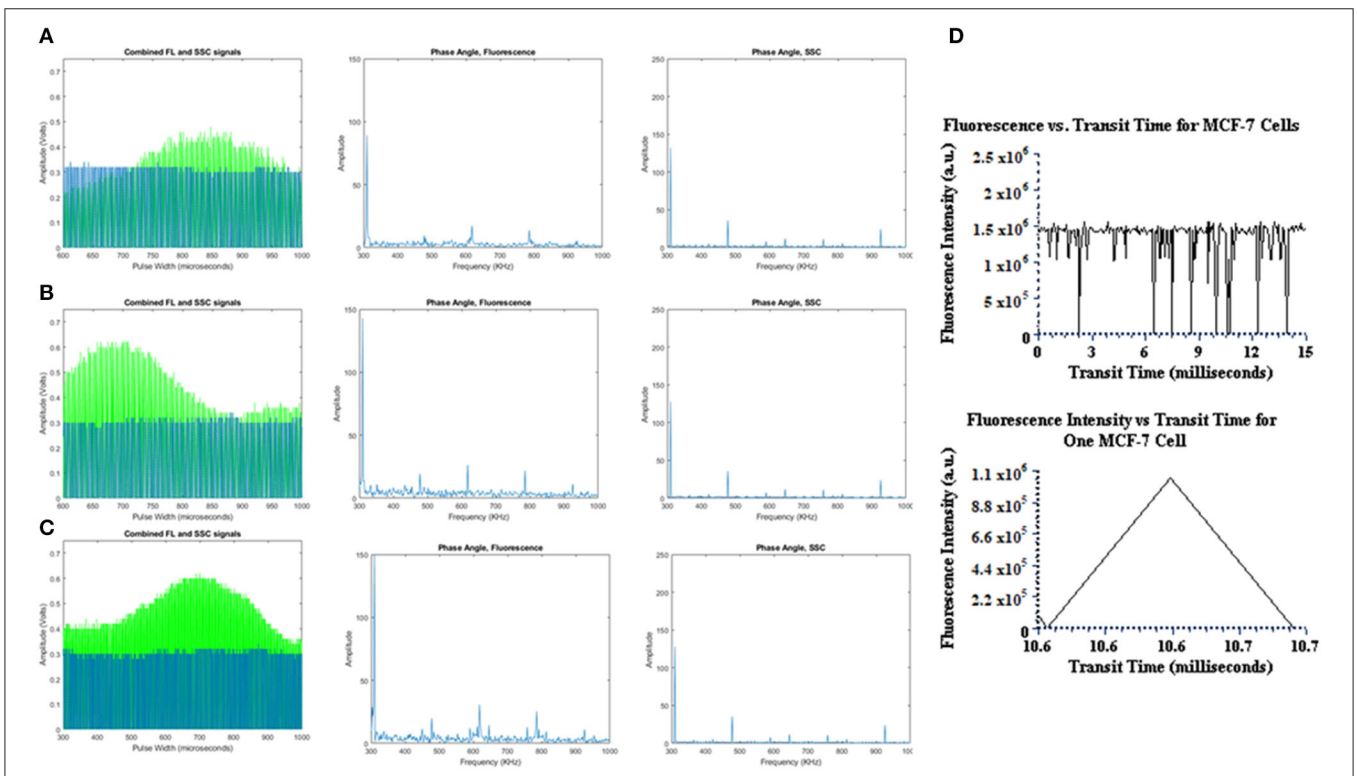

FIGURE 4 | Acoustic focusing performance. **(A)** Unfocused FlowCheck® particles passing through the device at 10 μL/min. White bar equals 100 pixels. **(B)** Acoustic field activated, and particles align to the pressure node in the center of the device's channel. **(C)** Graphical representation of acoustic focusing in-action. As the particles pass through the PZT generated SAW, alignment takes place along central pressure node. **(D)** Transit time in milliseconds vs. fluorescence intensity plotted for MCF-7 cells (up to 15 milliseconds) and the transit time (~200 μs) for a single MCF-7 cell in milliseconds.

analysis of the fluorescence lifetime. However, this did not hinder our ability to acquire fluorescence lifetimes in the nanosecond range. Time resolutions and transit time spreads for our DAQ, oscilloscope and PMT are 1 μs, 500 ps, and 1.5 ns, respectively. We found that reducing the sampling rate to 0.195 MHz, and ADC clocks to 1.56 MHz allowed for the capture of the entire fluorescence pulse. Another feature is that the DAQ offers the ability to control modulation cycles that are used to calculate the DFT, which calculates the phase shift needed for lifetime measurements. This is significant to our offline analysis. When we perform a Discrete Fourier Transform (DFT) on a single waveform or in bulk, we can expect the phase extracted from the frequency analysis to be very close to the actual phase value that is unique to the fluorophore. Increased modulation cycles minimizes phase errors. Error rates have been demonstrated in the past to be lower (phase shift errors at or below 0.4°) at modulating frequencies under 10 MHz. This translates to lifetime errors estimated to be around ∼0.10 ns. At smaller pulse widths, the increase in cycles would have a minimal effect whereas larger pulse widths see a more dramatic change with respect to error minimization. Although increased pulse widths can decrease the fluorescence lifetime standard deviation, when the modulation frequency is low, this variance is high. That is, at a higher the frequency the number of cycles increases; at the same high frequency a shorter pulse would have a less accurate DFT calculation compared to a longer pulse. Thus, in this work we show that the pulse width can be achieved and with adequate frequencies we should be able to achieve very high-resolution fluorescence lifetimes within tenths of a nanosecond.

ACOUSTIC FOCUSING

Finally, we determined that while acoustic focusing is possible there is a range of optimal frequencies that will dictate future measurements depending on the cell and sample measured. Upon evaluating the acoustic performance (**Figure 4**) we found that alignment was possible for particles as small as 3-micron with minor adjustments to acoustic parameters. Larger particle sizes aligned to the pressure nodes at higher flow rates which is also promising for higher-throughput measurements. In the data we present herein (cytometry histograms), cells alignment outperformed microsphere alignment (based on %cv), which is likely due to the density of the cells and the acoustic settings chosen. Owing to the fact that acoustic focusing has been optimized by others, we can draw on knowledge of what frequencies are optimal and identify the theoretical frequencies needed with our specific PZT (i.e., optimum resonant frequencies such as 1 vs. 0.1 kHz steps). These parameters are generally straightforward for optimization of our TRAFFC system.

Overall, this short report presents steps toward the development of a fully functional TRAFFC system. We provide evidence that fluorescence lifetimes can be measured from cells and microspheres with a goal to continue to refine the optofluidic design. We plan to focus on the limitations in the optical measurements as well as real-time data acquisition. Our goal is to use the TRAFFC system for key applications such as FRET, immunophenotyping, lanthanide-labeled vesicle detection, and metabolic mapping. Ultimately this instrument can be transformative for the flow cytometry field at large.

DATA AVAILABILITY STATEMENT

The original contributions presented in the study are included in the article/supplementary material, further inquiries can be directed to the corresponding authors.

AUTHOR CONTRIBUTIONS

JS wrote the paper, designed the technology, assembled the flow cytometer and performed all assessment and measurements to evaluate the operation of this tool. FR and JM participated in the assembly and design. JH directed the work and its interpretation and guarantee the integrity of its results.

FUNDING

This work was supported by the National Institutes of Health and the National Institute for General Medical Sciences grant number R01GM129859.

ACKNOWLEDGMENTS

We would like to extend a thank you to BennuBio for the acoustofluidic device used in the time-resolved acoustofluidic flow cytometer.

REFERENCES

1. Shapiro H. *Practical Flow Cytometry*. Hoboken: John Wiley & Sons (1995).
2. Houston JP, Naivar MA, Jenkins P, Freyer JP. Capture of fluorescence decay times by flow cytometry. *Curr Protocols Cytometry*. (2012) 59:1–21. doi: 10.1002/0471142956.cy0125s59
3. Cao R, Jenkins P, Peria W, Sands B, Naivar M, Brent R, et al. Phasor plotting with frequency-domain flow cytometry. *Opt Expr*. (2016) 24:14596–607. doi: 10.1364/OE.24.014596
4. Cao R, Pankayatselvan V, Houston JP. Cytometric sorting based on the fluorescence lifetime of spectrally overlapping signals. *Opt. Express*. (2013) 21:14816–31. doi: 10.1364/OE.21.014816
5. Jenkins P, Naivar MA, Houston JP. Toward the measurement of multiple fluorescence lifetimes in flow cytometry: maximizing multi-harmonic content from cells and microsphere. *J Biophotonics*. (2015) 8:908–17. doi: 10.1002/jbio.201400115
6. Alturkistany F, Nichani K, Houston KD, Houston JP. Fluorescence lifetime shifts of NAD (P) H during apoptosis measured by time-resolved flow cytometry. *Cytometry Part A*. (2019) 95:70–9. doi: 10.1002/cyto.a.23606
7. Cao R, Naivar MA, Wilder M, Houston JP. Expanding the potential of standard flow cytometry by extracting fluorescence lifetimes from cytometric pulse shifts. *Cytometry A*. (2014) 85:999–1010. doi: 10.1002/cyto.a.22574
8. Houston JP, Naivar MA, Freyer JP. Digital analysis and sorting of fluorescence lifetime by flow cytometry. *J Int Soc Analyt Cytol*. (2010) 77:861–72. doi: 10.1002/cyto.a.20930

9. Tabeling P. *Introduction to Microfluidics*. Oxford University Press on Demand (2005).
10. Whitesides GM. The origins and the future of microfluidics. *Nature*. (2006) 442:368–73. doi: 10.1038/nature05058
11. Verpoorte E, De Rooij NF. Microfluidics meets MEMS. *Proc IEEE*. (2003) 91:930–53. doi: 10.1109/JPROC.2003.813570
12. Çetin B, Li D. Dielectrophoresis in microfluidics technology. *Electrophoresis*. (2011) 32:2410–27. doi: 10.1002/elps.201100167
13. Zhou J, Papautsky I. Fundamentals of inertial focusing in microchannels. *Lab on a Chip*. (2013) 13:1121–32. doi: 10.1039/c2lc41248a
14. Shields IV, Reyes CD, López GP. Microfluidic cell sorting: a review of the advances in the separation of cells from debulking to rare cell isolation. *Lab on a Chip*. (2015) 15:1230–49. doi: 10.1039/C4LC01246A
15. Wiklund M, Green R, Ohlin M. Acoustofluidics 14: applications of acoustic streaming in microfluidic devices. *Lab on a Chip*. (2012) 12:2438–51. doi: 10.1039/c2lc40203c
16. Wang Y, Sayyadi N, Zheng X, Woods TA, Leif RC, Shi B, et al. Time-resolved microfluidic flow cytometer for decoding luminescence lifetimes in the microsecond region. *Lab on a Chip*. (2020) 20:655–64. doi: 10.1039/C9LC00895K

Conflict of Interest: The authors declare that the research was conducted in the absence of any commercial or financial relationships that could be construed as a potential conflict of interest.

frontiers in Physics

BRIEF RESEARCH REPORT
published: 28 May 2021
doi: 10.3389/fphy.2021.648016

Linear Behavior of the Phase Lifetime in Frequency-Domain Fluorescence Lifetime Imaging of FRET Constructs

*Daniel Sumetsky[1], James Y. Jiang[2], Marina A. Ayad[1], Timothy Mahon[1], Audrey Menaesse[3], Marina M. Cararo-Lopes[4], Mihir V. Patel[4], Bonnie L. Firestein[4] and Nada N. Boustany[1]**

[1] Department of Biomedical Engineering, Rutgers University, Piscataway, NJ, United States, [2] Thorlabs Inc., Newton, NJ, United States, [3] School of Life Sciences Engineering, Swiss Federal Institute of Technology (EPFL), Lausanne, Switzerland, [4] Department of Cell Biology and Neuroscience, Rutgers University, Piscataway, NJ, United States

We utilize a cost-effective frequency-domain fluorescence lifetime imaging microscope to measure the phase lifetime of mTFP1 in mTFP1-mVenus fluorescence resonance energy transfer (FRET) constructs relevant to the VinTS molecular tension probe. Our data were collected at 15 modulation frequencies $\omega/2\pi$ selected between 14 and 70 MHz. The lifetime of mTFP1 was $\tau_D = 3.11 \pm 0.02$ ns in the absence of acceptor. For modulation frequencies, ω, such that $(\omega \cdot \tau_D) < 1.1$, the phase lifetime of mTFP1in the presence of acceptor (mVenus), τ_ϕ^{DA}, was directly related to the amplitude-weighted lifetime τ_{ave}^{DA} inferred from the known FRET efficiency (E_{FRET}^{true}) of the constructs. A linear fit to a plot of $\left(\omega \cdot \tau_\phi^{DA}\right)$ *vs.* $\left(\omega \cdot \tau_{ave}^{DA}\right)$ yielded a slope of 0.79 ± 0.05 and intercept of 0.095 ± 0.029 ($R^2 = 0.952$). Thus, our results suggest that a linear relationship exists between the apparent E_{FRET}^{app} based on the measured phase lifetime and E_{FRET}^{true} for frequencies such that $(\omega \cdot \tau_D) < 1.1$. We had previously reported a similar relationship between E_{FRET}^{app} and E_{FRET}^{true} at 42 MHz. Our current results provide additional evidence in support of this observation, but further investigation is still required to fully characterize these results. A direct relationship between $\tau_\phi^{DA}$and τ_{ave}^{DA} has the potential to simplify significantly data acquisition and interpretation in fluorescence lifetime measurements of FRET constructs.

Keywords: fluorescence lifetime, imaging microscopy, live cell assays, fluorescence resonance energy transfer, frequency domain, mTFP1

OPEN ACCESS

Edited by:
Klaus Suhling, King's College London, United Kingdom

Reviewed by:
Theodorus Gadella, University of Amsterdam, Netherlands
Alessandro Esposito, University of Cambridge, United Kingdom

****Correspondence:***
Nada N. Boustany
nboustan@rutgers.edu

Specialty section:
This article was submitted to Optics and Photonics, a section of the journal Frontiers in Physics

Received: *31 December 2020*
Accepted: *16 April 2021*
Published: *28 May 2021*

Citation:
Sumetsky D, Jiang JY, Ayad MA, Mahon T, Menaesse A, Cararo-Lopes MM, Patel MV, Firestein BL and Boustany NN (2021) Linear Behavior of the Phase Lifetime in Frequency-Domain Fluorescence Lifetime Imaging of FRET Constructs. Front. Phys. 9:648016. doi: 10.3389/fphy.2021.648016

INTRODUCTION

Förster (or fluorescence) resonance energy transfer (FRET) is the non-radiative transfer of excitation energy from a donor fluorophore to an acceptor chromophore [1]. FRET occurs when the donor and acceptor are within close proximity, typically on the order of 1–10 nm, and depends on the inverse of this distance raised to the sixth power. The efficiency of energy transfer also depends on the physical optical properties of the two fluorophores, the alignment of their dipole moments, and the extent of overlap between the donor's emission spectrum and the acceptor's absorption band. FRET has important applications for measurements made in the biological sciences where one seeks to detect and characterize protein interactions. In addition, a multitude of biological sensors based on FRET have been designed to track cellular function, including intracellular changes to calcium, enzyme activation, or molecular tension [2]. We are interested in mechanical forces, which play an important role in the structure and function of a cell. For this reason, it is

important to investigate methods by which these forces can be measured. One method of measuring forces in cells is through the use of the vinculin tension sensor (VinTS), which consists of the tension module TSMod inserted between vinculin's head and tail [3]. TSMod itself consists of the fluorescent protein variants mTFP1 and mVenus acting as a donor-acceptor FRET pair connected by an elastic linker. The FRET efficiency between mTFP1 and mVenus can be related to the distance between the two fluorophores, and therefore, the tension force that the elastic linker is experiencing [3]. This measurement requires measuring absolute FRET efficiency as opposed to a relative FRET index.

Several techniques exist to measure FRET efficiency in living cells, including methods based on intensity measurements, such as the sensitized emission method [4], and fluorescence lifetime imaging microscopy (FLIM), including frequency-domain and time-domain techniques [5, 6]. The sensitized emission method, which can be achieved on a conventional epifluorescence microscope, utilizes intensity measurements in three channels, and requires calibration of the instrument to calculate FRET efficiency based on these measurements. In contrast, FLIM requires measuring the lifetime of the donor in a single imaging channel and does not rely on intensity calibration. FRET efficiency is obtained from the measured lifetimes of the donor in the presence and absence of the acceptor. Nonetheless, FLIM requires specialized instrumentation to resolve fluorescence lifetime. In addition, in the case of FRET sensors, data interpretation can be complex owing to the fact that FRET samples do not exhibit a single exponential decay. Thus, the FRET efficiency is given by the amplitude-weighted average lifetime of multi- or, more typically, bi-exponential decays. Fit-free techniques, which do not rely on fitting a multi-exponential decay model to the lifetime data, have been developed to interpret FLIM-FRET data. One example is the elegant phasor plot technique [7–12]. Methods incorporating deep learning and artificial intelligence to process lifetime data have also been demonstrated [13]. While powerful, the complexity of these methods and their reliance on costly instrumentation still present a barrier for the dissemination of FLIM-FRET measurements in biology.

In a recent study, we measured FRET efficiency by utilizing a cost-effective frequency-domain FLIM instrument operating at a single modulation frequency of 42 MHz [14]. We suggested that the apparent FRET efficiency obtained from phase lifetime measurements could be directly related to true FRET efficiency, which is given by the amplitude-weighted average lifetime, and that such a relationship could be used as a calibration curve to circumvent the need to fit a multi-exponential decay model to the data. In this study, we further, investigate the relationship between apparent FRET and true FRET for different choices of modulation frequencies. We measure the lifetime of the donor fluorophore mTFP1 at several modulation frequencies. We also measure the phase lifetime of mTFP1 in FRET constructs consisting of the mTFP1-mVenus FRET pair linked by peptides of various lengths relevant to the molecular tension probe, VinTS.

METHODS

Sample Preparation

Immortalized baby mouse kidney (iBMK) cells [15, 16]were a gift from Dr. Eileen White at the Rutgers Cancer Institute of New Jersey and were cultured on glass coverslips and maintained in Dulbecco's Modified Eagle's Medium (DMEM; Invitrogen) supplemented with 10% fetal bovine serum (FBS; Gemini), 100 U/ml penicillin and 100 μg/ml streptomycin (Invitrogen). The cells were maintained at 38°C in 8.5% CO_2. The cells were transfected as described previously [17]. For imaging, each coverslip with the attached cells was mounted on a homemade stainless-steel slide, and the growth medium was switched to Leibowitz L15 medium (Invitrogen) supplemented with FBS and penicillin/streptomycin as above. The imaging medium contained no phenol red. The cells were imaged between 24 and 48 h after transfection. Imaging was conducted at room temperature and room air.

The cells expressed either mTFP1 [18] or one of the following constructs consisting of mTFP1 and mVenus tethered by linkers of increasing lengths: mTFP1-$(GGSGGS)_1$-mVenus (6 amino acids), mTFP1-$(GGSGGS)_2$-mVenus (12 amino acids), mTFP1-$(GPGGA)_8$-mVenus (TSMod, 40 amino acids), and mTFP1-TRAF-mVenus (229 amino acids [19]). The constructs will herein be referred to as GGS1, GGS2, TSMod, and TRAF, respectively. We also note that TRAF typically forms a trimer [19]. TSMod was obtained from Addgene (TS module Plasmid # 26021). All the other plasmids were generously provided by Dr. Brenton Hoffman's laboratory at Duke University [4, 20]. The plasmids were amplified in DH5α competent *Escherichia coli*. DNA purification was carried out using NucleoBond® Xtra Midi endotoxin-free (Takara Bio USA, Inc.) according to the manufacturer's instructions.

Image Acquisition and Analysis

Fluorescence intensity and lifetime were acquired on a custom-built point scanning frequency-domain FLIM instrument, which was previously described in detail and utilizes sinusoidally modulated laser excitation [14]. Here, fluorescence intensity and phase lifetime images of mTFP1 were acquired using a laser diode with 450 nm excitation sinusoidally modulated at manually selected frequencies ranging between 14 and 70 MHz (**Supplementary Table 1**). The fluorescence signal was filtered by a 40 nm emission bandpass centered at 479 nm and measured with a photomultiplier tube. We had previously established that the fluorescence emission of mVenus in this acquisition channel is negligible. The microscope was fitted with a Nikon 40X dry objective with NA = 0.75. The excitation power was 20–23 μW at the sample. The images consisted of 1,024 × 1,024 scanned points with a dwell time of 6.8 μs per point. The instrument's phase offset was subtracted using a calibration sample of known lifetime as previously explained [14]. For this, we used a sample of Coumarin 6 (Sigma-Aldrich # 546283, ∼0.1 mM) dissolved in 100% ethanol (lifetime of 2.5 ns [21]) sandwiched between a glass slide and a coverslip using an adhesive well (Secure-Seal Spacers, Thermo-Fisher). The thickness of the sample was 0.12 mm. At the

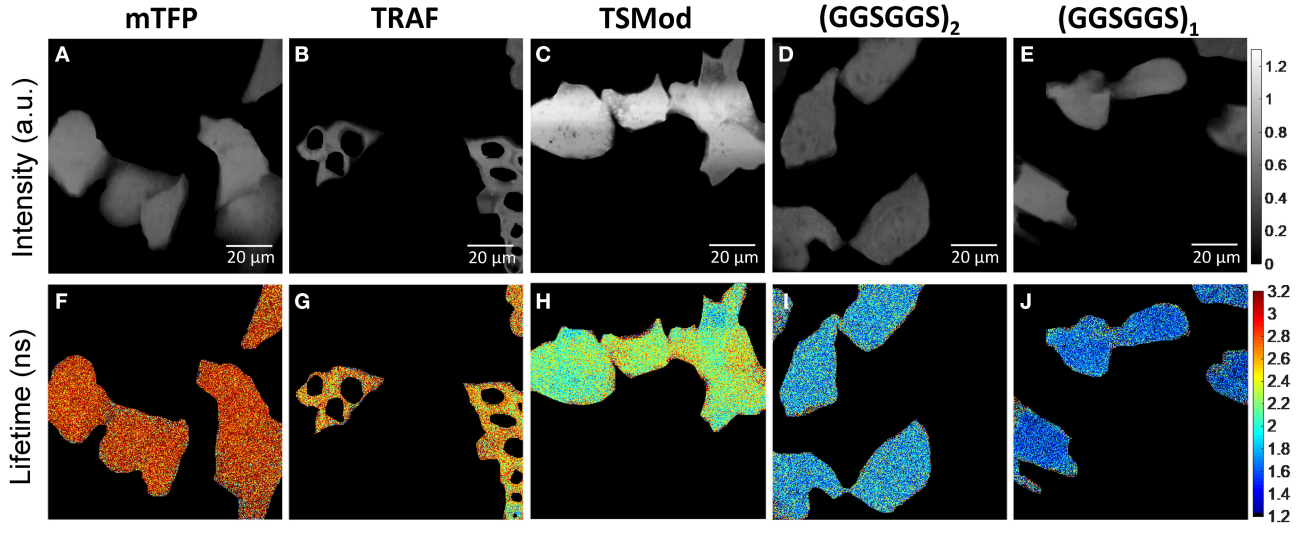

FIGURE 1 | Representative images of iBMK cells expressing mTFP1 and the FRET constructs mTFP1-TRAF-mVenus, mTFP1-TSMod-mVenus, mTFP1-$(GGSGGS)_2$-mVenus, and mTFP1-$(GGSGGS)_1$-mVenus acquired at 450 nm excitation with emission centered at 479 nm. **(A–E)** Fluorescence intensity in arbitrary units (a.u.). **(F–J)** Corresponding fluorescence lifetime images (color scale in ns). All images are captured with 1,024 × 1,024 points and 6.8 µs dwell-time per point. The cells were manually segmented.

beginning of every experiment, the calibration was performed at each of the modulation frequencies used during data acquisition. Once calibration is completed, the instrument measures at each image pixel, the phase difference, ϕ, between the sinusoidally modulated excitation and emission signals and calculates the sample's phase lifetime (or apparent lifetime) from [5]:

$$\tau_\phi \equiv \tau^{app} = \frac{\tan(\phi)}{\omega} = \frac{\tan(\phi)}{2 \cdot \pi \cdot f} \tag{1}$$

ω is the laser modulation frequency in rad/s; f is the frequency in Hz. Before analysis, the images were preprocessed by removing pixels with intensity signal below 0.02 intensity counts and for which an accurate measurement of lifetime cannot be made reliably. We also removed pixels with lifetime above 5 ns from the analysis. Finally, the images were manually segmented to ensure that the analysis was limited to the regions containing cells.

The measured phase lifetime is equal to the true lifetime of the fluorophore when the fluorescence can be modeled as a single exponential decay. This is expected to be the case for mTFP1 [18]. In contrast, the lifetime of mTFP1 within a FRET construct in presence of the mVenus acceptor is expected to exhibit more than one exponential decay [5]. The amplitude-weighted lifetime denoted here as τ_{ave}^{DA} is given by Equation 4.30 in [5]. If the FRET efficiency E_{FRET}^{true} is known, then the amplitude-weighted lifetime may be inferred from Equation 4.31–4.32 in [5]:

$$E_{FRET}^{true} = 1 - \frac{\tau_{ave}^{DA}}{\tau_D} \tag{2}$$

τ_D is the lifetime of the donor fluorophore in the absence of the acceptor fluorophore. Our donor is mTFP1, and our donor-acceptor FRET pairs are GGS1, GGS2, TSMod, and TRAF. In this paper, the FRET efficiency of all constructs was measured independently in our laboratory using the sensitized emission method with the calibration technique described previously in Menaesse et al. [17] These measurements gave (mean ± standard deviation of $N = 3$ experiments) $E_{FRET}^{true} = 0.567 \pm 0.021$ ($n = 64$ images) for GGS1, 0.524 ± 0.01 ($n = 90$ images) for GGS2, 0.285 ± 0.006 ($n = 90$ images) for TSMod, and 0.044 ± 0.01 ($n = 90$ images) for TRAF (**Supplementary Note 2**). Each value, together with the value of τ_D, may be used to obtain τ_{ave}^{DA} for each construct (**Supplementary Table 3**). We also define here the "apparent" FRET efficiency, E_{FRET}^{app}, obtained from the measured phase lifetime of the construct, τ_ϕ^{DA}, using the following equation:

$$E_{FRET}^{app} = 1 - \frac{\tau_\phi^{DA}}{\tau_D} \tag{3}$$

τ_ϕ^{DA} is the measured phase lifetime (apparent lifetime) of the donor fluorophore in the FRET construct while it is in the presence of the acceptor fluorophore. For a given modulation frequency ω, Equations 2, 3 may be re-written as:

$$\left(\omega \cdot \tau_{ave}^{DA}\right) = (1 - E_{FRET}^{true}) \cdot (\omega \cdot \tau_D) \tag{4}$$

and

$$\left(\omega \cdot \tau_\phi^{DA}\right) = (1 - E_{FRET}^{app}) \cdot (\omega \cdot \tau_D)\,. \tag{5}$$

Thus, we are able to compare directly the measurement of τ_ϕ^{DA} and E_{FRET}^{app} made in our FLIM system to τ_{ave}^{DA} and E_{FRET}^{true} measured by the intensity-based sensitized emission method. Unlike τ_{ave}^{DA}, which is expected to remain the same to the extent that the FRET efficiency of a given construct remains the same, τ_ϕ^{DA} and E_{FRET}^{app}

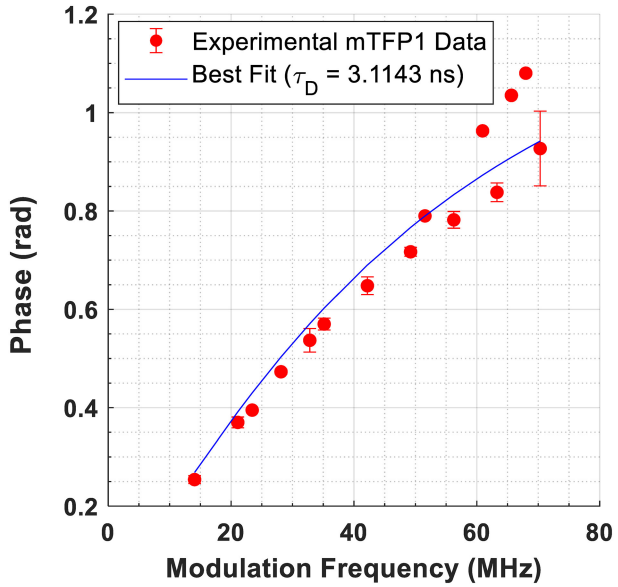

FIGURE 2 | Fit of $\phi = \tan^{-1}(2\pi f \cdot \tau_D)$ to data from cells expressing mTFP1 at 15 different modulation frequencies. The measured phase, ϕ, is obtained from Equation 1. The best fit yielded $\tau_D = 3.1143 \pm 0.017$ ns ($\chi^2 = 0.0699$).

are expected to change as a function of modulation frequency [5]. We therefore expect a priori that $\tau_{ave}^{DA} \neq \tau_{\phi}^{DA}$.

RESULTS

Representative images depicting the measured lifetime and intensity of each of the FRET constructs are shown in **Figure 1**. An estimate of fluorescence lifetime (τ_ϕ), was obtained from the mode (most frequent value) of the fluorescence lifetime distribution for each imaged field of view. We report the mean and standard deviation of τ_ϕ across N independent experimental repeats. Details of this analysis may be found in **Supplementary Note 3**. The measured fluorescence lifetime of mTFP1 expressed in the absence of mVenus, τ_ϕ^{TFP}, was converted to measured phase using Equation 1 and plotted as a function of modulation frequency (**Figure 2**). A fit of $(\omega \cdot \tau_D)$ to the measured phase as a function of modulation frequency yielded $\tau_D = 3.11 \pm 0.02$ns ($\chi^2 = 0.0699$) for mTFP1. The phase lifetime measurements made for the four FRET constructs at the different modulation frequencies are listed in **Supplementary Table 4**. At f = 42.1875 MHz, we obtained (mean ± standard deviation of n images) τ_ϕ^{DA} =1.72 ± 0.12 ($N = 5$) for GGS2; 2.13 ± 0.13 ns ($N = 4$) for TSMod, and 2.59 ± 0.08 ns ($N = 4$) for TRAF. In addition, we measured here $\tau_\phi^{DA} = 1.44 \pm 0.07$ ns ($N = 3$) for the GGS1 construct at 42.1875 MHz. Our results corroborate our previous values for TSMod and TRAF [14]. However, the mean GGS2 lifetime at 42.1875 MHz was 0.2 ns longer compared to our previous data.

To investigate the effect of modulation frequency on lifetime and FRET efficiency, we used $\tau_D = 3.11$ ns and the known true FRET efficiencies to obtain the expected lifetime τ_{ave}^{DA} of the constructs using Equation 2 (**Supplementary Table 3**). As explained in the Methods section, the FRET efficiency of the constructs was obtained independently using the intensity-based sensitized emission method. A relationship between τ_ϕ^{DA} measured at each frequency and τ_{ave}^{DA} is obtained for all constructs by plotting $\left(\omega \cdot \tau_\phi^{DA}\right)$ *vs.* $\left(\omega \cdot \tau_{ave}^{DA}\right)$ in **Figure 3A**. **Figure 3A** also includes a plot of $\left(\omega \cdot \tau_\phi^{TFP}\right)$ *vs.* $(\omega \cdot \tau_D)$ for mTFP1. The results in **Figure 3A** suggest that a linear relationship between τ_ϕ^{DA} and τ_{true}^{DA} holds for all constructs up to $\left(\omega \cdot \tau_{ave}^{DA}\right)\big|_{GGS1} = 0.478$ for GGS1 or $\omega = 353.429 \cdot 10^6 rad/s$ ($f = 56.25\ MHz$). Beyond this modulation frequency, $\left(\omega \cdot \tau_\phi^{DA}\right)$ begins to deviate significantly from this linear relationship, especially for the GGS1 and GGS2 constructs, which have short linkers and high FRET efficiency. Referring this value back to the constant lifetime of mTFP1, this frequency limit may be re-defined as $(\omega \cdot \tau_D) = 353.429 \cdot 3.11 \cdot 10^{-3} = 1.11$. A linear fit to the datapoints collected at frequencies up to and including 56.25 MHz is shown in **Figure 3B**. The slope and intercept of the fit are 0.79 (95% confidence interval ± 0.05) and 0.029 (95% confidence interval ± 0.031), respectively ($R^2 = 0.952$).

As expected from Equations 4, 5, a similar relationship should be obtained if we plot $\left[(1 - E_{FRET}^{app}) \cdot (\omega \cdot \tau_D)\right]$ vs. $\left[(1 - E_{FRET}^{true}) \cdot (\omega \cdot \tau_D)\right]$ where E_{FRET}^{app} is calculated using Equation 3 with τ_D =3.11 ns and the measured phase lifetimes (**Supplementary Table 4**), while E_{FRET}^{true} is based on the intensity-based FRET efficiency measurements of the constructs made independently (see Methods). In **Figure 4** we plot E_{FRET}^{app} vs. E_{FRET}^{true} for modulation frequencies up to and including 56.25 MHz. We note that for mTFP1, a non-zero intercept was taken as $\left(1 - \frac{\tau_\phi^{TFP}(\omega)}{\tau_D}\right)$, and results from the fluctuations in mTFP1 lifetime measured at each frequency. A linear fit is obtained at each modulation frequency (**Figure 4** top inset). As the modulation frequency increased, so did the y-intercept of the line of fit. However, the slope of the line of fit was consistently around 0.65, no matter the modulation frequency. The best fits occurred for modulation frequencies between 35 and 49 MHz with an $R^2 > 0.97$. In comparison, the slope of the linear fit in **Figure 3B** was 0.79. However, the difference between the slopes of **Figures 3B**, **4** is within experimental error.

DISCUSSION

In this report, we use frequency-domain FLIM to measure the phase lifetime of mTFP1 expressed alone or within mTFP1-mVenus FRET fusion constructs at different modulation frequencies. To calibrate our set up we used the 2.5 ns lifetime of Coumarin 6 in ethanol previously reported by Sun et al. [21] using frequency-domain FLIM. With this calibration value, the lifetime of Coumarin 6 in methanol (2.29 ns) was in close agreement with reported values [22] (**Supplementary Figure 3**). Still, variations in the measured lifetime of Coumarin 6 exist. For example, a lifetime of 2.4 ns was reported for Coumarin 6 in ethanol using time-domain FLIM [22]. Thus, a systematic

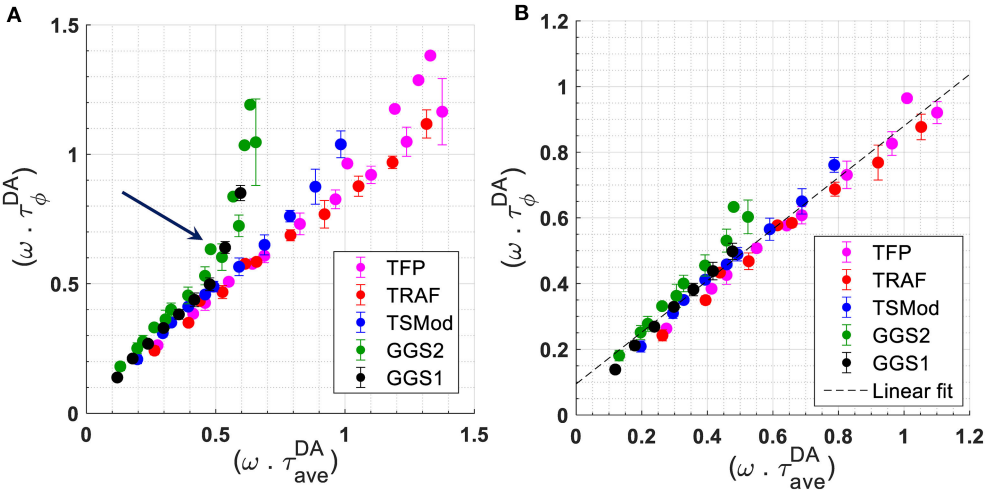

FIGURE 3 | (A): Relationship between $\left(\omega \cdot \tau_{\phi}^{DA}\right)$ *and* $\left(\omega \cdot \tau_{DA}^{ave}\right)$ for all FRET constructs. For mTFP1, we plotted $\left(\omega \cdot \tau_{\phi}^{TFP}\right)$ *vs* $(\omega \cdot \tau_D)$. For each frequency ω, τ_{ϕ}^{DA} (or τ_{ϕ}^{TFP}) is the measured phase lifetime at that frequency. The average lifetime was calculated using the known FRET efficiency of the constructs measured independently with the sensitized emission method, $\tau_D = 3.11$ ns, and Equation 2. The arrow denotes the point at which the data for GGS1 and GGS2 begin to deviate from a linear relationship. **(B)** Relationship between $\left(\omega \cdot \tau_{\phi}^{DA}\right)$ *and* $\left(\omega \cdot \tau_{ave}^{DA}\right)$ for all constructs, and between $\left(\omega \cdot \tau_{\phi}^{TFP}\right)$ *vs.* $(\omega \cdot \tau_D)$ for mTFP1, up to and including a modulation frequency of 56.25 MHz. The slope of best linear fit to these data is 0.79 (95% confidence interval of ±0.05). The intercept is 0.095 (95% confidence interval of ± 0.029). $R^2 = 0.952$.

error on the order of 0.1 ns may be attributed to the reference lifetime of the calibration sample. Such an error, however, would not affect the nature of the relationships in **Figures 3**,**4**.

A fit to the phase modulation data for mTFP1 between 14 and 70 MHz yielded a lifetime of $\tau_D = 3.11 \pm 0.02$ ns (**Figure 2**), which is slightly lower than the previously reported lifetime of 3.2 ns for mTFP1 in buffer [18]. In living cells, published measurements of mTFP1 yielded a lifetime of 2.98 ns based on a single exponential decay [3], phase and modulation lifetimes of 2.7 and 2.8 ns, respectively [23], or 2.65 ± 0.12 ns in the cytosol and 2.61 ± 0.11 ns in the nucleus based on a single exponential decay [24]. In that study, a bi-exponential model yielded a better fit to the data. However, the difference between the values of τ_1 and τ_2 obtained from the bi-exponential fits was <0.1 ns ($\tau_1 = 2.60$ ns, $\tau_2 = 2.67$ ns in the cytosol, and $\tau_1 = 2.61$ and $\tau_2 = 2.64$ ns in the nucleus) [24]. Taken together, published reports point to the fact that mTFP1 lifetime is monoexponential. A double exponential fit to our data in **Figure 2** results in two indistinguishable lifetimes ($\tau_{1D} = \tau_{2D} = 3.088e{-}9$ ns, α_1: 0.5, χ^2: 0.0683) (**Supplementary Figure 4**) and corroborates those previous results.

Our results for the FRET constructs suggest that for modulation frequencies such that $(\omega \cdot \tau_D) \lesssim 1$, the behavior of the measured phase lifetime of mTFP1 as a function of average lifetime was close to linear (**Figure 3B**). As explained in Methods, the average lifetime was determined using Equation 2 and the FRET efficiency measured separately with the intensity-based sensitized emission method. Based on the relationship in **Figure 3B**, we hypothesize that the apparent FRET efficiency, E_{FRET}^{app}, may be linearly related to E_{FRET}^{true} for frequencies, ω, such that $(\omega \cdot \tau_D) \lesssim 1.1$ or $f \lesssim 56.25$ MHz for our mTFP1-mVenus FRET constructs. These relationships are empirical and require further theoretical characterization. We had previously observed this linear behavior at f = 42 MHz [14]. Here, we show that such a relationship may hold at additional frequencies chosen such that $(\omega \cdot \tau_D) \lesssim 1.1$. Within this range, a linear fit to the experimental relationship between E_{FRET}^{app} and E_{FRET}^{true} at each modulation frequency resulted in slight differences in slope that are within the measurements' experimental error, while the intercept varied with fluctuations in mTFP1 lifetime measurements. These differences in slope and fluctuations in the measured lifetime of mTFP1 may explain the difference between the slope of the linear fits in **Figures 3B**, **4**. We also note here that the choice of frequency in frequency-domain FLIM can be based on a "best" frequency determined to optimize lifetime resolution and given by $\omega_{best}^2 = \frac{(1+\sqrt{3})}{2 \cdot \tau^2} = \frac{1.366}{\tau^2}$ [7]. Thus, $(\omega_{best} \cdot \tau_D) = 1.17$ and slightly exceeds the value of ~1.1 under which the linear relationships shown in this study would hold. This, however, suggests choosing the higher frequencies within our range of $(\omega \cdot \tau_D) \lesssim 1.1$ is expected to lead to a more precise characterization of the relationship between E_{FRET}^{app} and E_{FRET}^{true}.

For $(\omega \cdot \tau_D) \lesssim 1.1$, the relation between E_{FRET}^{app} and E_{FRET}^{true} may be used as a calibration curve to convert the measured phase lifetime at a single modulation frequency to a measurement of FRET efficiency and therefore, circumvent the need for fitting lifetime data to bi- or multi-exponential decay models or the need for more complex interpretation of the phase and demodulation data. Applications of frequency-domain FLIM in FRET experiments have extensively relied on the relationship between the phase and demodulation of the emission signal. Data fitting techniques applied to the

Frequency (MHz)	Slope	Intercept	Slope 95% Confidence Interval	Intercept 95% Confidence Interval	R^2
14.0625	0.66	0.062	+/- 0.34	+/- 0.124	0.923
21.0938	0.64	0.090	+/- 0.23	+/- 0.086	0.960
28.1250	0.66	0.090	+/- 0.26	+/- 0.095	0.955
35.1563	0.65	0.115	+/- 0.19	+/- 0.070	0.974
42.1875	0.68	0.124	+/- 0.16	+/- 0.058	0.984
49.2188	0.63	0.154	+/- 0.19	+/- 0.071	0.972
56.2500	0.61	0.162	+/- 0.20	+/- 0.075	0.967

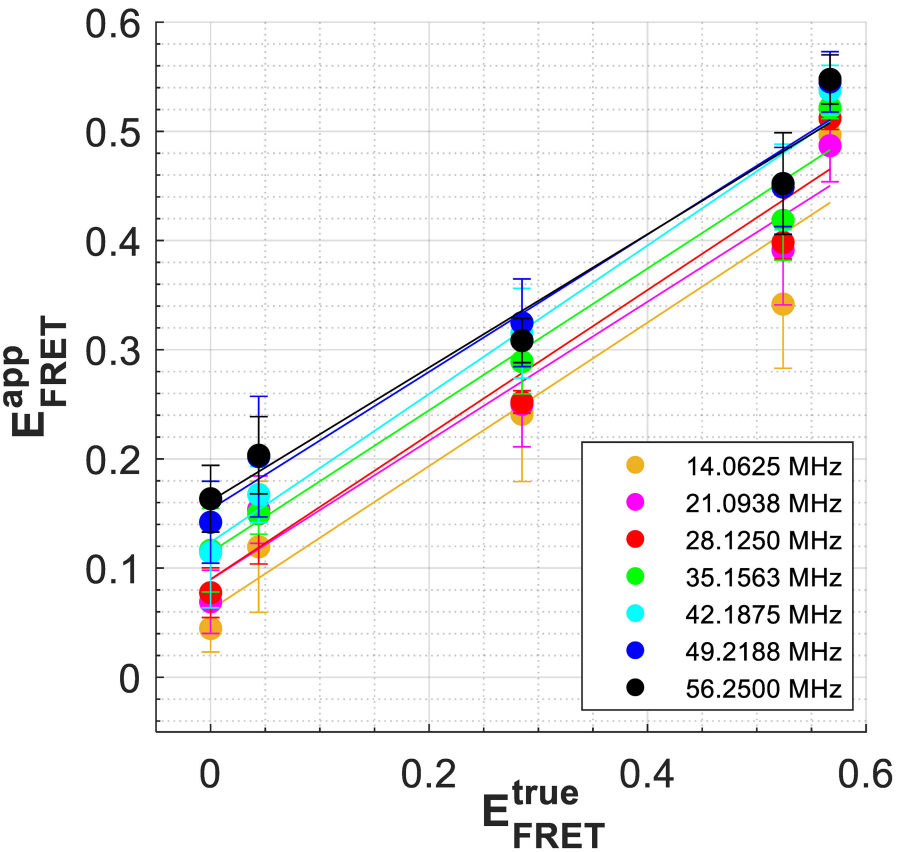

FIGURE 4 | Relationship between E_{FRET}^{app} and E_{FRET}^{true} for the protein constructs at each modulation frequency. E_{FRET}^{app} was calculated at each modulation frequency using the measured τ_ϕ^{DA}, $\tau_D = 3.11$ ns, and Equation 3. For mTFP1, a non-zero intercept was taken as $\left(1 - \tau_\phi^{TFP}(\omega)/\tau_D\right)$, and results from the slightly different mTFP1 lifetime measurements, τ_ϕ^{TFP}, that were made at each frequency While the slopes related to each modulation frequency are similar, the intercepts generally increase with increasing modulation frequency. Exact parameters of these linear fits are found in the top inset.

phase and demodulation measurements have been used to infer the fractional contributions of bi-exponential decays using single [25–27] or multiple [28] modulation frequencies. Phase and demodulation measurements have also been used to follow "FRET trajectories" by locating individual image pixels on the phasor plot to infer a FRET index [7–12]. By comparison, a direct relationship between E_{FRET}^{app} and E_{FRET}^{true} has the potential to simplify significantly acquisition and interpretation of FLIM-FRET data. Our studies are specifically relevant to the vinculin tension sensor, VinTS, which consists of TSMod inserted between the head and tail of vinculin [3]. We expect TSMod to stretch in the range of FRET efficiencies tested here. Therefore, we expect to be able to determine VinTS' FRET efficiency in an unknown sample using the measured phase lifetime at a single modulation frequency and the E_{FRET}^{app} vs. E_{FRET}^{true} relationship as we had previously suggested [14]. However, FRET sensors that operate outside this range or that have a different donor-acceptor pair would need to be recalibrated.

Deviations in the relationship between E_{FRET}^{true} based on the sensitized emission method and E_{FRET}^{app} based on FLIM could be due to the presence of unpaired donors or errors in the calibration of E_{FRET}^{true}. We had previously estimated the fraction of paired donors to be 1–1.03 or close to 1 in our constructs

(**Supplementary Note 2** in [17]). This is achieved by choosing an acceptor (mVenus) with short maturation time [29, 30] and observing cells at least 24 h post-transfection. Furthermore, the value of $E_{TSMod} = 0.286$ that we used to find the calibration factor G to infer E^{true}_{FRET} (See **Supplementary Note 2**) is based on the value reported by Gates et al. obtained with an error of 0.015 after pixel-based measurements from several hundred cells [4]. Such an error would result in <0.13 uncertainty in the G factor. We believe that a more significant source of variation in E_{FRET} values is the variation in the local cellular environment and biological variations across different cells. A limitation of our studies was, therefore, the use of a single global value of E^{true}_{FRET} measured in a separate set of cells and taken as representative of all the pixel data for a given construct. As such, we did not compare the relationship between E^{app}_{FRET} and E^{true}_{FRET} on a same-cell or even on a same-pixel basis. Still, our current results provide additional evidence to further investigate the validity of the linear relationships suggested by our data and the frequency regime in which they apply.

DATA AVAILABILITY STATEMENT

The raw data supporting the conclusions of this article will be made available by the authors, without undue reservation.

AUTHOR CONTRIBUTIONS

DS collected and analyzed data, produced all the figures in this article, and wrote and reviewed the manuscript. JJ designed, built and adapted the FLIM instrument for this study, collected and analyzed data, and reviewed and edited the manuscript. AM and MA collected data. TM analyzed FRET intensity-based data and provided cell samples. MP, MC-L, and BF provided purified plasmids and critical resources. AM, MA, TM, MP, MC-L, and BF reviewed and edited the manuscript. NB conceived the study, consulted on instrument design, provided cell samples and purified plasmids, collected and analyzed data, wrote and reviewed the manuscript, and managed the project. All authors contributed to the article and approved the submitted version.

FUNDING

This study was partially supported by a NSF GOALI grant under award CMMI-1825433 to NB and BF. Any opinions, findings, and conclusions or recommendations expressed in this material are those of the author(s) and do not necessarily reflect the views of the National Science Foundation. MC-L was supported by a Pre-doctoral Fellowship from the Coordination for the Improvement of Higher Education Personnel (CAPES), and MP was supported by NJCBIR Predoctoral Fellowship #CBIR15FEL009.

ACKNOWLEDGMENTS

We wish to thank Dr. Brenton Hoffman at Duke University for the plasmids used in this study, Dr. Eileen White at the Rutgers Cancer Institute of New Jersey for the iBMK cells, and the Université Paris-Saclay for internship support for AM.

SUPPLEMENTARY MATERIAL

The Supplementary Material for this article can be found online at: https://www.frontiersin.org/articles/10.3389/fphy.2021.648016/full#supplementary-material

REFERENCES

1. Clegg R. Fluorescence resonance energy transfer. *Curr Opin Biotechnol*. (1995) 6:103–10. doi: 10.1016/0958-1669(95)80016-6
2. Greenwald EC, Mehta S, Zhang J. Genetically encoded fluorescent biosensors illuminate the spatiotemporal regulation of signaling networks. *Chem Rev*. (2018) 118:11707–94. doi: 10.1021/acs.chemrev.8b00333
3. Grashoff C, Hoffman BD, Brenner MD, Zhou RB, Parsons M, Yang MT, et al. Measuring mechanical tension across vinculin reveals regulation of focal adhesion dynamics. *Nature*. (2010) 466:263–6. doi: 10.1038/nature09198
4. Gates EM, LaCroix AS, Rothenberg KE, Hoffman BD. Improving quality, reproducibility, and usability of FRET-based tension sensors. *Cytometry A*. (2019) 95A:201–13. doi: 10.1002/cyto.a.23688
5. Lakowicz JR. *Principles of Fluorescence Spectroscopy*. 3rd ed. New York, NY: Springer (2006). doi: 10.1007/978-0-387-46312-4
6. Periasamy A, Clegg RM. *FLIM Microscopy in Biology and Medicine*. Boca Raon, FL: CRC Press (2009). doi: 10.1201/9781420078916
7. Redford GI, Clegg RM. Polar plot representation for frequency-domain analysis of fluorescence lifetimes. *J Fluoresc*. (2005) 15:805–15. doi: 10.1007/s10895-005-2990-8
8. Digman MA, Caiolfa VR, Zamai M, Gratton E. The phasor approach to fluorescence lifetime imaging analysis. *Biophys J*. (2008) 94:L14–6. doi: 10.1529/biophysj.107.120154
9. Chen SJ, Sinsuebphon N, Rudkouskaya A, Barroso M, Intes X, Michalet X. *In vitro* and *in vivo* phasor analysis of stoichiometry and pharmacokinetics using short-lifetime near-infrared dyes and time-gated imaging. *J Biophotonics*. (2019) 12:e201800185. doi: 10.1002/jbio.201800185
10. Hinde E, Digman MA, Welch C, Hahn KM, Gratton E. Biosensor Forster resonance energy transfer detection by the phasor approach to fluorescence lifetime imaging microscopy. *Microsc Res Tech*. (2012) 75:271–81. doi: 10.1002/jemt.21054
11. Stringari C, Cinquin A, Cinquin O, Digman MA, Donovan PJ, Gratton E. Phasor approach to fluorescence lifetime microscopy distinguishes different metabolic states of germ cells in a live tissue. *Proc Natl Acad Sci U S A*. (2011) 108:13582–7. doi: 10.1073/pnas.1108161108
12. Ranjit S, Malacrida L, Jameson DM, Grafton E. Fit-free analysis of fluorescence lifetime imaging data using the phasor approach. *Nat Protoc*. (2018) 13:1979–2004. doi: 10.1038/s41596-018-0026-5
13. Smith JT, Yao RY, Sinsuebphon N, Rudkouskaya A, Un N, Mazurkiewicz J, et al. Fast fit-free analysis of fluorescence lifetime imaging *via* deep learning. *Proc Natl Acad Sci U S A*. (2019) 116:24019–30. doi: 10.1073/pnas.1912707116
14. Dumas JP, Jiang JY, Gates EM, Hoffman BD, Pierce MC, Boustany NN. FRET efficiency measurement in a molecular tension probe with a low-cost frequency-domain fluorescence lifetime imaging microscope. *J Biomed Opt*. (2019). 24:1–24. doi: 10.1117/1.JBO.24.12.126501
15. Mathew R, Degenhardt K, Haramaty L, Karp CM, White E. Immortalized mouse epithelial cell models to study the role of apoptosis in cancer. In: KhosraviFar R, et al. editors. *Programmed Cell Death, the Biology Therapeutic Implications of Cell Death, Part B*. London: Methods in Enzymology, Elsevier Inc., (2008). p. 77–106. doi: 10.1016/S0076-6879(08)01605-4

16. Mathew R, Karp CM, Beaudoin B, Vuong N, Chen GH, Chen HY, et al. Autophagy suppresses tumorigenesis through elimination of p62. *Cell*. (2009) 137:1062–75. doi: 10.1016/j.cell.2009.03.048
17. Menaesse A, Sumetsky D, Emanuely N, Stein JL, Gates EM, Hoffman BD, et al. Simplified instrument calibration for Wide-Field Fluorescence Resonance Energy Transfer (FRET) measured by the sensitized emission method. *Cytometry A*. (2021) 99:407–16. doi: 10.1002/cyto.a.24194
18. Ai HW, Henderson JN, Remington SJ, Campbell RE. Directed evolution of a monomeric, bright and photostable version of Clavularia cyan fluorescent protein: structural characterization and applications in fluorescence imaging. *Biochem J*. (2006) 400:531–40. doi: 10.1042/BJ20060874
19. Thaler C, Koushik SV, Blank PS, Vogel SS. Quantitative multiphoton spectral imaging and its use for measuring resonance energy transfer. *Biophys J*. (2005) 89:2736–49. doi: 10.1529/biophysj.105.061853
20. LaCroix AS, Lynch AD, Berginski ME, Hoffman BD. Tunable molecular tension sensors reveal extension-based control of vinculin loading. *Elife*. (2018) 7:e33927. doi: 10.7554/eLife.33927
21. Sun YS, Hays NM, Periasamy A, Davidson MW, Day RN. Monitoring protein interactions in living cells with fluorescence lifetime imaging microscopy. In: Conn PM, editor. *Methods in Enzymology. Vol. 204*. London: Methods in Enzymology, Elsevier Inc. (2012). p. 371–91. doi: 10.1016/B978-0-12-391857-4.00019-7
22. Kristoffersen AS, Erga SR, Hamre B, Frette Ø. Testing fluorescence lifetime standards using two-photon excitation and time-domain instrumentation: rhodamine B, coumarin 6 and lucifer yellow. *J Fluoresc*. (2014) 24:1015–24. doi: 10.1007/s10895-014-1368-1
23. Goedhart J, Van Weeren L, Hink MA, Vischer NOE, Jalink K, Gadella TWJ. Bright cyan fluorescent protein variants identified by fluorescence lifetime screening. *Nat Meth*. (2010) 7:137–9. doi: 10.1038/nmeth.1415
24. Day RN, Booker CF, Periasamy A. Characterization of an improved donor fluorescent protein for Forster resonance energy transfer microscopy. *J Biomed Opt*. (2008) 13:031203. doi: 10.1117/1.2939094
25. Verveer PJ, Squire A, Bastiaens PIH. Global analysis of fluorescence lifetime imaging microscopy data. *Biophys J*. (2000) 78:2127–37. doi: 10.1016/S0006-3495(00)76759-2
26. Clayton AHA, Hanley QS, Verveer PJ. Graphical representation and multicomponent analysis of single-frequency fluorescence lifetime imaging microscopy data. *J Microsc*. (2004) 213:1–5. doi: 10.1111/j.1365-2818.2004.01265.x
27. Esposito A, Gerritsen HC, Wouters FS. Fluorescence lifetime heterogeneity resolution in the frequency domain by lifetime moments analysis. *Biophys J*. (2005) 89:4286–99. doi: 10.1529/biophysj.104.053397
28. Schlachter S, Elder AD, Esposito A, Kaminski GS, Frank JH, Van Geest LK, et al. mhFLIM: resolution of heterogeneous fluorescence decays in widefield lifetime microscopy. *Opt Express*. (2009) 17:1557. doi: 10.1364/OE.17.001557
29. Nagai T, Ibata K, Park ES, Kubota M, Mikoshiba K, Miyawaki A. A variant of yellow fluorescent protein with fast and efficient maturation for cell-biological applications. *Nat Biotechnol*. (2002) 20:87–90. doi: 10.1038/nbt0102-87
30. Kremers GJ, Goedhart J, van Munster EB, Gadella TWJ. Cyan and yellow super fluorescent proteins with improved brightness, protein folding, and FRET Forster radius. *Biochemistry*. (2006) 45:6570–80. doi: 10.1021/bi0516273

Conflict of Interest: JJ was employed by Thorlabs Inc.

The remaining authors declare that the research was conducted in the absence of any commercial or financial relationships that could be construed as a potential conflict of interest.

frontiers in Physics

ORIGINAL RESEARCH
published: 02 March 2021
doi: 10.3389/fphy.2021.635645

On Synthetic Instrument Response Functions of Time-Correlated Single-Photon Counting Based Fluorescence Lifetime Imaging Analysis

Dong Xiao[1], Natakorn Sapermsap[2], Mohammed Safar[1], Margaret Rose Cunningham[1], Yu Chen[2] and David Day-Uei Li[1]*

[1]Strathclyde Institute of Pharmacy and Biomedical Sciences, University of Strathclyde, Glasgow, United Kingdom, [2]Department of Physics, University of Strathclyde, Glasgow, United Kingdom

Time-correlated single-photon counting (TCSPC) has been the gold standard for fluorescence lifetime imaging (FLIM) techniques due to its high signal-to-noize ratio and high temporal resolution. The sensor system's temporal instrument response function (IRF) should be considered in the deconvolution procedure to extract the real fluorescence decay to compensate for the distortion on measured decays contributed by the system imperfections. However, to measure the instrument response function is not trivial, and the measurement setup is different from measuring the real fluorescence. On the other hand, automatic synthetic IRFs can be directly derived from the recorded decay profiles and provide appropriate accuracy. This paper proposed and examined a synthetic IRF strategy. Compared with traditional automatic synthetic IRFs, the new proposed automatic synthetic IRF shows a broader dynamic range and better accuracy. To evaluate its performance, we examined simulated data using nonlinear least square deconvolution based on both the Levenberg-Marquardt algorithm and the Laguerre expansion method for bi-exponential fluorescence decays. Furthermore, experimental FLIM data of cells were also analyzed using the proposed synthetic IRF. The results from both the simulated data and experimental FLIM data show that the proposed synthetic IRF has a better performance compared to traditional synthetic IRFs. Our work provides a faster and precise method to obtain IRF, which may find various FLIM-based applications. We also reported in which conditions a measured or a synthesized IRF can be applied.

Keywords: time-resolved imaging, photon counting, deconvolution, fluorescence microscopy, instrument response function

OPEN ACCESS

Edited by:
Klaus Suhling,
King's College London,
United Kingdom

Reviewed by:
Nirmal Mazumder,
Manipal Academy of Higher Education, India
Jianming Wen,
Kennesaw State University,
United States

****Correspondence:***
Dong Xiao
dong.xiao@strath.ac.uk

Specialty section:
This article was submitted to Optics and Photonics, a section of the journal Frontiers in Physics

Received: *30 November 2020*
Accepted: *02 February 2021*
Published: *02 March 2021*

Citation:
Xiao D, Sapermsap N, Safar M, Cunningham MR, Chen Y and Li DD-U (2021) On Synthetic Instrument Response Functions of Time-Correlated Single-Photon Counting Based Fluorescence Lifetime Imaging Analysis. Front. Phys. 9:635645. doi: 10.3389/fphy.2021.635645

1 INTRODUCTION

Fluorescence lifetime imaging (FLIM) has become a versatile and powerful analytical tool for biomedical applications. Compared with fluorescence intensity imaging, FLIM is not only less susceptible to experimental artifacts in excitation/detection setups, optical paths, or fluorophore concentrations, but can also provide abundant cellular information [1–4]. FLIM offers a unique route for probing and visualizing intracellular physical parameters such as temperature, pH, O_2, and ion

concentrations, and it can be promising for cancer diagnosis [5–9]. Furthermore, in combination with Föster resonance energy transfer (FRET) techniques, FLIM-FRET techniques are excellent tools for studying protein-protein interactions, cellular metabolisms, and conformational changes of proteins in living cells [10–12].

Measurements of fluorescence lifetimes can be carried out either directly in the time domain or indirectly in the frequency domain. In particular, time-correlated single-photon counting (TCSPC) has become the gold standard. It is prevailing among scientific communities for its abilities to offer better temporal resolution and signal-to-noize ratio (SNR) performances [13, 14]. A typical TCSPC FLIM system has an ultrafast pulse laser to excite the specimens and a single photon detector, either a photomultiplier tube (PMT) or a single-photon avalanche diode (SPAD), and a time-to-digital converter (TDC) to time-tag captured photons. By repeating this process, a temporal decay histogram can be built. The fluorescence decay measured in the time domain can be described by a sum of multiexponential decays [1]:

$$f(t) = \sum_{i=1}^{n} \alpha_i e^{-t/\tau_i} + \varepsilon (t \geq 0) \tag{1}$$

where *f(t)* is the total fluorescence decay with *n* different exponential components. τ_i and α_i are the lifetime and corresponding fractional weight of the *ith* components, respectively. The sum of all fractional values, a1 + a2 +. . ., is normalized to 1 and ε represents the additional noise. However, since the duration of the excitation pulse and the temporal resolution of the TCSPC system cannot be ignored, the instrument response function (IRF) of the detection system should be considered. Therefore, the measured decay histogram *y(t)* is not the true fluorescence decay profile, *f(t)*, of the specimens under inspection. Instead, it is *f(t)* convolved with the IRF, *i(t)*.

$$y(t) = f(t) * i(t) = \int_{\tau=0}^{t} f(\tau)\, i(t-\tau) d\tau \tag{2}$$

The IRF is usually characterized by its full width at half maximum (FWHM), typically in several hundred picoseconds. It is a function of the uncertainties contributed from the laser excitation, the detector, and the TCSPC. To compensate the IRF and recover *f(t)*, the IRF of the system needs to be measured in advance. And the fluorescence lifetimes of specimens are retrieved by the iterative deconvolution of a pre-defined single or multiple decay model with the measured IRF using nonlinear least-squares deconvolution (NLSD) methods. The result is compared with the recorded decay profile until the residual error is sufficiently small [14].

Ideally, the IRF of the system can be measured using a sample with an ultrashort lifetime [15]. In real FLIM systems, the samples can be dyes with a fluorescence lifetime about tens of picoseconds such as Erythrosine B, pinacyanol iodide, or Allura Red [16–19]. However, the sample lifetime is comparable to the temporal resolution of the TCSPC system. The measured IRF using these samples have a pronounced effect on the measurement of specimens like NAD(P)H, which has multiexponential decays with short lifetime components. In real experiments, the IRF signal is often hard to be detected because the quantum yield of fast decay fluorophores is low. Another drawback is that the spectral ranges of the dyes are limited. It is reported that the emission spectra of dyes with short fluorescence lifetimes only exist at the range larger than about 525 nm [20]. For example, the emission spectrum of pinacyanol iodide starts from 550 nm, and that of Allura Red is from 550 nm to 750 nm [16, 19]. No dye has been found with an emission spectrum covering all visible wavelengths. Therefore, it is difficult to find suitable dyes for every spectra window of interest. For a two-photon FLIM system, some other IRF measurement techniques based on Hyper-Rayleigh scattering (HRS) or second harmonic generation (SHG) have been proposed [21–23]. For example, the plasmon-enhanced gold luminescence can yield a wide-range ultrafast second-harmonic HRS signal, which can be used as a calibration sample for IRF measurements for a multiphoton FLIM system [22]. The second harmonic signal generated on the surface of urea crystals, potassium dihydrogen phosphate crystals or collagen fibers is also widely applied to measure the IRF [23]. However, there are still many restrictions that limit their performances. The HRS or SHG signals are easily corrupted by many artificial reflected or scattered signals in optical systems within the instrument.

Furthermore, the wavelengths of both HRS and SHG signals are only half of the excitation wavelength. Emission filters are required to ensure that signals are detected. For a multispectral FLIM system with multiple detectors, the situation becomes much more complex as the whole optical path should be rearranged to allow all detectors to detect signals effectively. Strictly speaking, the entire experimental setup should exactly keep the same with that for fluorescence lifetime measurements, or the measured IRF would be inaccurate. But this is difficult or impossible for many practical FLIM systems. Additionally, some detectors, especially for SPAD, have a wavelength-dependent temporal response known as the color effect [1]. In this case, the HRS or SHG signals cannot be used as the IRF should be measured within the same spectra with the fluorescence signals.

Measurements of IRF increase experimental complexity and burden. What is worse, for some clinic or *in-vivo* FLIM-based applications, the IRF cannot be measured. Hence, it is desirable to directly extract the IRF information from the recorded decay profiles without extra measurements. One method uses synthetic gaussian or single exponential decay function to approximate to IRF by adjusting its width and position to give the best fit to the fluorescence decay signal. Such a method shows good precision and a wide dynamic range that can resolve lifetimes close to the FWHM of the IRF. However, one critical drawback for TCSPC FLIM is time-consuming curve-fitting analysis. It becomes worse for the synthetic IRF due to an extra fitting and optimization to determine the synthetic function pixel by pixel. Another method uses an automatic synthetic IRF or differential synthetic IRF, widely adopted in commercial FLIM data analysis software, e.g., SPCImage (Becker and Hickl, Berlin, Germany). The calculation procedure of such a synthetic IRF can be divided into two steps: 1) the rising edge of the recorded decay profile is fitted with a

suitable function $R(t)$; 2) the synthetic IRF is then calculated as $dR(t)/dt$ [24]. The synthetic IRF has been proved to yield precise fitting results in a deconvolution procedure. Nevertheless, the dynamic range of the synthetic IRF is limited. To obtain acceptable fitting results, the lifetimes of fluorescence signals should be several times longer than the FWHM of the IRF; otherwise, the analysis will be heavily biased. In this work, we proposed a new strategy to generate synthetic IRFs. This newly proposed synthetic IRF is directly extracted from the recorded summed decay histogram of all pixels, which has advantages: a broader dynamic range and higher accuracy. Bi-exponential fluorescence decay models were used in deconvolution procedures for more general FLIM-FRET applications. For better quantitively evaluations, simulated data was analyzed using a nonlinear least square deconvolution algorithm. Moreover, we also examined the fast deconvolution method's deconvolution performance based on the Laguerre expansion with the proposed synthetic IRF. The real experimental FLIM-FRET data obtained from the two-photon FLIM system were further analyzed and compared using different automatic synthetic IRFs.

2 THEORY AND METHOD

For simplification, considering a single exponential decay $f(t) = e^{-t/\tau}$. In order to evaluate $i(t)$ from $y(t)$, one can obtain the equation by performing both sides of **Eq. 2** with the *Laplace* transform:

$$I(s) = Y(s)/F(s) = sY(s) + \frac{1}{\tau}Y(s) \tag{3}$$

where $Y(s)$, $F(s)$, and $I(s)$ are the Laplace transform pairs of $y(t)$, $f(t)$, and $i(t)$, respectively. s is a complex-valued number. By performing the inverse *Laplace* transform on **Eq. 3**, The temporal IRF $i(t)$ is then expressed as

$$i(t) = \frac{dy(t)}{dt} + \frac{1}{\tau}y(t) \tag{4}$$

If the lifetime is large enough, the second item on the right side of **Eq. 4** can be neglected, and the IRF can be directly estimated from the measured decay. This only holds for decay components with lifetimes much larger than the FWHM of IRF. However, if the lifetime is close to the FWHM of IRF, the estimated IRF is significantly shortened, which biases the calculated lifetimes toward longer values. As for multiexponential decays, since the overall decay is the linear combination of single exponential decays described in **Eq. 1**, the conclusion is also suitable for this situation. Thus, a compensation method needs to be proposed to extend the applied range of a synthetic IRF.

A series of noiseless decay curves with different lifetimes and their corresponding synthetic IRFs were analyzed to investigate the effect of a fast decay component on the synthetic IRF. A Gaussian function approximates the IRF with a typical FWHM, w = 300 ps, referred to as "the true IRF", $i_0(t)$. The measured decays were then generated by convolving single exponential decays with $i_0(t)$ with 256 time-bins over a range of 10 ns. The synthetic IRF $i_s(t)$ was obtained by calculating the measured decays' difference and setting the negative values to zero. **Figure 1A** shows the measured decays with three different lifetimes and their corresponding synthetic IRFs ($i_s(t)$). It is evident that as the lifetime τ increases, the difference between $i_s(t)$ and $i_0(t)$ diminishes as **Eq. 4** suggests. On the contrary, when τ is approximate to w, for example, $\tau = 2w$, the FWHM of $i_s(t)$ is noticeably smaller than that of $i_0(t)$. The results agree well with the above theoretical analysis. Another essential feature is that the fast decay components have more influence on the descending edge of the $i_s(t)$, which accounts for the significant contribution to the decrement of the FWHM in $i_s(t)$. For a smaller τ, the descending edge of $i_s(t)$ has a steeper slope. On the contrary, the rising edge almost keeps unchanged as τ changes from $2w$ to $10w$. To compensate for the influence of the fast decay component, one possible approach is to use the mirror symmetry of the rising edge to replace the descending edge. The new synthetic IRF can be then referred to as the mirror-symmetric synthetic IRF and denoted by $i_m(t)$, which is calculated by

$$i_m(t) = \frac{dy}{dt}u(t_0 - t) + \frac{dy(t_0 - t)}{dt}u(t - t_0) \tag{5}$$

where t_0 is the peak position of the $i_s(t)$ and $u(t)$ is the step function. **Figure 1B** shows the relative error of FWHM. The relative error is defined as $|\ w_i - w|/w \times 100$ where w_i is the FWHM of $i_s(t)$ or $i_m(t)$. From **Figure 1B**, the error of $i_s(t)$ shows an exponential increase when τ/w moves toward 1. In contrast, $i_m(t)$ offers better performance. The error is much smaller than that of $i_s(t)$ within the whole dynamic range. Even when the lifetime is the same as the FWHM of the IRF ($\tau = w$), the error is still less than 10%. The precise evaluation of the IRF leads to better fitting results in the deconvolution procedure. Moreover, the dynamic range of the proposed IRF can be extended for faster decay components with a lifetime close to the FWHM of the IRF.

3 SIMULATIONS ON FLUORESCENCE LIFETIME IMAGING IMAGES

To compare the deconvolution performances of the two synthetic IRFs $i_s(t)$ and $i_m(t)$, both synthetic IRFs were tested with simulated TCSPC data. It is possible to calculate the bias accurately, and standard deviation since all simulated decays' parameters are already known. As shown in **Eqs 1**, **2**, different synthetic IRFs are applied in the deconvolution procedure of TCSPC data with a various number of decay components. Here a bi-exponential decay with fast and slow decay components is considered. A bi-exponential decay model has broad applications and can be used to describe the quenched and unquenched states of fluorophores, the decays of endogenous fluorophores, and FRET donors, to name just a few [12]. A bi-exponential decay model is defined as

$$f(t) = ae^{-t/\tau_1} + (1 - a)e^{-t/\tau_2} \tag{6}$$

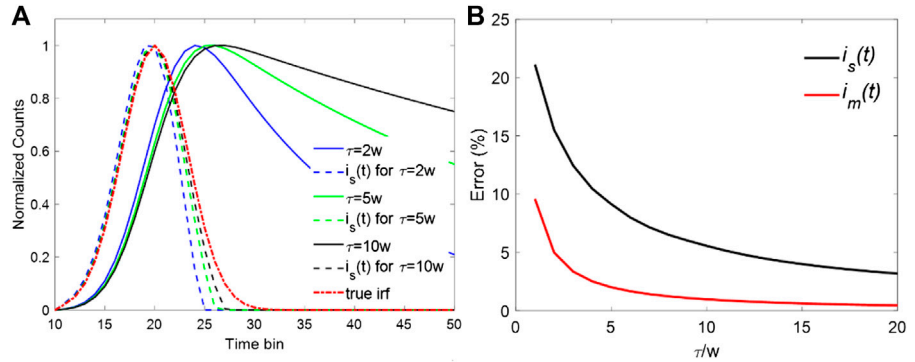

FIGURE 1 | (A) Decay curves with different lifetimes and their synthetic IRFs. **(B)** Errors for i_s(t) and i_m(t) when τ/w is changing from 1 to 10.

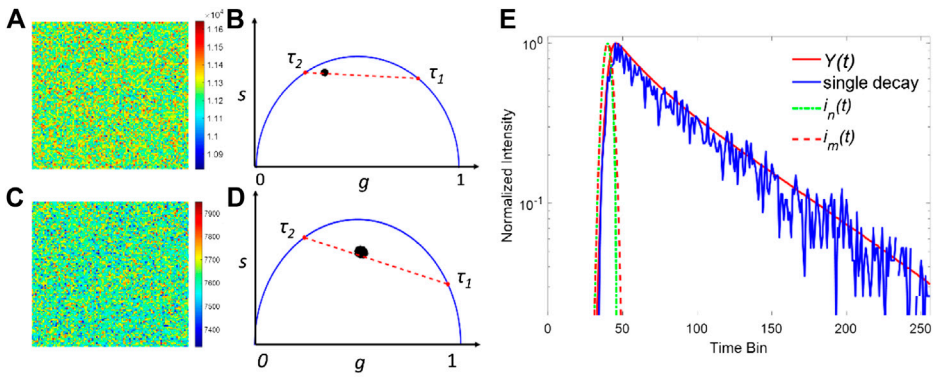

FIGURE 2 | Simulated FILM images with $a = 0.6$, $\tau_1 = 0.8$ ns, $\tau_2 = 2.8$ ns, and $N_c = 10{,}000$ for **(A)** and $a = 0.2$, $\tau_1 = 0.4$ ns, $\tau_2 = 2.8$, and $N_c = 5000$ for **(C)**. **(B,D)** are the corresponding phasor plots of **(A,C)**. **(E)** Normalized intensity plots for *Y(t)* and the single decay in a pixel in **(A)**. Generated synthetic IRFs using the total decay are depicted in dash lines.

where τ_1 and τ_2 are the two different lifetimes and a is the proportion ($0 < a < 1$). The synthetic measured decays can then be generated by convolving $f(t)$ and the pre-defined real IRF $i_r(t)$

$$y(t_m) = \sum_{k=0}^{m} i_r(t_m - t_k) f(t_k) + \varepsilon_m \qquad m = 1, 2, \ldots, 256 \qquad (7)$$

Here the observation window is $T = 10$ ns with 256 time-channels, and ε is the additive Poisson noise. $i_r(t)$ has a Gaussian profile with $w = 300$ ps. In the simulations, a series of TCSPC FLIM images with 100×100 pixels were generated, and the total photon count per pixel within the observation window was assumed to be N_c. τ_2 is the longer lifetime and fixed at 2.8 ns, whereas τ_1 is a short lifetime varying from 0.2 to 1.0 ns. The proportion a ranges from 0.2 to 0.8 with a 0.2 step interval. **Figures 2A,C** show two examples of the simulated FLIM images' intensity map. The parameters in (a) and (b) are $a = 0.4$, $\tau_1 = 0.8$ ns, $\tau_2 = 2.8$ ns, $N_c = 10{,}000$ and $a = 0.8$, $\tau_1 = 0.4$ ns, $\tau_2 = 2.8$ ns, $N_c = 5000$, respectively. Due to the Poisson noise, the intensity of each pixel is slightly different and fluctuated around N_c. The corresponding phasor plots of (a) and (c) are shown in (b) and (d), respectively. In the phasor plots, the real and imaginary parts of the *Fourier* transform of the decay profile correspond to the horizontal and vertical coordinates, respectively. And the fluorescence decay detected in each pixel can be projected to a single point on a phasor plot [25–27]. In **Figures 2B,D**, the projected point of a single exponential decay is located on the semicircle, whereas that of a bi-exponential is located on the straight line between two different lifetimes. For a FLIM image with a relative lower N_c, the points are spread within a larger area, indicating that the noise has a pronounced effect on the decay profiles. The traditional method to estimate IRF is computationally complicated and inaccurate because the peak position varies due to the noise and jitter. Here, we propose a new approach to extract the IRF based on the measured FLIM images obtained by a single-channel scanning sensor: we estimated the IRF by summing all pixels' histograms together. Since the SNR of the Poisson noise is proportional to the photon count, the total decay can be regarded as a noise-free decay curve and is used for calculating the synthetic IRF. As shown in **Figure 2E**, the summed decay of all pixels, $Y(t)$, and a decay in a pixel in

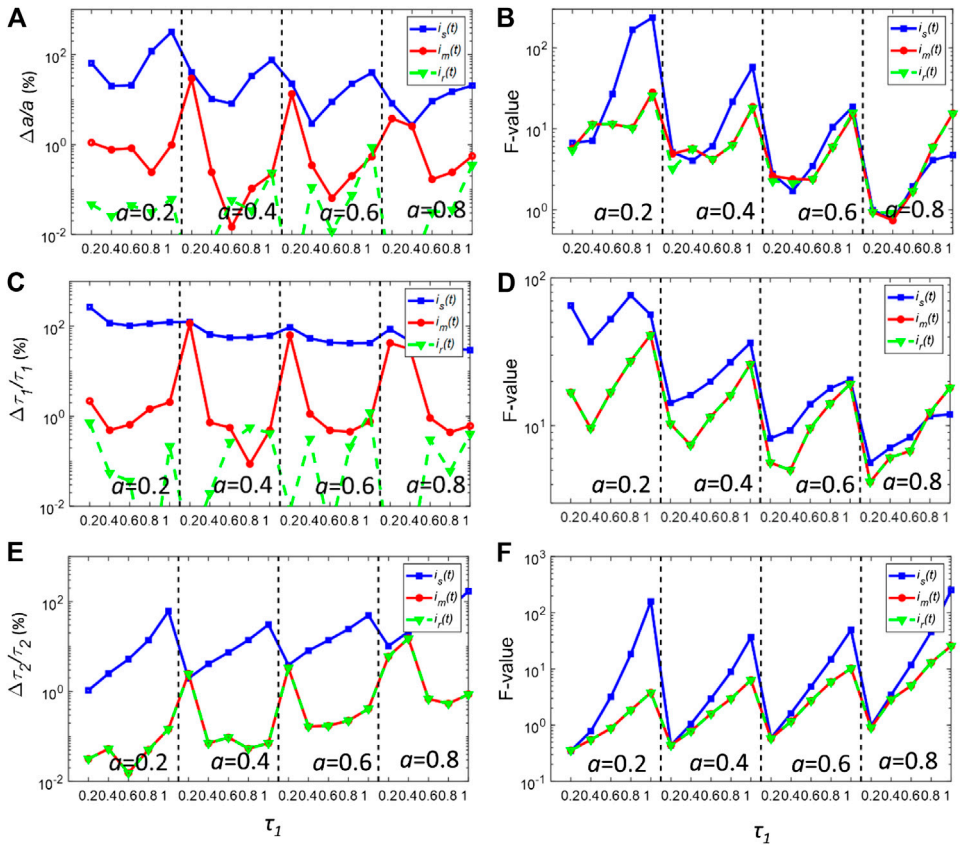

FIGURE 3 | (A,C,E) normalized bias plots for a, τ_1 and τ_2 when $N_c = 10^6$. The corresponding F-value plots are depicted in **(B,D,F)**.

Figure 2A are presented. Compared to a single decay curve, the noise has a negligible effect in $Y(t)$. The two synthetic IRFs were then obtained from $Y(t)$ and used for the deconvolution in each pixel.

Firstly, the nonlinear least-squares deconvolution (NLSD) based on the Levenberg-Marquardt algorithm was applied for recovering the parameters of the decays in **Eq. 6**. **Figures 3A,C,E** show the bias plots ($\Delta a/a$, $\Delta\tau_1/\tau_1$ and $\Delta\tau_2/\tau_2$) of the deconvolution fitting results using $i_s(t)$ and $i_m(t)$ with $N_c = 10^6$. For better comparing $i_s(t)$ and $i_m(t)$, the photon counts were intendedly set to a high value so that the decay curves are less affected by noise. As a reference, a, τ_1 *and* τ_2 were also calculated using the true IRF, $i_r(t)$, for each pixel. The calculated a, τ_1 and τ_2 using $i_s(t)$ have a larger bias within the whole dynamic range. When using $i_s(t)$, $\Delta a/a$ is generally larger than 10% and even reaches 100% when τ_1 is closed to 0.2 or 1 ns. The situation is worse for τ_1, where $\Delta\tau_1/\tau_1$ is around 100% for all cases, indicating that $i_s(t)$ cannot be used for resolving τ_1. $i_s(t)$ also failed to estimate τ_2 when τ_1 is closed to 1ns. In contrast, $\Delta a/a$, $\Delta\tau_1/\tau_1$ and $\Delta\tau_2/\tau_2$ are generally less than 1% using $i_r(t)$. As for $i_m(t)$, the biases are significantly reduced. The bias for all three parameters is lower than that of $i_r(t)$. In particular, the bias of τ_2 for $i_m(t)$ is the same as that of $i_r(t)$.

Figures 3B,D,E show the corresponding precision F-value = $(\sigma g/g)\cdot N_c^{0.5}$ ($g = a$, τ_1, or τ_2) plots for (a) (c) and (e), respectively, where σg is the standard deviation of g [28, 29]. For the ideal condition, $F = 1$. For most realistic FLIM analysis, $F >> 1$. The F-values for a, τ_1 and τ_2 using $i_s(t)$ are in general larger than those using $i_m(t)$ or $i_r(t)$. Surprisingly, the F-values for $i_m(t)$ and $i_r(t)$ are nearly the same throughout the whole dynamic range. It also shows that using $i_m(t)$ instead of $i_s(t)$, the instability effect of the synthetic IRF on the deconvolution procedure can be eliminated.

The deconvolution performances of $i_s(t)$ and $i_m(t)$ under relatively low photon counts were also assessed. For many applications such as real-time FLIM imaging for investigating cell dynamics or high-throughput screening, the acquisition time is usually kept low, resulting in low photon counts in pixels. **Figures 4A–F** show the bias, and F-value plots for simulated fluorescence decays with $N_c = 5000$ in each pixel. In this case, the noise considerably distorts the decay curve. As shown in **Figures 4A,C,E**, all three IRFs yield worse bias performances compared with those shown in **Figure 3**. Also, the gaps between the bias plots for all three parameters decrease, showing that in low photon counts, the deconvolution procedure becomes insensitive to the differences between IRFs. Nevertheless, $i_m(t)$ still shows better performances to resolve τ_2 when τ_1 is smaller than 1 ns. For determining τ_2, $i_m(t)$ also yields similar performances with $i_r(t)$. Moreover, $i_m(t)$ has similar precision performances with $i_r(t)$, showing smaller F-values for all variables

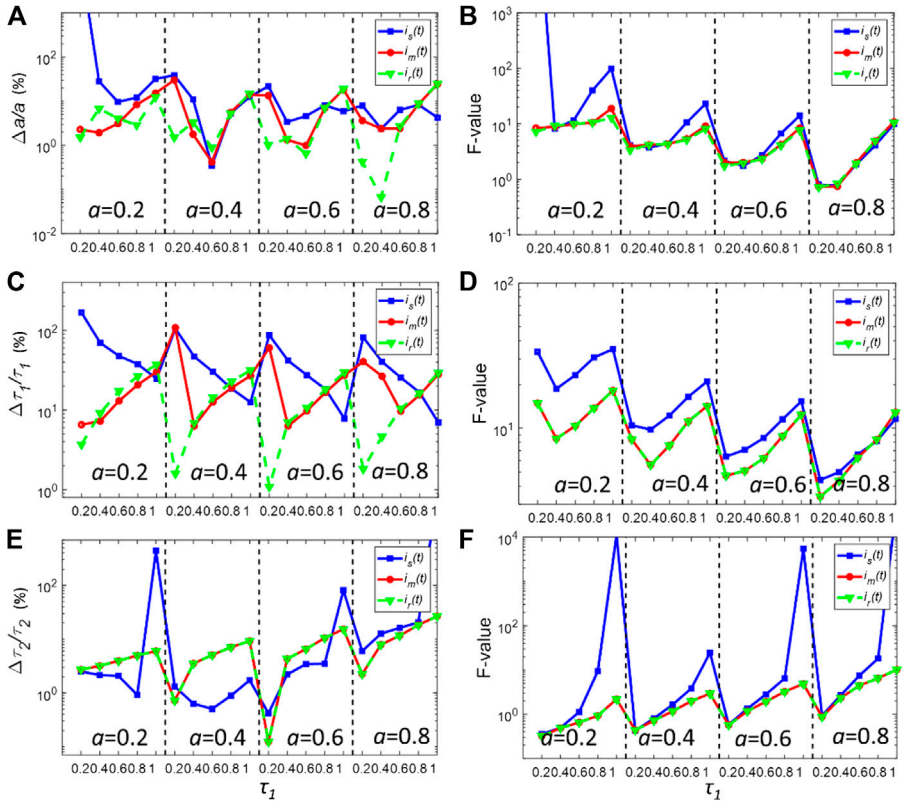

FIGURE 4 | (A,C,E) Normalized bias plots for a, τ_1 and τ_2 when N_c = 5000. The corresponding *F*-value plots are depicted in **(B,D,F)**.

compared with those of $i_s(t)$. On the other hand, $i_s(t)$ can yield an extremely large *F*-value for resolving τ_2. Therefore, it demonstrates that $i_m(t)$ can provide a better estimation of the true IRF.

Although NLSD fitting routines have been widely used for FLIM analysis, they still have intrinsic limitations. They are usually time-consuming and computationally intensive. Moreover, they are prone to overfitting problems when the fluorescence signal is heavily contaminated by noise. An alternative fast least-squares deconvolution based on Laguerre expansion (LSD-LE) was recently developed [30–34]. LSD-LE has been proven to be a robust and effective method showing much faster deconvolution speed than traditional methods. It also shows superior sensitivity in disease diagnoses. In brief, **Eqs. 2**, **6** can be rewritten in discrete forms ;

$$y(k) = \sum_{i=1}^{k} i(k-i)f(i) + \varepsilon(k),\ k = 1,\ 2,\ \ldots, N \tag{8}$$

$$f(k) = ae^{-(k-1)t_s/\tau_1} + (1-a)e^{-(k-1)t_s/\tau_2} \tag{9}$$

where t_s is the time bin width. LSD-LE expands the fluorescence single $f(t)$ onto an ordered set of orthonormal Laguerre basis functions $b_l(k;\ \alpha)$ as:

$$\widehat{f}(k) = \sum_{l=0}^{L-1} c_l b_l(k;\alpha) \tag{10}$$

where L is the Laguerre dimension and α ($0<\alpha<1$) is the scale parameter of LBF, and c_l is the *lth* expansion coefficient. The *lth* discrete LBF is defined as:

$$b_l(k;\alpha) = \alpha^{(k-1)}(1-\alpha)^{1/2}\sum_{l=0}^{L-1}(-1)^i\binom{k}{i}\cdot\binom{l}{i}\alpha^{1-i}(1-a)^i,$$
$$l = 0,\ 1,\ \ldots, L-1 \tag{11}$$

Under the Laguerre expansion, **Eq. 9** becomes:

$$y(k) = \sum_{i=0}^{k}\sum_{l=0}^{L-1} c_l i(k-i)b_l(i;\alpha) + \varepsilon_k \tag{12}$$

Equation 12 is the Laguerre expansion form of the fluorescence signal, which can be linearly parameterized by the expansion coefficient c_l. Also, the normalized sum of squared errors (NSSE) is defined as:

$$NSSE = \left\|\widehat{f} - f\right\|_2 \Big/ \left\|f\right\|_2^2 \tag{13}$$

To obtain the expansion coefficient c_l, the expansion of the fluorescence signal with LBFs becomes a fitting problem where NSSE reaches its minimal value. We would like to assess how i_s(t) behaves in **Eq. 13**. Therefore, the constrained LSD-LE is applied to recover the decay parameters using synthetic IRFs and the true

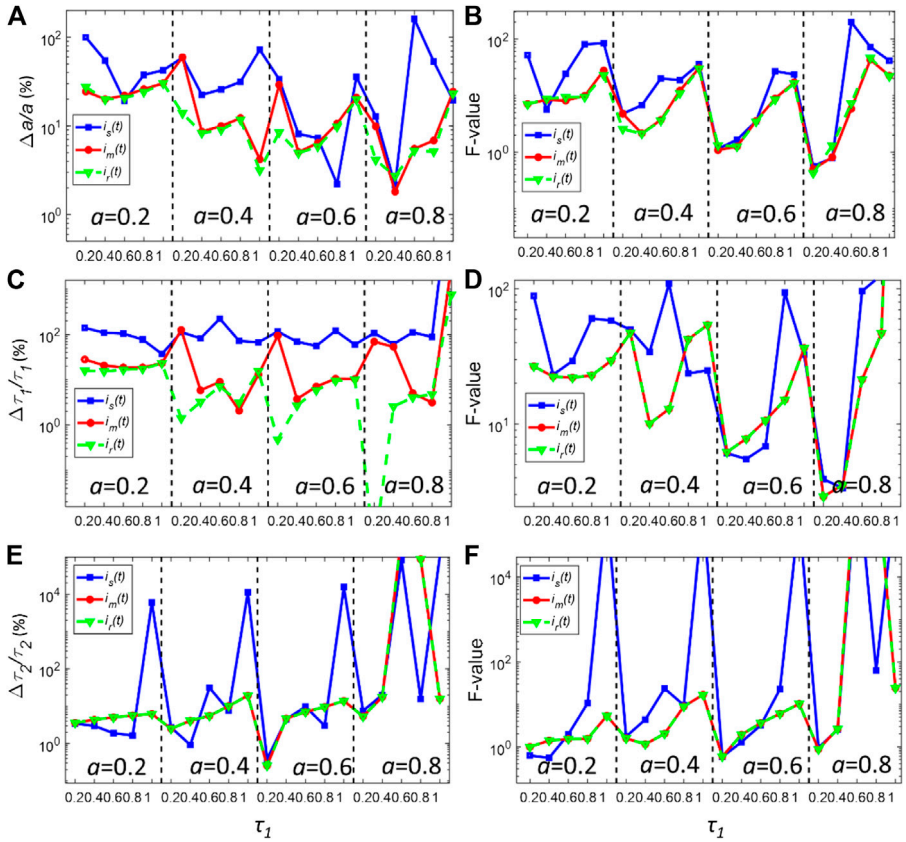

FIGURE 5 | (A,C,E) Normalized bias plots for a, τ_1 and τ_2 when N_c = 5000 using LSD-LE method with (α, L) = (0.92,16). The corresponding F-value plots are depicted in **(B,D,F)**.

IRF [30]. The LBF parameters were set as the optimized value as (α, L) = (0.92,16) [32]. The total photon counts in each pixel are N_c = 5000. The normalized bias and F-value plots are shown in **Figures 5A–F**. Not surprisingly, $i_s(t)$ still has the worse performance (larger bias and F-value). It is unable to estimate τ_1 robustly. Meanwhile, it fails to recover τ_2 when τ_1 approaches 1 ns. $i_m(t)$ has almost the same deconvolution results with the true IRF $i_r(t)$ in terms of the bias and F-value. It further demonstrates that compensating the descending edge of synthetic IRF is an effective way to improve the precision and the applied lifetime range of the synthetic IRF.

4 EXPERIMENTAL FLUORESCENCE LIFETIME IMAGING-FÖSTER RESONANCE ENERGY TRANSFER DATA ANALYSIS

To evaluate the performances of the new automatic synthetic IRF in real experiments, FLIM-FRET imaging data of tSA201 cells transfected with eCFP-eYFP (enhanced green fluorescent protein and enhanced cyan fluorescence protein) pair were investigated. FLIM-FRET is a well-established technique for studying protein-protein interactions within a nanometer scale. FRET refers to the non-radiative energy transfer between an excited fluorescent molecule (the donor) and a non-excited different fluorescent molecule (the acceptor) when they are close, which leads to the shortening the donor lifetime. The eCFP-eYFP pair is the most widely used donor-acceptor pair in various *in-vitro* or *in-vivo* FRET applications. The lifetimes of the eCFP-eYFP pair with/without FRET are known priorly, thus serving as a reference to evaluate the FRET between interacting proteins. Here the FLIM-FRET technique was used to assess the proximity of interacting proteins.

A two-photon FLIM system including a confocal microscope (LSM 510, Carl Zeiss), a femtosecond Ti: sapphire laser modulated source (Chameleon, Coherent) with excitation wavelength 800 nm, and the TCSPC acquisition system (SPC-830, Becker and Hickl GmbH) was used to obtain IRF and FLIM data. The exciting laser source's duration is less than 200 fs, and the repetition rate is 80 MHz. The bin width of the TCSPC is 0.039 ns, and each measured histogram contains 256 time bins. Firstly, the IRF of the system was measured using the SHG signal from the urea ($(NH_2)_2CO$) microcrystal. A thin layer of urea crystal obtained from air-dry concentrated urea droplet was placed on a microscope slide and was covered by a coverslip. The emitted SHG signal was then collected by a photomultiplier (PCM-100, Becker & Hickl GmbH) after passing through a ×63 water-immersion objective lens (N.A. = 1.0) and a

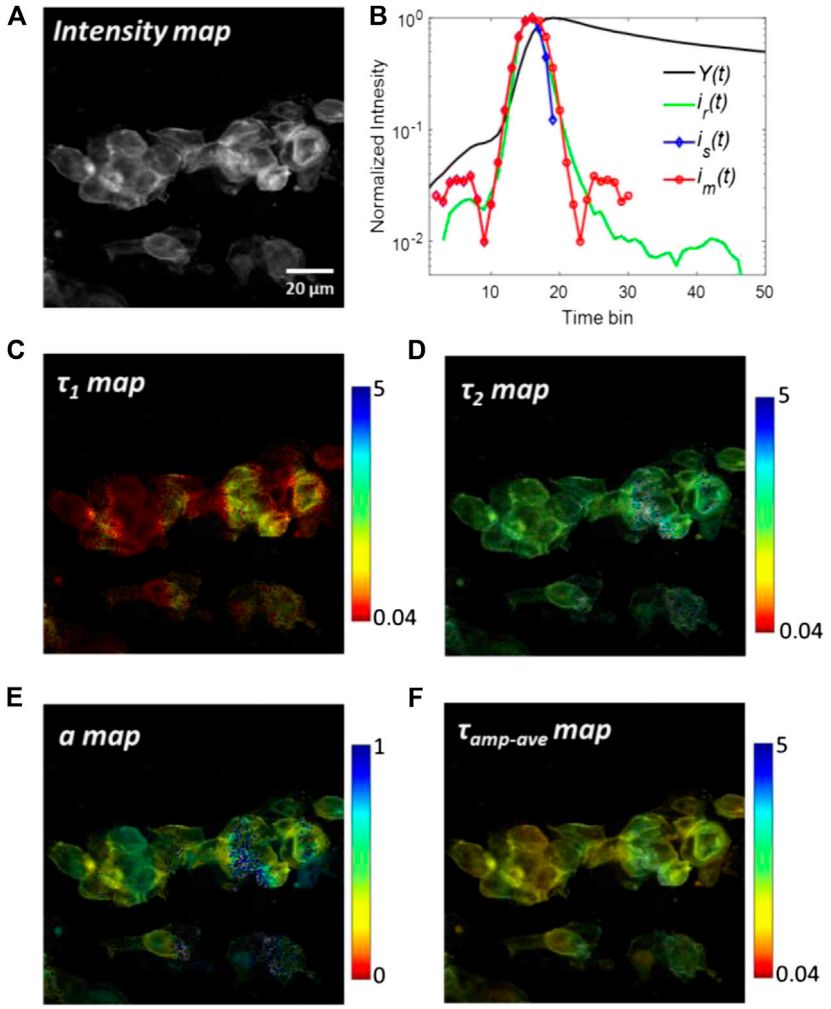

FIGURE 6 | Analyzed results of tSA201 cells with co-transfected eYFP. **(A)** Grey-scale fluorescence intensity image. **(B)** Measured IRF, $i_r(t)$, and the summed histogram, $Y(t)$, are plotted with a green and black solid line, respectively. $i_r(t)$ and $i_m(t)$ are shown in dash lines with markers. **(C–F)** τ_1, τ_2, a, and $\tau_{amp\text{-}ave}$ images using the experimental IRF ($i_r(t)$) and constrained LSD-LE method with (α, L) = (0.92,16).

650 nm short-pass filter. The emitted fluorescence signals from the cell samples were also collected using the same system except that a 535–590 nm bandpass filter was used.

The tSA201 cells were grown to 60% confluence on 13 mm glass coverslips located in 24 well plates. The cells were transfected with $hP2Y_{12}$-eCFP or co-transfected with $hP2Y_{12}$-eCFP and $hP2Y_1$-eYFP. After 48 h of transfection, the cells on the coverslips were washed once gently with PBS followed by fixation with ice-cold methanol for 10 min at room temperature. Then they were washed 3 times with PBS before they were mounted on to glass microscope slides with Mowiol. The microscope slides were then stored in the dark at room temperature overnight to allow the coverslips to dry, then held at 4°C for later use.

The analyzed results of tSA201cells with transfected co-transfected eYFP are shown in **Figure 6**. The eYFPs work as acceptors and their lifetimes increase when FRET occurs. **Figure 6A** shows the grey-scale fluorescence intensity image. Although the fluorescence intensity can be an indicator of FRET, it is susceptible to photobleaching and spectral cross-talk in FRET pairs, thus greatly limiting its application range in real scenarios. From the intensity image, it is difficult to evaluate the FRET among cells. The summed histogram $Y(t)$ of all pixels and the measured IRF $i_r(t)$ are shown in **Figure 6B**, in which $i_r(t)$ has already been aligned with the rising edge of $Y(t)$. Two synthetic IRFs $i_s(t)$ and $i_m(t)$ derived from $Y(t)$ are shown in lines with markers. The main peaks of synthetic IRFs are well agreed with the measured IRF. Also, the pre-pulse in $i_r(t)$ is slightly smaller than that in synthetic IRFs. The descending edge of $i_s(t)$ is quite short in the log-scale plot because the negative part of $i_s(t)$ is truncated to zero. This problem is mitigated by replacing the descending edge by the rising edge in $i_m(t)$. The FWHM of $i_m(t)$ is nearly the same with $i_r(t)$. It is worth noting that there are many complex sub-structures of after-pulse in $i_r(t)$, caused by ion-feedback in the PMT. However, the amplitudes of these after-pulses are two orders in the magnitude smaller than the peak of $i_r(t)$; therefore, the effect of these after-pulses can be neglected.

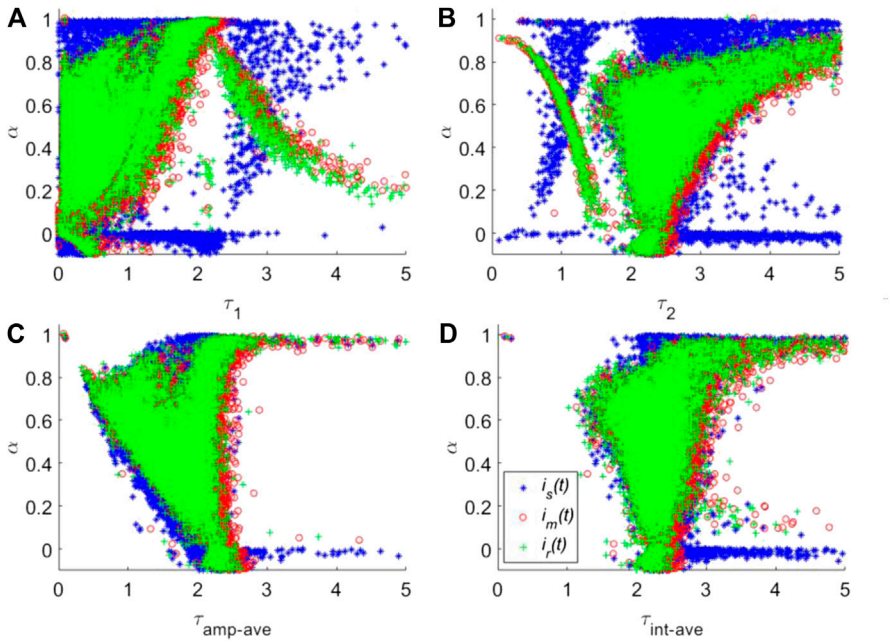

FIGURE 7 | Calculated τ_1 **(A)**, τ_2 **(B)**, $\tau_{amp\text{-}ave}$ **(C)** and $\tau_{int\text{-}ave}$ **(D)** vs. α using three different IRFs, $i_s(t)$, $i_m(t)$ and $i_r(t)$.

Figures 6C–F shows τ_1, τ_2, a and $\tau_{amp\text{-}ave}$ images for the bi-exponential model using the experimental IRF ($i_r(t)$) and constrained LSD-LE method with (α, L) = (0.92,16). The $\tau_{amp\text{-}ave}$ is the amplitude-average lifetime defined as $\tau_{amp\_ave} = a\tau_1 + (1\text{-}a)\tau_2$. The shorter lifetime τ_1 and longer lifetime τ_2 are depicted in **Figures 6C,D**, respectively. A better contrast can be observed form these two figures. The image of the proportion a is shown in **Figure 6E**, which is typically used to calculate the FRET efficiency. One remarkable phenomenon that can be observed from the image is the proportion a at the edges of the cells is relatively smaller than the surrounding, which is attributed to the lifetime of eYFP becoming longer due to a higher FRET efficiency. As a comparison, **Figure 6F** shows the amplitude-weighted average lifetime, from which we can observe the changed lifetime in the range of the whole cells.

To compare the deconvolution performances of $i_s(t)$ and $i_m(t)$ with that of $i_r(t)$, the corresponding lifetime images for two automatic synthetic IRFs were calculated. For a better comparison, the scatter plots of τ_1, τ_2, and two kinds of average lifetimes named amplitude-weighted average lifetime ($\tau_{amp\text{-}ave}$) and intensity-weighted average lifetime ($\tau_{int\text{-}ave}$) vs. α are shown in **Figures 7A–D**, respectively. $\tau_{int\text{-}ave}$ is also taken into consideration, defined as $\tau_{int-ave} = [a\tau_1^2 + (1-a)\tau_2^2]/[a\tau_1 + (1-a)\tau_2]$. For τ_1 and τ_2 in **Figures 7A,B**, it is easy to see that the lifetime distributions obtained from $i_s(t)$ (dots with blue "+" marker) are significantly different from that of $i_r(t)$ (green "." marker). The clusters obtained by $i_m(t)$ and $i_s(t)$ are discernible. It demonstrates that the deconvolution results using $i_s(t)$ can lead to a large bias compared to the results using $i_r(t)$ and a wrong interpretation of the data. For example, for τ_1 with sub-nanosecond lifetime, α should be less than 0.8 according to the $i_r(t)$ deconvolution results. Still, the results using $i_s(t)$ leads to large dots distributions at $\alpha > 0.8$ (top left corner in **Figure 7A**). This problem also happens for τ_2. On the other hand, for the proposed synthetic IRF $i_m(t)$, the cluster shape of the data is almost identical with that of $i_r(t)$, indicating that $i_m(t)$ is more suitable for recovering the real parameters. As for the average lifetimes $\tau_{amp\text{-}ave}$ and $\tau_{int\text{-}ave}$ in **Figures 7C,D**, interestingly, the cluster shapes of three IRFs are similar, but the deviation of the results with $i_s(t)$ from the other two is still noticeable. Compared to the cluster for $i_r(t)$, the overall clusters for $i_s(t)$ have a larger distribution range. Additionally, $i_s(t)$ can yield an obvious artificial cluster at $\alpha = 0$, which is eliminated for $i_m(t)$. Hence, it is safe to prove that $i_m(t)$ shows superior deconvolution performances than $i_s(t)$. It is worth noting that, for lifetimes down to or even smaller than the FWHM of the IRF, for example, the gold nanoparticles used as the biomarkers, both the synthetic IRFs would lead to a large deviation as shown in **Figure 1B**. Therefore, synthetic IRFs are not suitable for deconvolution analysis. Although our synthetic can well approximate the true IRF, it does not consider the pre-pulse and sub-structure after the main peak of IRF. However, both only cause negligible effects in TCSPC measurements because their magnitudes are generally two orders smaller than the main peak.

5 CONCLUSION

In conclusion, we proposed a strategy for obtaining the synthetic IRF of TCSPC based FLIM experiments. Compared to the simple differential synthetic IRF, the dynamic range of the mirror-symmetric synthetic IRF is significantly expanded. Even when the lifetime is close to the FWHM of the system's true IRF, the proposed synthetic IRF can resolve the lifetime with high accuracy. At the same time, the accuracy is also much improved

in the whole dynamic range. The proposed synthetic IRF was also applied to analyze bi-exponential decays with simulated data using both nonlinear least-square deconvolution and Laguerre expansion methods. The results show that the mirror-symmetric synthetic IRF has higher accuracy and a lower standard deviation. Additionally, the proposed synthetic IRF can resolve the more extended lifetime component in the whole dynamic range, unattainable in the simple differential synthetic IRF. We further investigated the proposed synthetic IRF with the real experimental FLIM-FRET data. Both simulated and experimental data show that the proposed synthetic IRF has superior performance than traditional synthetic IRF.

DATA AVAILABILITY STATEMENT

The raw data supporting the conclusions of this article will be made available by the authors, without undue reservation.

AUTHOR CONTRIBUTIONS

DX proposed the conceptualization and wrote the manuscript. MS and MC cultured and prepared the cell samples. NS and YC provided fluorescence lifetime imaging data and analysis. DL provided supervision and manuscript reviewing and editing. All authors reviewed the final manuscript.

FUNDING

The authors would like to acknowledge the Medical Research Scotland (1179-2017), Photon Force, Ltd., and the Engineering and Physical Sciences Research Council (EP/L01596X/1) for supporting this project. Photon Force supports the use of SPAD cameras in our project. The funder was not involved in the study design, collection, analysis, interpretation of data, the writing of this article or the decision to submit it for publication.

REFERENCES

1. Lakowicz JR. *Principles of fluorescence spectroscopy*. Boston, MA: Springer (2006).
2. Datta R, Heaster TM, Sharick JT, Gillette AA, Skala MC. Fluorescence lifetime imaging microscopy: fundamentals and advances in instrumentation, analysis, and applications. *J Biomed Opt* (2020) 25(7):1. doi:10.1117/1.JBO.25.7.071203
3. Suhling K, Hirvonen LM, Levitt JA, Chung P-H, Tregidgo C, Le Marois A, et al. Fluorescence lifetime imaging (FLIM): basic concepts and some recent developments. *Med Photon* (2015) 27:3–40. doi:10.1016/j.medpho.2014.12.001
4. Ntziachristos V. Going deeper than microscopy: the optical imaging Frontier in biology. *Nat Methods* (2010) 7(8):603–14. doi:10.1038/nmeth.1483
5. Bower AJ, Sorrells JE, Li J, Marjanovic M, Barkalifa R, Boppart SA. Tracking metabolic dynamics of apoptosis with high-speed two-photon fluorescence lifetime imaging microscopy. *Biomed* 10(12):6408–21. doi:10.1364/BOE.10.006408
6. Okabe K, Inada N, Gota C, Harada Y, Funatsu T, Uchiyama S. Intracellular temperature mapping with a fluorescent polymeric thermometer and fluorescence lifetime imaging microscopy. *Nat Commun* (2012) 3(1):705. doi:10.1038/ncomms1714
7. Sagolla K, Löhmannsröben HG, Hille C. Time-resolved fluorescence microscopy for quantitative Ca2+ imaging in living cells. *Anal Bioanal Chem* (2013) 405(26):8525–37. doi:10.1007/s00216-013-7290-6
8. Schmitt FJ, Thaa B, Junghans C, Vitali M, Veit M, Friedrich T. eGFP-pHsens as a highly sensitive fluorophore for cellular pH determination by fluorescence lifetime imaging microscopy (FLIM). *Biochim Biophys Acta Bioenerg* (2014) 1837(9):1581–93. doi:10.1016/j.bbabio.2014.04.003
9. Lukina MM, Shimolina LV, Kiselev NM, Zagainov VE, Komarov DV, Zagayanova EV, et al. Interrogation of tumor metabolism in tissue samples *ex vivo* using fluorescence lifetime imaging of NAD(P)H. *Methods Appl Fluoresc* (2020) 8(1):014002. doi:10.1088/2050-6120/ab4ed8
10. Shivalingam A, Izquierdo MA, Le Marois A, Vyšniauskas A, Suhling K, Kuimova MK, et al. The interactions between a small molecule and G-quadruplexes are visualized by fluorescence lifetime imaging microscopy. *Nat Commun* (2015) 6(1):8178. doi:10.1038/ncomms9178
11. Tardif C, Nadeau G, Labrecque S, Côté D, Lavoie-Cardinal F. Fluorescence lifetime imaging nanoscopy for measuring Förster resonance energy transfer in cellular nanodomains. *Neurophoton* (2019) 6(1):015002. doi:10.1117/1.nph.6.1.015002
12. Sparks H, Kondo H, Hooper S, Munro I, Kennedy G, Dunsby C, et al. Heterogeneity in tumor chromatin-doxorubicin binding revealed by *in vivo* fluorescence lifetime imaging confocal endomicroscopy. *Nat Commun* (2018) 9(1):2662. doi:10.1038/s41467-018-04820-6
13. Becker W. *Advanced time-correlated single photon counting techniques*. Berlin, Germany: Springer (2005)
14. Becker W. *Advanced time-correlated single photon counting applications*. Berlin, Germany: Springer (2015)
15. Luchowski R, Gryczynski Z, Sarkar P, Borejdo J, Szabelski M, Kapusta P, et al. Instrument response standard in time-resolved fluorescence. *Rev Sci Instrum* (2009) 80(3):033109. doi:10.1063/1.3095677
16. Chib R, Shah S, Gryczynski Z, Fudala R, Borejdo J, Zelent B, et al. Standard reference for instrument response function in fluorescence lifetime measurements in visible and near infrared. *Meas Sci Technol* (2016) 27(2):027001. doi:10.1088/0957-0233/27/2/027001
17. Szabelski M, Ilijev D, Sarkar P, Luchowski R, Gryczynski Z, Kapusta P, et al. Collisional quenching of erythrosine B as a potential reference dye for impulse response function evaluation. *Appl Spectrosc* (2009) 63(3):363–8. doi:10.1366/000370209787598979
18. Szabelski M, Luchowski R, Gryczynski Z, Kapusta P, Ortmann U, Gryczynski I. Evaluation of instrument response functions for lifetime imaging detectors using quenched Rose Bengal solutions. *Chem Phys Lett* (2009) 471(1-3):153–9. doi:10.1016/j.cplett.2009.02.001
19. van Oort B, Amunts A, Borst JW, van Hoek A, Nelson N, van Amerongen H, et al. Picosecond fluorescence of intact and dissolved PSI-LHCI crystals. *Biophys J* (2008) 95(12):5851–61. doi:10.1529/biophysj.108.140467
20. Wagnières GA, Star WM, Wilson BC. *In vivo* fluorescence spectroscopy and imaging for oncological applications. *Photochem Photobiol* (1998) 68(5):603–32. doi:10.1111/j.1751-1097.1998.tb02521.x
21. Habenicht A, Hjelm J, Mukhtar E, Bergström F, Johansson LB-Å. Two-photon excitation and time-resolved fluorescence: I. The proper response function for analysing single-photon counting experiments. *Chem Phys Lett* (2002) 354(5-6):367–75. doi:10.1016/s0009-2614(02)00141-0
22. Talbot CB, Patalay R, Munro I, Warren S, Ratto F, Matteini P, et al. Application of ultrafast gold luminescence to measuring the instrument response function for multispectral multiphoton fluorescence lifetime imaging. *Opt Express* (2011) 19(15):13848–61. doi:10.1364/oe.19.013848
23. *Recording the instrument response function of a multiphoton FLIM system, application note*. Becker & Hickl GmbH (2008). Available from: http://www.becker-hickl.de/pdf/irf-mp04.pdf.
24. Wolfgang B. *The bh TCSPC Handbook*. 8th ed. Available from: https://www.becker-hickl.com/literature/handbooks/the-bh-tcspc-handbook/ (Accessed September 2019).
25. Digman MA, Caiolfa VR, Zamai M, Gratton E. The phasor approach to fluorescence lifetime imaging analysis. *Biophys J* (2008) 94(2):L14–6. doi:10.1529/biophysj.107.120154

26. Ranjit S, Malacrida L, Jameson DM, Gratton E. Fit-free analysis of fluorescence lifetime imaging data using the phasor approach. *Nat Protoc* (2018) 13(9): 1979–2004. doi:10.1038/s41596-018-0026-5
27. Stringari C, Cinquin A, Cinquin O, Digman MA, Donovan PJ, Gratton E. Phasor approach to fluorescence lifetime microscopy distinguishes different metabolic states of germ cells in a live tissue. *Proc Natl Acad Sci USA* (2011) 108(33):13582–7. doi:10.1073/pnas.1108161108
28. Gerritsen HC, Asselbergs MA, Agronskaia AV, Van Sark WG. Fluorescence lifetime imaging in scanning microscopes: acquisition speed, photon economy and lifetime resolution. *J Microsc* (2002) 206(3):218–24. doi:10.1046/j.1365-2818.2002.01031.x
29. Li DD, Ameer-Beg S, Arlt J, Tyndall D, Walker R, Matthews DR, et al. Time-domain fluorescence lifetime imaging techniques suitable for solid-state imaging sensor arrays. *Sensors (Basel)* (2012) 12(5):5650–69. doi:10.3390/s120505650
30. Jo JA, Fang Q, Marcu L. Ultrafast method for the analysis of fluorescence lifetime imaging microscopy data based on the Laguerre expansion technique. *IEEE J Sel Top Quantum Electron* (2005) 11(4):835–45. doi:10.1109/JSTQE.2005.857685
31. Jo JA, Fang Q, Papaioannou T, Marcu L. Fast model-free deconvolution of fluorescence decay for analysis of biological systems. *J Biomed Opt* (2004) 9(4): 743–52. doi:10.1117/1.1752919
32. Liu J, Sun Y, Qi J, Marcu L. A novel method for fast and robust estimation of fluorescence decay dynamics using constrained least-squares deconvolution with Laguerre expansion. *Phys Med Biol* (2012) 57(4):843–65. doi:10.1088/0031-9155/57/4/843
33. Pande P, Jo JA. Automated analysis of fluorescence lifetime imaging microscopy (FLIM) data based on the Laguerre deconvolution method. *IEEE Trans Biomed Eng* (2011) 58(1):172–81. doi:10.1109/TBME.2010.2084086
34. Zhang Y, Chen Y, Chen Y, Li DD. Optimizing Laguerre expansion based deconvolution methods for analysing bi-exponential fluorescence lifetime images. *Opt Express* (2016) 24(13):13894–905. doi:10.1364/OE.24.013894

Conflict of Interest: The authors declare that the research was conducted in the absence of any commercial or financial relationships that could be construed as a potential conflict of interest.

frontiers in Physics

ORIGINAL RESEARCH
published: 27 May 2021
doi: 10.3389/fphy.2021.637123

Single-Cell Biochemical Multiplexing by Multidimensional Phasor Demixing and Spectral Fluorescence Lifetime Imaging Microscopy

Kalina T. Haas[1,2]*, *Maximilian W. Fries*[1], *Ashok R. Venkitaraman*[1] and *Alessandro Esposito*[1]

[1]The Medical Research Council Cancer Unit, University of Cambridge, Cambridge, United Kingdon, [2]Institut Jean-Pierre Bourgin, INRAE, AgroParisTech, Université Paris-Saclay, Versailles, France

Revealing mechanisms underpinning cell function requires understanding the relationship between different biochemical reactions in living cells. However, our capabilities to monitor more than two biochemical reactions in living cells are limited. Therefore, the development of methods for real-time biochemical multiplexing is of fundamental importance. Here, we show that data acquired with multicolor (mcFLIM) or spectrally resolved (sFLIM) fluorescence lifetime imaging can be conveniently described with multidimensional phasor transforms. We demonstrate a computational framework capable of demixing three Forster resonance energy transfer (FRET) probes and quantifying multiplexed biochemical activities in single living cells. We provide a comparison between mcFLIM and sFLIM suggesting that sFLIM might be advantageous for the future development of heavily multiplexed assays. However, mcFLIM—more readily available with commercial systems—can be applied for the concomitant monitoring of three enzymes in living cells without significant losses.

Keywords: sFLIM, FRET biosensors, TCSPC, spectral demixing, biochemical multiplexing

OPEN ACCESS

Edited by:
Klaus Suhling,
King's College London,
United Kingdom

Reviewed by:
Jianming Wen,
Kennesaw State University,
United States
Marc Tramier,
UMR6290 Institut de Genetique et de Developpement de Rennes (IGDR),
France

***Correspondence:**
Kalina T. Haas
kalina.haas@inrae.fr

Specialty section:
This article was submitted to Optics and Photonics, a section of the journal Frontiers in Physics

Received: *02 December 2020*
Accepted: *07 May 2021*
Published: *27 May 2021*

Citation:
Haas KT, Fries MW, Venkitaraman AR and Esposito A (2021) Single-Cell Biochemical Multiplexing by Multidimensional Phasor Demixing and Spectral Fluorescence Lifetime Imaging Microscopy. Front. Phys. 9:637123. doi: 10.3389/fphy.2021.637123

INTRODUCTION

The fluorescence lifetime (τ) is the average time a fluorescent molecule spends in the excited state before returning to the ground state with the emission of a photon [5, 44]. Often, τ depends on the physicochemical characteristics of the environment surrounding the fluorophore but does not depend on the fluorophore concentration; thus, fluorescence lifetime sensing has been applied successfully to probe cell biochemistry (e.g., pH, analyte concentration, enzymatic activities, protein–protein interactions, and conformational changes). Fluorescence lifetime imaging microscopy (FLIM) is commonly used to map cell biochemistry in a quantitative and low-invasive way [18, 28, 45, 46].

Genetically expressed (e.g., using fluorescent proteins) biosensors permit researchers to probe diverse biochemical reactions exploiting the use of Forster resonance energy transfer (FRET). FRET is the non-radiative transfer of energy from a donor fluorophore to an acceptor molecule that can occur when the two molecules are sufficiently close, typically <10 nm [13, 37]. FRET causes a loss in fluorescence intensity (quenching) and a decrease of the donor's fluorescence lifetime, both of which are directly proportional to the fraction of energy transferred from the donor to the acceptor. Thus, FRET can be exploited to quantify interactions at the nanometer scale *via* using a diffraction-limited microscope [75]. This property makes FRET an excellent tool for minimally invasive assays to probe molecular interactions, signal transduction, and biochemical activity in living cells [2, 48].

Historically, the estimation of fluorescence lifetime relied on the iterative fitting of the experimental decays [4, 31] or simple analytical relations between signals integrated in a few time-windows (e.g., [65]). Over the last decade, however, nonparametric data analysis using frequency-domain techniques [20, 33, 41], phasor-based representation [10, 18, 25, 35, 68], and extended phasors [8] have become very popular in the community. This strategy is simple, computationally efficient, and, more importantly, does not require model assumptions (e.g., mono or bi-exponential) that in complex, multiplexing assays might easily break down (e.g., because of background, cross-talks, and spurious signals). This is especially important at the low photon budget we must operate instrumentations to minimize phototoxicity.

With a large palette of fluorescent proteins that can be used to construct FRET biosensors of different colors (from the UV/blue to near infrared [3, 16, 27, 40, 53, 54, 66]), we can monitor multiple signaling events in living cells. Dual FRET biosensing was demonstrated with different experimental configurations and demixing analysis frameworks: multichannel ratiometric detection [1, 30, 57, 67], simultaneous homo-FRET and hetero-FRET detected with time-resolved anisotropy and global analysis [74], and dual-color FRET–FLIM to follow two biosensors using time-domain analysis [17]. However, the simultaneous detection of three and more FRET pairs remains challenging. Previously three-protein interaction was measured using "triple fluorophore" three-way FRET sensing [7, 29, 64, 69].

Recently, we have shown that the rational design of FRET pairs aimed to optimize the utilization of the visible spectrum enables multi-color FLIM (mcFLIM) to multiplex at least three FRET probes with a single excitation laser [27] at the speed and resolution necessary for live cell imaging [71]. The utilization of additional excitation wavelengths and hyperspectral detection might extend this strategy to the integration of a higher number of markers, biosensors, or optogenetic tools [39, 67, 71].

However, computational frameworks for the robust and sensitive multiplexing of FRET are at their infancy, and further work is necessary to improve our multiplexing capabilities. Phasor analysis of time decays has often been applied to quantify FRET for single probes by separating the two states of a typical sensor (low/high FRET) [10, 14, 18, 26, 35, 36, 38, 41, 47, 49, 50, 55, 60, 70, 72, 73]. Similarly, the integration of spectrally resolved FLIM (sFLIM) [34] and multidimensional phasor analysis has been successfully applied to the quantification of single FRET probes [25]. In Fries et al. [27], we have illustrated how to utilize multicolor FLIM and multidimensional phasors for demixing three FRET probes. However, to our knowledge, the demixing of multiple fluorescent species (donor, acceptors, and FRET for several probes simultaneously) has not been sufficiently explored.

In this work, first we briefly illustrate the development of a photon-efficient spectrally resolved FLIM based on off-the-shelf components. Second, we demonstrate the generalization of the NyxSense computational framework which we had first introduced for mcFLIM applications [27]. Most importantly, we provide a detailed comparison of various algorithms aimed to provide efficient dimensionality reduction by multidimensional phasors that can be used for demixing three FRET pairs by spectral FLIM (either multicolor or spectrally resolved FLIM).

We show that phasors of higher dimensionality significantly improve demixing algorithms for both mcFLIM and sFLIM. We demonstrate that while spectrally resolved FLIM could provide advantages in demixing of more than three FRET probes, state-of-the-art fast time-correlated single-photon counting (TCSPC) still attains very high performances with significant implications for future developments of multiplexing time-resolved platforms.

MATERIALS AND METHODS

Microscopy

We have developed a simple spectrally resolved FLIM (sFLIM) setup built with off-the-shelf components, including a 16-channel multi-anode GaAsP photomultiplier tube (PML-16-GASP16, Becker&Hick GmbH) placed at the de-scanned port of a SP5 Leica Confocal Microscope (Leica Microsystems United Kingdom, Ltd.). Spectral dispersion was achieved with a direct vision prism (G331120000, LINOS, GmbH) to provide a simple alignment and low optical losses. Notably, GaAsP photomultiplier tubes provide very high quantum efficiencies (45% at 500 nm) compared to the previous generation of photocathodes available (<20% for the bialkali PML-16-1), without compromising the instrument response function of the system significantly (220 vs 200 ps, nominal values provided by the manufacturer). The electrical signals from the photomultiplier assembly were routed to time-correlated single-photon counting electronics (SPC-150 by Becker & Hick GmbH) utilizing a single arm of the hyperdimensional imaging microscopy electronics we have described previously [19]. Single confocal plane images were acquired with a 40x oil objective (Leica HCX PL APO CS 40.0 × 1.25 OIL UV), 256 × 256 pixel image size, and 120 s acquisition time. A simultaneous two-photon excitation of the FRET pairs was achieved with a Ti:Sapphire Laser Chameleon Vision II (Coherent Inc.) tuned at 860 nm.

Cell Culture And Time-Lapse Imaging

For time-lapse imaging, we used HeLa-CCL2 cell lines (European Collection of Cell Cultures #93021013) expressing the three sensors with the plasmid described in [27]. The sensors have been fully characterized in our former publication: TagBFP-sREACh, mAmetrine-*ms*CP576, and mKeima-tdNirFP, fused with the flexible linkers containing the sequences VDTTD, DEVDR, and LEHD that are cleaved preferentially by caspase 2, caspase 3, and caspase 9, respectively. Cells were periodically mycoplasma-tested and STR profiled using the services of the CRUK Cambridge Institute. Cells were treated with the genotoxic drug cisplatin to induced cell death and imaged for 8 h at 1 h

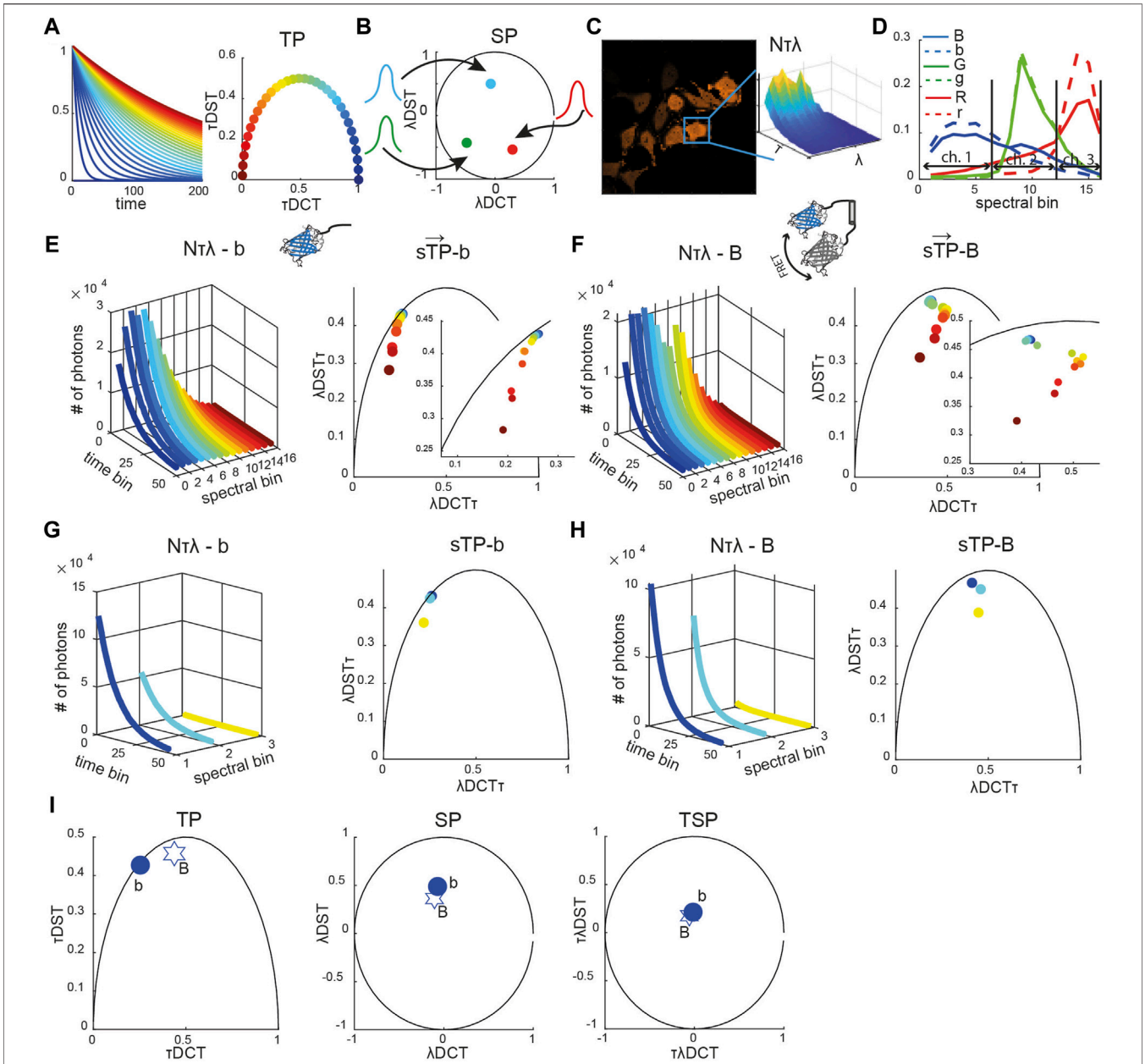

FIGURE 1 | Reference spectrally resolved fingerprint. **(A)** Diagrammatic representation of exponential decay curves (τ from ~0 ns in blue to 240 ns in crimson) shown in the time-domain (left) and time phasor space (circles, right panel). **(B)** Diagrammatic representation of Gaussian spectra (colored curves) and their representation as spectral phasors (solid circles). **(C)** Representative image of HeLa cells expressing a blue caspase-2 sensor (see **Supplemetary Figure S1** for green and red sensors) with the spectrally resolved time decay N (τ, λ) integrated over the mask of a single segmented cell is shown (inset). **(D)** Spectra of the blue (blue solid line), green (green solid line), and red (red solid line) positive controls (fusion constructs) and of the corresponding negative controls (only donors, dashed lines). Each curve was normalized to the total number of counts. The horizontal arrows indicate which spectral bins were used to emulate three-channel (ch.) multicolor FLIM (mcFLIM) data. Spectrally resolved time-decay N (τ, λ) (left panels in **(E–H)**) and corresponding spectrally resolved phasors ($s\overrightarrow{TP}$, right panel in **(E–H)**) for the blue donor **(E,G)** and positive control **(F,H)** for sFLIM **(E,F)** and emulated three-channel mcFLIM **(G,H)**. Inserts are magnifications of the same graphs. **(I)** The same data from the blue positive (stars markers and label *B*) and negative (round marker and label *b*) controls are shown transformed also as time-(TP), spectral-(SP), and time-spectral-phasor (TSP) space. Note, figure **(I)** is the same for spectrally resolved FLIM (sFLIM) and mcFLIM. In all panels, DCT-discrete cosine transform, DST-discrete sine transform; λ-marks spectral domain or spectral transformation (λDCT/λDST); τ-marks time-domain or time phasor transformation (τDCT/τDST).

intervals in LabTek II glass-bottom chambered slides (Nunc, #1.5) containing a 400 µl Leibovitz (L-15) medium supplemented with 10% FCS, 100 µM Cisplatin, and 0.9% NaCl. Multidimensional phasor fingerprinting of individual components was performed just before the time-lapse experiment, with HeLa-CCL2 cells transiently transfected with donor fluorophores not fused with an acceptor, and a donor–acceptor fusion pair (known FRET), as shown in [27].

Data Analysis

All the analyses were performed with custom-written Matlab script package freely available at https://github.com/inatamara/NyxSense. Segmentation, tracking, and application of NyxSense to mcFLIM have been described previously [27]. Briefly, cell segmentation was performed on the intensity images (decay curves and spectral channels were integrated) with the combination of an active contour algorithm [9] and a manual curation of the mask. Subsequently, cells were tracked between two consecutive images using a nearest neighbor approach, and mis-tracked cells were manually reassigned. A spectrally and time-resolved measurement for each cell was then achieved by summing the two-dimensional TCSPC histograms within the cell mask. The latest version of NyxSense (used here) also provides the capability to analyze spectrally resolved FLIM data. The performance of NyxSense for spectrally resolved or multicolor FLIM was evaluated using the same datasets. mcFLIM was generated by binning to the sFLIM spectral channels 1–6, 7–13, and 14–16, for channels 1, 2, and 3, respectively.

Multidimensional Phasor-Based Demixing of Spectrally Resolved Fluorescence Lifetime Imaging Microscopy Data

In the phasor space, single exponential decays are mapped to points on a semicircle described by the equation $(x\text{-}0.5)^2 + y^2 = 0.5^2$ (**Figure 1A**) [12, 18].

The time phasor coordinates are defined by the real and imaginary parts of the Fourier transform of the exponential decay function, and calculated as a discrete cosine (DCT) and a discrete sine (DST) transform, respectively. Points lying inside this semicircle correspond to mixed exponentials, being either inherently multi-exponential or a mixture of single-lifetime components. Similarly, all possible spectral phasors lie on arcs bounded by a circle $x^2 + y^2 = 1$, resulting from the Fourier transform of pure Gaussian spectra (**Figure 1B**) [22, 23, 23, 25]. The two-dimensional time-spectral phasor (TSP) is a two-dimensional Fourier transform, in which values are also bounded by a circle $x^2 + y^2 = 1$.

The phasor transform key advantage is additivity: a mixture of the spectral or lifetime components corresponding to a linear combination of phasors. This permits rapid demixing using a system of algebraic equations. A point in a phasor space corresponding to the combination of two lifetimes or spectra lies on the line connecting these two pure components. The distance to each pure component along connecting line segments translates directly to its fractional contribution within the mixture. In general, a phasor representing a mixture of n components is enclosed by a polygon with n vertices defined by the phasors of elementary components [23].

For every cell at each time point, we calculated multidimensional phasors: spectrally resolved time phasors (sTPs), spectrally integrated time phasors (TPs), spectral phasors (SPs), and time-spectral phasors (TSPs). The time-spectral phasor is a two-dimensional transformation along the time dimension followed by the transform along the spectral dimension.

Spectrally integrated time phasors (TPs) were obtained as TP = τDCT + i*τDST, where τDCT and τDST are discrete cosine and sine transforms, respectively (**Eqs. 1**,**2**).

$$\tau DCT = \sum_{\tau} N_{\tau} \cos(\varphi_{\tau}) \Big/ N_{TOT}, \quad (1)$$

$$\tau DST = \sum_{\tau} N_{\tau} \sin(\varphi_{\tau}) \Big/ N_{TOT}, \quad (2)$$

where $N_{TOT} = \sum_{\tau\lambda} N_{\tau\lambda}$ is the total number of photons detected for a given cell, $N_{\tau\lambda}$ denotes spectrally resolved time decay, $N_{\tau} = \sum_{\lambda} N_{\tau\lambda}$ is time decay, i denotes an imaginary unit, and $i^2 = -1$, $\varphi_{\tau} = 2\pi n * (S_{\tau}^{i} - 1/2)/S_{\tau}$ is a phase for time (τ) phasor computation, where S_{τ}^{i} is the ith time bin, S_{τ} is a number of time bins used to compute the phasor transform (here we used 46 out of 64), and n is a harmonic number.

Time-integrated spectral phasors (SPs) were obtained as SP = λDCT + i*λDST, where λDCT and λDST are the discrete cosine and sine transforms, respectively (**Eqs. 3**,**4**).

$$\lambda DCT = \sum_{\lambda} N_{\lambda} \cos(\varphi_{\lambda}) \Big/ N_{TOT}, \quad (3)$$

$$\lambda DST = \sum_{\lambda} N_{\lambda} \sin(\varphi_{\lambda}) \Big/ N_{TOT}, \quad (4)$$

where $N_{\lambda} = \sum_{\lambda} N_{\tau\lambda}$ is a spectrum and $\varphi_{\lambda} = 2\pi n * (S_{\lambda}^{i} - 1/2)/m$ is a phase for spectral (λ) phasor computation, where S_{λ}^{i} is the ith spectral bin, m is a number of spectral bins used to compute the phasor transform (16 for sFLIM and 3 for mcFLIM), and n is a harmonic number.

Time-spectral phasors (TPs) were obtained as TSP = τλDCT + i*τλDST, where τλDCT and τλDST are discrete cosine and sine transforms, respectively (**Eqs. 5**,**6**).

$$\tau\lambda DCT = \sum_{\lambda} \left(\sum_{\tau} N_{\tau\lambda} \cos(\varphi_{\tau}) \right) \cos(\varphi_{\lambda}) \Big/ N_{TOT}, \quad (5)$$

$$\tau\lambda DST = \sum_{\lambda} \left(\sum_{\tau} N_{\tau\lambda} \sin(\varphi_{\tau}) \right) \sin(\varphi_{\lambda}) \Big/ N_{TOT}. \quad (6)$$

Spectrally resolved time phasors (sTPs) were obtained as sTP = λDCTτ + i*λDSTτ, where λDCTτ and λDSTτ are discrete cosine and sine transforms for each spectral channel, respectively (**Eqs. 7**,**8**).

$$\lambda DCT\tau = \sum_{\tau} N_{\tau\lambda} \cos(\varphi_{\tau}) \Big/ N_{TOT}, \quad (7)$$

$$\lambda DST\tau = \sum_{\tau} N_{\tau\lambda} \sin(\varphi_{\tau}) \Big/ N_{TOT}. \quad (8)$$

The fluorescence signatures of cells or reference samples were then characterized by the multidimensional phasors defined by the complex vector $\overrightarrow{P_x} = [\, TP \quad SP \quad TSP \quad sTP_1 \quad \cdots \quad sTP_m \,]$, where the subscript x indicates the multidimensional phasors of the measurement or the reference fingerprints. The subscript m denotes the number of spectral channels for sFLIM (m = 16) or mcFLIM (m = 3).

Demixing of sFLIM can be achieved by minimization of a complex nonlinear multivariable constrained function (CF) with respect to fractional contributions of the six control signatures (C). At each minimization step, CF is computed as a squared residual between experimental phasors ($\overrightarrow{P_{exp}}$) and phasors estimated using the fractional contributions ($\overrightarrow{P_{est}}$): $CF = \sum_n (\overrightarrow{P_{exp}} - \overrightarrow{P_{est}})^2$, where n is a number of elements in $\overrightarrow{P_{est}}$, $\overrightarrow{P_{exp}}$, and the $\overrightarrow{P_{exp}} = [\overrightarrow{sTP}\ TP\ SP\ TSP]$. $\overrightarrow{P_{est}} = [\overrightarrow{sTP}_{est}\ TP_{est}\ SP_{est}\ TSP_{est}]$ is a nonlinear vectorial function of the fractional contributions $\overrightarrow{C} = (c_1 \cdots c_k)$. The spectrally resolved time phasors are estimated as $\overrightarrow{sTP}_{est} = \overrightarrow{PI} \odot \overrightarrow{RHO}^{-1}$, $\overrightarrow{RHO} = \overrightarrow{C}\,\widehat{BM}^T$, and $PI = \overrightarrow{C}\,((\widehat{BM} \odot \widehat{sTP_{ctr}})^T)^{\dagger}$, where $\odot$ denotes Hadamart operation, $\widehat{BM} = (\overrightarrow{N_\lambda^1} \cdots \overrightarrow{N_\lambda^k})$, $\widehat{sTP_{ctr}} = (\overrightarrow{sTP_1} \cdots \overrightarrow{sTP_k})$, where $\overrightarrow{N}_\lambda^k = \sum_\tau N_{\tau\lambda}^k$ is a column vector of spectrum and $\overrightarrow{sTP_k}$ is a column vector of spectrally resolved time phasors for the kth control signature. $TP_{est} = \sum_k C_k TP_k$, $SP_{est} = \sum_k C_k SP_k$, and $TSP_{est} = \sum_k C_k TSP_k$, where TP_k, SP_k, and TSP_k are time, spectral, and time-spectral phasors for the kth control signature. However, the minimization of the complex CF renders undetermined system for certain phasor combinations (e.g., $\overrightarrow{P_{est}} = [\,TP_{est}\ SP_{est}\ TSP_{est}\,]$, three equations for six unknown variables, and most of mcFLIM $\overrightarrow{P_{est}}$ combinations). To assure that the system of equations is not underdetermined, to compare mcFLIM and sFLIM, we used real and imaginary parts of $\overrightarrow{P_{exp}}$ and $\overrightarrow{P_{est}}$ separately, that is, $\overrightarrow{P_{exp}} = [real(\overrightarrow{sTP})\ imag(\overrightarrow{sTP})\ real(TP\ SP\ TSP)\ imag(TP\ SP\ TSP)]$ and $\overrightarrow{P_{est}} = [real(\overrightarrow{sTP_{est}})\ imag(\overrightarrow{sTP_{est}})\ real(TP_{est}\ SP_{est}\ TSP_{est})$ $imag(TP_{est}\ SP_{est}\ TSP_{est})]$ and the remainder is as described above. We note that the demixing results using complex CF and real CF (with twice as much equations) are almost the same even for the mcFLIM. In addition, for the minimization involving $\overrightarrow{P_{est}} = [\,TP_{est}\ SP_{est}\ TSP_{est}\,]$ for mcFLIM/sFLIM or $\overrightarrow{P_{est}} = [\,\overrightarrow{sTP_{est}}\,]$ for mcFLIM, the phasors were calculated at the first and the second harmonic. This assured that the number of equation is greater than the number of parameters to estimate, which was necessary to calculate the standardized residuals (see **Eq. 10**).

The minimization procedure was achieved using fmincon Matlab solver. The lower (LB) and upper bonds (UB) for the fractional contributions were constrained to 0 and 1, respectively. The initial values for the fractional contributions were typically 0 for all the control signatures.

The relative enzymatic activity (REA) for each FRET sensor (caspase) was calculated using the following equations:

$$REA = f_d / [f_d + f_{unc} / (1 - E)], \tag{9}$$

where f_d and f_{unc} are the fractional contribution of the donor-only and uncleavable sensor control signatures, respectively, E is FRET efficiency, and division by (1 − E) compensates for the change in brightness. To avoid the division by a very small number leading to large errors, REA was set to 0 for f_d and f_{unc} typically below 0.01–0.02. We note that in the specific case of proteolytic sensor, REA represents the cumulative enzymatic activity of the proteases as cleavage is irreversible (until new sensors are expressed *de novo*).

The standardized phasor residuals were calculated as a difference between experimental phasors and phasors calculated using the unmixed fractional contributions.

$$Res_{stand} = \left|\overrightarrow{P_{exp}} - \overrightarrow{P_{est}}\right| \Big/ \left(\hat{\sigma}\sqrt{1 - h_{ii}}\right), \tag{10}$$

where $\hat{\sigma}$ is the estimated residual standard deviation and h_{ii} is a leverage of the ith observation (i.e., ith element of the residual vector): $\hat{\sigma} = \sum_n (\overrightarrow{P_{exp}} - \overrightarrow{P_{est}})^2 / (n - p)$,where n is the number of equations (number of elements in $\overrightarrow{P_{est}}$ or $\overrightarrow{P_{exp}}$) and p is the number of parameters (six control signatures).

The root mean square deviation (RMSD) for the REA was computed as follows:

$$RMSD_{REA} = \sqrt{\sum_{t,P} (REA_0(t,P) - REA(t,P))^2 \Big/ N_t}, \tag{11}$$

where P is a FRET pair (B, G, R), $N_t = 8$ is the number of the experimental time points, REA_0 is the known enzymatic activity (the ground truth), and REA is obtained from the demixing.

Simulating Spectrally Resolved Fluorescence Lifetime Imaging Microscopy Data

The following equation was used to generate time- and spectrally resolved emission for each FRET pair (n):

$$E(t,\lambda)_n = \left(f_D \frac{e_D(\lambda)}{\tau_D}\right) \otimes e^{-\frac{t}{\tau_D}} + \left(r_0 \frac{e_A(\lambda)}{\tau_A} - (1 - f_D)(1 - r_0)\frac{(\tau_D - \tau_{DA})}{(\tau_A - \tau_{DA})\tau_D} e_A(\lambda)\right) \otimes e^{-\frac{t}{\tau_A}} + \left((1 - f_D)\frac{e_D(\lambda)}{\tau_D} - (1 - f_D)(1 - r_0)\frac{(\tau_D - \tau_{DA})}{(\tau_A - \tau_{DA})\tau_D} e_A(\lambda)\right) \otimes e^{-\frac{t}{\tau_{DA}}}, \tag{12}$$

where $e_D(\lambda)$, $e_A(\lambda)$ are the spectrally resolved normalized emission profiles, τ_D, τ_A are a lifetime of the donor and acceptor, respectively, and $\tau_{DA} = \tau_D(1 - E)$ is a donor lifetime in the presence of acceptor. f_D is a fraction of free donors and r_0 is a fraction of the directly excited acceptors. The donor and acceptor absorption cross-sections, quantum efficiencies, the transition rates, and the donor-to-acceptor ratio were set to 1. Finally, ⊗ is a convolution operation. The final counts per pixel was calculated as follows:

$$E(t,\lambda)_{tot} = N_1 E(t,\lambda)_1 + N_2 E(t,\lambda)_2 + N_3 E(t,\lambda)_3, \tag{13}$$

where N_1, N_2, N_3 are the total photon count for each FRET pair, respectively, which was set to 2,600 photons. The lifetime decays were modeled as a single exponential. The donor and acceptor emission spectra ($e_D(\lambda)$, $e_A(\lambda)$) were modeled as the Lorentzian curves. The synthetic images containing simulated three FRET pairs were generated with the following parameters: the donors' lifetimes (τ_D) were 2.3, 2.5, and 2.7 ns for FRET pairs 1–3, respectively, the acceptors' lifetimes (τ_A) was set to 0.3 ns, and FRET efficiencies 0.35 for each FRET pair. The donors' spectra maxima were 470, 515, and 570 nm and FWHM 55 nm, and the acceptors' spectra maxima were 505, 550, and 605 nm with FWHM 55 nm for each fluorophore. The acceptor direct

excitation relative to the donor excitation was set to 5 or 0%. The Poisson noise was added using the Matlab function imnoise and resulted in ~12% noise.

RESULTS

Multidimensional Phasor Fingerprint Provides an Efficient Method for Dimensionality Reduction

To test the capabilities of the computational framework presented in the Methods section, we used the NyxBits sensor platform we have described recently to sense cleavage of different substrates (the peptides VDTTD, DEVDR, and LEHD) that are preferentially cleaved by caspase 2, caspase 3, and caspase 9, respectively [27]. In our former work, we demonstrated the capability of mcFLIM to demix the blue (labeled as *B* in all figures, caspase 2), green (*G*, caspase 3), and red (*R*, caspase 9) FRET pairs excited at the same wavelength (**Figure 1**). Upon cleavage, each sensor yields two principal components with different lifetimes and spectra: an unquenched donor (labeled with the small *b*, *g*, and *r* letters in all figures) and the uncleaved donor–acceptor undergoing FRET (*B*, *G*, and *R*). Thanks to the large Stokes shifts of the probes and acceptor chromophores of a very low quantum yield, the free acceptors are excited with low efficiency and have a minor impact on our experiments. Here, we characterize the three FRET sensors and compare the performance of mcFLIM and sFLIM using a simple and optically efficient spectrally resolved FLIM (see Materials and Methods).

Each sFLIM image has two spatial dimensions (x, y–here 256 × 256), the time-resolved fluorescence decay histogrammed in 64 time bins (τ) and a spectral dimension represented with 16 spectral bins (λ). The spectrally and time-resolved fluorescence decay of each pixel can therefore be represented in an abstract space of high dimensionality (64 × 16 = 1,024 numbers, or photon-counts). Multidimensional phasor transforms permitted us to project this space onto a space of lower dimensionality where the fluorescence characteristics detected in each pixel are described by a vector $\overrightarrow{P_{exp}} = [\overrightarrow{sTP}\ TP\ SP\ TSP]$ (see **Eqs. 1–8**) of 19 complex components (6 for mcFLIM). Although different combinations of phasor transforms have been used previously, here we maintain a higher dimensionality of $\overrightarrow{P_{exp}}$ than other works [23, 52, 61] to ensure sufficient features are preserved during dimensionality reduction. Aiming to limit acquisition time and phototoxicity that affect biologically relevant measurements, we have acquired typically 1,000–1,500 photons per pixel. Rather than on pixel basis, we perform cell-based demixing by segmenting and thresholding (pixels with typically minimum ~200 photons are retained) individual cells and integrating photons collected within each cell. In the time-spectral domain (τλ), the biochemical state of a cell is thus described by a surface spanned by the number of photons (N), spectral information (λ), and time decay (τ) (**Figures 1C,D**).

The reference phasors were obtained by imaging cells expressing only one control signature, that is, only a donor or a sensor rendered non-cleavable by substituting the substrates with a proteolytically stable sequence. **Figures 1E,F** show the unquenched blue donor (b) and a blue uncleavable FRET pair (B) fingerprints, respectively, including spectrally resolved lifetime, decays (N[λτ]), spectrally resolved time phasors (sTPs), spectrally integrated time phasors (TPs), time-integrated spectral phasor (SP), and time-spectral phasors (TSPs) (see also **Supplementary Figure S1**). We compare the biochemical sensitivity of spectral FLIM to multicolor FLIM by binning the 16 spectral bins into three channels that numerically emulate multicolor detection (**Figures 1D,G,I**, **Supplementary Figure S1**, see also *Material and Methods*). This strategy permitted us to compare the computational performance of the two methods, without having to account for differences in the detection efficiency of two detection systems that would be otherwise difficult to control experimentally.

Multidimensional Phasor-Based Demixing Minimizes Cross-Talks Between Sensors

Subsets of the components of $\overrightarrow{P_{exp}}$ ($\overrightarrow{sTP}$) have been previously used to demix single FRET pair (donor and acceptor fluorescence, and interacting donor–acceptor pairs [25]). Different subsets of $\overrightarrow{P_{exp}}$ (TP, SP, and TSP) were applied to separate three fluorescence components using phasor plots [52], and blindly demix three signal components for contrast enhancement in tissue imaging [24, 61]. Here, we used the full complement of the features described by $\overrightarrow{P_{exp}}$ ($\overrightarrow{sTP}$ with the combination of TP, SP, and TSP) and experimental reference fingerprints to ensure robustness and reproducibility of the results. First, we tested our framework by demixing single FRET pair images containing only two reference components (b-B, g-G, or r-R; **Figure 2**). This approach permitted to evaluate false-positive detection of the four other components that were not present in a sample. For this, we recorded time-lapse sFLIM images of cells expressing individual sensors (*B*, *G*, or *R*) after exposure to the genotoxic drug cisplatin. Cisplatin induces irreparable DNA damage, leading to switch-like activation of caspases that execute apoptosis. **Figure 2A** shows that the biochemical trajectories of cells undergoing apoptosis (**Figure 2B**) tend to trace a line connecting two control fingerprints (i.e., FRET and no-FRET). The FRET control corresponds to uncleaved sensors; that is, no caspase is activated. During the apoptosis, caspases are activated, sensors get cleaved, and the experimental phasors (black line, **Figure 2A**) approach no-FRET control phasors signatures. In **Figure 3** and **Supplemetary Figures S2, S3**, we compare spectral demixing using different components of the multidimensional phasors $\overrightarrow{P_{exp}}$ for both sFLIM and mcFLIM. The single-cell traces of the blue- and green-emitting biosensors displayed linear trajectories in a phasor space (**Figure 2A**). The demixing correctly detected the fractional contribution of control fingerprints (**Figure 3**, **Supplemetary Figures S2, S3**), which resulted in ~80 and ~50% final sensor cleavage (cumulative relative enzymatic

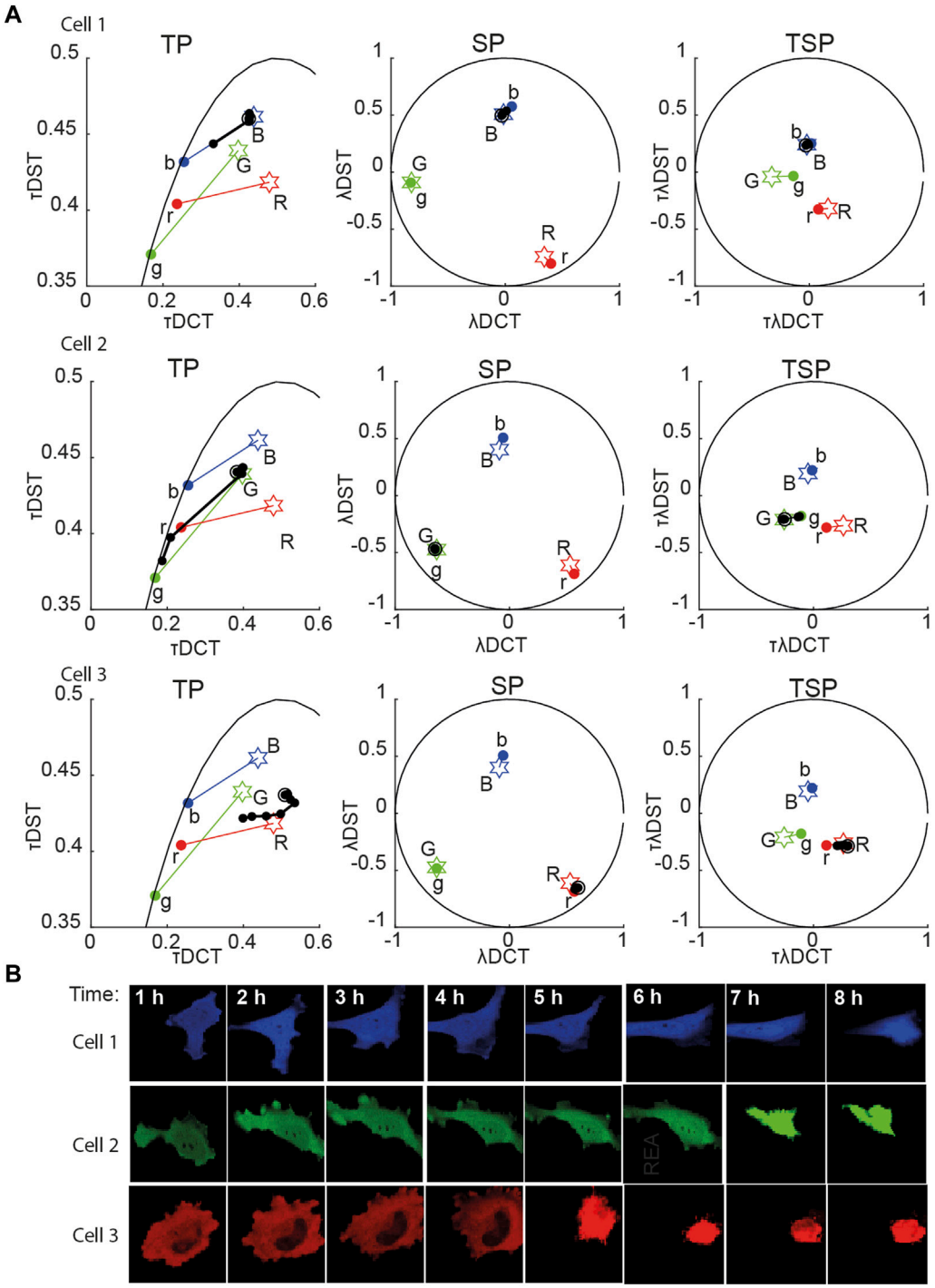

FIGURE 2 | Multidimensional phasor representation of time-lapse sFLIM of single FRET pairs. **(A)** Multidimensional phasor transforms (here, only TP, SP, and TSP are shown) of the representative cells expressing blue-only sensor **(top row,** cell 1), green-only sensor **(middle row,** cell 2), and red-only sensor **(bottom row,** cell 3). Cells were treated with cisplatin and imaged for 8 h. The black circles (experimental measurements taken every hour) and lines represent the biochemical trajectory of a cell projected on the different phasor spaces that should span from the negative control fingerprints (stars labeled *B*, *G*, and *R*, uncleavable sensors) to the donor-only references (colored circles labeled *b*, *g*, and *r*). **(B)** Intensity images (total photon-counts/pixel of sFLIM images) of the cells analyzed in **(A)**. In panel **(A)**, DCT-discrete cosine transform, DST-discrete sine transform; λ-marks spectral domain or spectral transformation (λDCT/λDST); τ-marks time-domain or time phasor transformation (τDCT/τDST).

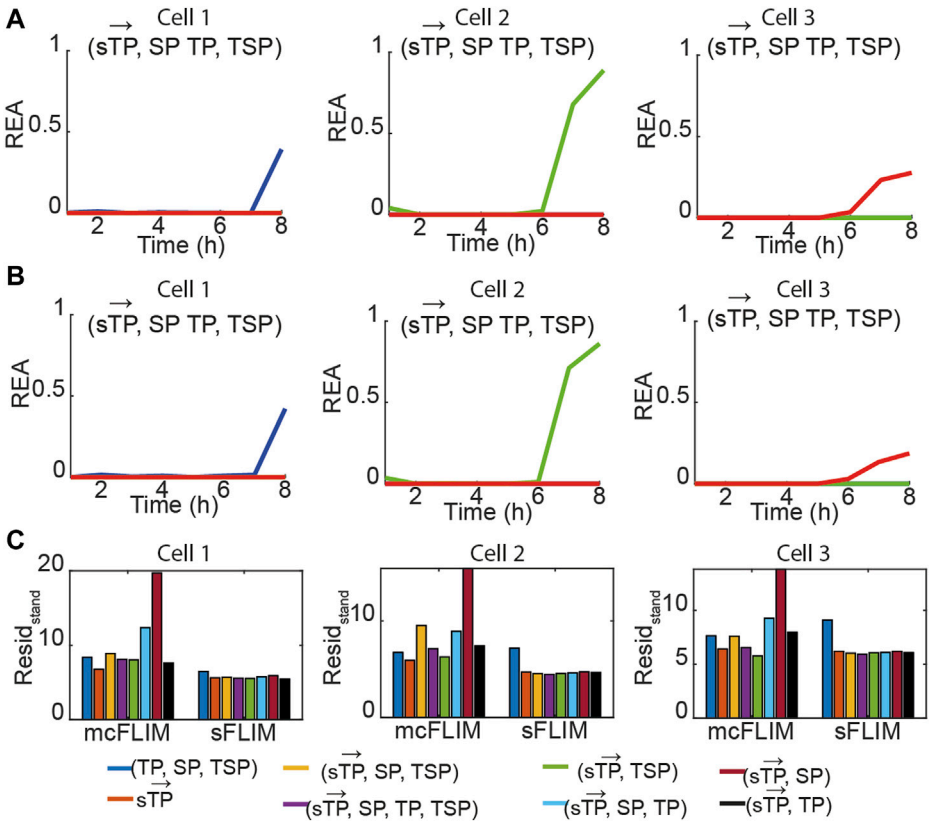

FIGURE 3 | Multiplexing biochemical reactions using multidimensional phasor-based demixing. **(A,B)** Results of the multidimensional phasor-based demixing of the time-lapse data shown in **Figure 2** using ($\overrightarrow{sTP}$, *TP*, *SP*, and *TSP*) phasors and presented as a relative enzymatic activity (REA, **top)** for sFLIM **(A)** and mcFLIM **(B)**. The complete set of results for each algorithm is shown in **Supplementary Figures S2, S3**. **(C)** The mean standardized phasor residuals summed over time for the demixing of the three cells shown in panels **(A,B)** and **Figure 2** (see **Eq. 10** *Materials and Methods*).

activity (REA)) for a cell expressing the green (*G*) or the blue (*B*) sensor, respectively. However, we note that the red sensor (*R*) can display curved trajectories in the phasor space in several experiments, observation we attribute to non-idealities of the mKeima/tdNirFP, including residual fluorescence of tdNirFP and occasional photo-conversion of mKeima that can occur at higher excitation regimes. However, despite these non-idealities, demixing of the red FRET pair is also sufficiently robust.

For the single FRET pairs (demixing of two components), we observed that the different combinations of $\overrightarrow{sTP}$ and *TP*, *SP*, and *TSP* components rendered comparable results as by the results shown in **Figure 3**, **Supplementary Figures S2, S3** for both mcFLIM and sFLIM. To compare different demixing methodologies, we provide two figures of merits, the mean standardized phasor residuals, where the mean is taken over observations (i.e., the number of equations) (see **Eq. 10**, *Materials and Methods*), either summed over time (**Figure 3**) or time-dependent (**Supplementary Figures S2D, S3D**). From **Figure 3C**, we see that the largest fitting errors for the sFLIM occur with the demixing using the smallest $\overrightarrow{P_{exp}}$ subset (*TP*, *SP*, and *TSP*) (see also **Supplementary Figure S2D**). Demixing with different combinations of $\overrightarrow{sTP}$ with *TP*, *SP*, and *TSP* rendered similar results. In comparison, mcFLIM showed higher residuals for $\overrightarrow{sTP}$ and *SP* than for $\overrightarrow{sTP}$ or *TP*, *SP*, and *TSP* alone. Yet, when $\overrightarrow{sTP}$ and *SP* demixing was calculated with the first and the second harmonic combined (as it is for $\overrightarrow{sTP}$ and (*TP*, *SP*, and *TSP*)), the residuals were lower (data not shown). However, to avoid errors caused by overfitting, we utilized the second harmonics when essential to have a determined system of equations (see also *Material and Methods*). For mcFLIM $\overrightarrow{sTP}$ or ($\overrightarrow{sTP}$, *TP*) alone, the wrongly detected components were not present in a sample (**Supplementary Figures S3A–C**). We conclude that the representation of data with a multidimensional phasor $\overrightarrow{P_{exp}}$ improves the overall performance of demixing algorithms for both spectrally resolved and multicolor FLIM even for the single FRET pair demixing.

Multidimensional Phasor-Based Demixing Achieves Efficient Multiplexing of Forster Resonance Energy Transfer Biosensors

Next, we validated the proposed methodology by summing photon counts recorded from cells expressing the individual FRET pairs. This strategy permitted us to test the demixing algorithms in the presence of typical cross-talks, providing an experimentally valid ground truth (the known fractional contributions, calculated in **Figure 3**). For example, **Figure 4** shows the same data displayed in **Figure 3**,

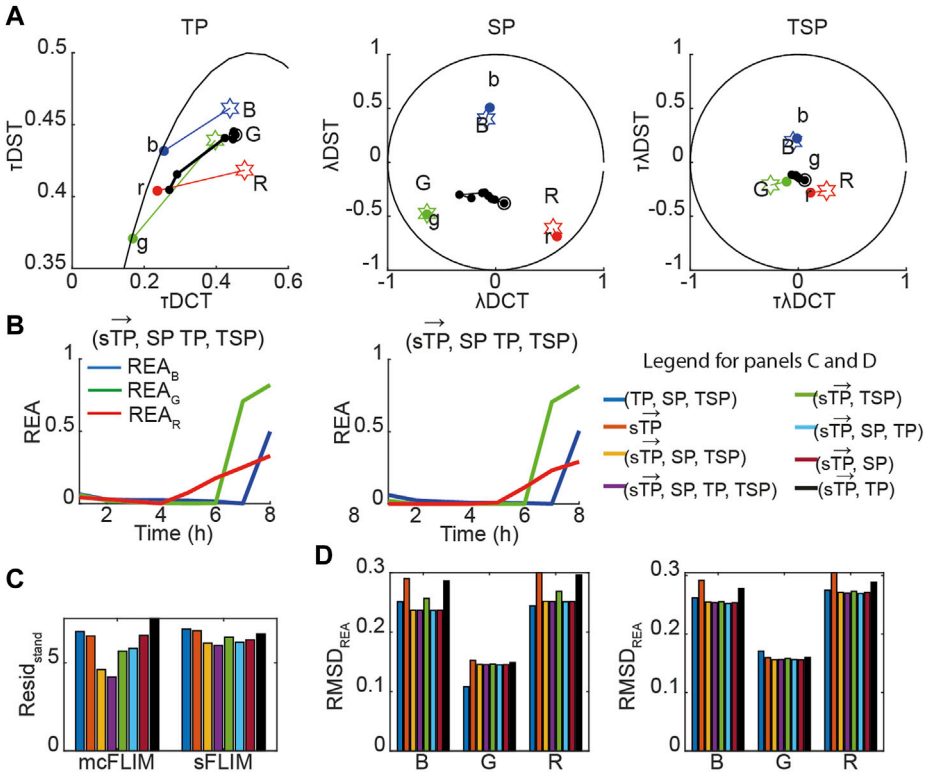

FIGURE 4 | Validation of the demixing algorithms. The experimental data shown in **Figures 2**, **3** were summed to generate a synthetic mixed signal (i.e., a cell expressing three sensors) of known ground truth. **(A)** The mixed signals are shown as different phasor subspaces. The black circles and lines represent the biochemical trajectory of a cell projected on the different phasor spaces. Stars represent the fingerprints of the uncleavable sensors (labeled *B*, *G*, and *R*), and the colored circles the donor-only fingerprints (labeled *b*, *g*, and *r*). **(B)** These data were demixed using ($\overrightarrow{sTP}$, *TP*, *SP*, and *TSP*) phasors of sFLIM data **(left)** and mcFLIM **(right)** (see also **Supplementary Figure S4**). **(C)** The standardized phasor residuals summed over time, and **(D)** REA RMSD for sFLIM **(left)** and mcFLIM **(right)**.

summed, and then demixed either using sFLIM or mcFLIM. With this validation dataset and the analysis of the residuals, we observe that both spectrally resolved and multicolor FLIM provide efficient and comparable demixing, see also **Supplementary Figure S4**. Most importantly, the residual analysis of both mcFLIM and sFLIM showed that the smallest fitting errors were observed for the largest $\overrightarrow{sTP}$ complement ($\overrightarrow{sTP}$, *TP*, *SP*, and *TSP* and the highest for *TP*, *SP*, and *TSP* and $\overrightarrow{sTP}$ or $\overrightarrow{sTP}$ and *TP*. For both mcFLIM and sFLIM $\overrightarrow{sTP}$ or $\overrightarrow{sTP}$ and *TP* alone were not able to detect the small rise in REA_R between 5 and 6 h (**Supplementary Figure S4**). We note that this rise is not an artifact as a clear apoptotic phenotype is seen at 5 h (**Figure 2B**, red cell).

As phasor residuals do not determine the accuracy in the estimation of relative enzymatic activities, we also estimated the root mean square deviation (RMSD) of the REA values when a ground truth can be estimated (see **Eq. 11**, *Materials and Methods*) by subtracting REA obtained with a single FRET pair denoted as REA_0 (**Figure 3**) from the REA obtained with triple FRET demixing (REA, **Figure 4B**). In **Figure 4D**, we show that the RMSD of sFLIM and mcFLIM is very similar.

Next, we applied the proposed methodology to the analysis of the experimental data with cells co-expressing all three sensors. **Figure 5A** shows the time evolution of biochemical traces of two cells (Cell-1 and 2) that exemplify the different responses we have described previously [27]. Cell-1 exhibits a robust activation of all three caspases, while Cell-2 does not. **Figures 5B, C** show the demixing results using $\overrightarrow{sTP}$, *TP*, *SP*, and *TSP* phasors (see also **Supplementary Figure S5**) for sFLIM and mcFLIM, respectively. The comparison between the 16 spectral-channel sFLIM and the three-channel mcFLIM demixing suggests that both modalities can efficiently retrieve the six signatures we analyzed. As for the semisynthetic data shown in **Figure 4**, the addition of spectral phasors and, more generally, the use of the multidimensional phasors $\overrightarrow{P_{exp}} = [\overrightarrow{sTP}\ TP\ SP\ TSP]$ improve fluorescence lifetime-based multiplexing of multiple FRET pairs. The residual analysis showed that $\overrightarrow{sTP}$, *TP*, *SP*, and *TSP* produce the smallest and *TP*, *SP*, and *TSP* and $\overrightarrow{sTP}$ or $\overrightarrow{sTP}$ and *TP* produce the highest fitting errors. In addition, with multicolor probes and detection channels optimized for FRET multiplexing, mcFLIM performs almost as well as spectrally resolved FLIM. However, comparing red traces in **Figures 4B,C**, **5B,C**, as well as **Supplementary Figures S4A,B, S5A,B**, suggests that sFLIM may be more robust for low fractional contributions of the individual components (typically below 2–5%). We conclude that the efficient demixing of three FRET pairs required the combination of $\overrightarrow{sTP}$ and spectral phasors *SP* and *TSP* for both mcFLIM and sFLIM and that, more generally, $\overrightarrow{P_{exp}} = [\overrightarrow{sTP}\ TP\ SP\ TSP]$ provides robust demixing.

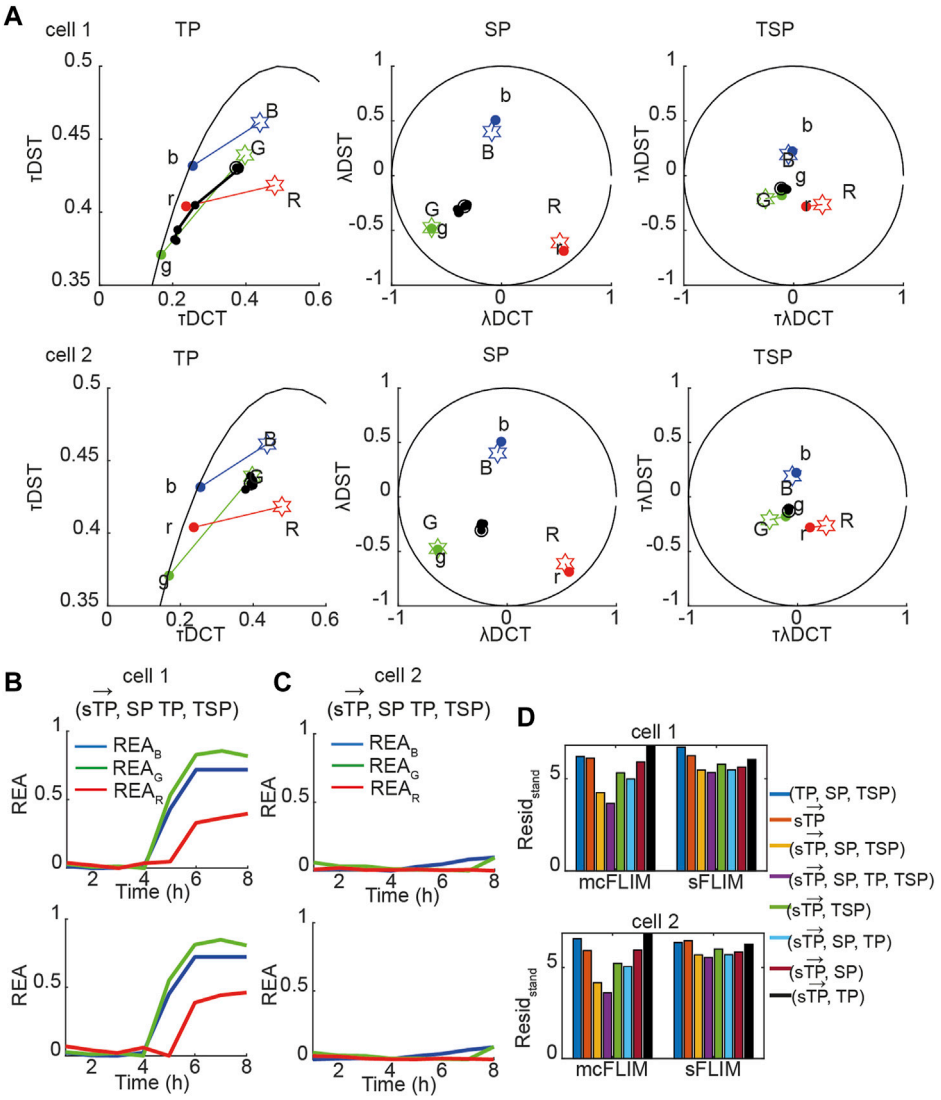

FIGURE 5 | Multidimensional phasor-based demixing of three biochemical reactions. **(A)** Time-lapse experiment showing two representative cells expressing all three sensors. Data are represented in the TP, SP, and TSP phasor subspaces. The black circles and lines represent the biochemical trajectory of a cell. Cells were treated with cisplatin and then imaged for 8 h every 1 h. Stars represent the reference fingerprints of the uncleavable sensors (labeled *B*, *G*, and *R*), and colored circles show the donor-only references (labeled *b*, *g*, and *r*). **(B,C)** The results of demixing using ($\overrightarrow{sTP}$, *TP*, *SP*, and *TSP*) phasors for sFLIM **(top)** and mcFLIM **(bottom)** for two different cells, respectively (see also **Supplementary Figure S5**). **(D,E)** The standardized phasor residuals summed over time for cell-1 **(top)** and cell-2 **(bottom)**.

Multidimensional Phasor-Based Demixing is Necessary for Demultiplexing High Cross-Talk Data

Taken together, the results shown suggest that multicolor FLIM is already an efficient technique for demix of three FRET pairs when analyzed with multidimensional phasors although it requires optimized FRET pairs. With the engineering of faster and efficient spectral FLIM system, we envisage that sFLIM might provide a significant advantage for demixing, for example, with FRET pairs not specifically designed for heavily multiplexed detection. We therefore investigated how more significant spectral overlaps might affect the performance of mcFLIM and sFLIM. We generated a fully synthetic triple FRET pair images (see **Eqs. 12,13**, *Material and Methods*, **Figure 6**, **Supplementary Figure S6**). In the presence of higher overlap, the spectrally resolved time phasors $\overrightarrow{sTP}$ [25] (*TP*, *SP*, *TSP*) or ($\overrightarrow{sTP}$, *TP*) phasors alone [24, 61] resulted in incorrect demixing for both mcFLIM and sFLIM, especially for the green and red FRET pairs that exhibit a larger spectral overlap, **Figures 6F,G**. The combination of (*TP*, *SP*, *TSP*) and $\overrightarrow{sTP}$ was necessary for robust demixing (**Figures 6E–G** and **Supplementary Figure S6**). Further increase in the overlap between the green and the blue FRET pair still led to correct demixing with sFLIM and mcFLIM, **Supplementary Figure S7**.

Once again, multidimensional phasors provided more robust demixing performing optimally in all the tested conditions. With low-to-medium spectral overlap, mcFLIM performs almost as

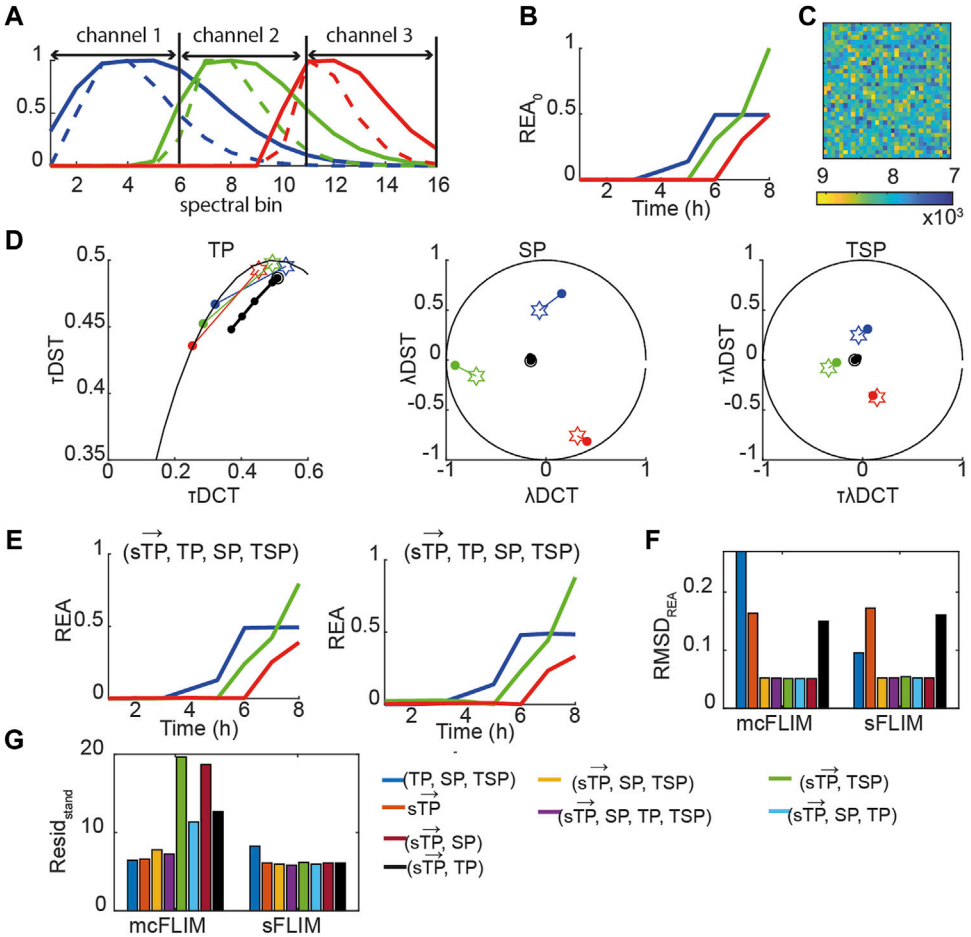

FIGURE 6 | Multidimensional phasor-based demixing of high multiplexed synthetic data. **(A)** Spectra of the simulated blue (blue solid line), green (green solid line), and red (red solid line) positive controls (uncleavable sensors) and of the corresponding negative controls (only donors, dashed lines). Each curve was normalized to the maximum. Data were simulated as 16 spectral bins, and channel 1–3 show which bins were summed to obtain three-channel mcFLIM. **(B)** A simulated REA_0 curves. **(C)** A simulated noisy image. **(D)** Time-lapse simulated data combining three sensors. Data are represented in the TP, SP, TSP phasor subspaces. The black circles and lines represent the biochemical trajectory of a simulated data. Stars represent the reference fingerprints of the uncleavable sensors (labeled *B*, *G*, and *R*), and colored circles show the donor-only references (labeled *b*, *g*, and *r*). **(E)** The results of demixing using ($\overrightarrow{sTP}$, *TP*, *SP*, and *TSP*) for sFLIM **(left)** and mcFLIM **(right)** (see also **Supplementary Figure S6**). **(F)** REA RMSD. **(G)**. The phasor standarised residuals for sFLIM **(left)** and mcFLIM **(right)** (see also **Supplementary Figure S7**).

well as spectral FLIM, but sFLIM (both supported by the open-source NyxSense code we provide) is more robust to the choice of algorithm and—intuitively—to increasing spectral overlaps.

DISCUSSION

Time- or spectrally resolved imaging has become very accessible, thanks to commercial confocal microscopes frequently installed in core facilities that can support these applications. Such technologies offer opportunities to match the increasing demands for enhanced multiplexing of fluorescent markers. The quantitative characterization of biochemical network dynamics is an invaluable application of multiplexed fluorescence to formulate or test hypotheses at the interface between cell and systems biology. Nevertheless, this application is comparatively immature, at least concerning more quantitative approaches extended to small biochemical networks. Demultiplexing several biochemical activities from complex photophysical datasets is still a challenge that requires breaking new grounds to enable the robust characterization of biochemical networks at single-cell resolution [7, 15, 30, 62]. This challenge is made harder by the nonideal conditions necessary to image living cells. For example, the need to minimize photon toxicity leads to low photon counts and spurious signals. In addition, the use of several fluorescent proteins that are determined by the need for multiplexing constraints (spacing between excitation/emission spectra) might exacerbate issues such as improper maturation of acceptor chromophores and brightness, photobleaching, and photochromism.

Therefore, here we contribute to this endeavor with a framework based on multidimensional phasor transforms, representing efficient and intuitive methods for demixing three

FRET pairs excited at a single wavelength. Building on work published by us and others (e.g., [21–23, 25, 27, 61]) we extended this computational framework, including higher phasor dimensionality. We demonstrate its efficacy to demix three FRET pairs imaged at a single excitation wavelength that we previously optimized for the multiplexing and by simulating synthetic triple FRET pair images with more spectral overlap. We provide a description of our methodology and the extension to spectrally resolved FLIM of the NyxSense computational platform that we had briefly described only for mcFLIM [27]. This platform is available in the public domain (https://github.com/inatamara/NyxSense) and could be used by the community to test, further improve, or simply use the methodology we proposed. Spectrally resolved FLIM is readily available commercially, and several bespoke implementations aimed to make available cost-effective and user-friendly solutions have been also published (e.g., [6, 42, 43, 51, 56, 58, 61, 63, 76], promising increased availability of such sophisticated assays in the near future. We showed that the combination of spectrally resolved time phasors ($\overrightarrow{sTP}$) with the spectral phasors (*SP* or *TSP*) permitted efficient demixing of three FRET pairs, presenting a low level of direct acceptor excitation using only six control signatures. Interestingly, the results for sFLIM (16 spectral bins) and mcFLIM (three spectral channels) were very similar for the data discussed here, that is, six main control signatures (donor-only and uncleavable sensors) with a low level of direct acceptor excitation. However, the sFLIM is more robust to unmix lower fractional contributions. Spectrally resolved FLIM will therefore be an essential tool either to demix common FRET pairs with large spectral overlaps or to further expand our capability to multiplex more than three biochemical reactions from single living cells.

However, we suggest that readily available equipment dedicated to multicolor FLIM, particularly instruments capable of fast detection, can already perform such complex experiments efficiently. Therefore, the innovation of detection technologies of both scanning and wide-field microscopes can make biochemical multiplexing a routine technique in the future [11, 32, 47, 59, 60]. We show that excellent demixing results can be achieved with the open-source toolbox NyxSense for both sFLIM and mcFLIM. NyxSense implements the multidimensional phasor transforms that facilitate the projection of complex multidimensional photophysical data onto biochemical spaces of lower dimensionality to represent the biochemical trajectory of single cells in response to stimuli.

DATA AVAILABILITY STATEMENT

The original contributions presented in the study are included in the article/**Supplementary Material**; further inquiries can be directed to the corresponding author.

AUTHOR CONTRIBUTIONS

AE, KH, and MF designed the experiments; KH and MF executed the experiments; AE built the microscope; KH and AE wrote the manuscript; KH analyzed the data and wrote the programs.

FUNDING

MF was funded by the Gates Foundation studentship. We acknowledge funding from the Medical Research Council core grants (MC_UU_12022/1 and MC_UU_12022/8) and the Wellcome Trust (090340/Z/09/Z) to AV, and from the Cancer Research UK (C54674/A27487) to AE.

SUPPLEMENTARY MATERIAL

The Supplementary Material for this article can be found online at: https://www.frontiersin.org/articles/10.3389/fphy.2021.637123/full#supplementary-material

REFERENCES

1. Ai H-w., Hazelwood KL, Davidson MW, and Campbell RE. Fluorescent Protein FRET Pairs for Ratiometric Imaging of Dual Biosensors. *Nat Methods* (2008) 5(5):401–3. doi:10.1038/nmeth.1207
2. Algar WR, Hildebrandt N, Vogel SS, and Medintz IL. FRET as a Biomolecular Research Tool - Understanding its Potential while Avoiding Pitfalls. *Nat Methods* (2019) 16(9):815–29. doi:10.1038/s41592-019-0530-8
3. Bajar B, Wang E, Zhang S, Lin M, and Chu J. A Guide to Fluorescent Protein FRET Pairs. *Sensors* (2016) 16(9):1488–24. doi:10.3390/s16091488
4. Barber PR, Ameer-Beg SM, Gilbey J, Carlin LM, Keppler M, Ng TC, et al. Multiphoton Time-Domain Fluorescence Lifetime Imaging Microscopy: Practical Application to Protein-Protein Interactions Using Global Analysis. *J R Soc Interf* (2009) 6, S93–S105. doi:10.1098/rsif.2008.0451.focus
5. Berezin MY, and Achilefu S. Fluorescence Lifetime Measurements and Biological Imaging. *Chem Rev* (2010) 110(5):2641–84. doi:10.1021/cr900343z
6. Bruschini C, Homulle H, Antolovic IM, Burri S, and Charbon E. Single-photon SPAD Imagers in Biophotonics: Review and Outlook. ArXiv (2019).
7. Bunt G, and Wouters FS. FRET from Single to Multiplexed Signaling Events. *Biophys Rev* (2017) 9(2):119–29. doi:10.1007/s12551-017-0252-z
8. Campos-Delgado DU, Navarro OG, Arce-Santana ER, and Jo JA. Extended Output Phasor Representation of Multi-Spectral Fluorescence Lifetime Imaging Microscopy. *Biomed Opt Express* (2015) 6(6):2088. doi:10.1364/boe.6.002088
9. Chan TF, and Vese LA. Active Contours without Edges. *IEEE Trans Image Process* (2001) 10(2):266–77. doi:10.1109/83.902291
10. Chen W, Avezov E, Schlachter SC, Gielen F, Laine RF, Harding HP, et al. A Method to Quantify FRET Stoichiometry with Phasor Plot Analysis and Acceptor Lifetime Ingrowth. *Biophysical J* (2015) 108(5):999–1002. doi:10.1016/j.bpj.2015.01.012
11. Chen H, Holst G, and Gratton E. Modulated CMOS Camera for Fluorescence Lifetime Microscopy. *Microsc Res Tech* (2015a) 78(12):1075–81. doi:10.1002/jemt.22587
12. Clayton AHA, Hanley QS, and Verveer PJ. Graphical Representation and Multicomponent Analysis of Single-Frequency Fluorescence Lifetime Imaging Microscopy Data. *J Microsc* (2004) 213(1):1–5. doi:10.1111/j.1365-2818.2004.01265.x

13. Clegg RM Chapter 1 Förster Resonance Energy Transfer-FRET what Is it, Why Do it, and How It's Done, *Laboratory Techniques in Biochemistry and Molecular Biology*, 33 (2009). p. 1–57. doi:10.1016/S0075-7535(08)00001-6
14. Colyer R, Siegmund O, Tremsin A, Vallerga J, Weiss S, and Michalet X. Phasor-based Single-Molecule Fluorescence Lifetime Imaging Using a Wide-Field Photon-Counting Detector. *Single Molecule Spectrosc Imaging* (2009) (71850T) 7185. doi:10.1117/12.809496
15. Dagher M, Kleinman M, Ng A, and Juncker D. Ensemble Multicolour FRET Model Enables Barcoding at Extreme FRET Levels. *Nat Nanotech* (2018) 13(10):925–32. doi:10.1038/s41565-018-0205-0
16. Dean KM, and Palmer AE. Advances in Fluorescence Labeling Strategies for Dynamic Cellular Imaging. *Nat Chem Biol* (2014) 10(7):512–23. doi:10.1038/nchembio.1556
17. Demeautis C, Sipieter F, Roul J, Chapuis C, Padilla-Parra S, Riquet FB, et al. Multiplexing PKA and ERK1&2 Kinases FRET Biosensors in Living Cells Using Single Excitation Wavelength Dual Colour FLIM. *Sci Rep* (2017) 7(December):1–14. doi:10.1038/srep41026
18. Digman MA, Caiolfa VR, Zamai M, and Gratton E. The Phasor Approach to Fluorescence Lifetime Imaging Analysis. *Biophysical J* (2008) 94(2):L14–L16. doi:10.1529/biophysj.107.120154
19. Esposito A, and Venkitaraman AR. Enhancing Biochemical Resolution by Hyperdimensional Imaging Microscopy. *Biophysical J* (2019) 116(10):1815–22. doi:10.1016/j.bpj.2019.04.015
20. Esposito A, Gerritsen HC, and Wouters FS. Fluorescence Lifetime Heterogeneity Resolution in the Frequency Domain by Lifetime Moments Analysis. *Biophysical J* (2005) 89(6):4286–99. doi:10.1529/biophysj.104.053397
21. Esposito A, Popleteeva M, and Venkitaraman AR. Maximizing the Biochemical Resolving Power of Fluorescence Microscopy. *PLoS ONE* (2013) 8(10):e77392. doi:10.1371/journal.pone.0077392
22. Fereidouni F, Bader AN, and Gerritsen HC. Spectral Phasor Analysis Allows Rapid and Reliable Unmixing of Fluorescence Microscopy Spectral Images. *Opt Express* (2012) 20(12):12729. doi:10.1364/oe.20.012729
23. Fereidouni F, Blab GA, and Gerritsen HC. Blind Unmixing of Spectrally Resolved Lifetime Images. *J Biomed Opt* (2013) 18(8):086006. doi:10.1117/1.jbo.18.8.086006
24. Fereidouni F, Reitsma K, and Gerritsen HC. High Speed Multispectral Fluorescence Lifetime Imaging. *Opt Express* (2013) 21(10):11769. doi:10.1364/oe.21.011769
25. Fereidouni F, Blab GA, and Gerritsen HC. Phasor Based Analysis of FRET Images Recorded Using Spectrally Resolved Lifetime Imaging. *Methods Appl Fluoresc* (2014) 2(3):035001. doi:10.1088/2050-6120/2/3/035001
26. Forde TS, and Hanley QS. Spectrally Resolved Frequency Domain Analysis of Multi-Fluorophore Systems Undergoing Energy Transfer. *Appl Spectrosc* (2006) 60(12):1442–52. doi:10.1366/000370206779321544
27. Fries MW, Haas KT, Ber S, Saganty J, Richardson EK, Venkitaraman AR, et al. Multiplexed Biochemical Imaging Reveals Caspase Activation Patterns Underlying Single Cell Fate. *BioRxiv* (2018). doi:10.1101/427237
28. Gadella TW, and Jovin TM. Oligomerization of Epidermal Growth Factor Receptors on A431 Cells Studied by Time-Resolved Fluorescence Imaging Microscopy. A Stereochemical Model for Tyrosine Kinase Receptor Activation. *J Cel Biol* (1995) 129(6):1543–58. doi:10.1083/jcb.129.6.1543
29. Galperin E, Verkhusha VV, and Sorkin A. Three-chromophore Fret Microscopy to Analyze Multiprotein Interactions in Living Cells. *Nat Methods* (2004) 1(3):209–17. doi:10.1038/nmeth720
30. Grant DM, Zhang W, McGhee EJ, Bunney TD, Talbot CB, Kumar S, et al. Multiplexed FRET to Image Multiple Signaling Events in Live Cells. *Biophysical J* (2008) 95(10):L69–L71. doi:10.1529/biophysj.108.139204
31. Grecco HE, Roda-Navarro P, and Verveer PJ. Global Analysis of Time Correlated Single Photon Counting FRET-FLIM Data. *Opt Express* (2009) 17(8):6493. doi:10.1364/oe.17.006493
32. Guerrieri F, Tisa S, Tosi A, and Zappa F. Two-dimensional SPAD Imaging Camera for Photon Counting. *IEEE Photon J.* (2010) 2(5):759–74. doi:10.1109/JPHOT.2010.2066554
33. Hanley QS, and Clayton AHA. AB-plot Assisted Determination of Fluorophore Mixtures in a Fluorescence Lifetime Microscope Using Spectra or Quenchers. *J Microsc* (2005) 218(1):62–7. doi:10.1111/j.1365-2818.2005.01463.x
34. Hanley QS. Spectrally Resolved Fluorescent Lifetime Imaging. *J R Soc Interf* (2009) 6. doi:10.1098/rsif.2008.0393.focus
35. Hinde E, Digman MA, Welch C, Hahn KM, and Gratton E. Biosensor Förster Resonance Energy Transfer Detection by the Phasor Approach to Fluorescence Lifetime Imaging Microscopy. *Microsc Res Tech* (2012) 75(3):271–81. doi:10.1002/jemt.21054
36. Hinde E, Digman MA, Hahn KM, and Gratton E. Millisecond Spatiotemporal Dynamics of FRET Biosensors by the Pair Correlation Function and the Phasor Approach to FLIM. *Proc Natl Acad Sci* (2013) 110(1):135–40. doi:10.1073/pnas.1211882110
37. Jares-Erijman EA, and Jovin TM. FRET Imaging. *Nat Biotechnol* (2003) 21(11):1387–95. doi:10.1038/nbt896
38. Kaufmann T, Herbert S, Hackl B, Besold JM, Schramek C, Gotzmann J, et al. Direct Measurement of Protein-Protein Interactions by FLIM-FRET at UV Laser-Induced DNA Damage Sites in Living Cells. *Nucleic Acids Res* (2020) 48(21):e122. doi:10.1093/nar/gkaa859
39. Kim J, and Heo WD. Synergistic Ensemble of Optogenetic Actuators and Dynamic Indicators in Cell Biology. *Mol Cell* (2018) 41(9):809–17. doi:10.14348/molcells.2018.0295
40. Kogure T, Karasawa S, Araki T, Saito K, Kinjo M, and Miyawaki A. A Fluorescent Variant of a Protein from the Stony Coral Montipora Facilitates Dual-Color Single-Laser Fluorescence Cross-Correlation Spectroscopy. *Nat Biotechnol* (2006) 24(5):577–81. doi:10.1038/nbt1207
41. Kremers G-J, Van Munster EB, Goedhart J, and Gadella TWJ. Quantitative Lifetime Unmixing of Multiexponentially Decaying Fluorophores Using Single-Frequency Fluorescence Lifetime Imaging Microscopy. *Biophysical J* (2008) 95(1):378–89. doi:10.1529/biophysj.107.125229
42. Krstajić N, Levitt J, Poland S, Ameer-Beg S, and Henderson R. 256 × 2 SPAD Line Sensor for Time Resolved Fluorescence Spectroscopy. *Opt Express* (2015) 23(5):5653–69. doi:10.1364/oe.23.005653
43. Lagarto JL, Villa F, Tisa S, Zappa F, Shcheslavskiy V, Pavone FS, et al. Real-time Multispectral Fluorescence Lifetime Imaging Using Single Photon Avalanche Diode Arrays. *Sci Rep* (2020) 10(1):1–10. doi:10.1038/s41598-020-65218-3
44. Lakowicz JR. *Principles of Fluorescence Spectroscopy*. Boston, MA: Springer. (2006). doi:10.1007/978-0-387-46312-4
45. Le Marois A, and Shuling K. *Multi-Parametric Live Cell Microscopy of 3D Tissue Models. Advances in Experimental Medicine and Biology*. Russia. Springer International Publishing. (2017). doi:10.1007/978-3-319-67358-5
46. Levitt JA, Matthews DR, Ameer-Beg SM, and Suhling K. Fluorescence Lifetime and Polarization-Resolved Imaging in Cell Biology. *Curr Opin Biotechnol* (2009) 20(1):28–36. doi:10.1016/j.copbio.2009.01.004
47. Levitt JA, Poland SP, Krstajic N, Pfisterer K, Erdogan A, Barber PR, et al. Quantitative Real-Time Imaging of Intracellular FRET Biosensor Dynamics Using Rapid Multi-Beam Confocal FLIM. *Sci Rep* (2020) 10(1):1–9. doi:10.1038/s41598-020-61478-1
48. Li IT, Pham E, and Truong K. Protein Biosensors Based on the Principle of Fluorescence Resonance Energy Transfer for Monitoring Cellular Dynamics. *Biotechnol Lett* (2006) 28(24):1971–82. doi:10.1007/s10529-006-9193-5
49. Liang Z, Lou J, Scipioni L, Gratton E, and Hinde E. Quantifying Nuclear Wide Chromatin Compaction by Phasor Analysis of Histone Förster Resonance Energy Transfer (FRET) in Frequency Domain Fluorescence Lifetime Imaging Microscopy (FLIM) Data. *Data in Brief* (2020) 30:105401. doi:10.1016/j.dib.2020.105401
50. Lou J, Scipioni L, Wright BK, Bartolec TK, Zhang J, Masamsetti VP, et al. Phasor Histone FLIM-FRET Microscopy Quantifies Spatiotemporal Rearrangement of Chromatin Architecture during the DNA Damage Response. *Proc Natl Acad Sci USA* (2019) 116(15):7323–32. doi:10.1073/pnas.1814965116
51. Mai H, Poland SP, Mattioli Della Rocca F, Treacy C, Aluko J, Nedbal J, et al. Flow Cytometry Visualization and Real-Time Processing with a CMOS SPAD Array and High-Speed Hardware Implementation Algorithm. *Proc.SPIE* (2020) 11243. doi:10.1117/12.2544759
52. Malacrida L, Jameson DM, and Gratton E. A Multidimensional Phasor Approach Reveals LAURDAN Photophysics in NIH-3T3 Cell Membranes. *Sci Rep* (2017) 7(1):1–11. doi:10.1038/s41598-017-08564-z
53. Mastop M, Bindels DS, Shaner NC, Postma M, Gadella TWJ, and Goedhart J. Characterization of a Spectrally Diverse Set of Fluorescent Proteins as FRET Acceptors for mTurquoise2. *Sci Rep* (2017) 7(1):1–18. doi:10.1038/s41598-017-12212-x

54. Miyawaki A, Shcherbakova DM, and Verkhusha VV. Red Fluorescent Proteins: Chromophore Formation and Cellular Applications. *Curr Opin Struct Biol* (2012) 22(5):679–88. doi:10.1016/j.sbi.2012.09.002
55. Molina-Guijarro JM, García C, Macías Á, García-Fernández LF, Moreno C, Reyes F, et al. Elisidepsin Interacts Directly with Glycosylceramides in the Plasma Membrane of Tumor Cells to Induce Necrotic Cell Death. *PLoS ONE* (2015) 10(10):e0140782–18. doi:10.1371/journal.pone.0140782
56. Niehörster T, Löschberger A, Gregor I, Krämer B, Rahn H-J, Patting M, et al. Multi-target Spectrally Resolved Fluorescence Lifetime Imaging Microscopy. *Nat Methods* (2016) 13(3):257–62. doi:10.1038/nmeth.3740
57. Niino Y, Hotta K, and Oka K. Simultaneous Live Cell Imaging Using Dual FRET Sensors with a Single Excitation Light. *PLoS ONE* (2009) 4(6):e6036–9. doi:10.1371/journal.pone.0006036
58. Pian Q, Yao R, Sinsuebphon N, and Intes X. Compressive Hyperspectral Time-Resolved Wide-Field Fluorescence Lifetime Imaging. *Nat Photon* (2017) 11(7):411–4. doi:10.1038/nphoton.2017.82
59. Poland SP, Krstajić N, Monypenny J, Coelho S, Tyndall D, Walker RJ, et al. A High Speed Multifocal Multiphoton Fluorescence Lifetime Imaging Microscope for Live-Cell FRET Imaging. *Biomed Opt Express* (2015) 6(2):277. doi:10.1364/boe.6.000277
60. Poland SP, Chan GK, Levitt JA, Krstajić N, Erdogan AT, Henderson RK, et al. Multifocal Multiphoton Volumetric Imaging Approach for High-Speed Time-Resolved Förster Resonance Energy Transfer Imaging In Vivo. *Opt Lett* (2018) 43(24):6057. doi:10.1364/ol.43.006057
61. Popleteeva M, Haas KT, Stoppa D, Pancheri L, Gasparini L, Kaminski CF, et al. Fast and Simple Spectral FLIM for Biochemical and Medical Imaging. *Opt Express* (2015) 23(18):23511. doi:10.1364/oe.23.023511
62. Qiu X, Guo J, Xu J, and Hildebrandt N. Three-Dimensional FRET Multiplexing for DNA Quantification with Attomolar Detection Limits. *J Phys Chem Lett* (2018) 9(15):4379–84. doi:10.1021/acs.jpclett.8b01944
63. Rück A, Hauser C, Mosch S, and Kalinina S. Spectrally Resolved Fluorescence Lifetime Imaging to Investigate Cell Metabolism in Malignant and Nonmalignant Oral Mucosa Cells. *J Biomed Opt* (2014) 19(9):96005–9. doi:10.1117/1.JBO.19.9.096005
64. Scott BL, and Hoppe AD. Three-dimensional Reconstruction of Three-Way FRET Microscopy Improves Imaging of Multiple Protein-Protein Interactions. *PLoS ONE* (2016) 11(3):e0152401–17. doi:10.1371/journal.pone.0152401
65. Sharman KK, Periasamy A, Ashworth H, Demas JN, and Snow NH. Error Analysis of the Rapid Lifetime Determination Method for Double-Exponential Decays and New Windowing Schemes. *Anal Chem* (1999) 71(5):947–52. doi:10.1021/ac981050d
66. Shcherbakova DM, Hink MA, Joosen L, Gadella TWJ, and Verkhusha VV. An orange Fluorescent Protein with a Large Stokes Shift for Single-Excitation Multicolor FCCS and FRET Imaging. *J Am Chem Soc* (2012) 134(18):7913–23. doi:10.1021/ja3018972
67. Shcherbakova DM, Cox Cammer N, Huisman TM, Verkhusha VV, and Hodgson L. Direct Multiplex Imaging and Optogenetics of Rho GTPases Enabled by Near-Infrared FRET. *Nat Chem Biol* (2018) 14(6):591–600. doi:10.1038/s41589-018-0044-1
68. Stringari C, Cinquin A, Cinquin O, Digman MA, Donovan PJ, and Gratton E. Phasor Approach to Fluorescence Lifetime Microscopy Distinguishes Different Metabolic States of Germ Cells in a Live Tissue. *Proc Natl Acad Sci* (2011) 108(33):13582–7. doi:10.1073/pnas.1108161108
69. Sun Y, Wallrabe H, Booker CF, Day RN, and Periasamy A. Three-color Spectral FRET Microscopy Localizes Three Interacting Proteins in Living Cells. *Biophysical J* (2010) 99(4):1274–83. doi:10.1016/j.bpj.2010.06.004
70. Szmacinski H, Toshchakov V, and Lakowicz JR. Application of Phasor Plot and Autofluorescence Correction for Study of Heterogeneous Cell Population. *J Biomed Opt* (2014) 19(4):046017. doi:10.1117/1.jbo.19.4.046017
71. Trinh AL, Ber S, Howitt A, Valls PO, and Fries MW Europe PMC Funders Group Fast Single-Cell Biochemistry : Theory, *open source Microsc Appl* (2020), 7. doi:10.1088/2050-6120/ab3bd2.Fast
72. Ulku A, Ardelean A, Antolovic M, Weiss S, Charbon E, Bruschini C, et al. Wide-field Time-Gated SPAD Imager for Phasor-Based FLIM Applications. *Methods Appl Fluoresc* (2020) 8(2):024002. doi:10.1088/2050-6120/ab6ed7
73. Wang S, Shen B, Ren S, Zhao Y, Zhang S, Qu J, et al. Implementation and Application of FRET-FLIM Technology. *J Innov Opt Health Sci* (2019) 12(5):1930010–2. doi:10.1142/S1793545819300106
74. Warren S, Margineanu A, Katan M, Dunsby C, and French P. Homo-FRET Based Biosensors and Their Application to Multiplexed Imaging of Signalling Events in Live Cells. *Ijms* (2015) 16(7):14695–716. doi:10.3390/ijms160714695
75. Zeug A, Woehler A, Neher E, and Ponimaskin EG. Quantitative Intensity-Based FRET Approaches-A Comparative Snapshot. *Biophysical J* (2012) 103(9):1821–7. doi:10.1016/j.bpj.2012.09.031
76. Zickus V, Wu M-L, Morimoto K, Kapitany V, Fatima A, Turpin A, et al. Fluorescence Lifetime Imaging with a Megapixel SPAD Camera and Neural Network Lifetime Estimation. *Sci Rep* (2020) 10(1):1–10. doi:10.1038/s41598-020-77737-0

Conflict of Interest: The authors declare that the research was conducted in the absence of any commercial or financial relationships that could be construed as a potential conflict of interest.

frontiers in Molecular Biosciences

ORIGINAL RESEARCH
published: 11 May 2021
doi: 10.3389/fmolb.2021.630107

Cannabidiol Modulates Mitochondrial Redox and Dynamics in MCF7 Cancer Cells: A Study Using Fluorescence Lifetime Imaging Microscopy of NAD(P)H

Rhys Richard Mould[1], *Stanley W. Botchway*[2], *James R. C. Parkinson*[1], *Elizabeth Louise Thomas*[1], *Geoffrey W Guy*[3], *Jimmy D. Bell*[1] *and Alistair V. W. Nunn*[1]*

[1]*Research Centre for Optimal Health, School of Life Sciences, University of Westminster, London, United Kingdom,* [2]*Central Laser Facility, Science and Technology Facilities Council, UKRI, Rutherford Appleton Laboratory, Harwell Campus, Oxford, United Kingdom,* [3]*GW Pharmaceuticals, Salisbury, United Kingdom*

OPEN ACCESS

Edited by:
Klaus Suhling, King's College London, United Kingdom

Reviewed by:
Alzbeta Marcek Chorvatova, International Laser Center, Slovakia
Thomas Blacker, University College London, United Kingdom

***Correspondence:**
Alistair V. W. Nunn
nunn@westminster.ac.uk

Specialty section:
This article was submitted to Biophysics, a section of the journal Frontiers in Molecular Biosciences

Received: *16 November 2020*
Accepted: *16 February 2021*
Published: *11 May 2021*

Citation:
Mould RR, Botchway SW, Parkinson JRC, Thomas EL, Guy GW, Bell JD and Nunn AVW (2021) Cannabidiol Modulates Mitochondrial Redox and Dynamics in MCF7 Cancer Cells: A Study Using Fluorescence Lifetime Imaging Microscopy of NAD(P)H. Front. Mol. Biosci. 8:630107. doi: 10.3389/fmolb.2021.630107

The cannabinoid, cannabidiol (CBD), is part of the plant's natural defense system that when given to animals has many useful medicinal properties, including activity against cancer cells, modulation of the immune system, and efficacy in epilepsy. Although there is no consensus on its precise mode of action as it affects many cellular targets, CBD does appear to influence mitochondrial function. This would suggest that there is a cross-kingdom ability to modulate stress resistance systems that enhance homeostasis. As NAD(P)H autofluorescence can be used as both a metabolic sensor and mitochondrial imaging modality, we assessed the potential of this technique to study the *in vitro* effects of CBD using 2-photon excitation and fluorescence lifetime imaging microscopy (2P-FLIM) of NAD(P)H against more traditional markers of mitochondrial morphology and cellular stress in MCF7 breast cancer cells. 2P-FLIM analysis revealed that the addition of CBD induced a dose-dependent decrease in bound NAD(P)H, with 20 μM treatments significantly decreased the contribution of bound NAD(P)H by 14.6% relative to the control ($p < 0.001$). CBD also increased mitochondrial concentrations of reactive oxygen species (ROS) (160 ± 53 vs. 97.6 ± 4.8%, 20 μM CBD vs. control, respectively, $p < 0.001$) and Ca^{2+} (187 ± 78 vs. 105 ± 10%, 20 μM CBD vs. the control, respectively, $p < 0.001$); this was associated with a significantly decreased mitochondrial branch length and increased fission. These are all suggestive of mitochondrial stress. Our results support the use of NAD(P)H autofluorescence as an investigative tool and provide further evidence that CBD can modulate mitochondrial function and morphology in a dose-dependent manner, with clear evidence of it inducing oxidative stress at higher concentrations. This continues to support emerging data in the literature and may provide further insight into its overall mode of action, not only in cancer, but potentially its function in the plant and why it can act as a medicine.

Keywords: cannabidiol, mitochondrial dynamics, imaging, redox, FLIM, NADH autofluorescence, multiphoton

INTRODUCTION

Uncontrolled cell growth, or cancer, is frequently associated with increased aerobic glycolysis (the Warburg effect) and alterations in mitochondrial function (Trigos et al., 2018). A plant's ability to develop tumors could explain why so many secondary plant phenolic compounds appear to have anticancer activity in both plant and animal models (Rasouli et al., 2016); over 3,000 species of plants have anticancer activity in animals, with many modulating mitochondrial function and apoptosis (Gali-Muhtasib et al., 2015). Due to the similarities between plant and animal metabolism, many plant compounds can be considered mitochondrially targeted drugs for treating cancer (Gorlach et al., 2015). In plants, mitochondria are central in managing oxidative stress *via* thermodynamic buffering, involving enhancement of antioxidant capacity and uncoupling, as well as detoxification and induction of programmed cell death (Popov, 2020; Gandin et al., 2021). This is supported by evidence that some bioactive plant compounds can protect plant mitochondria (Laus and Soccio, 2020). Critically, the stress response system has to not only be adaptive and protect cells but also induce cell death when necessary, suggesting a biphasic or hormetic dose–response curve. One such compound, cannabidiol (CBD), has demonstrated a plethora of pharmacological effects ranging from anti-inflammatory to anxiolytic, antiepileptic, anticancer, and even antibacterial (Mechoulam et al., 2002; Gray et al., 2020; Kis et al., 2019). However, there is still no clear consensus on its mode of action. Rather than focusing on individual receptors and channels, here we investigate how it might modulate a key nexus in cell function, the mitochondrion.

CBD, along with Δ9-tetrahydrocannabinol (THC), is a major phytocannabinoid and both are well described components of medicines. Unlike THC, CBD is not psychoactive and is now being used to treat epilepsy (O'Connell et al., 2017; Baker et al., 2000). A growing number of studies have demonstrated the anticancer properties of CBD, in both *in vitro* and *in vivo* models (Ramer and Hinz, 2017; Kis et al., 2019). Proposed mechanisms include induction of autophagy and mitochondrial-mediated apoptosis and inhibition of exosome and microvesicle release (Shrivastava et al., 2011; Armstrong et al., 2015; McAllister et al., 2015; Kosgodage et al., 2018). Although the exact cellular mechanisms by which CBD exerts its effects remain unclear (Ibeas Bih et al., 2015), one potential mechanism may relate to its ability to interact with the voltage-dependent anion channel 1 (VDAC1) (Rimmerman et al., 2013), which is central to metabolic reprogramming, apoptosis, and a cancer drug target (Shoshan-Barmatz et al., 2018). VDAC1 is also important in controlling mitochondrial morphology as part of the mitochondrial-associated membrane (MAM) complex and a key controller of calcium flux (Giorgi et al., 2015). Critically, cancer cells modulate mitochondrial dynamics to resist apoptosis (Senft and Ronai, 2016). We have preliminary data that indicate that CBD modulates mitochondrial dynamics (Nunn et al., 2013), supported by recent studies which suggest CBD modulates the membrane order and induces cholesterol biosynthesis (Guard et al., 2020).

Another important target for CBD, the transient receptor potential vanilloid 1 (TRPV1) (Bisogno et al., 2001; Iannotti et al., 2014) is critical in calcium signaling and can lead to its accumulation by mitochondria (Bujak et al., 2019). CBD stimulates neuronal survival in models of Parkinson's disease via the protein kinase B/mammalian target of rapamycin (AKT/mTOR) pathway through a mechanism involving TRPV1 (Gugliandolo et al., 2020) and can also induce cancer cell death by inhibiting AKT/mTOR (Pisanti et al., 2017). Similarly, CBD reduces oxidative stress, enhances mitochondrial function, and stimulates G6PDH activity and the pentose phosphate pathway (PPP) in cerebral ischemia (Sun et al., 2017). However, enhancing PPP pathway components in mitochondria, such as G6PDH could, by reducing oxidative stress, suppress apoptosis and thus enhance oncogenesis (Redhu and Bhat, 2020). This would begin to explain why a single compound can both be protective (e.g., in neurons) and capable of killing cancer cells.

It is possible that CBD directly modulates mitochondrial function as part of its mode of action. Balance between reduced nicotinamide adenine dinucleotide (NADH) and nicotinamide adenine dinucleotide phosphate (NADPH) plays a key role in balancing oxidative stress. This, in concert with markers such as reactive oxygen species (ROS), calcium, and mitochondrial dynamics could be informative in confirming this. In recent years, 2P-FLIM of the reduced forms of NADH and NADPH has emerged as a viable means of assessing the redox state of the cell (Yaseen et al., 2017) and is used to identify numerous pharmacological, physiological, and pathophysiological disruptions in NAD^+/NADH and $NADP^+$/NADPH metabolism (Yu and Heikal, 2009; Stringari et al., 2011; Skala et al., 2007a). The spectral properties of NADH and NADPH are indistinguishable and are therefore referred to as NAD(P)H. Moreover, NAD(P)H fluorescence is an effective way of imaging mitochondria, as NADH is predominantly found in the mitochondrion (Yu and Heikal, 2009).

NADH is a central cofactor in both anaerobic glycolysis and aerobic oxidative pathways and plays a critical role in controlling cellular energy production (Blacker and Duchen, 2016). The intrinsic fluorescence of NAD(P)H enables two photon fluorescence lifetime imaging (2P-FLIM) to differentiate between components of free or bound NAD(P)H species, thereby reflecting changes in enzymatic function and representing a potential label-free, direct marker of cellular metabolism. The excited state lifetime of a molecule allows for the extraction of additional information, as it is determined by a wide range of environmental parameters, including oxygen concentration, pH, ions, molecular binding, and the proximity to other molecules, making it currently the technique of choice for functional imaging in live cells and tissue. The use of two-photon excitation also provides further advantages; for example, using excitation wavelengths in the near infra-red (NIR) that are tissue-friendly compared to ultraviolet radiation, decreasing overall cell and tissue autofluorescence and light scattering, and improved tissue depth penetration which allows diffraction limited imaging selectivity, noninvasively confined to the focal volume (Suhling et al., 2015).

Here we report the use of FLIM to further assess the effects of CBD on mitochondrial metabolism and morphology in MCF7

breast adenocarcinoma cells. To achieve this, we used NAD(P)H autofluorescence by applying 2P-FLIM to provide a label-free marker of the metabolic state and mitochondrial morphology and more conventional fluorescent markers to study ROS and mitochondrial calcium levels.

MATERIALS AND METHODS

Cell Culture

MCF7 cells (from ATCC, provided by Central Laser Facility, UKRI) were cultured in minimal essential media (MEM), supplemented with 10% FBS and 1% penicillin/streptomycin. For the experiments, cells were seeded onto individual dishes or multiwell plates and treated with 0.005% v/v DMSO (Control) or 1, 5, 10, and 20 μM CBD (Sigma, United Kingdom) for 24 h prior to assessment at 37°C with 5% CO_2 humidified air.

2-Photon Fluorescence Lifetime Imaging Microscopy

2P-FLIM was used to image and quantify NAD(P)H lifetime decay as a measure of cellular and mitochondrial metabolism. MCF7 cells were seeded at densities of 1.5×10^5 onto individual glass bottom dishes (MatTek) and treated as described. Before imaging, cells were acclimatized for 15 min to room temperature. The 2P-FLIM setup has been described previously (Botchway et al., 2015). Images were obtained as follows: 750 nm wavelength light for 2-photon excitation of NADH was generated by a mode-locked titanium sapphire laser (Mira F900, Coherent Laser Ltd.), producing 180 fs pulses at 76 MHz. This laser was pumped by a solid-state continuous wave 532 nm laser (Verdi 18, Coherent Lasers Ltd.). Images were collected through a water immersion 60X 1.2 NA objective on a modified Nikon EC2 confocal scanning system attached to a TE2000-U microscope as described previously (Botchway et al., 2015). Emission was collected by the same objective, reflected off a 530 BK-25 filter (Comar Optics, United Kingdom), passed through a BG39 filter and detected with an external hybrid GaAsP (HPM-100–40, Becker and Hickl, Germany), linked to a time correlated single photon counting (TCSPC) module (SPC830, Becker and Hickl, Germany). In this configuration, together with an average laser power of 0.5 mW at the sample, we mostly observe the fluorescence signal from NAD(P)H with negligible contribution from the flavins. This was confirmed with solution phase studies of NAD(P)H and FAD (both purchased from Sigma, United Kingdom, and used without further purification). We have performed a dual channel FLIM setup containing BG39 with or without extra band pass filters (a 440–490 nm band pass filter for NADH and a 520–570 nm band pass filter for FAD and flavins), and we did not detect flavin emission in the NADH channel. Solution concentrations as high as 0.5 mM are observed in the flavin-detecting channel only. The intracellular FAD concentration has been estimated to be around 8 μM (Kimata et al., 2018). For each of the five experimental groups (Control, 1, 5, 10, and 20 μm CBD), five spatially distinct 2P-FLIM images were acquired. Within each image, five nonoverlapping cells with the highest signal-to-noise ratio were chosen, equating to 25 cells per treatment group. As NAD(P)H signal intensity aligns with mitochondrial morphology (See **Supplementary Figure S1**), pixels corresponding to the mitochondria or the cytosol could be manually selected (See **Supplementary Figure S2**) (the spatial resolution of the setup was determined to be ~350 nm) (Alam et al., 2017). Photon counts of at least 1,000 were used for the multiexponential analysis, which also excluded nuclear areas from analysis. The decay curve of each pixel from the 2P-FLIM image was modeled with a biexponential decay curve, according to **Eq. 1**, where I(t) represents fluorescence intensity at time t after the laser pulse. Goodness of fit was quantified by Chi-squared analysis (See **Supplementary Figure S3**). From each pixel two observed lifetimes were recorded: τ_{Free} for free NAD(P)H and τ_{Bound} for enzyme-bound NAD(P)H and the contributions of each lifetime to the overall decay curve, α_{Free} and α_{Bound}, respectively (Sharick et al., 2018; Blignaut et al., 2019).

$$I(t) = \alpha_{Free} exp^{-t/\tau_1} + \alpha_{Bound} exp^{-t/\tau_2} \quad [1]$$

Mitochondrial Reactive Oxygen Species and Ca^{2+}

Mitochondrial ROS and Ca^{2+} levels were quantified using the MitoSOX Red (ThermoFisher, United Kingdom) and Rhod2 (ThermoFisher, United Kingdom) stains, respectively, in octuplicate, as per manufacturer's instructions. Briefly, MCF7 cells were seeded at densities of 3.0×10^4 cells per well. Following treatment, cells were stained with either 5 μM MitoSOX Red or 1 μM Rhod2 for 30 min. Fluorescence was measured on a FLUOstar Optima microplate reader (BMG, Germany). Excitation/Emission: 510/580 nm for MitoSOX Red and 552/580 nm for Rhod2. Fluorescence intensities were normalized to total cellular protein, measured using the Bradford assay.

Mitochondrial Morphology Analysis

Mitochondrial morphology was analyzed as previously described (Valente et al., 2017). Briefly, MCF7 cells were seeded at densities of 1.0×10^5 cells per well and treated with DMSO (Control) or CBD for 24 h as described above. Following treatment, cells were stained with MitoTracker Deep Red and NucBlue (ThermoFisher, United Kingdom) and imaged using the ThermoFisher EVOS FL2 Auto using a 40X 0.65 NA plan fluorite objective. Five representative images were selected per treatment group and within each image, the mitochondria of three spatially distinct cells were selected for analysis. To quantify CBD-induced changes in morphology, the cells were analyzed with the MiNA plugin for ImageJ. This script, following a preprocessing stage of unsharp masking, local contrast enhancement (CLAHE), and median filtering, binarized and then skeletonized the mitochondrial image to produce an output of the mitochondrial footprint (the total area of the binary image), mean length of mitochondrial networks, mean branch length per network (the mean of the sum length of individual branches on separate networks) and mean number of networks. Three cells were analyzed per image for the five images. This experiment was carried out in triplicate.

Statistics

Data are presented as box plots, the box shows median with 25th and 75th percentiles, and the whiskers indicate minimum and

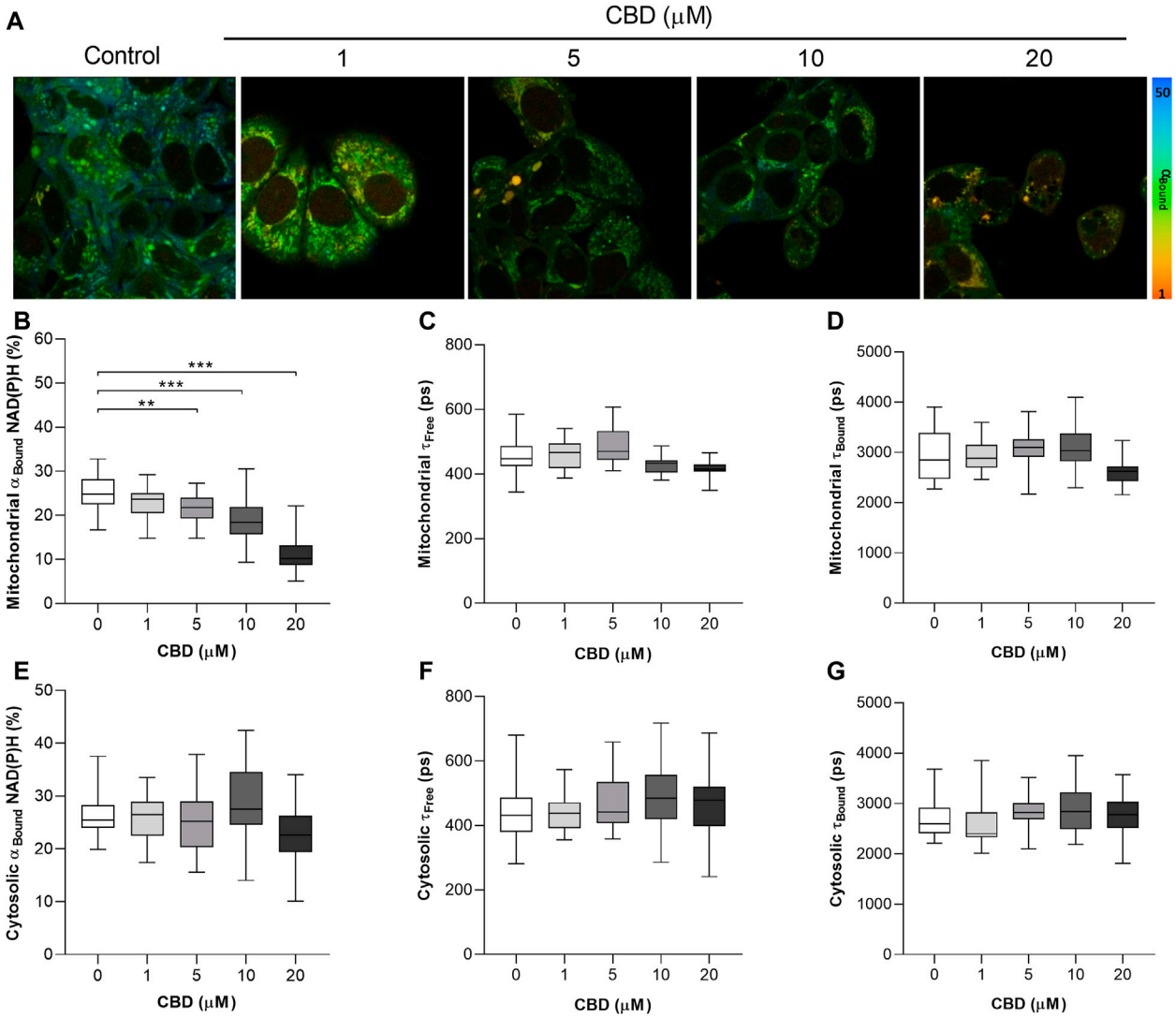

FIGURE 1 | *In vitro* effects of cannabidiol on NAD(P)H fluorescence decay as measured by 2P-FLIM. **(A)** 2P-FLIM–derived images of bound NAD(P)H (α_{Bound}). **(B–G)** Box plots showing the effect of CBD on **(B)** mitochondrial α_{Bound} NAD(P)H (%), **(C)** mitochondrial τ_{Free} (ps), **(D)** mitochondrial τ_{Bound} (ps), **(E)** cytosolic α_{Bound} NAD(P)H (%), **(F)** cytosolic τ_{Free} (ps), and **(G)** cytosolic τ_{Bound}. Box shows median with 25th and 75th percentiles, and whiskers indicate minimum and maximum values. n = 25/group; * = $p < 0.05$, ** = $p < 0.01$, *** = $p < 0.001$; data were analyzed by one-way ANOVA with Dunnett's test for multiple comparisons using GraphPad Prism (United States).

maximum values. Statistical significance was calculated by one-way ANOVA with Dunnett's multiple comparison using GraphPad Prism version 8.0 (GraphPad Software, La Jolla, California, United States). An adjusted $p < 0.05$ was considered statistically significant.

RESULTS

The significant dose-dependent effects of CBD on the mitochondrial NAD(P)H lifetime are shown in **Figure 1**. **Figure1A** are representative 2P-FLIM–derived images of bound NAD(P)H in MCF7 cells 24 h post-treatment with CBD. Each pixel represents the contribution of bound NAD(P)H to the overall fluorescence decay, $\alpha_{Bound,}$ and is color-coded between 50% (blue) and 1% (red). The images indicate a shift from high (blue-green) to lower α_{Bound} (yellow-orange) as the concentration of CBD increases. Quantitative changes in α_{Bound} are shown in **Figure 1B**. CBD was found to induce a dose-dependent decrease in α_{Bound} (Control: 25.3 ± 3.9% vs CBD 20 μM: 11.3 ± 4.1%, $p < 0.001$). CBD had no significant effect on the fluorescence lifetimes of mitochondrial free NAD(P)H (τ_{Free}) and bound NAD(P)H (τ_{Bound}), shown in **Figures 1C and D**, respectively. The mean values for each are consistent with the literature that describe free NAD(P)H as having a shorter lifetime of approximately 0.4 ns and bound NAD(P)H with a longer lifetime of approximately 2.4 ns. No significant effect of CBD was observed on cytosolic

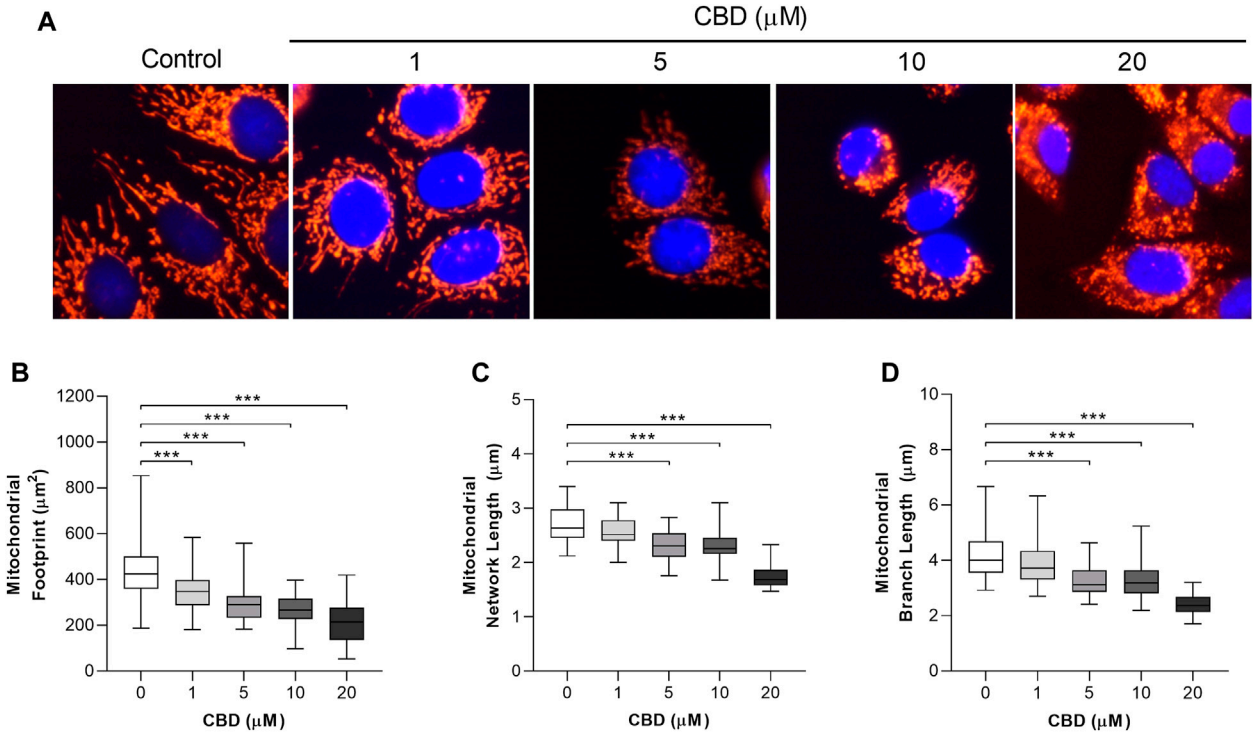

FIGURE 2 | *In vitro* effects of cannabidiol on mitochondrial morphology. **(A)** Representative images showing changes in mitochondrial morphology 24 h posttreatment with CBD (1, 5, 10, and 20 μM) or the control (DMSO). Cells were stained with MitoTracker Deep Red and NucBlue (ThermoFisher, United Kingdom) and imaged using the ThermoFisher EVOS FL2. **(B–D)** Box plots showing the effect of CBD on **(B)** mitochondrial footprint, **(C)** mitochondrial network length, and **(D)** mean mitochondrial branch length. Box shows median with 25th and 75th percentiles, and whiskers indicate minimum and maximum values. n = 45/group; *** = $p < 0.001$; data were analyzed by one-way ANOVA with Dunnett's test for multiple comparisons using GraphPad Prism (United States).

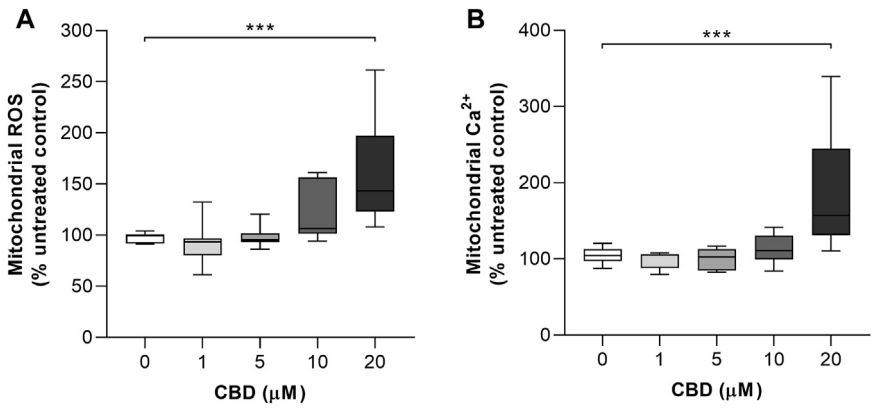

FIGURE 3 | *In vitro* effects of CBD on mitochondrial ROS and mitochondrial Ca^{2+} production in MCF7 cells. **(A)** Effects of cannabidiol (CBD) on normalized MitoSOX intensity as a marker of mitochondrial reactive oxygen species (ROS) production. **(B)** Effects of CBD on normalized Rhod2 intensity as a marker of mitochondrial Ca^{2+} production. Box shows median with 25th and 75th percentiles, and whiskers indicate minimum and maximum values. n = 8/group; ** = $p < 0.01$, *** = $p < 0.001$; data were analyzed by one-way ANOVA with Dunnett's test for multiple comparisons using GraphPad Prism (United States).

levels of α_{Bound} NAD(P)H (**Figure 1E**). CBD had no significant effect on the fluorescence lifetimes of cytosolic τ_{Free} and τ_{Bound} (shown in Figures 1F and G, respectively), and this again aligns with the literature describing the lifetimes of each species.

The *in vitro* effects of CBD on mitochondrial morphology in MCF7 cells are shown in **Figure 2**. Representative images are shown in **Figure 2A**. To quantify these changes in mitochondrial morphology we applied the MiNA plugin to assess the effects of

CBD on mitochondrial area (**Figure 2B**), network length (**Figure 2C**), and branch length (**Figure 2D**). CBD was found to induce a dose-dependent decrease in the mitochondrial footprint (control: 436 ± 133 μm^2 vs. CBD 20 μM: 214 ± 86 μm^2, $p < 0.001$, **Figure 2B**), mean network length (control: 2.7 ± 0.3 μm vs. CBD 20 μM: 1.8 ± 0.2 μm, $p < 0.001$, **Figure 2C**), and mean branch length (control: 4.2 ± 0.7 μm vs. CBD 20 μM: 2.4 ± 0.4 μm, $p < 0.001$, **Figure 2D**).

The effects of CBD treatment on mitochondrial ROS and mitochondrial Ca^{2+} levels are shown in **Figures 3A and B**, respectively. Compared to the controls, the highest dose of CBD significantly increased the mitochondrial levels of both ROS (Control: 97.6 ± 4.8% vs. CBD 20 μM: 160 ± 53, $p < 0.001$, **Figure 3B**) and Ca^{2+} (Control: 104.6 ± 10.3% vs. CBD 20 μM: 186.9 ± 78.2%, $p < 0.01$, **Figure 3C**).

DISCUSSION

In this study we used FLIM, fluorescence microscopy, and conventional ROS and calcium detecting stains to investigate the effects of CBD on NAD(P)H lifetime, calcium and ROS levels, and mitochondrial morphology in a breast cancer cell line. This study supports the use of FLIM to investigate how CBD may be working. The observed increase in mitochondrial ROS and calcium and enhanced mitochondrial fission and changes in bound NAD(P)H weighting are suggestive of CBD affecting mitochondrial function.

Studying mitochondrial function may be useful in explaining the beneficial actions of many natural products. This is reflected by the link between mitochondrial morphology and function in both immune cells (Rambold and Pearce, 2018) and cancer (Chen and Chan, 2017). Critically, many compounds that can suppress immunity are also antiproliferative; for instance, rapamycin, which modulates mTOR, is well known to be activated in cancer (Rad et al., 2018) and a modulator of mitochondrial function (Wei et al., 2015). In addition to metabolic reprogramming, mitochondria play a central role in regulating cell death, and resistance to proapoptotic signaling is a hallmark of cancer (Sayers, 2011).

Understanding Warburg to Understand Cannabidiol

A paradox in the understanding of the function of plant products, including CBD, is how they can enhance survival of normal cells, yet kill cancer cells. The Warburg shift, or aerobic glycolysis (Kroemer, 2006; Wallace, 2012), may be key, as it is overall antiapoptotic and probably key in the earlier stages of carcinogenesis, as more advanced cancers often upregulate mitochondrial function. This has led to the so called "Inverse Warburg Hypothesis", which, although not fully understood, suggests that high levels of mitochondrial metabolism underlie the observed inverse relationship between degenerative diseases and cancer. Mitochondria are pivotal in the detection of and adaptation to stress, sending out redox signals in response to stress, which may be an important mechanism explaining how plant secondary metabolites work as medicines via a process called mitohormesis (Tapia, 2006). Critically, evidence is accumulating that major plant stress signaling compounds, such as jasmonates, can modulate mitochondria in both plant and animal cells (Bömer et al., 2020). Moreover, plant compounds are known to interfere with glycolytic pathways and major controllers of metabolism, such as VDAC. Thus, they appear to inhibit carcinogenesis, but if a tumor does arise, they can alter its mitochondrial phenotype to restore cell death (Stevens et al., 2018).

Known Mitochondrial Effects for Cannabidiol–Controlling Calcium Flux

In cancer cells, reduced endoplasmic reticulum–mitochondria Ca^{2+} exchange contributes to apoptotic resistance; increased intracellular Ca^{2+} contributes to enhanced cell migration, facilitating metastasis (Marchi and Pinton, 2016). This is matched by changes in mitochondrial morphology, making cells more resistant to apoptosis (Senft and Ronai, 2016). Critically, mitochondrial function is tightly controlled by calcium, ranging from stimulation to enhance respiration, to overload to induce cell death (Rossi et al., 2019)—and in cancer, calcium flow is directed away from the mitochondrion (Danese et al., 2017).

CBD modulates TRPV1 and calcium influx into the cell and potentially into the mitochondrion (Ryan et al., 2009; Mato et al., 2010; Olivas-Aguirre et al., 2019). More directly, CBD has been shown to bind to and close VDAC1, a major channel responsible for transporting Ca^{2+}, potentially responsible for the immunosuppressive and anticancer effects of CBD (Rimmerman et al., 2013). In leukemic cells, CBD induces dose-related mitochondrial dysfunction, leading to apoptosis, which is associated with mitochondrial calcium overload, loss of mitochondrial membrane potential, and enhanced ROS production (Olivas-Aguirre et al., 2019). This all supports earlier data that CBD application can result in mitochondrial calcium overload and enhanced ROS production (Ryan et al., 2009; Mato et al., 2010).

Interpreting the FLIM Data

In response to CBD, we identified a dose-dependent decrease in mitochondrial bound NAD(P)H (α_{Bound}). This appears to indicate reduced activity of the ETC, as the oxidation of NADH by complex I is the first point where electrons enter the ETC (Chakraborty et al., 2016). Indeed, comparable reductions in NAD(P)H α_{Bound} have been observed in response to known mitochondrial toxins and inhibitors such as potassium cyanide and rotenone (Bird et al., 2005; Schneckenburger et al., 2004), while in contrast, agents which increase metabolic activity increase mitochondrial α_{Bound} NAD(P)H (Alam et al., 2017). So, in relation to our data, the increase in unbound NAD(P)H may represent an inhibition of the ETC and/or enhanced TCA leading to increased NADH, possibly coupled to inhibition of glycolysis and enhanced PPP activity, a generalized inhibition of metabolism leading more unbound NAD(P)H, and possibly, inhibition of $NADP^+$ binding

to G6PDH. The latter effect is a known ability of the polyphenol epigallocatechin gallate (EGCG) (Shin et al., 2008) which also modulates mitochondrial function (Oliveira et al., 2016). Inhibition of G6PD has also been observed for other phenolic compounds (Adem et al., 2014), while many have also been found to dissociate hexokinase from VDAC1, which inhibits glycolysis and can enhance apoptosis (Tewari et al., 2015; Tewari et al., 2017; Goldin et al., 2008). There is thus, perhaps, a generalization that many of these bioactive plant compounds have the capacity to induce metabolic reprogramming, which may also apply to CBD. Whilst the contribution of each species to the decay curve were affected by CBD treatment, there were no significant changes in the lifetimes of each species itself (τ_{free} and τ_{Bound}). Changes in τ_{Bound} are often associated with a redistribution of NAD(P)H binding sites as a result of a shift in metabolic pathways (Skala et al., 2007b). The absence of changes in this study may indicate no such pivot in specific metabolic pathways, although further studies comparing CBD-mediated τ_{free} and τ_{Bound} to agents known to perturb mitochondrial metabolism would be required to validate this.

In terms of intracellular localization, 2P-FLIM permits highly localized, label-free, sub-micron determination of the redox state, enabling the differentiation of the mitochondrial redox response from that of the cytosol. The lack of effect on free or bound cytosolic NAD(P)H in our results would seem to indicate that the actions of CBD are mitochondrial specific, which has been proposed based on the highly lipophilic properties of CBD (Huestis, 2007; Ryan et al., 2009). However, the subtle, interconnected relationships between the many cellular pathways maintaining stores of NADH are not fully deconvoluted in the aggregate FLIM signal (Blacker and Duchen, 2016), making full interpretation difficult. For example, while cancer cells shift their preferred energy-generating pathway to aerobic glycolysis (Trigos et al., 2018), the relative rates of glycolysis and OXPHOS do not appear to affect the intracellular NADH fluorescence lifetime (Blacker and Duchen, 2016; Guo et al., 2015).

Insight Into Mode of Action

It should be noted that the 24 h post-exposure protocol employed here was based on our earlier investigations into the actions of CBD (Kosgodage et al., 2018) and therefore limits our ability to define an accurate timescale for the specific cascade of intracellular events following CBD administration. However, previous studies have indicated that CBD-triggered increases in Ca^{2+} precede any mitochondrial changes in ROS, membrane potential, or morphology (Olivas-Aguirre et al., 2019). This might suggest a sequential modulation of various parts of the cells, starting on the outside and working inwards as this highly lipophilic compound is absorbed by the cell.

Overall, our FLIM data suggest that CBD induces mitochondrial oxidative stress in these cancer cells, which correlate with the dose-related increase in mitochondrial ROS and calcium and evidence of increased mitochondrial fission. Although cancer cells often display abnormal mitochondrial dynamics, mitochondrial fission is often a response to oxidative stress, especially if ROS originates from damaged mitochondria and is associated with a loss of the mitochondrial membrane potential and influx of calcium, leading to mitophagy and renewal or cell death (Sharma et al., 2019). Mitochondrial fission can also form part of a positive feedback cytosolic calcium signaling pathway that can promote autophagy, which also seems to be reliant on increased ROS production (Huang et al., 2019). Mitochondria have a pivotal role in maintaining cellular homeostasis by sequestering and releasing intracellular Ca^{2+}. Within the mitochondria, Ca^{2+} biphasically affects energy metabolism via activation/inhibition of mitochondrial enzymes and direct charge alteration of the mitochondrial membrane potential, which in turn regulates the supply of electrons into the respiratory chain and production of ROS (Danese et al., 2017). Ultimately however, prolonged accumulation of mitochondrial calcium, known as calcium overload, is associated with the mitochondrial permeability transition (MPT), a key step in the initiation of apoptosis, and has been identified in T-cells following treatment with CBD (Olivas-Aguirre et al., 2019). Indeed, these data support our previous observations of CBD-induced mitochondrial fission in a different cell line (Nunn et al., 2013) and our unpublished observations in several other cell lines. Overall, this supports the concept that CBD can induce ROS in a range of tissue types, including monocytes (Wu et al., 2018), glioma stem cells (Singer et al., 2015), and breast cancer cells (Kis et al., 2019).

To explain this, we suggest that CBD triggers calcium uptake via TRPV and/or release from endoplasmic stores, which is then taken up by the mitochondrion. In fact, TRPV1 is also expressed intracellularly, and it has been suggested to play a role in calcium signaling to the mitochondrion (Nita et al., 2016). Combined with data that it may also modulate VDAC1 (Rimmerman et al., 2013), we suggest that as CBD is absorbed by the cell, it sequentially modulates pathways that can result in either enhanced cellular protection or, potentially, induction of cell death; key in this is both direct and indirect modulation of mitochondrial function. Support for this comes from research that indicates that CBD can induce autophagy, which could be important in epilepsy (Hosseinzadeh et al., 2016), alcohol-induced liver damage (Yang et al., 2019), and cancer (Shrivastava et al., 2011). Autophagy is pivotal in maintaining overall mitochondrial health and involves VDAC1 and mTOR; a key trigger of the process is mitochondrial dysfunction (Li et al., 2020). Induction of mitochondrial stress could lead to mitophagy, which in some cells restores homeostasis, for instance, ensuring inflammation resolution, but in others, such as cancer cells, it results in death. **Figure 4** summarizes a possible mode of action. A key point here is that VDAC1 binds many different proteins, including HK and components of the Bcl2/Bax, so it is also central in controlling cell fate and a target for cancer treatment (Shoshan-Barmatz et al., 2017).

In broader terms, our data suggest that CBD, as its actions are often biphasic, could be mitohormetic (Nunn et al., 2020), inducing sublethal mitochondrial stress that results in an adaptive response via increased ROS production (Ristow and Schmeisser, 2014). In cancer cells, being at higher levels of stress than healthy cells, this tips them into a terminal oxidative stress. This selectivity has been observed following treatment of T-cells with CBD, inducing Ca^{2+} overload and apoptosis in cell lines derived from acute lymphobastic leukemia of T-lineage, but not in healthy T-cells (Olivas-Aguirre et al., 2019). This demonstrates

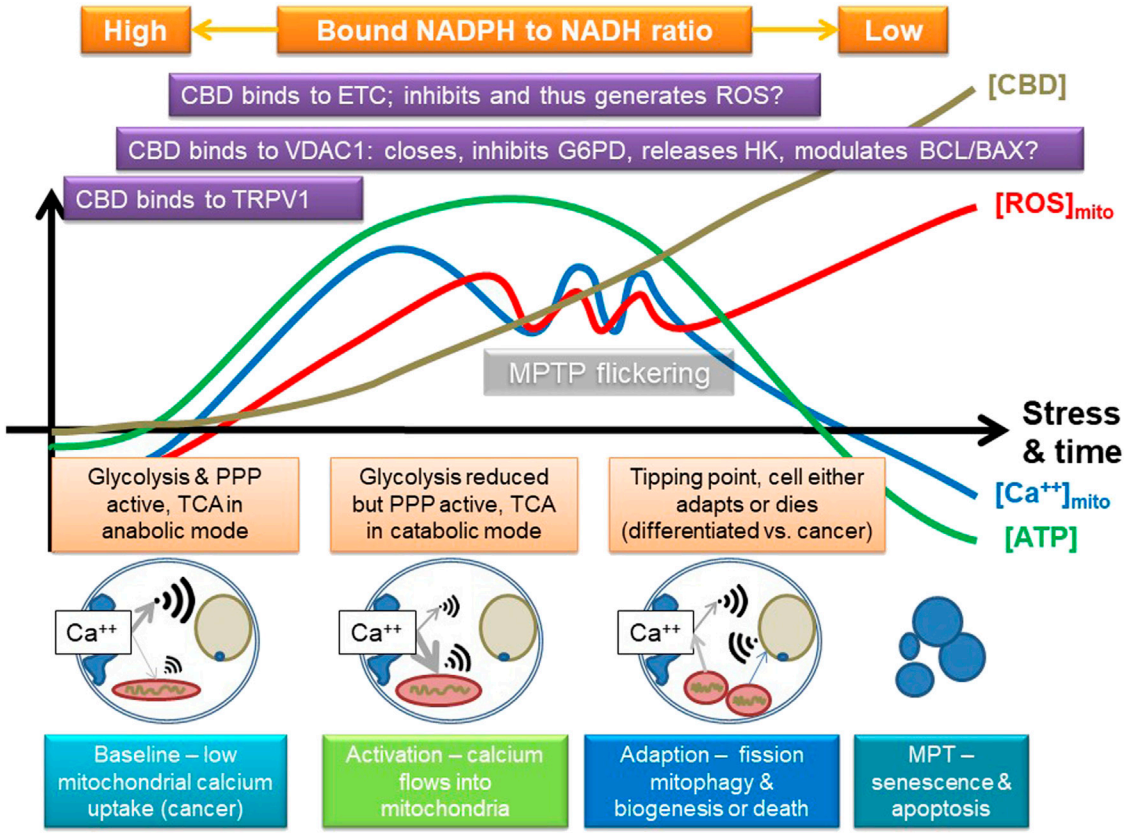

FIGURE 4 | Suggested mode of action of CBD, focusing on some of its known targets, and some inferred from other phenolic compounds. CBD may stimulate calcium uptake into the cell, possibly by channels like TRPV1 and then into the mitochondria, which may involve VDAC1. It could then eventually inhibit the electron transport chain (ETC) and potentially induce the release of hexokinase (HK, which binds to VDAC1; VDAC1 is also key in controlling apoptosis *via* the BCL/BAX system), and either directly, or indirectly (e.g., by ROS), inhibits other key enzymes in glycolysis, such as G6PDH or GAPDH. This could first stimulate and then inhibit mitochondrial function, providing a powerful adaptive signal; initially, the mitochondrion can swell while it buffers calcium. However, too much calcium influx will eventually lead to overload, loss of membrane potential, and inhibition of ATP production. If the amount of calcium influx is transient, or not too large, the mitochondrion has a number of adaptive strategies, such as mitochondrial permeability transition pore flickering (MPTP) to release excessive calcium and upregulation of antioxidant pathways, which could include the pentose phosphate pathway (PPP). However, if its membrane potential starts to fall, it could start to fission and stimulate mitophagy/autophagy and initially leads to mitochondrial biogenesis and eventually leads to induction of cell death; rapid fragmentation does seem to predispose to cell death. The key effect will be to switch off anabolic growth pathways and enhance stress resistance and catabolism, which could be indicated by a shift in bound NAD(P)H. The outcome is thus likely to be concentration and cell type dependent, as well as dependent on the initial metabolic state of the cell. A key tipping point in relation to cancer is that the sudden influx of calcium will potentially increase TCA activity and potentially flow through the ETC, which will increase ROS and shift carbohydrate flux away from growth to stress resistance, for instance, by inhibiting GAPDH. However, cancer cells are generally a lot more reliant on antioxidant defense systems, as generation of ROS is a key driver of proliferation, so suddenly enhancing mitochondrial ROS is a recognized anticancer strategy as it can tip cancer cells, but not normal cells, toward cell death.

the potential of CBD in anticancer therapy by "priming" cells, through sensitizing the mitochondria to respond better to chemotherapy and hence reducing the severity of treatment and side effects (Henley et al., 2017; Kosgodage et al., 2018).

CONCLUSION

Overall, our data support a consistent narrative regarding mitochondrial modulation by CBD. Our results align with those of previous studies demonstrating that CBD induces mitochondrial membrane changes that are not too dissimilar to a reduction in the mitochondrial membrane potential and the activation of intrinsic apoptotic pathways (Shrivastava et al., 2011; Wai and Langer, 2016; Olivas-Aguirre et al., 2019). Finally, we believe that the use of 2P-FLIM could be unique in unlocking further details of how CBD works, and we aim to use the technique to study different cell types to investigate the proposed mechanism further, for example, understanding its effects on NADH, NADPH, and FAD lifetimes. In particular, we will seek evidence of biphasic effects in response to different doses across a range of timescales.

DATA AVAILABILITY STATEMENT

The original contributions presented in the study are included in the article/**Supplementary Material**; further inquiries can be directed to the corresponding author.

AUTHOR CONTRIBUTIONS

AN, SB, JB, GG, and RM conceived and carried out the experiments. RM and SB analyzed the data. All authors were involved in writing and had final approval of the manuscript.

FUNDING

This project was partly funded by the Guy Foundation, and with access to the STFC Central Laser Facility, Octopus imaging cluster, application number 18130041.

SUPPLEMENTARY MATERIAL

The Supplementary Material for this article can be found online at: https://www.frontiersin.org/articles/10.3389/fmolb.2021.630107/full#supplementary-material

FIGURE S1 | NAD(P)H autofluorescence and mitochondrial staining overlap. Representative images of 2P-derived NAD(P)H autofluorescence and MitoTracker Red-stained MCF7 cells. Superimposed images show the NAD(P)H signal matching mitochondrial morphology.

FIGURE S2 | Identifying mitochondrial and cytosolic pixels for analysis. Representative 2P NAD(P)H FLIM image illustrating selection of pixels to be anaylsed.

FIGURE S3 | 2P NAD(P)H FLIM and the Goodness of Fit (Chi Squared). Representative 2P NAD(P)H FLIM-derived images for each treatment group, colour-coded to the obtained chi squared value (χ^2).

REFERENCES

Adem, S., Comakli, V., Kuzu, M., and Demirdag, R. (2014). Investigation of the effects of some phenolic compounds on the activities of glucose-6-phosphate dehydrogenase and 6-phosphogluconate dehydrogenase from human erythrocytes. *J. Biochem. Mol. Toxicol.* 28 (11), 510–514. doi:10.1002/jbt.21592

Alam, S. R., Wallrabe, H., Svindrych, Z., Chaudhary, A. K., Christopher, K. G., Chandra, D., et al. (2017). Investigation of mitochondrial metabolic response to doxorubicin in prostate cancer cells: An NADH, FAD and tryptophan FLIM Assay. *Sci. Rep.* 7 (1), 10451. doi:10.1038/s41598-017-10856-3

Armstrong, J. L., Hill, D. S., McKee, C. S., Hernandez-Tiedra, S., Lorente, M., Lopez-Valero, I., et al. (2015). Exploiting cannabinoid-induced cytotoxic autophagy to drive melanoma cell death. *J. Invest. Dermatol.* 135, 1629. doi:10.1038/jid.2015.45

Baker, D., Pryce, G., Croxford, J. L., Brown, P., Pertwee, R. G., Huffman, J. W., et al. (2000). Cannabinoids control spasticity and tremor in a multiple sclerosis model. *Nature* 404 (6773), 84–87. doi:10.1038/35003583

Bird, D. K., Yan, L., Vrotsos, K. M., Eliceiri, K. W., Vaughan, E. M., Keely, P. J., et al. (2005). Metabolic mapping of MCF10A human breast cells via multiphoton fluorescence lifetime imaging of the coenzyme NADH. *Cancer Res.* 65 (19), 8766–8773. doi:10.1158/0008-5472.CAN-04-3922

Bisogno, T., Hanuš, L., De Petrocellis, L., Tchilibon, S., Ponde, D. E., Brandi, I., et al. (2001). Molecular targets for cannabidiol and its synthetic analogues: effect on vanilloid VR1 receptors and on the cellular uptake and enzymatic hydrolysis of anandamide. *Br. J. Pharmacol.* 134 (4), 845–852. doi:10.1038/sj.bjp.0704327

Blacker, T. S., and Duchen, M. R. (2016). Investigating mitochondrial redox state using NADH and NADPH autofluorescence. *Free Radic. Biol. Med.* 100, 53–65. doi:10.1016/j.freeradbiomed.2016.08.010

Blignaut, M., Loos, B., Botchway, S. W., Parker, A. W., and Huisamen, B. (2019). Ataxia-Telangiectasia Mutated is located in cardiac mitochondria and impacts oxidative phosphorylation. *Sci. Rep.* 9 (1), 4782. doi:10.1038/s41598-019-41108-1

Bömer, M., Pérez-Salamó, I., Florance, H. V., Salmon, D., Dudenhoffer, J., Finch, P., et al. (2020). Jasmonates induce Arabidopsis bioactivities selectively inhibiting the growth of breast cancer cells through CDC6 and mTOR. *New Phytol.* 229 (4), 2120–2134. doi:10.1111/nph.17031

Botchway, S. W., Scherer, K. M., Hook, S., Stubbs, C. D., Weston, E., Bisby, R. H., et al. (2015). A series of flexible design adaptations to the Nikon E-C1 and E-C2 confocal microscope systems for UV, multiphoton and FLIM imaging. *J. Microsc.* 258, 68. doi:10.1111/jmi.12218

Bujak, J. K., Kosmala, D., Szopa, I. M., Majchrzak, K., and Bednarczyk, P. (2019). Inflammation, cancer and immunity—implication of TRPV1 channel. *Front. Oncol.* 9, 1087. doi:10.3389/fonc.2019.01087/full

Chakraborty, S., Nian, F-S., Tsai, J-W., Karmenyan, A., and Chiou, A. (2016). Quantification of the metabolic state in cell-model of Parkinson's disease by fluorescence lifetime imaging microscopy. *Sci. Rep.* 6, 19145. doi:10.1038/srep19145

Chen, H., and Chan, D. C. (2017). Mitochondrial dynamics in regulating the unique phenotypes of cancer and stem cells. *Cell Metab.* 26 (1), 39–48. doi:10.1016/j.cmet.2017.05.016

Danese, A., Patergnani, S., Bonora, M., Wieckowski, M. R., Previati, M., Giorgi, C., et al. (2017). Calcium regulates cell death in cancer: roles of the mitochondria and mitochondria-associated membranes (MAMs). *Biochim. Biophys. Acta* 1858 (8), 615–627. doi:10.1016/j.bbabio.2017.01.003

Gali-Muhtasib, H., Hmadi, R., Kareh, M., Tohme, R., and Darwiche, N. (2015). Cell death mechanisms of plant-derived anticancer drugs: beyond apoptosis. *Apoptosis* 20 (12), 1531–1562. doi:10.1007/s10495-015-1169-2

Gandin, A., Dizengremel, P., and Jolivet, Y. (2021). Integrative role of plant mitochondria facing oxidative stress: The case of ozone. *Plant Physiol. Biochem.* 159, 202–210. doi:10.1016/j.plaphy.2020.12.019

Giorgi, C., Missiroli, S., Patergnani, S., Duszynski, J., Wieckowski, M. R., and Pinton, P. (2015). Mitochondria-associated membranes: Composition, molecular mechanisms, and physiopathological implications. *Antioxid. Redox Signal.* 22 (12), 995–1019. doi:10.1089/ars.2014.6223

Goldin, N., Arzoine, L., Heyfets, A., Israelson, A., Zaslavsky, Z., Bravman, T., et al. (2008). Methyl jasmonate binds to and detaches mitochondria-bound hexokinase. *Oncogene* 27 (34), 4636–4643. doi:10.1038/onc.2008.108

Gorlach, S., Fichna, J., and Lewandowska, U. (2015). Polyphenols as mitochondria-targeted anticancer drugs. *Cancer Lett.* 366 (2), 141–149. doi:10.1016/j.canlet.2015.07.004

Gray, R. A., Stott, C. G., Jones, N. A., Di Marzo, V., and Whalley, B. J. (2020). Anticonvulsive properties of cannabidiol in a model of generalized seizure are transient receptor potential vanilloid 1 dependent. *Cannabis Cannabinoid Res.* 5 (2), 145–149. doi:10.1089/can.2019.0028

Guard, S. E., Chapnick, D. A., Poss, Z., Ebmeier, C. C., Jacobsen, J., Nemkov, T., et al. (2020). Multi-omic analysis reveals cannabidiol disruption of cholesterol homeostasis in human cell lines. bioRxiv. 10.1101/2020.06.03.130864.

Gugliandolo, A., Pollastro, F., Bramanti, P., and Mazzon, E. (2020). Cannabidiol exerts protective effects in an *in vitro* model of Parkinson's disease activating AKT/mTOR pathway. *Fitoterapia*. 143, 104553. doi:10.1101/2020.06.03.130864

Guo, H.-W., Yu, J.-S., Hsu, S.-H., Wei, Y.-H., Lee, O. K., Dong, C.-Y., et al. (2015). Correlation of NADH fluorescence lifetime and oxidative phosphorylation metabolism in the osteogenic differentiation of human mesenchymal stem cell. *J. Biomed. Opt.* 20 (1), 17004. doi:10.1117/1.JBO.20.1.017004

Henley, A. B., Yang, L., Chuang, K. L., Sahuri-Arisoylu, M., Wu, L. H., Bligh, S. W. A., et al. (2017). Withania somnifera root extract enhances chemotherapy through "priming". *PLoS One* 12 (1), e0170917. doi:10.1371/journal.pone.0170917

Hosseinzadeh, M., Nikseresht, S., Khodagholi, F., Naderi, N., and Maghsoudi, N. (2016). Cannabidiol post-treatment alleviates rat epileptic-related behaviors and activates hippocampal cell autophagy pathway along with antioxidant defense in chronic phase of pilocarpine-induced seizure. *J. Mol. Neurosci.* 58 (4), 432–440. doi:10.1007/s12031-015-0703-6

Huang, L., Yu, L-J., Zhang, X., Fan, B., Wang, F.-Z., Dai, Y.-S., et al. (2019). Autophagy regulates glucose-mediated root meristem activity by modulating ROS production in Arabidopsis. *Autophagy* 15 (3), 407–422. doi:10.1080/15548627.2018.1520547

Huestis, M. A. (2007). Human cannabinoid pharmacokinetics. *Chem. Biodivers* 4, 1770. doi:10.1002/cbdv.200790152

Iannotti, F. A., Hill, C. L., Leo, A., Alhusaini, A., Soubrane, C., Mazzarella, E., et al. (2014). Nonpsychotropic plant cannabinoids, cannabidivarin (CBDV) and cannabidiol (CBD), activate and desensitize transient receptor potential vanilloid 1 (TRPV1) channels *in Vitro*: potential for the treatment of neuronal hyperexcitability. *ACS Chem. Neurosci.* 5 (11), 1131–1141. doi:10.1021/cn5000524

Ibeas Bih, C., Chen, T., Nunn, A. V. W., Bazelot, M., Dallas, M., and Whalley, B. J. (2015). Molecular targets of cannabidiol in neurological disorders. *Neurotherapeutics* 12 (4), 699–730. doi:10.1007/s13311-015-0377-3

Kimata, S., Mochizuki, D., Satoh, J., Kitano, K., Kanesaki, Y., Takeda, K., et al. (2018). Intracellular free flavin and its associated enzymes participate in oxygen and iron metabolism in Amphibacillus xylanus lacking a respiratory chain. *FEBS Open Bio* 8 (6), 947–961. doi:10.1002/2211-5463.12425

Kis, B., Ifrim, F. C., Buda, V., Avram, S., Pavel, I. Z., Antal, D., et al. (2019). Cannabidiol-from plant to human body: A promising bioactive molecule with multi-target effects in cancer. *Int. J. Mol. Sci.* 20 (23), 5905. doi:10.3390/ijms20235905

Kosgodage, U. S., Mould, R., Henley, A. B., Nunn, A. V., Guy, G. W., Thomas, E. L., et al. (2018). Cannabidiol (CBD) is a novel inhibitor for exosome and microvesicle (EMV) release in cancer. *Front. Pharmacol.* 9, 889. doi:10.3389/fphar.2018.00889

Kroemer, G. (2006). Mitochondria in cancer. *Oncogene* 25, 4630. doi:10.1038/sj.onc.1209589

Laus, M. N., and Soccio, M. (2020). First evidence of a protective effect of plant bioactive compounds against H2O2-induced aconitase damage in durum wheat mitochondria. *Antioxidants* 9 (12), 1256. doi:10.3390/antiox9121256

Li, X., Zhang, W., Cao, Q., Wang, Z., Zhao, M., Xu, L., et al. (2020). Mitochondrial dysfunction in fibrotic diseases. *Cell Death Discov. Internet* 6 (1), 80. doi:10.1038/s41420-020-00316-9

Marchi, S., and Pinton, P. (2016). Alterations of calcium homeostasis in cancer cells. *Curr. Opin. Pharmacol.* 29, 1–6. doi:10.1016/j.coph.2016.03.002

Mato, S., Victoria Sánchez-Gómez, M., and Matute, C. (2010). Cannabidiol induces intracellular calcium elevation and cytotoxicity in oligodendrocytes. *Glia* 58 (14), 1739–1747. doi:10.1002/glia.21044

McAllister, S. D., Soroceanu, L., and Desprez, P. Y. (2015). The antitumor activity of plant-derived non-psychoactive cannabinoids. *J. Neuroimmune Pharmacol.* 10, 255. doi:10.1007/s11481-015-9608-y

Mechoulam, R., Parker, L. A., and Gallily, R. (2002). Cannabidiol: an overview of some pharmacological aspects. *J. Clin. Pharmacol.* 42 (S1), 11S–19S. doi:10.1002/j.1552-4604.2002.tb05998.x

Nita, I. I., Caspi, Y., Gudes, S., Fishman, D., Lev, S., Hersfinkel, M., et al. (2016). Privileged crosstalk between TRPV1 channels and mitochondrial calcium shuttling machinery controls nociception. *Biochim. Biophys. Acta* 1863 (12), 2868–2880. doi:10.1016/j.bbamcr.2016.09.009

Nunn, A. V., Henley, A., Brody, L. P., and Bell, J. D. (2013). *Phytocannabinoids modulate mitochondrial dynamics in cell lines; stress adaptation*. London, United Kingdom: European Workshop on Cannabinoid Research.

Nunn, A. V. W., Guy, G. W., Botchway, S. W., and Bell, J. D. (2020). From sunscreens to medicines: can a dissipation hypothesis explain the beneficial aspects of many plant compounds?. *Phytotherapy Res.* 34, 1868–1888. doi:10.1002/ptr.6654

Olivas-Aguirre, M., Torres-López, L., Valle-Reyes, J. S., Hernández-Cruz, A., Pottosin, I., and Dobrovinskaya, O. (2019). Cannabidiol directly targets mitochondria and disturbs calcium homeostasis in acute lymphoblastic leukemia. *Cell Death Dis.* 10 (10), 779. doi:10.1038/s41419-019-2024-0

Oliveira, M. R. d., Nabavi, S. F., Daglia, M., Rastrelli, L., and Nabavi, S. M. (2016). Epigallocatechin gallate and mitochondria—a story of life and death. *Pharmacol. Res.* 104, 70–85. doi:10.1016/j.phrs.2015.12.027

O'Connell, B. K., Gloss, D., and Devinsky, O. (2017). Cannabinoids in treatment-resistant epilepsy: A review. *Epilepsy Behav.* 70, 341–348. doi:10.1016/j.yebeh.2016.11.012

Pisanti, S., Malfitano, A. M., Ciaglia, E., Lamberti, A., Ranieri, R., Cuomo, G., et al. (2017). Cannabidiol: state of the art and new challenges for therapeutic applications. *Pharmacol. Ther.* 175, 133–150. doi:10.1016/j.pharmthera.2017.02.041

Popov, L. (2020). Mitochondrial biogenesis: An update. *J. Cell. Mol. Med.* 24 (9), 4892–4899. doi:10.1111/jcmm.15194

Rad, E., Murray, J., and Tee, A. (2018). Oncogenic signalling through mechanistic target of rapamycin (mTOR): A driver of metabolic transformation and cancer progression. *Cancers* 10 (1), 5. doi:10.3390/cancers10010005

Rambold, A. S., and Pearce, E. L. (2018). Mitochondrial dynamics at the interface of immune cell metabolism and function. *Trends Immunol.* 39 (1), 6–18. doi:10.1016/j.it.2017.08.006

Ramer, R., and Hinz, B. (2017). Cannabinoids as anticancer drugs. *Adv. Pharmacol.* 80, 397–436. doi:10.1016/bs.apha.2017.04.002

Rasouli, H., Farzaei, M. H., Mansouri, K., Mohammadzadeh, S., and Khodarahmi, R. (2016). Plant cell cancer: may natural phenolic compounds prevent onset and development of plant cell malignancy? A literature review. *Molecules* 21 (9), 21. doi:10.3390/molecules21091104

Redhu, A. K., and Bhat, J. P. (2020). Mitochondrial glucose 6-phosphate dehydrogenase and 6-phosphogluconate dehydrogenase abrogate p53 induced apoptosis in a yeast model: possible implications for apoptosis resistance in cancer cells. *Biochim. Biophys. Acta Gen. Subj* 1864 (3), 129504. doi:10.1016/j.bbagen.2019.129504

Rimmerman, N., Ben-Hail, D., Porat, Z., Juknat, A., Kozela, E., Daniels, M. P., et al. (2013). Direct modulation of the outer mitochondrial membrane channel, voltage-dependent anion channel 1 (VDAC1) by cannabidiol: A novel mechanism for cannabinoid-induced cell death. *Cell Death Dis.* 4 (12), e949. doi:10.1038/cddis.2013.471

Ristow, M., and Schmeisser, K. (2014). Mitohormesis: promoting health and lifespan by increased levels of reactive oxygen species (ROS). *Dose Response* 12, 288. doi:10.2203/dose-response.13-035.Ristow

Rossi, A., Pizzo, P., and Filadi, R. (2019). Calcium, mitochondria and cell metabolism: A functional triangle in bioenergetics. *Biochim. Biophys. Acta Mol. Cell. Res.* 1866 (7), 1068–1078. doi:10.1016/j.bbamcr.2018.10.016

Ryan, D., Drysdale, A. J., Lafourcade, C., Pertwee, R. G., and Platt, B. (2009). Cannabidiol targets mitochondria to regulate intracellular Ca2+ levels. *J. Neurosci.* 29 (7), 2053–2063. doi:10.1523/JNEUROSCI.4212-08.2009

Sayers, T. J. (2011). Targeting the extrinsic apoptosis signaling pathway for cancer therapy. *Cancer Immunol. Immunother.* 60 (8), 1173–1180. doi:10.1007/s00262-011-1008-4

Schneckenburger, H., Wagner, M., Weber, P., Strauss, W. S., and Sailer, R. (2004). Autofluorescence lifetime imaging of cultivated cells using a UV picosecond laser diode. *J. Fluoresc* 14 (5), 649–654. doi:10.1023/b:jofl.0000039351.09916.cc

Senft, D., and Ronai, Z. A. (2016). Regulators of mitochondrial dynamics in cancer. *Curr. Opin. Cell Biol.* 39, 43–52. doi:10.1016/j.ceb.2016.02.001

Sharick, J. T., Favreau, P. F., Gillette, A. A., Sdao, S. M., Merrins, M. J., and Skala, M. C. (2018). Protein-bound NAD(P)H lifetime is sensitive to multiple fates of glucose carbon. *Sci. Rep.* 8 (1), 5456. doi:10.1038/s41598-018-23691-x

Sharma, A., Smith, H. J., Yao, P., and Mair, W. B. (2019). Causal roles of mitochondrial dynamics in longevity and healthy aging. *EMBO Rep.* 20 (12), e48395. doi:10.15252/embr.201948395

Shin, E. S., Park, J., Shin, J-M., Cho, D., Cho, S. Y., Shin, D. W., et al. (2008). Catechin gallates are NADP+-competitive inhibitors of glucose-6-phosphate dehydrogenase and other enzymes that employ NADP+ as a coenzyme. *Bioorg. Med. Chem.* 16 (7), 3580–3586. doi:10.1016/j.bmc.2008.02.030

Shoshan-Barmatz, V., De, S., and Meir, A. (2017). The mitochondrial voltage-dependent anion channel 1, Ca2+ transport, apoptosis, and their regulation. *Front. Oncol.* 7, 60. doi:10.3389/fonc.2017.00060/full

Shoshan-Barmatz, V., Krelin, Y., and Shteinfer-Kuzmine, A. (2018). VDAC1 functions in Ca2+ homeostasis and cell life and death in health and disease. *Cell Calcium* 69, 81–100. doi:10.1016/j.ceca.2017.06.007

Shrivastava, A., Kuzontkoski, P. M., Groopman, J. E., and Prasad, A. (2011). Cannabidiol induces programmed cell death in breast cancer cells by coordinating the cross-talk between apoptosis and autophagy. *Mol. Cancer Ther.* 10 (7), 1161–1172. doi:10.1158/1535-7163.MCT-10-1100

Singer, E., Judkins, J., Salomonis, N., Matlaf, L., Soteropoulos, P., McAllister, S., et al. (2015). Reactive oxygen species-mediated therapeutic response and resistance in glioblastoma. *Cell Death Dis.* 6, e1601. doi:10.1038/cddis.2014.566

Skala, M. C., Riching, K. M., Bird, D. K., Gendron-Fitzpatrick, A., Eickhoff, J., Eliceiri, K. W., et al. (2007a). In vivo multiphoton fluorescence lifetime imaging of protein-bound and free nicotinamide adenine dinucleotide in normal and precancerous epithelia. *J. Biomed. Opt.* 12 (2), 024014. doi:10.1117/1.2717503

Skala, M. C., Riching, K. M., Gendron-Fitzpatrick, A., Eickhoff, J., Eliceiri, K. W., White, J. G., et al. (2007b). *In vivo* multiphoton microscopy of NADH and FAD

redox states, fluorescence lifetimes, and cellular morphology in precancerous epithelia. *Proc. Natl. Acad. Sci. U.S.A.* 104 (49), 19494–19499. doi:10.1073/pnas.0708425104

Stevens, J. F., Revel, J. S., and Maier, C. S. (2018). Mitochondria-centric review of polyphenol bioactivity in cancer models. *Antioxid. Redox Signal.* 29 (16), 1589. doi:10.1089/ars.2017.7404

Stringari, C., Cinquin, A., Cinquin, O., Digman, M. A., Donovan, P. J., and Gratton, E. (2011). Phasor approach to fluorescence lifetime microscopy distinguishes different metabolic states of germ cells in a live tissue. *Proc. Natl. Acad. Sci. U.S.A* 108 (33), 13582–13587. doi:10.1073/pnas.1108161108

Suhling, K., Hirvonen, L. M., Levitt, J. A., Chung, P.-H., Tregidgo, C., Le Marois, A., et al. (2015). Fluorescence lifetime imaging (FLIM): Basic concepts and some recent developments. *Med. Photon.* 27, 3–40. doi:10.1016/j.medpho.2014.12.001

Sun, S., Hu, F., Wu, J., and Zhang, S. (2017). Cannabidiol attenuates OGD/R-induced damage by enhancing mitochondrial bioenergetics and modulating glucose metabolism via pentose-phosphate pathway in hippocampal neurons. *Redox Biol.* 11, 577–585. doi:10.1016/j.redox.2016.12.029

Tapia, P. C. (2006). Sublethal mitochondrial stress with an attendant stoichiometric augmentation of reactive oxygen species may precipitate many of the beneficial alterations in cellular physiology produced by caloric restriction, intermittent fasting, exercise and dietary phytonutrients: "Mitohormesis" for health and vitality. *Med. Hypotheses* 66 (4), 832–843. doi:10.1016/j.mehy.2005.09.009

Tewari, D., Ahmed, T., Chirasani, V. R., Singh, P. K., Maji, S. K., Senapati, S., et al. (2015). Modulation of the mitochondrial voltage dependent anion channel (VDAC) by curcumin. *Biochim. Biophys. Acta* 1848, 151–158. doi:10.1016/j.bbamem.2014.10.014

Tewari, D., Majumdar, D., Vallabhaneni, S., and Bera, A. K. (2017). Aspirin induces cell death by directly modulating mitochondrial voltage-dependent anion channel (VDAC). *Sci. Rep.* 7 (1), 45184. doi:10.1038/srep45184

Trigos, A. S., Pearson, R. B., Papenfuss, A. T., and Goode, D. L. (2018). How the evolution of multicellularity set the stage for cancer. *Br. J. Cancer* 118 (2), 145–152. doi:10.1038/bjc.2017.398

Valente, A. J., Maddalena, L. A., Robb, E. L., Moradi, F., and Stuart, J. A. (2017). A simple ImageJ macro tool for analyzing mitochondrial network morphology in mammalian cell culture. *Acta Histochem.* 119 (3), 315–326. doi:10.1016/j.acthis.2017.03.001

Wai, T., and Langer, T. (2016). Mitochondrial dynamics and metabolic regulation. *Trends Endocrinol. Metab.* 212 (4), 379–387. doi:10.1016/j.tem.2015.12.001

Wallace, D. C. (2012). Mitochondria and cancer. *Nat. Rev. Cancer* 12 (10), 685–698. doi:10.1038/nrc3365

Wei, Y., Zhang, Y.-J., Cai, Y., and Xu, M.-H. (2015). The role of mitochondria in mTOR-regulated longevity. *Biol. Rev. Camb. Philos. Soc.* 90 (1), 167–181. doi:10.1111/brv.12103

Wu, H.-Y., Huang, C.-H., Lin, Y.-H., Wang, C.-C., and Jan, T.-R. (2018). Cannabidiol induced apoptosis in human monocytes through mitochondrial permeability transition pore-mediated ROS production. *Free Radic. Biol. Med.* 124, 311–318. doi:10.1016/j.freeradbiomed.2018.06.023

Yang, L., Yang, C., Thomes, P. G., Kharbanda, K. K., Casey, C. A., McNiven, M. A., et al. (2019). Lipophagy and alcohol-induced fatty liver. *Front. Pharmacol.* 10, 495. doi:10.3389/fphar.2019.00495/full

Yaseen, M. A., Sutin, J., Wu, W., Fu, B., Uhlirova, H., Devor, A., et al. (2017). Fluorescence lifetime microscopy of NADH distinguishes alterations in cerebral metabolism *in vivo*. *Biomed. Opt. Express* 8 (5), 2368–2385. doi:10.1364/BOE.8.002368

Yu, Q., and Heikal, A. A. (2009). Two-photon autofluorescence dynamics imaging reveals sensitivity of intracellular NADH concentration and conformation to cell physiology at the single-cell level. *J. Photochem. Photobiol. B.* 95 (1), 46–57. doi:10.1016/j.jphotobiol.2008.12.010

Conflict of Interest: GG is the founder and chairman of GW Pharmaceuticals, and AN is a consultant to GW Pharmaceuticals.

The remaining authors declare that the research was conducted in the absence of any commercial or financial relationships that could be construed as a potential conflict of interest.

frontiers in Physics

ORIGINAL RESEARCH
published: 12 April 2021
doi: 10.3389/fphy.2021.634324

Biosensing the Presence of Metal Nanoparticles by Spectrally- and Time-Resolved Endogenous Fluorescence in Water Moss *Fontinalis antipyretica*

Alzbeta Marcek Chorvatova[1,2]*, *Martin Uherek*[1] *and Dusan Chorvat*[1]

[1]Department of Biophotonics, International Laser Centre of the Slovak Centre of Scientific and Technical Information, Bratislava, Slovakia, [2]Department of Biophysics, Faculty of Natural Sciences, University of St. Cyril and Methodius, Trnava, Slovakia

Pollution by heavy metals represents a significant environmental burden. We employed confocal microscopy with spectral detection and fluorescence lifetime imaging (FLIM) to evaluate the effect of nanoparticles (NPs) from various metals (Zinc, Nickel, Cobalt, Copper) on endogenous fluorescence of *Fontinalis antipyretica* moss. Short term (3–5 day) exposure to NPs, designed and fabricated by direct synthesis using femtosecond laser ablation in water, was studied. The green flavonoid and/or lignin endogenous fluorescence peaking between 500 and 560 nm was found to be increased by Zn and significantly reduced by Cu. The overall red chlorophyll fluorescence intensity with a maximum of 680 nm remained largely unchanged after exposure to Ni and Zn, but was decreased in the presence of Co and completely abolished by Cu. All NPs but Zn induced changes in the fluorescence lifetimes, demonstrating increased sensitivity of this parameter to environmental pollution. Gathered data indicate fast responsiveness of the endogenous fluorescence in the *Fontinalis antipyretica* moss to the presence of heavy metals that can thus potentially serve as a biosensing tool for monitoring environmental pollution in the moss natural environment.

Keywords: Autofluorescence (AF), FLIM (fluorescence lifetime imaging microscopy), nanoparticle (NP), chlorophyll, moss, heavy metal, biosensor

OPEN ACCESS

Edited by:
Klaus Suhling,
King's College London,
United Kingdom

Reviewed by:
Saikiran Vadavalli,
Gandhi Institute of Technology and Management (GITAM), India
Nirmal Mazumder,
Manipal Academy of Higher Education, India

***Correspondence:**
Alzbeta Marcek Chorvatova
alzbeta.marcekchorvatova@cvtisr.sk

Specialty section:
This article was submitted to Optics and Photonics, a section of the journal Frontiers in Physics

Received: *27 November 2020*
Accepted: *18 January 2021*
Published: *12 April 2021*

Citation:
Marcek Chorvatova A, Uherek M and Chorvat D (2021) Biosensing the Presence of Metal Nanoparticles by Spectrally- and Time-Resolved Endogenous Fluorescence in Water Moss Fontinalis antipyretica. *Front. Phys. 9:634324. doi: 10.3389/fphy.2021.634324*

INTRODUCTION

In the last decades, the environment has been severely polluted by heavy metals. Despite the fact that some heavy metals are essential trace elements for the functioning of living organisms, most can be toxic due to formation of complex compounds within the cells [1]. Excessive levels of metals such as Co, Cu, or Zn, induced by industrial developments, thus often lead to detrimental effects on living cells and organisms [2]. Heavy metals induce lipid peroxidation and DNA damage leading to several diseases, namely various types of cancer [3]. Other potential harmful effects include metabolic disorders, lung inflammation, hepatic and/or heart diseases, as well as nervous system problems and foetal as well as birth defects [4, 5]. Mosses, together with algae and higher plants, are highly sensitive to environmental pollution including that of heavy metals that they are also capable to accumulate [6]. The decrease in the photosynthetic capacity, inhibition of growth, as well as reduced biosynthesis

of chlorophylls and/or carotenoids often accompanies metal toxicity [7, 8]. In the past, diverse investigations proved the suitability of *Fontinalis antipyretica* for heavy metal biomonitoring in natural habitats [9, 10]. Previous research has demonstrated that aquatic moss *Fontinalis antipyretica* can be used as an indicator of heavy metal toxicity [11, 12]. For that reason, we opted for the *Fontinalis antipyretica* moss and evaluated its responsiveness to heavy metals using spectrally- and time-resolved monitoring of their endogenous fluorescence.

The choice of the appropriate detection method for environmental monitoring of the presence of heavy metals in aqueous solution is broadly important. Among available methods, fluorescence emission spectroscopy is an attractive approach because of its non-invasiveness, easy-to-use operation and the widespread availability of equipment for analysis. We employed both spectrally- and time-resolved fluorescence monitoring. Time-resolved imaging presents an advanced tool to monitor changes of the endogenous fluorophores to their environment directly in living cells [13, 14]. Chlorophyll *a* is a well-established fluorescing pigment employed in photosynthesis [15]. In addition to the chlorophyll fluorescence, NADPH dependent blue-green fluorescence (BGF) was also described in isolated chloroplasts [16, 17], while most of the green fluorescence in the intercellular space was associated with lignins of the intermediate lamella [18]. We previously demonstrated a sensitivity of endogenous fluorescence to various environmental stressors employing the spectrally and time-resolved microscopy in algae [19, 20]. In this contribution, we focus on endogenous fluorescence, derived primarily from chlorophylls, but also from flavonoids and/or lignins, studied by spectrally- and time-resolved imaging in moss.

To study the effect of heavy metals, we have chosen heavy metal NPs produced by femtosecond laser ablation, as previously described [21]. NPs possess particular properties related to their small size, as well as composition. Consequently, they offer a large number of applications [22–24]. Their interaction with living organisms was broadly investigated. CuO, as well as ZnO NPs were shown to have antimicrobial properties [25–27]. Ni and Co NPs were also demonstrated to induce stress in the microalgae [28, 29]. Under heavy metals exposure, the growth and the chemical composition of several substances, including chlorophylls, have been reduced within the first 48 h [30]. We also noted the capacity of heavy metal NPs to reduce the chlorophyll fluorescence after 10–14 days of exposure in algae [31].

In this contribution, we focus on the effect of heavy metals on endogenous fluorescence in the *Fontinalis antipyretica* moss. Water is an exceptionally essential source for the presence of life on the Earth. The water quality has been seriously affected by human activities. Heavy metals enter into the aquatic system through the agricultural runoff and industrial discharges [32]. Previously, we have demonstrated the sensitivity of marine algae *Dunalliela tertiolecta* to laboratory-induced stress with heavy metal cadmium [19, 33]. The study showed an appearance of the stress-related light-harvesting complex (LHC), as well as changes at the endogenous fluorescence levels. We also demonstrated that endogenous fluorescence can potentially serve as a biosensing tool for monitoring environmental pollution [34]. Our aim in this work is to evaluate non-invasively the short term (in terms of days) exposure of *Fontinalis antipyretica* moss to chosen heavy metal NPs (Zn, Ni, Co, Cu), employing spectrally- and time-resolved studies of their endogenous fluorescence.

MATERIALS AND METHODS

Sample

Water bryophyte green moss species *Fontinalis antipyretica* was gathered commercially from aquashop (Aquasymbioza, Bratislava, Slovakia) and grown under ambient light. For the measurements, green moss fyloides were cut and placed on a microscope slide without further modification.

Preparation of Metal Nanoparticles

NPs of the size in the range 10–100 nm were prepared by laser ablation of metal surfaces, as described previously [21, 31]. In brief, discs from pure metals were covered by deionised water and we have employed ultrafast spirit ytterbium amplified laser (HighQ, SpectraPhysics, Newport, 300 fs pulse width, 1,040 nm wavelength; 4 W mean power operated at 100 kHz) that was focused at the metal disc surface by Plan N 10×/0.25 UIS2 objective (Olympus). The laser beam movement over the surface was done by motorized XYZ micropositioner (Walter Uhl Technische Mikroskopie GmbH & Co.) via a joystick interface.

Substrates for the fabrication of NPs included following metal discs of pure elements (Goodfellow Cambridge Ltd.):

Cobalt	Co (99.9%),	diameter 25 mm,	thickness 1.0 mm
Zinc	Zn (99.99%),	diameter 25 mm,	thickness 3.0 mm
Nickel	Ni (99.99%),	diameter 25 mm,	thickness 3.2 mm
Copper	Cu (99.99%),	diameter 25 mm,	thickness 3.0 mm

The size of the NPs, determined by Scanning Electron Microscopy [21] reached under 20 nm for Co and Cu, between 10 and 20 nm for Zn (often aggregating into chunks up to 80 nm) and between 20 and 80 nm for Ni.

NPs were prepared in distilled water and 20 µl of the solution with NPs was added without additional modification to *Fontinalis antipyretica* moss in 0.5 ml of pure water. In the control sample, the equivalent of deionized water was added. NPs were maintained with the moss leaves during 3–5 days before use. All procedures complied with the Institutional rules and guidelines of the International Laser Center in Bratislava.

Confocal Imaging

Confocal autofluorescence images were gathered using the laser scanning confocal microscope Axiovert 200 LSM 510 Meta (Carl Zeiss, Germany) equipped with objective C-Apochromat 40×, 1.2 W Corr. Moss leaves were excited with the 450 nm laser (Kvant, Slovakia), fluorescence was detected using two photomultipliers and 16 channel META detector. Channel 1 was recorded with BP 500–550 IR filter and channel 2 using BP 650–710 IR filter. Spectrally-resolved blue/green images were recorded between 477 and 638 nm with 11 nm step using 472–643 filter. Spectrally-resolved red images were gathered between 638 and 713 nm with 11 nm step using 632–718 filter.

Fluorescence Lifetime Imaging Microscopy

FLIM images were recorded using time-correlated single-photon counting (TCSPC) technique equipped with a 475 nm picosecond pulsed laser diode (BDL-475, Becker&Hickl, Germany) [14]. The laser beam was reflected to the sample through an epifluorescence path of the Axiovert 200 LSM 510 Meta (Zeiss, Germany) inverted microscope and LP 500 nm filter was used to separate emitted fluorescence from laser excitation. HPM 100–40 photomultiplier and SPC-830 TCSPC board were used for detection of time-resolved signals (both Becker&Hickl, Germany).

Data Analysis

Confocal images were analyzed by ZEN 2011 software (Zeiss, Germany). FLIM images were analyzed using proprietary software packages SPCImage (Becker&Hickl, Germany). In the data fitting procedure, the synthetic IRF function produced by SPCImage software (Becker Hickl, Germany) was employed as an instrument response function. Statistical comparison was done by Origin 6.0 Professional using one-way Anova, with $p < 0.05$ considered as significant.

RESULTS

Our aim was to examine changes in the spectrally- and time-resolved endogenous fluorescence of the green moss water bryophyte species *Fontinalis antipyretica* following the short-term (3–5 days) exposure to diverse heavy metal NPs.

Spectrally-Resolved Imaging of the Effect of Nanoparticles on Endogenous Fluorescence in Moss

The endogenous fluorescence of the moss was evaluated in the presence of NPs at two emission windows: first in the green spectral region, 500–550 nm, and second in the red spectral region, 650–710 nm in response to excitation at 450 nm (**Figure 1A** green and red windows). The two different channels were chosen because the red chlorophyll fluorescence was several times higher than the green one. The intensity in the red spectral region was comprised within the cell chloroplasts (**Figure 1B** red "balls"), as expected for the contribution of chlorophylls [15]. The green fluorescence was mainly situated in the intercellular space (**Figure 1B** green "fibres") and, in part, also recorded intracellularly. The green fluorescence is most likely related to the fluorescence of intracellular flavins and flavonoids when recorded inside the cells and/or lignins when measured as green "fibres" in the intercellular environment [18].

In the presence of heavy metal NPs, we have observed changes in the endogenous fluorescence in the moss (**Figure 1C**). Zn induced a clear rise in the green fluorescence in the intercellular space, while Cu attenuated both the green and the red

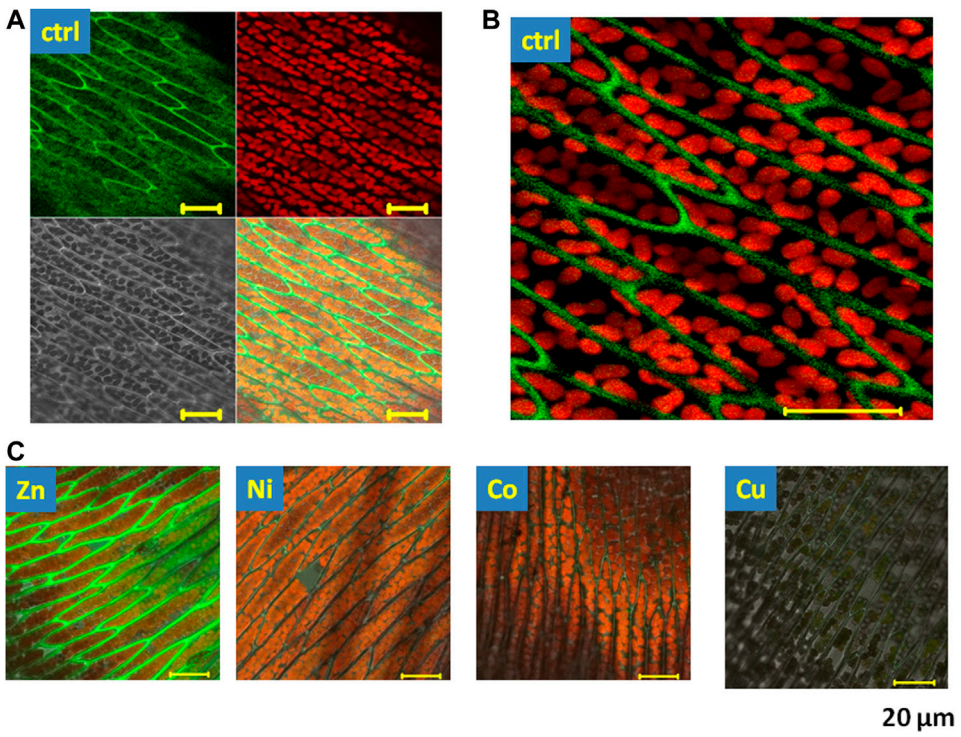

FIGURE 1 | Fluorescence microscopy images of endogenous fluorescence of *Fontinalis antipyretica* in control conditions and in the presence of heavy metal NPs. **(A)** Images recorded by laser scanning confocal microscopy in control conditions, excitation 450 nm. Green fluorescence channel 1) emission 550–550 nm, red fluorescence channel 2) emission 650–710 nm, grey channel 3) transmission image, mixed channel 4) overlay of channels 1–3. **(B)** Amplified section of the overlaid green and red fluorescence image, **(C)** the overlay of all channels in the presence of the tested heavy metal NPs (Zn, Ni, Co, and Cu); scale 20 µm.

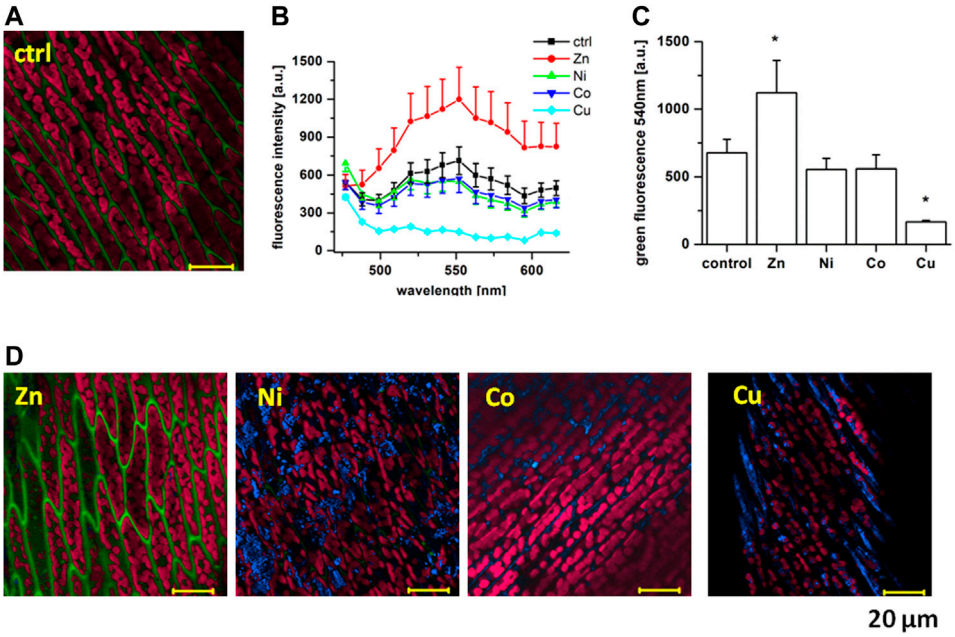

FIGURE 2 | Spectrally-resolved images of *Fontinalis antipyretica* blue/green fluorescence. **(A)** An original lambda-coded image in control conditions taken with an 11 nm step between 477 and 638 nm, excitation 450 nm. **(B)** Comparison of the recorded spectra in the presence of individual NPs ($n = 28$ in Ctrl, $n = 20$ in Zn, $n = 30$ in Ni, $n = 28$ in Co, $n = 37$ in Cu). **(C)** Statistical comparison at 540 nm, $^*p < 0.05$ with one-way Anova. **(D)** Original recordings in the presence of Zn, Ni, Co and Cu NPs, scale 20 µm.

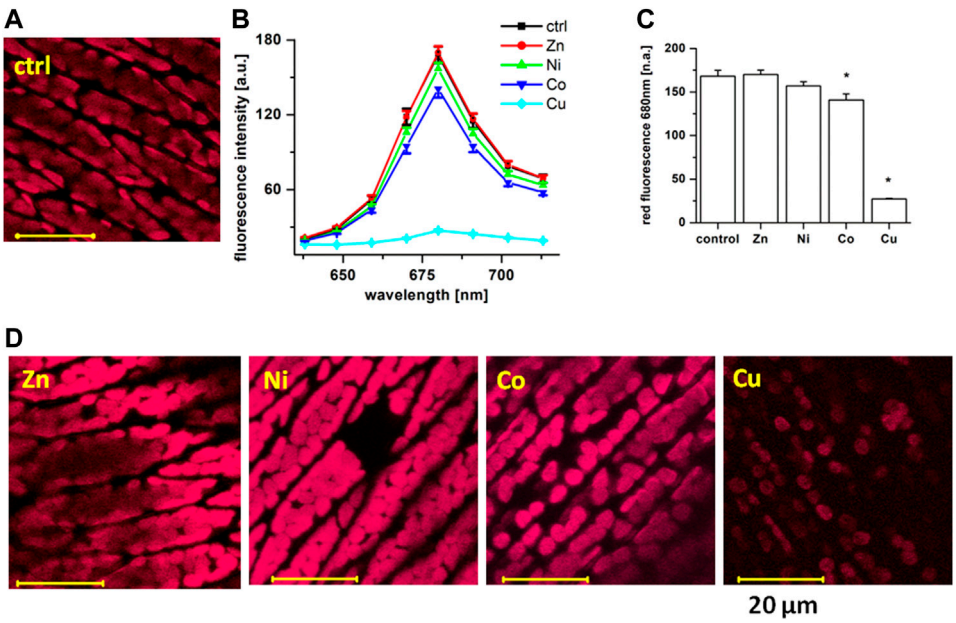

FIGURE 3 | Spectrally-resolved confocal microscopy images of *Fontinalis antipyretica* red fluorescence. **(A)** An original lambda-coded image in control conditions taken with an 11 nm step between 638 and 713 nm, excitation 450 nm. **(B)** Comparison of the recorded spectra in the presence of individual NPs ($n = 42$ in Ctrl, $n = 28$ in Zn, $n = 26$ in Ni, $n = 36$ in Co, $n = 31$ in Cu). **(C)** Statistical comparison at 680 nm, $^*p < 0.05$ with one-way Anova. **(D)** Spectrally-resolved confocal microscopy imaging of the red fluorescence in the presence of Zn, Ni, Co, and Cu NPs, scale 20 µm.

fluorescence of the moss. Next, to evaluate the spectral characteristics of the fluorescence that was affected by heavy metals, we have therefore employed the spectrally-resolved fluorescence. Spectral changes in the endogenous fluorescence of the moss were evaluated by spectrally-resolved images taken in the blue/green spectral region, using an 11 nm step between 477 and 638 nm (**Figure 2A**). In these conditions, endogenous fluorescence in control conditions was recordable between 520 and 560 nm (**Figure 2B**). Using this protocol in control conditions, the fluorescence peaked at 540 nm. When recorded at this wavelength, we noted a significant rise in the presence of Zn (**Figure 2C**). On the other hand, Cu induced a significant decrease in this fluorescence, while Ni and Co had a tendency to reduce it, but this effect did not reach significance. At **Figure 2D**, representative images in the presence of NPs are shown. Aggregation was proposed to play role in the modification of the lignin fluorescence [35] and we advance that it can also play a role in this action.

We have also recorded a rise in the blue signal at 477–488 nm in the presence of all but Zn NPs (**Figure 2D**, blue colour). This signal was mostly lacking in control conditions and, as we already reported previously [31], is most likely related to the reflection on the metal particles. This fluorescence was mainly situated in the intercellular space and its lack in the presence of Zn can thus be related to the rise in the stronger green fluorescence in this condition.

Red fluorescence of the moss represents the typical chlorophyll fluorescence [15]. When evaluated using spectrally-resolved confocal imaging, the fluorescence was taken in the red spectral region between 638 and 713 nm with an 11 nm step (see **Figure 3A** for the original recording in control conditions, with spectra at **Figure 3B**). In these conditions, the moss fluorescence in the chloroplasts peaked at 680 nm, as expected for the chlorophylls. At this emission wavelength, no change in the fluorescence was recorded in the presence of Zn (**Figure 3C**, with the original recording at **Figure 3D**). On the other hand, Co and Cu significantly reduced the red fluorescence at 680 nm (**Figures 3C,D**). Ni tends to decrease the chlorophyll signal, but this effect did not reach significance. The gathered result uncovered different sensitivities of the chlorophyll fluorescence to NPs.

Time-Resolved Imaging of the Effect of Nanoparticles on Endogenous Fluorescence in Moss

In order to better understand the observed reduction in the chlorophyll fluorescence in the presence of NPs, we have employed FLIM. Time-resolved fluorescence was recorded by TCSPC following excitation at 475 nm, using LP 500 nm emission filter (**Figure 4**). In such settings, most of the recorded fluorescence is situated intracellularly and is derived from chloroplasts inside *Fontinalis anripyretica* cells (*see* **Figure 4A** for the original recording of the FLIM image in control conditions). Fluorescence decays (*see* example of the decay curve in control conditions at **Supplementary Figure S1**) presented the best χ^2 (under 1.2–1.6) for a 3-exponential decomposition (*see* lifetime values with corresponding

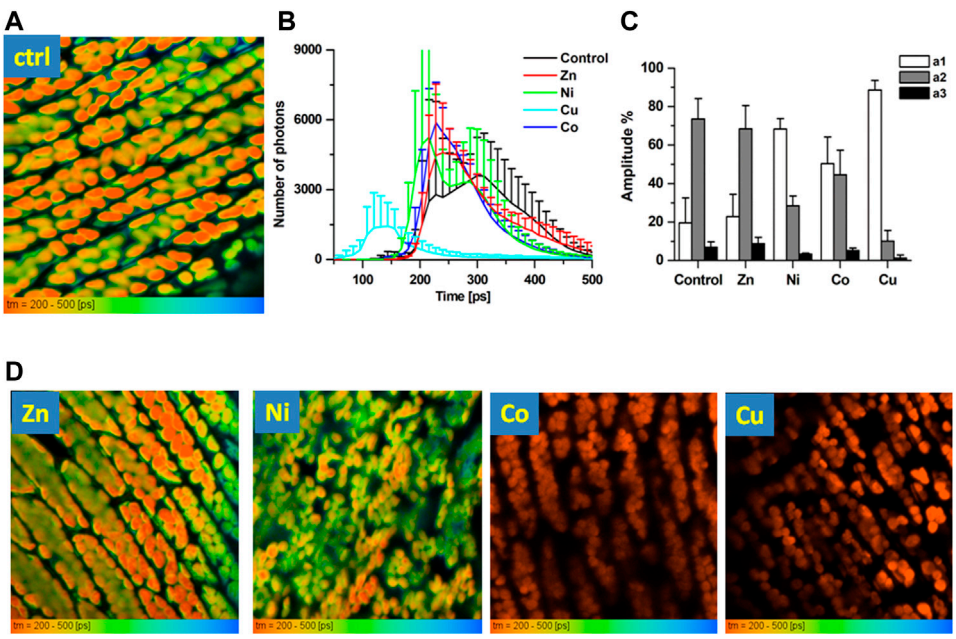

FIGURE 4 | FLIM images of *Fontinalis antipyretica* moss. **(A)** An original FLIM image in control conditions (CTRL) following excitation at 475 nm, using LP 500 nm emission filter. Lifetime distribution showed in the range 200–500 ps; **(B)** histograms of fluorescence lifetimes in the recorded conditions illustrated between 50 and 500 ps. **(C)** Amplitudes gathered by a 3-exponential decay for fixed lifetimes of 100 ps (a1, component 1) and 350 ps (a2, component 2), with residual third component a3 (n = 6 in Ctrl, n = 5 in Zn, n = 7 in Ni, n = 6 in Co, n = 4 in Cu). **(D)** Representative FLIM images in the presence of Zn, Ni, Co and Cu NPs, scale 200–500 ps.

amplitudes at **Supplementary Table S1**). At the same time, most of the fluorescence decayed at tau1. Such fluorescence lifetime situated between 200 and 500 ps (**Figure 4B**) which corresponds well to the chlorophyll fluorescence [20, 36]. In addition to fluorescence lifetime histograms (**Figure 4B**), we therefore also evaluated amplitudes related to the fixed lifetime of 100 ps (close to low lifetime values recorded in conditions such as Cu) and 350 ps (recorded in most conditions, including the control ones). In control conditions, the a1/a2 ratio for these fixed lifetimes was 20/73% with a small (7%) residual third component (**Figure 4C**).

When NPs were applied to *Fontinalis anripyretica* cells, statistical comparison of the recorded lifetime histograms (**Figure 4B**) revealed that, when compared to control conditions, Zn induced little or no change in the lifetime distribution for this fluorescence (**Figures 4B**,**D**), with the a1/a2 unaffected (23/68%, **Figure 4C**). On the other hand, in the presence of Co, the a1/a2 ratio reached close to parity (50/45%). Interestingly, Ni that was unable to induce a significant change in the overall fluorescence reversed the a1/a2 ratio to 68/28%. Such reverse of the a1/a2 ratio was even more pronounced in the presence of Cu, where it reached 89/10% (**Figure 4C**). This effect of Cu was also observable at the lifetime histograms (**Figure 4B**): as the Cu shortened the fluorescence lifetimes, an appearance of a very short lifetime around 150 ps was noted. Observed effects of NPs on the chlorophyll fluorescence lifetimes indicate that the recorded decrease in the chlorophyll fluorescence in the presence of NPs is most likely related to the change in the molecular environment. These results also suggest higher sensitivity of the fluorescence lifetimes than that of the fluorescence intensity to environmental stress, making this parameter a potential biosensing tool for rapid responsiveness of the moss to the heavy metal presence.

DISCUSSION

Data gathered in this contribution demonstrate that the short-term exposure for 3–5 days of the *Fontinalis anripyretica* moss to NPs produced from various metal targets using fs laser ablation [21] induced changes in its endogenous fluorescence. More precisely, we observed an increase of the green fluorescence in the spectral region 500–560 nm by the Zn and its decrease by the Cu NPs. On the other hand, the red chlorophyll fluorescence was reduced by the Co and Cu NPs and this effect was accompanied by changes in the fluorescence lifetimes induced by all but Zn NPs.

Heavy metal pollution is one of the most sensitive environmental issues due to production and a discharge into the environment of wastes containing different heavy metals by various industries. The presence of heavy metals in water and wastewater is thus increasing [2, 6]. An inhibited biosynthesis of chlorophylls, together with the decrease of growth-limiting photosynthesis and respiration [7, 8, 30] belong to the most frequent symptoms of the metal toxicity. In the present study, we evaluate the sensitivity of endogenous fluorescence to short-term exposure of heavy metal NPs in water bryophyte species *Fontinalis antipyretica* moss. This green moss is naturally occurring in sweet water lakes and is thus a good choice for the study of environmental pollution in water environments [37, 38]. It occurs on submerged rocks and wood in flowing or standing waters, including sweet water lakes, where it forms refuge for fish eggs. This moss was found to have good accumulation properties for metals when used in active biomonitoring in the river environment [11]. In addition, the *Fontinalis antipyretica* moss presents high sensitivity of chlorophyll fluorescence parameters to environmental changes [38] and can adsorb some of the heavy metals (Cd, Zn) [39].

Endogenous fluorescence was evaluated in two spectral regions: the green (peaking between 540 and 560 nm) and the red (peaking at 680 nm). Previously, the NADPH dependent blue-green fluorescence (BGF) was described in isolated chloroplasts [16, 17]. In our experiments, green/yellow fluorescence stimulated by excitation at 450 nm was most pronounced between 510 and 560 nm and this fluorescence inside the cells is most likely derived from NADPH-related flavins and flavonoids. In addition to the blue-green fluorescence inside the cells, most of the green fluorescence was observed in the intercellular space. Such green fluorescence can be derived from lignins of the intermediate lamella [18]. This fluorescence was clearly increased in the presence of Zn NPs and completely abolished in the presence of the Cu NPs. Metal oxide NPs of ZnO are known to have antimicrobial properties associated with an increase in the ROS production [26]. At the same time, aggregation-induced conjugation from phenylpropane units was believed to be the main source of the visible emission of lignin and different phenylpropane aggregates consequently forming the multi-fluorophore system in lignin micelle [40]. Lignin aggregation fluorescence behavior has great potential in its microstructure analysis and a case study of pH/ionic strength-induced solution behaviour analysis was presented [40]. We propose that such an oxidative-stress related aggregation-dependent mechanism can play role in the observed effect of the rise in the intercellular space green fluorescence by Zn and its decrease by Cu in the *Fontinalis antipyretica* moss.

Most of the endogenous fluorescence recorded in our sample of living moss was in the red spectral region and reached maximum at 680 nm. This finding is in agreement with previous observations that the main fluorescence recorded naturally in all plants is derived from chlorophyll a, a light-absorbing pigment [15]. Chlorophyll fluorescence is highly sensitive to changes in the functional state and we employed it previously as a biosensing tool for tracking algae responsiveness to environmental modulators [20]. In the presented study, heavy metal NPs Co and Cu significantly lowered the chlorophyll fluorescence intensity. A comparable effect was previously noted in the *Chlorella sp.* algae after 2 weeks exposure to NPs [31]. It is well known that heavy metals change the chlorophyll fluorescence yield and content of photosynthetic pigments representing sensitive indicators of environmental stress [41]. The toxic effect of Cu was proposed to be due to its oxidative potential causing the reduction of chlorophylls, leading to a decrease of oxygen rates and depletion of ATP. The observed effect of Cu can also be related to the fact that the Cu was

demonstrated to have a higher adsorption capacity than Ni and Zn in the moss [42]. On the other hand, Co NPs were shown to inhibit fresh water algal bloom by decreasing super oxide dismutase (SOD) activity with increased NPs concentration, indicating the formation of stress in the microalgae [29]. Notwithstanding, even though cellular alterations were described by NiO NPs, including effects on the photosynthetic apparatus via chlorophyll synthesis, photochemical reactions of photosynthesis and oxidative stress [28], we noted little or no effect of the Ni NPs on the overall fluorescence intensity. This indicates lesser sensitivity of the moss to Ni and/or the need for longer exposure times.

In order to better understand the action of NPs on the red chlorophyll fluorescence, we have employed time-resolved fluorescence imaging microscopy. Fluorescence lifetimes depend on multiple factors that include pH, temperature, oxygenation, density, as well as presence or absence of quenchers {reviewed in [43]} and its use represents an important instrumental advancement. Temporal characteristics of the endogenous fluorescence served as a biomarker for changing environment, namely evidencing Cd toxicity noninvasively in algal cells [44]. In this contribution, FLIM recordings showed that most of the fluorescence signal in the *Fontinalis antipyretica* was situated inside the cell chloroplasts of the moss leaves. In control conditions, moss leafs exhibited short fluorescence lifetimes (200–350 ps), which is in agreement with others [36, 45–47], as well as with our findings in algae [19, 20]. In pine wood middle lamella, lignin was also shown to have a 300 ns lifetime. However, in our settings, FLIM images did not reveal fluorescence in the intercellular space due to its weak fluorescence when compared to chlorophylls; time-resolved fluorescence evaluated in this contribution are therefore related mostly to chlorophylls.

Following exposure to all NPs but Zn, we noted changes in the fluorescence lifetimes. More precisely, the ratio of a1/a2 components, fixed at 100 and 350 ps, was modified: while in control conditions, the a2 component was prevailing, in the presence of Ni, Co and mainly Cu, the contribution of the a1 (100 ps) component became more pronounced. Surprisingly, this modification was also observed in the presence of Ni, where the overall fluorescence was unchanged, suggesting higher sensitivity of the fluorescence lifetimes to environmental stress than that of the overall fluorescence. Shortening of the chlorophyll fluorescence lifetime was noted following water stress in plants [48]. Our previous results in algae demonstrated a decrease in the chlorophyll fluorescence with acidification, related to the shortening of the fluorescence lifetimes [20]. Heavy metals are known to affect the chloroplast ultrastructure, causing lipid peroxidation in photosynthetic membranes, degradation of photosynthetic pigments, inhibition of photosystem II (PSII) activity and electron transport, thus restraining the net photosynthetic rate [49]. Previously, we have demonstrated the sensitivity of marine algae *Dunalliela tertiolecta* to laboratory-induced stress with heavy metal cadmium [19, 33], with the role of stress-related light-harvesting complexes (LHC). The comparable effect can also be involved in the observed actions, but the exact mechanisms involved still remain to be elucidated. Nevertheless, our findings indicate that the observed change in the fluorescence lifetime component ratio, induced by heavy metals, can be employed for tracing their presence in the sweet water environment.

One of the problems faced in detecting metal ions with fluorescent sensors is the emission suppressing effects of some metal ions, which results in strong quenching of the fluorescence. Inherently quenching metal ions such as Hg^{2+}, Cu^{2+}, Co^{2+}, Ni^{2+}, and Fe^{3+} can interfere with the fluorescent signal of the sensors in detecting other metals [50]. Non-photochemical quenching of the chlorophyll fluorescence, described in the presence of heavy metals [38, 51], can a play role in the observed effect of the decrease in the fluorescence by both Co and Cu, accompanied by a rise in the contribution of the shorter fluorescence lifetime component a1. At the same time, our experiments demonstrate accumulation of the NPs mainly in the intercellular space, while the red fluorescence was derived from chloroplasts inside the cells. This fact, together with the lack of changes in the fluorescence lifetime during the decrease in the red chlorophyll fluorescence in the monocellular algae *Chlorella sp.* after NPs exposure [31] rather suggests an employment of intracellular pathways, the effect on LHC, PSII and/or modification in the intrachloroplast environment in this action than a direct non-photochemical quenching. Various parameters, including pH, temperature and water quality were proposed to play role in the heavy metal adsorption by the *Fontinalis antipyretica* moss [38]. However, an exact mechanism explaining how the NPs enter and/or attach to the *Fontinalis antipyretica* moss leaves was not yet elucidated and needs to be the subject of future studies. Also, the concentration effects, as well as the time-dependence of the effects of NPs on the moss should be explored in more details.

Since heavy metals are nonbiodegradable, they accumulate in the environment and subsequently contaminate the food chain. This contamination poses a risk to environmental and human health. The biomass of the aquatic moss *Fontinalis antipyretica* was proposed to be suitable for the removal of Cd and Zn from aqueous solutions [39], as this natural material is widely available in most European lakes and rivers. An improved understanding of heavy metal uptake by plants from soil can thus help in promoting phytomining - plant-based eco-friendly mining of metals, which can be used for the extraction of metals even from low-grade ores [52]. Data gathered in this contribution demonstrate the fast capacity of the *Fontinalis antipyretica* moss to reabsorb heavy metals, including small size NPs, from the environment. It can thus be considered as a sorbent for purification of metal-bearing wastewaters and play role in water cleansing and remediation.

CONCLUSION

In conclusion, we present the application of spectrally- and time-resolved imaging of endogenous fluorescence in biosensing of environmental pollution by heavy metal NPs (Zn, Ni, Co, Cu). Gathered results demonstrate the sensitivity of both, the green flavonoid and/or lignin fluorescence and the red chlorophyll fluorescence of *Fontinalis antipyretica* moss to the short

(3–5 day) presence of various heavy metal (mostly Zn, Co and Cu) NPs. The action of all NPs but Zn also uncovered changes in the fluorescence lifetimes of the red chlorophyll fluorescence, suggesting an effect on the molecular environment, as well as increased sensitivity of this parameter to environmental stress. Our work is the first step towards fast and non-invasive biosensing of environmental pollution in living moss cells and their potential use in remediation.

DATA AVAILABILITY STATEMENT

The raw data supporting the conclusions of this article will be made available by the authors, without undue reservation.

AUTHOR CONTRIBUTIONS

All authors contributed equally to the paper. MCA overviewed the work presented in the ms, performed key experiments together with their analysis and wrote the ms. CD participated in the preparation of setups and experimental protocols, as well as in the data analysis and UM performed a large part of experiments and analysed primarily the FLIM data.

FUNDING

This publication was supported by the Grant Agency of the Ministry of Education, Science, Research and Sports of the Slovak Republic under the contract No. VEGA 2/0070/21. This work also received funding from the European Union's Horizon 2020 research and innovation programme under the grant agreement no 871124 Laserlab-Europe. The authors would like to thank T. Teplicky and J. Bruncko for their help with NPs preparation.

SUPPLEMENTARY MATERIAL

The Supplementary Material for this article can be found online at: https://www.frontiersin.org/articles/10.3389/fphy.2021.634324/full#supplementary-material.

REFERENCES

1. Mohammed AS, Kapri A, Goel R. Heavy metal pollution: source, impact, and remedies. In: M Khan, A Zaidi, R Goel, J Musarrat, editors. *Biomanagement of metal-contaminated soils. Environmental pollution*, 20. Dordrecht: Springer (2011) doi:10.1007/978-94-007-1914-9_1
2. Srivastava NK, Majumder CB. Novel biofiltration methods for the treatment of heavy metals from industrial wastewater. *J Hazard Mater* (2008) 151:1–8. doi:10.1016/j.jhazmat.2007.09.101
3. Jadoon S, Malik A. DNA damage by heavy metals in animals and human beings: an overview. *Biochem Pharmacol* (2017) 06:1000235. doi:10.4172/2167-0501.1000235
4. Hoet PH, Brüske-Hohlfeld I, Salata OV. Nanoparticles – known and unknown health risks. *J Nanobiotechnol* (2004) 2:12. doi:10.1186/1477-3155-2-12
5. Jaishankar M, Tseten T, Anbalagan N, Mathew BB, Beeregowda KN. Toxicity, mechanism and health effects of some heavy metals. *Interdiscip Toxicol* (2014) 7(2):60–72. doi:10.2478/intox-2014-0009
6. Wilde EW, Benemann JR. Bioremoval of heavy metals by the use of microalgae. *Biotechnol Adv* (1993) 11:781–812. doi:10.1016/0734-9750(93)90003-6
7. Parys E, Romanowska E, Siedlecka M, Poskuta JW. The effect of lead on photosynthesis and respiration in detached leaves and in mesophyll protoplasts of *Pisum sativum*. *Acta Physiol Plant* (1998) 20:313. doi:10.1007/s11738-998-0064-7
8. Prasad MNV. *Heavy metal stress in plants - from biomolecules to ecosystems*. Berlin, Germany: Springer-Verlag (2004).
9. Cenci RM. The use of aquatic moss (*Fontinalis antipyretica*) as monitor of contamination in standing and running waters: litmits and advantages. *J Limnol* (2001) 60: 53–61. doi:10.4081/jlimnol.2001.s1.53
10. de Traubenberg C, Ah-Peng C. A procedure to purify and culture a clonal strain of the aquatic moss *Fontinalis antipyretica* for use as a bioindicator of heavy metals. *Arch Environ Contam Toxicol* (2004) 46:289–295. doi:10.1007/s00244-003-3040-7
11. Bruns I, Friese K, Markert B, Krauss G-J. The use of Fontinalis antipyretica L. ex Hedw. as a bioindicator for heavy metals. 2. Heavy metal accumulation and physiological reaction of Fontinalis antipyretica L. ex Hedw. in active biomonitoring in the River Elbe. *Sci The Total Environ* (1997) 204(2): 161–76. doi:10.1016/S0048-9697(97)00174-5
12. Rau S, Miersch J, Neumann D, Weber E, Krauss G-J. Biochemical responses of the aquatic moss Fontinalis antipyretica to Cd, Cu, Pb and Zn determined by chlorophyll fluorescence and protein levels. *Environ Exp Bot* (2007) 59(3): 299–306. doi:10.1016/j.envexpbot.2006.03.001
13. Chorvatova A, Chorvat D, Jr. Tissue fluorophores and their spectroscopic characteristics. In: L Marcu, PMW French, DSV Elson, editors. *Fluorescence lifetime spectroscopy and imaging for tissue biomedical diagnostics*. Boca Raton, FL: CRC Press Publ (2014). 47–84. doi:10.1201/b17018-5
14. Becker W. *Advanced time-correlated single photon counting applications*. New York, NY: Springer (2015). doi:10.1007/978-3-319-14929-5
15. Govindjee G, Rabinowitch E Chlorophyll fluorescence and photosynthesis. In: GG Guilbaut, editor. *Fluorescence instrumentation and practice*. Newyork, NY: Marcel Dekker Inc. (1967). p. 511–64.
16. Cerovic ZG, Bergher M, Goulas Y, Tosti S, Moya I. Simultaneous measurement of changes in red and blue fluorescence in illuminated isolated chloroplasts and leaf pieces: the contribution of NADPH to the blue fluorescence signal. *Photosynth Res* (1993) 36:193–204. doi:10.1007/BF00033038
17. Cerovic ZG, Langrand E, Latouche G, Morales F, Moya I. Spectral characterization of NAD(P)H fluorescence in intact isolated chloroplasts and leaves: effect of chlorophyll concentration on reabsorption of blue-green fluorescence. *Photosynth Res* (1998) 56:291–301. doi:10.1023/a:1006081209887
18. Donaldson L Autofluorescence in plants. *Molecules* (2020) 25(10):2393. doi:10.3390/molecules25102393
19. Pavlinska Z, Chorvat D, Jr., Mateasik A, Jerigova M, Velic D, Ivošević DeNardis N, et al. Fluorescence responsiveness of unicellular marine algae *Dunaliella* to stressors under laboratory conditions. *J Biotechnol X* (2020) 6: 100018. doi:10.1016/j.btecx.2020.100018
20. Marcek Chorvatova A, Uherek M, Mateasik A, Chorvat D, Jr. Time-resolved endogenous chlorophyll fluorescence sensitivity to pH: study on Chlorella sp. algae. *Methods Appl Fluoresc* (2020b) 8:024007. doi:10.1088/2050-6120/ab77f4
21. Teplicky T, Chorvat D, Michalka M, Chorvatova AM. Preparation of metal nanoparticles by femtosecond laser ablation. *Nova Biotechnologica Chim* (2018) 17(1):38–47. doi:10.2478/nbec-2018-0004
22. Gupta SM, Tripathi M. A review of TiO2 nanoparticles. *Chin Sci Bull* (2011) 56:1639–57. doi:10.1007/s11434-011-4476-1
23. Kim JS, Kuk E, Yu KN, Kim J-H, Park SJ, Lee HJ, et al. Antimicrobial effects of silver nanoparticles. *Nanomedicine: Nanotechnology, Biol Med* (2007) 3(1): 95–101. doi:10.1016/j.nano.2006.12.001
24. Langer J, Novikov SM, Liz-Marzán LM. Sensing using plasmonic nanostructures and nanoparticles. *Nanotechnology* (2015) 26(32):322001. doi:10.1088/0957-4484/26/32/322001
25. Padmavathy N, Vijayaraghavan R. Enhanced bioactivity of ZnO nanoparticles-an antimicrobial study. *Sci Technol Adv Mater* (2008) 9(3): 035004. doi:10.1088/1468-6996/9/3/035004

26. Li M, Ahammed GJ, Li C, Bao X, Yu J, Huang C, et al. Brassinosteroid ameliorates zinc oxide nanoparticles-induced oxidative stress by improving antioxidant potential and redox homeostasis in tomato seedling. *Front Plant Sci* (2016) 7:615. doi:10.3389/fpls.2016.00615
27. El-Kassas HY, Okbah MAE-A. Phytotoxic effects of seaweed mediated copper nanoparticles against the harmful alga: lyngbya majuscula. *J Genet Eng Biotechnol* (2017) 15(1):41–8. doi:10.1016/j.jgeb.2017.01.002
28. Oukarroum A, Zaidi W, Samadi M, Dewez D. Toxicity of nickel oxide nanoparticles on a freshwater green algal strain of *Chlorella vulgaris*. *Biomedresearch Int* (2017) 8:9528180. doi:10.1155/2017/9528180
29. Anusha L, Chingangbam Sushmita D, Sibi G. Inhibition effects of Cobalt nano particles against fresh water algal blooms caused by microcystis and oscillatoria. *Am J Appl Scientific Res* (2017) 3(4):26–32. doi:10.11648/j.ajasr.20170304.12
30. Bajguz A. Suppression of Chlorella vulgaris growth by cadmium, lead, and copper stress and its restoration by endogenous brassinolide growth by cadmium, lead, and copper stress and its restoration by endogenous brassinolide. *Arch Environ Contam Toxicol* (2011) 60(3):406–16. doi:10.1007/s00244-010-9551-0
31. Marcek Chorvatova A, Teplicky T, Valica M, Mateasik A, Chorvat D, Jr. Biosensing the presence of nanoparticles using endogenous fluorescence in live algae. In: AN Cartwright DV Nicolau, editors. Proceedings of SPIE on Nanoscale imaging, sensing and actuation for biomedical applications XVII book series. 11254 (2020a). p. 1125402–1. doi:10.1117/12.2543332
32. Alkorta I, Hernández-Allica J, Becerril JM, Amezaga I, Albizu I, Garbisu C. Recent findings on the phytoremediation of soils contaminated with environmentally toxic heavy metals and metalloids such as zinc, cadmium, lead, and arsenic. *Re/Views Environ Sci Bio/Technology* (2004) 3:71–90. doi:10.1023/b:resb.0000040059.70899.3d
33. Ivošević DeNardis N, Pečar Ilić J, Ružić I, Novosel N, Mišić Radić T, Weber A, et al. Algal cell response to laboratory-induced cadmium stress: a multimethod approach. *Eur.Biophys J* (2019) 48(2):124–42. doi:10.1007/s00249-019-01347-6
34. Marcek Chorvatova A, Teplicky T, Pavlinska Z, Kronekova Z, Trelova D, Razga, et al. A bio-inspired design of live-cell biosensors. *Proc SPIE* (2018) 10506:105060R–1. doi:10.1117/12.2288789
35. Xue Y, Qiu X, Wu Y, Qian Y, Zhou M, Deng Y, et al. Aggregation-induced emission: the origin of lignin fluorescence Polymer chemistry. *Polym Chem* (2016) 7:3502–8. doi:10.1039/C6PY00244G
36. Kristoffersen AS, Hamre B, Frette Ø, Erga SR. Chlorophyll a fluorescence lifetime reveals reversible UV-induced photosynthetic activity in the green algae Tetraselmis. *Eur Biophys J* (2016) 45:259–68. doi:10.1007/s00249-015-1092-z
37. Martínez-Abaigar J, Nuñez-Olivera E, Crespo MA, Tomas R, Beaucourt N, Otero S. *Effects ultraviolet Radiat Aquat bryophytes Limnetica* (2006) 25(1-2): 81–94. doi:10.23818/limn.25.06
38. Chen Y-E, Wu N, Zhang Z-W, Yuan M, Yuan S. Perspective of monitoring heavy metals by moss visible chlorophyll fluorescence parameters. *Front Plant Sci* (2019) 10(35):1–7. doi:10.3389/fpls.2019.00035
39. Martins RJE, Pardo R, Boaventura RAR. Cadmium(II) and zinc(II) adsorption by the aquatic moss Fontinalis antipyretica: effect of temperature, pH and water hardness. *Water Res* (2004) 38(3):693–9. doi:10.1016/j.watres.2003.10.013
40. Xue Y, Qiu X, Ouyang X. Insights into the effect of aggregation on lignin fluorescence and its application for microstructure analysis. *Int J Biol Macromolecules* (2020) 154:981–8. doi:10.1016/j.ijbiomac.2020.03.056
41. Lichtenthaler HK, Miehé JA Fluorescence imaging as a diagnostic tool for plant stressRemoval of copper from solution using moss. *Trends in Plant ScienceEnviron Technology Lett* (1997) 2:316–20. doi:10.1016/s1360-1385(97)89954-242
42. Lee CK, Low KS. Removal of copper from solution using moss. *Environ Technology Lett* (1989) 10(4):395–404. doi:10.1080/09593338909384755
43. Berezin MY, Achilefu S Fluorescence lifetime measurements and biological imaging. *Chem Rev* (2010) 110(5):2641–84. doi:10.1021/cr900343z
44. Zeng Y, Wu Y, Li D, Zheng W, Wang W-X, Qu JY. Two-photon excitation chlorophyll fluorescence lifetime imaging: a rapid and noninvasive method for *in vivo* assessment of cadmium toxicity in a marine diatom Thalassiosira weissflogii. *Planta* (2012) 236(5):1653–63. doi:10.1007/s00425-012-1703-1
45. Singhal GS, Rabinowitch E, Camenen L, Goulas YGG, Cerovic ZG, Schmuck G. Measurement of the fluorescence lifetime of chlorophyll a *in vivo*. *Biophysical JRemote Sens Environ* (1969) 9:586–91. doi:10.1016/S0006-3495(69)86405-2
46. Moya I. Estimation of the chlorophyll fluorescence lifetime of plant canopies: validation of a deconvolution method based on the use of a 3-D Canopy Mockup58157168. *Remote Sens Environ* (1996) 58:157–68.
47. Nordlund TM, Knox WH. Lifetime of fluorescence from light-harvesting chlorophyll a/b proteins. Excitation intensity dependence. *Biophysical J* (1981) 36(1):193–201. doi:10.1016/S0006-3495(81)84723-6
48. Schmuck G, Moya I, Pedrini A, van der Linde D, Lichtenthaler HK, Stober F, et al. Chlorophyll fluorescence lifetime determination of waterstressed C3- and C4-plants. *Radiat Environ Biophys* (1992) 31:141–51. doi:10.1007/bf01211212
49. Mishra S, Dubey R. Heavy metal toxicity induced alterations in photosynthetic metabolism in plants. In: M Pessarakli, editor. *Handbook of photosynthesis*. Boca Raton, FL: CRC Press (2005). p. 827–44.
50. Tan SS, Kim SJ, Kool ET. Differentiating between fluorescence-quenching metal ions with polyfluorophore sensors built on a DNA backbone. *J Am Chem Soc* (2011) 133(8):2664–71. doi:10.1021/ja109561e
51. Niyogi KK, Truong TB. Evolution of flexible non-photochemical quenching mechanisms that regulate light harvesting in oxygenic photosynthesis. *Curr Opin Plant Biol* (2013) 16:307–14. doi:10.1016/j.pbi.2013.03.011
52. Ali H, Khan E, Sajad MA. Phytoremediation of heavy metals-Concepts and applications. *Chemosphere* (2013) 91:869–81. doi:10.1016/j.chemosphere.2013.01.075

Conflict of Interest: The authors declare that the research was conducted in the absence of any commercial or financial relationships that could be construed as a potential conflict of interest.

frontiers in Physics

BRIEF RESEARCH REPORT
published: 27 January 2021
doi: 10.3389/fphy.2020.625424

A Highly Sensitive Time-Gated Fluorescence Immunoassay Platform Using Mn-Doped AgZnInS/ZnS Nanocrystals as Signal Transducers

Brandon Gallian[1,2], *Masoumeh Saber Zaeimian*[1,2], *Derrick Hau*[3], *David AuCoin*[3] *and Xiaoshan Zhu*[1,2]*

[1]Department of Electrical and Biomedical Engineering, University of Nevada, Reno, NV, United States, [2]Biomedical Engineering Program, University of Nevada, Reno, NV, United States, [3]Department of Microbiology and Immunology, School of Medicine, University of Nevada, Reno, NV, United States

In this work, a time-gated immunoassay platform using low-energy excitable and fluorescence long-lived Mn:AgZnInS/ZnS nanocrystals as signal transducers was developed and applied to the detection of the capsular polysaccharide (CPS) of *Burkholderia pseudomallei*, a Gram-negative bacterium that is the causative agent of melioidosis. CPS is a high molecular weight antigen displayed and is shed from the outer membrane of *B. pseudomallei*. The immunoassay using the time-gated platform presents a limit of detection at around 23 pg/ml when CPS is spiked in human serum.

Keywords: nanocrystals, Mn doping, time-gated fluorescence, immunoassay, analytical platform

OPEN ACCESS

Edited by:
Yiqing Lu,
Macquarie University, Australia

Reviewed by:
Run Zhang,
The University of Queensland, Australia
Luca De Stefano,
Institute of Applied Sciences and Intelligent Systems (ISASI), Italy

***Correspondence:**
Xiaoshan Zhu
xzhu@unr.edu

Specialty section:
This article was submitted to Optics and Photonics, a section of the journal Frontiers in Physics

Received: *03 November 2020*
Accepted: *14 December 2020*
Published: *27 January 2021*

Citation:
Gallian B, Zaeimian MS, Hau D, AuCoin D and Zhu X (2021) A Highly Sensitive Time-Gated Fluorescence Immunoassay Platform Using Mn-Doped AgZnInS/ZnS Nanocrystals as Signal Transducers. Front. Phys. 8:625424. doi: 10.3389/fphy.2020.625424

INTRODUCTION

Time-gated fluorescence measurement using long-lived fluorescence probes is a highly sensitive signal transduction method in biomedical research [1–5]. In the time-gated measurement, biological samples are excited using a pulsed optical source. After the excitation, autofluorescence from biological samples fades out quickly in tens to hundreds of nanoseconds. However, the long-lived probes continue emitting fluorescence up to milliseconds. Through detecting the time-gated emission from the probes, the signal-to-background ratio can be significantly enhanced to yield improved analytical sensitivity or a limit of detection (LOD).

The widely used probes for time-gated measurements mainly include lanthanide complexes or lanthanide-based nanoparticles, which have long fluorescence lifetimes at microseconds to milliseconds due to the unique energy bands (i.e., forbidden nature of the 4f transitions) of lanthanide elements [6]. For biosensing applications utilizing lanthanide-based probes, bulky laboratory-based instruments are routinely used for time-gated measurements; however, portable or small benchtop "personal" time-gated instruments are preferred to facilitate point-of-care or in-field testing [7–11]. One of the challenges is that the absorption spectra of lanthanide-based probes are generally in the ultraviolet (UV) range, and high-energy optical sources (e.g., 200–365 nm wavelength with tens or hundreds of milliwatts optical power) are needed to excite these probes in their applications. For instance, costly light-emitting diodes (LED) at 365 nm wavelength from Prizmatix (Mic-LEDs, > 200 mW, ~ $1,500) were reported as the excitation light sources for lanthanide-based probes [8]. Expensive UV-grade optics are also needed in order to avoid UV-induced (e.g., 365 nm) strong autofluorescence from glass/optics. Xenon lamps, broadly used in various instruments as excitation sources, are cheap but relatively large in size, and they need more strict operating conditions, including high current and kilovolts pulsed voltage to initiate light.

Additionally, xenon lamps have a long trailing afterglow (hundreds of microseconds) but are hard to pulse rapidly [9, 10, 12]. UV laser diodes (e.g., <375 nm) as excitation sources are more expensive (~$4,000), and their output powers are also limited. As a result, the UV laser diodes may not be ideal excitation sources for lanthanide-based probes. High-energy optical sources not only complicate the instrument development but also increase the cost. It is important to find new high-quality probes for time-gated measurement under low-energy excitation.

Among various probes with long-lived luminescence for time-gated (or time-resolved) biosensing/imaging [13, 14], manganese- (Mn-) doped nanocrystals (NCs) including I(II)-III-VI NCs are attractive in biomedical research (i.e., biosensing/imaging) [15, 16]. Mn-doped I(II)-III-VI NCs can be synthesized in a relatively low temperature and a short time (<200°C, 1–2 h, an energy-saving procedure) and have low toxicity synthesis/handling/disposal. They also possess excellent optical properties, including high brightness and long fluorescence lifetimes resulting from the spin relaxation and slow inversion between $^4T_1$ and $^6A_1$ states of Mn. In spite of these merits, some recent works on Mn doping into I(II)-III-VI NCs show significant variations on their absorption/fluorescence spectra and lifetimes (hundreds of nanoseconds to milliseconds) of the doped NCs depending on the synthesis approaches/conditions [17, 18]. Recognizing that the electronic energy bands of the host NCs could interact with the energy levels of Mn dopants and thus determine the optical properties of Mn-doped quaternary NCs [15, 19], we have specifically investigated the interaction between Mn dopants and host AgZnInS/ZnS NCs by tuning host composition and also changing Mn spatial distribution and its concentration in host NCs [19]. Therefore, we achieved Mn-doped AgZnInS/ZnS (Mn:AgZnInS/ZnS) NCs with optimal optical properties, including long fluorescence lifetimes (1.33 milliseconds), low excitation energy (excitable at 405 nm wavelength), minimal emission reabsorption, and adequate brightness (>40% quantum yield). Compared to lanthanide-based probes, Mn:AgZnInS/ZnS NC-based probes would not replace them in all their applications. However, due to their unique optical properties and the availability of compact and cheap excitation sources at 405 nm wavelength with appropriate optical power outputs, Mn:AgZnInS/ZnS NC-based probes could be more efficient in facilitating the development of cost-effective small benchtop "personal" instruments. These instruments could have broader in-field sensing applications and avoid the need/use of central laboratories.

We have recently presented a compact time-gated fluorescence instrument using Mn:AgZnInS/ZnS NC-based probes as signal reporters and applied it for sensitive detection of copper(II) ions in highly autofluorescent rum (alcoholic beverage) [20]. Nevertheless, this system adopted a quartz cuvette with a volume of several milliliters as the sample holder and an optical path corresponding to such a cuvette. It is hard for this system to be used in microplate-based immunoassays, which can handle small sample volumes and also have wide applications in disease diagnosis, environmental monitoring, food safety analysis, and so on. It would be more interesting to develop a small and highly sensitive time-gated immunoassay platform using microplates and adopting Mn:AgZnInS/ZnS NC-based probes as signal transducers. Additionally, we have recently reported poly(maleic anhydride-alt-1-octadecene) (PMAO) based zwitterionic amphiphiles to encapsulate hydrophobic ligand coated nanoparticles for water solubility, minimal nonspecific binding, excellent colloidal stability, and bioconjugation [21]. In this work, we redesigned the instrument for the analysis/measurement on a small sample volume and also applied the zwitterionic amphiphiles to encapsulate hydrophobic Mn:AgZnInS/ZnS NCs to form water-soluble probes for immunoassay. We then mainly investigated whether such a redesigned instrument together with the Mn:AgZnInS ZnS NC-based probes can significantly enhance the immunoassay performance (i.e., lowering the LOD of immunoassay, which is a major advantage of time-gated measurement).

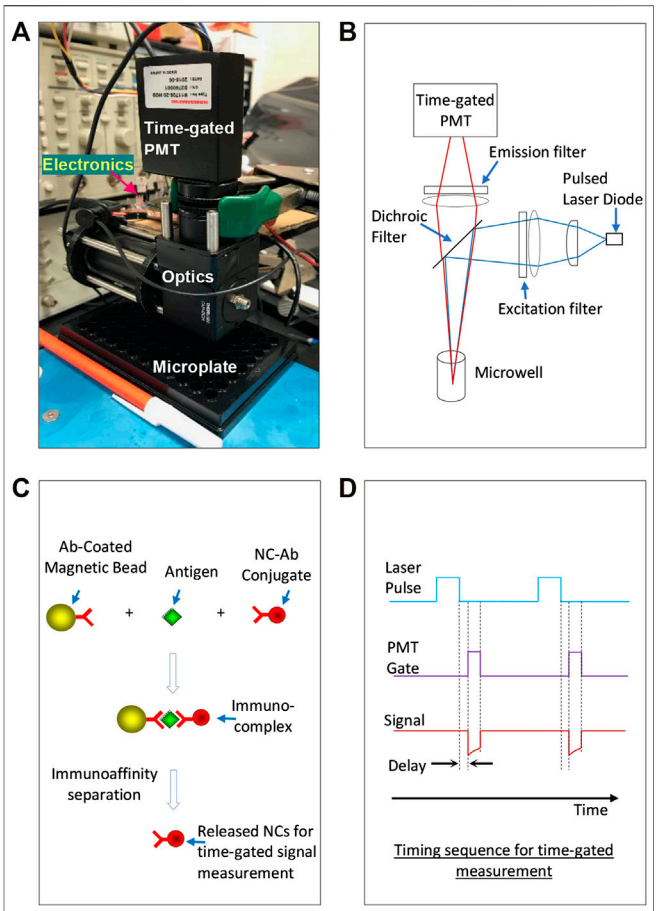

FIGURE 1 | (A) A small time-gated immunoassay platform integrating a time-gated optical detector and microplate-based immunoassay using Mn:AgZnInS/ZnS NC probes as signal transducers. **(B)** Principle illustration of the optical unit. **(C)** The immunoassay format performed in microwells of microplates: after antigens are switched between antibody-coated magnetic microbeads and antibody-conjugated NC probes, the NC probes are released from the immuno-switch-complexes into supernatants for time-gated signal measurement. **(D)** The timing sequence for time-gated measurement on the excitation laser and the PMT.

For the immunoassay, we utilized a high-affinity monoclonal antibody (mAb 4C4) to detect purified *B. pseudomallei* CPS spiked in human serum. mAb 4C4 was confirmed to be suitable for use in an antibody-based detection assay for the diagnosis of *B. pseudomallei* infections [22–24]. CPS is expressed on the cell envelopes of *B. pseudomallei*, which is listed as Tier 1 select agent by the CDC and is a Gram-negative bacterial pathogen affecting both human beings and animals to cause melioidosis [25, 26]. The immunoassay for the detection of CPS in human biological fluid can be potentially used in mobile laboratories for in-field melioidosis diagnosis. It should be noted that culture of *B. pseudomallei* from blood or other body fluids is still the gold standard for diagnosis of melioidosis, but it needs central laboratories and also takes 3–5 days before a definitive diagnosis can be made. Thus, developing a compact highly sensitive immunoassay platform for CPS detection is of important significance for melioidosis diagnosis and rapid administration of effective antibiotics.

MATERIALS AND METHODS

The detailed experimental approaches/methods are described in the **Supplementary Material**.

RESULTS AND DISCUSSION

Figure 1A presents the small time-gated immunoassay platform integrating a time-gated optical detector and a microplate-based immunoassay using Mn:AgZnInS/ZnS NC probes as signal transducers. Compared to our previously reported instrument [20], we kept all electronics but redesigned the optical path for microwell-based detection. **Figure 1B** illustrates the design of the optical unit using a dichroic-filter ZT514rc (Chroma) to split excitation and emission light. The dichroic filter reflects light with short wavelengths (<514 nm) to the sensing surface/volume but allows light with long wavelengths (>514 nm) to pass through the dichroic filter. On the excitation (or laser diode) side, one planoconvex lens and one biconvex lens direct the laser light to the dichroic filter. To avoid any possible autofluorescence from lenses and harmonic wavelengths from the laser diode, a bandpass optical filter (405 ± 10 nm, Chroma) filter is placed at the innermost end of the excitation-side slotted lens tube. On the microwell side, the reflected laser light is focused on a region of the microwell. The emission light from the sample passes through the dichroic filter, a biconvex lens, and an emission filter (655 ± 20 nm, Chroma) and then is focused into a time-gated photomultiplier tube (PMT). The whole optical path is built in two lens tubes and a dichroic-filter cage cube with necessary adapters. The PMT is directly placed at the end of a lens tube using a PMT-to-C-mount adapter, C-mount-to-SM1 adapter, and a silicone gasket to block out stray light at the junction of the PMT and C-mount adapter. An adapter surrounded with a rubber gasket (as a part of the optical detector) is used to align/seal with each microwell without touching samples loaded in the microwell. The microplate under the testing can be manually shifted; thus, each microwell can be read by the optical detector (with good alignment and sealing with the optical detector). Before the use of the instrument, with the continuous turn-on of the laser diode, the lenses in the excitation branch were manually adjusted/tuned in their positions to achieve the highest signal/background ratio for a probe solution with a certain concentration (e.g., 1 μg/ml) and a blank, which were loaded in a microwell with a certain volume (e.g., 100 μL). The cost for the optical detector, including optics and electronics, is ~$4,000, with the major spending on PMT and optical filters.

Figure 1C shows the immunoassay format performed in microwells as we reported before (Ref. 27). In principle, antigens are first switched between antibody-coated magnetic microbeads and antibody-conjugated NC probes, and then the probes are released from the switched immunocomplexes into supernatant using an appropriate immunoaffinity separation solution to denature antibodies in complexes. The released probes were separated from magnetic microbeads and suspended in the immunoaffinity separation solution for signal reading under the time-gated mode. The separation of NC probes from immunocomplexes can avoid the interference of magnetic beads in fluorescence measurement. In this immunoassay format, the suspended microbeads have advantages in efficiently capturing and separating antigens from complex sample matrices and facilitating all wash procedures in the assay. **Figure 1D** illustrates the timing sequence for time-gated measurement on the excitation laser and the PMT.

The Mn:AgZnInS/ZnS NCs were synthesized according to our previous report [19]. In the first step, Mn:AgZnInS were synthesized by using 0.2 mmol Zn precursor, 0.2 mmol In precursor, 0.025 mmol Mn precursor, 0.8 mmol sulfur precursor, and 0.05 mmol Ag precursor. After Mn atoms were homogenously doped into AgZnInS NCs, a ZnS shell was grown on NCs to form Mn:AgZnInS/ZnS NCs. **Supplementary Figure S1** shows the material characterization of the prepared Mn: AgZnInS/ZnS NCs, including their energy-dispersive X-ray (EDX) spectrum and transmission electron microscopy (TEM) image. **Supplementary Figure S2A** presents the absorption and fluorescence spectra when these NCs were suspended in hexane. **Supplementary Figure S2B** shows the fluorescence decay of these NCs. It can be seen that >40% light intensity remains within the first 200 μs delay, which is good for time-gated measurement.

These NCs were produced in organic solvents with naturally hydrophobic surfaces and needed to transfer water for further bioapplications. Poly(maleic anhydride-alt-1-octadecene) (PMAO) can be modified to incorporate zwitterions such as carboxybetaine (CB) and sulfobetaine (SB) on PMAO backbones to form amphiphilic polymer PMAO-CB-SB [21]. Here, we applied PMAO-CB-SB to Mn:AgZnInS/ZnS NCs for NC surface modification. **Figure 2A** illustrates the basic method for surface modification. PMAO-CB-SB and NCs mixed in an organic solvent were added on top of water. With sonication, organic droplets containing polymers and

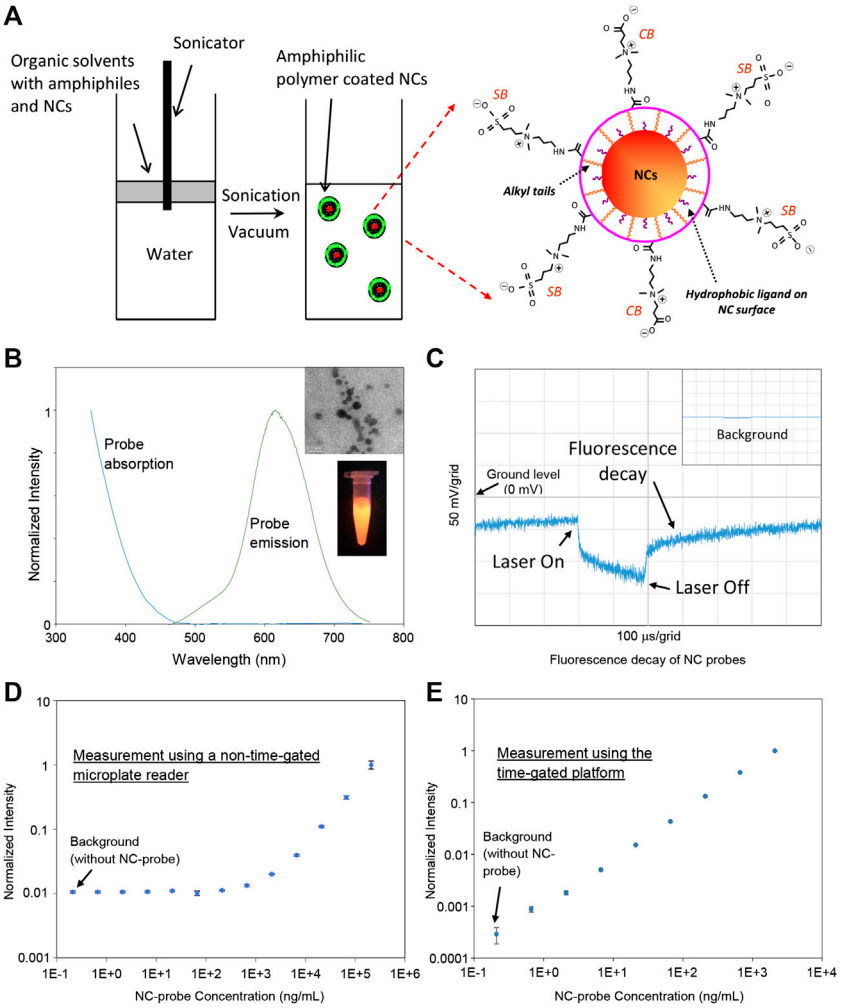

FIGURE 2 | (A) Illustration on the preparation method of NC probes for immunoassay. **(B)** The fluorescence and absorption spectra of the NC probes. The inset images present a representative TEM image of the prepared NC probes and their emission under UV light. **(C)** Representative fluorescence decay of the NC probes diluted in pure water—the NC probes emit fluorescence after laser-off. The inset presents the background for pure water. **(D)** Calibration curve of the NC probes in water (with 5% BSA mimicking a high autofluorescent sample matrix) measured using a nongated microplate reader. **(E)** Calibration curve of the NC probes in water (with 5% BSA) measured using the time-gated platform.

NCs were further broken down and dispersed into water. Followed up by rotary evaporation, organic solvents in the droplets were removed and self-assembly between PMAO-CB-SB and NCs occurred through hydrophobic interaction, while CB and SB groups are exposed to aqueous solutions. CB and SB groups coated on NC probes can prevent their aggregation and significantly lower their nonspecific binding because these zwitterions can interact with water molecules to form a stable hydration layer. CB can be further used for bioconjugation through covalent cross-linking chemistry using 1-ethyl-3-(3-dimethylaminopropyl)carbodiimide (EDC) and N-hydroxysulfosuccinimide (Sulfo-NHS) [27]. In the preparation of the NC probes, they were filtrated through a 0.2 µm membrane filter. **Figure 2B** presents the absorption and fluorescence spectra of the water-soluble NC probes and their TEM image and a digital image of these probes exposed under UV light. **Figure 2C** shows a representative decay of the diluted NC probes under a single pulse of a laser diode (1 kHz repetition with a 200 µs pulse width). As shown in this figure, the NC probes present a long-time fluorescence decay in the time domain after laser-off and the fluorescence of NC probes after laser-off does not totally fade out before the next moment of laser-on. The NC probes are suitable for the time-gated measurement (picking up a signal after the excitation light is off).

In order to demonstrate the detection capability of the time-gated platform, we compared the LODs between this platform and a standard non-time-gated microplate reader by measuring a series of diluted solutions with a probe concentration range from 0.66 ng/ml to 2.1 µg/ml in 5% bovine serum albumin (BSA). The use of 5% BSA is to mimic a high autofluorescent sample matrix. In this work, the non-time-gated microplate

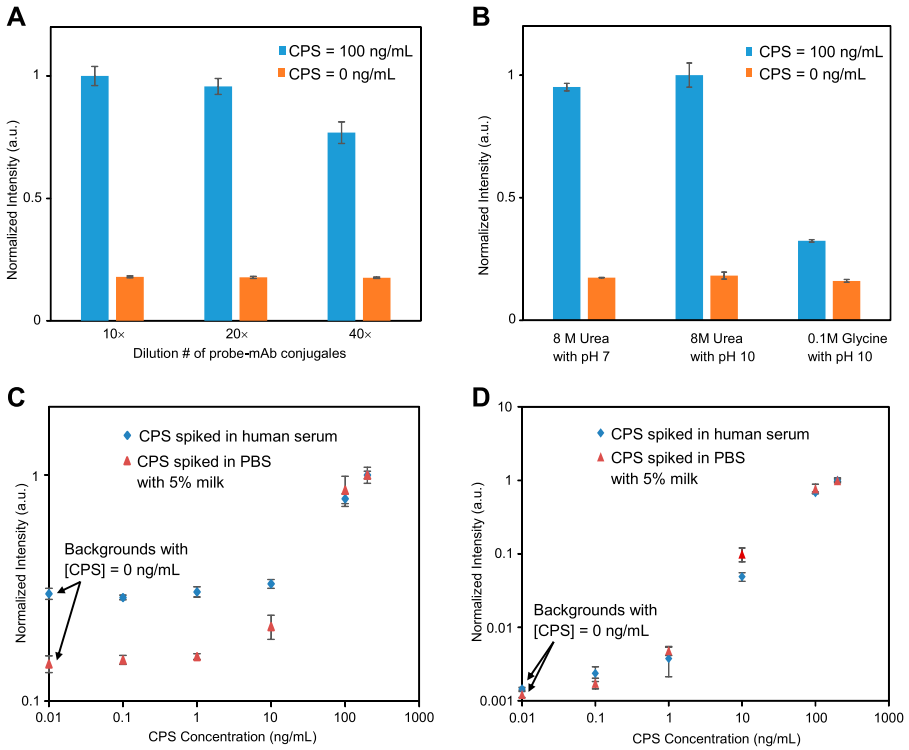

FIGURE 3 | (A) Dilution optimization of antibody-coated NC probes for immunoassay. **(B)** Optimal selection of immunoaffinity separation solutions for immunoassay (all separation solutions contain 0.1% BSA and 1% SDS, and the optimization experiments were done with measurements using a standard non-time-gated microplate reader). **(C)** Calibration curves of immunoassays measured using a standard nongated microplate reader. **(D)** Calibration curves of immunoassays measured using the time-gated platform.

reader from PerkinElmer was used as a standard instrument, which is usually used in a central analytical laboratory. As shown in **Figure 2D**, the calibration curve established by the non-time-gated microplate reader (with 405 nm excitation) indicates a LOD at ~273 ng/ml. For the time-gated system, its electronics design/setting and the data processing of this platform are the same as what we reported [20]: the gain control voltage of PMT is at 1.080 V (a maximum value) to achieve the highest gain for the input light to current conversion, the laser diode is pulsed with 200 μs for excitation with a repetition rate of 1.024 kHz, and the delay time after laser-off is 50 μs, and the time period to pick up the signal (the detection window) is 100 μs. The calibration curve measured using this platform (with a 405 nm laser as excitation) is shown in **Figure 2E** and presents a LOD of ~354 pg/ml. Although two instruments have different optics and electronics, the difference in LODs clearly indicates that the time-gated platform as a standalone instrument is more sensitive or capable of detecting a lower level of NC probes because it can avoid the high autofluorescence from BSA.

The immunoassay for the detection of CPS in a microplate was developed in a format illustrated in **Figure 1C**. In the assay, anti-CPS mAb 4C4 was conjugated on both magnetic microbeads and the NC probes for CPS capture and detection (CPS has multiple binding sites), respectively. In this assay development, the experimental approach went through two steps. In the first step, using the non-time-gated microplate reader as the signal measurement tool, the assay was optimized and its calibration curve was then established. In the second step, the same microplates (used to set up the calibration curve under the measurement of the nongated microplate reader) was read out by our time-gated optical detector, and then the LODs by two different measurement tools were extracted and compared. Both instruments use the light at 405 nm wavelength for the probe excitation.

For assay optimization, two sets of magnetic microbeads were incubated with 0 ng/ml and 100 ng/ml CPS spiked in phosphate-buffered saline (PBS) with 5% milk, respectively. Afterward, conjugates (anti-CPS coated probes) diluted from the stock were applied to each microbead set to form immunocomplexes. The probes were released from the immunocomplexes for signal reading using an appropriate immunoaffinity separation solution to denature antibodies in the immunocomplexes. The readings from 0 ng/ml and 100 ng/ml CPS were designated as the background and the signal, respectively. In the assay optimization experiments, we mainly aimed to identify the dilution number of the stock conjugates and the appropriate immunoaffinity separation solution that can achieve higher signal/background ratios. **Figure 3A** presents the signals and the backgrounds when

different dilutions of the stock conjugates were applied for assay labeling. It can be seen that 10× dilution of the stock conjugates can achieve a higher signal/background ratio. Thus, this dilution condition was used in the sequential assays. In the assay, an appropriate immunoaffinity separation solution is used to denature antibodies in switched immunocomplexes so that the NC probes can be released to separate from magnetic microbeads for signal measurement. The immunoaffinity separation solution is expected to efficiently release NC probes from magnetic beads and also stabilize the fluorescence signal of the released NC probes for reliable signal measurement. Several immunoaffinity separation solutions (8M urea with pH7, 8M urea with pH10, and 0.1M glycine with pH10) were tested. Note that these solutions are supplemented with 0.1% BSA and 1% sodium dodecyl sulfate (SDS) [27]. The fluorescence stability of the anti-CPS-conjugated NC probes was tested for 2 h with different dilutions of the stock conjugates in these separation solutions and are presented in **Supplementary Figure S3**, which indicates that all separation solutions present a good capability to stabilize the NC probes. **Figure 3B** shows the signals and the backgrounds when these immunoaffinity separation solutions were applied to release probes for signal reading. As shown in **Figure 3B**, the signal/background ratios using 8M urea (pH7) and 8M urea (pH10) are similar to each other without significant difference but higher than that using 0.1M glycine (pH 10). Although both 8M urea (pH7) and 8M urea (pH10) can be used, 8M urea (pH7) is easier to prepare, handle, and dispose due to its neutral pH and was used further.

With the optimized conditions, different concentrations of CPS spiked in PBS with 5% milk or human serum were prepared and assayed. **Figure 3C** presents two assay calibration curves when CPS was spiked in PBS with 5% milk and human serum, respectively. These calibration curves were established using the non-time-gated microplate reader as the measurement tool. From these curves, using the 3σ method, the calculated LODs of assays are ~5 ng/ml for CPS spiked in PBS with 5% milk and ~14 ng/ml for CPS in human serum. With triplicate running of the calibration experiments using the non-time-gated microplate reader, the LOD for CPS spiked in PBS with 5% milk presents an average value with a standard deviation at 9 ± 4 ng/ml, and the LOD for CPS spiked in human serum is at 10 ± 5 ng/ml. The same microplates used to set up the calibration curves in **Figure 3C** were also read out using the time-gated optical detector, and the calibration curves under the time-gated measurement are presented in **Figure 3D**. Through the direct comparison between the curves in **Figures 3C,D**, it can be clearly seen that the CPS concentrations at 0.1 ng/ml and 1 ng/ml are buried in the background under non-time-gated measurement but can be read out under time-gated measurement. From **Figure 3D**, the LODs of assays for CPS spiked in PBS with 5% milk and human serum are calculated to be ~65 pg/ml and ~23 pg/ml, respectively. With triplicate running of the calibration experiments using the time-gated instrument, the LOD for CPS spiked in PBS with 5% milk present an average value with a standard deviation at 64 ± 4 pg/ml, and the LOD for CPS spiked in human serum is at 23 ± 1 pg/ml. When compared to the non-time-gated microplate reader, the time-gated instrument as a standalone measurement tool can achieve a much lower LOD (at least two ordera lower). Through the assay development, it can be seen that the time-gated immunoassay for the highly sensitive detection of CPS in human biological fluid is feasible and has the potential to be used for melioidosis diagnosis.

After the time-gated assay calibration curve (with CPS spiked in human serum) was established, the assay reliability was tested by measuring the signals of 100 ng/ml CPS in human serum and then comparing them to the signal of 100 ng/ml CPS resulting from the calibration curve. The average recovery is ~91%, with a standard deviation at ~8.8%. The recoveries for triplicates of lower concentrations (1 ng/ml, 0.1 ng/ml) of CPS in human serum were also tested. The average recovery for 1 ng/ml CPS is ~94% with a standard deviation at ~9.9%, and the average recovery for 0.1 ng/ml CPS is ~89% with a standard deviation at ~0.5%. The assay accuracy reflected by the average recoveries is in the range of 89–94%. This study suggests that the time-gated immunoassay on the detection of CPS in human serum is reliable.

Supplementary Table S1 presents a comparison with several recently reported assays on CPS detection. An optimized lateral flow immunoassay (LFIA) using gold nanoparticles as probes/labels shows LOD at ~200 pg/ml [23, 28]. An enzyme-based microplate immunoassay using horseradish peroxidase (HRP) to react with substrates (3,3',5,5'-tetramethylbenzidine (TMB) and H_2O_2) presents LOD at ~200 pg/ml [23]. A very recent LFIA using gold nanoparticles as labels presents LOD at ~20 pg/ml, but it was only tested using CPS spiked in PBS buffer with a large volume (~50 ml) [29]: 50 ml of CPS-spiked PBS buffer was filtrated and preconcentrated through a membrane. Please note that although the filtration/preconcentration approach is a very good way to enhance assay sensitivities, filtrating a 50 ml of human serum sample (or samples with complex matrices) could cause the membrane to be clogged very quickly. Our assay under the time-gated measurement used 50 μL of samples and can achieve a LOD at ~23 pg/ml.

CONCLUSION

In this work, a time-gated immunoassay platform was developed and applied for the detection of CPS (a biomarker of melioidosis). This platform integrates a time-gated optical detector and microplate-based immunoassay using Mn:AgZnInS/ZnS NC probes as signal transducers. Compared to the immunoassay under non-time-gated measurement, the immunoassay measured by the time-gated optical detector presented more than two orders lower LOD at ~23 pg/ml (with CPS spiked in human serum) and broader detection range.

DATA AVAILABILITY STATEMENT

The original contributions presented in the study are included in the article/**Supplementary Material**; further inquiries can be directed to the corresponding author.

AUTHOR CONTRIBUTIONS

BG developed the instrument. BG, MZ, and DH worked on NC probe preparation and immunoassay development. DA produced and provided antibodies. BG, DA, and XZ discussed and initiated the concept. BG, DA, and XZ prepared the manuscript.

FUNDING

Research reported in this work was supported by the NIGMS grant, R15GM135855, and Nevada Research and Innovation Corporation under the InNEVenture Fund. The content is solely the responsibility of the authors and does not necessarily represent the official views of the funding agencies.

ACKNOWLEDGMENTS

Purified CPS was graciously provided by P. Brett and M. Burtnick (School of Medicine, University of Nevada, Reno).

SUPPLEMENTARY MATERIAL

The Supplementary Material for this article can be found online at: https://www.frontiersin.org/articles/10.3389/fphy.2020.625424/full#supplementary-material

REFERENCES

1. Soini E, Kojola H. Time-resolved fluorometer for lanthanide chelates–a new generation of nonisotopic immunoassays. *Clin Chem* (1983) 29:65–8. doi:10.1093/clinchem/29.1.65
2. Dickson EF, Pollak A, Diamandis EP. Ultrasensitive bioanalytical assays using time-resolved fluorescence detection. *Pharmacol Ther* (1995) 66:207–35. doi:10.1016/0163-7258(94)00078-h
3. Lövgren T, Meriö L, Mitrunen K, Mäkinen ML, Mäkelä M, Blomberg K, et al. One-step all-in-one dry reagent immunoassays with fluorescent europium chelate label and time-resolved fluorometry. *Clin Chem* (1996) 42:1196–201. doi:10.1093/clinchem/42.8.1196
4. Hemmilá I, Mukkala VM. Time-resolution in fluorometry technologies, labels, and applications in bioanalytical assays. *Crit Rev Clin Lab Sci* (2001) 38:441–519. doi:10.1080/20014091084254
5. Collier BB, Mcshane MJ. Time-resolved measurements of luminescence. *J Lumin* (2013) 144:180–90. doi:10.1016/j.jlumin.2013.06.034
6. Wang X, Chang H, Xie J, Zhao B, Liu B, Xu S, et al. Recent developments in lanthanide-based luminescent probes. *Coord Chem Rev* (2014) 273:201–12. doi:10.1016/j.ccr.2014.02.001
7. Song X, Knotts M. Time-resolved luminescent lateral flow assay technology. *Anal Chim Acta* (2008) 626:186–92. doi:10.1016/j.aca.2008.08.006
8. Jin D, Lu Y, Leif RC, Yang S, Rajendran M, Miller LW. How to build a time-gated luminescence microscope. *Curr Protoc Cytom* (2014) 67:2.22.1–36. doi:10.1002/0471142956.cy0222s67
9. Rodenko O, Fodgaard H, Tidemand-Lichtenberg P, Petersen PM, Pedersen C. 340 nm pulsed UV LED system for europium-based time-resolved fluorescence detection of immunoassays. *Opt Express* (2016) 24:22135–43. doi:10.1364/OE.24.022135
10. Rodenko O, Eriksson S, Tidemand-Lichtenberg P, Troldborg CP, Fodgaard H, van Os S, et al. High-sensitivity detection of cardiac troponin I with UV LED excitation for use in point-of-care immunoassay. *Biomed Opt Express* (2017) 8:3749–62. doi:10.1364/BOE.8.003749
11. Kim KR, Han YD, Chun HJ, Lee KW, Hong DK, Lee KN, et al. Encapsulation-stabilized, europium containing nanoparticle as a probe for time-resolved luminescence detection of cardiac troponin I. *Biosensors* (2017) 7:48. doi:10.3390/bios7040048
12. Connally R, Veal D, Piper J. Flash lamp-excited time-resolved fluorescence microscope suppresses autofluorescence in water concentrates to deliver an 11-fold increase in signal-to-noise ratio. *J Biomed Opt* (2004) 9:725–34. doi:10.1117/1.1756594
13. Suárez PL, García-Cortés M, Fernández-Argüelles MT, Encinar JR, Valledor M, Ferrero FJ, et al. Functionalized phosphorescent nanoparticles in (bio) chemical sensing and imaging – a review. *Anal Chim* (2019) 1046:16–31. doi:10.1016/j.aca.2018.08.018
14. Schiattarella C, Moretta R, Defforge T, Gautier G, Della Ventura B, Terracciano M, et al. Time-gated luminescence imaging of positively charged poly-l-lysine-coated highly microporous silicon nanoparticles in living Hydra polyp. *J Biophotonics* (2020) 13:e202000272. doi:10.1002/jbio.202000272
15. Pradhan N. Red-tuned Mn d–d emission in doped semiconductor nanocrystals. *Chem Phys Chem* (2016) 17:1087–94. doi:10.1002/cphc.201500953
16. Pradhan N. Mn-doped semiconductor nanocrystals: 25 years and beyond. *J Phys Chem Lett* (2019) 10:2574–7. doi:10.1021/acs.jpclett.9b01107
17. Manna G, Jana S, Bose R, Pradhan N. Mn-doped multinary CIZS and AIZS nanocrystals. *J Phys Chem Lett* (2012) 3:2528–34. doi:10.1021/jz300978r
18. Tang X, Zu Z, Bian L, Du J, Chen W, Zeng X, et al. Synthesis of Mn doping Ag-In-Zn-S nanoparticles and their photoluminescence properties. *Mater Des* (2016) 91:256–61. doi:10.1016/j.matdes.2015.11.080
19. Zaeimian MS, Gallian B, Harrison C, Wang Y, Zhao J, Zhu X. Mn doped AZIS/ZnS nanocrystals(NCs): effects of Ag and Mn on NC optical properties. *J Alloys Compd* (2018) 765:236–44. doi:10.1016/j.jallcom.2018.06.173
20. Gallian B, Dong G, Zhu X. A compact time-gated instrument for QDs with low excitation energy and millisecond fluorescence lifetime as signal reporters, and its detection application. *Rev Sci Instrum* (2019) 90:104701. doi:10.1063/1.5111147
21. Demillo VG, Zhu X. Zwitterionic amphiphile coated magnetofluorescent nanoparticles – synthesis, characterization and tumor cell targeting. *J Mater Chem B Mater Biol Med* (2015) 3:8328–36. doi:10.1039/C5TB01116G
22. Brett PJ, Burtnick MN, Heiss C, Azadi P, DeShazer D, Woods DE, et al. *Burkholderia thailandensis oacA* mutants facilitate the expression of *Burkholderia mallei*-like O polysaccharides. *Infect Immun* (2011) 79:961–9. doi:10.1128/IAI.01023-10
23. Houghton RL, Reed DE, Hubbard MA, Dillon MJ, Chen H, Currie BJ, et al. Development of a prototype lateral flow immunoassay (LFI) for the rapid diagnosis of melioidosis. *PLOS Negl Trop Dis* (2014) 8(3):e2727. doi:10.1371/journal.pntd.0002727
24. Marchetti R, Dillon MJ, Burtnick MN, Hubbard MA, Kenfack MT, Blériot Y, et al.. *Burkholderia pseudomallei* capsular polysaccharide recognition by a monoclonal antibody reveals key details toward a biodefense vaccine and diagnostics against melioidosis. *ACS Chem Biol* (2015) 10:2295–302. doi:10.1021/acschembio.5b00502
25. Currie BJ, Kaestli M. Epidemiology: a global picture of melioidosis. *Nature* (2016) 529:290–1. doi:10.1038/529290a
26. Limmathurotsakul D, Golding N, Dance DA, Messina JP, Pigott DM, Moyes CL, et al. Predicted global distribution of *Burkholderia pseudomallei* and burden of melioidosis. *Nat Microbiol* (2016) 1:15008. doi:10.1038/nmicrobiol.2015.8

27. Zhu X, Duan D, Publicover NG. Magnetic bead based assay for C-reactive protein using quantum-dot fluorescence labeling and immunoaffinity separation. *Analyst* (2010) 135:381–9. doi:10.1039/b918623a
28. Nualnoi T, Kirosingh A, Pandit SG, Thorkildson P, Brett PJ, Burtnick MN, et al. *In vivo* distribution and clearance of purified capsular polysaccharide from *Burkholderia pseudomallei* in a murine model. *PLOS Negl Trop Dis* (2016) 10(12):e0005217. doi:10.1371/journal.pntd.0005217
29. Chen P, Gates-Hollingsworth M, Pandit S, Park A, Montgomery D, AuCoin D, et al. Paper-based vertical flow immunoassay (VFI) for detection of bio-threat pathogens. *Talanta* (2019) 191:81–8. doi:10.1016/j.talanta.2018.08.043

Conflict of Interest: The authors declare that the research was conducted in the absence of any commercial or financial relationships that could be construed as a potential conflict of interest.

frontiers in Molecular Biosciences

TECHNOLOGY AND CODE
published: 17 March 2021
doi: 10.3389/fmolb.2021.631774

Combining Multicolor FISH with Fluorescence Lifetime Imaging for Chromosomal Identification and Chromosomal Sub Structure Investigation

Archana Bhartiya[1,2], *Ian Robinson*[1,3], *Mohammed Yusuf*[1,2,4]* *and Stanley W. Botchway*[5]*

[1]London Centre for Nanotechnology, University College London, London, United Kingdom, [2]Research Complex at Harwell Rutherford Appleton Laboratory, Didcot, United Kingdom, [3]Condensed Matter Physics and Materials Science Division, Brookhaven National Lab, Upton, NY, United States, [4]Centre for Regenerative Medicine and Stem Cell Research, Aga Khan University, Karachi, Pakistan, [5]Central Laser Facility, Science and Technology Facilities Council, Rutherford Appleton Laboratory, Oxon, United Kingdom

OPEN ACCESS

Edited by:
Klaus Suhling,
King's College London,
United Kingdom

Reviewed by:
James McGinty,
Imperial College London,
United Kingdom
Sobhan Sen,
Jawaharlal Nehru University, India

***Correspondence:**
Mohammed Yusuf
yusuf.mohammed@ucl.ac.uk
Stanley W. Botchway
Stan.Botchway@stfc.ac.uk
ucanymo@ucl.ac.uk

Specialty section:
This article was submitted to Biophysics, a section of the journal Frontiers in Molecular Biosciences

Received: 20 November 2020
Accepted: 02 February 2021
Published: 17 March 2021

Citation:
Bhartiya A, Robinson I, Yusuf M and Botchway SW (2021) Combining Multicolor FISH with Fluorescence Lifetime Imaging for Chromosomal Identification and Chromosomal Sub Structure Investigation. Front. Mol. Biosci. 8:631774. doi: 10.3389/fmolb.2021.631774

Understanding the structure of chromatin in chromosomes during normal and diseased state of cells is still one of the key challenges in structural biology. Using DAPI staining alone together with Fluorescence lifetime imaging (FLIM), the environment of chromatin in chromosomes can be explored. Fluorescence lifetime can be used to probe the environment of a fluorophore such as energy transfer, pH and viscosity. Multicolor FISH (M-FISH) is a technique that allows individual chromosome identification, classification as well as assessment of the entire genome. Here we describe a combined approach using DAPI as a DNA environment sensor together with FLIM and M-FISH to understand the nanometer structure of all 46 chromosomes in the nucleus covering the entire human genome at the single cell level. Upon DAPI binding to DNA minor groove followed by fluorescence lifetime measurement and imaging by multiphoton excitation, structural differences in the chromosomes can be studied and observed. This manuscript provides a blow by blow account of the protocol required to perform M-FISH-FLIM of whole chromosomes.

Keywords: chromosome, fluorescence lifetime imaging, multicolor FISH, microscopy, multiphoton, karyotyping

INTRODUCTION

Nuclear chromosomes are composed of chromatin, primarily a complex of deoxyribonucleic acid (DNA) and proteins, which are arranged into elementary structural units of nucleosomes, each made up of 147 base pairs. The nucleosome is composed of eight core histone proteins, in a bead on a string structure forming 11 nm fibers with DNA wrapped around the nucleosomes. Further coiling of these units leads to highly compact structures. The organization of chromatin into these higher-order structures and how they are controlled play a role in the so-called DNA condensation process which still remain a subject of debate as well as representing one of the key challenges in structural biology. Traditional methods for identifying chromosomes based on large scale (> 100 nm) structure include Giemsa banding (G-banding) method that displays chromosomes having dark (AT rich regions) and light (GC rich regions) band, heterochromatin and euchromatin respectively (Sumner, 1982). This

method is still currently the gold standard for clinical hospital laboratories and involves analysis at the microscope stage and requires highly specialized training (Liehr, 2017). More recently, a modern and user-friendly Fluorescence *in situ* Hybridization (FISH)-based protocols for karyotyping include Multiplex FISH (M-FISH) is being explored. M-FISH is a fluorescence technique that uses computer-generated colors from a coding scheme, which analyses the fluorescence from various pairs of five paints (probes) and uses DAPI as a counterstain (Speicher et al., 1996). Although M-FISH is an invaluable and powerful karyotyping tool that provides detailed analysis of structural rearrangements and marker chromosomes and does not require intensive training (Yusuf et al., 2013), it lacks detailed information at the sub 500 nm level. Its use has been expanded into validating and karyotyping complex clinical cases after G-banding (Jalal and Law, 1999) on the same sample. Furthermore, its use has been demonstrated well in identifying and karyotyping chromosomes after contrast (Shemilt et al., 2015) and fluorescence (Yusuf et al., 2011) imaging methods. Fluorescence lifetime imaging microscopy (FLIM) is a technique that can map the spatial nature of excited state lifetime and can act as a reporter when combined with a sensor to changes in the fluorophore's environment (Anthony et al., 2009; Ahmed et al., 2019). FLIM can be generally applied to a broad field of research including viruses, plants, mammalian and material research to name a few (Danquah, et al., 2012; Breeze et al., 2016; Ahmed et al., 2020). The fluorescence lifetime of a molecule in a particular environment is fixed and defines the average time the molecule spends in the excited state before returning to the ground state, which is typically in the range of several nanoseconds (ns). Changes in the measured excited state life values is a characteristic of the fluorophore's environment such as pH, viscosity, proximity to other molecules and energy transfer events via dipole-dipole interactions. FLIM allows the excited state lifetime of a sample to be measured and imaged on a pixel by pixel basis. FLIM may be constructed around epifluorescence microscope configuration, confocal single and multiphoton excitation microscopy together with intensified charged coupled device (iCCD) or time-correlated single photon counting (TCSPC). Epifluorescence-FLIM mostly use the iCCD method, although recently a wide array single-photon avalanche photo-diode has been demonstrated) (Suhling et al., 2019). The application of frequency-domain lifetime imaging has also been described (Lakowicz, 2006; Schoberer and Botchway, 2014). However, confocal and multiphoton FLIM via TCSPC currently provide the best special and temporal resolution. Although the operation of the different systems varies, the data interpretation is similar. The principle of a TCSPC FLIM system is shown in Schematic 1 (and also detailed in Botchway et al., 2015; Schoberer and Botchway, 2014). FLIM (or the excited state lifetime value) is less influenced by molecule concentration and photo-bleaching whilst providing another method of image contrast. Although the lower the concentration, the longer is the data collection time. Generally, when photo-bleaching is observed, this can be easily accounted for by a Stern-Volmer equation.

Recently, chromosome compaction at nanometer length scales has been suggested along the length of chromosomes imaged using multiphoton FLIM after DAPI staining (Estandarte et al., 2016) alone. This was performed on a classical spread of chromosomes whereby excited state lifetime measurements have been obtained on all 46 chromosomes. Crucial for analyzing the FLIM data is the identification of each chromosome whereby M-FISH plays an important role. Here we describe a step by step procedure combining FLIM together with DAPI staining acting as an environment sensor for investigating chromosome substructure and M-FISH for chromosome identification and karyotyping.

MATERIALS

All solutions must be prepared using Milli-Q® Millipore water (prepared by purifying deionized water, to attain a sensitivity of 18 MΩ -cm at 25°C).

Consumable for Extraction of Primary T-Lymphocytes

(1) 10 ml of blood obtained from a human donor.
(2) BD Vacutainer® lithium heparin tubes (Becton Dickinson).
(3) 5 ml of Histopaque-1077 (Sigma-Aldrich).
(4) Hank's Balanced Salt Solution (HBSS, Life Technologies)
(5) Sterile pastette (Alpha Laboratories, Eastleigh, United Kingdom).

Requirements for T-Lymphocytes Cell Culture

(1) A sterile cryovial containing 3×10^6 T-lymphocytes cells.
(2) Lymphoblastoid cell growth medium (LCGM): consisting of Roswell Park Memorial Institute [RPMI-1640 (1X)] medium supplemented with 20% heat inactivated fetal bovine serum (FBS), 1 mM sodium pyruvate, 2 mM L-glutamine, 100 U/ml penicillin, 100 μg/ml streptomycin (all from Invitrogen/Life Technologies).
(3) Stimulating growth medium (SR10): comprised of RPMI 1640 supplemented with 10% heat inactivated FBS, 1 mM sodium pyruvate, 2 mM L-glutamine, 100 U/ml penicillin, 100 μg/ml streptomycin, 50 μM, 2-mercaptoethanol (GIBCO/Life Technologies), 20 U/ml recombinant interleukin-2 (IL2; Sigma-Aldrich) and 0.4 μg/ml phytohaemagglutinin (PHA; Sigma-Aldrich).
(4) Growth medium (GR10) comprised of SR10 without PHA.
(5) Lethally irradiated lymphoblastoid GM 1899A as feeder cells.
(6) Incubator at 37°C temperature with 5% $C0_2$ supply.
(7) Freeze mix: 10% dimethyl sulfoxide (DMSO, Sigma-Aldrich Company Ltd., Gillingham, United Kingdom) and 90% of FBS (Life Technologies).

Reagents for Chromosome Preparation

(1) Colcemid (Karyomax, Gibco by Life technologies (10 μg/ml): to arrest the cells at metaphase stage.
(2) KCL (75 mM) to lyse the cells (Sigma-Aldrich).
(3) Methanol: acetic acid at the ratio of 3:1 (v/v) for fixation.
(4) Vectashield mounting medium containing 4′,6-Diamidine-2′-phenylindole dihydrochloride stain (5 μg/ml) DAPI, Victor Laboratories, H-1200).
(5) DAPI (4 μM) (ThermoFisher Scientific) in Milli-Q® Millipore water from stock of 40 μM DAPI.

Equipment

(1) Counting cells: The ADAM or equivalent cell counter (Labtech International Ltd., Uckfield, United Kingdom), 20 μl of cell media of a stimulated T-cells and 20 μl of each accuStain T and N solutions for total cell count with a propidium iodide dye and non-viable cells count with fluorescent dye respectively.
(2) Epifluorescence microscope (Zeiss Z2Axioimager or equivalent) with 6 filters such as DAPI (counterstain, SP-100), aqua (31036v2), green (MF-101, orange (31003), red (SP-107 (SP-103v1) and near infrared (SP-104v2).
(3) ISIS imaging software (MetaSystems) for capturing images and analysis.
(4) Excitation sources for the multiphoton FLIM were from a Mira 900 F (Ti-sapphire laser (Coherent Ltd., United Kingdom, Tunable 700–980 nm, pulse length 180–200 fs) pumped by a Verdi V18, operating at 532 nm with a CW outputs. Here the laser was tuned to 760 nm. Photons were detected by a hybrid detector HPM 100–40, connected to a time correlated single photon counting PC module, SPC830, Becker and Hickl, Germany.

Solutions for M-FISH

(1) 0.1× Saline-sodium citrate buffer (SSC) stock: Add 1 ml of 20 x SSC (Sigma-Aldrich) in a 200 ml Milli-Q® Millipore water, pH 7.25. Transfer ~50 ml of solution in a two Coplin jars, keeping one jar at room temperature and another in a fridge at 4 C.
(2) Repeat the above procedure to prepare 2× SSC stock: Add 20 ml of 20× SSC in a 200 ml Milli-Q® water, pH 7.45. Pour ~50 ml of solution in a two Coplin jars, keep one jar at 70 C (±1°C) in a hot water bath and another in a fridge at 4 C.
(3) Prepare 0.07 mol/L: add 1 ml of 7 M stock solution in a 100 ml of Milli-Q® water and transfer ~50 ml of solution in Coplin jar and stored at room temperature.
(4) 100, 95 and 70% of ethanol series prepared in a Milli-Q® water. Keep at room temperature.
(5) 0.4× SSC: mix 1 ml of 20× SSC in a 50 ml of Milli-Q® water, pH 7.2. Keep at 72 C (± 1°C).
(6) 2× SSCT: dissolving 0.05% Tween-20 (Polyoxyethylenesorbitan-monolaurate syrup, sigma P-1379) in a 50 ml of a 2× SSC, pH 7.45 and keep at room temperature.

METHODS

Cell Culture

Lymphoblastoid Cell Line Culture

(1) Thaw a cryovial containing 3×10^6 cells at 37°C in a water bath for 2 min (mins).
(2) Transfer contents into a 15 ml conical bottom tube containing 10 ml of lymphoblastoid cell growth medium (LCGM). Mix the cells by inverting the tube and centrifuged for 5 min at 1200 rpm (revolution per minute). Remove the supernatant followed by resuspending the cell pellet in 10 ml of LCGM.
(3) Transfer the suspended cells into a vented 25 cm^2 culturing flask.
(4) Incubate the flask with cells, in the upright position for three days. At this stage, cells become disaggregated. Count the cells at daily intervals using the Adam cell counter [*Equipment* (1)].
(5) Check if the cell number has reached 0.8×10^6, then add 10 ml of fresh LCGM and transfer the cells to 75 cm^2 flask.

Feeder Cell Preparation

(1) Lethally irradiated (40 Gy) lymphoblastoid GM1899A cells are used as feeder cells for human T-lymphocytes (see 4 below).
(2) The culturing conditions for this lymphoblastoid cell line are described in the Section *Lymphoblastoid Cell Line Culture*.
(3) Prepare feeder cells as follows: when cell number reaches 5×10^7 cells per ml, transfer the cells into one or two, 50 ml conical bottom tubes (depending on the volume) and centrifuge at room temperature for 5 min at 1200 rpm. Aspirate the supernatant and resuspend the cell pellet in 5 ml of LCGM.
(4) Lethally irradiate the cells at room temperature with an X-ray source at dose of 40 Gy (Gray), at dose rate 1.7 Gy per min.
(5) Dilute the lethally irradiated feeder cells in the freeze mix [see *Requirements for T-lymphocytes cell Culture*. (7)], Aliquot 1 ml of mixture (cells in 1 ml freeze mix) in each cryovials and freeze at –80 C in a Mr. Frosty™ (Thermo Scientific) containers which allow cooling at rate of 1 C per min. After 24 h, vials are transferred to the liquid nitrogen container for long term storage.

Extraction of Human Stimulated T-Lymphocytes

(1) Collect 10 ml of blood from a donor (22 years old female was used in our case) into BD Vacutainer® lithium heparin tubes.
(2) Aliquot 5 ml of Histopaque-1077 into a four ~15 ml conical bottom centrifuge tubes at room temperature. Mix 10 ml of blood with 10 ml of Hank's Balanced Salt Solution at a room temperature in ~50 ml tube.
(3) Layer ~5 ml of diluted blood slowly onto each of the four tubes containing Histopaque-1077 using a sterile pastette. Centrifuge the tubes at 1600 rpm for 20 min.

(4) Aspirate the top serum layer after phase separation from each tube leaving around 0.5 cm of liquid above the buffy coat cell layer. Collect the buffy coat using a sterile pastette and transfer into a 15 ml tube containing ~10 ml of HBSS.
(5) After mixing by inverting the tubes, centrifuge at 1200 rpm for 5 min at room temperature. Aspirate the supernatant and re-suspend the cell pellet with ~5 ml of HBSS.
(6) Centrifuge the cell suspensions at 1200 rpm for 5 min at room temperature. Aspirate the supernatant and wash the cells with ~10 ml of HBSS once. Perform cell counting using 20 µl aliquot of cell suspension. Centrifuge the tubes at 1200 rpm for 5 min at room temperature and aspirate the supernatant.
(7) Next re-suspend the cells at concentration of 3×10^6 cells per ml in freeze mix.
(8) Freeze cells at –80 C and transfer the cryogenic vials in Mr. Frosty™ container. The next day transfer vials to liquid nitrogen container for long-term storage.

Culturing Conditions of T-Lymphocytes

(1) Thaw cryovial containing 3×10^6 cells at 37 C in a water bath for 2 min.
(2) Transfer cells with sterile pastette into a 15 ml conical bottom tube containing 10 ml of stimulating growth medium.
(3) Mix the cells by inverting the tube and centrifuge for 5 min at 1200 rpm, room temperature.
(4) Aspirate the supernatant and re-suspend the cell pellet in 10 ml of SR10 and centrifuge for 5 min at 1200 rpm, room temperature.
(5) In the meantime, thaw a cryovial of feeder cells in the water bath at 37°C for 2 min.
(6) Aspirate the supernatant from T-lymphocytes and re-suspend the cells in 10 ml of SR10.
(7) Transfer the feeder cells with sterile pastette into a 15 ml conical bottom tube containing T-lymphocytes, mix the tube by inverting several times and centrifuge at room temperature for 5 min at 1200 rpm. Aspirate the supernatant and again re-suspend the cell pellet in 10 ml of SR10.
(8) Transfer the cell suspension into a vented 25 cm^2 flask and incubate at 37°C with 5% CO_2 at an angle of about 10° from horizontal position.
(9) Leave in incubator for 4 days to grow.
(10) Disaggregate cells and count cells daily.
(11) When cells reached a density of 0.8×10^5 cells per ml, perform a dilution of 1:2 with growth medium.

Cell Counting and Viability

(1) Use the ADAM cell counter or equivalent for cell counting and viability.
(2) For every cell count, aliquot 20 µl of each "T" and "N" solutions in two separate Eppendorf. Disaggregate the cells by shaking vigorously. Aliquot 20 µl of cell media and mix with T and N solutions separately and incubate for 2 min at room temperature. After 2 min of incubation, load the samples into an appropriate T and N positions in the cartridge and load into the ADAM.
(3) The cell counter provides a value for total cell number (T), viable cell number (N) and percentage of viable cells.

Chromosome Preparation

(1) Arrest chromosomes at the mitotic stage when the cells are confluent up to 75–80%.
(2) Transfer the cell media from the culturing flasks into a 50 ml falcon tube and centrifuge at 1000 rpm for 10 min.
(3) In the meantime, use 20 µl of cell media to count the cells using an ADAM cell counter. The cell count ranged between $0.32–0.35 \times 10^6$ cells per ml.
(4) Aspirate the supernatant and then slowly add 6 ml of pre-warmed (37°C), hypotonic KCL solution (75 mM), in a falcon tube.
(5) Immediately, transfer the tube to 37°C water bath for 8–10 min and then centrifuge at 1000 rpm for 10 min.
(6) Meanwhile, prepare fresh fixative of methanol: acetic acid solution (MAA) also known as carnoys solution at the ratio of 3:1.
(7) Aspirate the supernatant and quickly add carnoys solution in the tube, centrifuge the tube at 1000 rpm for 10 min. Repeat the washing procedure with carnoys solution three washes.
(8) Store the prepared chromosome solutions in –20°C for future use.

Chromosome Mounting

(1) Clean glass slides (Supersoft, VWR international) by soaking them overnight in 70% ethanol: water solution which effectively removes grease.
(2) Wipe the slides with colourless soft tissues and place in the freezer for 30 min before use.
(3) To prepare chromosome spreads, retrieve the cleaned frozen slides from the freezer, blow on the slides to humidify it and then drop 20 µl–30 µl carnoys fixed chromosomes from a height of around 30 cm to obtain good spreads of chromosomes on the slides.
(4) Place the slides on the hot plate (45°C) to dry. Once the slides are dried, stain with DAPI/antifade (5 µg/ml) then covered with a 22×50 mm^2 cover slip.
(5) Incubate the slides with DAPI for 10 min then observe using an epifluorescence microscope.

Sample Preparation for Multiphoton Fluorescence Lifetime Imaging Microscopy (FLIM)

(1) For lifetime measurement and FLIM of chromosomes, prepare chromosome spreads according to the sections *Chromosome Preparation* and *Chromosome Mounting*.
(2) Stain fixed chromosomes using 4 µM DAPI and incubate for 20 min in the dark.
(3) Following incubation, soak slides in 1× phosphate buffered saline (PBS, pH-7.4) for 4 min.
(4) Before imaging, mount DAPI stained slides with 1 drop of water and cover with a cover slip (22×50 mm^2, No. 1 or 1.5

depending on the cover glass thickness specifications of the imaging objective).

Procedure for DNA Hybridization

(1) Prepare 0.1× SSC and 0.2× SSC, pour into Coplin jars and place into the refrigerator at 4°C.
(2) Prepare 2× SSC, pour into a Coplin jar and place into a water bath at 70°C (±1°C).
(3) Carefully remove coverslip from the glass slide following the FLIM data acquisition.
(4) Place slide in a series of ethanol: 70, 95, and 100% for 30 s in each solution and leave to dry in air.
(5) Incubate the slides for 30 min in the prewarmed 2× SSC at 70°C (±±1°C) Coplin jar.
(6) Remove the Coplin jar from the water bath and let it cool for 20 min at room temperature.
(7) Meanwhile prepare the M-FISH probe cocktail according to the intended area for hybridization e.g., 9 µl for an 18 × 18 mm^2 cover slip, 12 µl for a 22 × 22 mm^2 cover slip.
(8) Denature the probe by incubating at 75°C (±1°C) for 5 min on the prewarmed hot plate.
(9) Place on ice for 15 s.
(10) Incubate at 37 C (±1°C) for 30 min on the prewarmed hot plate.
(11) Once the slides have cooled to room temperature, place the slides in the Coplin jar containing 0.1× SSC at room temperature for 1 min.
(12) Denature slides in 0.07 N NaoH at room temperature for 1 min.
(13) Place slides into 0.1× SSC 4°C for 1 min.
(14) Place slides into 2× SSC 4°C for 1 min.
(15) Transfer to a Coplin jar with 70% ethanol for 1 min.
(16) Transfer to a Coplin jar with 95 and 100% ethanol and incubate for 1 min. Allow the slides to air dry.
(17) Pipette the denatured probe cocktail onto the denatured chromosome preparation and cover with the required sized coverslip prior to fluorescence imaging.
(18) Seal the coverslip to the slide using rubber cement.
(19) Incubate for 1–2 days in a humidified chamber at 37°C (±1°C).
(20) Following incubation, carefully remove the rubber cement and the cover slips.
(21) Place slides into the Coplin containing prewarmed (72°C (±1°C) 0.4× SSC for 2 min.
(22) Incubate slides into the Coplin containing 2× SSCT for 30 s.
(23) Briefly, wash with Milli-Q® water to avoid crystal formation and leave to dry in air at room temperature.
(24) Apply 20 µl of the DAPI/antifade and overlay with a 24 × 60 mm^2 cover slip and incubate for 10 min.
(25) Proceed with imaging and analysis. Store at –20°C for up to 2 weeks.

Calibrations Prior to FLIM Imaging

(1) Calibrate the motorized sample stage of the FLIM microscope to the epi-fluorescence microscope.
(2) To correlate chromosome images between two microscopes, use a reference glass slide "The England Finder" also known as graticules (Pyser-SGI Ltd.). The graticules is 3″ × 1″ in size, same as standard glass slides. This has a marked square grid at 1 mm intervals. Record approximately 20 x, y coordinates on the graticules using both microscopes. Generate a linear equation for both X and Y directions from the obtained coordinates and then apply the same linear equation to re-locate the chromosome spreads during the imaging with epifluorescence microscope and FLIM.
(3) This helps to locate the same chromosome spreads imaged from an inverted-multiphoton confocal to an upright-epifluorescence microscope.
(4) Measure the instrument response function (IRF) of the FLIM setup prior to any data acquisition. The reason for this is to check the excitation pulse profile of the instrument as well as correct for noise introduced into the system by for example radio-frequency pickup by the detector and electrical cables. Poorly shielded detectors may also be sources of noise. Where the noise cannot be completely eliminated, the IRF data can be used to deconvolute the noise from the data. The IRF peak should be sharp and narrow and depending on the laser pulse width and detector response, this should not be larger than the detector response if the laser width is narrower. Generally, photomultiplier tubes (PMTs) give a secondary peak in the IRF while hybrid detectors do not. It is therefore preferable to use hybrid detectors where possible. These are also less prone to damage by very high fluorescence intensities and photon count rates. Use crystals of either urea, potassium dihydrogen phosphate (KDP) or gold nanoparticles to determine the IRF when using multiphoton excitation. The NIR laser is tuned to 740–760 nm to excite the crystal followed by detection of a second harmonic signal. When using one photon excitation, a highly dilute solution of ludox may be used with the emission filters replaced by several ND filters to avoid too much laser power reaching the detector (See Section *FLIM Data Analysis* for software generated IRF modes). The use of multiphoton excitation also has several advantages over one photon excitation. For example, the use of NIR light that this less phototoxic to biological samples (in live cell experiments), reduced detector sensitivity in the red region, thus reducing background and reduced general autofluorescence. We found that the use of multiphoton excitation provided better time lifetime difference between the centromere and chromosome arm regions than using a standard 405 nm one photon excitation using light with more than 40 ps pulse-width. However, we did not investigate using 365 nm excitation where DAPI maximally absorbs. In our set up, we obtain 20 ps for a detector with a 25 ps response (Becker and Hickl HPM-100–06) or 110 ps for a detector with 110 ps response (Becker and Hickl HPM-100–40). A 3 mm BG39 band filter is used to remove the NIR laser light and transmit the fluorescence of the DAPI signal. Although photobleching does not generally affect excited state lifetime values, excessively high excitation average laser powers may lead to photo-induced fluorescent products. It is therefore best to determine any

bleaching effects and to avoid higher than necessary excitation average laser powers. We used 0.1–1.0 mW, 750 nm laser power at the sample.

(5) Calibrate the setup with known fluorophores such as 10–100 μM rhodamine B, 10–100 μM erythrosin B and 10 μM fluorescein, all prepared in water, Aliquot 50 μl of the required fluorophore solution on a round glass coverslip, thickness number –1 or 1.5 (VWR international). Place on the multiphoton confocal microscope stage and raster scan using NIR light, in the dark to avoid damage to the detector. Excited fluorescence signals are detected by a hybrid detector HPM 100–40. Lifetime value of the fluorophores, 1.65, 0.12 and 4.0 ns respectively were obtained. This is within 5% error of the standard literature value and in line with our daily calibration operation values.

(6) Once an instrument test and calibration are completed, locate and record the coordinates of the slide references on the epi-fluorescence microscope on which the chromosome images have been captured (see above, *Calibrations Prior to FLIM Imaging*, subsections 1 and 2).

FLIM Data Acquisition

(1) Prepare a slide with chromosomes, stained with 4 μM DAPI. Locate the x, y coordinates of the chromosomes using the epifluorescence microscope initially followed by the multiphoton FLIM microscope. Please note there are now FLIM instruments with combined epifluorescence attachment for chromosome identifications.

(2) Where the multiphoton microscope has a UV light (365–405 nm), it is easier to initially use a 405 nm excitation wavelength before multiphoton FLIM.

(3) Prior to multiphoton imaging mode, make sure the 405 nm laser is switched off. Due to chromatic aberration in our microscopes there is a need to adjust the focus for the 760 nm multiphoton excitation wavelength. Choose optimal excitation average power to avoid too much photobleaching of DAPI during multiphoton or confocal scanning.

(4) For TCSPC FLIM, we use the Becker and Hickl system although other systems are equally adequate such as the PicoQuant system. Using the Becker and Hickl data acquisition software SPCM (version 9.80, 64 bit), set out parameters such as number of cycles or image frames to accumulate and the pixels of the image, 512 × 512, to acquire a clear set of FLIM data (10–30 s) with each chromatid visible. Image pixel size of 128 × 128 to 2048 × 2048 may be acquired as well as lifetime decay resolution of 64–1024 (known as time bins). It is worth noting that low photon counts will determine the pixel resolution as well as the time resolution. Once the pixel number and time bins are selected, the acquisition may be operated in the scan-syn in mode where the data is stored on the TCSPC PC card, FiFo (file-in file-out) mode, where the data is stored as photon arrival time and x, y coordinates directly onto the PC memory (**Figure 1**).

FLIM Data Analysis

(1) To analyze the raw acquired data, the data file from the TCSPC is imported into the SPCImage software (version 6.4) for processing.

(2) During FLIM data acquisition, it is often difficult to or near impossible to acquire IRF that works well for every pixel in the image. SPCImage therefore offers several options to generate an IRF. The Becker and Hickl SPCImage software uses data from an area around the brightest spot in the image to calculate an IRF. When "Auto" has been set the IRF calculation is done automatically after loading data.

(3) In the SPCImage software, it is necessary to discard pixels with poor photon signal to noise ratio and by adjusting the threshold range between 25 and 35 or allowing the software to automatically determine this. Ideally pixel binning should be kept to a minimum between 1 and 3, depending upon intensity of the image. Higher binning values likely degrade the final FLIM image.

(4) In our case we chose "Incomplete Multiexponential" decay model as our fitting model to calculate accurate fluorescence lifetime of a fluorophore (under "Option-Model-Incomplete Multiexponential") due to our laser running at around 80 MHz (12.5 ns between laser pulses) and the lifetime of DAPI does not decay to the baseline before the next pulse.

(5) Chi-square (χ^2) is used to determine the goodness of the decay fitting. A chi-square value of unity indicates a perfect decay curve fitting that is desirable. Chi-square (>1.4) denotes presence of multiple fluorophore components and (<0.8) represents poor fit of the data point.

(6) Set appropriate "scatter" and "shift" values then run decay matrix (under "calculate-Decay Matrix"), for whole image to obtain the lifetime distribution of whole image. BH software converts intensity image to false-colored image to generate lifetime values at each pixel.

(7) It is also necessary to set a false-color range from "Minimum" and "Maximum" (opt continuous color mode), (under "Option-Color"). This generally "spreads" out the lifetime range (example in **Figure 2**).

(8) Following the analysis, pseudo colored histogram denotes range of short and long lifetime of a fluorophore stained to chromosomes. Here, we consider red representing shorter lifetime and blue representing longer lifetime.

(9) The median, minimum and maximum values of the lifetime values from the distribution curve may be taken to generate the range of lifetimes per chromosome and sub-region.

(10) At least three areas of a sample slide and at least three independent biological samples per chromosome preparation combination were analyzed, and the average of the ranges were taken.

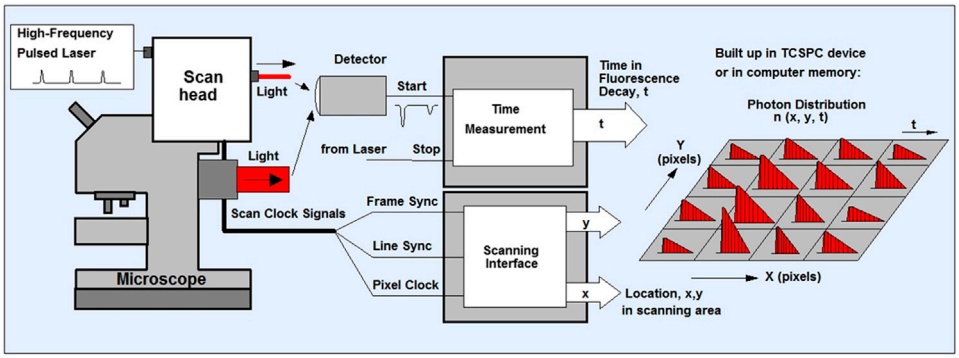

FIGURE 1 | Schematics of TCSPC- FLIM. The sample is scanned using a laser scanning microscope that has a focused beam of a high-repetition-rate pulsed laser ion. The system can either be one or multiphoton depending on the laser used. The TCSPC detector is attaches to either the confocal or non-descanned port of the microscope. The detector sends an electrical pulse into the TCSPC module upon detection of every photon. The TCSPC module i) determines the decay time (t) of the photon ii) receives scan clock signals (pixel, line and frame clock) from the scan controller of the microscope and also iii) is configured as a scanning interface with two counters X, Y, for the x and y location in the scanning area. With permission from: W. Becker, The bh TCSPC handbook. 8th edition (2019) available on www.becker-hickl.com Also see (Schoberer and Botchway, 2014; Suhling et al., 2019).

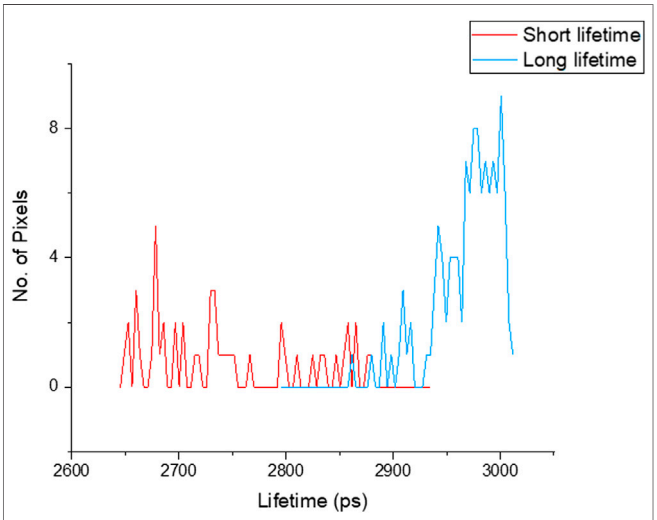

FIGURE 2 | Lifetime distribution of chromosomes measured from image **Figure 3**, showed shorter lifetime (red 2.76 ± 0.07 ns) and longer lifetime (blue 2.95 ± 0.04 ns) values of DAPI stained chromosomes.

(11) Here, FLIM measurement of the chromosome sample indicates that chromosome 1, 9, 15, 16 have a shorter lifetime at the heterochromatin regions compared to the rest of the chromosomes (**Figures 3–5**).

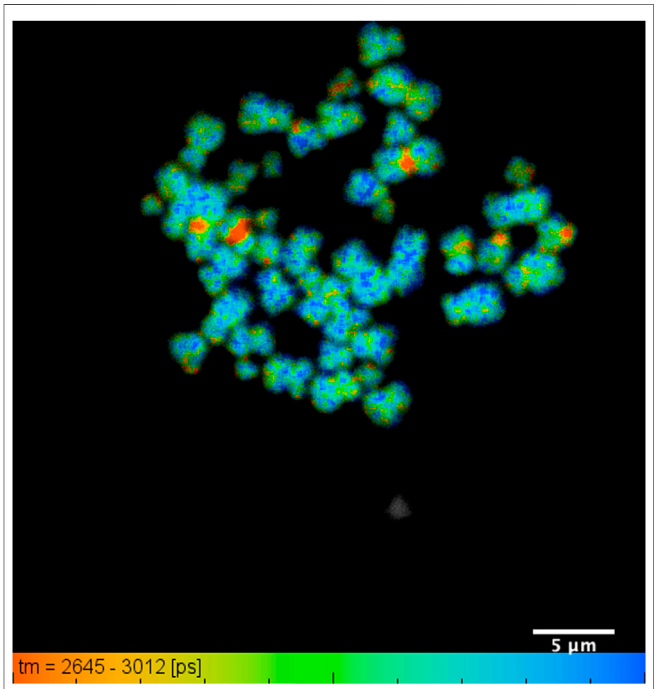

FIGURE 3 | DAPI lifetime map of a typical chromosome spread with all 46 human chromosomes identified: showing lifetime change along the length of an individual chromosome, obtained from human T-lymphocytes. The lifetime values range from 2.76 ± 0.07 ns to 2.95 ± 0.04 ns within a field of view of 35 µm and scale bar of 5 µm.

NOTES

(1) To remove unbound DAPI rinsed with milli Q water.
(2) Prepared slides were first observed under fluorescence microscope (Zeiss Z2 Axio imager with Isis software) for quality assurance of chromosome spreads then transferred to the FLIM imaging.
(3) A 10× objectives was used to locate the chromosomes and observed the quality of the prepared chromosome spreads. A 60× (water immersion) or 63× objective (with immersion oil) was used to visualize the DAPI stained chromosomes at high resolution.
(4) Store the probe away from the light during the process of denaturation.
(5) Once M-FISH cocktail is prehybridized, spin briefly to obtain probe cocktail.

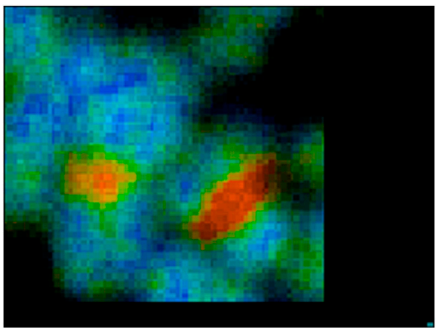

FIGURE 4 | Zoomed image of chromosome 1 and 9 from image **Figure 3**.

(6) The fluorescence decay function (f) at time, t, is obtained from the intensities data to obtain the excited state lifetime (τ) exponential decay as follows:

- a homogeneous population of molecules in the same environment giving a single exponential.
- $f(t) = e^{-t/\tau}$
- The equation for triple exponential is: $f(t) = ae^{-t/\tau 1} + be^{-t/\tau 2}$
- That for a triple exponential is: $f(t) = ae^{-t/\tau 1} + be^{-t/\tau 2} + ce^{-t/\tau 3}$

the amplitudes of the exponential components, a, b and c define the contributions to each lifetime (example in **Figure 6**).

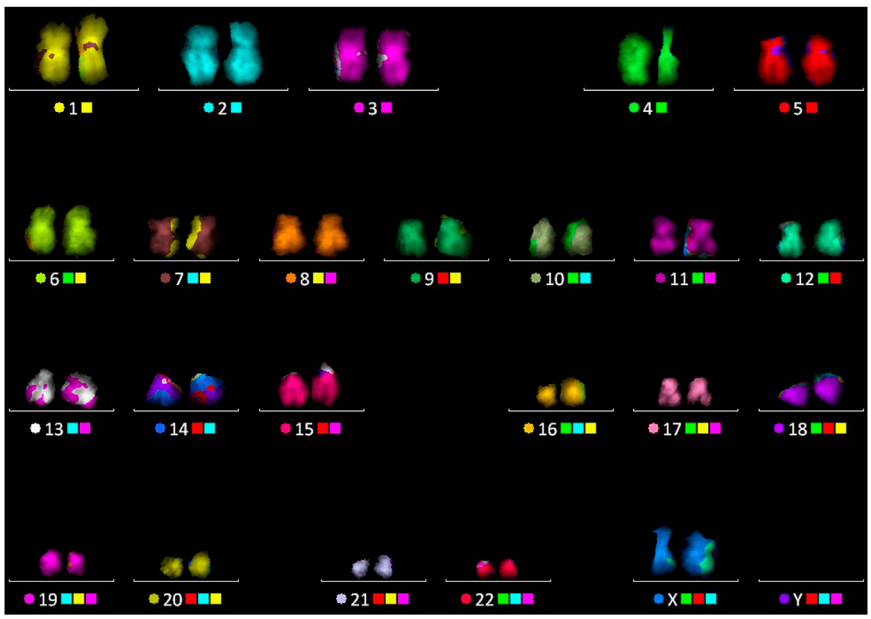

FIGURE 5 | Multicolor FISH performed on the chromosome spread, after the FLIM imaging, followed by karyotype as shown in image.

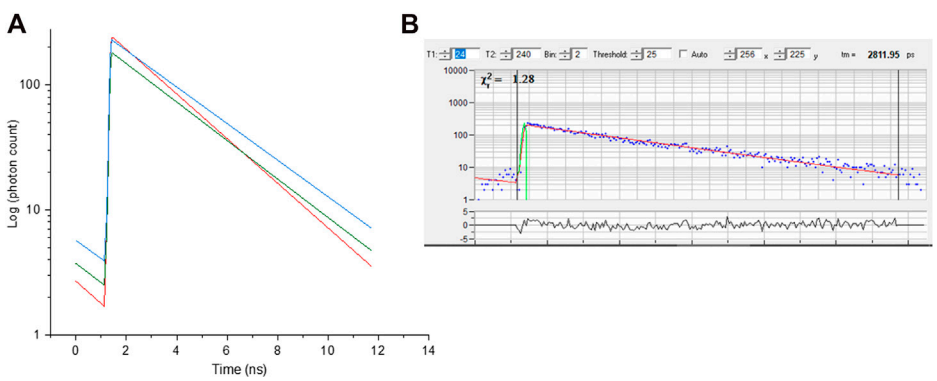

FIGURE 6 | (A) Fluorescence decay curve obtained from selected pixel of red, green and blue regions of chromosome 9 from image **Figure 3**. **(B)**- representative raw decay data with a single exponential fitting.

DATA AVAILABILITY STATEMENT

The raw data supporting the conclusions of this article will be made available by the authors, without undue reservation.

AUTHOR CONTRIBUTIONS

SB, IR, and MY conceived the idea. AB carried out the experiments with help from MY and SB. AB and SB analyzed the FLIM data with help from SB. AB analyzed the MFISH data with the help of MY. All authors were involved in writing and had final approval of the manuscript.

FUNDING

We acknowledge funding in the Research Complex at Harwell from a BBSRC Professorial Fellowship "Diamond Professorial Fellowship for imaging chromosomes by coherent X-ray diffraction." AB is grateful to EPSRC for a studentship supported by the UCL Molecular Modelling and Materials Science Centre for Doctoral Training with co-sponsorship from the ERC Advanced Grant 227711. Access to the STFC Central Laser Facility Octopus Imaging is also acknowledge.

ACKNOWLEDGMENTS

The authors are grateful to Ken Raj of Public Health England for providing T-cells. MY would also like to acknowledge the ongoing support of Professor El-Nasir MA Lalani of the Centre for Regenerative Medicine and Stem Cell Research at the Aga Khan University, the Aga Khan University.

REFERENCES

Ahmed, A. R., Owens, R. J., Stubbs, C. D., Parker, A. W., Hitchman, R., Yadav, R. B., et al. (2019). Direct imaging of the recruitment and phosphorylation of S6K1 in the mTORC1 pathway in living cells. *Sci. Rep.* 9 (1), 3408–3414. doi:10.1038/s41598-019-39410-z

Ahmed, A., Schoberer, J., Cooke, E., and Botchway, S. W. (2020). "Multicolor FRET-FLIM microscopy to analyze multiprotein interactions in live cells," in *Methods in molecular biology*. Editor A. Poterszman 2247th Edn. (New York, NY: Humana Press), 287–301. doi:10.1007/978-1-0716-1126-5_16

Anthony, N., Guo, P., and Berland, K. (2009). "Principles of fluorescence for quantitative fluorescence microscopy," in *FLIM microscopy in biology and medicine*. Editors A. Periasamy and R. M. Clegg 1st edn. (New York, NY: Taylor & Francis Group, LLC), 35–59. doi:10.1201/9781420078916

Botchway, S. W., Scherer, K. M., Hook, S., Stubbs, C. D., Weston, E., Bisby, R. H., et al. (2015). A series of flexible design adaptations to the Nikon E-C1 and E-C2 confocal microscope systems for UV, multiphoton and FLIM imaging. *J. Microsc.* 258 (1), 68–78. doi:10.1111/jmi.12218

Breeze, E., Dzimitrowicz, N., Kriechbaumer, V., Brooks, R., Botchway, S. W., Brady, P., et al. (2016). C-terminal amphipathic helix is necessary for the *in vivo* tubule-shaping function of a plant reticulon. *Proc. Natl. Acad. Sci.* 113 (39), 10902–10907. doi:10.1073/pnas.1605434113

Danquah, J. O., Botchway, S., Jeshtadi, A., and King, L. A. (2012). Direct interaction of baculovirus capsid proteins VP39 and EXON0 with kinesin-1 in insect cells determined by fluorescence resonance energy transfer-fluorescence lifetime imaging microscopy. *J. Virol.* 86 (2), 844–853. doi:10.1128/JVI.06109-11

Estandarte, A. K., Botchway, S., Lynch, C., Yusuf, M., and Robinson, I. (2016). The use of DAPI fluorescence lifetime imaging for investigating chromatin condensation in human chromosomes. *Sci. Rep.* 6 (31417), 31417–31512. doi:10.1038/srep31417

Jalal, S. M., and Law, M. E. (1999). Utility of multicolor fluorescent *in situ* hybridization in clinical cytogenetics. *Genet. Med.* 1 (5), 181–186. doi:10.1097/00125817-199907000-00003

Lakowicz, J. R. (2006). *Principles of fluorescence spectroscopy*. 3rd Edn. Philadelphia, NY: Springer US. doi:10.1007/978-0-387-46312-4

Liehr, T. (2017). "Classical cytogenetics" is not equal to "banding cytogenetics". *Mol. Cytogenet.* 10 (3), 1–3. doi:10.1186/s13039-017-0305-9

Schoberer, J., and Botchway, S. W. (2014). "Investigating protein-protein interactions in the plant endomembrane system using multiphoton-induced FRET-FLIM," in *Methods in molecular biology*. Editor M. S. Otegui 1209th Edn. (New York, NY: Humana Press), 1209, 81–95. doi:10.1007/978-1-4939-1420-3_6

Shemilt, L., Verbanis, E., Schwenke, J., Estandarte, A. K., Xiong, G., Harder, R., et al. (2015). Karyotyping human chromosomes by optical and X-ray ptychography methods. *Biophys. J.* 108 (3), 706–713. doi:10.1016/j.bpj.2014.11.3456

Speicher, M. R., Gwyn Ballard, S., and Ward, D. C. (1996). Karyotyping human chromosomes by combinatorial multi-fluor FISH. *Nat. Genet.* 12, 368–375. doi:10.1038/ng0496-368

Suhling, K., Hirvonen, L. M., Becker, W., Smietana, S., Netz, H., Milnes, J., et al. (2019). "Wide-field time-correlated single photon counting-based fluorescence lifetime imaging microscopy," in *Nuclear instruments and methods in physics research, section A: accelerators, spectrometers, detectors and associated equipment*. (Amsterdam, Netherlands: Elsevier Ltd.), Vol. 942, 162365. doi:10.1016/j.nima.2019.162365

Sumner, A. T. (1982). The nature and mechanisms of chromosome banding. *Cancer Genet. Cytogenet.* 6 (1), 59–87. doi:10.1016/0165-4608(82)90022-X

Yusuf, M., Bauer, D. L., Lipinski, D. M., MacLaren, R. E., Wade-Martins, R., Mir, K. U., et al. (2011). Combining M-FISH and quantum dot technology for fast chromosomal assignment of transgenic insertions. *BMC Biotechnol.* 11 (121), 121–210. doi:10.1186/1472-6750-11-121

Yusuf, M., Leung, K., Morris, K. J., and Volpi, E. V. (2013). Comprehensive cytogenomic profile of the *in vitro* neuronal model SH-SY5Y. *Neurogenetics* 14 (1), 63–70. doi:10.1007/s10048-012-0350-9

Conflict of Interest: The authors declare that the research was conducted in the absence of any commercial or financial relationships that could be construed as a potential conflict of interest.

Advantages of publishing in Frontiers

OPEN ACCESS
Articles are free to read for greatest visibility and readership

FAST PUBLICATION
Around 90 days from submission to decision

HIGH QUALITY PEER-REVIEW
Rigorous, collaborative, and constructive peer-review

TRANSPARENT PEER-REVIEW
Editors and reviewers acknowledged by name on published articles

Frontiers
Avenue du Tribunal-Fédéral 34
1005 Lausanne | Switzerland

Visit us: www.frontiersin.org
Contact us: frontiersin.org/about/contact

REPRODUCIBILITY OF RESEARCH
Support open data and methods to enhance research reproducibility

DIGITAL PUBLISHING
Articles designed for optimal readership across devices

FOLLOW US
@frontiersin

IMPACT METRICS
Advanced article metrics track visibility across digital media

EXTENSIVE PROMOTION
Marketing and promotion of impactful research

LOOP RESEARCH NETWORK
Our network increases your article's readership